

**TYPE-II BEHAVIOR OF
CERAMIC SUPERCONDUCTORS - GRANULARITY,
IRREVERSIBILITY AND HYSTERESIS**

THESIS

*Submitted in partial fulfillment
of the requirements for the degree of*
DOCTOR OF PHILOSOPHY

By

SUBIR SAHA

Under the supervision of

DR. B.K. DAS

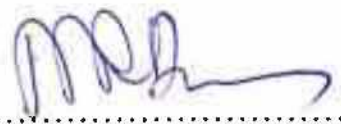
**BIRLA INSTITUTE OF TECHNOLOGY AND SCIENCE
PILANI (RAJASTHAN) INDIA**

1993

BIRLA INSTITUTE OF TECHNOLOGY & SCIENCE
PILANI RAJASTHAN

CERTIFICATE

This is to certify that the thesis entitled " **Type-II Behavior of Ceramic Superconductors - Granularity, Irreversibility and Hysteresis** " and submitted by **Subir Saha**, ID No. *90PZYF008* for award of Ph.D. Degree of the Institute, embodies original work done by him under my supervision.

Signature of the Supervisor

Name - **DR. B. K. DAS**

Date : 18/12/93

Designation : Scientist-'F'

-: ACKNOWLEDGEMENTS :-

The author takes pleasure to express a deep sense of gratitude and his indebtedness to Dr. B.K. Das, *Scientist-F, National Physical Laboratory, New Delhi* under whose able supervision the present work has been carried out. The author also gratefully acknowledges the liberty and constant encouragement that has been offered by Dr. Das throughout the period of this work. It is his liberal view that made it possible to undertake the kind of study and his able guidance that paved the way forward. In the early stages of instrumentation, he was always available with his clear notions and best suggestions. His patience and logical approach, in the course of the numerical modelling proved to be a boon.

Encouragement of Prof. E.S.R. Gopal, *Director, National Physical Laboratory, New Delhi* inspired the author to overcome the difficulties during his tenure. The author gratefully acknowledges his wise advice.

The author would like to acknowledge Prof. A.K. Roychowdhury, *Saha Institute of Nuclear Physics, Salt Lake, Calcutta*, whose lecture inspired him to start the kind of research.

The best possible suggestions offered by Dr. R.B. Tripathi, *Scientist-EI, National Physical Laboratory, New Delhi*, during the course of this work are also worth acknowledgement.

The author finds it important to acknowledge the valuable suggestions that Dr. R.B. Bhattacharya, *Scientist-EII*, Dr. A.C. Rastogi *Scientist-EII*, and Dr. S.N. Singh, *Scientist-EII, National Physical Laboratory, New Delhi* offered to him at various times.

Dr. P.K. Singh, *Scientist-C*, deserves a special mention for his help in numerical calculations is being acknowledged sincerely.

The friendly behaviour and active suggestions of Dr. S.T. Lakshmikumar, *Scientist-EI* were always available. It is a pleasure for the author to acknowledge Dr. Lakshmikumar for his constant inspiration and the invaluable teaching in the course work.

A special mention is due for Mrs. Kiran Jain, *Scientist-C*, who offered her best possible assistance. Discussion with her was also helpful for the author. Thanks are due to Dr. G.K. Padam, *R.A.*, for her friendly cooperations.

Dr. S.N. Ekbote, *Scientist-EI* and Dr. Pushpa Upadhyay, *Scientist-B* deserve very special thanks for many useful discussions which helped the author in improving his understanding of the subject.

Acknowledgements are due to Mr. Mukul Sharma of *Materials Division* who offered best of his knowledge and active help in designing and improvising all the experimental setups throughout this work. His friendship was a constant source of inspiration to the author.

Mr. B.S. Khurana, *Technical officer*, who offered the author timely assistance needs to be

mentioned along with Mr. R.C. Goel, *Technical officer*, Mr. S.K. Sharda, *Technical officer* and all other staff members in the group.

The author would fail in his duty if he does not acknowledge Dr. P. Banerjee, *Scientist-EII*, Dr. A. Sengupta, *Scientist-EI*, Dr. A.K. Hanjura, *Scientist-EI*, and others of the Time and Frequency Standard who allowed their computer and laser printer at the author's disposal, which made it possible the state of the art publication of the thesis.

The helpful attitude of the staff in Central Computer Facility, especially of Mr. Sanjay Raizada needs to be mentioned.

Thanks are due to all the research fellows specially to Mr. Sandeep Dhara, Mr. Pavas Asthana, Mr. R.N. Sharma, Miss. I. Dhingra and Mr. N. Deepak Kumar. The author is grateful to Mr. Pavas and Mr. Deepak for their help in editing.

Finally, the author would like to thank all of those who were involved directly or indirectly in the work and worth a mention.

-: ABSTRACT :-

TYPE-II BEHAVIOR OF CERAMIC SUPERCONDUCTORS - GRANULARITY, IRREVERSIBILITY AND HYSTERESIS

SUBIR SAHA

Assuming that the ceramic bulk contains two distinct components viz., the grains with a high critical current density(J_{c1}) and the grain boundaries(GB) with poor critical current density(J_{c2}), a two component critical state model appropriate to the ceramic bulk was solved numerically. The model can accommodate for two different grain and bulk shapes, slab and cylindrical and different type of $J_{c1}(H)$ and $J_{c2}(H)$ (viz., Bean, Kim or exponential type of $J_c(H)$) could be selected for the GB and the grain. For the first time, the model explained the low field anomalous M-H loops of the ceramic bulk. It was seen that a close to Bean type $J_{c1}(H)$ of the grains and Kim type $J_{c2}(H)$ for the GB gave best qualitative agreement with experimental loops. It also could explain the problem of calculating magnetic J_c from the M-H loops on the basis standard formula. The model being a two component one, was not range specific. The loops for higher field range were also calculated and gave good agreement to the actual data. It brought out the right evolution of the M-H loops over the field range variations. The grain size dependence of the M-H loops, as studied in this model gave good agreement to already published data. It was also seen, that an addition of a phenomenological correction due to shielding current could produce the Z-shaped M-H loops.

The model was further extended to calculate AC susceptibility and the $\chi'(H)$ and $\chi''(H)$ were studied in detail. The model, for the first time was able to show that even in the premise of conventional critical state model, the $\chi''(H)$ loops could show hysteresis depending on the amplitude and J_{c0} parameters. The consideration of demagnetization correction due to grain as well as the bulk, made the model a realistic one. The $\chi'(H)$ and $\chi''(H)$ loops were generated for different field ranges with demagnetization factors of 0.3 and 1.0 for the bulk and the grain respectively. For the first time, the hysteresis in both $\chi'(H)$ and $\chi''(H)$ loops were seen in these calculation for different amplitudes and different J_{c0} parameters. The excellent qualitative agreement of the $\chi'(H)$ loops with the experimental data was encouraging. For the $\chi''(H)$ loops, though the features were similar to the experimental loops, the extra large hysteresis of the experimental loops was not seen in the theoretical curves. Once again the model was tested for different field ranges and was seen to be continuous.

The model was then extended for studying the χ' and $\chi''(H)$ as a function of AC amplitude for different constant DC bias field. In zero bias, the model correctly yielded two peaks on the $\chi''(H_{DC})$ curves - the peak at lower amplitude was due to the GB contribution and other one due to the grain contribution. The agreement of this $\chi'(H_{DC})$ and $\chi''(H_{DC})$ with experimental data of others was remarkable. At a non-zero bias a third peak was seen to appear on the $\chi''(H_{DC})$ curves and was in agreement to already published experimental data of others.

The model was also used for harmonic generations and hysteresis in higher harmonics with respect to DC bias field was justified.

In an effort to consider different "non-critical" (flux creep, flux flow etc.) contributions a phenomenological approach was followed. The effect of the non-critical" contributions was considered indirectly through modifying the J_{c1} or J_{c2} . The results of this calculations was important for explanation of the frequency

dependence of the $\chi'(H)$ and $\chi''(H)$ loops.

In order to justify the results of the model calculation on the $\chi'(H)$ and $\chi''(H)$ similar experiments were carried out for different DC bias ranges, amplitudes and frequencies of the AC field, two different field configuration of the fields and for different samples (i.e., different J_{\parallel} and J_{\perp} parameters). The experimental results were justified in light with the model calculations. In coaxial case, the low field $\chi'(H)$ and $\chi''(H)$ loops were in good agreement with the calculated loops. Below certain DC field range there was no hysteresis seen in the $\chi'(H)$ and $\chi''(H)$ loops. The study on the $\chi'(H)$ and $\chi''(H)$ loops for different AC amplitude could be explained qualitatively within the model. The study on frequency dependence of the $\chi'(H)$ loops were also carried out.

The high field $\chi'(H)$ and $\chi''(H)$ loops in the case when the AC and the DC fields were mutually perpendicular, were tested for all the features in light with the model which was in fact for the co-axial case. This implied that so long the amplitude was low one could consider the AC field as an probe and hence the $\chi'(H)$ and $\chi''(H)$ loops in both field configurations would be similar. The high field loops were compared for different bulk sizes, amplitudes and frequencies of AC field. All the results could be explained qualitatively in the premise of the model calculations.

Response of the samples in an alternating current were also carried out through study of FFT of voltage signal, AC I-V for different frequencies and irreversibility of magneto-resistance.

-: CONTENT :-

1. CHAPTER 1 :	INTRODUCTION	1
2. CHAPTER 2 :	EXPERIMENTAL TECHNIQUES	38
3. CHAPTER 3 :	MODEL CALCULATIONS	67
PART A :	A TWO COMPONENT CRITICAL STATE MODEL APPROPRIATE TO THE GRANULAR SUPERCONDUCTORS	67
PART B :	EXTENSION OF THE CRITICAL STATE MODEL.	97
4. CHAPTER 4 :	EXPERIMENTAL DATA	164
PART A :	STUDIES ON THE RESPONSE OF THE HIGH TEMPERATURE SUPERCONDUCTORS IN ALTERNATING CURRENTS	164
PART B :	HYSTERESIS IN COMPLEX AC SUSCEPTIBILITY WHEN THE AC AND DC FIELDS ARE COAXIAL	196
PART C :	HYSTERESIS IN COMPLEX AC SUSCEPTIBILITY WITH MUTUALLY PERPENDICULAR AC AND DC FIELDS	244
PART D :	A CLOSER LOOK INTO THE FREQUENCY DEPENDENCE	279
5.	: CONCLUSIONS	285

INTRODUCTION

This chapter starts with a brief history of superconductivity. Next, different terms and parameters of importance have been defined in a semi-quantitative way. High temperature superconductor has been introduced in continuation with the conventional one. As a background for this work different experimental results of high temperature superconductors have been described briefly.

1.1.	HISTORY - THE JOURNEY FROM 1911 TO....	1
1.2.	MAGNETIC PROPERTIES OF SUPERCONDUCTORS	6
1.2.1.	PERFECT CONDUCTORS VS. SUPERCONDUCTORS	6
1.2.2.	TYPE-I AND TYPE-II SUPERCONDUCTORS	6
1.2.3.	LONDON EQUATION AND TYPE-I SUPERCONDUCTORS	7
1.2.4.	GINZBURG-LANDAU FORMALISM	9
1.2.5.	THE EFFECT OF THE TWO LENGTH PARAMETERS	12
1.2.6.	FURTHER IMPORTANCE OF NEGATIVE SURFACE ENERGY...	13
1.2.7.	IRREVERSIBLE MAGNETIC BEHAVIOR	17
1.3.	HIGH TEMPERATURE SUPERCONDUCTORS AND SUPERCONDUCTIVITY	22
1.3.1.	INTRODUCTION	22
1.3.2.	MACROSCOPIC MAGNETIC PROPERTIES	23
	A. DC MAGNETIZATION MEASUREMENTS	24
	B. AC SUSCEPTIBILITY	28
1.3.3.	RESISTIVITY VS. TEMPERATURE AND FIELD	29
1.3.4.	MAGNETIC DECORATION OF FLUX LINE LATTICE	29
1.3.5.	SUMMING UP THE PICTURE	29
1.4.	THE AIM AND THE SCOPE OF THE WORK	32
	REFERENCE	35

1.1. HISTORY - THE JOURNEY FROM 1911 TO

It is almost 83 years since Kamerling Onnes discovered the phenomenon of superconductivity in mercury. Immediately he conceived the idea of making an electromagnet for large magnetic field having no loss. However, he failed as even at a few hundred orested of magnetic field superconductivity of mercury got destroyed. The field as we now understand is the critical field (H_c). At the same time it became known that there is a critical current density, J_c , above which mercury loses its superconductivity. Silsbee(1916) immediately recognized that the two effects have the same origin.

The loss of resistance in superconductors below T_c stole the lime light and until 1933 the physics of superconductivity had the same bearings as of a perfect conductor. But in that year Meissner and Ochsenfeld discovered the so called Meissner effect which made the distinction between a perfect conductor and a superconductor and which Hübener[1] described as, "perhaps more fundamental aspect" than vanishing of resistance. Instead of $E=0$ in perfect conductors, superconductors are to be characterized by both $E=0$ and $B=0$. Paramount possibility of technological utility with the vanishing resistance initiated a search for materials with higher and higher T_c , J_c and H_c . At the same time physicists got busy in discovering the laws of the mother nature behind the phenomenon of superconductivity.

The search for a material with higher J_c and H_c led to some alloys which sustained superconductivity even at a field \approx 1-2 Tesla. Mendelssohn and Moore(1935) found that these alloys did not show complete Meissner effect and showed hysteretic behavior in magnetic field. They proposed the "sponge" model which until late fifties was the only explanation for this high field behavior.

As it happens in most fields of physics, the experimentalist and the technologists were one step ahead and they succeeded and in 1941 came the NbN, the first high field superconductor[8] with $T_c=15$ K and $H_c=15$ T. But the physics was still unknown. Then in a row new materials with better parameters started to be available.

It was only in 1957 that the BCS theory and Abrikosov's theory came into picture. While the BCS opened the new horizon of understanding of the superconductivity from a microscopic view, the Abrikosov's theory introduced a new dimension in our understanding. While the BCS

pioneered the electron pairing through virtual phonon exchange which brought them the first Nobel prize in superconductivity. Abrikosov proposed the surface energy between the normal and superconducting region to have positive or negative values. Abrikosov's work led to the classification of superconductors into two classes; Type-I, with positive surface energy and Type-II, with negative surface energy. It immediately became clear that alloys and some others which showed incomplete Meissner effect and had quite higher critical field belonged to the Type-II. As it is now known that the technologically important superconductors are the Type-II. With the recognition of Type-II superconductors the magnetic properties of superconductivity got serious attention. The essence of negative surface energy is that it favours the presence of magnetic field inside the bulk. More over the entered flux was required to be divided in to smallest "flux quanta" which are now known as flux lines. Abrikosov solved the Ginzburg-Landau equation for limiting values of field and showed that a triangular "flux line lattice" is a favourable configuration for the penetrated flux inside the bulk. In case of Type-I, entry of flux is not favourable. However for irregular shaped samples with large demagnetizing factor "intermediate state" may persists. In both cases flux line seen to be quantised with $\phi = h/2e = 2.07 \times 10^{-15}$ webers.

With the introduction of flux lines(FL) and so called flux line lattice(FLL), the interaction of flux lines assumed central attraction both in Type-I and Type-II. It became clear that the transport properties of Type-II superconductors are very much dependent on the interaction of the FLL with different parameters. The motion of FLL is dissipative and flux line have to be "pinned" for a superconductor to have high J_c [1-7]. In this context the understanding of "pinning mechanism" becomes most important. The presence of a pinned FLL, as one can visualize, must introduce irreversibility or hysteresis in magnetic behavior. In this context came the phenomenological models to help our understanding and to have better knowledge on material parameters which affect the superconducting properties. In 1964 C.P Bean[10] proposed his "critical state" model, which succeeded in deriving the theoretical MH loops of Type-II in close agreement with the experimental result. Particularly, the complexity in formulating microscopic theories for "pinning mechanism" has led more and more people to study using critical state model. It also offers scope for study of AC response and harmonics generation.

In the mean time, more materials with higher and higher T_c , J_c and H_c were added to the

list of superconducting materials and the industrial application started for high magnetic field usages. In 1973 came the Nb₃Ge with T_c = 23.2 K, H_{c2} = 38 T and J_c(4.2 K) 10⁴ Amp/cm². But here the quest for higher T_c seemed to saturate. BCS theory put the upper limit of T_c through the relation[3],

$$T_c = 1.14h\omega_D e^{(-1/N(0)V)}.$$

Assuming a limiting values of the parameters maximum T_c comes out to be 20 to 40 K.

Certain draw backs, present in the famous BCS theory viz., the absence of direct experimental evidence of phonon mediated pairing of electron as proposed in this theory made some people not to be serious about the BCS predicted limit of T_c and the search for higher and higher T_c continued. Ultimately came the success in the January of 1986, after 13 years of discovery of the Nb₃Ge. Bednorze and Müller[9] discovered the "new generation" superconductors, the La_{2-x}Sr_xCuO₄ with T_c ≈ 30 K which brought them a Nobel prize, the second one in superconductivity. The material is ceramic and structurally known as oxygen deficient perovskites. Within few months C.W. (Paul) Chu[11] discovered YBa₂Cu₃O_{7-x}(1987), with a critical temperature T_c 90 K, which is also a oxygen deficient perovskites. The physics community saw the biggest euphoria of the last few decades with all pervading activities in every branch of physical science. Obviously YBa₂Cu₃O_{7-x} having its T_c higher than the liquid nitrogen became the most popular and extensively studied. In fact this discovery made study of superconductivity possible at almost every university and research institute. The result is an enormous amount of study in a very short period of time rendering it almost impossible to keep track of what is happening. Immediately it become clear that YBa₂Cu₃O_{7-x} is a type-II system with unexpectedly high H_{c2} (a few hundred teslas) and J_c at 77 K for the thin film or single crystal > 10⁵ Amp/cm². With the euphoria of higher T_c and H_c came the despair that the critical current density, J_c of the bulk poly-crystalline was ≈ 1000 Amp/cm². A closer look at this problem initiated more fundamental work regarding the flux dynamics and pinning mechanism.

After YBa₂Cu₃O_{7-x}, other two major systems have been reported in quick succession - the Bismuth[12, 13] (Bi-Sr-Ca-CuO)(1988) and the Thallium[14, 15] (Tl-Ba-Ca-Cu-O)(1988). Till

the date of this writing, the Mercury (Hg-Ba-Ca-Cu)(1993)[16] system has been reported with the highest T_c of 140 K. All are copper oxide based and have structures related to the same oxygen deficient perovskites structure as $YBa_2Cu_3O_{7-x}$. While the T_c jumped to 140 K in Mercury and to 125 K in Thallium system, technological problem remains the same. Once Barnard Shaw commented in his famous welcome message to Einstein " ... science never solves a problem without creating ten other problems.", finds it justification. As the newer and newer superconductors add to the list, physics becomes more and more complicated with new physical phenomena which were never seen in conventional superconductors. Having T_c higher, it is now possible to see flux lines at a higher ambient temperature than before. This factor alone, probably, has made it possible to see a lot of interesting flux related phenomena,[17-19] viz., thermally activated flux flow, giant flux jumps, irreversibility line, large relaxation effect. But for theoretician problems is more sever.

As BCS can not explain this much high T_c , newer pairing mechanism has to be invoked. Theories started to pour in considering all possible pair mechanisms along with modification in BCS line. As Sir Nevil Mott[24] wrote in Nature, " ..there are as many theories of this superconductors as theorists." But the problems remains, leaving a scope for perhaps the third Nobel in superconductivity. Starting from its birth the subject never has been understood in full length. It has always been burdened with new discoveries which put forth serious confusion on the proposed theories.

In the theoretical front, Anderson and his school tried to establish the famous RVB[20] (resonance valence bond) where charge and spin were seen to be separated creating "holon"s and "spinon"s. In other front, the BCS like school tried all possible exchange interactions through which electrons may form a pair[25]. Obviously none stood the test of time. Whatever the theory, it is now beyond doubt that the copper oxygen planes and chains are the main point of interest.

The huge funding in last 6-7 years in this field has its demand for direct technological use of this superconductors. But here lies the saga of despair. As conceived by most of the "pundits", the bulk usages of the superconductors are going to be case where they require substantial critical current density, J_c . The plus point about the high temperature superconductors is that the refrigeration cost is quite less since liquid nitrogen is cheaper than helium, cost benefit

for refrigeration is by a factor of 20 to 30. But it is an apparent benefit only. As one can imagine the penalty for fabricating this fragile and brittle material into a superconducting coil which can withstand tremendous force of magnetic field that we are expecting, will, by no means, suppress the cost benefit of the cheap coolant, because the refrigeration cost for such bulk use is only around 10% of the total cost. Another important point, more serious, is that can we really use liquid nitrogen for a optimum performance? The answer up to this time is probably no. For an optimum performance working temperature should be half way below T_c which, even for the Thallium system with T_c around 125 K, is lower than the liquid nitrogen temperature. So the commercial feasibility for high current application of high temperature superconductors is a matter of future technology only.

In the mean time endeavor will continue in the field of our understanding the complexity of this new class of superconductors. The work in this thesis is in that line.

1.2. MAGNETIC PROPERTIES OF SUPERCONDUCTORS:

1.2.1 Perfect-conductors vs. Superconductors:

Magnetic properties of superconductors are more fundamental than their electrical properties. In fact magnetic properties distinguish a superconductor from a "perfect conductor" leading to exact definition of superconductivity. A superconductor, as we now understand, must exhibit both flux exclusion and expulsion unlike a "perfect conductor" which is capable only of flux expulsion not exclusion(Fig. 1.1.1a,b).

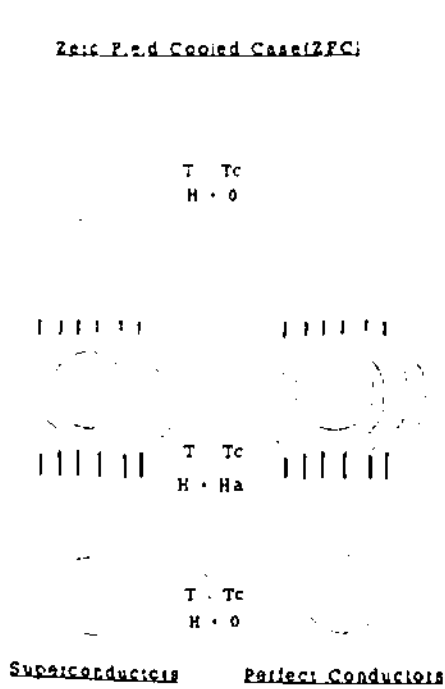


Figure 1.1.1A: Flux expulsion - no difference between perfect-conductors and superconductors.

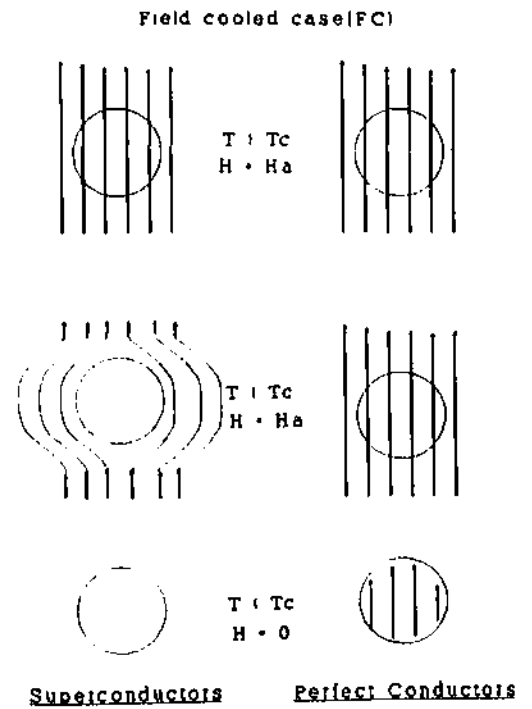


Figure 1.1.1B: Flux exclusion - differentiating perfect-conductors and superconductors.

1.2.2. Type-I and Type-II Superconductors:

Depending upon the magnetic properties, superconductors can be divided into two distinct types, viz., Type-I and Type-II. In Fig. 1.1.2 the M-H curves for the two type has been given. In type-I if the magnetic field is below a certain upper value called the critical field, (H_c), the total field is excluded leading to its diamagnetic susceptibility, $\chi = -1$ i.e., perfect diamagnetism(Fig. 1.1.2). Magnetic field above this critical field destroys the superconductivity of the Type-I materials. But in the other type there are two critical field, viz., lower(H_{c1}) and

upper(H_{c2}) critical fields. Below the lower critical field Type-II shows same behavior as that of a Type-I. However at a field higher than H_{c1} magnetic field starts penetrating inside the bulk leading to partial Meissner effect. This state continues upto the upper critical field H_{c2} and is known as mixed or vortex state. Above the upper critical field superconductivity of type-II vanishes (Fig.1.1.2). The magnetic behavior of the Type-II superconductors is most important from technological point of view.

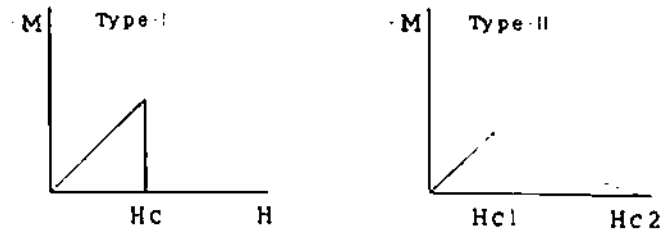


Figure 1.1.2: M-H curves showing type-I and type-II.

1.2.3. LONDON EQUATION AND TYPE-I SUPERCONDUCTIVITY:

A. Penetration depth:

As have been discussed above, due to Meissner-Ocshenfeld effect any external field subjected to superconductor will be rejected i.e., a surface current will be establish which will cancel the external field on point to point basis. Obviously surface current will require a finite depth of the surface to exist. This depth through which magnetic field will reduce to zero is known as penetration depth.

Starting from the electrodynamics of perfect conductors F. and H. London derived;

$$\chi_L^2 \bar{\nabla} \times \bar{\nabla} \times \vec{h} + \vec{h} = 0 \quad (1.1.1)$$

where,

$$\lambda_L = \sqrt{\frac{m}{\mu_0 n_s e^2}} = \text{London penetration depth}, \quad (1.1.2)$$

n_s is the number density of super-electron and h is the microscopic magnetic field others parameters are same as in conventional electrodynamics. Solving the eqn. (1.1.1) in one dimension one can get,

$$\dot{h}(x) = \dot{h}(0)\exp\left(\frac{-x}{\lambda_L}\right) \quad (1.1.3)$$

which implies that well inside a perfect conductor time variation of h will be zero, i.e., h will be constant indicating the basic properties of perfect conductors.

In superconductors well inside the bulk not only time variation of h is constant but also that the constant be zero which is minimum requirement for Meissner-Ochsenfeld effect. With this view in mind F. and H. London removed the time dependence from eqn. (1.1.1) to get the London equation for superconductors;

$$\lambda_L^2 \nabla \times \nabla \times \bar{h} + \bar{h} = 0 \quad (1.1.4)$$

yielding the solution,

$$h(x) = h(0)\exp\left(\frac{-x}{\lambda_L}\right) \quad (1.1.5)$$

which implies that λ_L is the length scale over which any magnetic field is confined at the surface. It is now well known as London penetration depth. Experimental value of λ_L is seen to be upto 5 times larger than predicted by eqn. (1.1.2).

B. The Coherence Length, ξ :

The discrepancy of experimental value of λ_L from London's prediction is due to non-local nature of superconducting properties. This range of non-locality appears to be another fundamental length parameter called coherence length, ξ . This was introduced by Pippard as a generalization to extend London's electrodynamics for the non-local cases. It is conceived as the range over which the averaging has to be done to account for the non-local effect. It has same meaning as that of ordinary mean free path(l) in normal materials. When the mean free path, l is comparable to ξ the effective coherence length is given by;

$$\frac{1}{\xi} = \frac{1}{\xi_0} + \frac{1}{l} \quad (1.1.6)$$

where ξ_0 is the coherence length of the pure material given by;

$$\xi_0 = a \frac{\hbar v_f}{kT_c} \quad (1.1.7)$$

with a as a numerical constant close to unity and v_f the Fermi velocity. With this introduction of coherence length, penetration depth is given by,

$$\lambda = \lambda_L \left(1 + \frac{\xi_0}{l}\right)^{\frac{1}{2}} \quad (1.1.8)$$

1.2.4. GINZBURG-LANDAU FORMALISM:

Starting with the free energy expression for a general second order phase transitions Ginzburg and Landau have been able to formulate phenomenological equations for superconductivity. The free energy is given by,

$$f = f_n + \alpha |\psi|^2 + \frac{\beta}{2} |\psi|^4 + \frac{1}{2m^*} \left| \frac{\hbar}{i} \bar{\nabla} - e^* \bar{A} \right|^2 + \frac{\mu_o \hbar^2}{2} \quad (1.1.9)$$

Minimizing the free energy with respect to the order parameter, ψ and setting boundary condition to,

$$\left(\frac{\hbar}{i} \bar{\nabla} - e^* \bar{A} \right) \psi = 0 \quad (1.1.10)$$

the two famous phenomenological G-L equations are derived as,

$$\alpha\psi + \beta|\psi|^2\psi + \frac{1}{2m^*}(\frac{\hbar}{i}\bar{\nabla} - e^*A)^2\psi = 0 \quad (1.1.11)$$

and

$$\bar{J}_s = \frac{e^*\hbar}{2m^*i}(\psi^*\bar{\nabla}\psi - \psi\bar{\nabla}\psi^*) - \frac{e^*2}{m^*}\psi^*\psi\bar{A} \quad (1.1.12)$$

THE LENGTH PARAMETERS IN G-L CONTEXT:

A. The Temperature dependent coherence length, $\xi(T)$:

The two length parameters in G-L theory have more fundamental consequence at least in the non-local case. From the first G-L eqn. one can see,

$$g''(x) = \left(\frac{2}{\xi^2}\right)g \quad (1.1.13)$$

where $g(x)$ is a small disturbance on normalized wavefunction, $f(x) = 1 + g(x)$ and

$$\xi(T)^2 = \frac{\hbar^2}{2m^*|\alpha(t)|} \quad (1.1.14)$$

The solution to eqn. (1.1.13) indicates that the disturbance $g(x)$ will die down over a distance $\xi(T)$. Obviously the definition of ξ in the G-L and Pippard theories are not fundamentally same.

Substituting different values from the microscopic theories(BCS) values of ξ , in the two extreme limit can be calculated as,

$$\xi(T) = 0.74 \frac{\xi_0}{(1-t)^{\frac{1}{2}}} \quad (\text{pure: } \xi_0 \ll l) \quad (1.1.15)$$

and

$$\xi(T) = 0.855 \frac{(\xi_0 l)^{\frac{1}{2}}}{(1-t)^{\frac{1}{2}}} \quad (\text{dirty: } \xi_0 \gg l) \quad (1.1.16)$$

where $t = T/T_c$, is the reduced parameter.

B. The G-L Penetration depth:

The other length parameter i.e., the penetration depth, λ can be obtained from the second G-L equation (eqn. (1.1.12)) and appears as,

$$\lambda(T) = \left[\frac{m^*}{\mu_0 e^2 \psi_0^2} \right]^{\frac{1}{2}} \quad (1.1.17)$$

and once again by substituting appropriate values of the parameters in the two extreme limit one gets,

$$\lambda(T) = \frac{\lambda_L(0)}{\sqrt{2}(1-t)^{\frac{1}{2}}} \quad (\text{pure}) \quad (1.1.18)$$

and

$$\lambda(T) = \frac{\lambda_L(0)}{\sqrt{2}(1-t)^{\frac{1}{2}}} \left(\frac{\xi_0}{1.33l} \right)^{\frac{1}{2}} \quad (\text{dirty}) \quad (1.1.19)$$

Unlike the coherence length the penetration depth as derived above has same physical meaning as the London penetration depth.

C. The Ginzburg-Landau Parameter:

In the G-L formulation both ξ and λ have same temperature dependence. Thus one can define a temperature independent parameter by,

$$\kappa = \frac{\lambda(T)}{\xi(T)} \quad (1.1.20)$$

Obviously in the two extreme limit κ can be evaluated by using eqn. (1.1.16-17) and eqn. (1.1.18-19). In the pure limit κ is dependent on $\lambda_L(0)$ and ξ and in the dirty limit $\lambda_L(0)$ and 1.

1.2.5. THE EFFECT OF THE TWO LENGTH PARAMETERS: THE SURFACE ENERGY AND EXACT DEFINITION OF TYPE-I AND TYPE-II.

The implication of the length parameter can be easily understood from the Fig. 1.1.3. Penetration of the magnetic field into a superconductors comes with some decrease in the free energy. Because the expulsion of a field, H due to Meissner-Ocshenfeld effect raises the energy of the superconductor by $H^2/8\pi$ per unit volume. At the same time there is a increase of free energy due to decrease of order parameter. The problem can further be simplified to have semi-quantitative calculation of surface energy by applying a external magnetic field, H_{c1} . The decrease of free energy due to field penetration can be approximated by $H_{c1}^2\lambda/8\pi$ and the increase due to reduction of order parameter by $H_{c1}^2\xi/8\pi$. Thus the resultant increase is given by $H_{c1}^2(\xi - \lambda)/8\pi$. Obviously if $\lambda > \xi$, then surface energy is negative and penetration of field will be favoured(Fig.

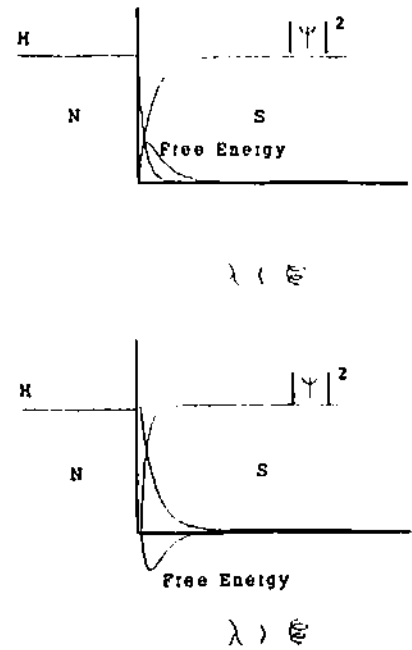


Figure 1.1.3: Significance of length parameters.

1.1.3). However if $\lambda < \xi$ then surface energy is positive(Fig. 1.1.3) and field penetration is energetically unfavourable. Thus in terms of κ , the critical value will be for $\kappa = 1$. However accurate calculation on the basis of the G-L theory shows this critical value to be $\kappa = 1/\sqrt{2}$.

G-L theory gives exact calculation of surface energy in the two limiting values of κ ,

i. $\kappa \ll 1/\sqrt{2}$:

$$\sigma_{ns} = 1.89\xi(T) \frac{\mu_0 H_c^2}{2} \quad (1.1.21)$$

This obviously happens in Type-I superconductors where complete Meissner effect is seen at all field upto a field H_c .

ii. $\kappa \gg 1/\sqrt{2}$:

$$\sigma_{ns} = -\lambda(T) \frac{\mu_0 H_c^2}{2} \quad (1.1.22)$$

This belongs to Type-II. As the field is raised above H_{c1} , flux start penetrating and this penetration, being energetically favourable this process continues upto a field H_{c2} .

1.2.6. FURTHER IMPORTANCE OF NEGATIVE SURFACE ENERGY - FORMATION OF FLUX LINES IN TYPE-II SUPERCONDUCTORS.

A. Flux lines: Quantization of flux.

The consequence of negative surface energy is far reaching. It will also determine the state of the penetrated flux. As one can visualize any penetrated flux will get divided into finer and finer "structures" leading to increase in total surface area and hence decreasing the free energy. However there must be some limiting dimension of these "structures" and one can see, indeed there is a limiting value which can be identified with the "flux quantum", Φ_0 as proposed by London for multiply connected Type-I superconductors and is given by,

$$\Phi_0 = \frac{h}{2e} = 2.07 \times 10^{-15} \text{ Webers} \quad (1.1.23)$$

The quantization of magnetic flux inside a superconductor can theoretically be shown both from London equation as well as second G-L equation for multiply connected Type-I superconductors. The extension of this for the type-II in the mixed state is straight forward by physical argument that normal cores in the mixed state are like "holes" within the bulk making

a large number of multiply connected regions.

C. Shape of an isolated flux line:

At H_{c1} flux lines are sparsely distributed and so long as the separation between the lines, $d \gg \lambda$, flux lines can be considered to be isolated. In that case one can loosely consider the flux lines as a normal core of radius $\xi(T)$. At the center of the core order parameter is zero and magnetic field is maximum. Away from the center order parameter increases exponentially over a length $\xi(T)$ and magnetic field decreases over a length $\lambda(T)$ (Fig. 1.1.4).

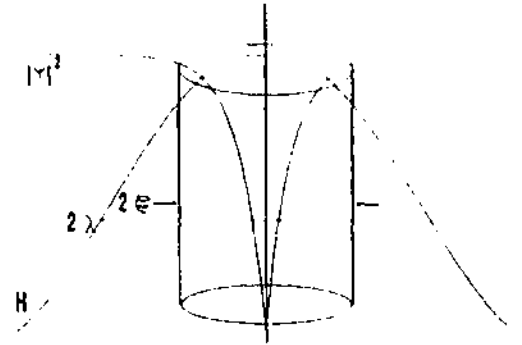


Figure 1.1.4: Schematics of isolated vortex line.

D. Flux Line Lattice:

As the field increases beyond H_{c1} , more and more flux penetrates increasing the number of flux lines and decreasing the spacing between the lines. As a consequence of this, repulsion between the lines increases. Because of these two processes a stable configuration of flux line is achieved. This configuration of flux line is known as flux line lattice (FLL).

1.2.6. PINNING OF FLUX LINES : THE HARD SUPERCONDUCTORS.

The presence of FLL in the mixed state of Type-II superconductors makes it a complicated physical system for theoretical studies. At the same time technological utility is also largely dependent on the interaction of FLL with different parameters.

A. Critical Current density in Type-II superconductors:

Unlike the Type-I case where the critical current density (J_c) equals the depairing current density in case of the Type-II J_c is not well defined experimentally and is fundamentally different from the depairing critical current density. This is because of the presence of flux lines due to external magnetic field or self field of the measuring current.

When a current with density J_x is forced along the x direction, flux lines are subjected to a Lorentz force $(J_x \times \phi)/c$ which moves the flux line with a velocity V_θ along a direction determined by the Hall angle, θ with the y-axis. If this force is not sufficient to impede flux lines start moving and dissipation sets in due to eddy current in the normal cores[27] Thus critical current density is zero. However in reality for most cases there is a measurable non-zero critical current density and the usual current voltage curves is shown in Fig. 1.1.5.

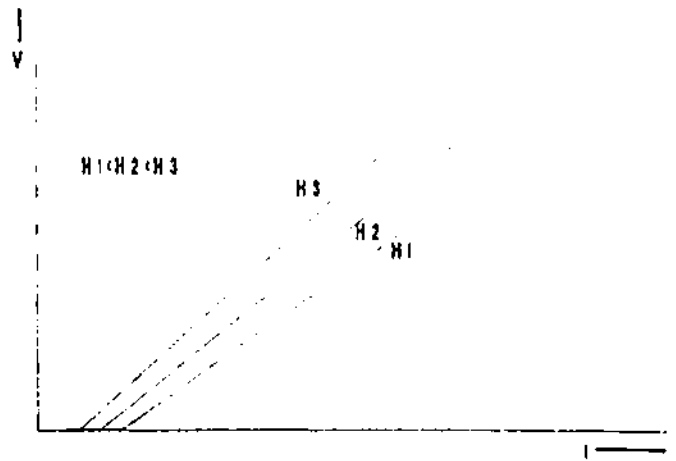


Figure 1.1.5: Schematic I-V for ideal condition.

This implies that there is some "pinning mechanism" which impedes the motion of

flux lines upto a certain level of current density leading to finite critical current density, J_c .

B. Ideal Type-II and hard superconductors:

Thus the type-II superconductors can further be divided into two groups:

- i. Ideal Type-II: No pinning force present and critical current density is zero. Here the force balance equation of flux lines becomes,

$$(\bar{J}_x \times \bar{\phi}) - f n_s \bar{v}_\theta \times \bar{\phi} - \eta \bar{v}_\theta = 0 \quad (1.1.24)$$

where second term represents the magnus force [1] and the third term resulting from all shorts of dissipation due to viscous drag. Obviously η represents the viscosity co-efficient.

- ii. Hard Superconductors: Strong pinning force impedes the motion of flux lines leading to large current density. In this case the force balance equation is given by,

$$(\bar{J}_x \times \bar{\phi}) - f n_s \bar{v}_\theta \times \bar{\phi} - \eta \bar{v}_\theta - \bar{f}_p = 0 \quad (1.1.25)$$

where the last term represents the pinning force.

The definition of critical current density for the hard superconductors can be becomes,

$$\bar{J}_c \times \bar{\phi} = \bar{f}_p \quad (1.1.26)$$

Obviously the technologically important superconductors are in the second group.

C. Flux Flow In Hard Superconductors:

As can be seen from eqn. (1.1.25), when the current is such that Lorentz force exceeds the pinning force, the dynamics of the lines is determined by the viscous force allowing flux line motions and hence dissipation thereof (assuming the magnus force negligible). Obviously the current in question is the critical current for the sample.

From Faraday's law if flux lines moves with velocity, V_θ , the induced emf is given by,

$$\bar{E} = -(\bar{v}_\theta \times \bar{B}) \quad (1.1.27)$$

Using eqn. (1.1.25-27) one gets,

$$E_x = \frac{\phi B}{\eta} (J_x - J_c) \quad (1.1.28)$$

Thus the flux flow resistivity $\rho_f = \phi B / \eta c^2$ is the slope of I-V curve away from the critical current.

D. Thermally activated flux creep in hard superconductors:

Flux pinning allows the establishment of stationary distribution of magnetic fields and currents which are far away from the thermodynamic equilibrium. At a finite temperature, even if $F_L > F_p$ relaxation is attempted through "creeping out of flux lines from the potential well of pinning by thermal excitation of lines which is of the order of kT ". If there is no flux gradient, obviously creep will be in all direction with same probability with zero net creep velocity.

Anderson[28] argued that this creep may involve bundles of several flux lines instead of individual lines. He proposed the creep rate,

$$v_{\pm} = \nu_0 \exp\left(-\frac{E_{eff}}{KT}\right) \quad (1.1.29)$$

where E_{eff} is the effective barrier height of the pinning potential well and ν_0 is a characteristic frequency. If there is driving force, δE net creep rate is given by[3],

$$v = v_{+} + v_{-} = \nu_0 e^{-E_0/kT} (e^{\delta E/kT} - e^{-\delta E/kT}) \quad (1.1.30)$$

Starting from eqn. (1.1.30) one can show,

$$B_{in} \sim B_c (1 - \beta \ln t) \quad (1.1.31)$$

which gives the logarithmic time decay of the flux density inside the material due to flux creep.

1.2.7. IRREVERSIBLE MAGNETIC BEHAVIOR OF HARD SUPERCONDUCTORS.

The most direct implication of the pinning of flux lines is the irreversible magnetic behavior of the hard superconductors. In Fig. 1.1.6 one such M-H loops have shown for a hard superconductor which indicates large hysteresis.

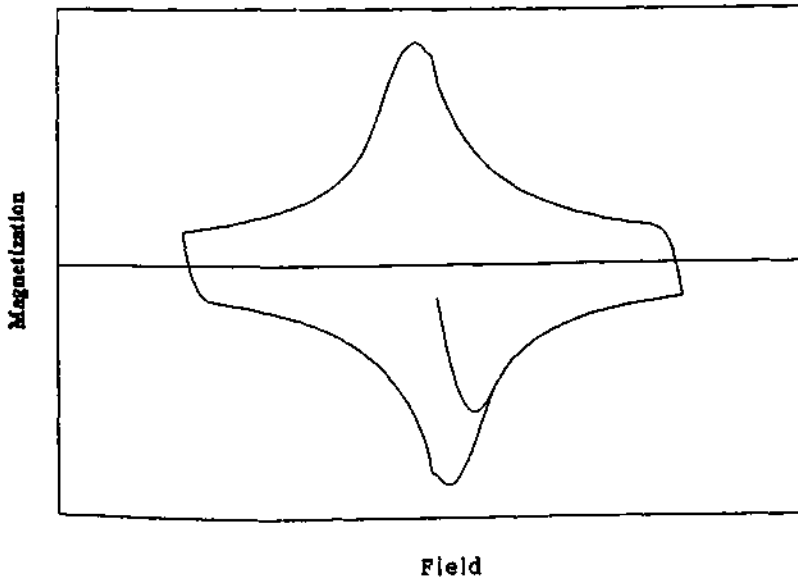


Figure 1.1.6: M-H loop showing hysteresis.

A. THE CRITICAL STATE:

At an external field, $H > H_{c1}$, flux start penetrating within the bulk and form a stable situation mediated by mutual interaction. In the presence of strong pinning a thermodynamic inequilibrium is set up where even after the decrease of field a large number of lines remains trapped inside.

Although pinning forces and driving forces presumably act on individual vortices, it is appropriate to adopt a more macroscopic view because the motion of individual vortices is largely prevented by their mutual repulsion, which tends to impose a crystalline structure on the array. Thus one must expect flux to move in "bundles" when the driving force exceeds the pinning force in the same volume. Since the force per unit volume is,

$$\vec{F} = \vec{J}_{ext} \times \vec{B} = \vec{\nabla} \times \vec{H} \times \vec{B} \quad (1.1.31)$$

the condition for zero dissipation is that F never exceeds the maximum available pinning force per unit volume, F_p .

The implication of this concept is made clear by considering the case of a hollow cylinder having a large field B_0 inside. So long as $B_0 > H_{c1}$, flux lines immediately start to enter the wall, and the decrease in the flux in the bore will induce a current in the wall. Since this current density is $J = dH/dr$, there will be very strong current if $H(r)$ drops abruptly from B_0 to 0 in the wall. As seen from eqn. (1.1.32) this high current, J and high field, B_0 will lead to $F > F_p$. In this case, vortices will penetrate further into the wall, tending to reduce the gradient term. This process will continue until,

$$F = |\vec{F}| = J_{ext} B = B \frac{dH}{dr} \leq F_p \quad (1.1.32)$$

everywhere. This situation is called the critical state.

B. The Two Ways To Reach The Critical State :

- i). The driving force, F may drop below F_p before the flux penetrates all the way to the outside, so that all the initial flux is still in the bore or in the wall.

- ii.) The wall thickness is inadequate to confine the initial amount of flux. So flux will leak out through the wall until that the remaining flux fulfill the condition, $F \leq F_p$ every where.

C. Solution to Critical State Equation -Bean's Model For Infinite Slab :

As Bean[10] argued, " the basic premise of this theory is that there exists a limiting microscopic superconducting current density, $J_c(H)$ that a superconductor can carry; and further, that any electromotive force, however small, will induce this full current to flow locally. On this picture only three state of current flow are possible with a given axis of magnetic field, zero current for those regions which never felt the magnetic field and full current flow perpendicular to the field axis, the sense depending on the sense of electromotive force that accompanied the last local change of field".

He further assumed for simplicity that J_c is independent of magnetic field. Thus the process of magnetization in an infinite slab in a magnetic field, parallel to slab surface can be visualized as in Fig. 1.1.7 showing the flux profile and corresponding current density profile. From Ampere's circuital law,

$$\nabla \times \vec{H} = \vec{J} \tag{1.1.33}$$

one can see that the field within the specimen decreases linearly with field (this is obviously due to the fact that J_c is independent of field). As one can see from the current profile, initially the current flows within a thickness, $\delta = H/J_c$ which is sufficient to reduce the field to zero. This field dependent penetration depth is the central result of Bean's model. At fields of $H \geq H^*$, current flows through the whole sample. This upper limit of field is called the penetration field and is given by,

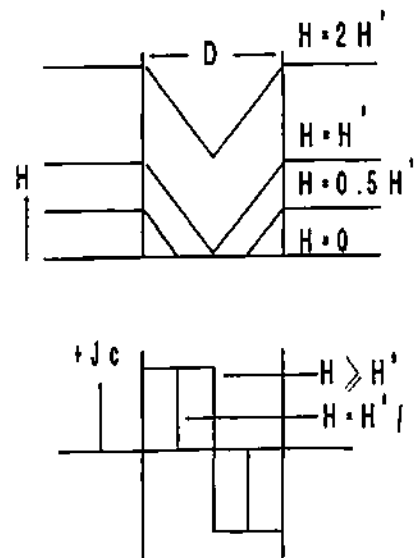


Figure 1.1.7: Schematic flux profile in Bean model.

$$H^* = \frac{J_c D}{2} \quad (1.1.34)$$

where D is the width of the slab. In principle once the flux profile is known one can get B and M from their definition as,

$$\bar{B} = \frac{\mu_0 \int \bar{H} dv}{\int dv} \quad (1.1.35)$$

$$\bar{M} = \bar{B} - \bar{H} \quad (1.1.36)$$

Employing eqns. (1.1.36-37) Bean calculated for initial magnetization curves as,

$$-M = H - H^2/2H^*, \quad (H \leq H^*) \quad (1.1.37)$$

and,

$$-M = H^*/2, \quad (H \geq H^*) \quad (1.1.38)$$

For the hysteretic loops he derived,

$$\frac{1}{\mu_0} B = H \pm H_0/2H^* \pm (H^2 - H_0^2)/4H^*, \quad (H_0 \leq H^*) \quad (1.1.39)$$

where + sign apply for the field traverse from $-H_0$ to H_0 and minus sign for the field traverse from H_0 to $-H_0$.

Though Bean had not included in his first calculation[10] the range, $H > H^*$, modifications latter on by other workers provide the expression for M for this range as[29],

For H increasing:

$$\frac{1}{\mu_0} B = H - H^*/2 + (H + H_0 - 2H^*)^2/4H^* \quad (-H_0 < H < -H_0 + 2H^*) \quad (1.1.40)$$

$$\frac{1}{\mu_0} B = H - H^*/2 \quad (-H_0 + 2H^* < H < H_0) \quad (1.1.41)$$

For H decreasing:

$$\frac{1}{\mu_0} B = H + H^*/2 - (H - H_0 + 2H^*)/4H^* \quad (H_0 > H > H_0 - 2H^*) \quad (1.1.42)$$

$$\frac{1}{\mu_0} B = H + H^*/2 \quad (H_0 - 2H^* > H > -H_0) \quad (1.1.43)$$

D. Calculation of current density from Bean's Model:

Bean's model became popular because of its ability to predict critical current density with good accuracy in the conventional superconductors. The simple expression of J_c given by,

$$J_c = k \Delta M \quad (1.1.44)$$

where $\Delta M = M^+ - M^-$ is the width of the hysteresis at a given field and k is constant depending on geometry of the sample. It is important to note that the eqn. (1.1.45) is valid for field excursion quite larger than the bulk penetration field, H^* .

E. Extension of critical state models:

In Bean's simple model critical current density, J_c has been considered to be independent of magnetic field which is not true for most of the real cases. Further, the sample shape has

been such that demagnetization effect can be neglected. The lower critical field, H_{c1} has also been set to zero.

In order to make the model a realistic one, a large number of modification and extension have been proposed to account for different $J_c(H)$ as well as non-zero H_{c1} and finite demagnetization factors[30-43].

1.3. HIGH TEMPERATURE SUPERCONDUCTORS AND SUPERCONDUCTIVITY:

1.3.1. INTRODUCTION:

A discussion of the different phenomena of high temperature superconductors (HTSC) vis-a-vis the conventional one is a must to understand the complexity in the new material and to pursue any change in the existing theories and models to account for the experimental results. As here the interest is in macroscopic Type-II properties, only the relevant topics will be considered.

The failure of BCS theory to account for such a high critical temperature in this new class of material has led to search for new microscopic theories. In this context phenomenological theories are better[17]. GL theory may still be contextual in this respect. Thus it will be assumed that all the terms and definition in the GL frame work, just described in the context of conventional superconductors are equally valid in this new class of materials.

It is seen that this new class of materials have a short coherence length, $\xi(T)$. Though there is no experimental convergence of actual dimension of ξ , it is surely, in all probability, of the order of a few angstrom only. At the same time it seen that magnetic penetration depth, $\lambda(T)$ is also very large. The small coherence length, $\xi(T)$ and large penetration depth, $\lambda(T)$ have rendered this superconductors as extreme Type-II. More over in the case of HTSC both $\lambda(T)$ and $\xi(T)$ have strong anisotropy. The typical values of these parameters are;

Materials	ξ (nm)		λ (nm)	
	//	\perp	//	\perp
YBaCuO	3.1	0.4	80	180
BiSrCaCuO	3.1	0.4	300	40
Nb ₃ Ge	3		100	

// : parallel to ab plane
 \perp : perpendicular to ab plane
 Taken from: J. Talvecchio[46]

The large anisotropy of the length parameters is another complexity that one has to take into account. The anisotropy of $\lambda(T)$ and $\xi(T)$ will also cause anisotropy of other parameters like, H_{c1} , H_{c2} , resistivity(ρ) etc. Thus this anisotropy has to be included in a real GL theory to get actual picture of these materials. The major contribution due to anisotropy is going to in modifying the elastic properties of the FLL [45]. However such a formulation is too complicated. Therefore in the simple case of GL theory, $\xi(T)$ and $\lambda(T)$ may be replaced by their suitable mean value.

The consequence of short coherence length, ξ , can be felt from the simple calculation of critical fields. ξ being small, $H_{c2} \approx \phi_0/2\pi\xi^2$, is quite large and as λ is high, $H_{c1} \approx \phi_0/2\pi\lambda^2$, is quite less.

Let us now look at different parameters H_{c1} , H_{c2} , J_c at 0 K in YBCO.

Material	$H_{c1}(T)$	$H_{c2}(T)$	$J_c(0)(\text{Amp}/\text{cm}^2)$
Yba ₂ Cu ₃ O ₇	8×10^{-2}	90	≈ 1000

1.3.2. MACROSCOPIC MAGNETIC PROPERTIES:

The macroscopic properties of high temperature superconductors have now attracted more interest and have become center of controversy. These features include the unusual irreversibility line in the H-T plane, the possible melting of the vortex lattice above this line, the large non-exponential time-relaxation of magnetic properties and its aging effect, discrepancy between magnetic and transport critical current density, J_c of the ceramic materials, the almost exponential fall-off of critical current density with temperature and magnetic field, the unusual field dependence of field-cooled susceptibility and few others.

1.3.2A. DC MAGNETIZATION MEASUREMENTS

I. THE IRREVERSIBILITY LINE:

Even in the first study of DC susceptibility [47], it was seen that zero-field-cooled (ZFC) and field-cooled (FC) susceptibility vs temperature curves do not coincide. Figure 1.1.8 shows the difference. It is seen that the point, X where the ZFC and FC curves separates is also a function of DC bias field. This point, X in the H-T plane has been plotted giving the so called "irreversibility line". What it imply, is that above this line in H-T plane ZFC and FC curves coincide and below it does not. The irreversibility line in H-T plane is represented by,

$$1 - \left(\frac{T}{T_c}\right)^q \propto H^q \quad (1.1.45)$$

where T is point of irreversibility and q has typical values in between 1/2 to 3/4. A similar behavior is seen in spin-glass systems and has same mathematical relation as given by de Almeida and Thouless[48].

This is probably the major support for early theories of granularity mediated spin-glass approach. The irreversibility line can also be drawn from AC susceptibility as well as resistivity measurements. However the irreversibility line in AC susceptibility measurements are more accurate because in DC magnetic measurements or resistive measurements the instrumental resolution will change the position of an irreversibility point.

The presence of "irreversibility line"(IL) has evoked a serious doubt about the so called phase diagram of magnetic states in HTSC(A detailed discussions and comments on IL can be seen at the end of ref[70]).

II. SCREENING EFFECT:

In this study, sample is cooled in zero field (a small residual field may still be there) and then a field is applied. This is also known as zero field cooled (ZFC) flux expulsion. In conventional superconductors ZFC susceptibility is -1. It is to remember that ZFC expulsion can give full diamagnetic signal even when only a small surface layer of the

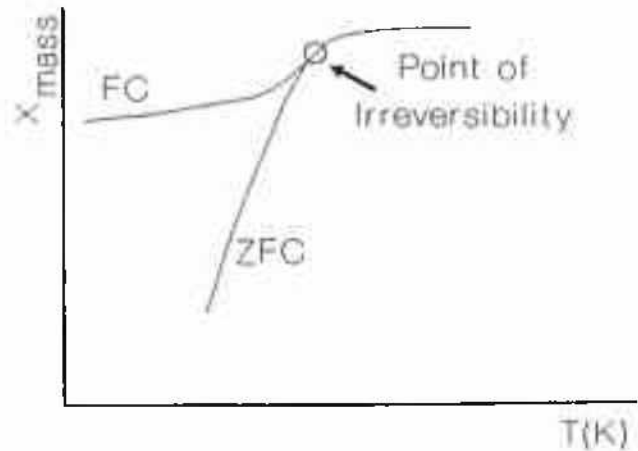


Figure 1.1.8: FC and ZFC susceptibility(DC).(Taken from [47])

sample is superconducting. But in HTSC complete screening has hardly been observed even after a proper demagnetizing correction due to sample shape. The incomplete screening effect can be understood from a premature flux penetration at a field as low as few millioersted[51].

III. MEISSNER EFFECT:

Magnetic field is applied at a temperature higher than T_c and then the temperature is brought down below T_c . This differs from the screening effect because it is basically flux exclusion from inside the bulk. Obviously this gives a true measure of the superconducting volume fraction in at least conventional case. In HTSC Meissner effect gives $M_{fc} > -1$. This possibly indicates; i. flux pinning may present, ii. system may be glass-like, or iii. system may contain non-superconducting phases.

However it is now clear that at quite low field (sub-oersted) at least, there is full flux exclusion. Thus the method of finding volume fraction of superconducting matter in analogy with conventional method as employed earlier is not sure one and may be utilized only at very low field.

IV. REMANENT MOMENT:

If the magnetic field is put off after the field cooling, one can measure the remanent moment. It can be seen that below the irreversibility line one has; $M_{rem} = M_{fc} - M_{zfc}$ and above irreversibility line M_{rem} is zero. This behavior is basically the side effect of the irreversibility line. It is to be seen what causes this non-zero M_{rem} .

V. EXPERIMENTAL HYSTERESIS LOOPS:

Hysteresis study through M-H or B-H loops are one of the most important experimental tools for Type-II materials. It gives insight into the flux line lattice, pinning mechanisms, and all other irreversible properties of Type-II materials. In fact this study initiated the "granularity" picture of the bulk ceramics of HTSC. In case of conventional superconductors MH loops have some monotonic nature with respect to field range: loop area increases with increasing field range. The peculiarity of the bulk ceramics, as now it is well known, is that even at very low field range of a few oersted a small MH loop opens up and then closes at a higher field of tens of oersted. More interesting is that this is not seen in powdered or good quality single crystal samples indicating that the peculiarity may

be due to the "granularity" or so called "weak links"[52] present in ceramic bulk. At higher field of a few Koe, the M-H loop for a ceramic sample take a new shape quite different from the low field loops but similar to the conventional one. It has also been seen that powdered and single crystal samples give similar MH loops in this range. In between these two ranges, some times a peculiar Z-shaped loops are also seen. It is argued qualitatively that the Z-shaped loops are due to the presence of shielding currents. The temperature dependence of the loops are monotonic with loop areas shrinking at higher temperature.

VI. CRITICAL STATE MODEL AS APPLIED TO HTSC:

Critical state model has been extensively used for calculating "magnetic J_c " from MH loops by the standard formula for slab of thickness D;

$$J_c = 20 | -M^+ + M^- | / D \quad (1.1.46)$$

From high field M-H loops, using the grain size instead of bulk, very high magnetic J_c for the grains have been predicted. And from low field MH loops with bulk dimension of the sample, magnetic J_c of the order of 1000 Amp/cm² have been predicted. In conventional case, critical state has no confusion of this kind.

VII. THE GRANULARITY PICTURE OR THE WEAK LINK MODELS OF HTSC:

Particularly the hysteresis data has clearly indicated some sort of weak links through which grains are connected within a ceramic bulk. Though single crystal and good quality thin film have high J_c ($\approx 10^6$ amp/cm² at zero field), the transport J_c of ceramic bulk is quite low (≈ 1000 Amp/cm²). Even the magnetic J_c as calculated from high field MH loops of the polycrystalline sample indicates large J_c ($> 10^5$ amp/cm²) for the grain. Drastic magnetic field dependence of transport critical current density, J_c as compared to magnetic J_c is further in support of the weak link model. The strong field suppression of transport J_c has been looked as due to the well known effect of magnetic field on Josephson junctions. Thus the transport current can be represented by the diffraction equation;

$$J_c(H) = J_{c0} \left| \frac{\sin(\pi H/H_0)}{\pi H/H_0} \right|$$

In this model the bulk is considered as having two critical current densities J_{cj} , for the bulk

and $J_{c,g}$ for the grains.

VIII. GRANULARITY WITHIN A CRYSTAL:

Here is the confusion as to how far is the weak link hierarchy is extended. Possibly down to inside a so called crystal or an individual grain. Possible weak link effect within a grain or crystal may be due to twin planes. This is probably the biggest draw back in the model of HTSC on the basis of granularity induced "Glassy superconductors"[52,53].

IX. MAGNETIC RELAXATION:

Magnetic relaxation has assumed another important parameter in HTSC. Quite large and non-exponential magnetic relaxation has been reported[72,55]. More complicated thing is that the normalized relaxation rate, $(1/M) dM/d\ln(t)$, is seen to have a peak at around 20 to 30 K in $YBa_2Cu_3O_{7-x}$. This is not expected in conventional flux creep model for LTS where creep should increase monotonically with temperature approaching T_c , where it will be largest. The problem of this unusual relaxation behavior becomes more complex when Yeshuran and Malozemoff[54-55] reported similar effects in single crystal of $YBa_2Cu_3O_{7-x}$ signifying that this peculiarity may not be due to granularity.

X. CRITICAL CURRENT DENSITY - DEPENDENCE ON TEMPERATURE AND MAGNETIC FIELD:

Critical current density, the most technologically important parameter, is least understood in this materials. The dependence of transport J_c on magnetic field and temperature is not yet well documented mainly because of the problem in sending the large current through the contacts for this measurements. While for a bulk polycrystal the transport is very much retarded due to weak links creating sharply decreasing $J_c(B)$, for the case of single crystal the behavior is complicated. There is a discrepancy of magnetic and transport $J_c(T)$ which possibly indicates the irreversibility line.

XI. THE MECHANICAL OSCILLATOR EXPERIMENT:

The superconductor is subjected to resonant oscillation and frequency shift and the dissipation are plotted as a function of temperature keeping the DC field constant. The observed peak in the dissipation as function of temperature is explained as a consequence of flux melting[56].

1.3.2B. AC SUSCEPTIBILITY:

AC susceptibility is the most common measurements to characterize a superconductor and a large number of data is available both on conventional and ceramic superconductors. The measurements of real and imaginary part of AC susceptibility gives valuable information on the intricacy of the flux dynamics.

I. TEMPERATURE VS. χ' AND χ'' :

The complexity in HTSC comes with the presence of a large peak in $\chi''(T)$ along with a smaller one for bulk ceramics samples. In fact some of the first[57] evidence for granularity have derived from this data. The lower temperature peak is due to the weak links which disappears on powdering the ceramic. Further the position of the large peak at lower temperature, is dependent on DC biased field and excitation frequency. In fact, this peak in the H-T diagram has been argued to represent the so called irreversibility line.

II. HIGHER HARMONICS:

AC susceptibility has also been studied for different harmonics. The striking features is that the presence of large even harmonics. In conventional materials even harmonics have not been found in agreement with Beans model prediction.

III. χ' AND χ'' AS A FUNCTION OF FREQUENCY AND AMPLITUDE OF THE AC EXCITATION FIELD:

Measurement of AC susceptibility as a function of amplitude and frequency of the AC excitation field have shown novel features[43,59]. Two distinct peaks have been seen in case of amplitude versus χ'' curves showing clear evidence for granularity in ceramic samples. Strong frequency dependance of susceptibility is also unique of this new class[66-67].

IV. HYSTERESIS OF $\chi'(H)$ AND $\chi''(H)$:

If the DC bias field is varied and the maximum of the excursion is higher than certain field then the $\chi'(H)$ and $\chi''(H)$ will trace two loops showing hysteresis[60,64]. This hysteresis have been studied mainly at low DC fields. By modifying Bean model for field dependence of current density Kim et al. have been explained the field dependence of $\chi'(H)$

and $\chi''(H)$. But the hysteresis is still unaccounted. In conventional superconductors this sort of hysteresis were not studied much. However there is a recent study on this aspect of hysteresis of $\chi(H)$ in filamentary structures of conventional superconductors[65].

1.3.3. RESISTIVITY VERSUS TEMPERATURE AND FIELD:

Extra large broadening of resistivity versus temperature curves with increasing magnetic field is another new phenomenon in these materials. In conventional homogeneous superconductors, in presence of magnetic field, resistive transition shifts to lower temperature along with broadening. But the broadening is usually less than the shift permitting one to calculate H_{c2} accurately. The large broadening has also been reported for HTSC single crystal. This broadening creates a problem for defining the temperature corresponding to H_{c2} causing the definition very much obscure. Further, H_{c2} calculated with this definition shows varying temperature dependence, sometimes linear or sometimes curved following $(1 - T/T_c) \propto H^{2/3}$. Thus the doubt is that it is possibly the irreversibility line not the $H_{c2}(T)$ line[73].

1.3.4. MAGNETIC DECORATION OF FLUX LINE LATTICE:

The most direct evidence of the flux line lattice is achieved through the magnetic decoration technique. In conventional superconductors this technique has yielded valuable information on the FLL. In HTSC, at 4.2 K well defined FLL has been observed in single crystal of YBCO in ab plane. However no pattern was seen at 77 K. "Melting" of flux line is one of the possible causes for this[44]. Also it may be due to the fact that at high temperature λ , the penetration depth may be too large making the vortices magnetically ill-defined.

1.3.5. SUMMING UP THE PICTURE:

The whole aim of all the discussion on HTSC is with an aim to have a clarity of the problems to be faced in the next few chapters. So let us now define our problem and set the goal of the thesis.

As per the title of the thesis - "Granularity, irreversibility and hysteresis" of the ceramic bulk are the points of interest in our work. Thus let us first list experimental results that are known.

WHAT IS KNOWN :

1. the HTSC:

- * All HTSC belong to type-II with high κ .
- * All have small $\xi(T)$ and quite large $\lambda(T)$.
- * All are intrinsically as well as macroscopically anisotropic.
- * In thin film and good single crystal J_c is high ($> 10^5$ amp/cm²).

2. the ceramic bulks:

- * It is seen to be "granular system" connected by "weak links".
- * Two "irreversibility lines" are seen.
- * Peculiar evolution of M-H (B-H) loops through three distinct phases over the increasing maximum of field excursion.
- * Transport $J_c < 1000$ amp/cm².
- * High magnetic J_{cg} ($> 10^{5-6}$ amp/cm²) for the grains.
- * Discrepancy between bulk magnetic J_c and transport J_c .
- * $J_c(H)$ shows strong irreversibility.
- * $\chi''(T)$ shows two peaks, grains and the grain boundaries.
- * χ'' as a function of AC amplitude also shows two peaks.
- * Irreversibility in $\chi'(H)$ and $\chi''(H)$ is seen.
- * Strong even harmonics are seen.
- * Strong magnetic relaxation is seen.
- * In melt textured or the like J_c close to 10^5 amp/cm² have been achieved.

Now it is to see what we can explain and how. Initially the tendency was to assign all the artifacts of the HTSC as due to the granularity induced "glassiness" as an extension of Ebner-Stroud model. However with the extension of almost all properties of bulk ceramic into single crystals, the doubt arises as to the length scale of granularity. It is seen that the granularity length scale may even be down to 100 Å. With the evidence of flux line lattice by magnetic decoration technique, the attention has been shifted to theories incorporating the FLL or better the "vortex matter" and involving different approach of phase transitions or pinning-depinning models. It is by now certain that because of high ambient temperature, low $\xi(T)$ a large number of flux related phenomenon may be appreciable in this new class of materials which, in conventional superconductors were never realized. Though there is

confusion in these flux related models, as to what the right phase is, beyond doubt they have been successful in explaining the most confusing "irreversibility line" with sufficient confidence. However, there is one important discrepancy between the prediction from different vortex theories - in TAFF (thermally activated flux flow) as proposed by Malozemoff et al.[71] IL does not exist for zero frequency i.e., in the DC limit where as in vortex-glass picture, conceived by Fisher et al.[50], a finite IL is present in the DC limit.

Though the success of the theories of "vortex matter" has overshadowed the "glassy superconductor" models, for granular systems (bulk ceramic) the presence of "weak link" is beyond doubt[68,69] and experiments reporting junctions between grains are well known. Therefore, for the granular system glass models are still important particularly to explain some of the experimental data pertaining to the granular nature of this materials.

What we can explain and how -

*	Irreversibility line : Vortex theory /glass theory			
*	Two IL's	:	? /	do
*	Magnetic relaxation :		do /	?
*	Evolution of			
	M-H loops	:	? /	do
*	Two $\chi''(T)$ peaks	:	? /	do
*	Two $\chi''(H_{ac})$ peaks	:	? /	do
*	$J_c(H)$ low field	:	do /	do
*	$J_c(T)$:	do /	do
*	$J_c(H)$ hysteresis	:	? /	do
*	$\chi(H)$ hysteresis	:	? /	do

Though the chart looks quite favourable for a superconducting glass model, it is to be remembered that the a exact quantitative calculation in this model is much complex and tedious.

At this point, one "terminology problem" must be cleared. The "GLASS model", as concerned here is the glassiness of the superconductor itself due to randomness of the granular system and not the "glassiness" of the vortex lines due to random pinning[17] or thermal fluctuations[50].

1.4. THE AIM AND SCOPE OF THE WORK:

The above discussion gives the background for the work of this thesis. However the discussion is not to the point but a little general. With the picture as depicted above, it is clear that the HTSC is still a living problem. Particularly, the macroscopic magnetic properties are not yet well understood. As described above, the low field anomalous M-H loops of the ceramic is still not well explained. Though, there are large number of experimental and theoretical reports on this, exact explanations are yet to come. There are a lot of calculations on the basis of critical state model which are very range specific and are unable to give true picture -particularly the evolution of M-H loops with increasing range of field excursion. The work in this thesis starts from this point - searching for a realistic model to give a better picture of the actual physical situation.

Assuming the results of the superconducting glass model for the granular system, a two component critical state model will be solved numerically. This will form the content of the Chapter 3 of this thesis. In the first part of Chapter 3(Part-A), the model will be developed and solved for M-H loops. First it will be shown that a two component model can account for the anomalous low field M-H loops. The model will also be tested for higher field ranges and the evolution of M-H loops will be addressed. It will further be shown that the Z-shaped M-H loops, seen in the middle range of the field can be derived from the model by adding a shielding contribution. Grain size dependence of the M-H loops have also been included.

Measurement of AC susceptibility as a function of temperature, DC bias field, frequency and amplitude of AC excitation field is the most important experimental tool to probe into the flux dynamics of any superconductor - conventional or new. There are a large number of data on $\chi(T)$ for different frequencies which have been qualitatively explained by considering flux creep to account for the effect of frequency. However, the study of AC susceptibility as a function of DC bias field is relatively rare. Further, the $\chi'(H)$ and $\chi''(H)$ have shown hysteresis with respect to DC field. Though there are some calculations justifying the field dependence of the χ' and χ'' , there is no success in explaining the hysteresis in $\chi'(H)$ and $\chi''(H)$.

In the second part (Part-B) of Chapter 3, the same model as above will be extended for the AC susceptibility calculations as a function of DC bias field and amplitude of AC excitation. Instead of considering different features and comparing them, always the full loop has been plotted. This way of representation, though makes the study a little complicated,

is helpful for the reader to see for himself all the details of an individual loop. This calculation, for the first time will show the hysteresis of $\chi'(H)$ and $\chi''(H)$ as seen in experimental data of different researchers[60-65]. The model has been tested for different field ranges (a few mT to a few hundreds of mT) and seen to be consistent with experimental data. To bring out the significance of J_c parameters and hence of pinning mechanism, the model has been tested for different critical current parameters as well as different $J_{cj}(H)$ and $J_{cg}(H)$ (Bean, Kim as well as exponential type of $J_c(H)$). The amplitude dependence of AC susceptibility has been studied. These results are in good agreement with already published data. The important point about the model is that it produces continuous $\chi'(H_{ac})$ and $\chi''(H_{ac})$ over the full range of amplitude. Calculation by other workers consider different ranges of amplitude in a discontinuous manner. The AC susceptibility calculation has also been extended for harmonic generation and the results are in agreement with that of others. Further, it will be shown that the higher harmonics also show hysteresis.

In the next section of the Part-B of Chapter 3, the effect of flux creep and flux flow have been considered in the model in a phenomenological way. This calculation will be crucial in explaining our own data on the frequency dependence of the $\chi'(H)$ and $\chi''(H)$ loops.

It is already mentioned that the study of χ' and χ'' as a function DC field are numerous. Further, the model yields more interesting results which require verification. With this view, some experiments were planned. In the 4th Chapter, all the experimental data have been presented and attempt was made to correlate the data with model calculation. In order to perform these experiments, some experimental arrangements were devised. A brief description of the experimental arrangements has been included in Chapter 2.

As a systematic sample series is must for a systematic study, a few series of samples were also made. As YBCO is already a well characterized material, it has been considered for the study here. In order to have a systematic variation of the sample properties, liquid phase sintering was attempted and PbO was used as liquid phase sintering agent. The description of the sample preparation and initial characterization have also been included in Chapter 2.

As mentioned above, the 4th Chapter contains all the experimental results. This Chapter has 4 main parts. In the first part (Part A), the response of the samples in an AC current has been studied. As the quest was for hysteresis or irreversibility of HTSC fast Fourier analysis(FFT) of the voltage signal to see the different harmonics was also attempted

and included in this part. Hysteresis of magneto-resistance (instead of $J_c(H)$ hysteresis) was done at different frequencies with the aim to see the effect of frequency on the overall on the hysteresis and so pinning mechanism . Extension of these studies for three probe measurements, i.e, for the apparent contact resistance also was also considered to emphasize the "weak-link-like" behavior at the metal-superconductor junction.

The next two parts of Chapter 4 (i.e., part B and C) contain the measurements on the $\chi'(H)$ and $\chi''(H)$ loops for different DC bias ranges, amplitudes and frequencies of AC excitation field for two configurations of the AC and the DC fields, co-axial and mutually perpendicular. In part B, the two fields (AC and DC) were co-axial and hence the data could directly be analysed on the basis of the model calculations in Chapter 3. The qualitative agreement of the experimental data with the model prediction is noticeable. The data on the $\chi'(H)$ and $\chi''(H)$ loops for different range of DC bias field shows that only above a certain DC bias field, the hysteresis starts to appear. The amplitude dependence of the $\chi'(H)$ and $\chi''(H)$ loops also shows strong variation of the shapes of the loops. The range of frequency in this study was 11 to 97770 Hz. The dependence of the $\chi'(H)$ and $\chi''(H)$ on frequency is quite obvious and probably indicates the presence of "non-critical(Flux flow or creep)" components originated from the weakly pinned Josephson vortices.

In view of the fact that conceiving a model for the case of the AC and the DC fields mutually perpendicular is not easy and is not available, substantial experimental data were generated for the purpose of understanding the problem. The question is, can one fit these data in the model as above(where fields are co-axial)? The answer is given in Part-C of Chapter 4. The $\chi'(H)$ and $\chi''(H)$ loops were studied for the bulk size dependence to bring out the essence of critical state in this case. It is already described above that the $\chi'(T)$ and $\chi''(T)$ show strong frequency dependence which can partially be explained by considering the flux creep[66-67]. With this view, the effect of frequency on the $\chi'(H)$ and $\chi''(H)$ hysteresis loops was seriously considered and the effect of frequency was established for lower range of frequency.

This chapter concludes in 4th part with the discussion frequency dependence of $\chi(H)$ loops on the basis of "non-critical" components - flux creep and flux flow.

The thesis concludes with the listing of the salient features of this work.

REFERENCES:

- [1] R.P. Hübener 1979 "Magnetic Flux Structures in Superconductors", Springer-Verlag
- [2] D. Saint-James, G. Sharma and E.J. Thomas 1969 "Type-II Superconductivity", Pergamon press
- [3] M. Tinkham 1975 "Introduction to Superconductivity", McGraw-Hill, New York
- [4] A.C. Rose-Innes and E.H. Rhoderick 1988 Introduction to superconductivity(Pergamon press)
- [5] R.D. Perk ed. "Supperconductivity" Vol. 2
- [6] D.J. Doss 1989 "Engineering Guide to High Temperature Superconductivity" N.York, Willy
- [7] A.M. Campbell and J.E. Evettes 1972 Ad. Phys. **21**, 199
- [8] D. Dew-Hughes 1979 Treaties on Materials Science and Technology vol. 14 ed. T. Luhman and D. Dew-Hughes and references therein.
- [9] J.B. Bednorze and K.A. Müller 1986 Z. Phys. B **64**, 189
- [10] C. P. Bean , Review of modern physics, **34**, 31 (1964)
- [11] Wu, M.K., J.R. Ashburn, C.J. Torng, P.H. Hor, R.L. Meng, L. Gao, Z.J. Huang, Y.Q. Wang and C.W. Chu 1987 Phys. Rev. Lett. **58**, 908
- [12] C.W. Chu, J. Bechtold, L. Gao, P.H. Hor, R.L. Meng, Y.Y. Sun, Y.Q. Wang and Y.Y. Xue 1988 Phys. Rev. Lett. **60**, 941
- [13] H. Maeda, Y. Tanaka, M. Fukutomi and T A. Asano 1988 J. J. Appl. Phys. **20**, L209
- [14] R. M. Hazen, L.W. Finger, R.J. Angel, C.T. Prewitt, R.L. Ross, C.G. Hadidiacos, P.J. Heaney, D.R. Veblen, Z.Z. Sheng, A.El. Ali and A.M. Hermann
- [15] A.M. Hermann, Z.Z. 1988 Sheng Nature **332**, 138
- [16] A. Schilling, M. Cantoni, J.D. Gno, H.R. Ott 1993 Nature **363**, 56
- [17] E.H. Brandt, Physica C **195**,1-27 (1992)
- [18] E.H. Brandt 1991 Jl. Mod. Phys. **B5**, 751
- [14] E.H. Brandt Z. Phys. B (cond. Matter) **80**, 167
- [19] G.M. Ginsburg 1989 "Physical Properties of High Temperature Superconductors", ed. G.M. Ginsburg World Scientific, Singapore
- [20] P.W. Anderson 1987 Science **235**, 1196
- [21] A discussion between Anderson and Schrieffer, Phys. Today 1991, June
- [22] P.W. Anderson and Z, Zou 1988 Phys. Rev. Lett. **60**, 153
- [23] N. Nagoasa and P.A. Lee 1990 Phys. Rev. **64**, 2450

- [24] Nevil Mott 1987 *Nature* **327**, 363
- [25] J.P. Carbotte 1990 *Rev. Mod. Phys.* **62**, 1027
- [26] V.L. Ginsburg 1992 *Contemporary Phys.* **33**, 15
- [27] J. Bardeen and M.J. Stephen 1965 **140**, A1197
- [28] P.W. Anderson 1962 *Phys. Rev. Lett.* **9**, 309
- [29] L. Ji, R.H. Sohn, G.C. Spalding, C.G. Lobb and M. Tinkham 1989 *Phys. Rev.* **B40**, 10936
- [30] Y. B. Kim, C. F. Hempstead and A. R. Strand 1962 *Phys. Rev. Lett.* **9**, 306
- [31] Y. B. Kim, C. F. Hempstead and A. R. Strand 1963 *Phys. Rev.* **129**, 528
- [32] F. Irie and K. Yamafuji 1967 *J. Phys. Soc. Jpn.* **23**, 255
- [33] I. M. Green and P. Hlawiczka, 1967 *Proc. IEE* **114**, 1329
- [34] V. R. Karasik, N. G. Vasil'ev and V. G. Ershov 1964 *Sov. Phys. Rev.* **136**, A335
- [35] G. Ravi Kumar and P. Chaddah 1989 *Phys. Rev.* **B39**, 4704
- [36] D.-X. Chen, A. Sanchez, J. Nogues, and J.S. Munoz 1990 *Phys. Rev.* **B41**, 9510
- [37] K. V. Bhagwat and P. Chaddah 1990 *Physica C*, **190**, 444
- [38] Y. Kim, Q. H. Lamb and C.D. Jeffries 1991 *Phys. Rev.* **B43**, 11404
- [39] T. Ishida and R. B. Goldfarb 1990 *Phys. Rev.* **B41**, 8937
- [40] K. H. Müller 1989 *Physica C*, **159**, 717
- [41] K.H. Müller 1991 *Magnetic Susceptibility of Superconductors and Other Spin Systems* ed R.A. Hein, T.L. Francavilla and D.H. Liebenberg p229
- [42] K. Yamamoto, H. Mazaki and H. Yasuoka 1993 *Phys. Rev.* **B47**, 915
- [43] D.-X Chen, A. Sanchez, T. Puig, L.M. Martinez and J.S. Munoz 1990 *Physica C* **168**, 652
- [44] A.P. Malozemoff 1989 *Physical Properties of High Temperature of Superconductors* ed. D.M. Ginsburg, World Scientific, Singapore pp-71
- [45] P.H. Kes *Physica C* **153-155(1988)** 1121-1126
- [46] J. Talvacchio 1989 *IEEE Trans, CHMT* **12**, 21
- [47] K.A. Müller, M. Takashige, J.G. Bednorz 1987 *Phys. Rev. Lett.* **58**, 408
- [48] J. R. L. de Almeida and D.J. Thouless 1978 *J. Phys.* **A11**, 983; **C11**, L871
- [49] D.S. Fisher M.P.A. Fisher and D.A. Huse 1991 *Phys Rev B* **43**, 130
- [50] M. P. A. Fisher, *Phys. Rev. Lett.* **62**, 1415 (1989)

- [51] L. Civale, H. Safar, F. de la Cruz, D.A. Esparza and C.A. D'Ovidio 1988 Solid State Comm. **65**, 129
- [52] M. Tinkham and C.J. Lobb 1990 Solid state Physis **40**, 92
- [53] J. Clem 1988 Physica C, **153-155**, 50
- [54] Y. Ysehurun, A.P. Malozemoff 1988 Phys. Rev. Lett **60**, 2262
- [55] Y. Ysehurun, A.P. Malozemof, F. Holtzberg and T.R. Dingher Phys. Rev. B **38**,
- [56] P.L.Gammel, L.F. Schneemeyer, J.V. Wazczak and D. Bishop 1988 Phys. Rev. Lett. **61**, 1666
- [57] H. K pfer, I. Apfelstedt, R. Fl kiger, C. Keller, R. Meier-Hirmer, B. Runtsch, A. Turowski, U. Wiech and T. Wolf 1988 Cryogenicis **28**, 650
- [58] D.-X. Chen, A. Sanchez, T. Puig, L.M. Martinez and J. S. Munoz 1990 Physica C **168**, 652
- [59] Lamb et al Ampli vs. χ
- [60] Y. Kim, Q. H. Lamb and C. D. Jeffries 1991 Phys. Rev. **B43**, 11404
- [61] Y. Yamaguchi, M. Tokumoto, and K. Mitsugi 1991 Physica C **179**, 447
- [62] Y. Yang, C. Beduz, Z. Yi and R. G. Scurlock 1992 Physica C, **201**, 325
- [63] A. Kompany, Y. J. Qian, M-F. Xu, H-P. Baum, W. Millman and M. Levy 1990 Solid State Comm., **75**, 579
- [64] C.Y. Lee, L.W. Song and Y.H. Kao 1992 Physica C **191**, 429
- [65] R.B. Goldfarb and A.F. Clarke 1985 IEEE Trans. **MAG21**, 332
- [66] K.H. M ller 1990 Physica C **168**, 585
- [67] S. Takacs, F. Gomory and P. Lobotka 1991 IEEE **MAG27**, 1057
- [68] C.E. Gough 1988 Physica C **153-155**, 1569
- [69] R.H. Koch, C.P. Umbach, M.M. Oprysko, J.D. Mannhart, B. Bumble, G.J. Clark, W.J. Gollagher, A. Gupta, A. Kleinsasser, R.B. Laibowitz, R.B. Sandstrom and M.R. Scheuermann 1988 Physica C **153-155**, 1685
- [70] Magnetic Susceptibility of Superconductors and Other Spin Systems ed R.A. Hein, T.L. Francavilla and D.H. Liebenberg (Plenum press-1990)
- [71] A.P. Malozemoff, T.K. Worthington, Y. Yeshurun, F. Holtzberg and P.H. Kes 1988 Phys. Rev. **B38**, 7203
- [72] M.E. McHenry, M. Foldeaki, J. McKittrick, R.C. O'Handly and G. Kalonji
- [73] M. Tinkham 1988 Phys. Rev. Lett. **61**, 1658

EXPERIMENTAL TECHNIQUES

This chapter contains a brief description of experimental arrangements. A description of the sample preparation and initial characterization is also included.

2.1.	ELECTRICAL MEASUREMENTS	38
1.	FOUR PROBE AC RESISTIVITY	38
2.	AC RESISTIVITY AS A FUNCTION OF TEMPERATURE	39
3.	V-I MEASUREMENTS AT DIFFERENT FREQUENCIES AND MAGNETIC FIELDS	43
4.	HYSTERESIS OF MAGNETO-RESISTANCE	44
2.2.	MAGNETIC MEASUREMENTS	46
1.	MAGNETIC AC SUSCEPTIBILITY MEASUREMENTS	47
2.	AC SUSCEPTIBILITY AS A FUNCTION OF TEMPERATURE	51
3.	AC SUSCEPTIBILITY AS A FUNCTION OF SUPERIMPOSED DC BIAS	52
4.	SUPPORT FOR FREQUENCY DEPENDENCE STUDY OF $\chi(H)$	54
2.3.	SAMPLE PREPARATION AND INITIAL CHARACTERIZATION	57
1.	SAMPLE PREPARATION - CERAMIC ROUTE	57
2.	LIQUID PHASE SINTERING OF YBCO IN PRESENCE OF PbO	59
3.	BASIC CHARACTERIZATION	61
	REFERENCES	65

2. MEASUREMENT TECHNIQUES:

To study the flux dynamics in the HTSC's, it is essential to study the transport and magnetic properties of the material. In order to accomplish this, several experimental set-ups to measure the electrical resistivity, magneto-resistance and ac magnetic susceptibility were fabricated. Several YBCO samples were also synthesized. This chapter gives a detail description of all experimental techniques used during the present work.

2.1. ELECTRICAL MEASUREMENTS:

2.1.1. FOUR PROBE AC-RESISTIVITY:

Usually resistivity is measured using a DC four probe method. However the draw backs in the DC method are[2-4]:

- i. Thermo-emf: This is due to the presence of temperature gradient and the junctions creating thermo-emf. However this can be removed by averaging over the readings taken by reversing the DC current. Obviously this makes the experiment slower.
- ii. Instrumental Limitation: Usually low voltage DC signal detection requires costly equipment and is slower (vis-a-vis same order of AC signal).

On the other hand, an AC measurement technique has no thermo-emf problem. If a Lock-in-amplifier(LIA) is used, it offers much better signal to noise ratio. (An LIA of 1 nV resolution does not cost as much as a DMM of same resolution). An AC measurement is fundamentally more versatile as;

- i. it offers study of frequency response.
- ii. it offers study of complex resistivity (or conductivity).

In figure 2.1 the schematic of the four probe AC resistivity measurement system has been shown. The lock-in-amplifier used here is EG&G make model 5210(dual phase) which offers

resolution of 1 nV and signal to noise ratio (SNR) of 120 dB. This model offers full computer-interface through IEEE bus making it a potential tool for low signal experiments.

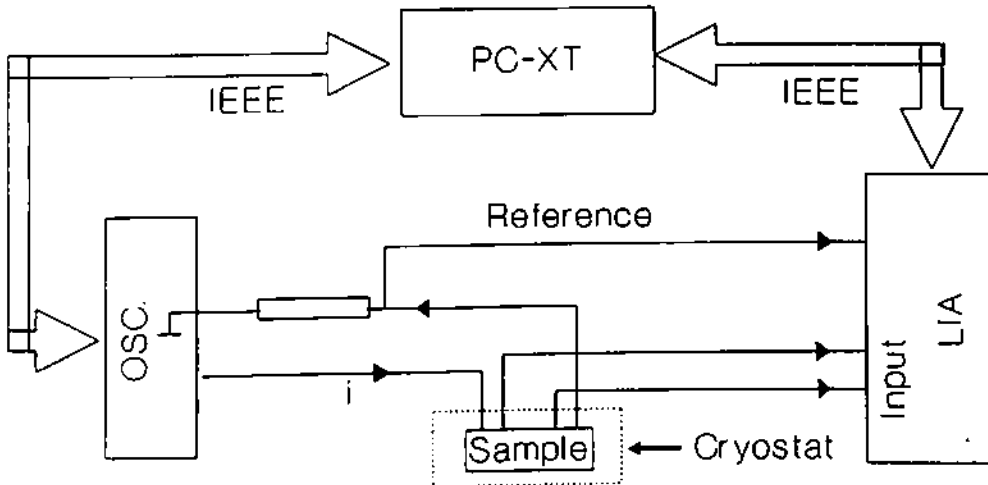


Figure 2.1: Schematic for AC four probe resistivity measurement.

2.1.2. AC-RESISTIVITY AS A FUNCTION OF TEMPERATURE :

Resistivity as a function of temperature is the most obvious study to determine the critical temperature (T_c) of the material. At critical temperature, resistivity shows a sudden steep decrease (in the cooling mode) indicating the point of transition[5]. However, as discussed in chapter 1, in high temperature superconductors this transition is not sharp and hence an artificial definition has to be introduced[5,6], viz., point of onset of transition (T_{con}), point of vanishing resistivity (T_{c0}) etc. There is no agreement, however, as to which will be the right one.

Precise measurement of resistivity as a function of temperature requires thermodynamic equilibrium at the point of measurement. Thus a quasi-static variation of temperature is a must. In practice resistivity measured by quasi-static method is time consuming. Thus measurement is carried out in a continuous slow cooling (or heating) mode. However, accurate measurement of resistivity as a function of temperature is to be done in a quasi-static mode only.

A. SIMPLE ARRANGEMENT FOR CONTINUOUS COOLING (HEATING):

In figure 2.2 a simple design has been shown. Sample was pasted on the copper block(A) by varnish. The copper container(B) could be tightened to the sample holder side by thread. All the electrical connections for sample as well as thermocouple and Pt-100(platinum resistance thermometer) were taken out through the stainless steel tube leads . The whole tube was sealed through out its length (1 meter approx.) by a rubberized chemical. Thus the space inside the sample chamber could be evacuated to a vacuum better than 10^{-1} tor. Before measurement small zirconia balls (around 50 gm) were kept inside the chamber which absorbed the humidity on dipping inside the liquid nitrogen dewar and saved the samples from moisture. However, the lowest temperature that could be reached was only 80-82 K. But it was sufficient for the experiments concerned here.

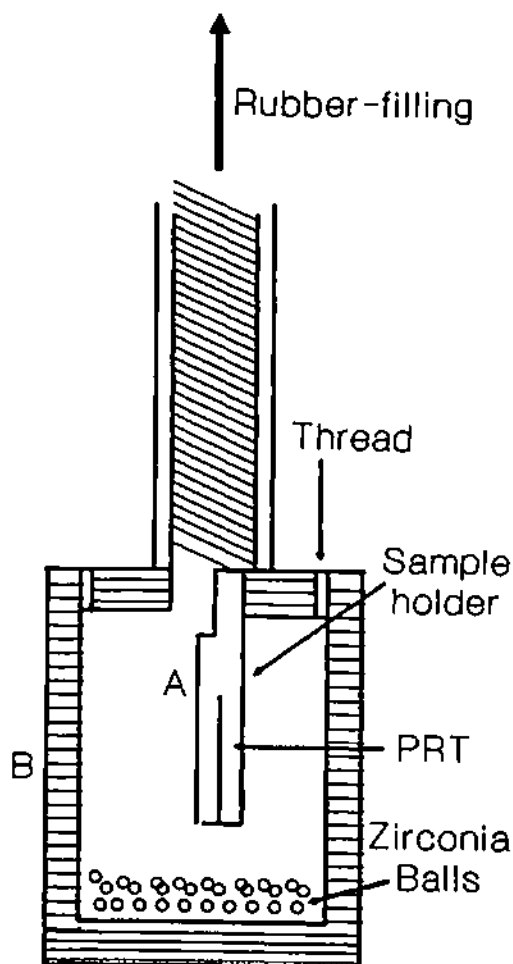


Figure 2.2: Simple arrangement for slow but continuous cooling or heating.

B. THE CRYOSTAT:

For accurate measurement of resistivity vs. temperature a simple cryostat has been devised. In figure 2.3 the schematic diagram is given. The nozzle(A) at the bottom of

the main chamber is the most important part of the design. Ultra dry Nitrogen was passed through this nozzles within the chamber which could be controlled by the valve(B). All the electrical connections were through hermetically shielded BNCs(C).

Vacuum was obtained by rotary pump of larger capacity. The operational steps were;

B1. Cooling down to 80 K:

i. After closing all the valves rotary pump was started.

ii. The valve was opened to allow a full N_2 gas flow to flush out water vapour, CO_2 etc.

iii. The valve was closed and had to wait for maximum vacuum to reach.

iv. Liquid nitrogen was poured in.

v. If this was continued for sufficient time temperature could settle around 80 K.

B2. Cooling below 80 K:

i. Same steps as above were taken till a temperature of 80 K was reached.

ii. The valve was opened all on a sudden to allow full flow of N_2 gas. Within 2-3 minutes the temperature fell down to 63 K (triple point of nitrogen). Sometimes a few cycles of the above steps were required to go down to 63 K.

iii. The N_2 flow was continued and temperature increased and settled at 77 K.

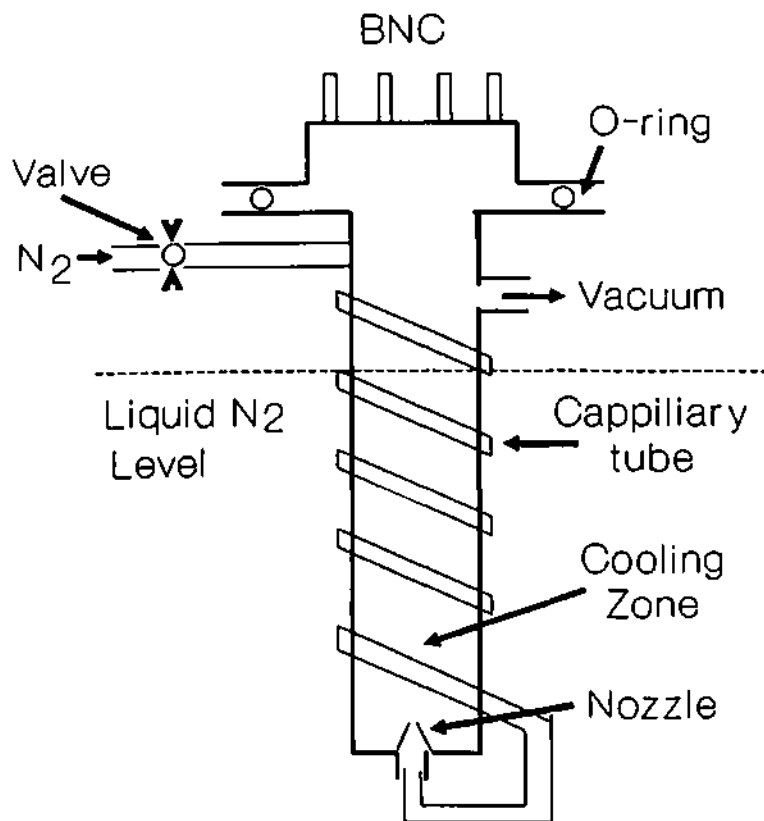


Figure 2.3: Schematic diagram of the cryostat.

B3. Heating mode:

Actual data acquisition was done only in the heating mode which gave better thermal stability.

- i. After going to the lowest temperature the computer controlled heater was put on to obtain programmed temperature and held it for as long a time as required for the measurement at that point of temperature.
- ii. Above 80 K the gas flow was required to be stopped and heater was run with new "PID" parameters.

B4. Temperature Stability:

Temperature stability in heating mode was 0.1 K.

B5. Resolution:

Resolution of temperature measurement was 0.1 K.

B6. Cooling below 63 K - down to 50 K !

It was quite interesting to see that this cryostat could go down to 50 K. However, working within this range was not reliable because this was a short duration process. The operational steps were:

- i. The lowest temperature of 63 K was reached as described above (in point 2. Cooling below 80 K).
- ii. All on a sudden the valve was put off and N₂ flow was stopped. It was seen that temperature started to go below 63 K.
- iii. This situation was continued till 49-50 K was achieved. Sometimes it was required to repeat this process for a few cycles. Time to reach 50 K was only few minutes. It must be noted here that in usual process of boiling off of liquid nitrogen, it takes quite a long time to go below 63 K.

iv. If this situation was continued for a long time (around 10 minutes) temperature started to rise and gradually reached a temperature around 80 K as in the first step.

2.1.3. V-I MEASUREMENT AT DIFFERENT FREQUENCY AND MAGNETIC FIELD:

Measurements of V-I at different frequencies were done at different magnetic field. Usually I-V measurements (An rms current of 1 to 5 amp was used in the experiments concerned here) faced serious problem from high contact resistivity[6,7-23]. Moreover, the generation of high alternating current was also a technical difficulty. The problem of high AC had been solved by designing a voltage to current converter which took the oscillatory voltage as input and gave proportional current through the sample. The contact problem was considered seriously and low resistivity contact was achieved as described below. Figure 2.4 is showing the experimental configuration.

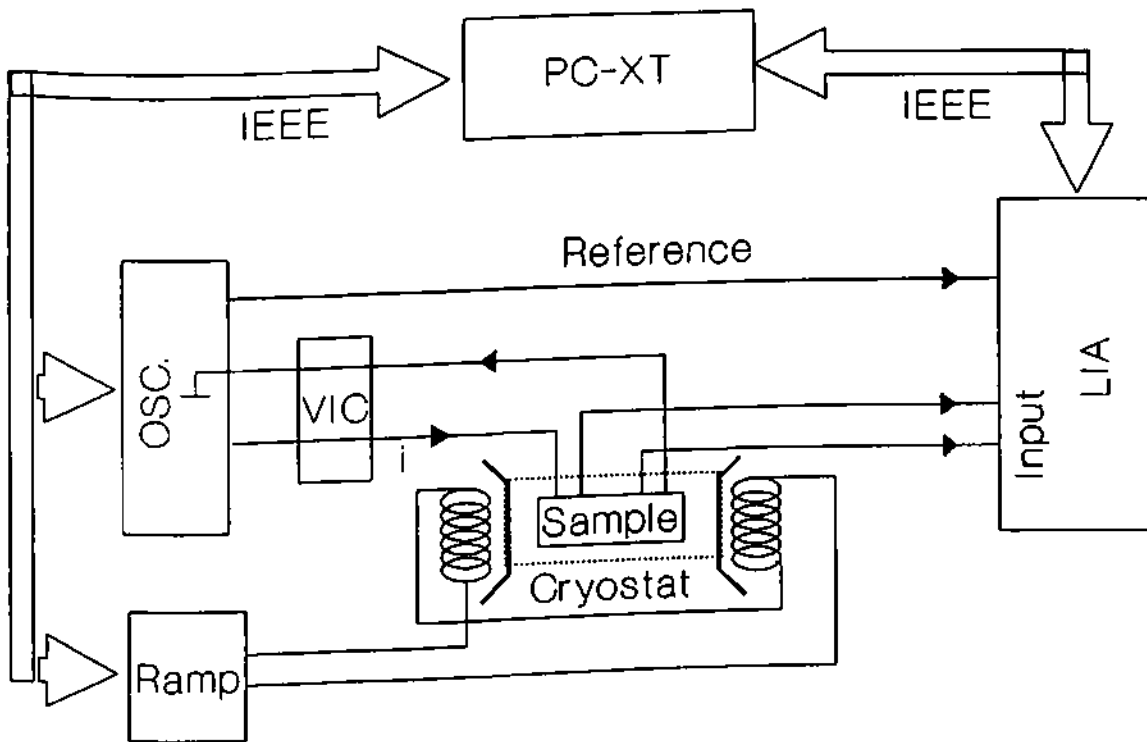
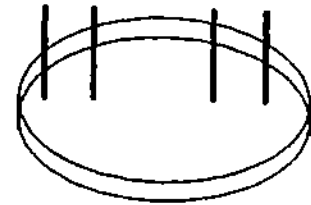


Figure 2.4: Experimental set-up for I-V measurement.

A. DEVELOPMENT OF LOW RESISTIVITY CONTACTS:

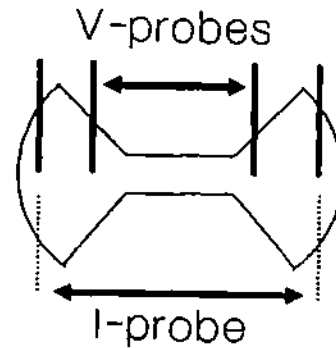
Low resistivity contact was developed by [24] co-sintering of the contact silver wire fixed with the sample which gave a resistivity of $\approx 10^{-6}$ ohm.cm². The contact configuration has been shown in figure 2.5. For resistivity measurements the whole pellet could be used. However, for J_c measurements, the pellet was grooved as shown in figure 2.5.



Full Sample

B. MEASUREMENT OF CONTACT RESISTIVITY:

Measurements of apparent contact resistance was done by usual three probe technique.



Grooved Sample

C. HIGH CURRENT AC SOURCE (VOLTAGE TO CURRENT CONVERTER):

As high current AC source with variable frequency was not available, a voltage to current converter was fabricated which gave very less distortion upto a frequency of 10 KHz and reasonably low distortion upto a frequency of 30 KHz. Though the harmonics contribution was not studied directly, it was likely to be negligible being a push-pull type of configuration of the amplifier. While discussing the data in chapter 4, it will be seen that indeed the harmonics generation was not present.

Figure 2.5: Contact configuration.

2.1.4. HYSTERESIS OF MAGNETO-RESISTANCE:

In chapter 1, the hysteresis of $J_c(H)$ of high temperature superconductors has been discussed. Here instead of directly studying $J_c(H)$ hysteresis, hysteresis of the magneto-resistance was performed. Obviously this data could be converted to $J_c(H)$ by assuming some functional

of $J_c(E)$. In order to perform the experiments involving the hysteresis of magneto-resistance, the I-V set up as above was modified by replacing the constant magnetic field with a continuously variable (ramp) or quasi-statically variable magnetic field and continuously monitoring the voltage at a given constant sample current. The ramp was designed based on an analog integrator. The ramp was not linear near the zero-cross over point and was quite slower in the this region. In fact this is an inherent problem with an ordinary integrator. It will be seen, while discussing the data, that this was essentially not a problem because of nominal dependence of the data on the ramp rate.

A. DESIGNING THE RAMP FOR CONTINUOUS FIELD:

An analog input was fed into an analog integrator and the output was used to drive a pair of power transistors (TIP142, TIP147) through one intermediate current boosting by another pair of TIPs (BD 167,168). Care was taken to avoid zero-cross over distortion by proper biasing by diodes.

- i. Inductive load of a solenoid is difficult to drive in the constant current mode.
- ii. Thus the inductive load of the coil was not included in the feed back loop.
- iii. This made it possible to reach zero current while ramping the field, to and fro.

B. QUASI-STATIC FIELD:

For the quasi-static field generation, a programmable constant current source (Keithley model 228A) was used. As discussed above it was difficult to realize a proper zero current state in this mode.

C. MEASUREMENT OF MAGNETIC FIELDS AND ADJUSTMENT FOR HYSTERESIS OF POLE PIECES.

i. Solenoid:

In this case the field was calculated from the measured current (field was not measured directly). Further the problem of hysteresis of the field itself was not present.

ii. Electromagnet:

Magnetic field was calibrated against the drive current. Hysteresis for the pole gap was corrected by polynomial fitting for increasing and decreasing fields separately.

Obviously for different maximum field excursions the fitting parameters were different. A typical calibration curve is shown in figure 2.6.

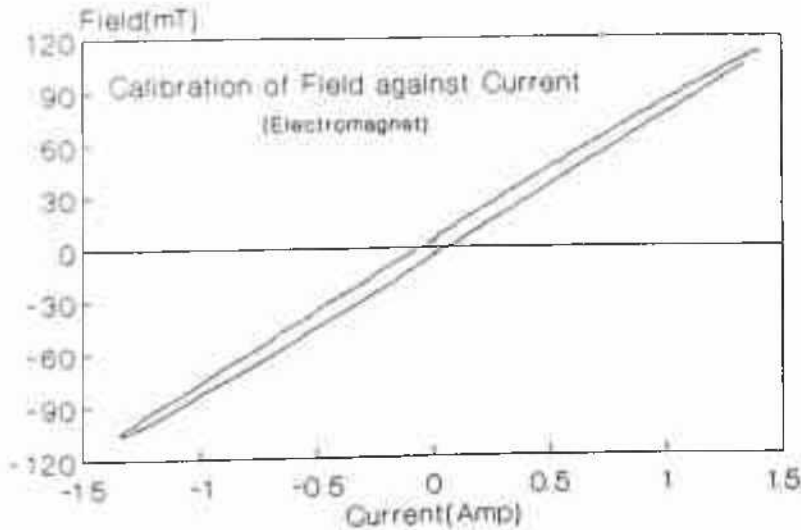


Figure 2.6: Magnetic field calibration against drive current.

2.2. MAGNETIC MEASUREMENTS:

Measurements of AC susceptibility as a function of temperature, frequency, amplitude of AC excitation or DC bias field superimposed on the AC field are the most important and common experimental tools used in the study of superconductivity. The importance of AC susceptibility over the DC one, is due to the fact that here one has more parameters viz., frequency, amplitude, DC bias field superimposed on the AC field, to vary to probe into the complex nature of the magnetic properties. A detailed discussion of the experimental aspects of AC susceptibility has been compiled by R. A. Hein et al[1].

2.2.1. MAGNETIC AC SUSCEPTIBILITY MEASUREMENTS:

The principle of measurement of AC susceptibility is simple. The basic experimental arrangement is given in figure 2.7. The primary was driven by the in-built oscillator of the Lock-in-amplifier(LIA -model 5210 EG&G). The output of the secondary was detected by the same LIA as above which was capable of giving the two phases simultaneously. The frequency, amplitude and all other parameters of the LIA were controlled through a computer. The readings were also continuously monitored by the computer.

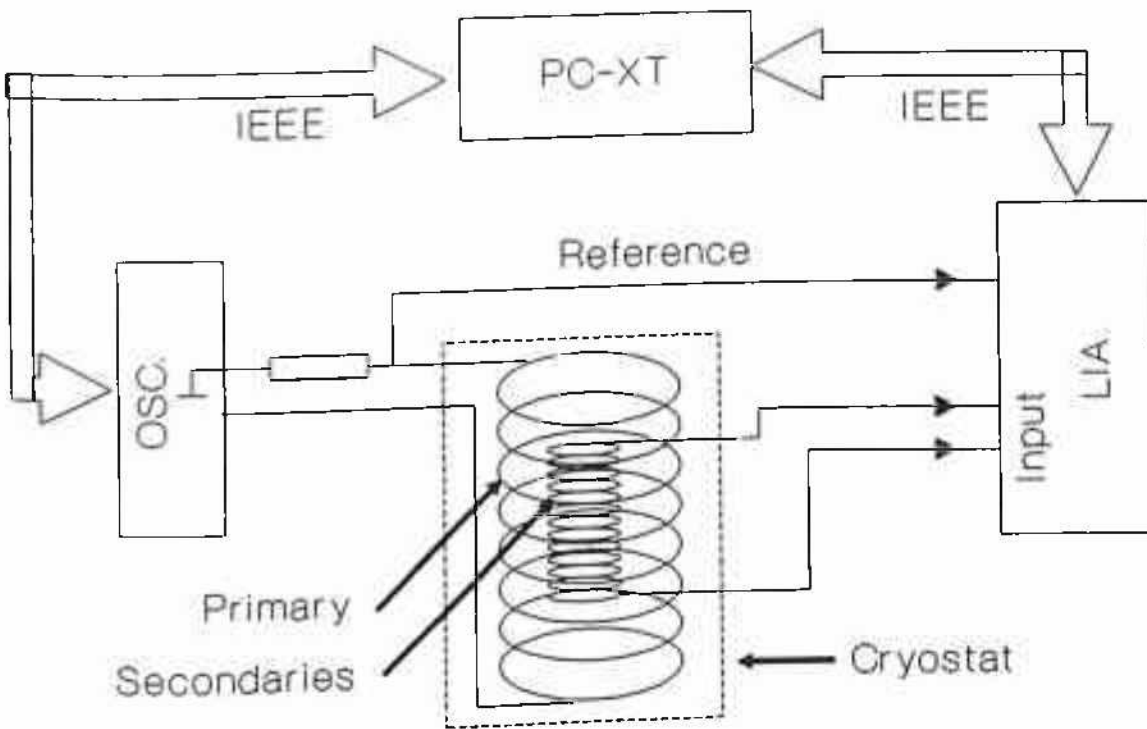


Figure 2.7: Schematic of the experimental set-up for AC susceptibility measurement.

A. BASIC PRINCIPLE:

The basic principle is simple and is based on the lock-in-detection of the change in the mutual inductance produced in the oppositely wound coils by the presence of a magnetic sample[25]. When in the absence of the sample, a current $i_{ac}(t) = i_0 \cos(\omega t)$ is passed through the primary coil because of the non-exact

compensation of the coils and a background emf, $U_b(t)$, is always present,

$$\begin{aligned} U_b(t) &= (M_1 - M_2) di_{ac} / dt \\ &= -(M_1 - M_2) i_0 \omega \sin(\omega t) \end{aligned} \quad (2.1)$$

where M_1 and M_2 are the mutual inductances of the two secondaries with the primary. When a magnetic sample is placed in one of the secondary coils the mutual inductance changes and a new term, U_s , appears and is given by,

$$U_s(t) = -N_1 S_1 f \chi_{ac} dh_{ac}(t) / dt. \quad (2.2)$$

where N_1 and S_1 is the number of turns and cross-section of the first coil i.e., sample coil. Thus the total emf from the pair of secondary is, $U_t = U_b + U_s$. Thus by noting U_t and U_b one can find out U_s easily.

Obviously, the real(χ') and imaginary(χ'') parts of AC susceptibility, will be proportional to the in- and out-of-phase components of the secondary output as below,

$$\begin{aligned} \chi' &\propto \frac{V'}{fh} \\ \chi'' &\propto \frac{V''}{fh} \end{aligned}$$

Though the principle is simple, it is very often masked with different stray effects which must be looked into carefully for an accurate measurement.

1. Right frequency that one can work safely: As one can see from eqn. 2.1 that the background emf, U_b increases linearly with frequency provided M_1 and M_2 are unequal which is most practical case. Thus at higher frequency due to higher U_b values one has to work at higher scale i.e., lower gain of the amplifier (and so lower

sensitivity). If U_s is less or comparable to U_b , this artifact may lead to a situation where one ends up with wrong interpretation of data, possibly indicating reduction of susceptibility signal with frequency. Thus some sort of compensation is required to reduce the signal before passing to the amplifier. Though electronic balancing circuit can be utilized, they are avoided because: i). they are costly, ii). add further noise, iii). difficult to automate, iv). time consuming.[26]

2. Lower Frequency Limit: The lower limit of detection is set by the gain of the amplifier. As one can see by increasing the number of turns in the secondary this limiting frequency can further be push down. However, as can be seen in the next paragraph this will also bring down the upper limit of the safe frequency.
3. Upper Limit of Frequency: The presence of inductance of the coil as well as self capacitance leads to presence of a resonance frequency. As this resonance frequency is approached, U_b increases dramatically[26]. On the other hand, the sensitivity is reduced by partial capacitive shortening of the coils, obviously thus decreasing number of turns in the coils will increase the upper limit of frequency.

B. DESIGNING THE SOLENOID COILS:

1. Primary: In order to get uniform field over the sample length uniform winding of the coil is important. This has been achieved by winding in a semiautomatic winding machine on a well finished hylam former of dimension given in Table. 2.1.
2. Secondaries : The two secondaries were designed to the maximum

possible similarity. They were separated by 3 mm. In order to reduce the capacitive coupling of the coils (between the primary and the secondaries) the two secondaries were wound on separate hylam former(single piece). The secondary pair was inserted within the core of the primary with slight tolerance such that they can be moved with respect to each other. One small quartz bucket was placed in one of the secondary for holding the cylindrical sample.

Table-2.1
(Specifications of the coils)

Parameters	Primary	Secondaries
Length(mm)	40	5x2
Inner diameter(mm)	11	4
Outer diameter(mm)	16	11
No. of turns	500	2x450
Wire diameter(mm)	.08 (#46)	.08(#46)
Resonance frequency	40 KHz	

C. BALANCING THE COILS: It is impossible to produce a perfectly uniform field within the primary core. This non-uniformity was, in fact, utilized here for balancing the coil. If the secondary pairs have good enough similarity, i.e., they have same resistance and give almost same mutual inductance with respect to the primary, then by moving the secondaries with respect to the primary over the non-uniform field of primary, one can have rest of the balance. However it is impossible to have balance over the full range of frequency. Therefore after balancing at a suitable

frequency, preferably at low frequency range (where proper balancing is more important) the secondary coils were fixed permanently using GE varnish.

2.2.2. AC Susceptibility As A function of Temperature:

The whole coil set-up was placed within the cryostat described earlier and subjected to programmed temperature in quasi-static mode and the output from the was monitored dynamically. All of the necessary software was developed by the author only. The following points are important and were considered in the experiments,

1. Temperature Uniformity: The requirement of temperature uniformity over the full length of the solenoid was achieved by designing the whole coil set-up as small as possible because the other means for achieving the same i.e., larger uniform zone in the cryostat was beyond scope of present set-up.
2. Minimization Of Resistive Imbalance Between The Secondaries: Large resistive mismatch between the secondaries leads to temperature dependent offset i.e., U_b becomes function of temperature and measurements become difficult. Thus uniform solenoid wire was taken and moderate numbers of turns were wound keeping in mind the range of frequency. Obviously if number of turns were high then resistive balance could be easily achieved.
3. Temperature Stability: The cryostat could give a temperature stability of 0.1 K (max) over a time window of few minutes. This was sufficient to take average of large number of data points at a given temperature.
4. Signal To Noise Ratio: Though the LIA was capable of giving signal to noise ratio better than 10^5 (120 dB), it was not possible to achieve the same in true

sense mainly because the rotary pump for the vacuum requirement added strong noise to the actual signal. In fact by putting the rotary pump off and compromising for temperature stability one could decrease the noise. Better solution is to provide proper isolation of the vacuum system and use of low-noise pump which was not available at the present time.

5. Arbitrary Scaling: It is almost impossible to design an AC susceptometer which can give absolute measurements without proper calibration with a laboratory standard (LS) magnetic sample. As getting a LS for diamagnetic calibration in temperature range of 77K and onward is difficult, we had to be happy with arbitrary scaling and relative measurement. However as can be seen in the following chapters, a good amount of information can be gathered from these measurements without scale calibration.

2.2.3. AC SUSCEPTIBILITY AS A FUNCTION OF SUPERIMPOSED DC BIAS FIELD - $\chi'(H)$ AND $\chi''(H)$:

Measurement of AC susceptibility as a function of DC bias field is relatively new. These measurements form a major part of this thesis.

If a large enough DC field is superimposed coaxial with the AC field, the situation can be simplified as being traversing of minor loops by the AC field at different DC fields. The same extension become obscure in the case where the fields are mutually perpendicular.

The experimental set-up was same as that used for $J_c(H)$ hysteresis shown in figure 2.4 with exception that the sample was replaced by the solenoid set including the sample. The DC bias field (parallel or perpendicular to the AC field) is changed continuously or quasi-statically and real and imaginary parts of voltages from the secondary were monitored keeping the whole sample and coil set-up immersed in liquid nitrogen. The basic modules have already been discussed. Some further points to be considered are:

1. Uniformity Of DC Bias Field Over The Sample Length: This is important and was achieved by using smaller sample (usually 2.5 to 3 mm). In case of electromagnet uniformity was easy to achieve but for the solenoid (to generate

coaxial DC field) which was hand made and 10 cm long uniformity was not good.

2. Time Constant of LIA and Ramp Rate of Bias Field: The experimental results on ramp rate dependence can be obscured by the experimental limitation set by the integration time of the LIA. If the time constant was set too low reading was faster and followed the magnetic field closely but there was an increase in the noise. But on the other hand an increase in the time constant introduced a lag between the correspondence of magnetic field and the LIA output because of the ramping of the field. However, as will be seen in later chapters the ramp rate dependence was only nominal.
3. Non-Linearity at Zero-Cross-Over in the Ramp Field: Because of the logarithmic time dependence in ordinary analog integrator, the field variation at the zero-cross-over became quite slow. Thus zero-cross-over region had a very slow ramp rate as compared to the higher field region where it was linear. But since the ramp rate dependence of the sample response was negligible, the zero-cross-over problem did not affect the data.
4. The Problem of Arbitrary Scaling: Though arbitrary scaling and relative measurements are most often used, here it has created some confusion in explaining the data. As one of the aims of the experiment was to find out frequency dependence, if any, in this class of materials, the algorithm of the software was in that orientation. Maximum care was taken to exploit this aspect. Thus it was required to maintain all other conditions same while frequency was varied for a given sample. As there was no automated sample exchanger it was very difficult to preserve the same condition for different frequencies if the sample was taken out every time for offsetting the background emf, U_b . Thus it was required to make an arbitrary offsetting and measure the change of χ' (or χ'') as a function of field. This surely should reflect the possible change due to different frequencies. However as one can visualize, this arbitrary "offsetting"

can give some problem in interpreting the data.

2.2.4. SUPPORT FOR FREQUENCY DEPENDENCE STUDY OF $\chi(H)$:

The study of frequency dependence of $\chi'(H)$ and $\chi''(H)$ in this experimental set-up requires further justification. As discussed above for a given coil set there is a resonance frequency[25,26] where the response becomes non-linear. Further, there is a phase reversal by 180 degree at this resonance frequency[25]. Moreover closer to the resonance frequency, due to capacitive shorting between the primary and secondary, time dependent stability is greatly reduced[26]

In figure 2.8 one typical frequency response of a unbalanced solenoid has been shown where ratio of the moduli of signal with a standard sample and with out any sample (i.e., the offset, $U_b(\omega)$) has been plotted as a function of frequency. The peak corresponds to the resonance frequency. It shows that with the increase of frequency, offset overtakes

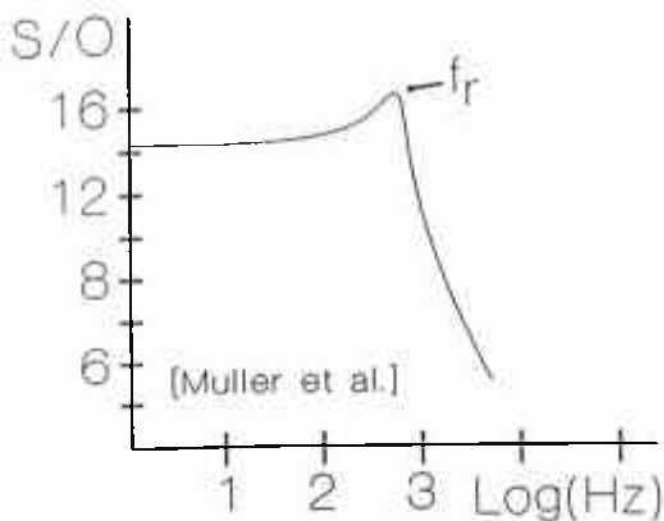


Figure 2.8: Frequency vs. ratio of moduli of χ with LS to the offset of the empty coil.[taken from P.H. Muller et al.]

the sample signal. If the ratio gets too small, the reproducibility of the experiment suffers, because noise and apparatus drifts are mainly proportional to the overall signal [26].

With this in mind it is important to go into the exact experimental situation here. As already discussed the whole exercise was aimed at possible frequency dependence of $\chi'(H)$ or $\chi''(H)$ and the experimental steps were as follows,

- i. Samples were put in the quartz bucket. The whole arrangement was put within the magnetic field and liquid nitrogen was poured (FC case).

- ii. The frequency and amplitude of AC excitation field were set at required values.
- iii. Both the channels were offset by in built utility of the LIA.
- iv. The field was then cycled and outputs from the x,y channels of the LIA were continuously monitored.
- v. After one full cycling of the DC field excursion, the same cycle (steps iii to iv as above) was repeated for the next frequency.
- vi. After full range of frequency scan, frequency was set to the lowest value and amplitude was set to new value and the same cycle (step iii to v as above) was repeated.

Usually for experimental easiness offsetting was done at the highest field. Now after offsetting the reading to zero in both the channels(V' and V'' , $V'(H)$ and $V''(H)$) started varying with DC field. Thus if one plots this variation as a function DC field, there should be no effect of the solenoid. Further one should note the following points,

- i. The offset of the empty coil was independent of DC bias field for frequency less than 50 KHz.
- ii. Above 50 KHz though the curves were straight lines(almost parallel to field axis) but sometimes the two lines were not close showing strong apparatus drift.

It is instructive to consider a specific case e.g., at 57770 Hz. The offset was seen to be 1.2 mV in the real part and 8 mV in the imaginary part where as the total change in signal for a field change of 100 mT was about 6 mV in real part and 8 mV in the imaginary part [because the imaginary part was measured in the x-channel with an additional gain of 10 as available in the LIA here]. Thus even at 57770 Hz the total signal was around 10% of the full scale of measurement. This was not too low to be masked by noise or drift. In fact, as will be discussed in results section, the dependence on frequency showed systematic dependence on sample properties indicating the fact that the frequency effect as observed in the experiments here was not an artifact of measurement.

This point of argument may further be strengthened by considering figure 2.9, where the plot of the offset in the absence of sample and the ratio of the signal magnitude of a ferrite sample to the offset of the empty coil as a function of frequency has been given for the solenoid considered here. The ferrite was tested to have little frequency dependence below 100 KHz. It is clear from the figure 2.9 that the offset was almost linear upto a frequency of 60 KHz and also in the other graph, ratio of the signal (of the ferrite sample) to the offset (of the empty coil) remained almost independent of frequency below 50 KHz and did not change drastically even above 50 KHz.

Further, there is another point in support of high frequency measurements. It is clear from above discussion that if there was any effect due to high frequency, this was in all possibility, going to reduce actual signal contribution. However, as will be seen latter in the results section, that depending upon amplitude of AC excitation the total change of $V'(H)$ and $V''(H)$ signal for full excursion of DC field increased with frequency for some samples. All this argument, in all possibility, indicates that a systematic study of frequency dependance is possible even in this experimental set-up.

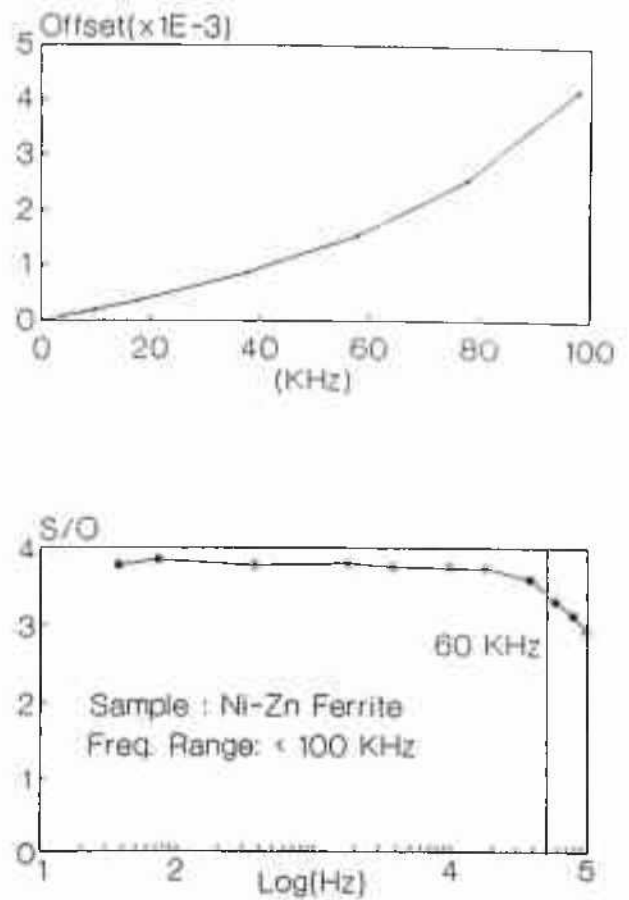


Figure 2.9: Frequency response of the coil set-up.

2.3. SAMPLE PREPARATION AND INITIAL CHARACTERIZATION:

A systematic study requires a systematic series of samples. This is further important in this work, because the thesis involves the measurements which are relatively new and not yet exploited for studying of sample properties. Moreover, there is a model calculation included in this thesis which is required to be verified for some of its predictions. Obviously, a study on a systematic sample series will make the job much simple.

2.3.1. SAMPLE PREPARATION - CERAMIC ROUTE:

As the thesis is about ceramic superconductors, the basic preparation technique was ceramic route as shown in the flow chart in figure 2.10. The main features of the technique were;

A. WEIGHING OF DIFFERENT POWDERS IN STOICHIOMETRIC RATIO:

The basic raw materials were high purity powders of Yttrium Oxide(Y_2O_3), Barium Carbonate($BaCO_3$), Copper Oxide(CuO) and Lead Oxide(PbO). As the nominal composition of the product was $YBa_2Cu_3O_{7-x}$, the mole ratio in which the oxides were taken was ($\frac{1}{2}$ mole of Y_2O_3):(2 moles of $BaCO_3$):(3 moles of CuO).

B. MIXING OF THE POWDER:

In order to have homogeneous mixture of the powders in order to ensure a better calcination output, mixing was dry ball milled using

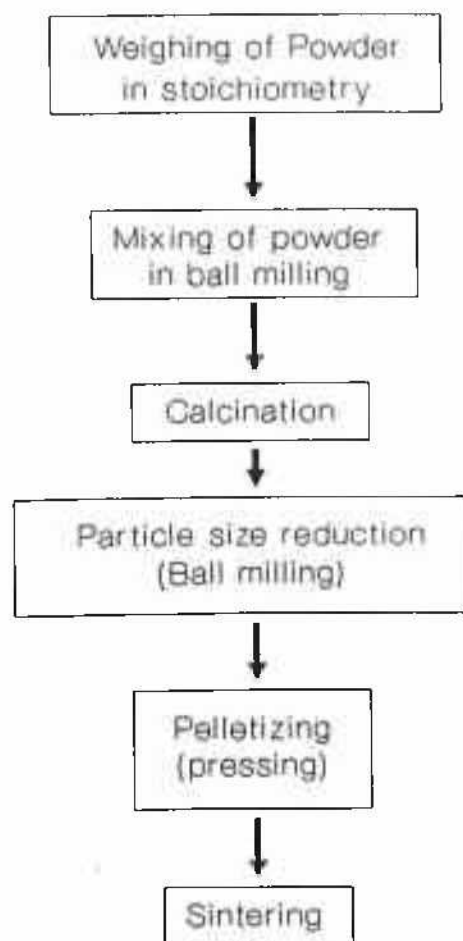


Figure 2.10: Flow chart of ceramic processing.

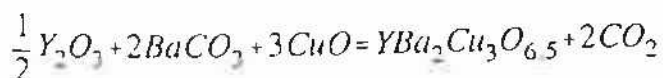
poly-propylene jars with yttria-stabilized- zirconia balls. Usual time of ball milling was 24 hours.

C. CALCINATION OF THE MIXTURE:

The aim of this step was to achieve;

- * complete chemical reaction,
- * homogeneous powder.

The reaction concerned is given by,



Usual calcination temperature is 100 to 200 degrees centigrade below the sintering temperature. The calcination temperature is usually determined from the following two first principles,

- * Too less a temperature : chemical reaction will be incomplete.
- * Too high a temperature : Too hard a material for the next step of particle size reduction.

All the powders concerned in this thesis were calcined at 890° C for 24 hours.

D. PARTICLE SIZE REDUCTION: Particle size reduction was done once again by the same ball milling arrangement. The aim of this step was to ensure a suitable particle size distribution to ensure;

- * required densification,
- * appropriate microstructure.

The average particle size in this work was 1.2 micron.

E. PELLETIZING: In this step of pelletizing, the powder was compacted into the required form using a laboratory hydraulic press. In this work all the samples were prepared in pellet form (tablet of 10 mm diameter and 2 to 4 mm thickness).

F. SINTERING: The most important and the final step of the ceramic route is the sintering.

The aims of this step were;

- * Completion of uncompleted reaction in calcination process: If some reaction was left incomplete in calcination step, it would be completed here.
- * Formation: The loose particles formed a compact shape.
- * Densification: The required densification could be achieved by selecting right temperature and time schedule.
- * Microstructure: This includes i). grain size, ii). porosity, iii) other phases.
- * Maintaining right Oxygen stoichiometry: The final product was $\text{YBa}_2\text{Cu}_3\text{O}_{7-x}$ ($0.5 < x < 1$). The value of x determines the T_c of the sample. For $0.5 < x < 1$ the T_c is close to 90 K and is important for the work here.

2.3.2. LIQUID PHASE SINTERING OF YBCO IN PRESENCE OF PbO:

Liquid phase sintering is a well known technique in material science to activate microstructural change in ceramic processing. As microstructure plays an important role in determining the current carrying properties of superconductors, here the aim of adding PbO was to modify the microstructure in the required way - to give better grain to grain connectivity, uniform grain growth and possible texturing if at all.

A. CONFIRMATION OF PRESENCE OF LIQUID PHASE IN YBCO-PbO MIXTURE:

PbO has melting point (886°C) which is lower than the usual sintering temperature ($900-940^\circ\text{C}$) of YBCO. Different weight percents of PbO were added in well calcined YBCO powder and mixed thoroughly. This mixture was subjected to simultaneous TGA/DTA study. In figure 2.10 the TGA/DTA curve is shown. It is apparent from the figure that there was a phase transition peak at 886°C , i.e., at melting point of PbO. The small peak at 805°C was for phase transformation of BaCO_3 . Thus there was no reaction of YBCO with PbO. In fact the same

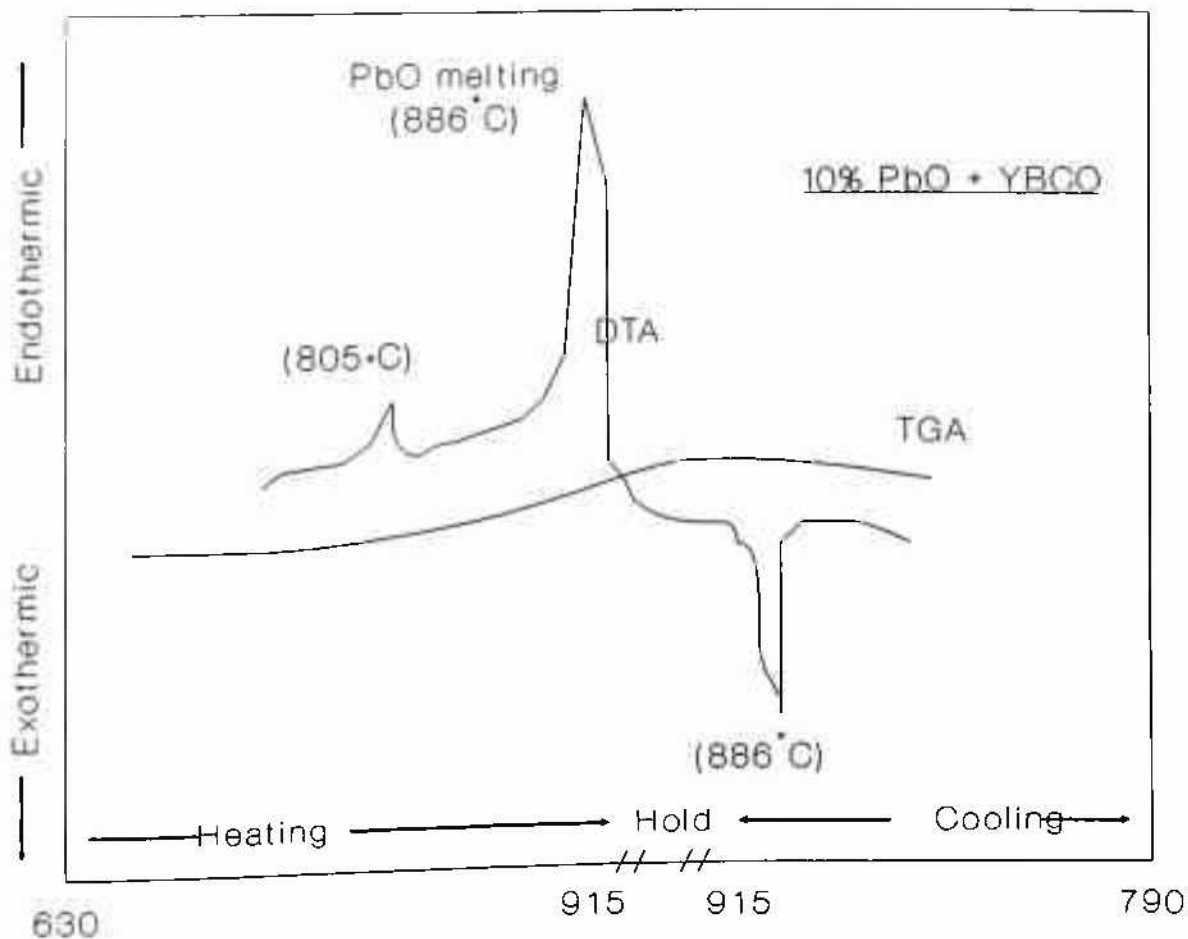


Figure 2.11: TGA/DTA of YBCO+PbO showing presence of solid-liquid phase formation.

experiment was repeated for other oxides e.g. Sb_2O_3 , V_2O_3 and Mo_2O_3 (all having melting points below the sintering temperature of YBCO) but all of them showed strong reactions with YBCO. Thus PbO was selected as the liquid phase sintering agent.

B. PREPARATION OF PbO DOPED YBCO SAMPLES:

1. **PREPARATION OF BASE MATERIAL(YBCO):** The base material was calcined YBCO as described above. Calcination was done in two steps. After the first calcination at 890°C for 24 hours the material was cooled and ball-milled for 24 hours and then once again subjected to a firing of 24 hours at 890°C . Final

ball milling was done for 24 hours and particle size was measured. Average particle size was 1.2 μm .

2. **DOPING OF PbO IN YBCO:** 0.8, 2, 4, 6, 10% (by weight) PbO was added to the calcined YBCO and mixed thoroughly by ball milling in smaller poly-propylene bottles in propanol medium for several hours.

3. **PRESSING AND SINTERING:** Dried powder with different PbO content were pelletized and sintered for different time and temperature schedules. For all the batches rates of oxygen flow were fixed at 30 cc/min. and rates were also same and were 20°C/hour. The Time and temperature schedule is given in Table. 2.2.

Table-2.2 (Sintering Schedule)		
Batch	Temperature(°C)	Time(Hour)
A	930	16
B	920 600(anneal)	24 6
C	940 600(anneal)	24 6
D	945	24

2.3.2. BASIC CHARACTERIZATION:

1. R-T measurements:

The first characterization was to determine the T_c . The T_c was determined by plotting resistance of the sample as a function of temperature. Exact measurement technique have already been described above. The results from the R-T measurements are;

- i). There was no observable variation of T_c as a function of PbO content. Even though there was a variation of ± 1 K, it could not be correlated to PbO content.

- Probably, the variation in the T_c was due to slight variation in oxygen content.
- ii). All the samples in all the batches had almost same T_c which was within 90 to 92 K(T_{co}).
 - iii). There was a minimum in normalized room temperature resistivity close to PbO content of 0.8% to 2.0%. This was seen in all the batches. This was probably because of improvement in densification due to liquid phase sintering. At higher concentration of PbO, the grains became coated with insulating PbO layer and hence resulted in higher resistivity.

2. AC SUSCEPTIBILITY AS A FUNCTION OF TEMPERATURE:

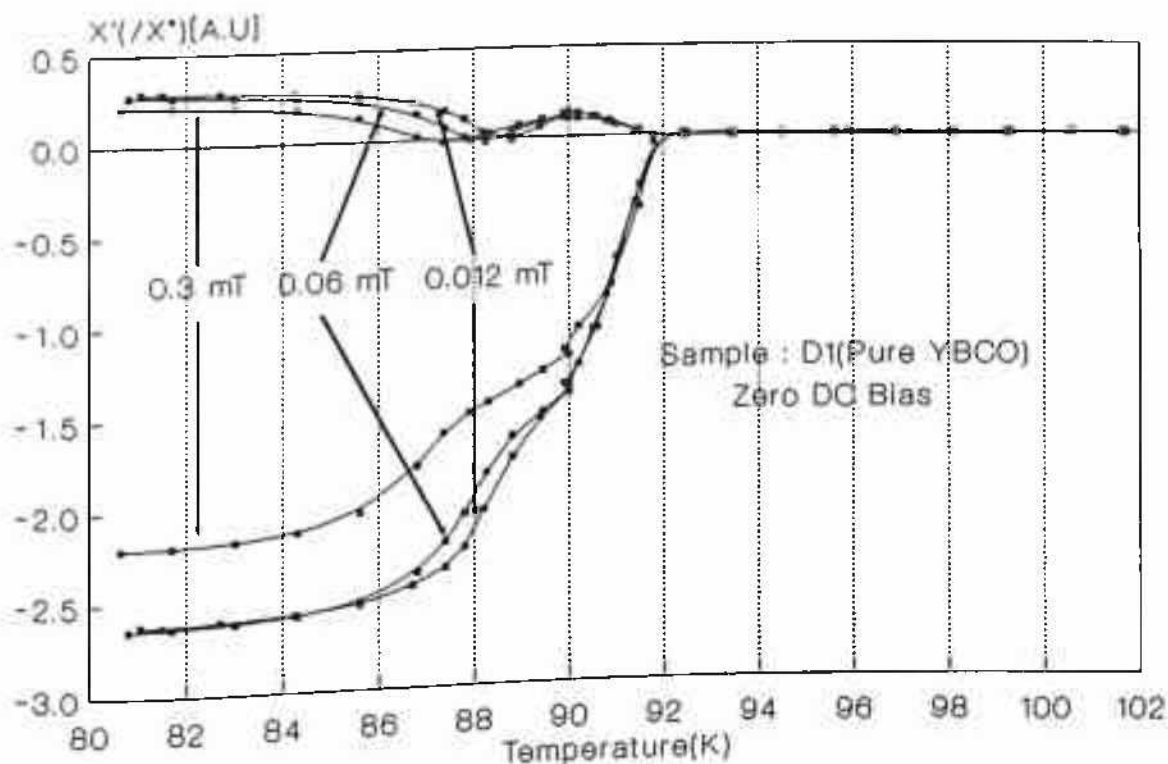


Figure 2.12: AC susceptibility as a function temperature for three AC amplitudes for a frequency of 73 Hz. (Sample: Pure of Batch D)

Magnetic AC susceptibility was measured as a function temperature. Though the studies could be utilized for a rigorous analysis of magnetic behavior grain and grain boundaries[27],

here the use was only to find the T_c . In figure 2.12 the χ' and χ'' are plotted as a function of temperature for different amplitudes and zero DC bias.

The grain and the grain boundary contributions (the peak on $\chi''(T)$ at higher temperature was due to grain and other due to grain boundary) are clearly seen on the $\chi''(T)$ curves. It is clearly seen in the figure that the variation of amplitude was to affect the grain boundary contribution because the amplitude was too low to affect the grains.

The essential result from this AC susceptibility measurements was that all samples in all batches had critical temperatures around 90 to 92 K. This data is further indicative of the fact that the coil set-up was properly balanced.

3. Volume density:

Volume density was measured by immersion method. The results of batch A have been given in table-2.3.

4. Transport J_c and Magnetization J_c :

Transport J_c was measured using 1 second pulse current and $1\mu\text{V}/\text{cm}$ criterion. Magnetization J_c was calculated by using the Bean's model formula for the slab from M-H loops at low enough field where "phase locking" was not destroyed. The M-H loops were studied by a commercial VSM at liquid Nitrogen temperature. The results for batch A have been included in the table-2.3.

5. X-ray and SEM data:

Detailed X-ray study indicated that PbO, indeed was an inert liquid phase sintering agent and showed no extra peaks than that of PbO and pure YBCO. However PbO peaks were quite weak in comparison to that of YBCO.

SEM (scanning electron microscope) study was also undertaken. The essential finding was that there was a gradual decrease of grain size including some homogeneity with increasing PbO content. However, at higher concentrations of PbO, grain boundaries were seen to contain excess PbO layer.

Table-2.3

PbO content (mole %) Batch A	Transport J_c (Amp/cm ²)	Magnetiza- -tion J_c (Amp/cm ²)	Density (gm/cc)
0.0(1)	240	340	5.69
0.8(2)	210	330	5.89
2.0(3)	165	254	5.79
4.0(4)	145	200	5.81
6.0(5)	140	200	5.64
8.0(6)	160	180	5.67
10.0(7)	120	170	5.63

REFERENCE:

- [1] Magnetic Susceptibility of Superconductors and Other Spin System, 1991 R.A. Hein, T.L. Francavilla and D.H. Liebenberg
- [2] L. Valdes Proc 1954 IRE **42**, 420
- [3] L.J. Vander Pauw 1958 Phil. Res. Reports **13**, 1
- [4] D.J. DOSS 1989 "Engineering Guide to High Temperature Superconductivity", N.York, Willy
- [5] Charles P. Poole, Jr., Timir Dutta and Horacio A. Farach 1988 ed. Copper Oxide Superconductors p.71
- [6] J.E. Evetts 1992 ed. Concise Encyclopedia of Magnetic and Superconducting Materials
- [7] L.F. Goodrich and S.L. Bray 1990 Cryogenics **30**, 667
- [8] J.E. Evetts and B.A. Glowacki 1988 Cryogenics **28**, 641
- [9] J. Talvachio 1989 IEEE Trans CHMT **12**, 21
- [10] S.T. Lakshmikummar and A.C. Rastogi 1989 Appl. Phys.A **48**, 325
- [11] J.W. Ekin, A.J. Panson and B.A. Blankenship 1988 Appl. Phys. Lett. **52**, 331
- [12] V.G. Bessergenev, N.V. Gelfond, I.K. Igumenov, S.Sh. Ilyasov, R.D. Kangiev, Yu A. Kovalevskya, V.S. Kravchenko, S.A. Slobodyan, V.I. Motorin and A.F. Shestak 1991 Supercond. Sci. Technol. **4**, 273
- [13] J.W. Ekin, T.M. Larson, N.F. Bregren, A.L. Nelson, A.B. Swartzlander, L. L. Kazmerski, A. J. Panson, and B. A. Blankenship 1988 Appl. Phys. Lett. **52**, 1819
- [14] C.L.Huang, G.Sh.Gildenblat and S.J. Fonash 1989 J.Vac. Sci. Technol. A **716**, 3371
- [15] Y.Iye, T. Tamegai, H. Takeya and H. Takei 1988 Jpn. J. Appl. Phys. **27**, L658
- [16] R. Selim, R. Caton, A.M. Bouncristiani, C.E.Byvik, R.A. Edahl,jr. and S. Wise 1990 J. Appl. Phys. **67**, 376
- [17] A.D. Wieck 1988 Appl. Phys. Lett. **52**, 1017
- [18] S. Jin, M.E. Davis, T.H. Tiefel, R.B. van Dover, R.C. Sherwood, H.M. O'Bryan, G.W. Kammlott and R.A. Fastnacht 1989 Appl. Phys. Lett.**54**, 2605
- [19] R. Caton, R. Selim, A.M. Bouncristiani and C.E. Byvik 1988 Appl. Phys. Lett **52**, 1014
- [20] N. Khare, S.K. Arora, G.S.N. Reddy, V.S. Reddy, V.S. Tomar, V.N. Ojha, N.D. Katria and A.K. Gupta 1989 Pramana-J.Phys. **33**, L333

- [21] B. Dwir, M. Affronte and D. Pavuna 1989 Appl. Phys. Lett. **55**, 399
N. Shimizu, K. Michishita, Y. Higashida, H. Yokoyama, Y. Hayami, Y. Kubo, E. Inukai, A. Saji, N. Kuroda, and H. Yoshida 1989 J. Appl. Phys. (part 2) Lett. **28**, L1955
- [22] Yue Sun and Hongchuan Yang 1991 Cryogenics **31**, 760
- [23] S. Jin, J.E. Graebner, T.H. Tiefel, and G.W. Kammlott 1990 Appl. Phys. Lett. **56**, 186
- [24] Subir Saha, R.B. Tripathy and B.K. Das 1992 Supercond. Sci. Technol. **5**, 703
- [25] C. Rillo, F. Lera, A. Bandia, L.A. Angurel, J. Bartolome, F. Palacio, R. Navarro and A. J. van Duyneveldt Magnetic Susceptibility of Superconductors and other Spin Systems ed. R.A. Hein et al.
- [26] P.H Muller, M. Schienle and A. Kasten, Journal of Mag. Mag. Mater. **28**, 341 (1982).
- [27] H. Küpfer, I. Apfelstedt, R. Flükiger, C. Keller, R. Meier-Hirmer, B. Runtsch, A. Turowski, U. Wiech and T. Wolf 1988 Cryogenics **28**, 650

A TWO COMPONENT CRITICAL STATE MODEL APPROPRIATE TO THE GRANULAR SUPERCONDUCTORS:

This part of Chapter 3 gives the description of a two component critical state model. It describes the solution of the model for M-H loops and gives a comparative analysis of results for different input parameters of the model.

3.1.1.	BACKGROUND - THE GLASSY SUPERCONDUCTOR MODEL	67
3.1.2.	IMPORTANT FINDINGS OF THE GRANULARITY MODEL	68
3.1.3.	THE CRITICAL STATE MODEL - STUDY ON M-H LOOPS	71
3.1.4.	REVIEW	71
3.1.5.	DESCRIPTION OF THE MODEL	74
3.1.6.	OUT COME - M-H LOOPS	77
A.	LOW FIELD M-H LOOPS : ANSWER TO THE ANOMALY	78
B.	THE INSIDE - HOW IT HAS BEEN POSSIBLE	78
C.	TEMPERATURE DEPENDENCE OF M-H LOOPS	83
D.	OVER ESTIMATION OF MAGNETIC J_c	83
E.	TEST FOR A TRUE TWO COMPONENT MODEL - EVOLUTION OF M-H LOOPS OVER FIELD RANGE	85
F.	EXACT FIELD DEPENDENCE OF J_{c1}	85
G.	EFFECT OF GRAIN SIZE	89
3.1.7.	SUMMARY	89
3.1.8.	PHENOMENOLOGICAL CORRECTION FOR SHIELDING CURRENT - DETAILS ON EVOLUTION OF M-H LOOPS OVER FIELD RANGE	89
	REFERENCES	94

3. A TWO COMPONENT CRITICAL STATE MODEL APPROPRIATE TO GRANULAR SUPERCONDUCTORS:

3.1.1. BACKGROUND - THE GLASSY SUPERCONDUCTOR MODEL:

THE GRANULARITY INDUCED GLASS MODEL:

Glass models[1,11,12] are in analogy to the so called magnetic-spin-glass system. We have already seen in Chapter 1, that the irreversibility line in high temperature superconductors(HTSC) has similarity with the same prediction in spin-glass by de Almeida and Thouless[5]. This similarity of this line with that of spin-glass one, has given the first clue to superconducting glass models.

A disordered array of weak links coupling together small superconducting grains is the basis of the "superconducting-glass" models developed principally by Ebner and Stroud [6]. However, a simpler version of glass model as developed by Clem[7] and also by Tinkham and Lobb [8] will be used here.

This model describes the bulk ceramic as an agglomerate of grains connected between them by some sort of "weak links". Existence of weak links is now experimentally verified through exhibition of grain boundary SQUID in polycrystalline materials[2-4]. However it is not yet certain as to what the origin of weak links is. But beyond doubt, unclean grain boundary, miss-orientation between adjacent grains are two of the most obvious hindering factors[9]. This can be verified by noting the fact that there is now confirmed report of high current in BSSCO as well as YBCO prepared by proper melt texturing [12,13] which must have improved the weak links drastically. However it is important to notice that even in the highest critical current samples weak links are very much present, though they have better performance.

For simplicity, the model assumes the material to be a cubic array of identical grains of volume V_g with lattice parameter a_0 . Also it is assumed that the nearest neighbour grains are coupled by identical Josephson junctions of maximum Josephson current I_0 . The problem is tackled by proposing a Ginzburg-Landau-like free energy functional which accounts for only the intragranular condensation energy and the intergranular Josephson coupling energy[7]. Clem[7] has introduced an important dimensionless parameter,

$$\epsilon = \frac{E_j}{E_g} \quad (3.1.1)$$

where,

$$E_j = (\hbar/2e)I_0 \quad (3.1.2)$$

$$E_g = (H_{c1}^2/8\pi)V_g \quad (3.1.3)$$

are the Josephson coupling energy and intragranular condensation energy respectively. Here J (for Josephson) and g (for grain) subscripts denotes intergranular and intragranular quantities respectively. Tinkham, for the purpose of generality, assumed this dimensional parameter as the ratio of J_{cj} to J_{cg} .

Depending upon the value of ϵ , one has two limiting regimes in granular superconductors. Obviously we are interested in the $\epsilon \ll 1$ regime, where grains are weakly coupled and critical current density, J_c is limited by the critical current density of the Josephson junction. In HTSC, with representative values of parameters [$H_{c1} \simeq 10^6$ Oe, $I_0 = 100 \mu\text{A}$, $a_0 = 1 \mu\text{m}$,] we get $\epsilon \simeq 10^{-3}$. With this low value of ϵ , Clem as well as Tinkham and Lobb argued that the effect of **granularity** will be pronounced and a **weakly coupled regime** prevail from a low temperature to close to T_c .

3.1.2. IMPORTANT FINDINGS OF THE GRANULARITY MODEL:

A. PHASE LOCKING TEMPERATURE:

The basic prediction of this theory is that there exists a temperature below the critical temperature of grains (T_{co}) where all the grains become "phase locked". This, we will call as phase locking temperature, T_{cl} . Below this T_{cl} , the bulk behaves as a **whole**.

B. PENETRATION DEPTHS, λ_G AND λ_j :

Below T_{cl} , when the grains are phase locked, application of small magnetic field to a bulk sample of HTSC will induce screening currents that flow around the outer surface of the sample.

The depth to which the applied field penetrates inside the grains is, λ_g . Because of the weakness of the intergranular coupling, the magnetic field penetrates more easily and deeply between the grains, to a depth λ_j , along the grain boundaries.

In our choice of material, we have $\lambda_j \gg \lambda_g$.

C. EFFECTIVE PERMEABILITY, μ_{EFF} & λ_j :

Further, Clem assumed $\lambda_j \gg a_0$ and showed that for $r_g (=a_0/2) > \lambda_g$, the junction penetration depth,

$$\lambda_j = (c\phi_0/8\pi^2 a_0 J_0 \mu_{\text{eff}})^{1/2} \quad (3.1.4)$$

where $\mu_{\text{eff}}(T)$ is the temperature dependent permeability of the granular material given by,

$$\mu_{\text{eff}} = f_n + f_s \frac{2I_1(r_g/\lambda_g)}{(r_g/\lambda_g)I_0(r_g/\lambda_g)} \quad (3.1.5)$$

The implicit assumption in the expression for μ_{eff} is that the grains are infinite cylinder. However the expression for λ_j is not confined by the geometry and all the effect for different grain shapes will be accounted through the μ_{eff} only. Introduction of μ_{eff} , as we will see, is one of the most significant step in handling this complex situation of a granular ensemble.

D. COHERENCE LENGTH, $\xi_j(T)$ OF GRANULAR SYSTEM:

Unfortunately the other length parameter is not as well defined as λ_j in this model for our limiting value of ϵ . In fact Clem[7] has defined it phenomenologically as,

$$\xi_j^2(T) = \epsilon a_0^2 / 2 \quad (3.1.6)$$

We will like to follow this definition because it bears better rationale than the definition of Tinkham[8].

E. CRITICAL FIELDS:

Clem derived the expression for lower critical fields for the grain junction as,

$$H_{c1j} = \frac{\Phi_0}{4\pi\lambda_j^2/a_0\mu_{eff}} \ln(2\lambda_j/a_0) \quad (3.1.7)$$

which, for our choice of parameters alongwith reasonable $\mu_{eff} = 0.3$, becomes of the order of 1 orested.

The other critical field, H_{c2j} , can be derived recalling our expression for H_{c2} in Chapter 1 and H_{c2j} is,

$$H_{c2j} = \frac{\Phi_0}{2\pi\xi_j^2} \quad (3.1.8)$$

F. BEHAVIOR IN MAGNETIC FIELD:

From the above discussion one can sum up the response of a granular material to magnetic field as follows:

- i. When the magnetic field is below the lower critical field, H_{c1j} , magnetic field is screened by the bulk as a whole in a distance λ_j .
- ii. For $H_{c1j} < H < H_{c2j}$, the field penetrates (within the intergranular region) through a distance satisfying the corresponding critical state equation,

$$\frac{dH}{dx} = \pm J_c \quad (3.1.9)$$

Here we are in the mixed state of the phase diagram of the junction and vortex lines are present. The shapes of the lines are to be determined by ξ_j , and λ_j . However, as Clem[7] has argued, for $\epsilon \ll 1$ which is the case here, there is no suppressed order parameter in the core of these vortex lines.

- iii. As H increases towards or beyond H_{c2j} , the effective critical current density, J_{cj} is reduced by a factor $\approx H_{c2j}/H$ by the phase randomization, allowing even deeper

penetration, to distance $\approx H/J_c \approx H^2$ [8].

- iv. For $H_{c2} < H < H_{c1g}$, the field penetrates to a depth of λ_g into the grains and above H_{c1g} the field penetrates into individual grains following the critical state equation, appropriate to the grains.

G. PINNING OF JOSEPHSON VORTEX LINES:

Implicit in the assumption of the critical state of the junction is that there is "pinning" actively holding the VLs in their positions. The origin of this pinning is most likely the implied discreteness of the Josephson junctions array or the inhomogeneity of the junction coupling strength.

3.1.3. THE CRITICAL MODEL- STUDY ON M-H LOOPS:

In Chapter 1, the critical state model as proposed and solved by Bean[14,15] has been discussed. Here a two component model will be discussed as appropriate for the HTSC in the background of glass model. In last twenty years, after the first work of C.P. Bean critical state model has gone through a systematic change. It is important to have a detail look into this history and justify the modifications that has been arrived at.

3.1.4. REVIEW :

Critical state model of Bean[14,15] and its different variants have been extensively used for conventional type-II superconductors to predict critical current density, $J_c(H)$ from magnetization measurements.

The original model of Bean was immediately extended by Kim et al.[16,17] and Anderson[18] for more realistic field dependence of $J_c(H)$ given by:

$$J_c(H) = \frac{k}{H_0 + |H|} \quad (3.1.10)$$

where k , H_0 are two positive constants (Kim model). Irie and Yamafuji[19], and Green et al[20], have proposed a power law model where $J_c(H)$ is given by;

$$J_c(H) = K|H|^q \quad (3.1.11)$$

where K and q are two positive constant. The exponential $J_c(H)$ model was proposed by Karasik et. al.[21] as;

$$J_c(H) = a_1 \exp\left(-\frac{|H|}{a_2}\right) \quad (3.1.12)$$

where a_1 and a_2 are two positive constants.

A large number of theoretical derivation of the M-H loops of high T_c ceramic bulk have been reported on the basis of critical state models with different $J_c(H)$. But none of these models has been successful in deriving the low field anomalous M-H loops of the bulk polycrystalline ceramics. It is now well understood as per our above discussion that the ceramic bulk has two components to their electromagnetic response, one from the good superconducting grains with high enough critical current densities ($J_{cg}(0)$ of the order of 10^6 amp/cm²) and weaker magnetic field dependence and the poor superconducting grain boundary with low critical current density ($J_{cj}(0)$ of the order of 10^3 amp/cm²) with strong magnetic field dependence[8]. Qualitative explanation of this M-H loops is; at a low field excursion the grains remain well phase locked[8] and give rise to a M-H loop determined by the $J_c(H)$ (i.e., $J_{cg}(H)$). As the field range is increased this loop increases by size. But as the field increases beyond the H_{c2j} of the material, the grains become isolated by phase randomization and the M-H loop collapses. At higher field excursions, the loop is determined by the $J_c(H)$ of the grains(i.e., J_{cg}). Most of the theoretical treatment, on the basis of critical state model, assumes a single $J_c(H)$ appropriate to the field range. Hence, most of these models are crude approximations of the exact situation as depicted above.

Chaddah and Ravi Kumar[23] have extended the exponential critical state model and calculated analytically virgin magnetization curve and numerically hysteresis loops but they have not considered contributions of both the components, i.e., grains and GB simultaneously. Chen et al.[24] have given a comparative study of all the three models i.e., Bean, Kim and exponential. Bhagwat and Chaddah[25] have given analytical solution for M-H loops for general

ellipsoid and also have considered non-zero demagnetization factor.

However, in a realistic model both the components - the grain boundaries and the grains, have to be present. Though Chen et al.[24] have discussed the basic idea of including both the components they have not extended their model in that line. Though explicit derivation of M-H loops at low field from critical state models is yet not seen, calculation of AC susceptibility and harmonics on the basis of same model shows good enough agreement with experimental data[26-28]. Particularly calculation of magnetic field dependence of real and imaginary parts of AC susceptibility by Kim et. al.[26] have good agreement with experimental data for Kim type field dependence of $J_c(H)$. Further Ji et al.[27], have shown that the very low field M-H loops can be derived as ;

$$M - M_{Bean} = aH \quad (3.1.13)$$

where M_{Bean} is the Bean like contribution given by;

$$M_{Bean} = B_{Bean} - H \quad (3.1.14)$$

and $a=0.3$ gives the constant of proportionality signifying diamagnetic contribution from the grain. Obviously this is quite an arbitrary method.

In fact as we have already argued that none of these models includes both the components and hence are not applicable over the wide field range, i.e., from a few millitesla to a few tesla.

The only critical state model considering both the contributions has been proposed by Müller[29,33]. This model has been successful in deriving the AC susceptibility as a function of temperature for different AC amplitudes as well as for different DC biasing fields. However a detail study on this model, involving M-H loops at different field, has yet not been reported. We have extended this model and studied M-H loops with different parameters.

The success of critical state models in explaining experimental data lies on the proper selection of $J_c(H)$. In a two components model like that of Müller, selecting the right $J_c(H)$ has to be done carefully because one pair of $J_c(H)$ have to be selected.

At low field ($< H_{c1g}$) grains show Miessner effect and the contribution to magnetization is reversible. In critical state models, in general, H_{c1} is assumed to be zero. But still at low field

one will get loops which are quite narrow and can be considered to be almost reversible. This reversible component can be comparable to the magnetization due to grain boundary and can substantially modify the M-H loops. The low field AC susceptibility and harmonics calculation as a function of DC field with Kim type $J_c(H)$ shows good agreement with experimental data[26,28] because of the fact that these measurements are not sensitive to the above mentioned reversible contribution from the grain. However, it is obvious that a better quantitative agreement of AC susceptibility data will come only from the consideration of both the components, grain and GB. Obviously for a poor $J_{c_j}(H)$ more grains will contribute to the reversible component at low field and in that case this model will yield better result. However, at very high field GB contribution will be vanishingly small and this model must lead to the same result as that of a single component model with appropriate $J_{c_g}(H)$ for the grains.

3.1.5. DESCRIPTION OF THE MODEL :

Following above discussion, it is assumed that the bulk, consists of two distinguishable physical components of different superconducting properties; the grains with high critical current density, $J_{c_g}(0)$ (10^6 amp/cm²) and $J_{c_g}(H)$ of Bean, Kim or exponential type and the grain boundaries with poor critical current density, $J_{c_j}(0)$ (10^3 amp/cm²) and $J_{c_j}(H)$ of Kim type. Obviously, we are not away from that as proposed in ref. [29] by Müller. The grains are embedded in GB matrix in such a way that a macroscopic flux profile is set up contributed by J_{c_j} . Under this macroscopic flux profile different grains are subjected to different amounts of field resulting in a different microscopic flux profile for each grain. As one can visualize the complexity in solving the problem analytically, we have resorted to numerical solution, though analytical equation for M-H loops for different models as well as different sample shapes are available. As will be seen, that the easiness of handling a numerical problem, has given us quite a bit advantage in making a large variation of $J_c(H)$ models and other parameters input for the our model and also has yielded some results which other workers have not been able to get.

Instead of using the conventional form of Kim expression for $J_c(H)$ we slightly changed

the from as;

$$J_{cgij}(H_i) = \frac{J_{cgij}(0)}{1 + \alpha_{gij} * |H_i|} \quad (3.1.15)$$

where α_{gij} is the constant given by;

$$\alpha_{gij} = \frac{J_{cgij}(0)}{J_{cgij}(0.1)} - 1 \quad (3.1.16)$$

where $J_{cgij}(0)$ and $J_{cgij}(0.1)$ are the two critical current density values at 0.0 and 0.1 Tesla fields. This direct expression involving experimental parameters gives better visualization of the internal functioning of $J_{cgij}(H)$. Bean regime can be achieved simply by setting this two current values equal; $J_{cgij}(0) = J_{cgij}(0.1)$ giving $\alpha = 0$ and $J_c(H)$ independent of field.

Having the $J_{cg}(H)$ defined, the bulk of the sample is assumed to be an infinite slab or cylinder parallel to the magnetic field direction (Figure 3.1.1). Considering the sample divided into numbers of strips (incase of slab) parallel to length we can step the field gradually and at every point of field we can calculate the flux profile within the sample by the following relation;

$$dH(x) = -sgn(H)J_{cg}(H) * dx \quad (3.1.17)$$

where $sgn(H)$ returns the sign of the field. Now after calculating the macroscopic flux profile, the GB contribution can be evaluated by integrating the flux profile which gives $\langle B \rangle_j$, the volume average of macroscopic flux density. So GB contribution to magnetization is;

$$M_j = \langle B \rangle_j - H_i \quad (3.1.18)$$

where H_i is the externally applied field.

To get the grain contribution, the microscopic flux profile of individual grain is then calculated using the macroscopic local magnetic field as external field for the grain. Then the process is simple and extension of the same thing as in the GB case. Combining all the magnetization contribution of individual grains the total grain contribution at that external field can be obtained. Now the requirement is to combine the two contributions in a meaningful way. Ob-

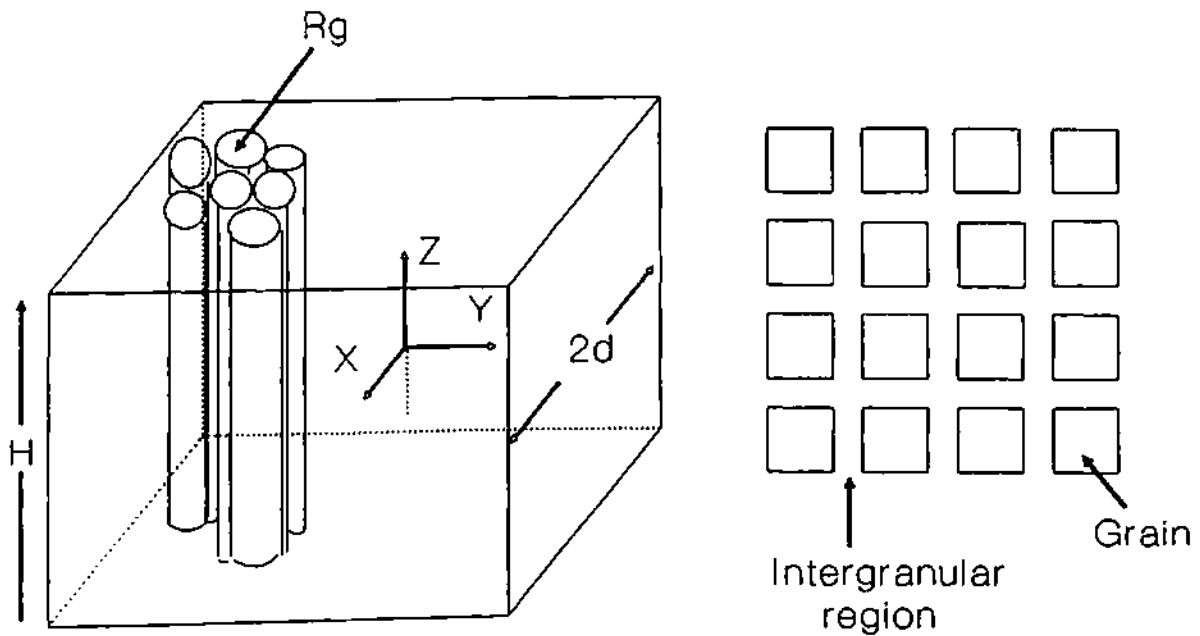


Figure 3.1.1: Schematics showing grain and grain boundaries.

viously some weighing factor has to be introduced to combine the two different contributions, the grains and the GB. Following Clem[7] and Müller[29,33] the effective permeability, μ_{eff} is introduced as the required weighing factor. Thus the total magnetization contribution will be given by;

$$M_t = \mu_{eff} \cdot \langle B \rangle_g + (1 - \mu_{eff}) \cdot \langle B \rangle_{gb} - H_a \quad (3.1.19)$$

where $\langle B \rangle_g$ and $\langle B \rangle_{gb}$ are the average macroscopic GB and microscopic grain contributions to flux. We have also calculated μ_{eff} following Clem's prescription as discussed above[7] and for our choice of parameter $\mu_{eff} = 0.37337$ equal for all the data discussed here.

3.1.6. THE OUT COME - M-H LOOPS:

$J_c(0)$ and $J_c(0.1)$ has been used in Kim expression instead of more conventional constant k and H_0 as in equation (1). The equivalence with equation (1) is given by;

$$k = \frac{J_c(0)}{\alpha} \quad (3.1.20)$$

$$H_0 = \frac{1}{\alpha} \quad (3.1.21)$$

There is no direct expression for the so called penetration field, H^* in the present numerical model. However, one can always have approximate idea by calculating the flux profile. Also knowing the equivalence of $J_{ej}(H)$ in the present model with others, one can write the analytic expression of H^* for a cylinder of radius a as given by Yamamoto et. al.[31] (in this ref. penetration field is defined as H_p);

$$H^* = \frac{(1 + 2J_{ej}(0)a\alpha)^{\frac{1}{2}} - 1}{\alpha} \quad (3.1.22)$$

With appropriate parameters one can calculate both macroscopic (junction or GB) or microscopic (grain) penetration field.

The particular choice of constant viz, $J_c(0)$ and $J_c(0.1)$ in this model gives easy visualization of the plotted result. In principle, by keeping these two constants fixed one can still select different $J_c(H)$ like $1/H$, $1/H^2$, or exponential. Thus exact functional dependence of $J_c(H)$ can be compared in M-H loops. Further for stronger field dependence for a given $J_c(H)$ we can replace $J_c(0.1)$ by $J_c(0.01)$ or so. Thus we have better choice over the experimental parameters to be selected for the model.

3.1.6A. LOW FIELD M-H LOOPS : ANSWER TO THE ANOMALY:

Figure 3.1.2. is showing complete M-H loops for different ranges of field for Bean (Figure 3.1.2a), Kim (Figure 3.1.2b) and exponential (Figure 3.1.2c) $J_{cg}(H)$ for the grains while the $J_{cj}(H)$ for GB is fixed at Kim type. In all the three cases in figure 3.1.2, $J_{cg}(0)$ is same. In figure 3.1.3, three loops with fixed J_{cj} parameter and different J_{cg} parameters are plotted. These loops have striking similarity with reported experimental low field results [22, 33-40]. In fact by selecting proper J_{cg} and J_{cj} parameters it is possible to have exact agreement with experimental data. As seen in the Figure 3.1.3 for a given J_{cj} parameters and $J_{cg}(0)$ fixed at 10^6 amp/cm² the loops become narrower as one goes towards less field dependence of $J_{cj}(H)$ like Bean, the widest being for the case of Kim type. Further the slope of the loops (i.e., the slope of the line connecting the end points of the loops) increases as one goes toward Bean model. These findings of this model calculation are physically justified. As one goes toward less field dependence of $J_c(H)$, like Bean, the reversible component (as discussed earlier) will increase, making the loops narrower. Again as the $J_{cj}(0)$ increases, these loops become wider both along M and H directions. To our knowledge, these are first theoretical M-H loops showing the anomalous behavior as in the experimental loops. One can immediately identify the "kink" in these figure with the so called "granularity kink" in the experimental data [22] and many others.

3.1.6B. THE INSIDE - HOW IT HAS BEEN POSSIBLE:

One can examine how the contribution of the GB has been modified by the presence of the contribution of the grains. In figure 3.1.4, the contribution due to the grain boundary for

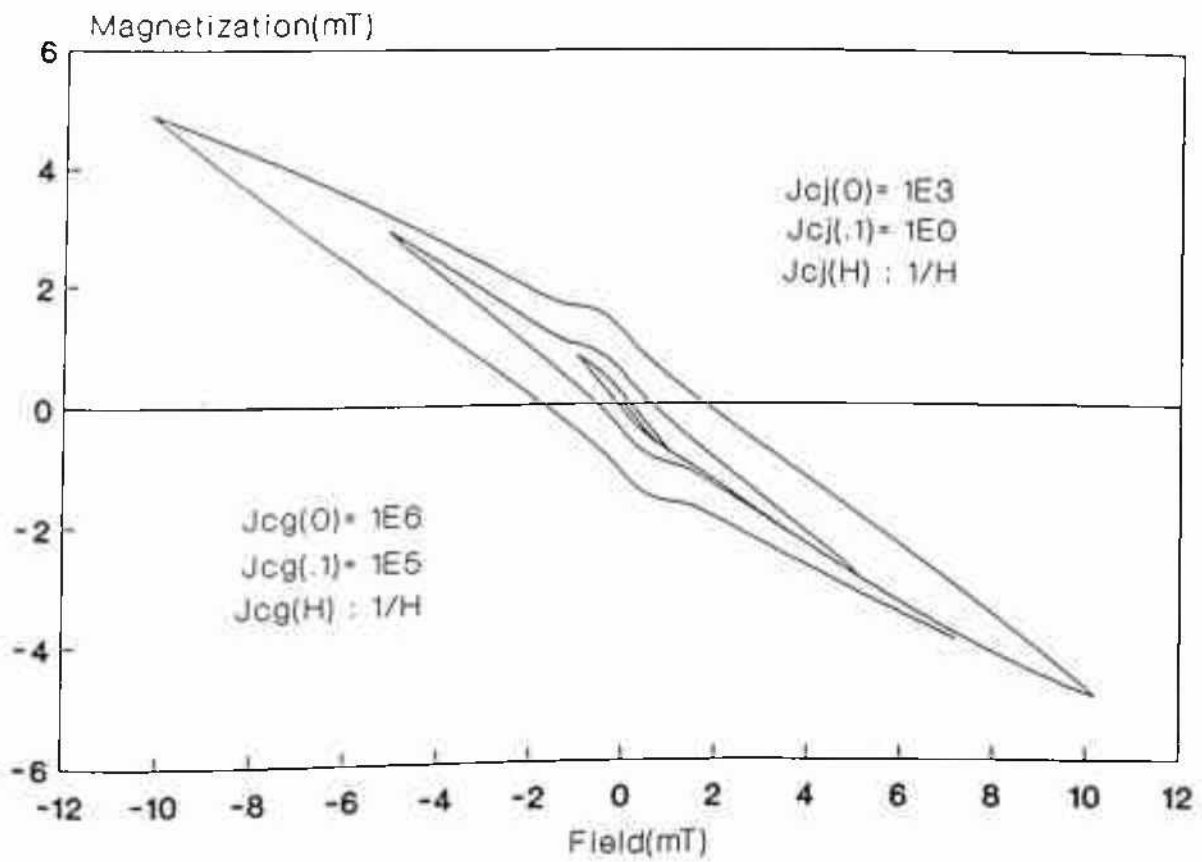


Figure 3.1.2a: M-H loops for Kim type $J_{cg}(H)$ (shown as $1/H$) for the grain. J_{cj} of the GB is Kim type (shown as $1/H$).

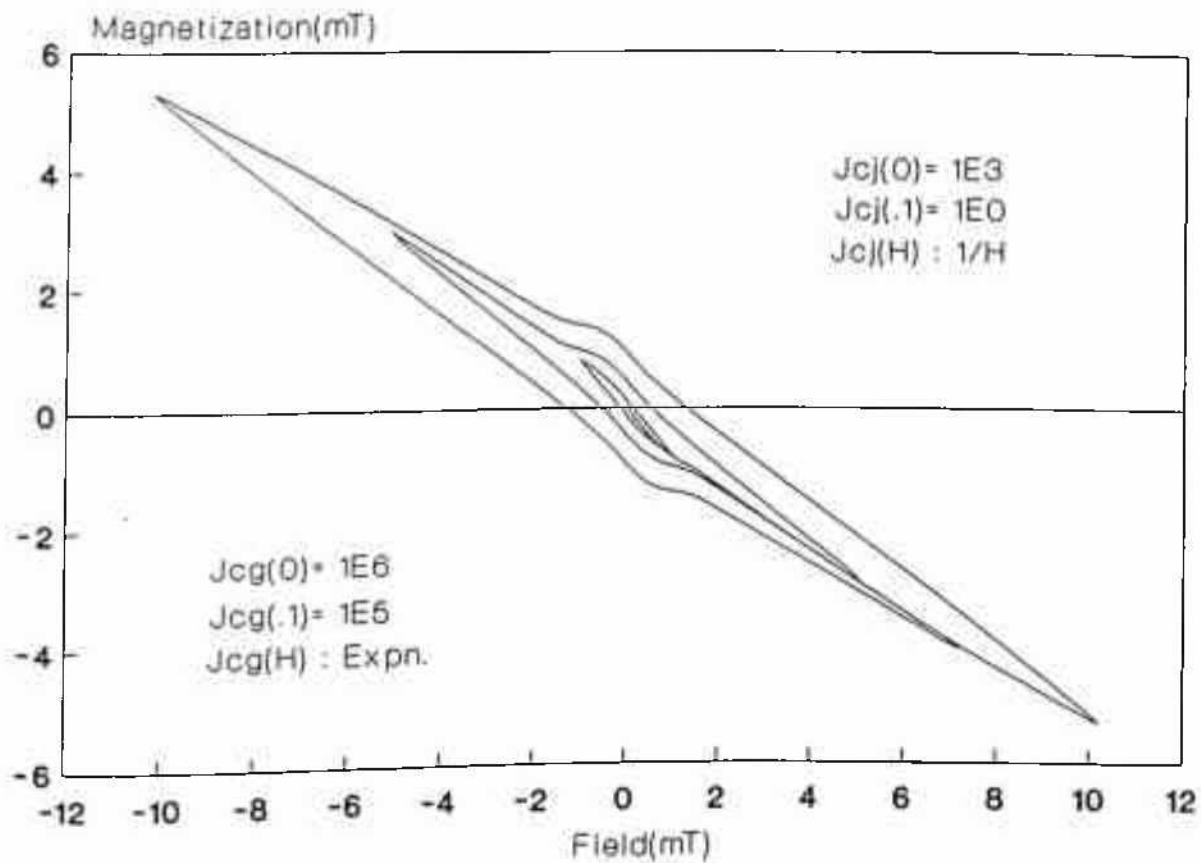


Figure 3.1.2b: M-H loops for exponential $J_{cg}(H)$ for the grain. J_c of the GB is Kim type (shown as $1/H$).

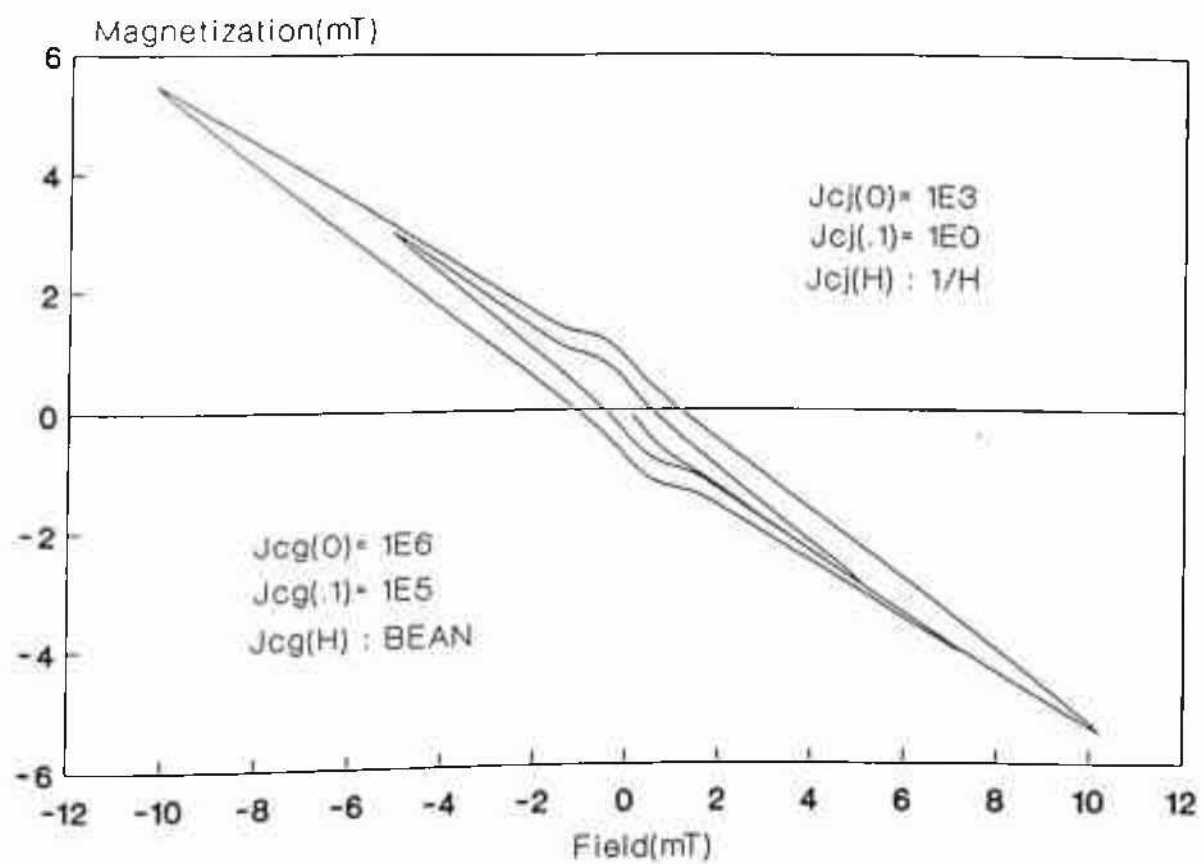


Figure 3.1.2c: M-H loops for Bean type $J_{cg}(H)$ for the grain. J_{cj} of the GB is Kim type.

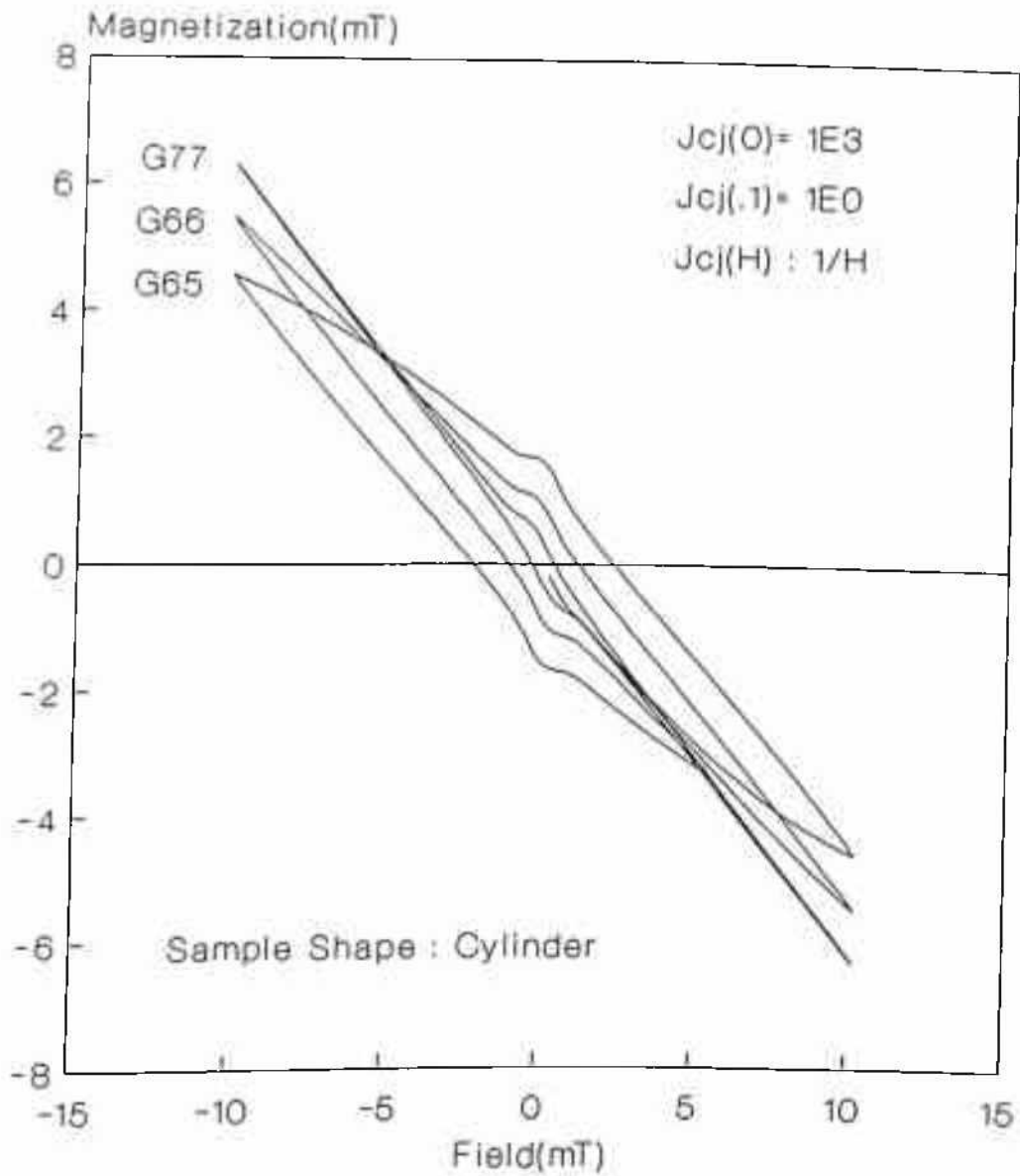


Figure 3.1.3: M-H loops for three $J_{cg}(H)$ s. J_{cj} is same. [Gmn : m is the exponent of $J_{cg}(0)$, i.e., 10^m and n is exponent of $J_{cg}(0.1)$]

different field ranges with given J_{c_j} parameters is shown. This is what is expected in a single component model with Kim type $J_{c_j}(H)$. We know from single components model for grain (not shown here), in this field range M-H loop will be very narrow or almost straight line with slope close to +1 or -1 (i.e. reversible contribution). Thus the combined effect can be visualized as shown in figure 3.1.2.

3.1.6C. TEMPERATURE DEPENDANCE OF M-H LOOPS:

These calculations can be utilized to explain qualitatively almost all the low field features of M-H loops including temperature dependence. However there is an apparent complexity as to the temperature dependance of $J_{cg}(T)$ and $J_{c_j}(T)$ and hence of M-H loops. Experimental data shows $J_{c_{trans}} \simeq (T_{c0}-T)^n$, with $n = 1$ to 3.5 [41]. In this model two complimentary things can happen :

1). If one assume that as the temperature increases, the J_{cg} parameters deteriorate faster than the J_{c_j} parameters, then from figure 3.1.3 it is apparent that loops may be narrower with increasing temperature. However, at the same time, because of poor J_{cg} and hence lower H_g^* , more and more irreversible grain contribution will be available resulting in a wider loop. This assumption of $J_c(T)$ is in-built in the superconducting glass model as described by Clem (see discussion by Clem[7] and Tinkham and Lobb[8] on the cross-over regime of glassy model), where $J_{cg}(T) \simeq J_{cg}(\text{depairing}) \simeq (T_{c0}-T)^{3/2}$ and $J_{c_j}(T) \simeq (T_{c0}-T)$. Thus recalling more important experimental facts that M-H loops monotonically reduce, the second proposition for this assumption of $J_c(T)$, should be rejected;

2). There are at least some results where $J_{c_j}(T)$ deteriorates faster than $J_{cg}(T)$ [42] implies that the reduction of loops with increasing temperature is probably due the second fact i.e., due to more grain contribution.

3.1.6D. OVER-ESTIMATION OF MAGNETIC J_c :

Obviously, it can be seen (figure 3.1.3) that a wider loop does not necessarily imply better J_{c_j} parameters (i.e., higher $J_{c_j}(0)$ or weaker $J_{c_j}(H)$) but may indicate worse J_{cg} parameters

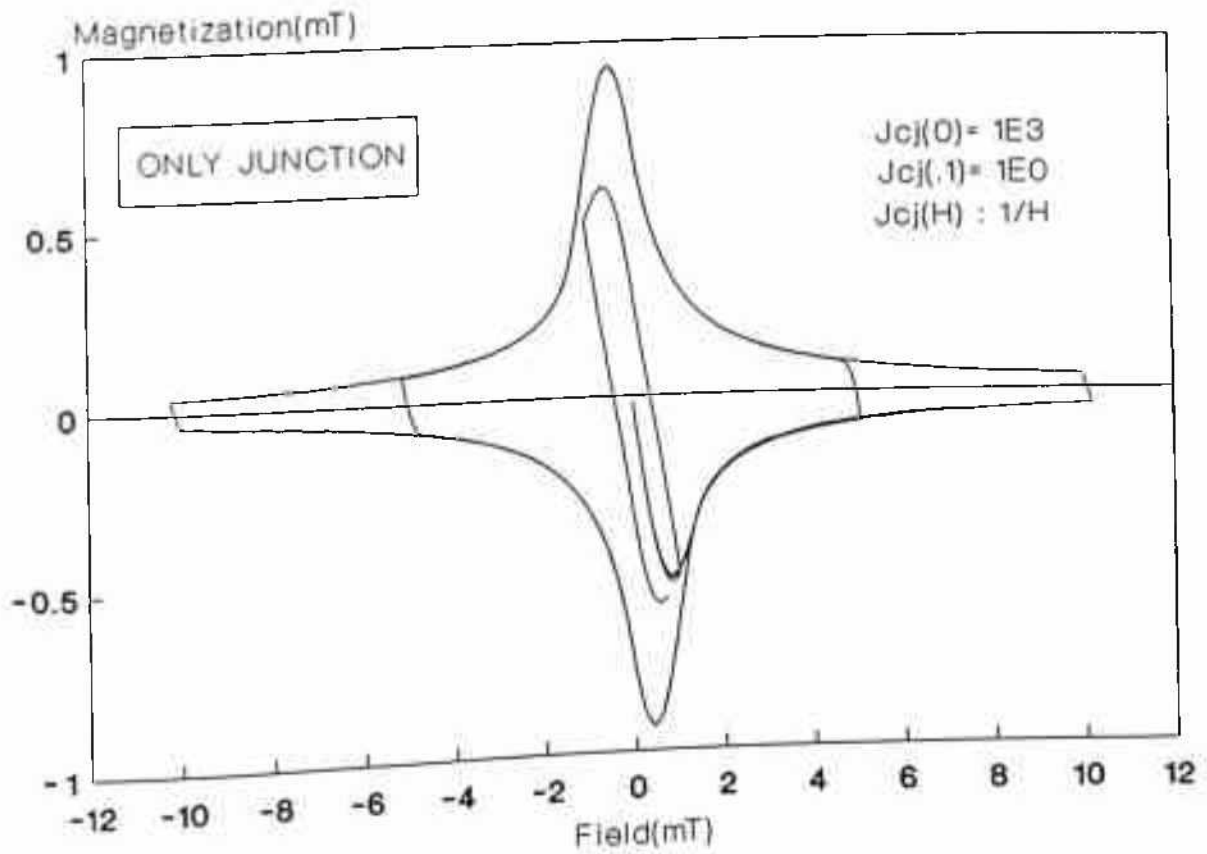


Figure 3.1.4: M-H loops considering only GB(junction) contribution.

(lower $J_{cg}(0)$ or stronger field dependence of $J_{cg}(H)$). Thus these calculations justify the problem of calculating $J_{cj}(H)$ from experimental M-H loops at low fields. As can be seen in figure 3.1.3, the loops become narrower with better J_{cg} parameters though J_{cj} parameters are the same, indicating possible false-estimation of magnetic J_c using standard Bean's formula alongwith bulk dimension. It should, further be noticed, that if one compares figure 3.1.4 and figure 3.1.1.a,b,c it is clear that the grain contribution increases with worse J_{cg} parameters making the loops wider. Thus in the usual cases where grains are not very good (e.g. $J_{cg}(0) \approx 10^6$ amp/cm²), there will be an over-estimation of magnetic J_c with respect to actual transport J_c .

3.1.6E. TEST FOR A TRUE TWO COMPONENT MODEL - EVOLUTION OF M-H LOOPS OVER FIELD RANGE:

The dry test for a successful two component model is that it should be equally valid in the whole field range starting from a few millitesla to a few Tesla.

In Figure 3.1.5 the same M-H loops as in figure 3.1.2 except that the field range is higher (120 mT). These loops are also in complete agreement with the already published calculations(on the basis of single component model) and experimental data, except the small kink close to zero field. This kink decreases on decreasing μ_{eff} , or decreasing $J_{cj}(0)$ since both lead to a decrease in magnetization contribution due to GB. However the high field experimental M-H loops do not show this kink. It is for the first time that such a systematic evolution of M-H loops in HTSC has been presented.

3.1.6F. EXACT FIELD DEPENDENCE OF J_{cj} :

As has been discussed earlier our way of considering the parameters offer a better comparison of field dependence of $J_c(H)$, two M-H loops for different $J_{cj}(H)$; one $J_{cj}(H) \approx 1/(1+k | H |)$ and other $J_{cj}(H) \approx 1/(1+k | H |)^2$ for given set of $J_{cj}(0)$ and $J_{cj}(0.1)$ have been plotted in figure 3.1.6(a,b). Obviously the second $J_{cj}(H)$ is power law type. It is obvious in this figure that for stronger field dependence of $J_{cj}(H)$ the loops are wider, which further indicates the problem of calculating J_{cj} values from these loops. This is because, for stronger field dependence of $J_{cj}(H)$ more flux will penetrate the bulk making more grains subjected to that field and increasing the contribution of grain magnetization.

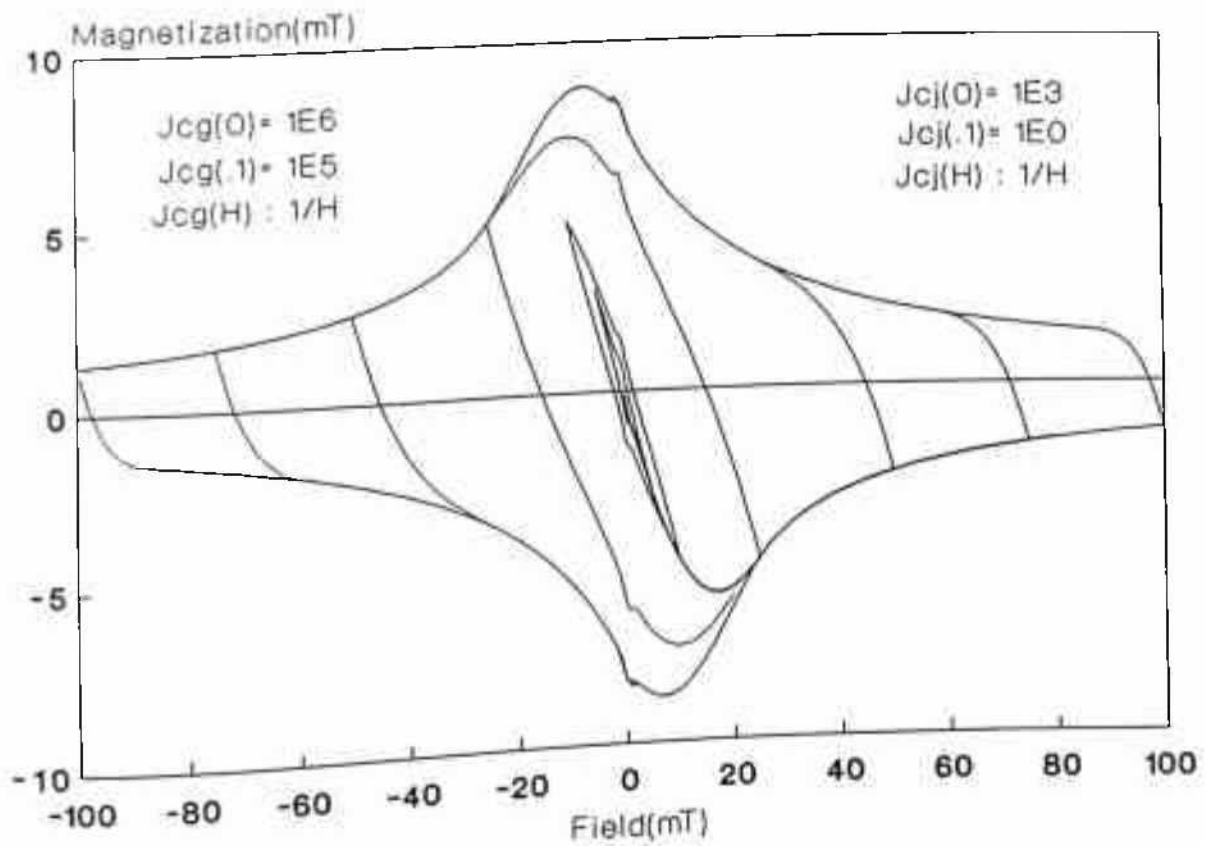


Figure 3.1.5a: M-H loops for Kim type $J_{cg}(H)$ (shown as $1/H$) of the grain. J_{cj} of the GB is Kim type ($1/H$).

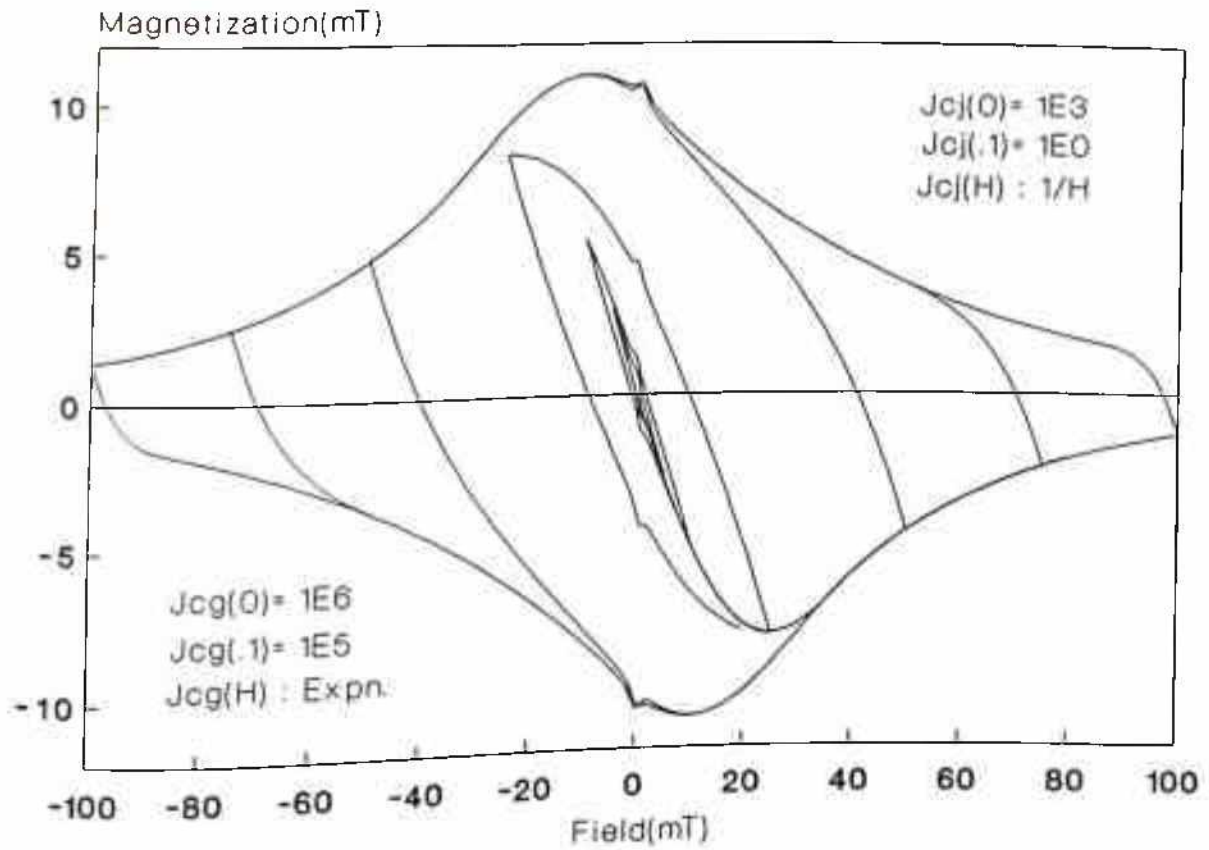


Figure 3.1.5b: M-H loops for exponential type $J_{cg}(H)$ (shown as $1/H$) of the grain. J_{cj} of the GB is Kim type ($1/H$).

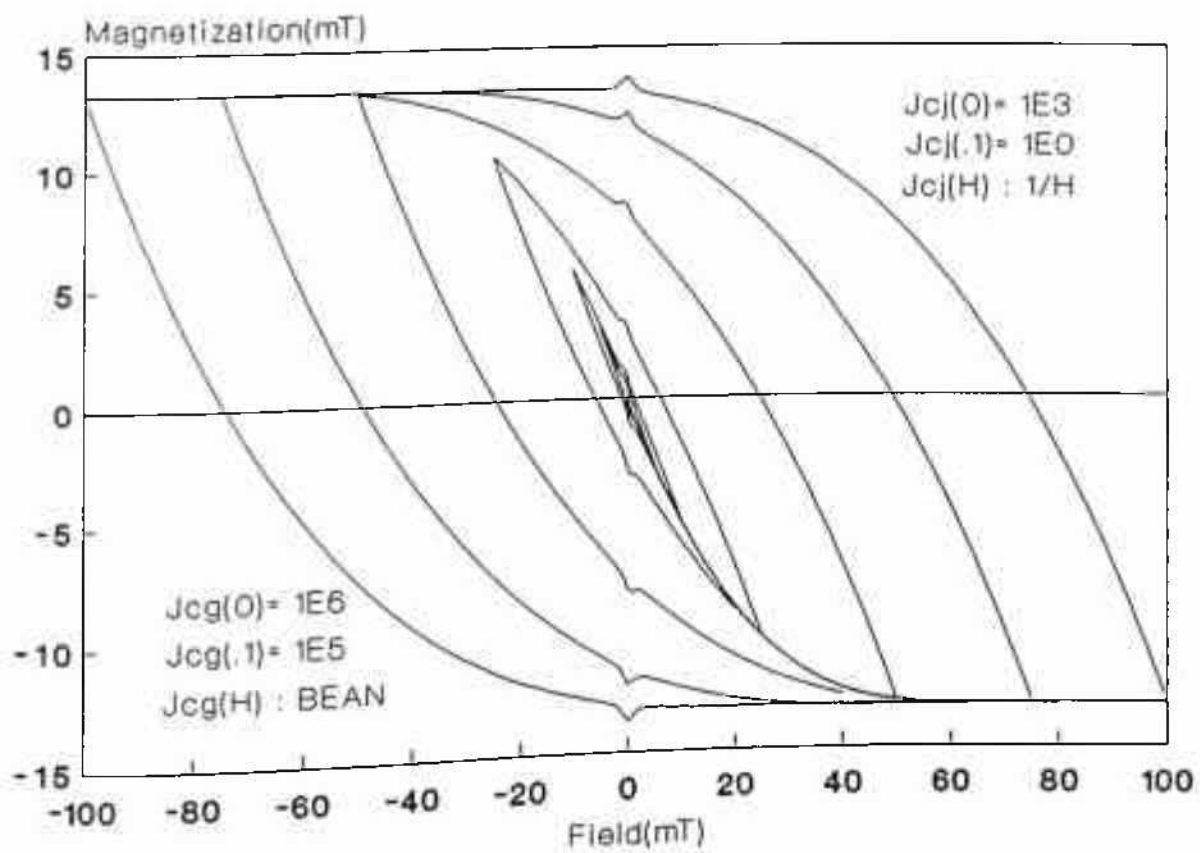


Figure 3.1.5c: M-H loops for Bean type $J_{cg}(H)$ of the grain. J_{cj} of the GB is Kim type ($1/H$).

3.1.6G. EFFECT OF GRAIN SIZE:

The effect of grain size can be investigated in this model. In figure 3.1.7 M-H loops for different grain sizes have been plotted for given parameters as shown in the figure. As one can visualize, with the decrease of grain size more number of grains are exposed to macroscopic field. Moreover with decrease of grain size the corresponding H^* of the grains decreases allowing more flux to penetrate within the grains which implies that the irreversible contribution from the grain will increase. Thus with the decrease of grain size M-H loops will become wider in size. The calculation in figure 3.1.5. has good qualitative agreement with the experimental data of Muary et. al.[33].

3.1.7. SUMMARY:

The results can now be summarized showing the significant achievements in this two component model;

- i. Anomalous Behavior in M-H loops: It is shown here that the low field anomalous behavior can be explained quantitatively in this model.
- ii. Evolution of M-H loops: A systematic evolution of M-H loops over the field range variation has been presented.
- iii. Estimation of magnetic J_c : It is clearly shown that there is a chance of over-estimation of transport J_c from magnetic measurements.
- iv. Grain size effect: Systematic grain size dependence has been discussed which finds good agreement with published results.

3.1.8. PHENOMENOLOGICAL CORRECTION FOR SHIELDING CURRENT

- DETAILS ON EVOLUTION OF M-H LOOPS OVER FIELD RANGE:

In Chapter 1 the peculiar evolution of M-H loops in HTSC over the variation of field range has been discussed. In the above calculation it is not possible to see the middle step (the Z-shaped M-H loops which is often seen in the middle range of field excursions) of the evolution of M-H loops because, in all probability, this step has a large contribution from the shield-

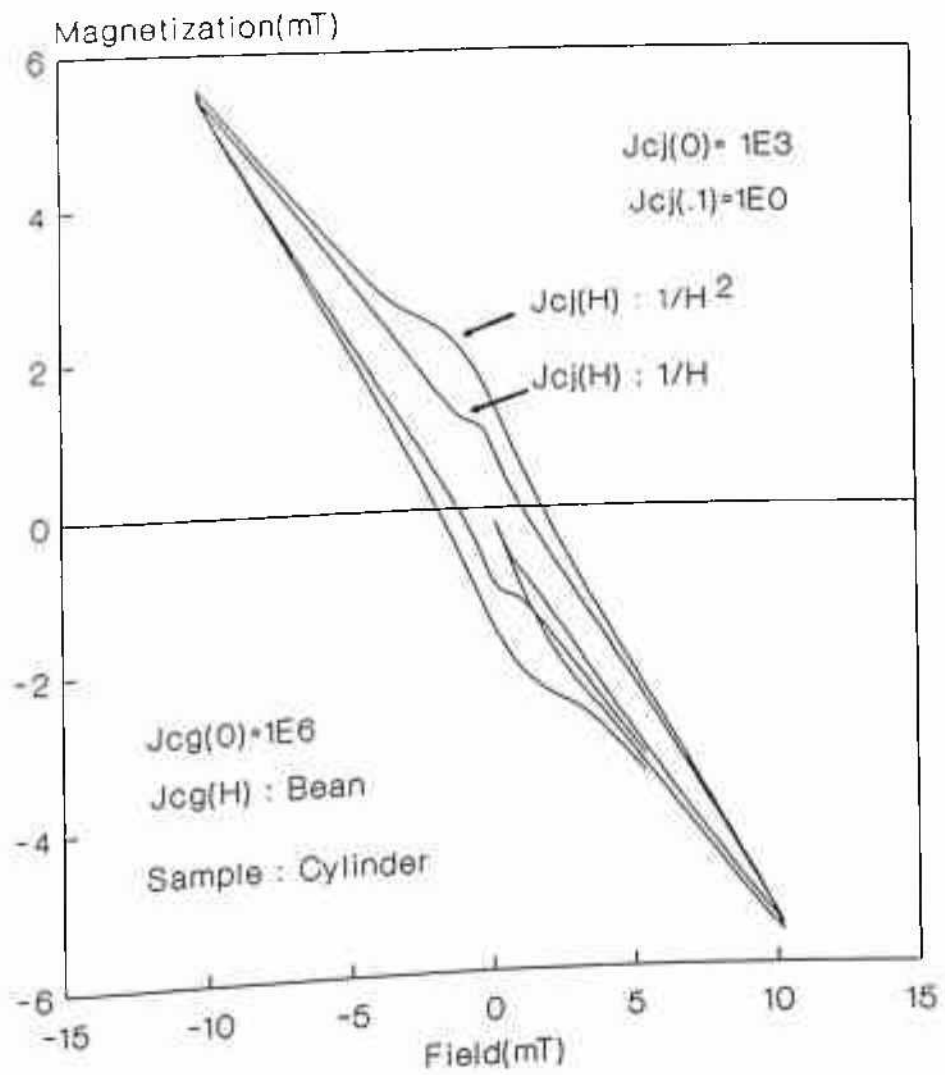


Figure 3.1.6a: M-H loops for two $J_{c1}(H)$ s [$\beta=1, 1/H$ and $\beta=2, 1/H^2$]. $J_{c2}(H)$ is same and is Bean type.

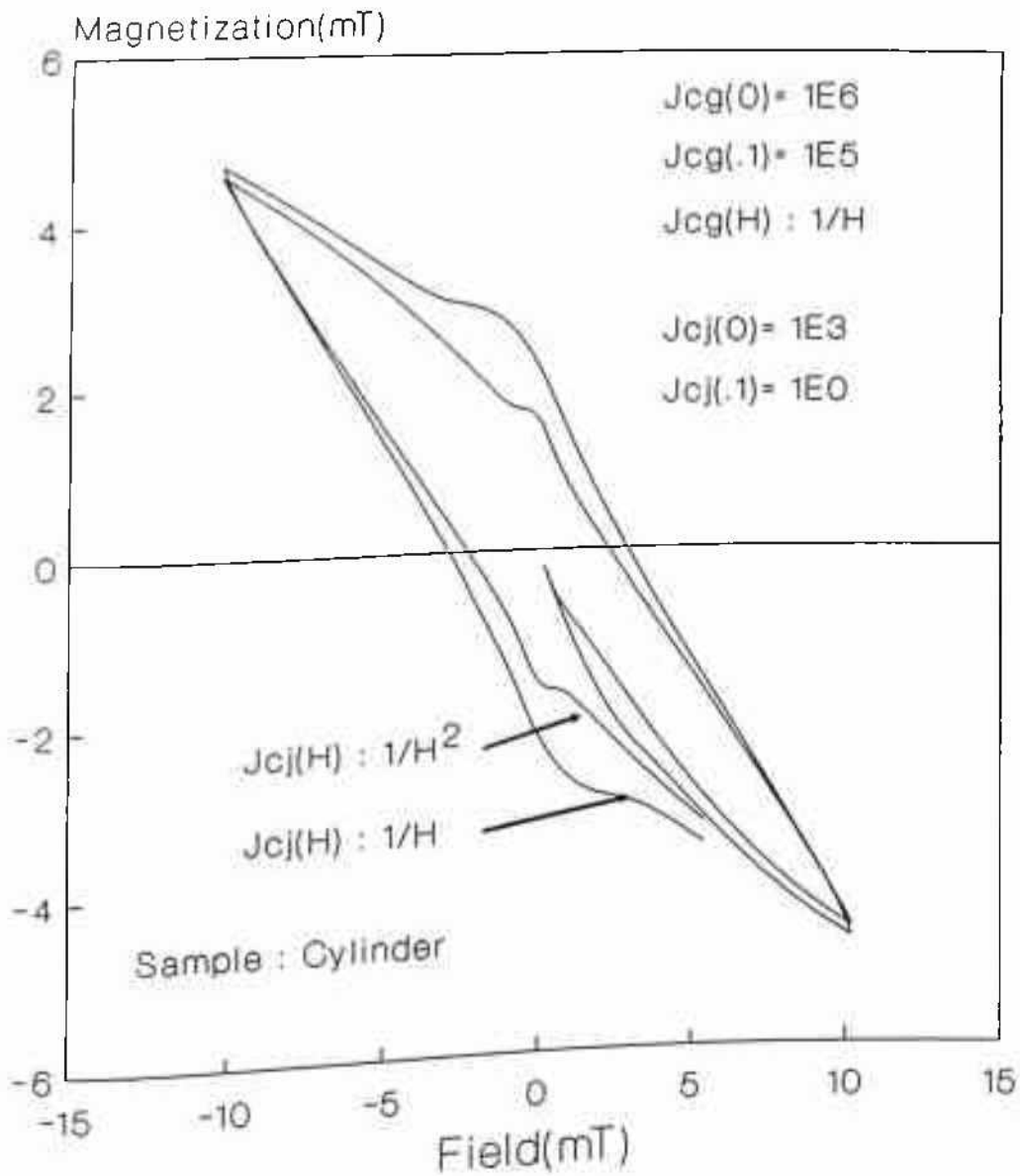


Figure 3.1.6b: M-H loops for two $J_{cj}(H)$ s [$\beta=1, 1/H$ and $\beta=2, 1/H^2$]. $J_{cg}(H)$ is same and is Kim type.

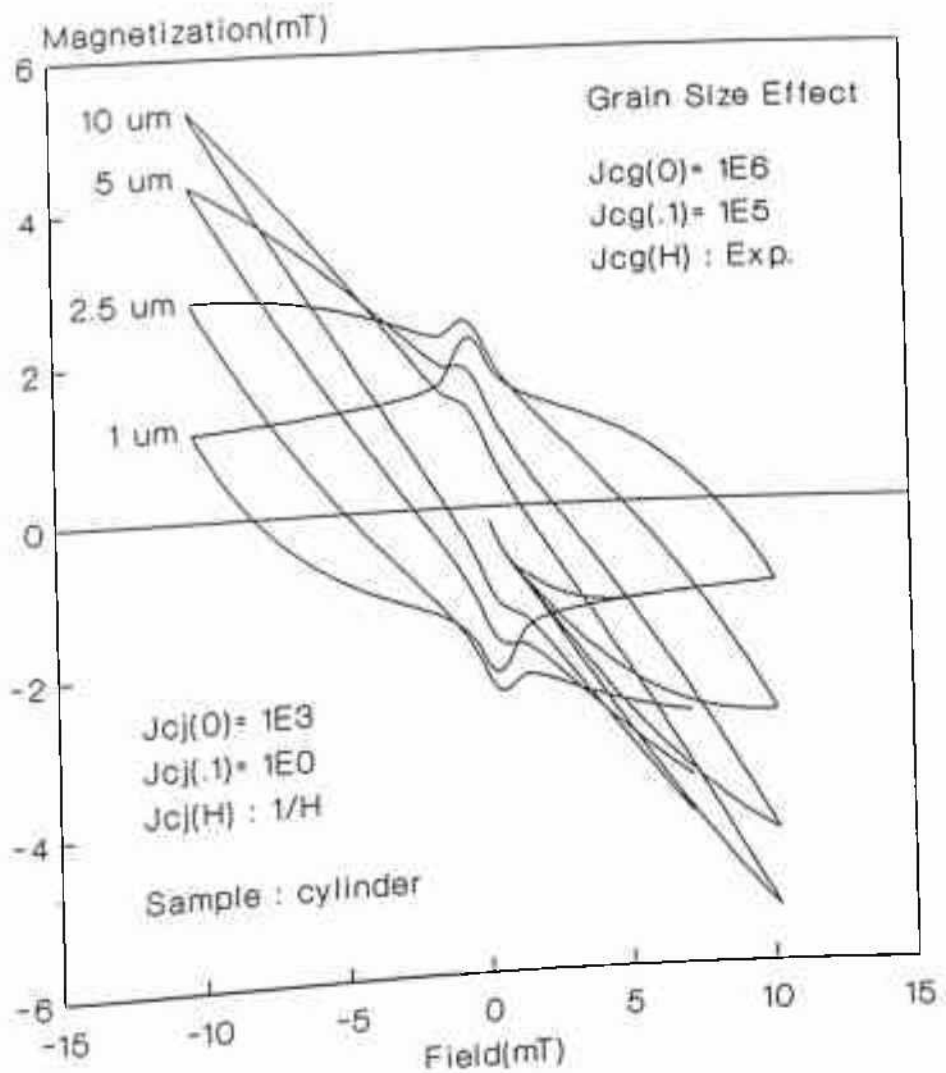


Figure 3.1.7: Grain Size effect on M-H loops. Results in agreement with data of Maury et al. [ref. 29].

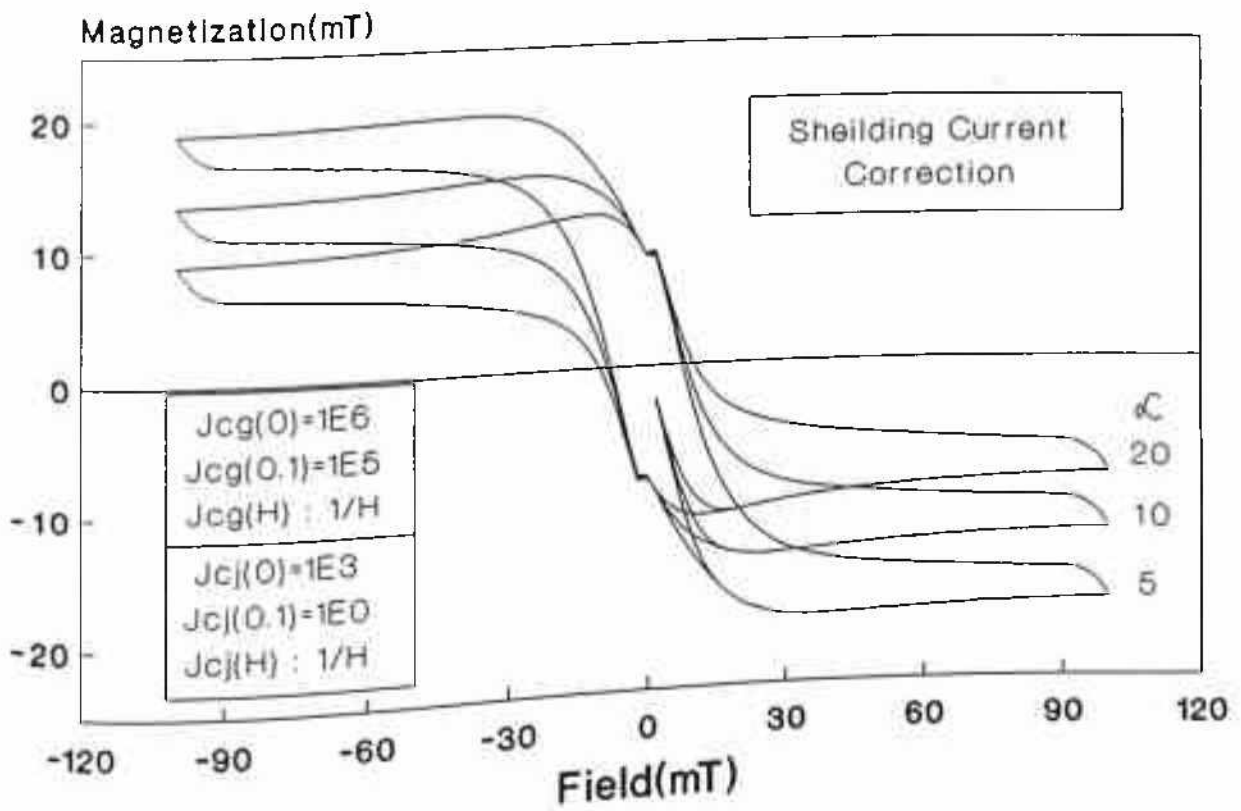


Figure 3.1.13: M-H loops including shielding current correction.

ing currents[43] and that there is no scope for handling any shielding currents in the critical state model, which by its nature requires the magnetic response to be irreversible. One important point must be taken note of here, that this limitation is inherent in critical state calculations and because of this limitation most work on this model assumes lower critical field, H_{c1} to be zero. In conventional LTSC also, where the reversible contribution is usually quite negligible as compared to the irreversible component, Kim et al.[17] tried to consider the same reversible contribution.

Thus, here, the shielding contribution of the grains (because H_{c1j} being very small, junction as such has very less reversible contribution) is considered phenomenologically in modifying the critical state M-H loops. Unlike Chen et al., no surface barrier to entry and exit field is assumed to exist. Thus it is a crude mathematical manipulation that have been tried here and is not based on rigid physical ground. However a justification is being sought on the basis that magnetization due to a reversible shielding current increases linearly with the applied external field upto a field equal to H_{c1g} . Above this field, flux starts penetrating. Handling this problem in a mathematical model is difficult because this jump from Meissner state to vortex state is a discontinuous process at H_{c1g} . This problem has been seriously faced by others also and Chen et al[43] have not been able get continuous M-H loops on this model.

With this in mind and to have a glimpse of the effect of the shielding current on the M-H loops, it is assumed that the reversible component is given by,

$$M_{rev} \propto H_0 \text{Exp}\left(-\frac{|H_0|}{\alpha}\right) \quad (3.1.23)$$

The advantage of this form is that it is a self-limiting function at a field to be determined by the constant α and hence does not require artificial limiting logic (in the software) to manage the discontinuity at H_{c1g} and has only one arbitrary parametric constant, α . The compromisation is that the slope of the virgin M-H curve below H_{c1g} is not ± 1 . However as an initial approximation this is good enough to bring out the essence.

In figure 3.1.8, three such M-H loops have been included where the component due to shielding current has been added to the critical state M-H loops with parameters as shown within the diagram. The excellent agreement of this calculated loops with the reported data[34,39,43-

48] justifies the assumption here.

References :

- [1] I. Morgenstern 1990 Earlier and Recent Aspects of Superconductivity (Springer Series in Solid State Science, Vol. 90) Ed. J.G. Bednorze and K.A. Müller pp240
- [2] M.S. Colclough, C.E. Gough, M. Keene, C.M Muirhead, N. Thomas, J.S. Abell and S. Sutton 1987 Nature **328**, 47
- [3] C.M. Pegrum, G.B. Donaldson, A.H. Cart and A. Hendry 1987 Appl. Phys. Lett. **51**, 1364
- [4] R. Tichy, M. Odehnal, V. Petricek, S. Safrata, E. Pollert, J. Kamarad, J. Hejtmanek, O. Smrckova and D. Sykorova, 1988 J. Low Temp. Phys. **70**, 187
- [5] J. R. L. de Almeida and D.J. Thouless 1978 J. Phys. **A11**, 983; **C11**, L871
- [6] C. Ebner and D. Stroud, Phys. Rev. **B31**, 165 (1987)
- [7] J.R. Clem. Physica C, **153-155**, 50 (1988)
- [8] M. Tinkham and C. J. Lobb Solid State Physics **42**, 91 (1989)
- [9] A.P. Malozemoff Physical 1989 Properties of High Temperature Superconductors ed. D.M. Ginsberg, World Scientific, Vol. 1, p71
- [10] G. Deutscher 1990 Earlier and Recent Aspects of Superconductivity (Springer Series in Solid State Science, Vol. 90) Ed. J.G. Bednorze and K.A. Müller
- [11] J. Mannhart 1990 Earlier and Recent Aspects of Superconductivity (Springer Series in Solid State Science, Vol. 90) Ed. J.G. Bednorze and K.A. Müller
- [12] S. X. Dou and H.K. Liu 1993 Supercond. Sci. Technol, **8**, 297
- [13] M. Murakami 1992 Supercond. Sci. Technol. **5**, 185
- [14] C.P. Bean 1962 Phys. Rev. Lett. **8**, 250
- [15] C.P. Bean 1964 Rev. Mod. Phys. **36**, 31
- [16] Y. B. Kim, C. F. Hempstead and A. R. Strand 1962 Phys. Rev. Lett. **9**, 306
- [17] Y. B. Kim, C. F. Hempstead and A. R. Strand 1963 Phys. Rev. **129**, 528
- [18] P. W. Anderson, 1962 Phys. Rev. Lett. **9**, 309
- [19] F. Irie and K. Yamafuji 1967 J. Phys. Soc. Jpn. **23**, 255
- [20] I. M. Green and P. Hlawiczka, 1967 Proc. IEE **114**, 1329

- [21] V. R. Karasik, N. G. Vasil'ev and V. G. Ershov 1964 Sov. Phys. Rev. **136**, A335
- [22] Subir Saha, R.B. Tripathi and B.K. Das. 1992 Solid State Phenomena **25-26**, 387
- [23] G. Ravi Kumar and P. Chaddah 1989 Phys. Rev. **B39**, 4704
- [24] D.-X. Chen, A. Sanchez, J. Nogues, and J.S. Munoz 1990 Phys. Rev. **B41**, 9510
- [25] K. V. Bhagwat and P. Chaddah 1990 Physica C, **190**, 444
- [26] Y. Kim, Q. H. Lamb and C.D. Jeffries 1991 Phys. Rev. **B43**, 11404
- [27] L. Ji, R.H. Sohn, G.C. Spalding, C.G. Lobb and M. Tinkham 1989 Phys. Rev. **B40**, 10936
- [28] T. Ishida and R. B. Goldfarb 1990 Phys. Rev. **B41**, 8937
- [29] K. H. Müller 1989 Physica C, **159**, 717
- [30] K.H. Müller 1991 Magnetic Susceptibility of Superconductors and Other Spin Systems ed R.A. Hein, T.L. Francavilla and D.H. Liebenberg p229
- [31] K. Yamamoto, H. Mazaki and H. Yasuoka 1993 Phys. Rev. **B47**, 915
- [32] D.-X Chen, A. Sanchez, T. Puig, L.M. Martinez and J.S. Munoz 1990 Physica C **168**, 652
- [33] R. Maury, A. R. Fert, J. P. Redoules, J. Ayache, J. Sabras and C. Monty 1990 Physica C, **167**, 591
- [34] S. Senoussi, M. Oussena, M. Ribault and G. Collin 1987 Phys. Rev. **B36**, 4003
- [35] H. Zhang, S. S. Yan, H. Ma, J. L. Peng, Y. X. Sun, G. Z. Li, Q. Z. Wen and W. B. Zhang 1988 Solid State Comm. **65**, 1125
- [36] G. J. Nieuwenhuys, T. A. Friedmann, J. P. Rice, P. M. Gehring, M. B. Salamon and D. M. Ginsberg 1988 Solid State Comm., **67**, 253
- [37] Hong Zhang, Shou-sheng Yan, Wen-bin Zhang, Zhao-bui Shen, Yun-xi Sun, Guo-zhong Li, and Ke Wu 1988 Solid State Comm., **67**, 1183
- [38] M. Cizek, J. Olejniczak, E. Trojnar, A. J. Zaleski, J. Klamut, A. J. M. Roovers and L.J.M. Van de Klundert, 1988. Physica C, **152**, 247
- [39] S. Senoussi, M. Oussena and S. Hadjoudj 1988 J. Appl. Phys. **63**, 4176
- [40] R. B. Goldfarb, R. W. Cross, L. F. Goodrich and N. F. Bergren 1993 Crogenics **33**, 3
- [41] S.X. Dou and H.K. Liu Supercond. Sci. Technol. **6**, 297 (1993)
- [42] N. Savvide, A. Katsaros and S.X. Dou, Physica C, **179**, 361 (1991)
- [43] D. X. Chen and A Sanchez 1991 Magnetic Susceptibility of Superconductors and Other Spin Systems ed R.A. Hein, T.L. Francavilla and D.H. Liebenberg p259

- [44] M. Polak, F. Hanic, I. Hlasnik, M. Majoros, F. Chovanec, I. Horvath, L. Krempsky, P. Kottman, M. Kedrova and L. Galikova 1988 *Physica C* **156**, 79
- [45] D. X. Chen, R.W. Cross and A. Sanchez 1993 *Cryogenics* **33**, 695
- [46] D. X. Chen and A. Sanchez 1992 *Phys. Rev. B* **45**, 10793
- [47] A. Ding, Z. Yu, K. Shi and J. Yan 1988 *Physica C* **153-155**, 1509
- [48] H. Dersch and G. Blatter 1988 *Phys. Rev. B* **38**, 11391

MODEL CALCULATIONS

EXTENSION OF THE CRITICAL STATE MODEL:

In this part of Chapter 3 the model as described in Part A, will be extended for AC susceptibility calculations.

3.2.1.	FIELD DEPENDENCE OF AC MAGNETIC SUSCEPTIBILITY OF HTSC AND ITS HYSTERESIS	97
A.	REVIEW	97
B.i.	MODEL CALCULATION	99
B.ii.	EFFECT OF DEMAGNETIZATION	100
C.	RESULTS AND DISCUSSION	101
i.	DEMAGNETIZATION EFFECT ABSENT	101
ii.	EFFECT OF DEMAGNETIZATION -BETTER REALIZATION OF HYSTERESIS OF $\chi(H)$	111
iii.	EFFECT OF PARAMETERS	113
iv.	EFFECT OF GRAIN SIZE	120
D.	SUM UP	127
3.2.2.	AC AMPLITUDE DEPENDENCE OF χ' AND χ''	128
A.	ZERO BIAS	128
B.	NON-ZERO DC BIAS	135
C.	SIZE EFFECT - BULK AND GRAIN	140
D.	EXPERIMENTAL EVIDENCE	142
E.	SUM UP	142
3.2.3.	HIGHER HARMONICS - FIELD DEPENDENCE	149
A.	WITHOUT DEMAGNETIZATION CORRECTION	149
B.	DEMAGNETIZATION CORRECTION AND HYSTERESIS	152
3.2.4A.	MODIFICATION IN THE MODEL- ACCOUNTING FOR THE FLUX CREEP	152
3.2.4B.	AC FIELD MEDIATED DEPINNING LEADING TO ENHANCE FLUX FLOW - FURTHER MODIFICATION IN THE MODEL	154
3.2.5.	INCORPORATING THE NON-CRITICAL PHENOMENON IN THE MODEL	156
3.2.6.	EXPERIMENTAL EVIDENCE IN SUPPORT OF THE LAST TWO MODIFICATIONS	159

3.2 EXTENSION OF THE CRITICAL STATE MODEL :-

3.2.1. FIELD DEPENDENCE OF AC MAGNETIC SUSCEPTIBILITY OF HTSC AND ITS HYSTERESIS.

It is now time to extend this model for calculating AC susceptibility, the most easily available experimental data with enormous information on the magnetic properties of superconductors, conventional or new. First a brief review of the background on which these calculations have been done to extend the model will be given. Next the model as an extension to the above critical state model will be described. Then a detailed description of the simulated results will be presented.

3.2.1A) REVIEW:

AC magnetic susceptibility has been considered to be one of the most important experimental tools for the study of superconductivity. It is often used for rapid characterization of critical temperature and superconducting volume fraction. But a careful measurement of complex AC magnetic susceptibility as a function of temperature, amplitude and frequency of AC excitation or DC bias field provides good insight into the different magnetic properties[5]. Though a large number of studies on temperature and frequency dependence of AC susceptibility for the high temperature superconductors(HTS) has been reported, its dependence on the superimposed DC field and AC amplitude has not been studied in detail. In high temperature ceramic bulk superconductors, these measurements assume further importance because of their capability in recognizing the presence of two separate contributions to magnetization - one from grains and other from grain boundaries (GB). In particular, the superimposition of a DC field on the AC field has been instrumental in the study of high temperature granular superconductors providing good resolution to the so called inter- and intra-grain contributions[6].

In Chapter 1, it has been discussed that measurements of real(χ') and imaginary(χ'') parts of AC susceptibility as a function of DC bias field have shown hysteresis for high temperature superconducting ceramics[1-3,7,8] as well as in single crystals[9]. Sen et al.[2] have further

shown that the higher harmonics of AC magnetic susceptibility also exhibit hysteresis with respect to DC field.

This strong hysteresis has yet not been explained. Several workers[1-3] have tried to build up the case in line with Evetts et al.'s model[10] which qualitatively explains the hysteresis of $J_c(H)$ in granular system. Mumsurova et al.[9] have tried to do quantitative analysis of the observed hysteresis in single crystals on the basis of flux line oscillation around their equilibrium position due to the AC field and have argued that the possible origin of this hysteresis may be due to the "local reversible shift of the vortex lattice when changing the DC field scan direction". However, they have not been able to derive the hysteresis loops, $\chi(H)$ explicitly.

It must be recalled that the hysteresis in AC susceptibility has also been reported for conventional NbTi multifilamentary superconductors[11] where hysteresis of $J_c(H)$ has not been reported. Goldfarb and Clark[11] have also tried to derive the loops theoretically on the basis of differential susceptibility and were able to show small hysteresis in calculated loops. Though the agreement of their calculated result with experimental data is poor, it is probably the first theoretical analysis showing that the hysteresis in AC susceptibility is possible even in the critical state model.

Theoretical calculations of AC susceptibility and its harmonics for HTSC's on the basis of critical state models have been done by several groups[1,23,24]. The results of Ji et al.[23] and Ishida et al.[24] show that a better agreement with experimental data is achieved for the case of Kim type $J_c(H)$ while calculation of Kim et al. demands a $J_c(H)$ of power law type given by,

$$J_c(H) = \frac{k}{(H+H_0)^n} \quad (3.2.1)$$

Moreover, most of these model calculations do not consider the complex situation in granular system, instead they oversimplify the problem by assuming a single component with appropriate $J_c(H)$.

Here, extension of the same model as described above (in the first part of Chapter 3) will be presented to derive the observed hysteresis in $\chi'(H)$ and $\chi''(H)$ on complete theoretical basis. In the following, it will be shown that a critical state model even without further

correction can account for some hysteresis in the imaginary part($\chi''(H)$) at low AC amplitude and an additional contribution from demagnetization correction due to finite bulk and grain size leads to better realization of experimental data showing hysteresis in both real and imaginary parts as well as at all amplitudes depending on the parameters of the models.

3.2.1B.i) MODEL CALCULATION:

In presence of an alternating field of amplitude H_{ac} defined as,

$$H(t) = H_{ac} \operatorname{Im}(e^{i\omega t}) = H_{ac} \sin(\omega t) \quad (3.2.2)$$

where $\operatorname{Im}()$ denotes the imaginary part of its complex argument, magnetization can be written as[24];

$$M(t) = H_{ac} \sum_{n=1}^{\infty} \operatorname{Im}(\chi_n e^{i n \omega t}) \quad (3.2.3)$$

where $\chi_n = \chi'_n - i\chi''_n$ ($n = 1, 2, 3 \dots$). Thus from this $M(t)$ one can find magnetic susceptibilities χ'_n and χ''_n by,

$$\chi'_n = \frac{1}{\pi H_{ac}} \int_0^{2\pi} M(t) \sin(n\omega t) d(\omega t) \quad (3.2.4)$$

$$\chi''_n = \frac{-1}{\pi H_{ac}} \int_0^{2\pi} M(t) \cos(n\omega t) d(\omega t) \quad (3.2.5)$$

The definition remains valid even in the presence of a DC field superimposed on the AC.

Here the definition of $J_c(H)$ for the grain and the grain boundary is expressed in a compact way as,

$$J_{c,j} = \frac{J_{c,j}(0)}{(1 + \alpha_{c,j} |H|)^n} \quad (3.2.6)$$

where g and j are representation for the grain and the GB respectively and β is a positive constant whose value is 1 for grain and 1 or 2 for GB. Instead of using the constants α_g and α_j directly one can calculate them in terms of two J_c values as described earlier.

Now assuming appropriate J_{cg} and J_{cj} parameters it is simple to calculate the $M(H)$ loops following above model calculation. First a macroscopic flux profile is allowed to be built up as per the J_{cj} parameters which causes different grains to be subjected to different local fields. On this macroscopic flux profile a microscopic contribution is added because of the grains with different J_{cg} parameters. While integrating the macroscopic flux profile to obtain the magnetization (M), one gets the GB contribution to magnetization, the grain contribution will be summed up after integration of microscopic profiles of individual grains. The two components have to be weighed by a suitable factor [25,26] considered to be effective permeability μ_{eff} . Now at every point of DC field, the AC excitation is allowed to disturb the flux profile from which one can calculate the change of M , i.e., ΔM due this AC field. Then using equation 4 and 5 χ'_n and χ''_n can be found out. In fact one can calculate ΔM in steps over one cycle, the FFT of which will give different harmonics. As one can visualize, the disturbance to flux profile due to superposition of AC field at every DC field will take certain time to stabilize and ΔM should be calculated after the stabilization. The first half cycle (time required for stabilization) has not been included in this calculation and the numerical integrations in equation 4 and 5 have been done, in effect, over one cycle after first half cycle.

3.2.1B.ii) EFFECT OF DEMAGNETIZATION :

Most calculations assume the sample and the grains inside it to be either slabs or infinite cylinders. In practice, this is far from actual case. Samples have finite size and grains have a finite shape and size. Therefore, demagnetization correction to grain and grain boundary contributions have to be accounted. The grains being quite irregular, it is not possible to have a definite demagnetization factor for all the grains. The intrinsic anisotropy of these superconductors will further complicate the situation. For a homogeneous sample, Chen, Brug and Goldfarb [28] have calculated the demagnetization factors of a cylinder as a function of susceptibility, χ and aspect ratio, γ . As discussed by Senoussi et al. [29] for higher packing fraction samples, the bulk demagnetization factor will be important whereas in lower density

samples individual grains determine the demagnetization correction. Therefore, for practical cases where packing fraction of grains in the bulk is not too high, demagnetization contribution due to grains will have to be included. Demagnetization correction assumes further complexity in the granular samples because of magnetic field dependence of shielded fraction[30,31] . Because of all these complications, inclusion of demagnetization correction in this model is not easy. Following Yaron et al[30]., a simplification of the problem is achieved by correcting for demagnetization in two steps. The macroscopic internal field which determines J_{cj} is given by[30],

$$H_i = H_0 - NM$$

where H_0 and H_i are external and corrected internal fields respectively and N and M are the demagnetization factor for the bulk and volume average of magnetization respectively. But J_{cg} will be determined by a corrected field, H_g given by,

$$H_g = H - nM_g \tag{3.2.8}$$

where H is the field, appears as applied field in the grains, n is the demagnetization factor corresponding to the grains and M_g is the magnetization due to grain. Then J_{cj} is calculated using equations (6) and (7) and J_{cg} is calculated using equations (6) and (8). Thereafter, flux profile and magnetic susceptibilities have been calculated.

3.2.1C. RESULTS AND DISCUSSION:

3.2.1C.i) DEMAGNETIZATION EFFECT ABSENT:

In figure 3.2.1a, $\text{real}(\chi')$ parts of the AC susceptibility have been plotted as a function of DC bias field for different AC amplitudes as indicated within the figure for DC bias field range of 10 mT. Unless and otherwise mentioned, the default bulk diameter and grain size in our calculation are 2 mm and 10 μm respectively. All the critical current values indicated in all the figures are in amp/cm^2 . Here the field dependence of both $J_{cj}(H)$ and $J_{cg}(H)$ is of Kim type,

i.e., $\beta=1$. It can be seen in this figure that as the amplitude decreases the field dependence in the real parts becomes smoother. The peak at zero bias decreases with decrease of AC amplitudes. With decrease of amplitude, the valleys on both sides shift to lower fields (magnitude wise) as shown in the inset (figure 3.2.1a) and coincide with each other for lowest amplitude at zero DC field. These results are in agreement with those of Kim et al.[1].

In figure 3.2.1b imaginary parts, (χ'') of AC susceptibility have been plotted for parameters same as in figure 3.2.1a. With increase in AC amplitude, the valleys on these curves appear at higher DC fields and the peak at the zero DC field gets enhanced. The inset shows this amplitude dependence of the valley position. The main features in these curves are; i). the presence of a peak at zero bias field height of which decreases with amplitude of AC field, ii). the presence of valley at a DC bias value close to the AC amplitude and iii). the presence of hysteresis at lower amplitudes of AC field. The field dependence, as seen in figure 3.2.1b, once again has good agreement with results of Kim et al.[1]. However, the striking difference is the appearance of hysteresis specially for low AC amplitudes. Further it is clear that the hysteresis depends on the amplitude of the AC excitation. The argument of Kim et al.[1] that the presence of hysteresis can not be explained in terms of critical state model does not find support in our calculations. They further argued that the observed hysteresis in $\chi'(H)$ and $\chi''(H)$ is possibly due to the hysteresis of $J_c(H)$. In fact it is seen (results not shown here) that the hysteresis in imaginary part is quite possible even in a single component model which implies that the observed hysteresis must have at least, part contribution from the critical state hysteresis. The success of the model is probably because of the straight forward approach as available in a numerical model calculation and exploring a wide AC amplitude range.

It is difficult to look into the physical origin of the features in the field dependence of $\chi'(H)$ and $\chi''(H)$ as described in figures 3.2.1a and 3.2.1b. However, a qualitative argument can be tried on the basis of the evolution of the major M-H loops due to DC bias and minor M-H loops due to AC field. At zero DC bias the AC field traces full minor loops during which bulk annihilation loss dominates[27] and so the χ'' increases along with a decrease in diamagnetic response, χ' . This bulk annihilation loss increases with amplitude of AC field and in the absence of surface barrier and lower critical field this loss decreases with increase of DC bias field. This decrease continues upto a DC bias close to AC amplitude. This can explain the peak at zero DC

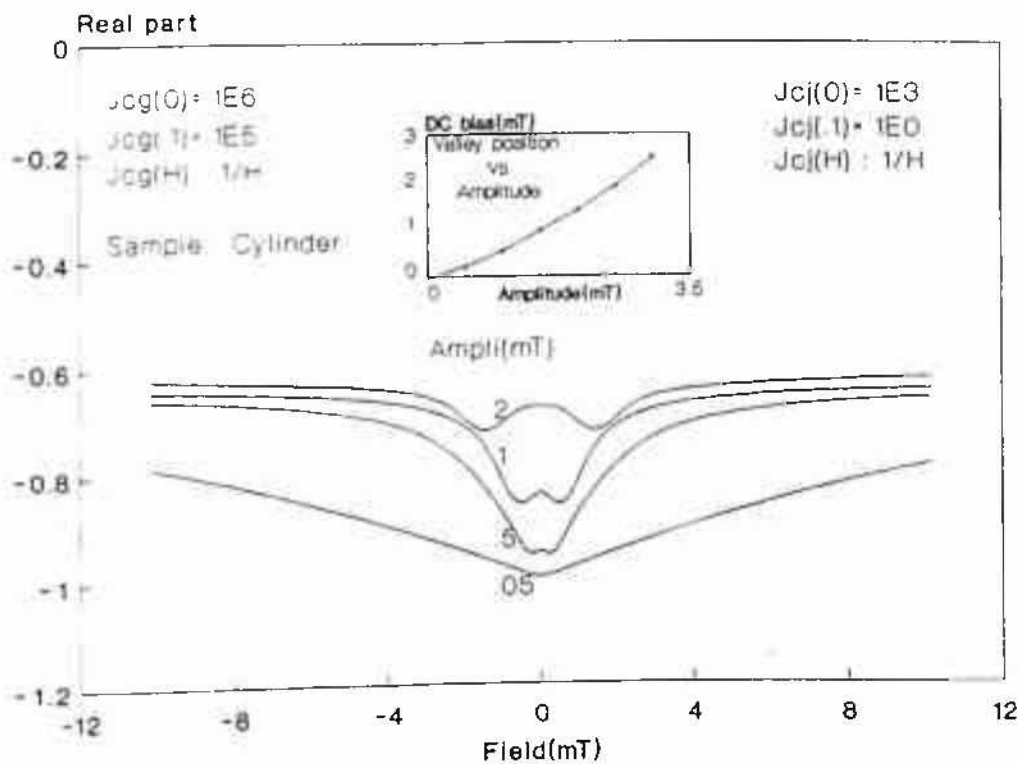


Figure 3.2.1a: $\chi'(H)$ curves for four AC amplitudes without considering demagnetization correction.

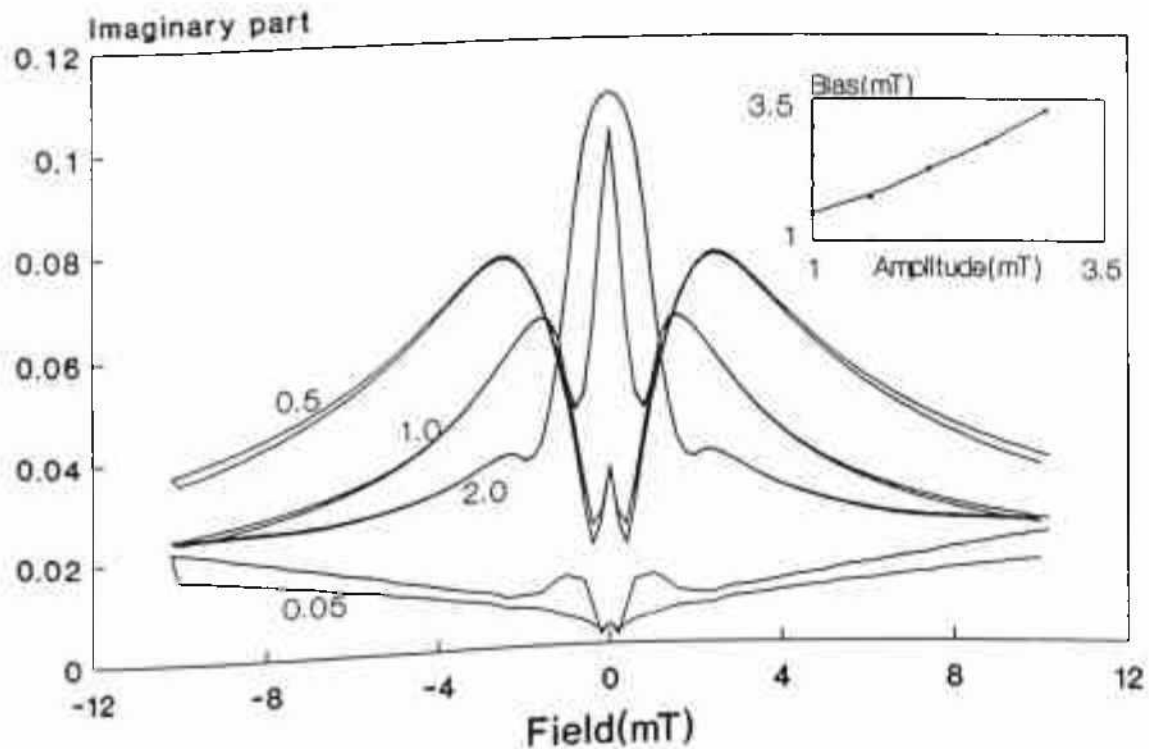


Figure 3.2.1b: Imaginary counter part of figure 3.2.1a.

bias in the imaginary($\chi''(H)$) as well as real($\chi'(H)$) loops. As seen in figure 3.2.1a,b the peak at zero bias decreases with decrease of AC amplitude and the valley shift to lower DC bias (magnitude wise) in agreement with above explanation. As the DC bias is increased the hysteretic (bulk pinning loss as described by Clem [27]) loss dominates and χ'' starts to increase. At a sufficiently higher bias, when the major loop becomes almost parallel to field axis, the area and the slope of the minor loops also become constant and the χ'' and χ' curves saturate which is obvious in figure 3.2.1a,b.

The similar curves (as shown in figure 3.2.1a,b) have also drawn for other $J_{ej}(0.1)$ parameters which essentially show the same behavior except that with increase of $J_{ej}(0.1)$ to 10^1 or 10^2 , the $\chi'(H)$ and $\chi''(H)$ become less field dependent. However, they have not been included being similar to what Kim et al. have reported except the hysteresis at low amplitudes of AC field.

In figures 3.2.2(a,b), 3.2.3(a,b) and 3.2.4(a,b) the real and imaginary parts have been plotted upto a higher field range of 100 mT for three different junction parameters (i.e., different $J_{ej}(0.1)$) while J_{ej} 's are same for all. Field dependence of J_{ej} as well of J_{cg} is Kim type, i.e., $\beta=1$. As one can visualize, in this field range the grain and grain boundary contributions will be substantial and it will be difficult to understand the nature of these curves. The peaks at zero bias in the χ' curves, as seen in the low field curves (figure 3.2.1a) can not be seen here. However, in the case of χ'' curves the zero bias peaks are prominent and even higher than the corresponding low field peaks (however, it is seen that the virgin value of χ'' at zero DC bias is same in both low and high field cases). It is apparent from the figure that the peak at a finite DC bias shifts to higher DC bias field as the AC amplitude decreases and can not be seen for amplitude = 0.01 mT as in figure 3.2.2b. In the case of $J_{ej}(0.1) = 10^1$ (figure 3.2.3b) the peaks in the $\chi''(H)$ curves at a finite DC bias appear at a relatively lower DC bias as compared to figure 3.2.2b for $J_{ej}(0.01)=1$. It is also seen that at lower AC amplitudes, though the peak at finite DC bias vanishes, a third peak appear at the position of DC bias independent of AC amplitude only on the increasing (by magnitude) arm of the $\chi''(H)$ loops. This is further clear in figure 3.2.4b for $J_{ej}(0.1)=10^2$ where the above mentioned peak at finite DC bias is not seen but the third peak appears at all amplitude on the increasing (magnitude wise) arm of $\chi''(H)$ loops. It is obvious from these figures that more hysteresis in imaginary part is seen in com-

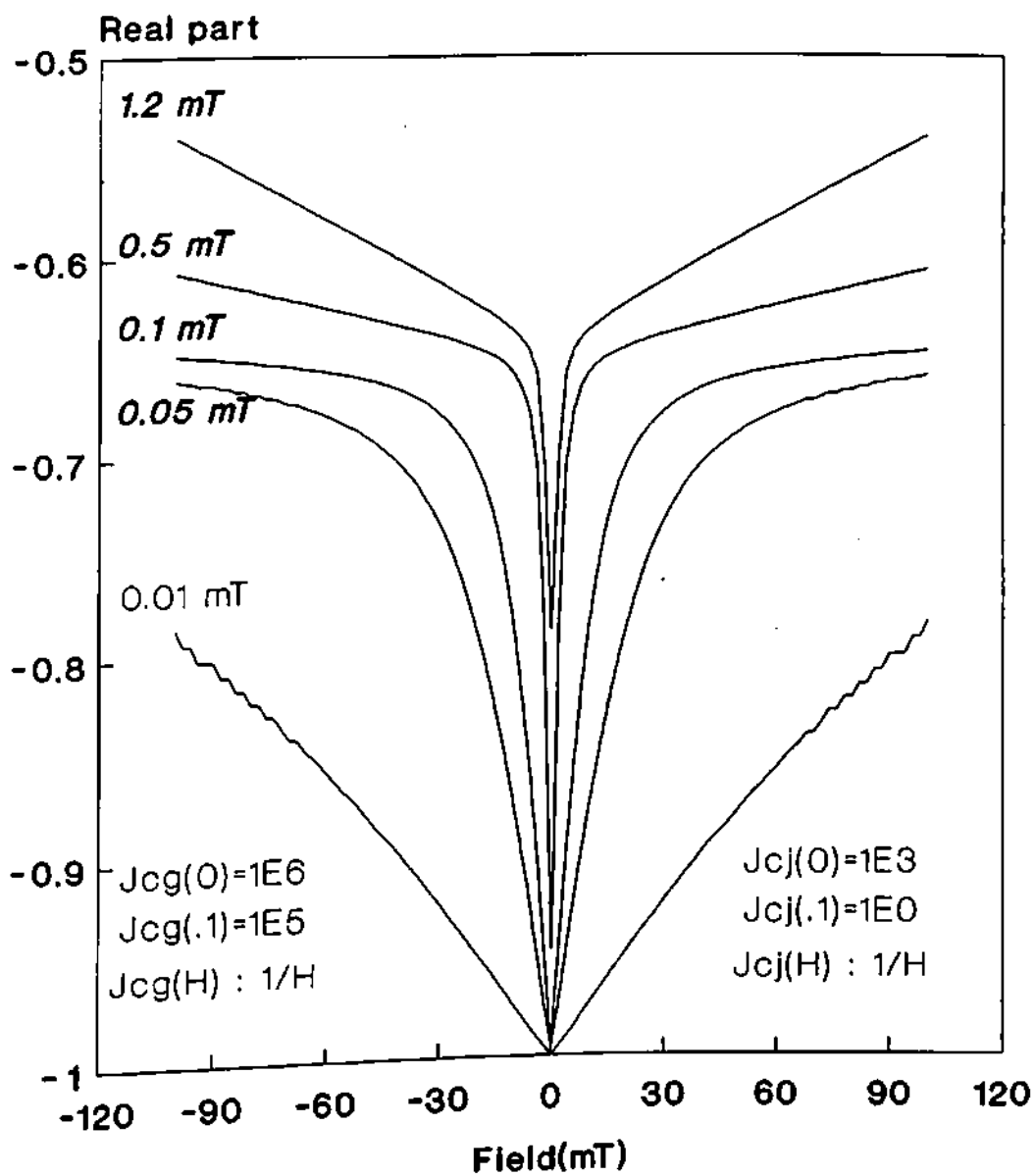


Figure 3.2.2a: $\chi'(H)$ curves for four AC amplitudes without considering demagnetization correction.

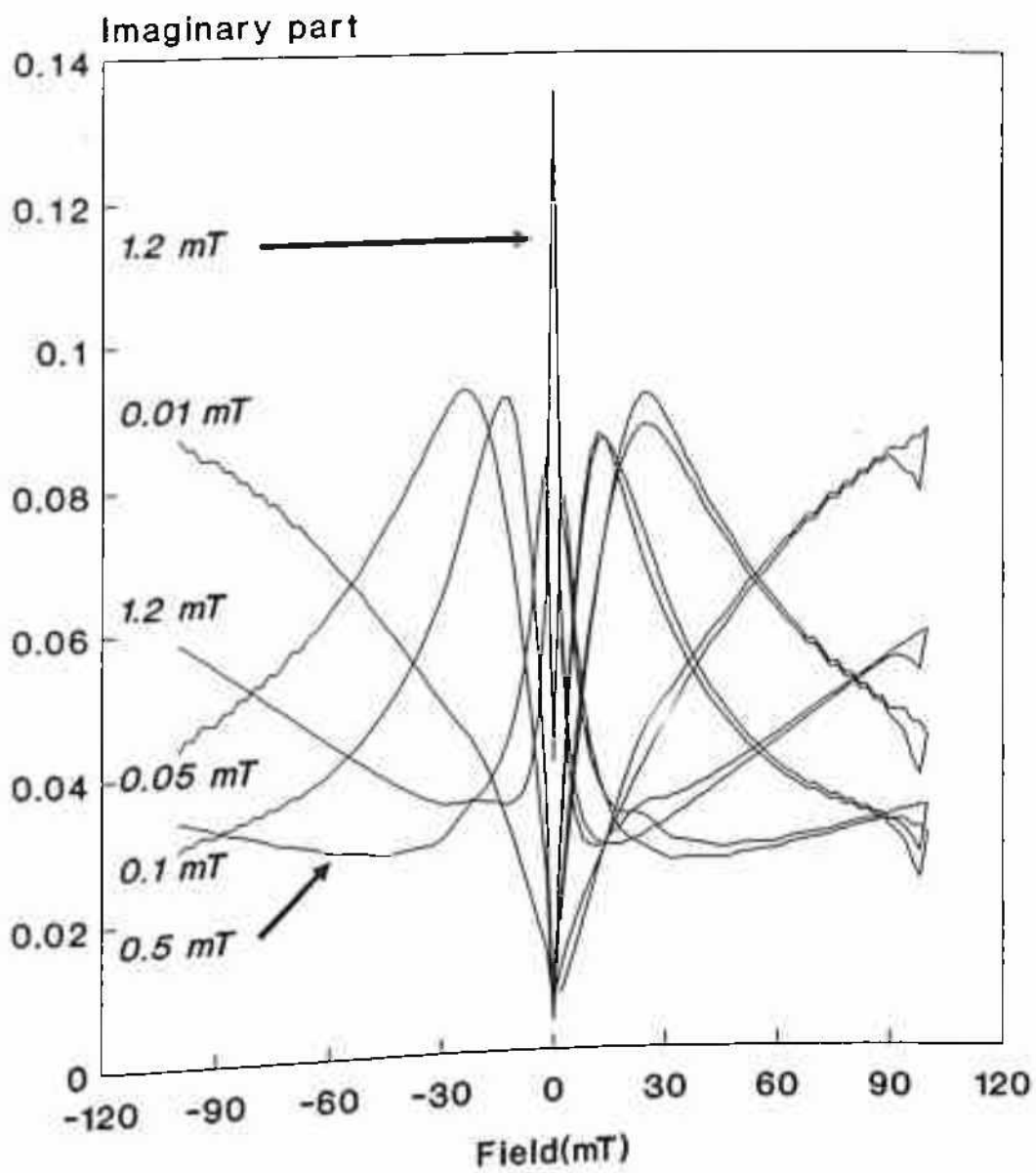


Figure 3.2.2b: Imaginary counter part of figure 3.2.2a.

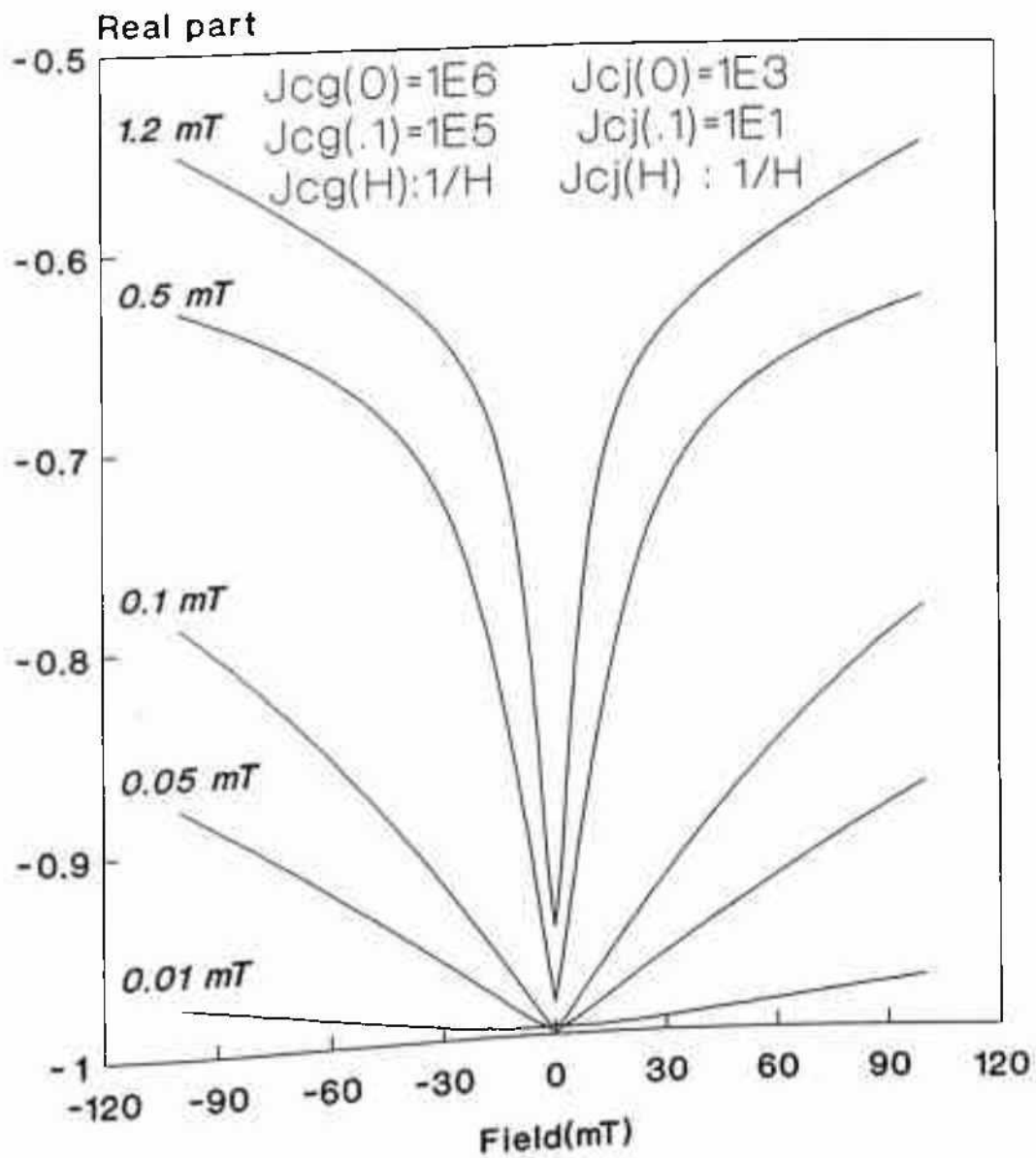


Figure 3.2.3a: $\chi'(H)$ curves for four AC amplitudes without considering demagnetization correction.

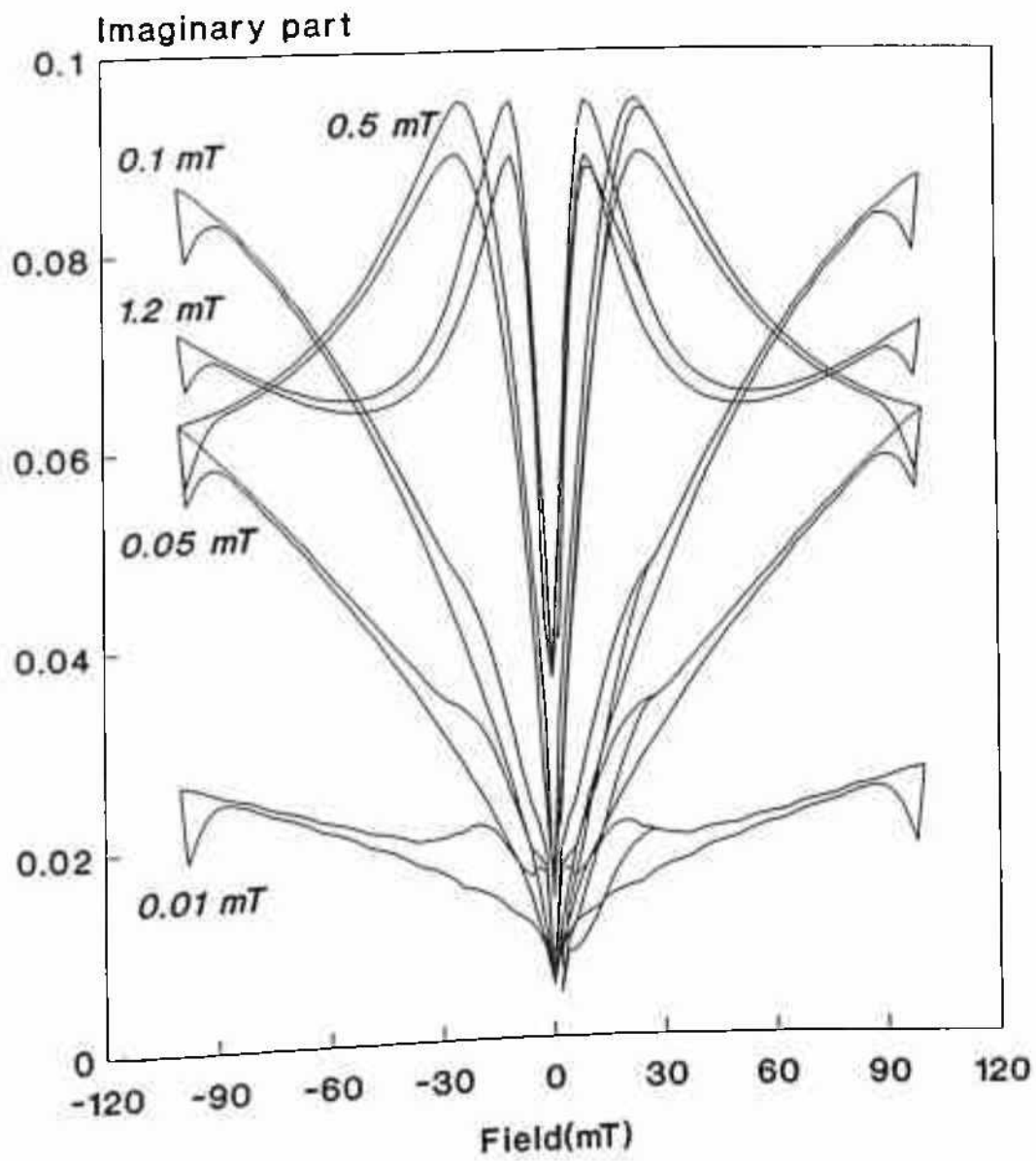


Figure 3.2.3b: Imaginary counter part of figure 3.2.3a.

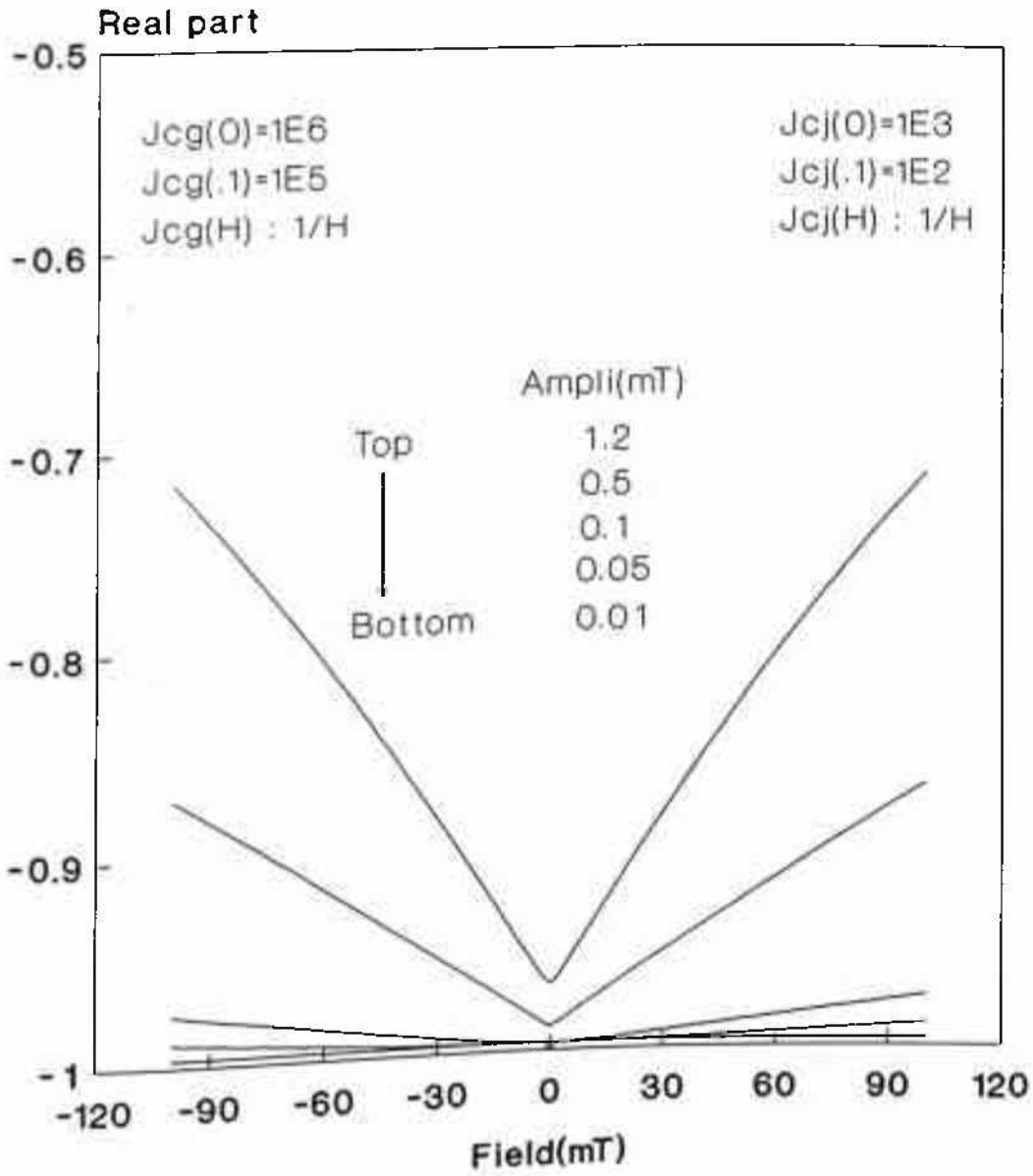


Figure 3.2.4a: $\chi'(H)$ curves for four AC amplitudes without considering demagnetization correction.

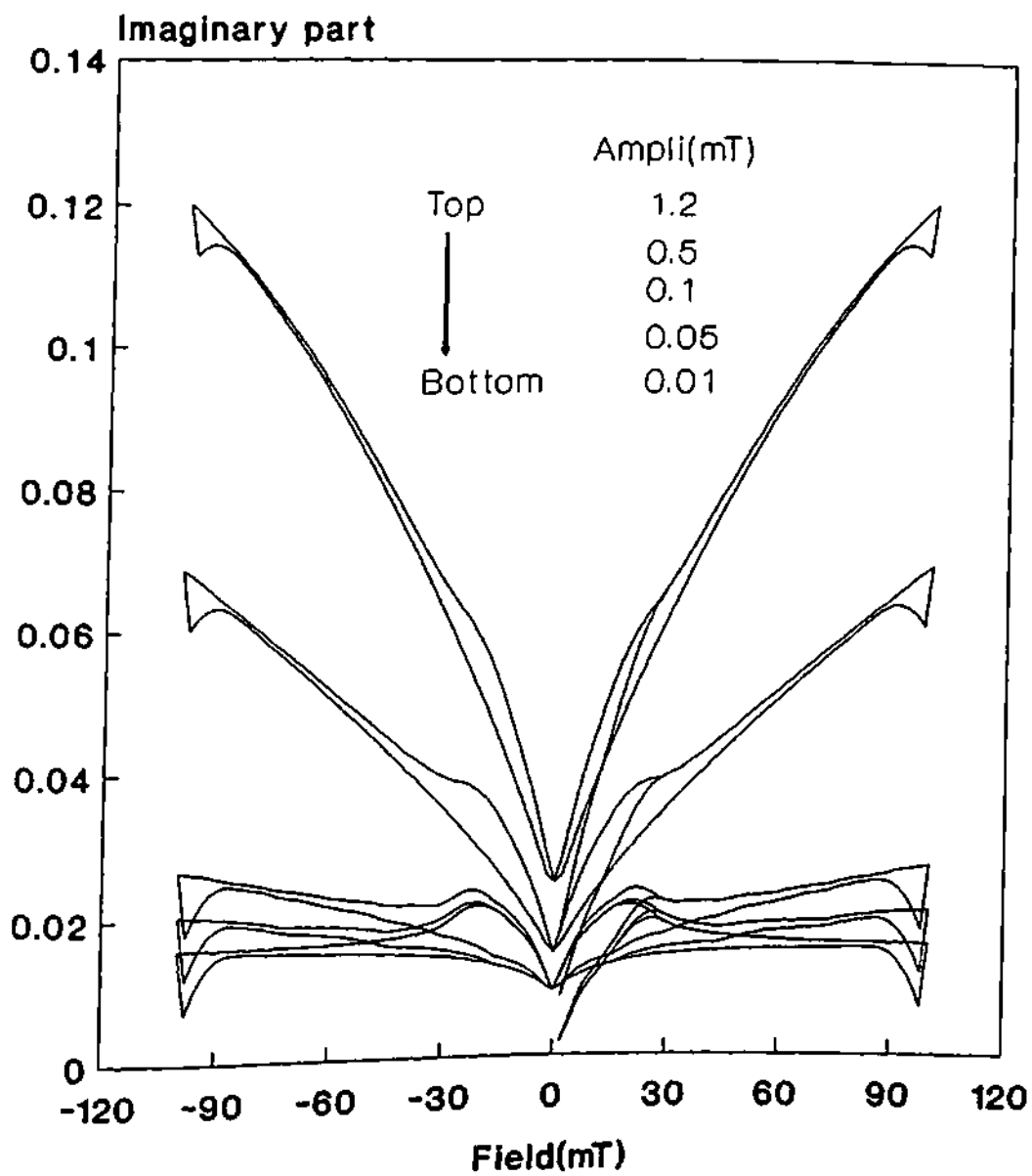


Figure 3.2.4b: Imaginary counter part of figure 3.2.4a.

parison to the low field calculations (figure 3.2.1b). But, even in this field range, the real part does not show any hysteresis in all the cases. Further, it is to be noticed in comparing figures 3.2.2, 3.2.3 and 3.2.4 that the hysteresis in imaginary part increases with increase of $J_c(0.1)$ (i.e., as one goes towards Bean model) while the field dependence of real part decreases.

3.2.1C.ii) EFFECT OF DEMAGNETIZATION - BETTER REALIZATION OF HYSTERESIS OF $\chi'(H)$ and $\chi''(H)$:

As the effort is not to do exact fit of the results to some experimental data, a moderate value of 0.3 for the demagnetization factor for the bulk and an extreme value of 1 for the demagnetization factor of the grains which are appropriate for usual samples used in experiments have been selected to illustrate the effect of demagnetization correction. Figure 3.2.5 shows real (χ' , figure 3.2.5a) and imaginary (χ'' , figure 3.2.5b) parts of AC magnetic susceptibility as a function of DC bias field for different AC amplitudes. Other parameters are shown in the figure and are same as in figure 3.2.1. As seen in these two figures, hysteresis is seen in both real and imaginary parts at all AC amplitudes. This is for the first time that the hysteresis in AC susceptibility has been successfully described theoretically. In these calculations, the hysteresis of $J_c(H)$ has not been included at all. The field dependence of $\chi'(H)$ and $\chi''(H)$ is same as in figures 3.2.1a and 3.2.1b except for the shift causing the hysteresis. In case of real parts, the curves for increasing and decreasing field seem to get sheared while the basic shape are same as in the figure 3.2.1a. The origin of this shift is that as the DC field is decreased, some flux get trapped causing the local field to become somewhat higher, resulting in a shift, ΔH of the decreasing (magnitude wise) field arms to higher (by magnitude) field side. Thus the local zero field is seen to appear at somewhat higher field than the external zero field. Due to this split, the zero bias peak on the $\chi''(H)$ curves as seen in figure 3.2.1b have shifted apart by ΔH (for simplicity still these shifted peaks will be referred as "zero bias peaks"). Kim et al[1], have used this amount of split as the measure of hysteresis. As seen in figure 3.2.5a, with increase of AC amplitude, the split (ΔH) does not change appreciably. But at the same time, it is apparent from the figure 3.2.5a that with decrease of amplitude, the area of individual loops initially increases and after an optimal value of AC amplitude the area starts decreasing. Thus it is not justified to consider only the split as the measure of hysteresis. In fact, one must take the area of individual loops as a measure of hysteresis.

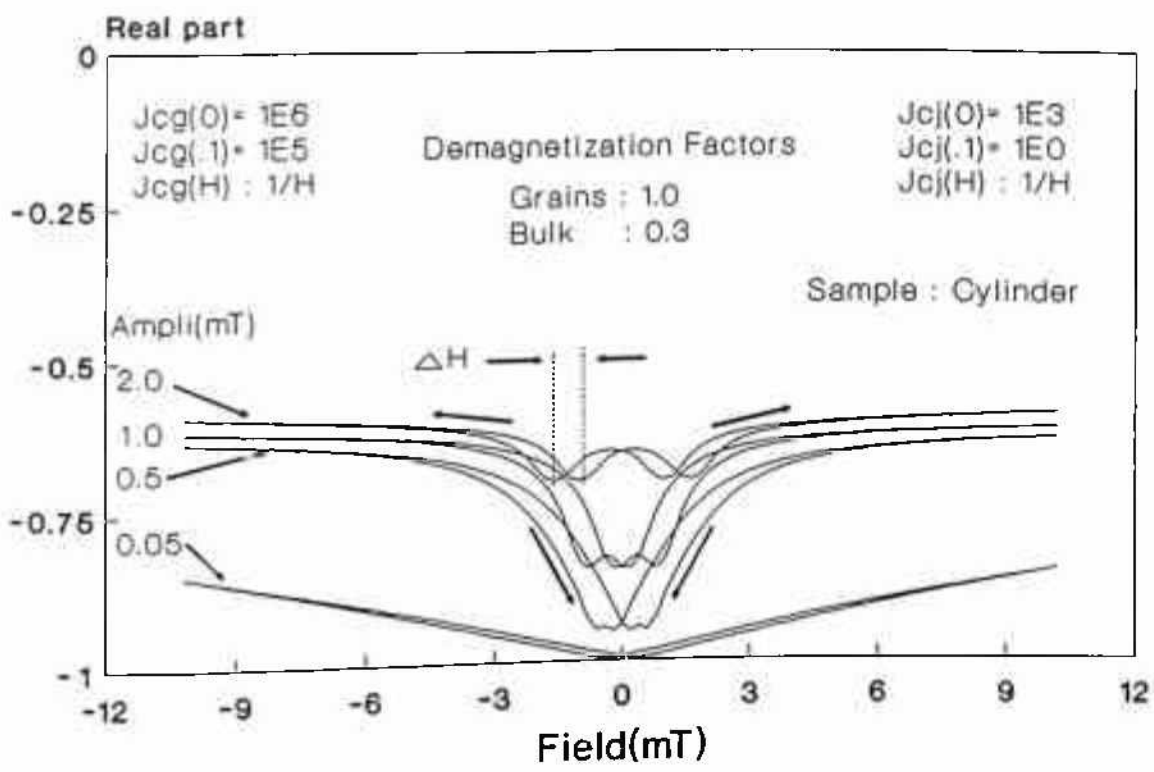


Figure 3.2.5a: $\chi'(H)$ loops for four AC amplitudes considering demagnetization correction.

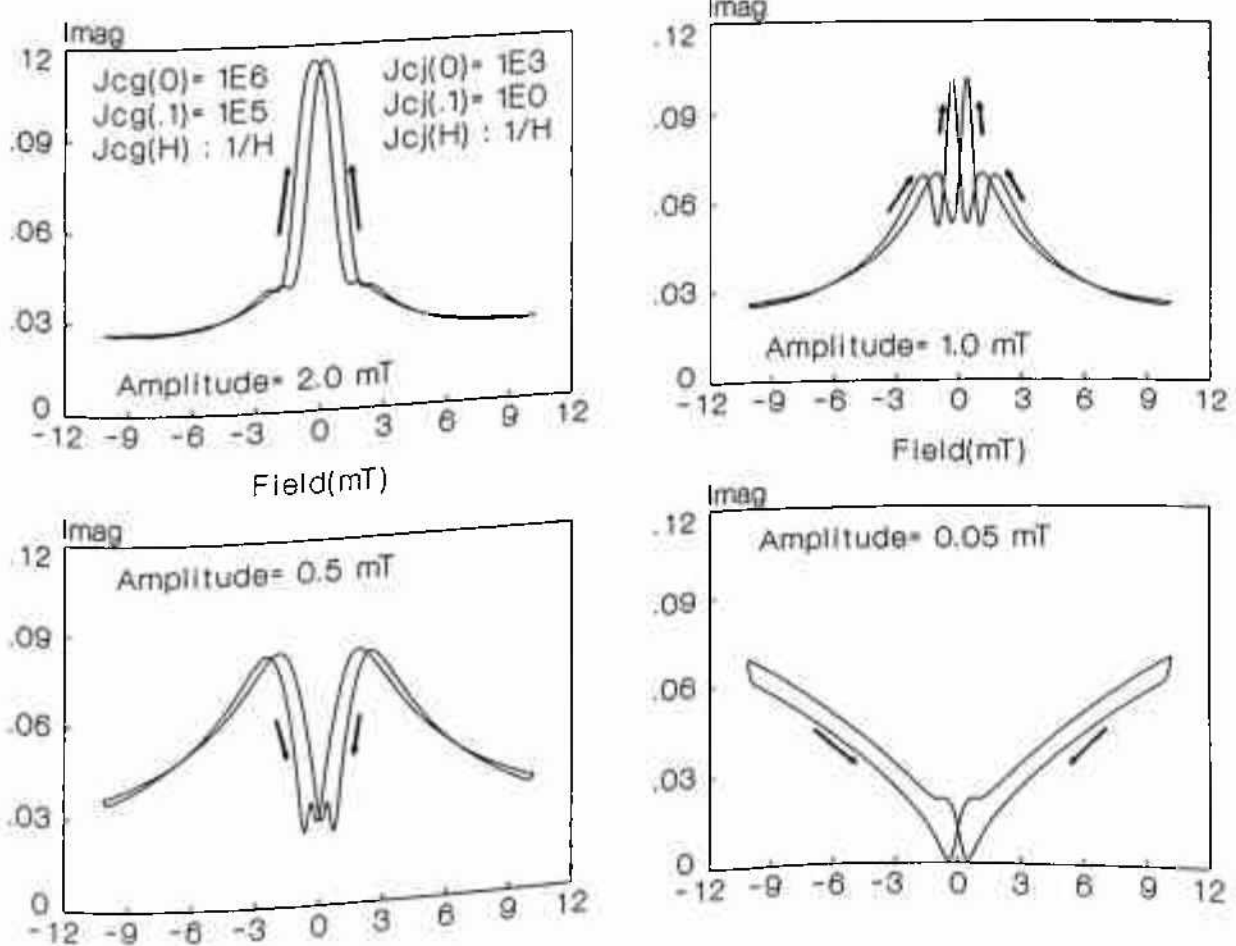


Figure 3.2.5b: Imaginary counter part of figure 3.2.5a.

For the case of imaginary loops the behavior is more complicated (figure 3.2.5b.). However, the same split appears at all amplitudes but like the real part, the split does not seem to depend on AC amplitudes. Considering the area as the measure of hysteresis one can see, while for $\chi'(H)$ hysteresis is maximum at an optimum amplitude, for $\chi''(H)$ it is monotonically increasing with decreasing AC amplitude. The area between the increasing and decreasing curves as seen in figure 3.2.5b clearly decreases at higher bias fields.

3.2.1C.iii) DEPENDENCE ON PARAMETERS :

It is important to compare the calculations for different critical current density parameters. In figures 3.2.6 and 3.2.7 $\chi'(H)$ (figures 3.2.6a, 3.2.7a) and $\chi''(H)$ (figures 3.2.6b, 3.2.7b) have been plotted for three different J_{cg} parameters of the grains for two given amplitudes with J_{cj} parameters of the GB remaining same. Since fields are low, grain contribution is small and loops are determined mainly by J_{cj} parameters. Thus all the three loops in figures 3.2.6a, 3.2.7a and 3.2.6b, 3.2.7b are of similar shape. Further, it is apparent from these figures that loop height and area decrease as one goes towards less field dependent J_{cg} parameters. The reduction of height of the loops is physically justified since one must expect better screening from the grains with less field dependence of J_{cg} . For $\chi''(H)$ the effect of better J_{cg} parameters is due to less contribution to loss from the grains at all DC fields. However, the reduction of hysteresis with better grain parameters is puzzling and indicates the problem of this study in characterizing the granular system. Thus a reduction in $\chi'(H)$ or $\chi''(H)$ loops does not necessarily mean worse transport properties (i.e., GB J_{cj} parameters) but may indicate better grain parameters(J_{cg} parameters). This reduction of hysteresis becomes more obvious at lower amplitudes as seen in figure 3.2.7a,b. The dependence of hysteresis on J_{cg} parameters indicates that a contribution from the grains is partly responsible for the hysteresis even at low field like this. This finding makes it further clear that a one component model will be unable to give good fit to experimental data even at low fields. This also clarifies the experimental observation [1] of sample dependence of hysteresis in $\chi(H)$.

So far the field dependence of $J_{cj}(H)$ has been taken as $J_{cj}(H) = J_{cj}(0)/(1 + \alpha|H|)$ which is typically accepted for a bulk ceramic. However, as discussed earlier $J_{cj}(H) = J_{cj}(0)/(1 + \alpha|H|)^\beta$, $\beta > 1$ may also be good choice. It is important to consider higher values of

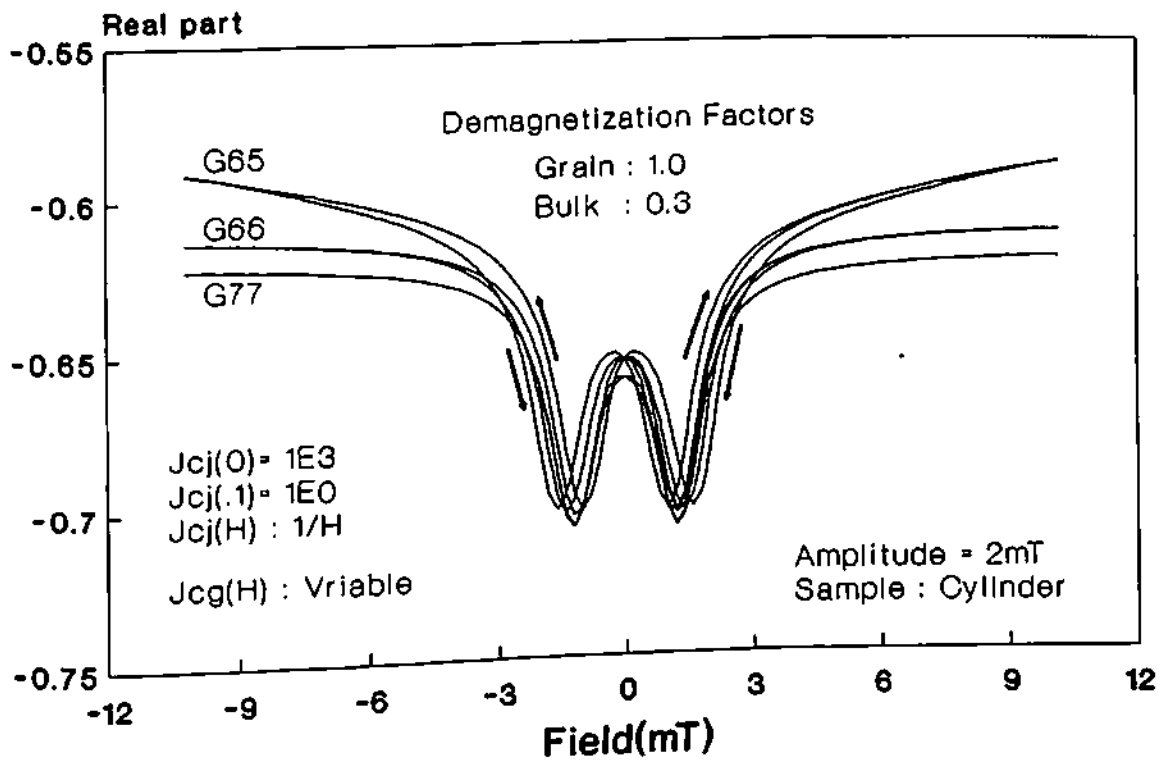


Figure 3.2.6a: $\chi'(H)$ loops for 2 different $J_{cg}(H)$'s. [Gmn : m is the exponent of $J_{cg}(0)$ and n that of $J_{cg}(0.1)$]

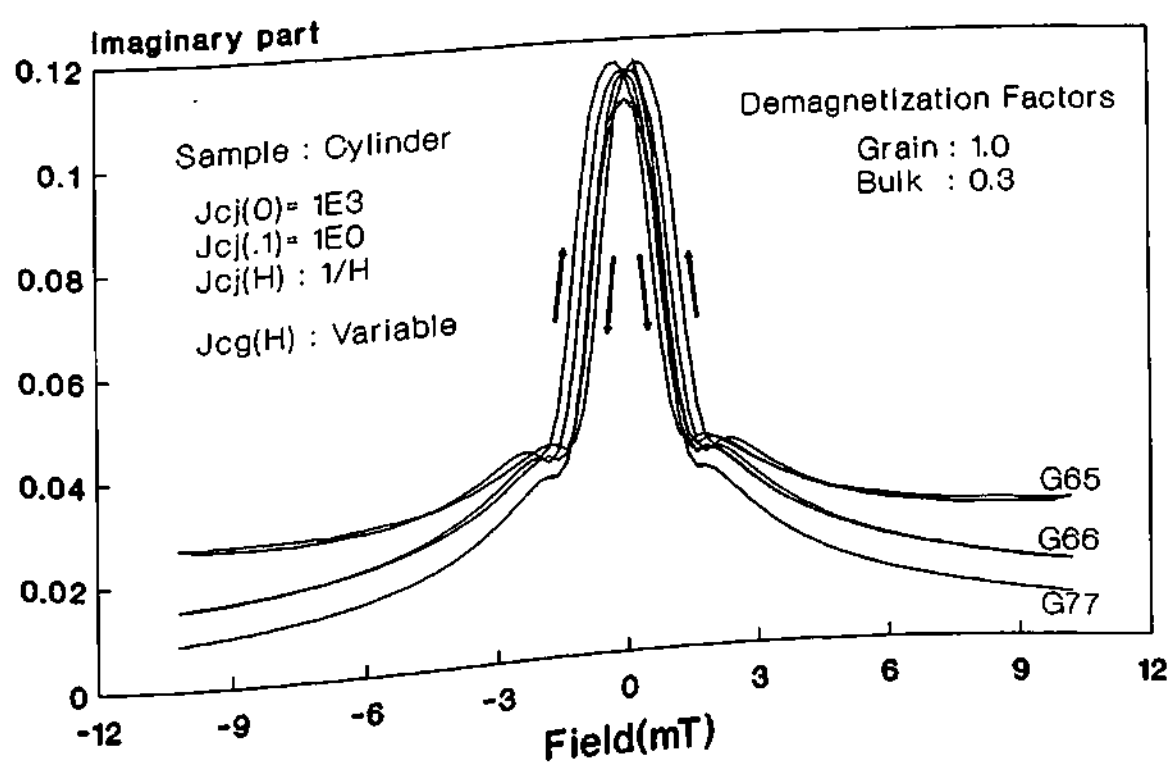


Figure 3.2.6b: Imaginary counter part of figure 3.2.6a.

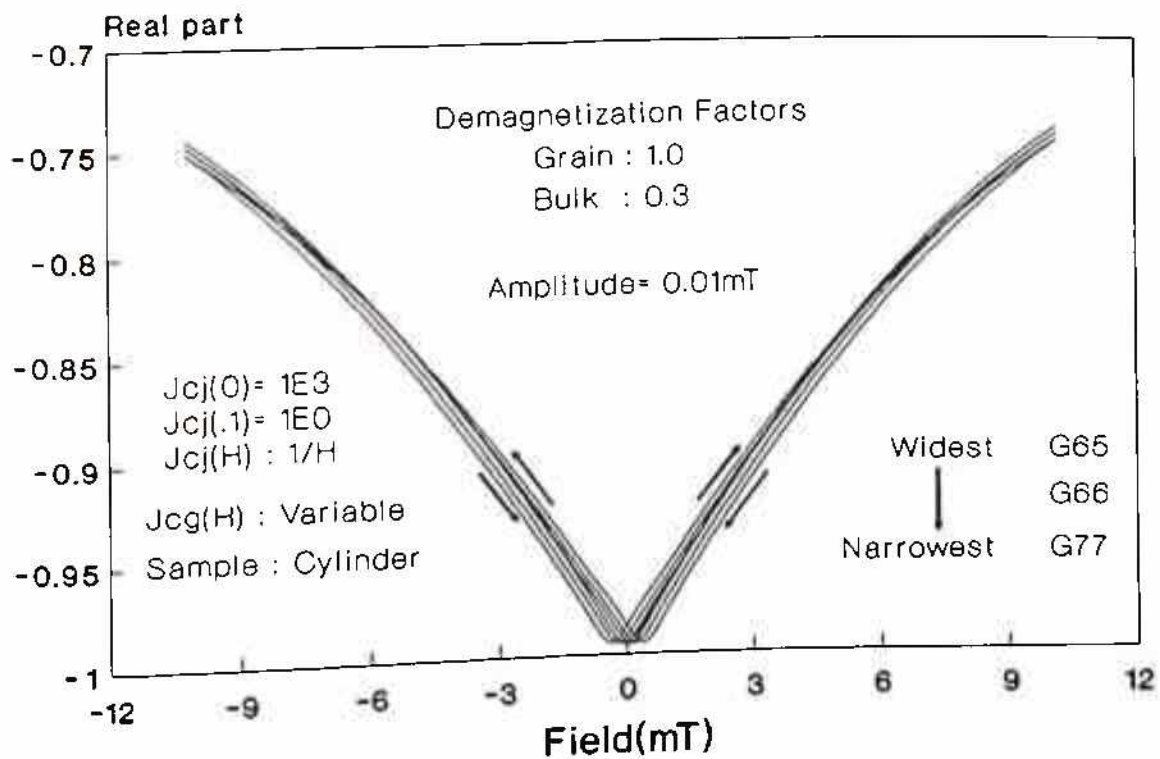


Figure 3.2.7a: $\chi'(H)$ loops for 2 different $J_{cg}(H)$'s. [Gmn : m is the exponent of $J_{cg}(0)$ and n that of $J_{cg}(0.1)$]

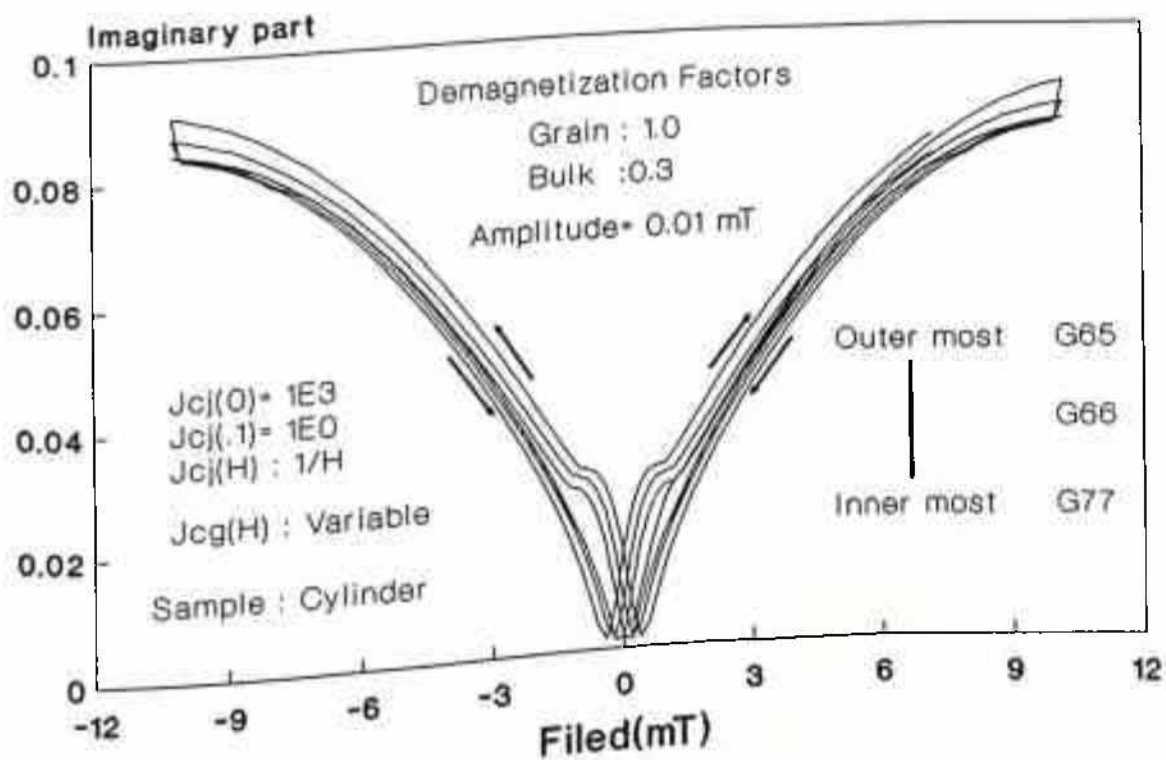


Figure 3.2.7b: Imaginary counter part of figure 3.2.6a.

β also, viz, $\beta=2$, $J_c(0)=100$ amp/cm² and $J_{c1}(0.01)=1$ amp/cm² (instead of $J_{c1}(0.1)=1$ amp/cm²). Therefore a comparative study of different values of β must be considered. Thus in figure 3.2.8 the $\chi'(H)$ (figure 3.2.8a) and $\chi''(H)$ (figure 3.2.8b) loops with $J_c(0)=1000$ and $J_{c1}(0.1)=1$ have been plotted for $\beta=2$ keeping all the parameters for the grains same as in figure 3.2.5. It is apparent from figure 3.2.8a that with $\beta=2$ (in diagrams $J_{c1}(H)\propto 1/H^2$ means $\beta=2$) the peak at zero DC bias vanishes and also the field dependence becomes smoother. It can also be seen that with higher β hysteresis decreases in real parts provided all other parameters including $J_c(0)$ and $J_{c1}(0.1)$ remain the same. The imaginary loops ($\chi''(H)$) in figure 3.2.8b for $\beta=2$ are also quite different from that in the figure 3.2.5b where $\beta=1$. Except for the loop for amplitude of 0.5 mT in all other amplitudes as shown in these two figures, the field dependence in the $\beta=2$ case is less than for the case with $\beta=1$.

In figure 3.2.9 the $\chi'(H)$ (figure 3.2.9a) and $\chi''(H)$ (figure 3.2.9b) loops with $J_c(0)=100$ and $J_{c1}(0.01)=1$ have been plotted for $\beta=2$, keeping all the parameters for the grains same as in figure 3.2.5. As seen in figure 3.2.9a, the real part has good agreement with the data of Kim et al.[1]. In fact it is possible to select the parameters to achieve the right fit to experimental data. On comparing figures 3.2.9a and 3.2.9b with figures 3.2.5a and 3.2.5b, both having same grain parameters (J_{cg}), one can see that though the nature of the $\chi'(H)$ loops are almost the same in both cases, hysteresis is more and the zero DC bias peak in χ'' appears at a smaller AC amplitude for $\beta=2$ along with $J_c(0)=100$ and $J_{c1}(0.01)=1$. In figure 3.2.10 the $\chi'(H)$ and $\chi''(H)$ loops with same J_c parameters as in figure 3.2.8 has been plotted except that in figure 3.2.10 the value of β is 1. It is apparent from 3.2.10a that the zero bias peak in $\chi'(H)$ is seen to come back which is not seen in figure 3.2.9a. Moreover though at higher amplitudes the curvatures of individual arms of $\chi'(H)$ loops are same, at lowest amplitude (0.01 mT) they are opposite. The same observation is seen in figures 3.2.8a and 3.2.5a where all parameters except β are same. In fact for $\beta=2$ the curvatures of arms of $\chi'(H)$ loops at different amplitudes show a transition from downward at higher amplitudes to upward at lower amplitudes and this critical value of amplitude is higher for better J_{c1} parameters. As one can visualize, comparing the $\chi''(H)$ loops is more difficult than the $\chi'(H)$ loops because of the strong dependence of these loops on parameters particularly at higher amplitudes. These can be seen to be true even in all the figures, e.g. figures 3.2.5b, 3.2.8b, 3.2.8b, 3.2.10b where, at lower amplitudes (like 0.05 or 0.01 mT)

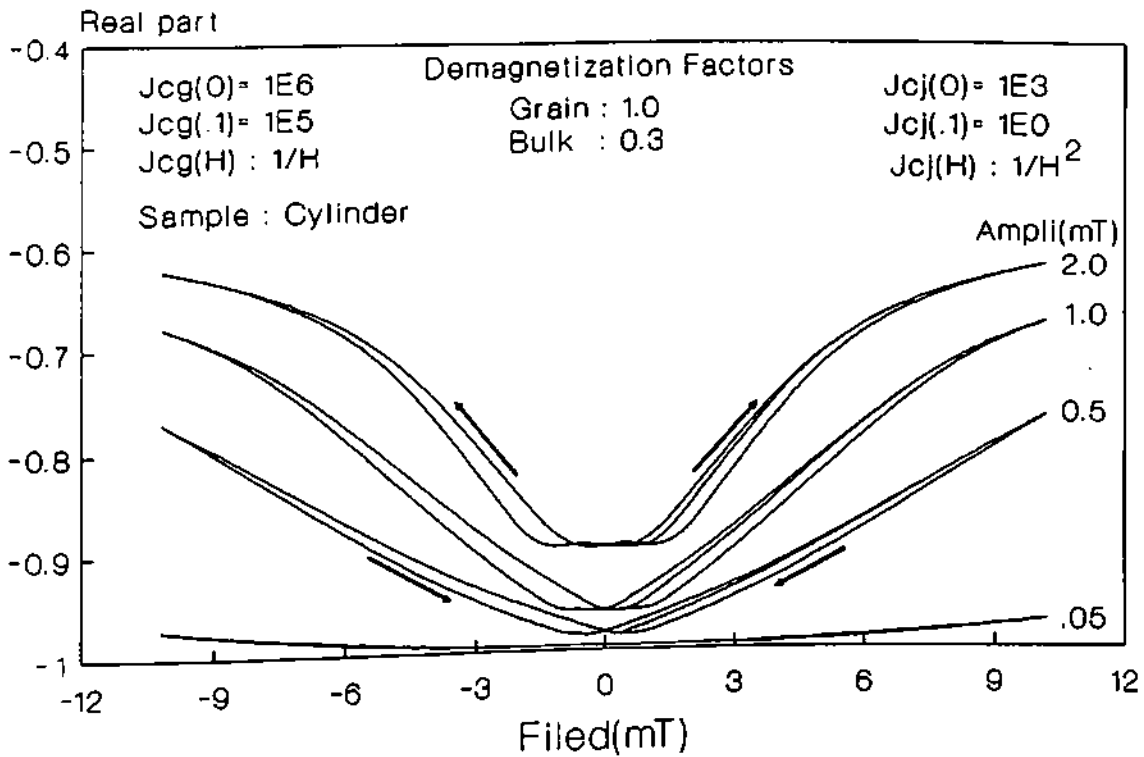


Figure 3.2.8a: $\chi'(H)$ loops for four AC amplitudes considering demagnetization correction. [$\beta=2$]

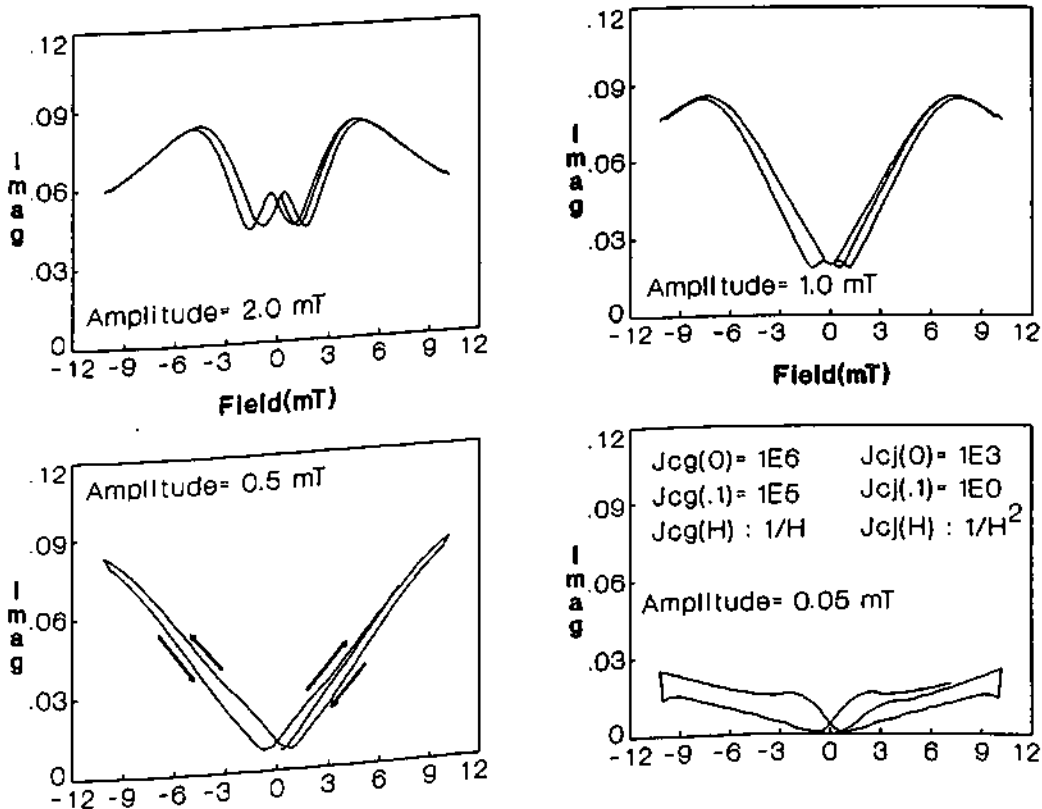


Figure 3.2.8b: Imaginary counter part of figure 3.2.8a.

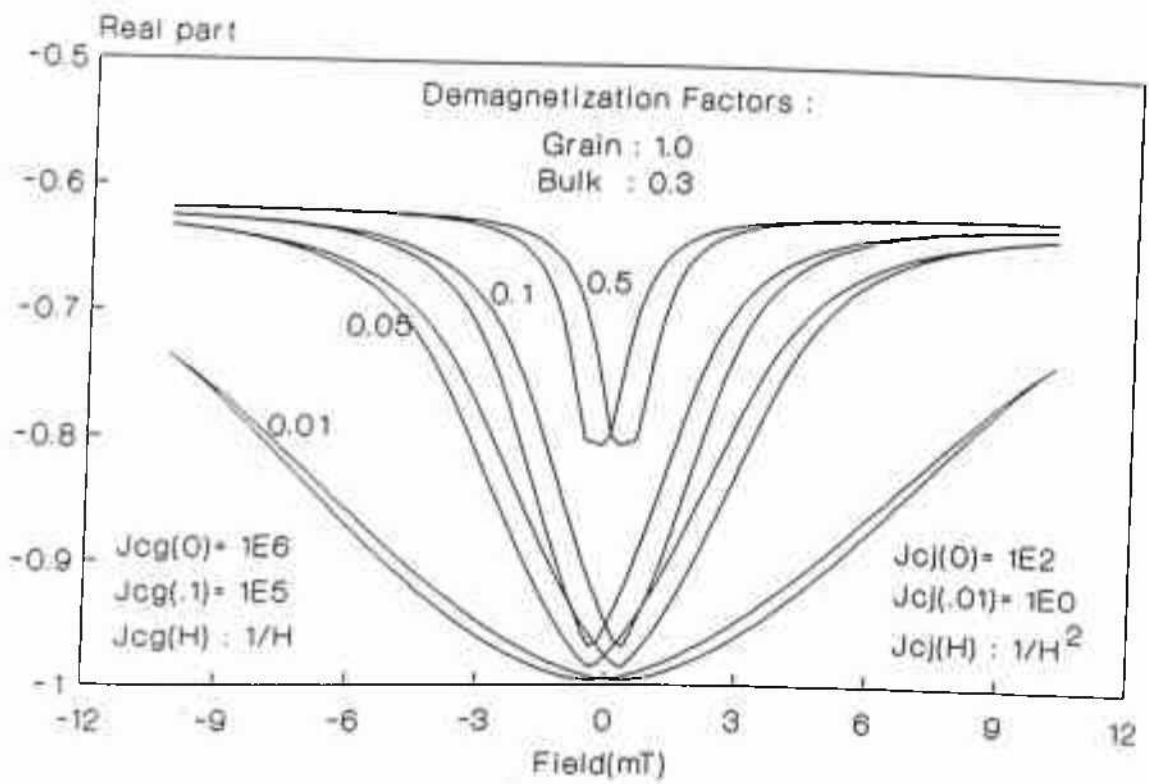


Figure 3.2.9a: $\chi'(H)$ loops for four AC amplitudes considering demagnetization correction. [$\beta=2$]

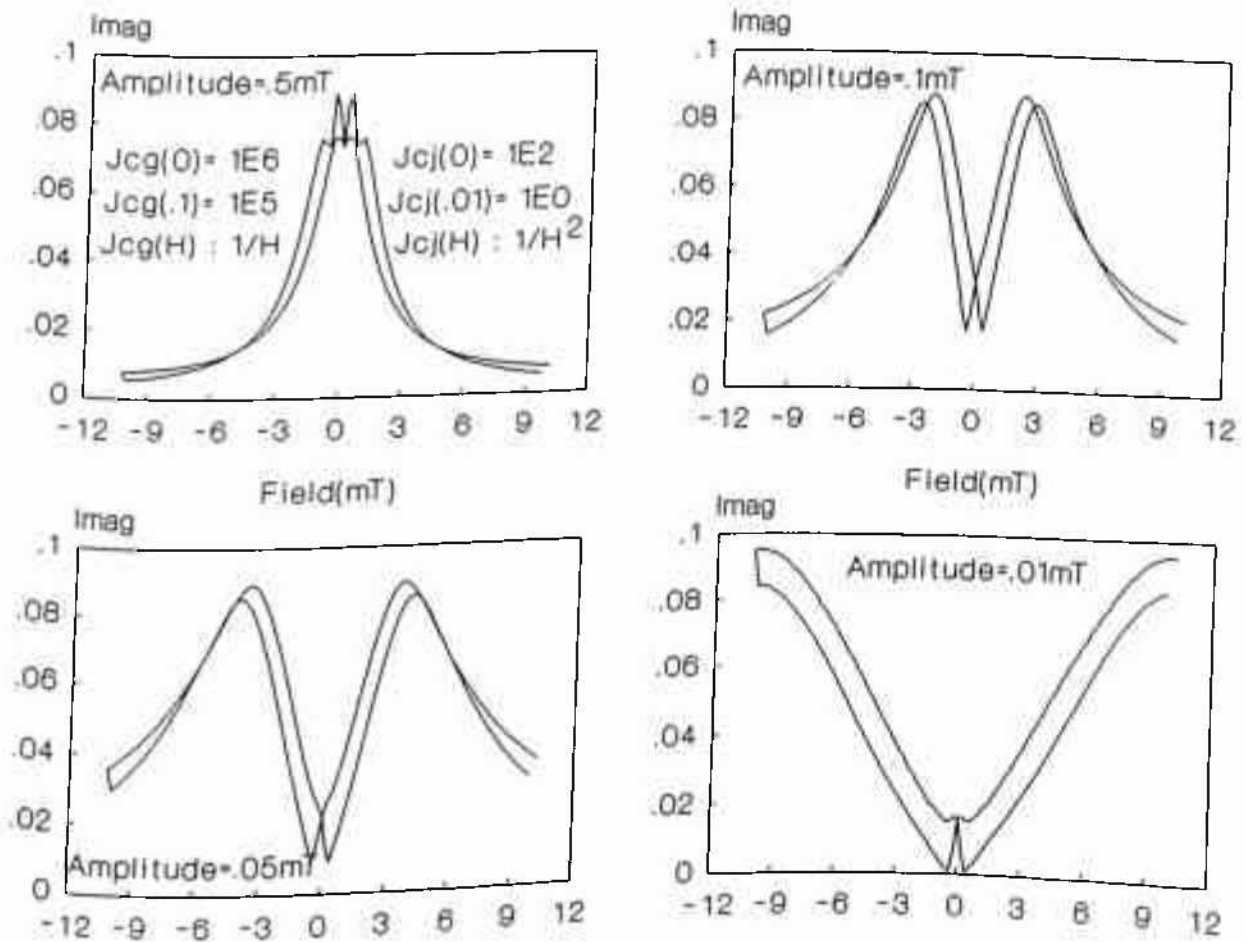


Figure 3.2.9b: Imaginary counter part of figure 3.2.9a.

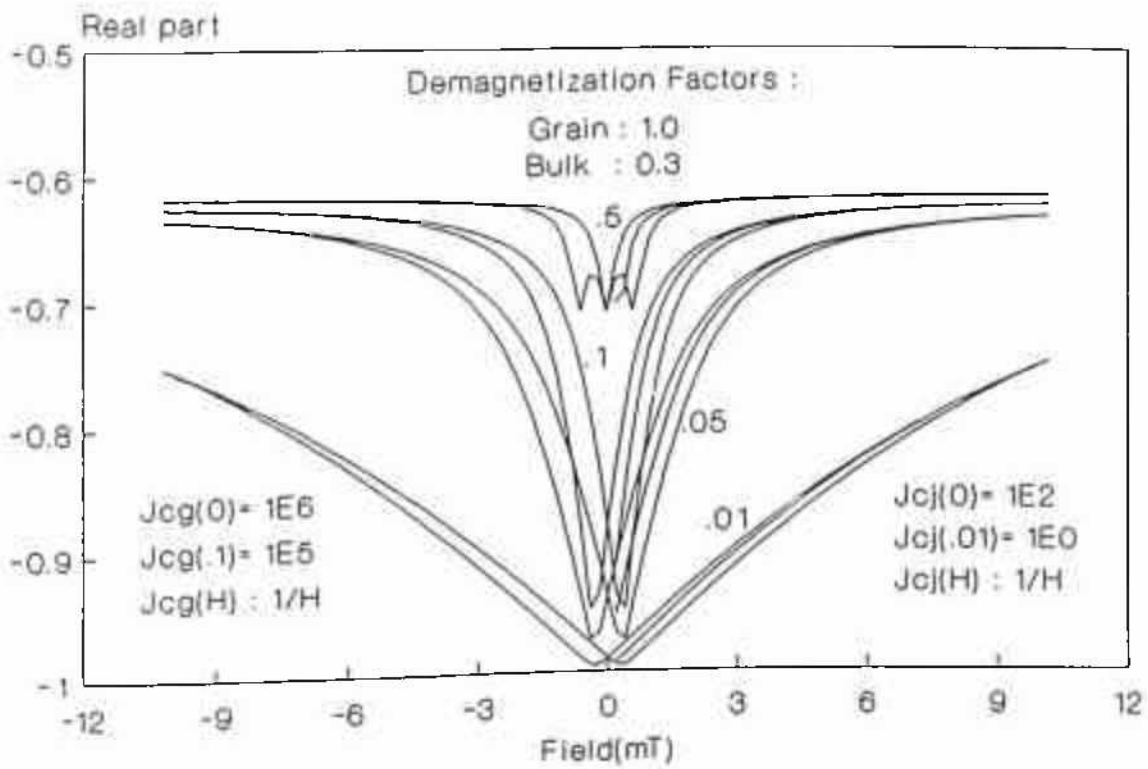


Figure 3.2.10a: $\chi'(H)$ loops for four AC amplitudes considering demagnetization correction. [$\beta = 1$]

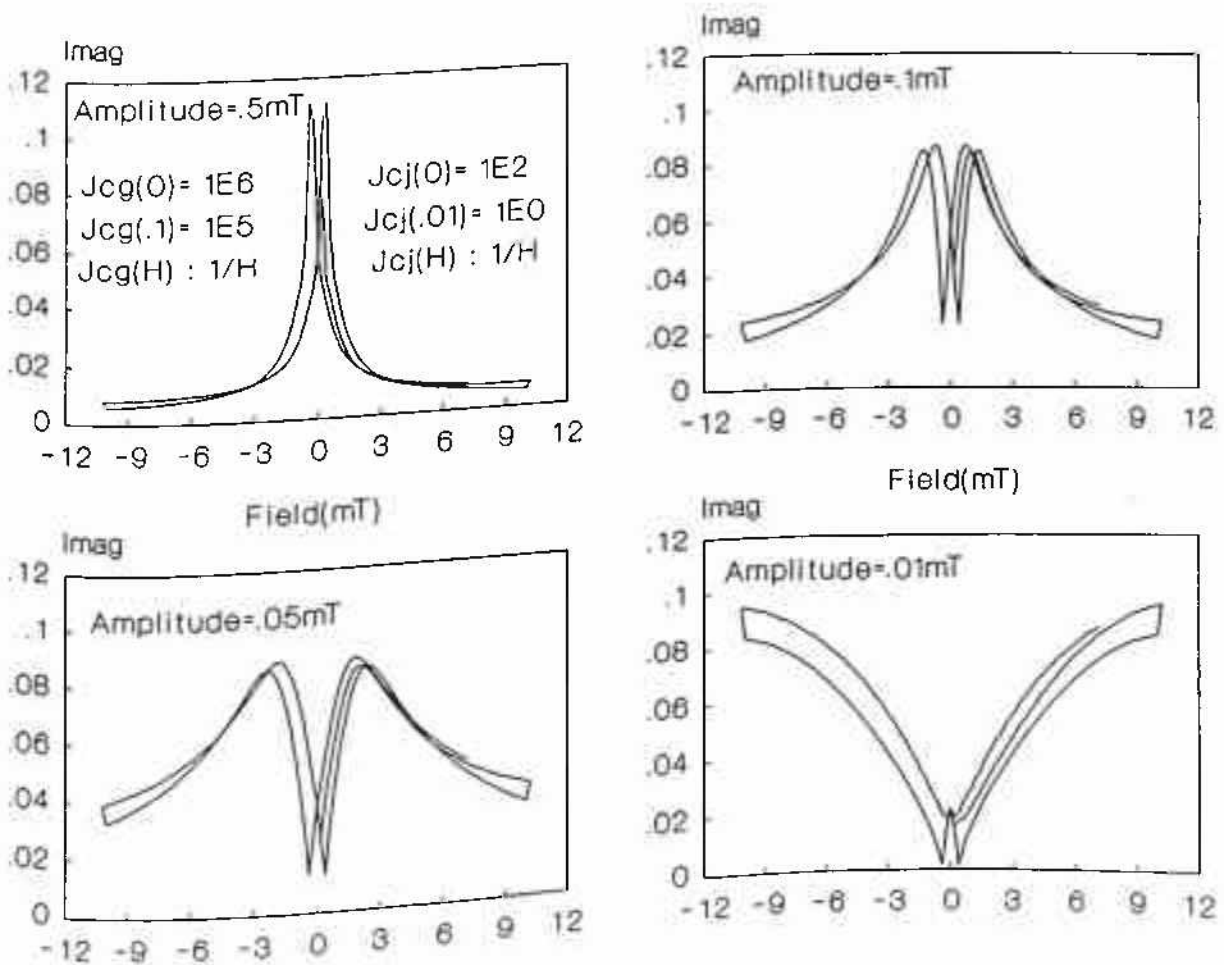


Figure 3.2.10b: Imaginary counter part of figure 3.2.10a.

the basic shapes of the $\chi''(H)$ loops are same. However, at higher amplitudes the shapes are drastically different. The similarity of shapes of $\chi''(H)$ loops at low amplitudes may be due to the fact that for amplitudes much smaller than the bulk penetration field, H_p^* the basic shapes are determined essentially by the major M-H loops. Because when the amplitude is small enough, perturbation due to amplitude is negligible and the AC excitation can simply be considered as a signal probe. In fact, by observing the effect of amplitudes of the AC field on the M-H loops one can see that at lower amplitudes the M-H loops are not much disturbed (figure not shown).

3.2.1C.iv) EFFECT OF GRAIN SIZE:

The complex situation of magnetic state in a granular system can further be probed by studying the effect of grain size in this model. As the grain size decreases, the number of grains per unit volume increases. At the same time with decrease of the grain size, the so called grain penetration field, H_p^* will also decrease making grains more responsive to magnetic field. This view can be justified in figures 3.2.11a and 3.2.11b where real and imaginary parts of AC susceptibility have been plotted as a function of DC bias field for different grain sizes. It can be seen in the real part in figure 3.2.11a, that with increase of the grain size, the field dependence decreases but the width of the χ' loops increases, reaches a maximum at around a grain size of $5 \mu\text{m}$ and then once again starts to decrease. The optimality of the width of the loops with respect to grain size, indicates the presence of mutually opposite processes scaling with grain size. The imaginary part, $\chi''(H)$ (figure 3.2.11b) also shows the same tendency. As grain size decreases the field dependence decreases and the height of the loops decreases but the loops as a whole get shifted to higher loss values.

3.2.1C.v) EFFECT OF FIELD RANGE :

The utility of a successful two components model will be in its ability to yield correct calculated results at all field ranges, i.e., from a few mTesla where grain boundary contribution is dominant to few hundred mTesla or higher where grains are dominant. It has been already seen in case of figures 3.2.2, 3.2.3 and 3.2.4 that the model is correct even at a field range of 120 mT and gives physically consistent field dependence of $\chi''(H)$ and $\chi''(H)$. Now the model

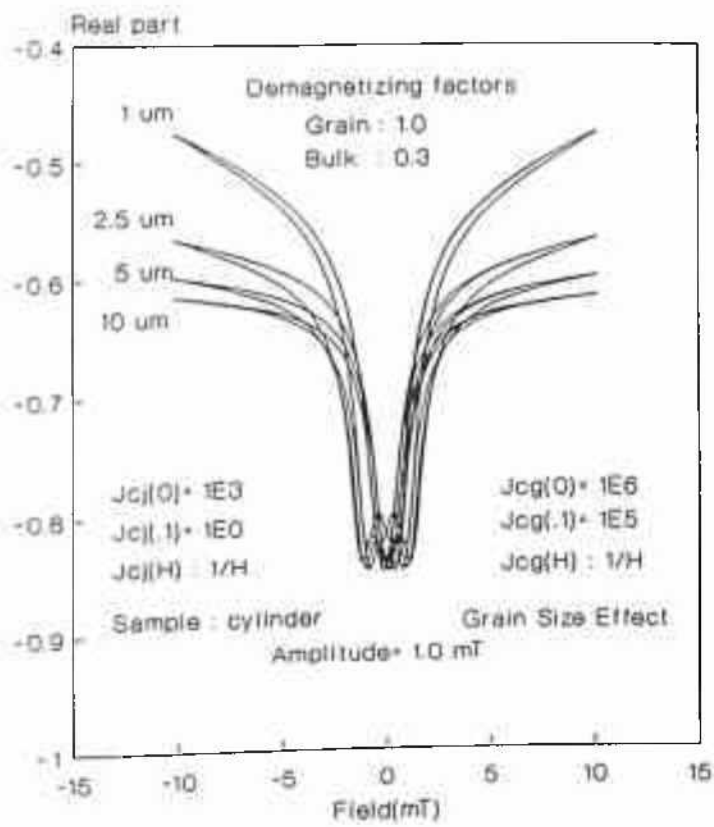


Figure 3.2.11a: Grain size (in micron) effect of $\chi'(H)$ loops for AC amplitude 1.0 mT.

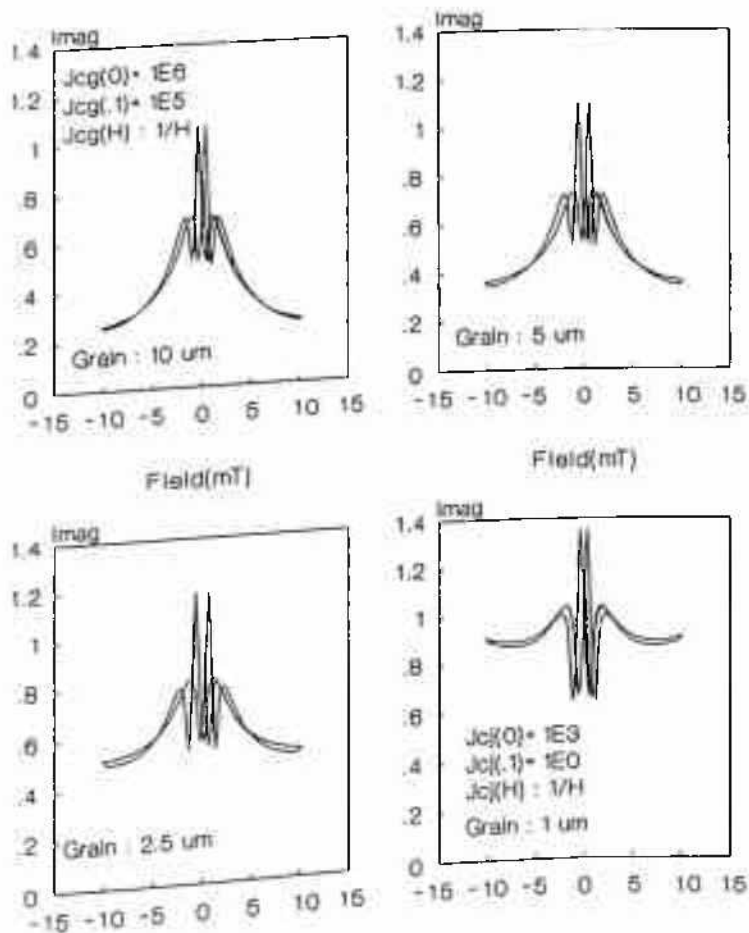


Figure 3.2.11b: Imaginary counter part of figure 3.2.11a.

will be tested for higher field range to see whether it gives physically justified hysteresis in $\chi'(H)$ and $\chi''(H)$.

In figures 3.2.12a and 3.2.12b the plot of $\chi'(H)$ and $\chi''(H)$ loops for a maximum DC field of 100 mT have been given for four different amplitudes and parameters are same as in figure 3.2.5 for $\beta=1$. The real loops still maintain the same shape as in low field range loops of figure 3.2.5a. These also are in agreement with Kim et al.'s data[1]. The $\chi''(H)$ loops, however, have strong amplitude dependence and are not similar to those at low field range. Further, though the hysteresis in $\chi'(H)$ loops is in agreement with that taken at low field range, the hysteresis in $\chi''(H)$ loops is different from their low field range counter parts indicating a decreasing trend in hysteresis (area of loops) with decreasing amplitude. It can be seen in the $\chi''(H)$ loops that at lower AC amplitudes hysteresis at higher DC fields becomes less. For example, in case of AC amplitude of 0.01 mT there is no hysteresis seen at higher DC field (> 40 mT), whereas in case of AC amplitude of 1.0 mT, even at a DC field of 100 mT hysteresis is seen. It is quite interesting to see that at higher amplitude ($>> 0.1$ mT) and at lower amplitude ($<< 0.1$ mT) the nature of the loops is apparently same. The appearance of peaks in these two extreme cases in the decreasing arms of the χ'' loops is important. It can further be noticed that the peak position is almost invariant of amplitude where as the valleys in these loops appear at a lower DC field with the decrease of amplitudes. The peaks probably indicate the point of "phase randomization" [34] by way of which grains get decoupled in an actual experimental situation. In fact the experimental data of Lee et al.[8], indicates appearance of such peaks in-out-of phase components(χ''). However, Lee et al.[8] have argued the valley to be due to H_{c1g} of the grains. They further suggested to use these valleys for predicting H_{c1g} of the grains. However, calculations here show the dependence of the valleys with amplitudes indicating the error in this process of calculating H_{c1g} .

In figures 3.2.13a, 3.2.14a the $\chi'(H)$ loops and in figures 3.2.13b and 3.2.14b the $\chi''(H)$ loops have been plotted for β values of 1 and 2 respectively, while all others parameters are same in both cases. As in these figures the J_{ej} parameters are worse than those in figure 3.2.12, one can realize the stronger field dependence of χ' in the low field region (close to the zero cross over region) to be justified and with higher β (figure 3.2.14a) this dependence is more pronounced. In case of the χ'' as seen in figure 3.2.13b, at higher amplitudes (0.5 and 0.1 mT)

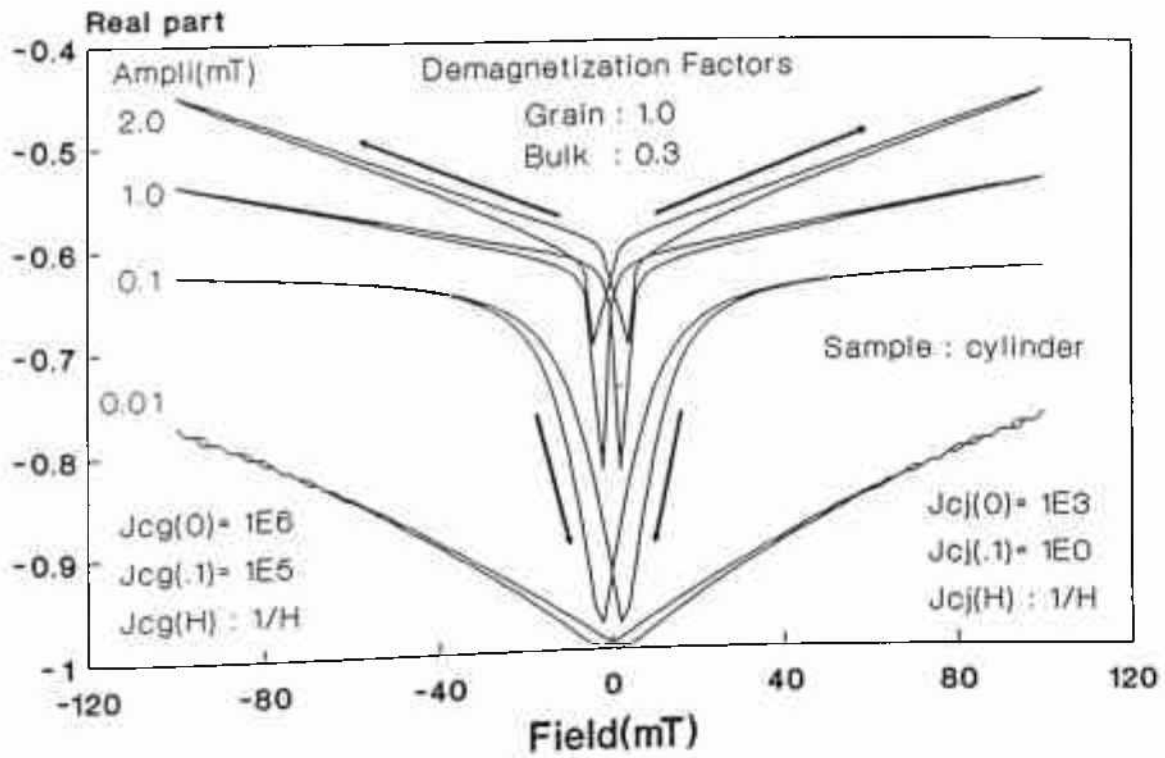


Figure 3.2.12a: $\chi'(H)$ loops for four AC amplitudes considering demagnetization correction. [$\beta=1$]

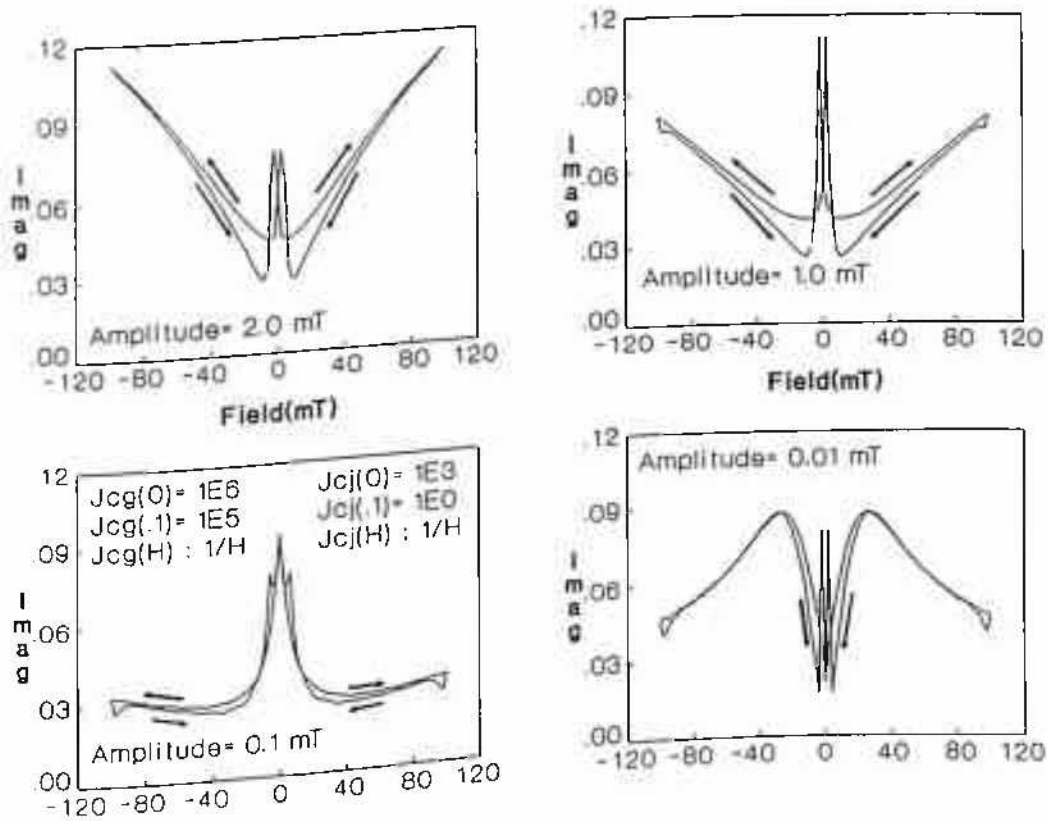


Figure 3.2.12b: Imaginary counter part of figure 3.2.12a.

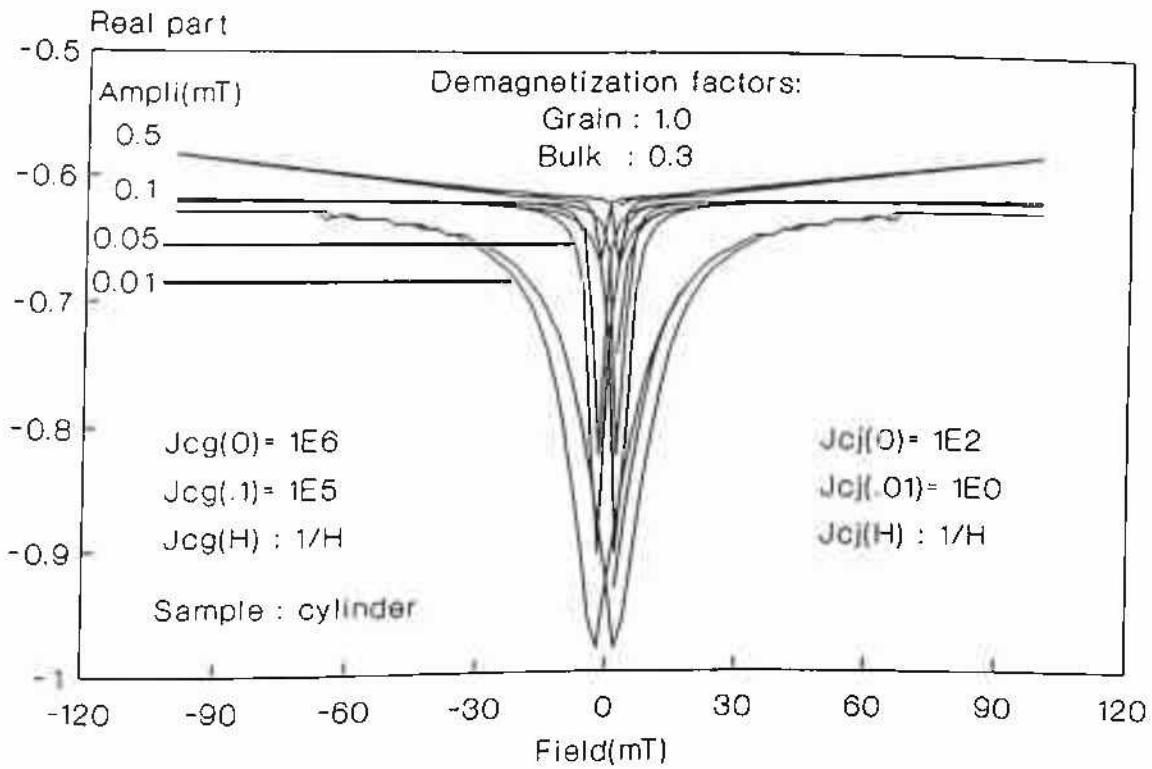


Figure 3.2.13a: $\chi'(H)$ loops for four AC amplitudes considering demagnetization correction. [$\beta = 1$]

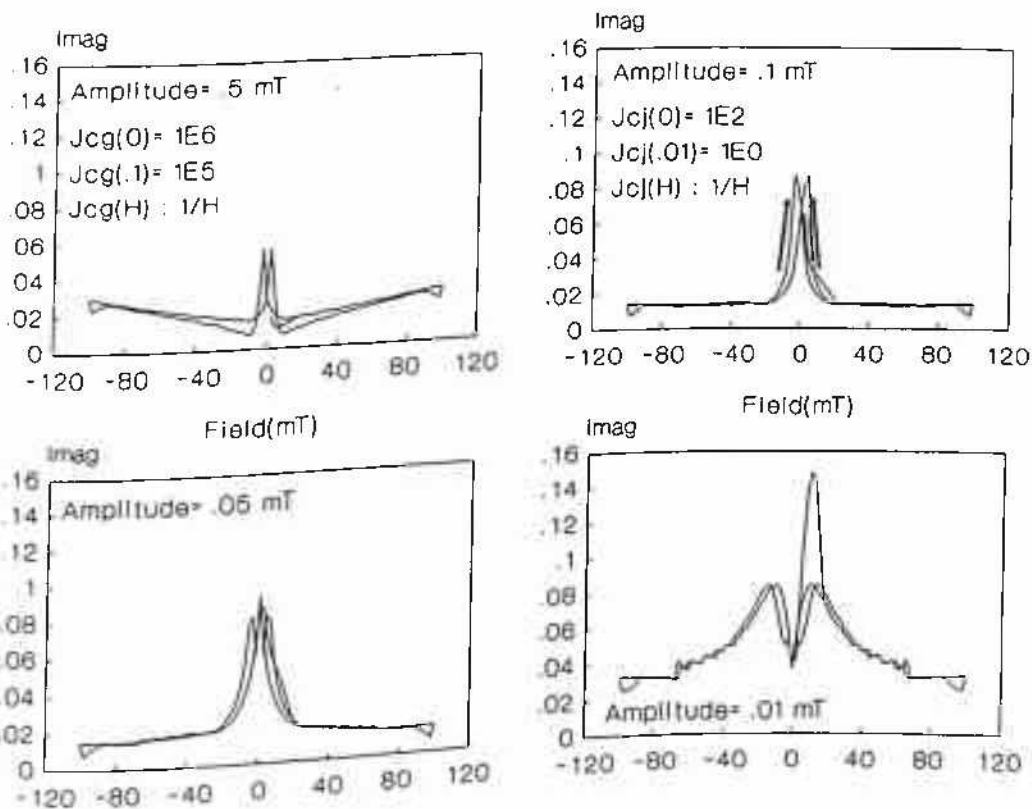


Figure 3.2.13b: Imaginary counter part of figure 3.2.13a.

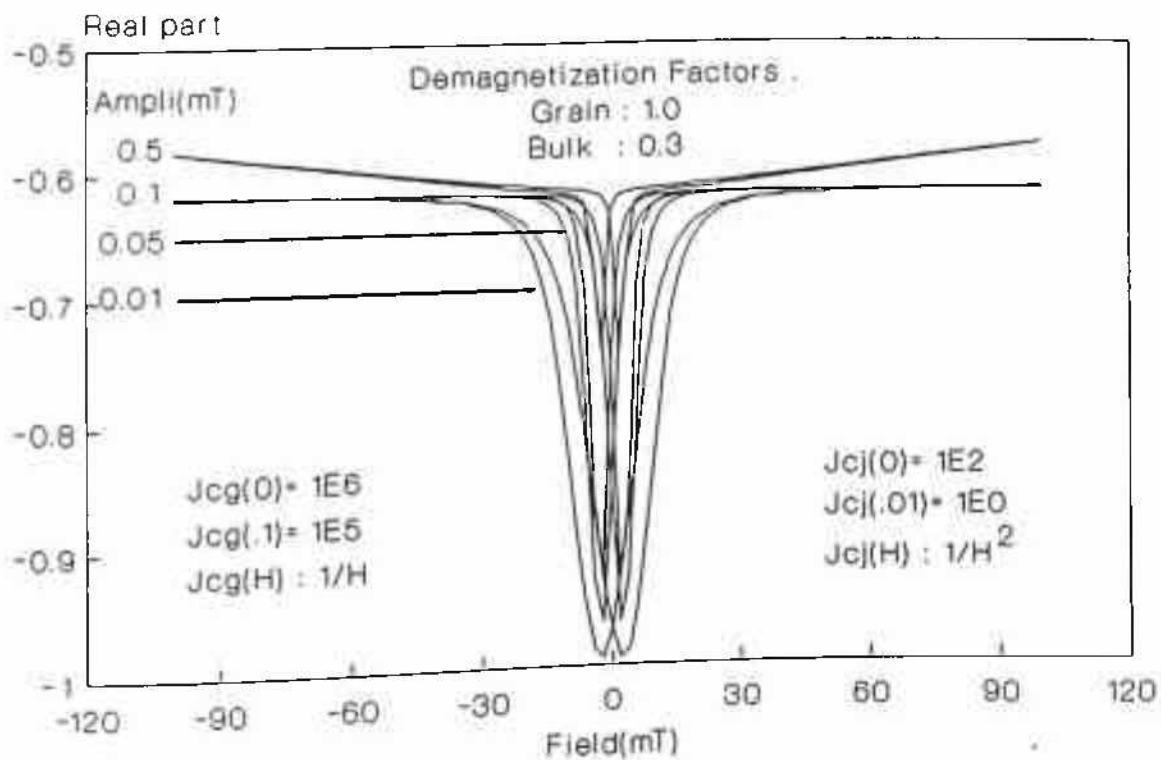


Figure 3.2.14a: $\chi'(H)$ loops for four AC amplitudes considering demagnetization correction. [$\beta=2$]

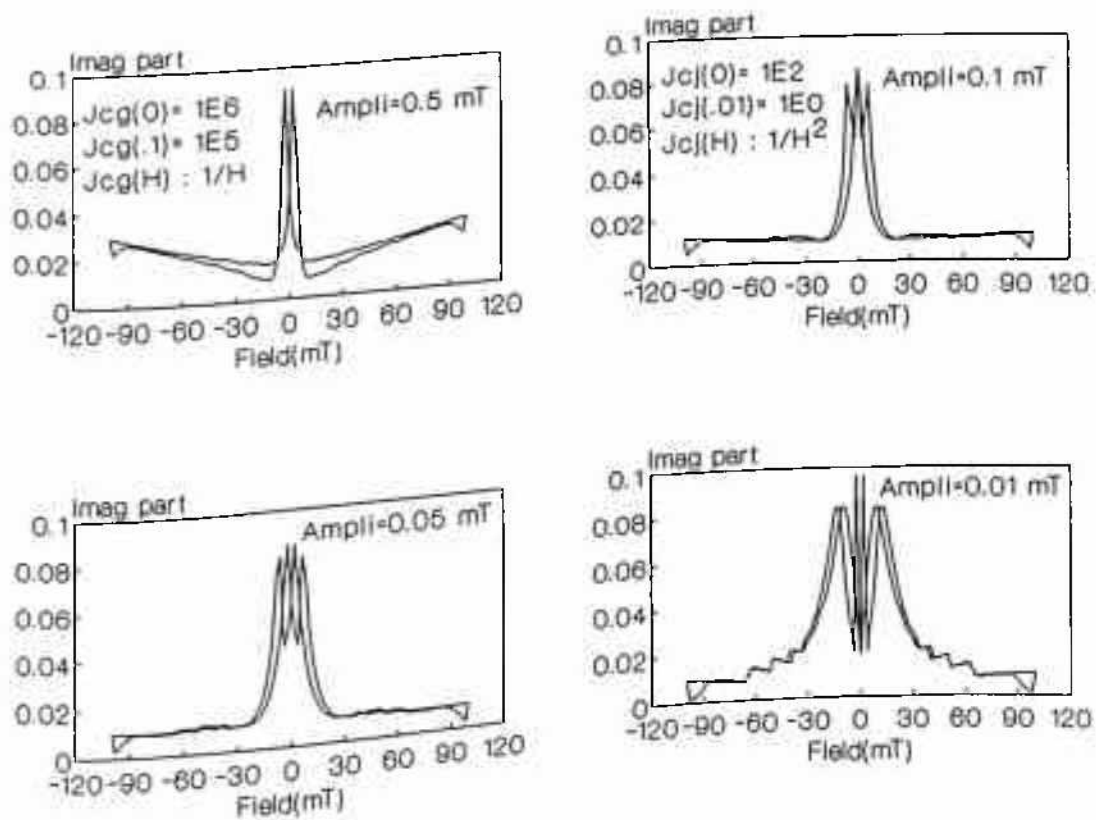


Figure 3.2.14b: Imaginary counter part of figure 3.2.14a.

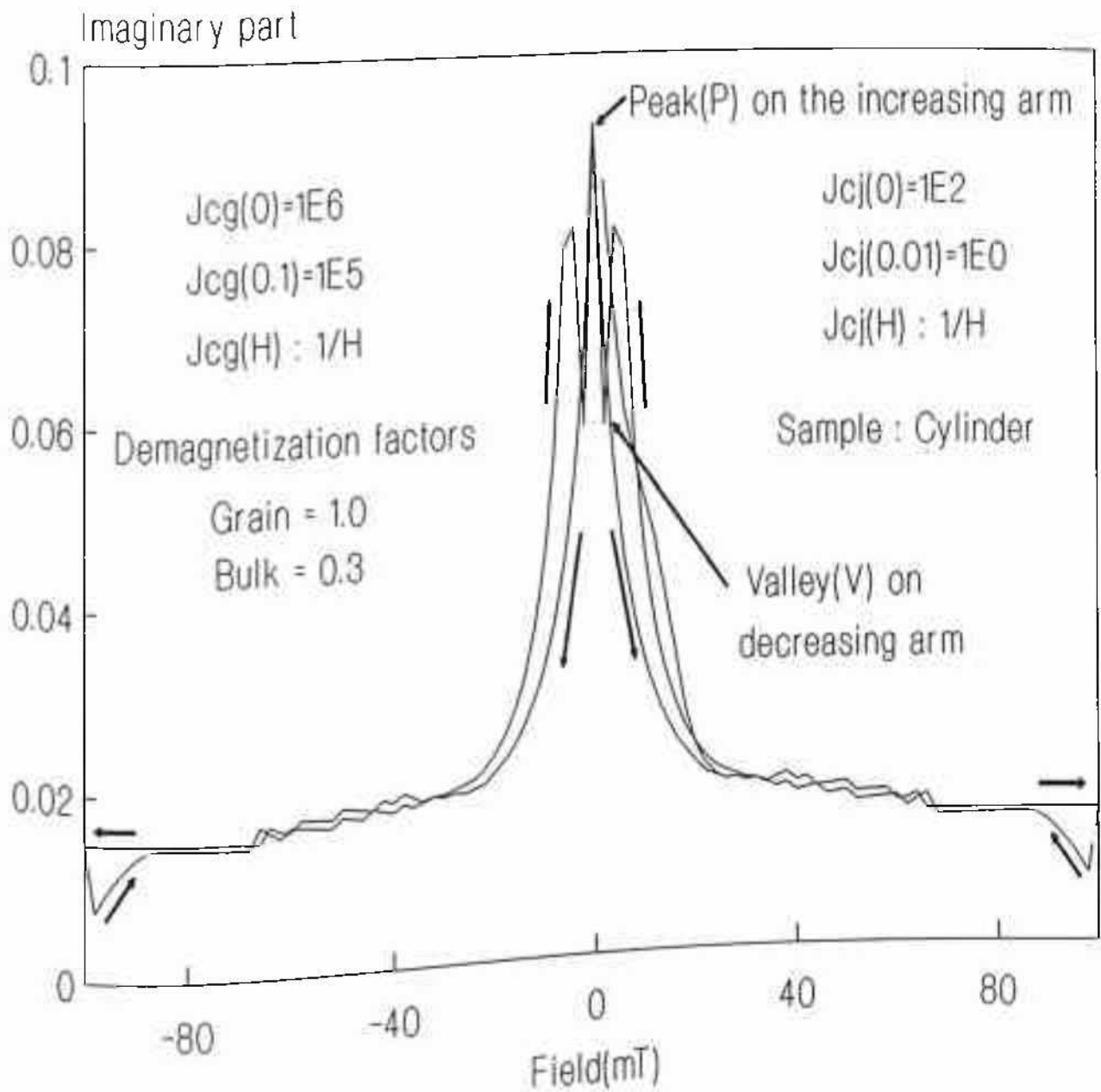


Figure 3.2.15: A single $\chi''(H)$ loop, demonstrating different features. AC amplitude is 0.1 mT. [$\beta=2$]

he $\chi''(H)$ loops are similar to figure 3.2.12b and with decrease of amplitude the high field regions of $\chi''(H)$ loops gradually become parallel to the DC field axis. At amplitude of 0.05 mT, as in figure 3.2.13b, the loops take a different look and as will be discussed in next chapter, these loops are quite similar to the experimental loops reported in this thesis. Thus it is important to see such a loop in full size. In figure 3.2.15 the $\chi''(H)$ loop for amplitude of 0.05 mT has been shown. The features (figure 3.2.15) appearing on the decreasing arms (magnitude wise) at a low DC bias are quite interesting and will be important in explaining experimental data in the next chapter. In figure 3.2.14b (for $\beta=2$) these features are more prominent and increases with decrease in the AC amplitude. One more important feature in figure 3.2.13b is that a large peak is seen in the virgin $\chi''(H)$ curve (when H_{DC} increases from zero the first time) at 0.01 mT which is difficult to understand on physical ground.

3.2.1D) SUM UP:

Main points of the above discussion can be summed up as follows;

- * DC bias field dependence of AC susceptibility have been explained using a two component critical state model.
- * DC bias field dependence of AC susceptibility in low field range ≤ 10 mT as shown here, are in agreement with already published data and calculations.
- * DC bias field dependence in the high field range $\simeq 100$ mT is being reported for the first time.
- * The model is continuous for the whole range of DC fields.
- * With out considering demagnetization factors real part does not exhibit hysteresis whereas, the imaginary part shows hysteresis in all field ranges and this hysteresis increases with decrease of AC amplitude.
- * For the first time demagnetization corrections have been considered in a phenomenological way, which has resulted in hysteresis in both real and imaginary parts of the AC susceptibility with respect to DC bias field at all field regimes. The excellent agreement of this hysteresis of real part particularly in the low field regime of DC bias fields with published data is encouraging. The hysteresis in imaginary part has also been experimentally verified for its different

features.

- The $\chi'(H)$ and $\chi''(H)$ hysteresis loops at high field regime are not much studied experimentally. However, our calculation seems to be in agreement with at least one reported case. In the next chapter, further justification of this hysteresis will be presented on the basis of our own data.
- Systematic variation has been studied for different critical current parameters which appears to be physically consistent.
- Grain size dependence have been presented which shows some critical size discriminating two opposite processes.

The inherent problem of assumed zero lower critical fields in critical state models makes difficult to correlate the calculated results with the experimental ones, since obviously the critical fields are never zero. However, the macroscopic situation as simplified in these models are close analogous of the true experimental results. Current crowding at the GB's due to flux expulsion from grains affecting J_{c1} can be considered by modifying equation (7) as per Muller and Matthews[35];

$$H_i = H_0 - NM - nM_g \quad (3.2.9)$$

As one can see that this modification may increase the hysteresis resulting in better fit to experimental data. However, in this work we have not included this modification to avoid further complication in understanding the basic nature of the observed hysteresis in AC susceptibility.

3.2.2. AC AMPLITUDE DEPENDENCE OF χ' AND χ'' :

It is important, at this point to see the amplitude dependence of both the components of AC susceptibility for different DC bias fields as well as for different critical current parameters. In fact the most prominent experimental support of presence of two components in the ceramic bulk is seen in the dependence of AC susceptibility on AC amplitude because the loss (imaginary) component clearly shows two prominent peaks.

3.2.2A) ZERO BIAS:

In figures 3.2.16a and 3.2.16b real and imaginary parts of AC susceptibility for slab geometry have been plotted as a function of amplitude for different J_{cg} parameters for a zero DC bias field while J_{cj} parameters are same for all and shown in the diagram. It can be inferred from these figures that the low field peak in χ'' is due to the grain boundary and hence remains almost unchanged by variation of J_{cg} parameters while the peak at higher field is due to grain contribution and thus is affected very much by the variation J_{cg} parameters. There is a shift in the grain peak in figure 3.2.16b to a lower AC amplitude with poor J_{cg} parameters. This is due to the fact that with poor J_{cg} parameters the grain penetration field, H_g^* decreases and since the peak appears at an amplitude close to this H_g^* , the grain peak shifts to lower amplitude. It is obvious from figure 3.2.16b that with bad J_{cg} parameters grain peaks become more prominent. In the same way in the real part (figure 3.2.16a) there is not much variation in the low amplitude values of χ' while at higher amplitude χ' significantly changes with different grain parameter. Thus in experimental study on grain properties one has to employ higher amplitude AC field in order to probe the grain properties.

In figures 3.2.17a, 3.2.18a χ' and 3.2.17b, 3.2.18b χ'' have been plotted for different J_{cj} and two given J_{cg} (G66 and G77 respectively) parameters for slab geometry. All these figures, further clarify the above argument that the first peak is due to grain boundary contribution and hence is strongly modified by variation of J_{cj} parameters. The shift of GB peak to lower AC amplitudes for poor J_{cj} as seen in figure 3.2.17b and 3.2.18b is due to the fact that with poor J_{cj} the bulk penetration field, H_j^* for the GB is decreased resulting in the shift of χ'' peak to lower AC amplitudes. In figures 3.2.19(a,b) and 3.2.20(a,b) the same $\chi'(H)$ and $\chi''(H)$ loops as in the figures 3.2.17(a,b) and 3.2.18(a,b) respectively have been plotted for a cylindrical sample of radius 2mm. It is obvious from these figures that for change in sample shape (slab to cylindrical) the AC amplitude dependence of AC susceptibility remains qualitatively same except for the peak positions which shift depending on H^* , the penetration field. As seen in figure 3.2.16b and comparing figures 3.2.17b and 3.2.18b as well as 3.2.19b and 3.2.20b, it can be inferred that with better grain parameters (J_{cg}) not only grain peaks decrease but also there is some reduction in the grain boundary peaks.

In order to see the effect of field dependence of critical currents on the amplitude dependence of susceptibility, it is instructive to plot the same curves as in figures 3.2.19 and

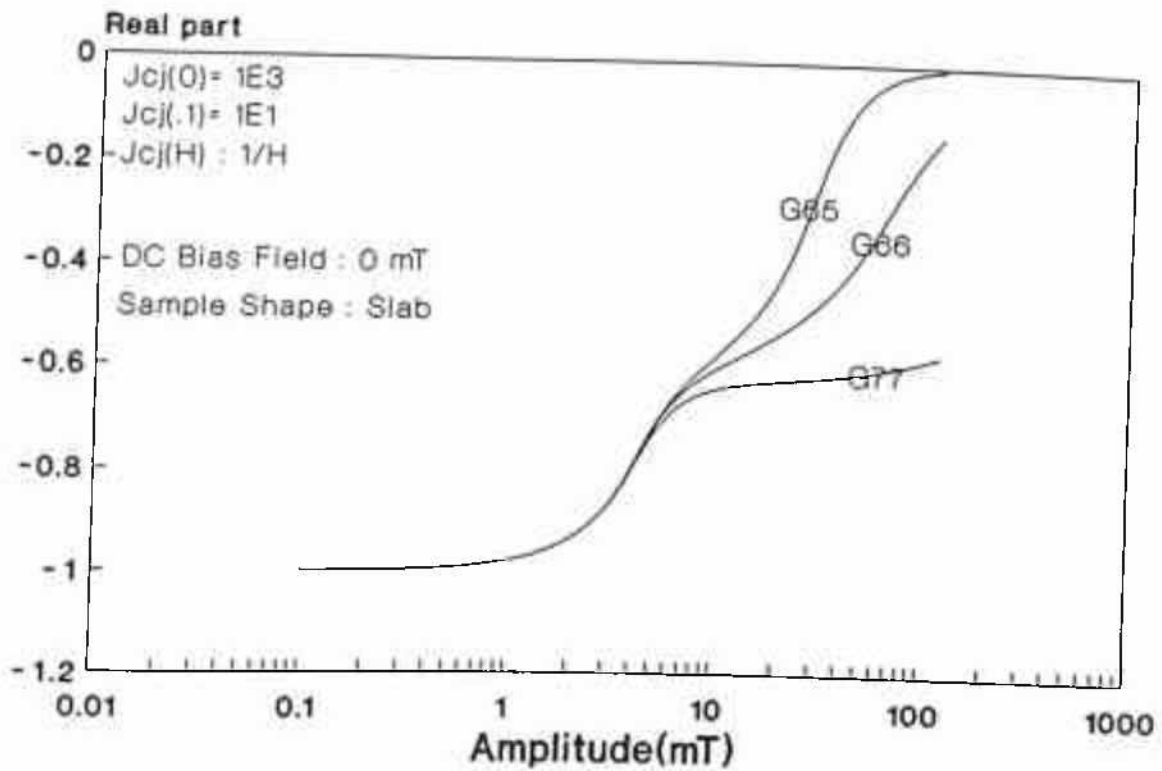


Figure 3.2.16a: χ' as a function of AC amplitude for two different $J_{cg}(H)$ [G65 Kim and G77, G66 Bean type]

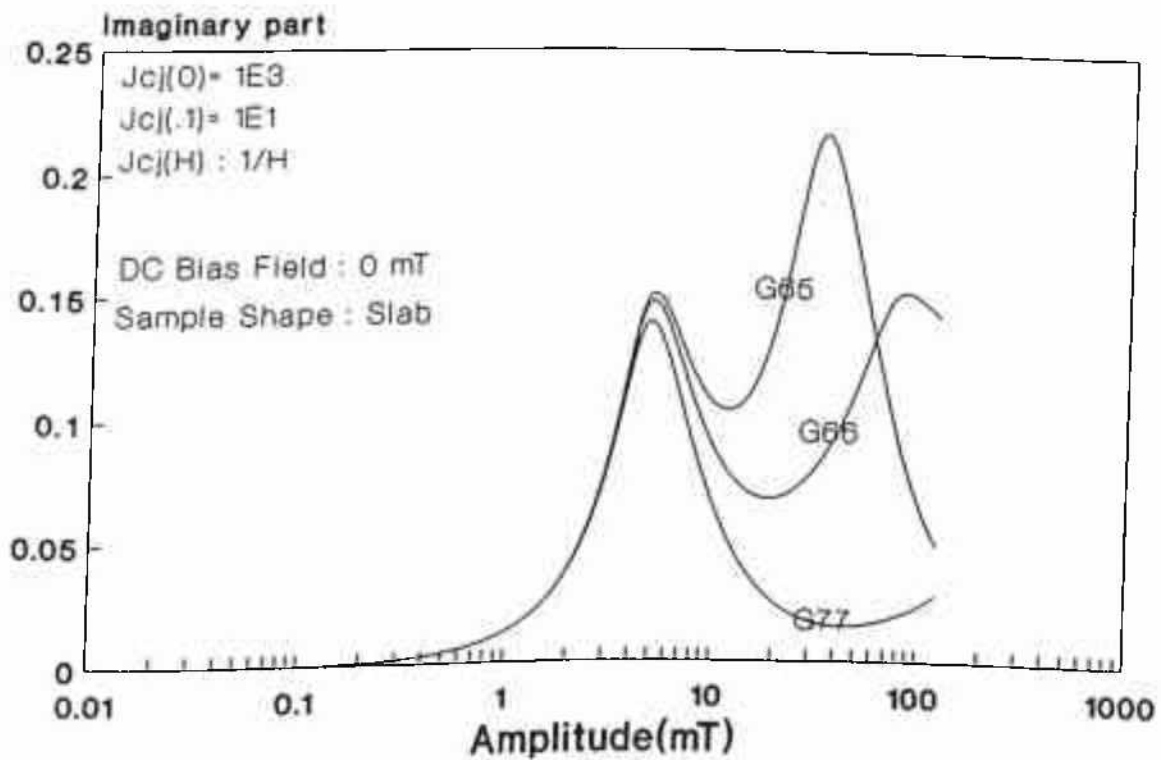


Figure 3.2.16b: Imaginary counter part of figure 3.2.16a.

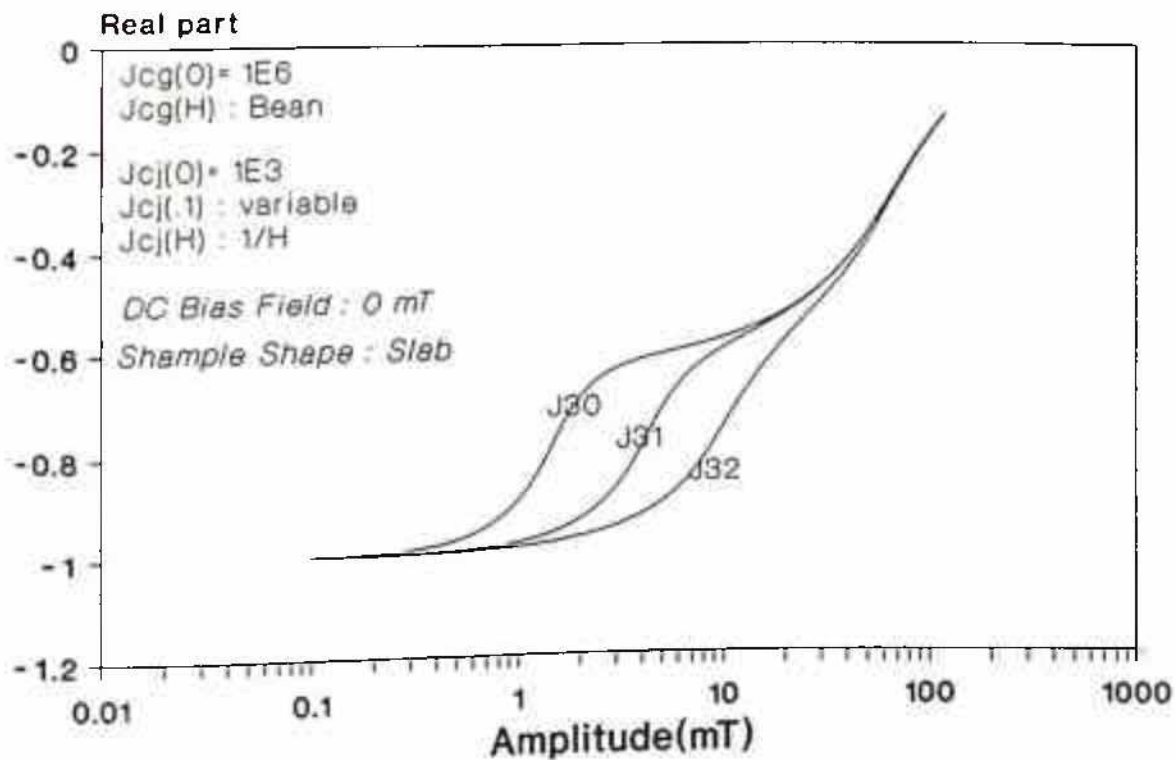


Figure 3.2.17a: χ' as a function of AC amplitude for 3 different $J_{cj}(0.1)$. [Jmn : m,n exponent of $J_{cj}(0)$ and $J_{cj}(0.1)$ respectively]

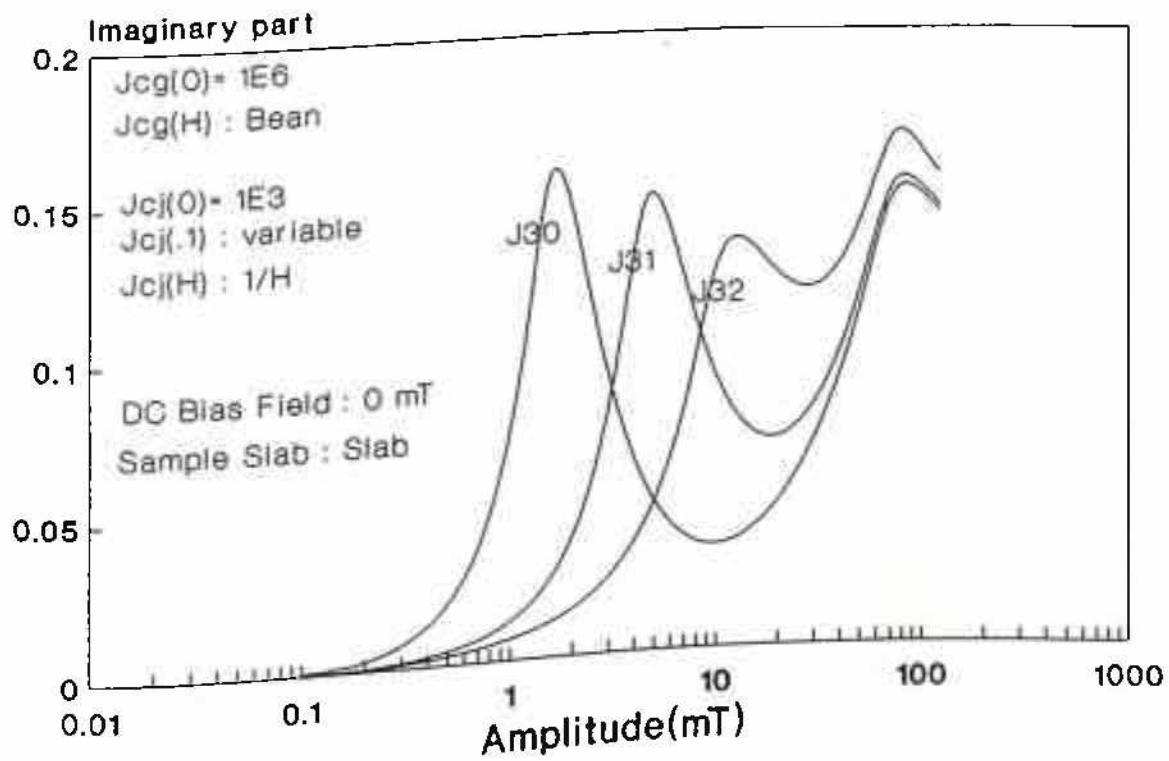


Figure 3.2.17b: Imaginary counter part of figure 3.2.17a.

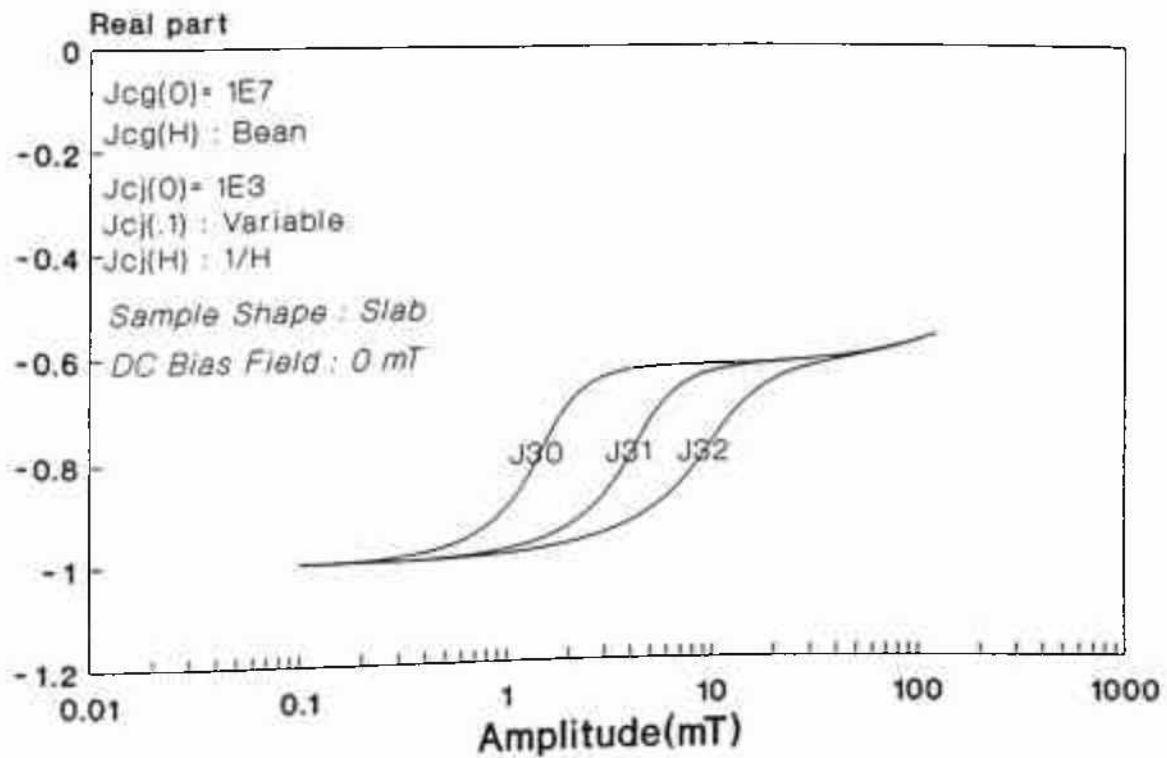


Figure 3.2.18a: χ' as a function of AC amplitude for 3 different $J_{cj}(0.1)$. [Jmn : m,n exponent of $J_{cj}(0)$ and $J_{cj}(0.1)$ respectively]

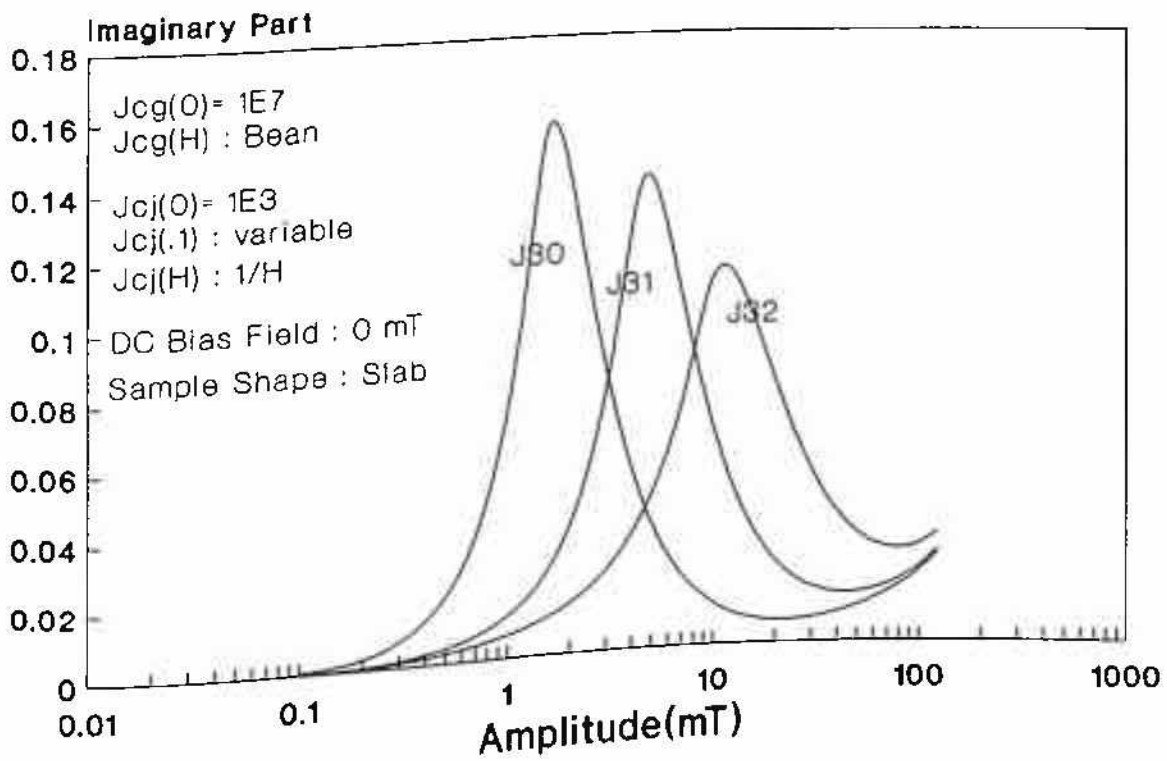


Figure 3.2.18b: Imaginary counter part of figure 3.2.18a.

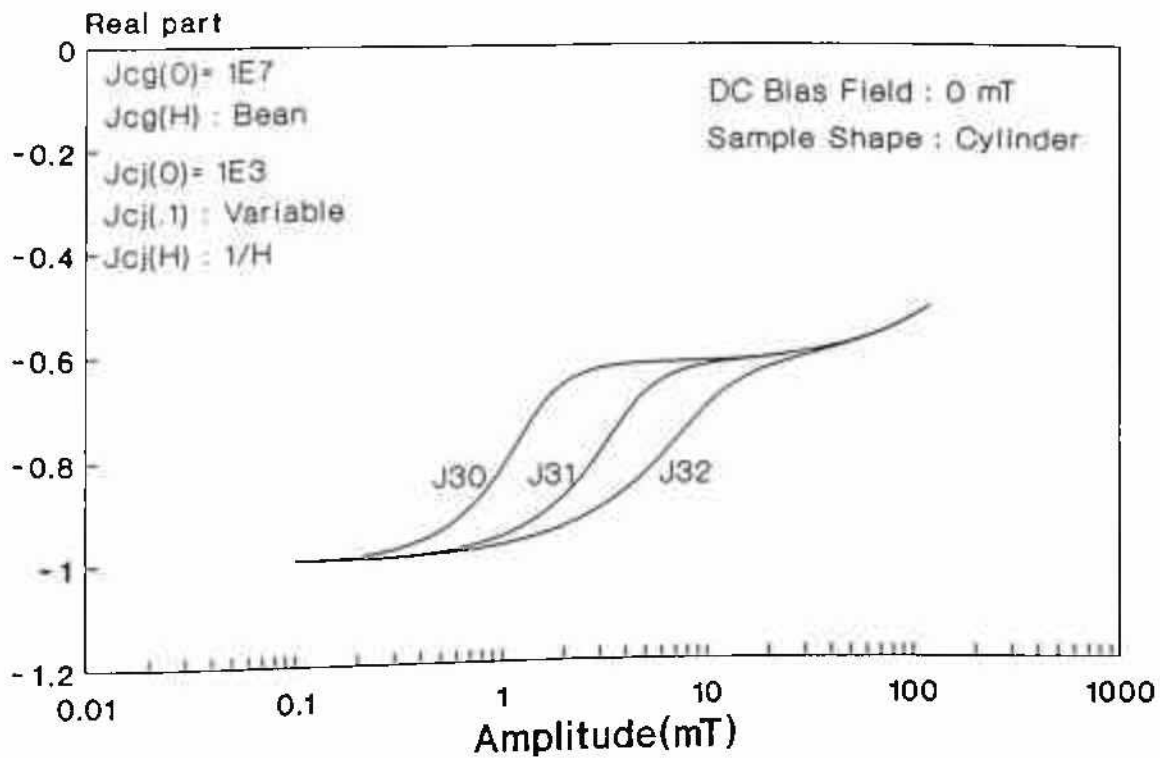


Figure 3.2.19a: χ' as a function of AC amplitude for 3 different $J_{cj}(0.1)$. [J_{mn} m,n exponent of $J_{cj}(0)$ and $J_{cj}(0.1)$ respectively]

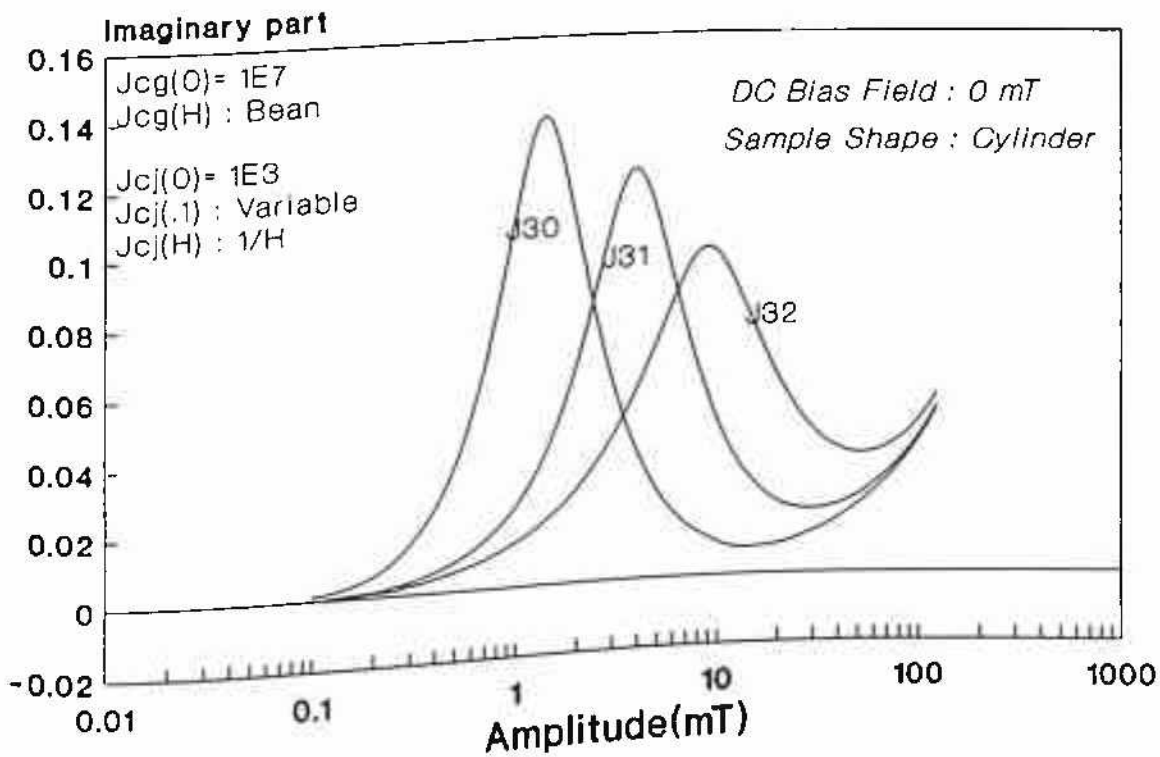


Figure 3.2.19b: Imaginary counter part of figure 3.2.19a.

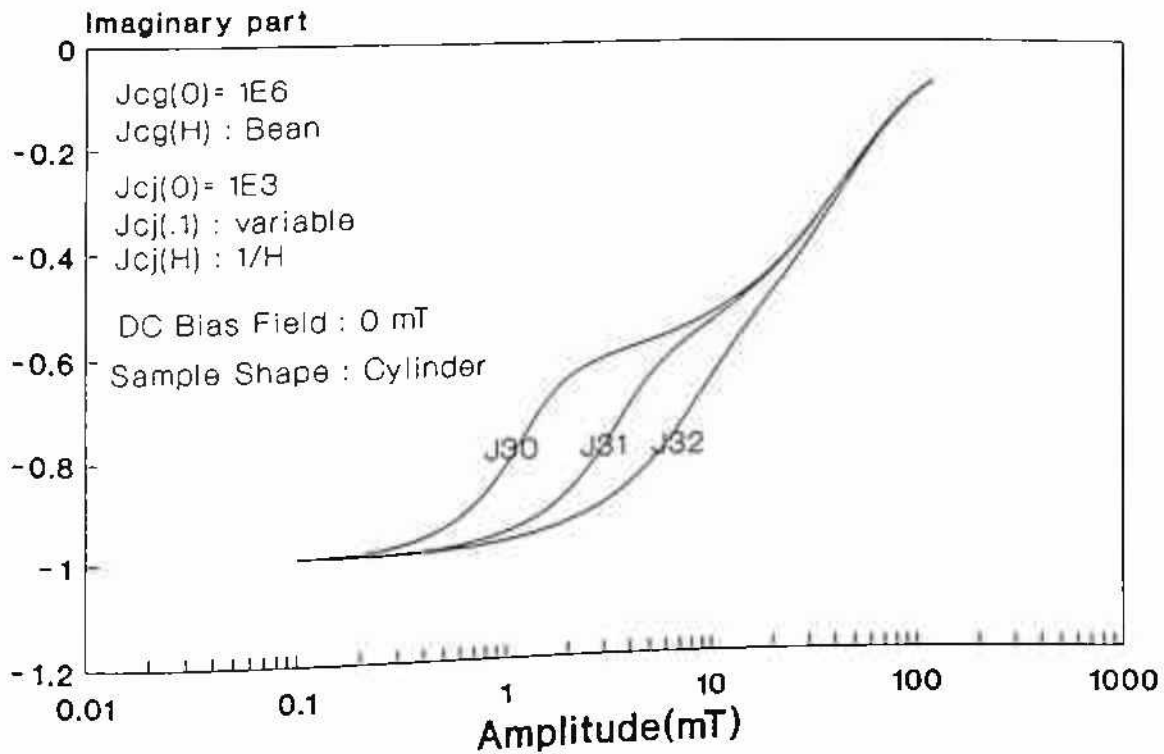


Figure 3.2.20a: χ' as a function of AC amplitude for 3 different $J_{cj}(0.1)$. [Jmn : m,n exponent of $J_{cj}(0)$ and $J_{cj}(0.1)$ respectively]

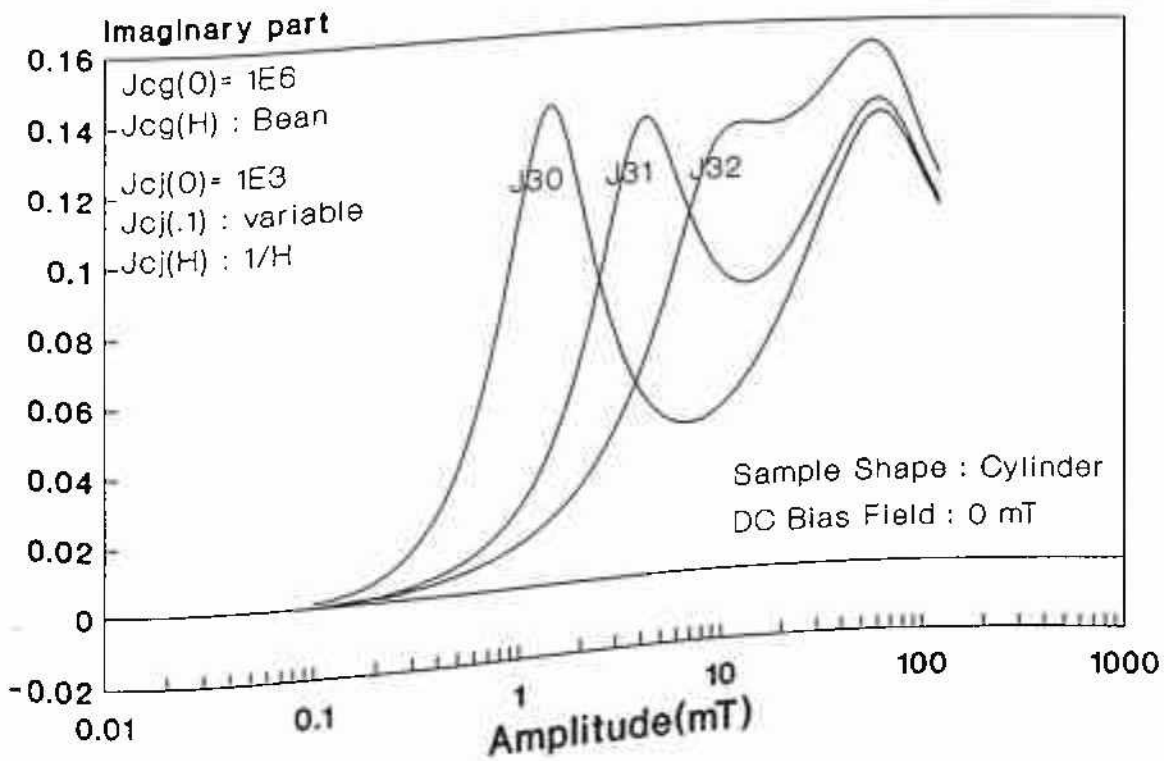


Figure 3.2.20b: Imaginary counter part of figure 3.2.20a.

3.2.20 for $\beta=2$. In figures 3.2.21(a,b) and 3.2.22(a,b) the real and imaginary parts have been plotted as a function of amplitude for $\beta=2$ and all other parameters are same as in figures 3.2.19 and 3.2.20 respectively. It can be seen by comparing figures 3.2.19a, 3.2.21a and figures 3.2.20a, 3.2.22a that with $\beta=2$, the three curves for different $J_{c_j}(0.1)$'s (i.e., J30, J31 and J32) become closer to each other. Further, from comparison of figures 3.2.19b, 3.2.21b and figures 3.2.20b, 3.2.22b, it is clear that for $\beta=2$, the bulk penetration field is higher than that for $\beta=1$. This apparent contradiction is due to the choice of parameters. Though $\beta=2$ means stronger field dependence of $J_{c_j}(H)$ but at the same time if one keep $J_{c_j}(0)$ and $J_{c_j}(0.1)$ fixed for different β values it appears that α_j in eqn. 3.2.6 is less for higher β values. In fact what is more important is the values of $J_{c_j}(0)$ and $J_{c_j}(0.1)$ and as one can visualize, if these two are kept constant the physical effect of higher β is not realized properly. It is an important conclusion from this calculation and must be considered while looking for a rational J_{c_j} parameter to have better fit to experimental data.

3.2.2B) NON-ZERO DC BIAS:

In figures 3.2.23a, 3.2.24a, 3.2.25a χ' and in figures 3.2.23b, 3.2.24b, 3.2.25b χ'' have been plotted as a function of amplitude for different DC bias fields for parameters as shown within the diagram. The complicated interaction of the DC bias can be seen in figures 3.2.23, 3.2.24 and 3.2.25. As can be seen figure 3.2.23a, in case of real part, as the DC bias field is increased beyond 3 mT a small hump is seen to appear which then moves to higher amplitudes with increase of DC bias field and at the same time the hump becomes smaller and smaller. The imaginary part shows more complicated behavior (figure 3.2.23b). At zero bias there are two peaks, one due to GB which is at lower amplitude (GB peak) and other due to grains and appears at higher amplitude (grain peak). Physically the first peak at zero bias is at an amplitude equal to the bulk penetration field, H^* , when the amplitude is just sufficient to reach to the center of the sample resulting in maximum loss. Other way one can explain the GB peak at zero DC bias as when the end points of the minor loops traced during the AC cycling touch the humps of the corresponding major M-H loops of the GB. In the same way the second maximum (Grain peak) appears at an amplitude equal to the grain penetration field, H_g^* . With increase of DC bias, the first peak (i.e., GB peak) height decreases rapidly and moves towards higher

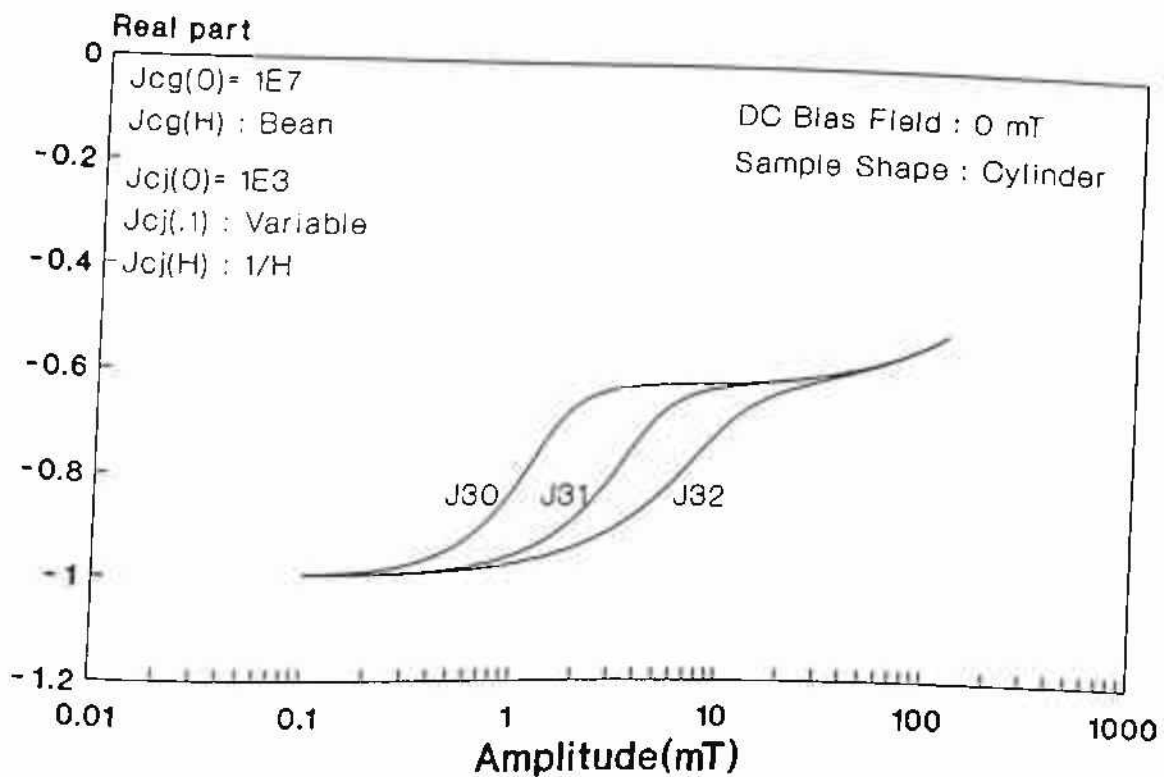


Figure 3.2.21a: χ' as a function of AC amplitude for 3 different $J_{cj}(0.1)$. [Jmn : m,n exponent of $J_{cj}(0)$ and $J_{cj}(0.1)$ respectively]

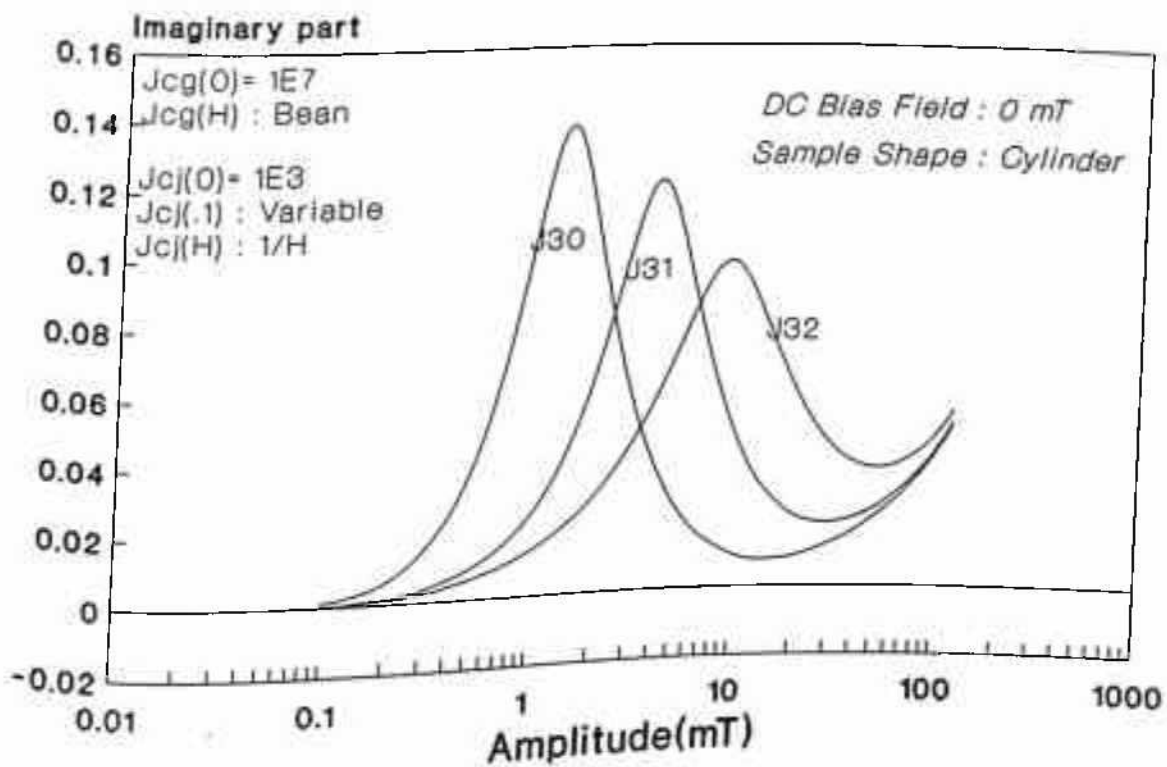


Figure 3.2.21b: Imaginary counter part of figure 3.2.21a.

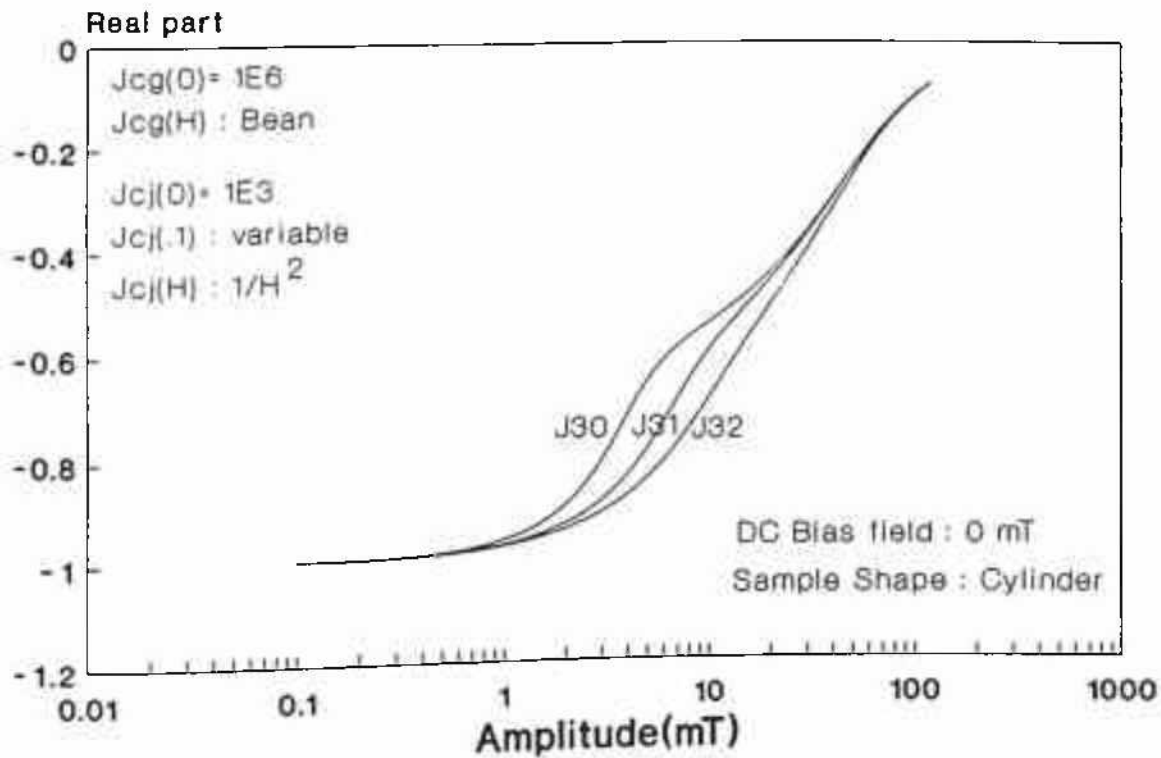


Figure 3.2.22a: χ' as a function of AC amplitude for 3 different $J_{cj}(0.1)$. [Jmn : m,n exponent of $J_{cj}(0)$ and $J_{cj}(0.1)$ respectively]

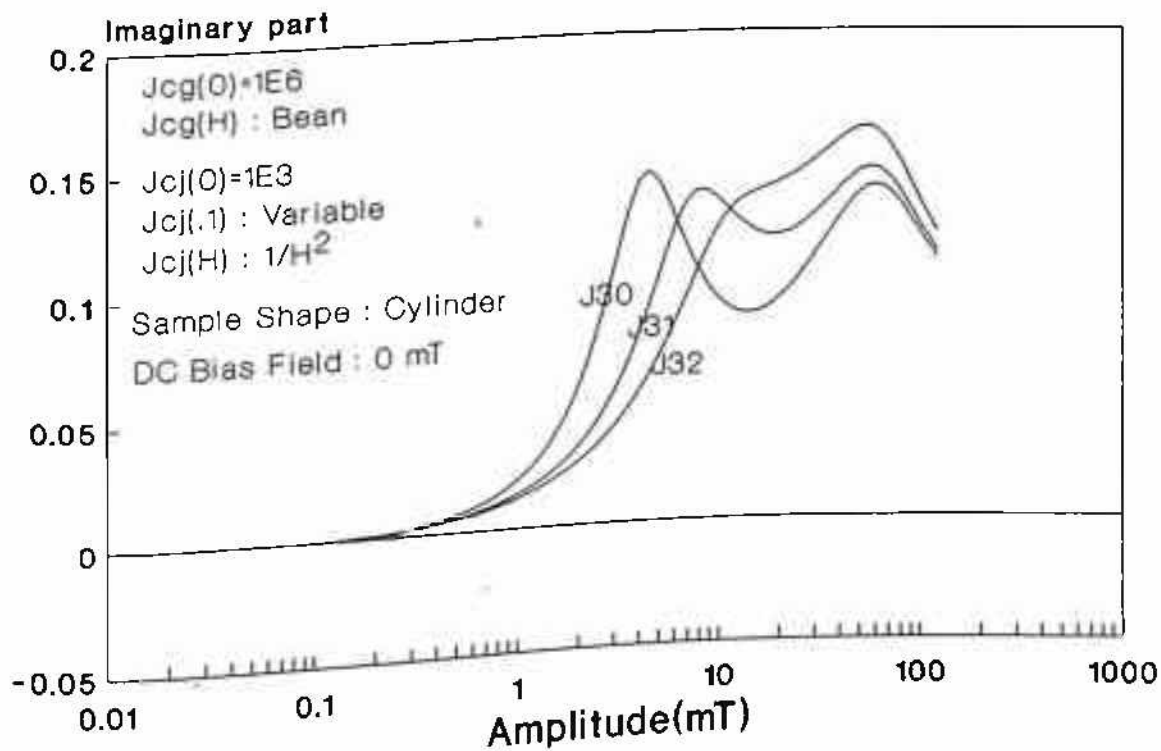


Figure 3.2.22b: Imaginary counter part of figure 3.2.22a.

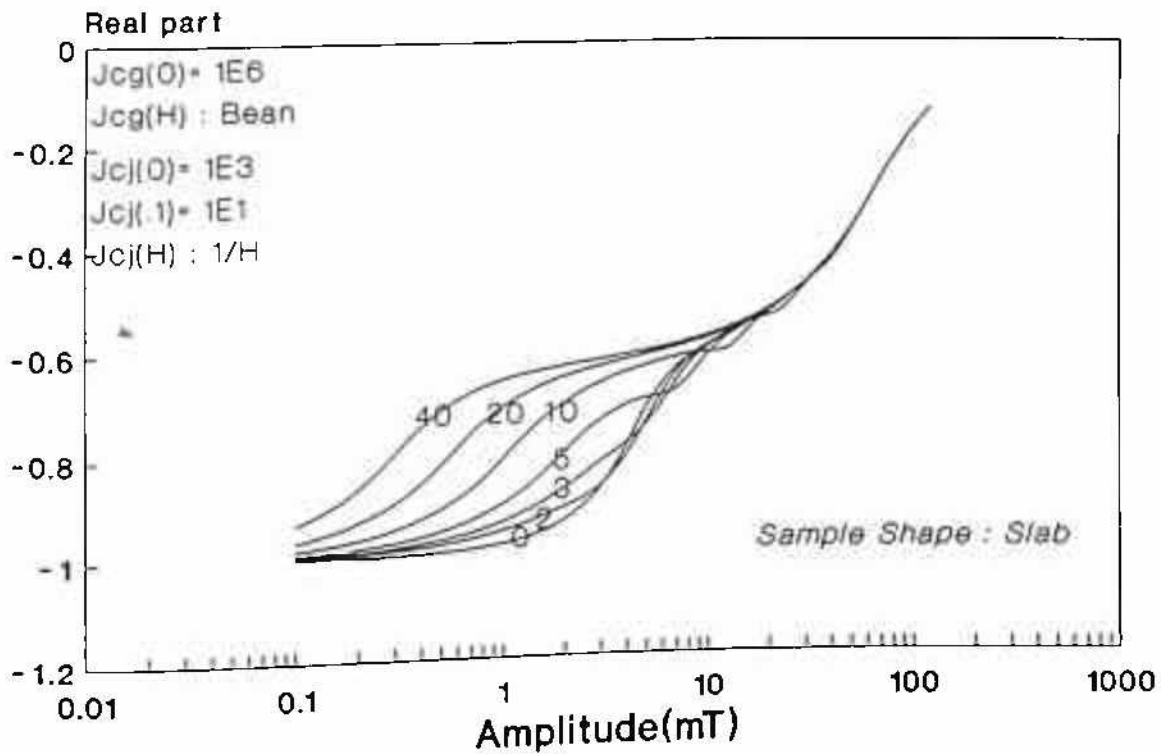


Figure 3.2.23a: χ' as a function of AC amplitude for DC bias field. [Numbers indicating DC bias in mT]

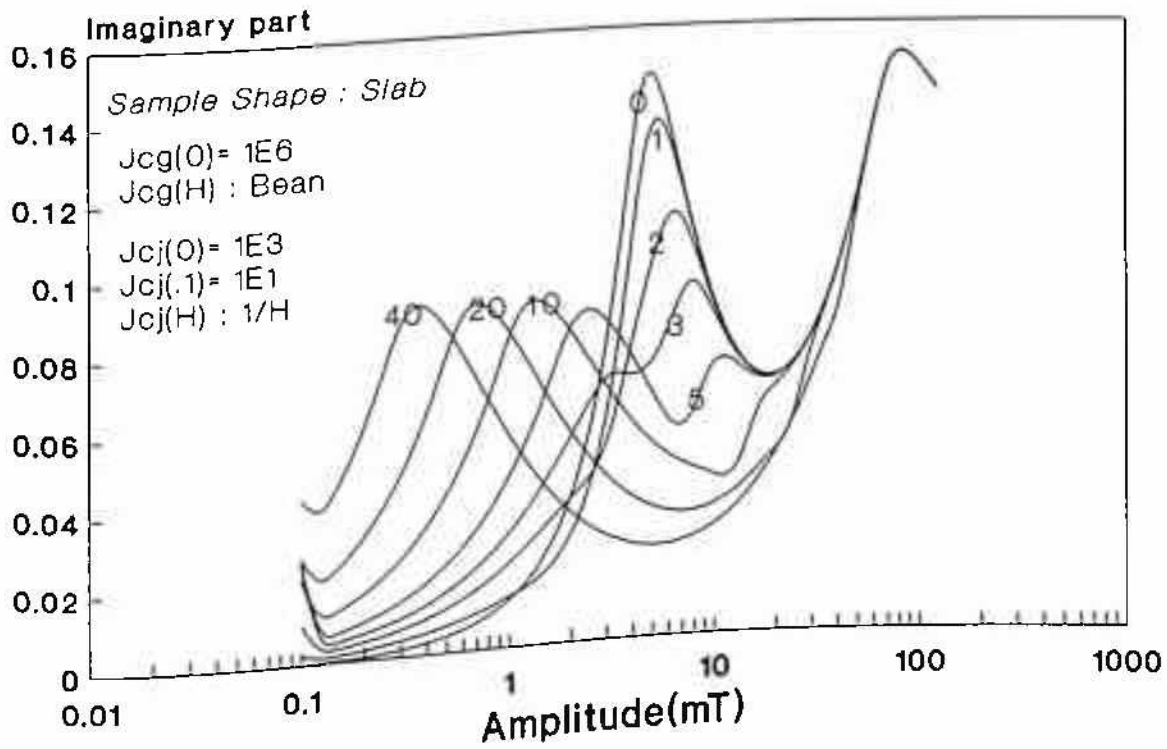


Figure 3.2.23b: Imaginary counter part of figure 3.2.23a.

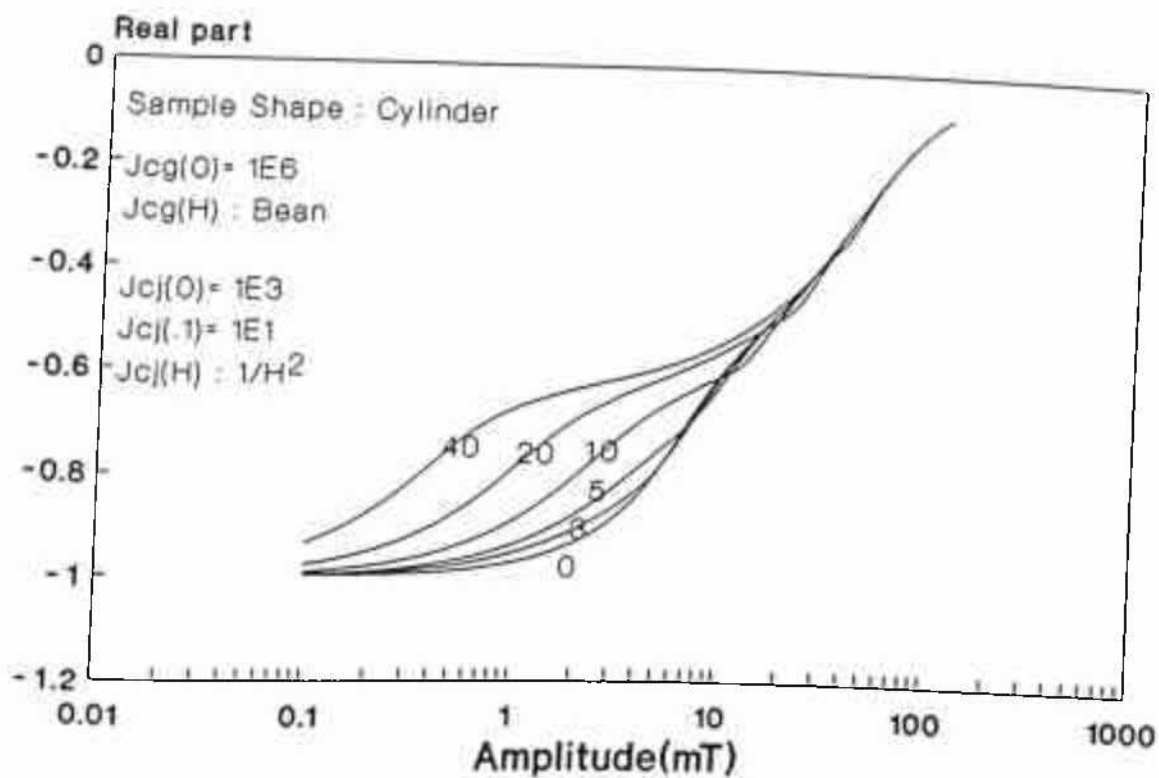


Figure 3.2.24a: χ' as a function of AC amplitude for DC bias field. [Numbers indicating DC bias in mT]

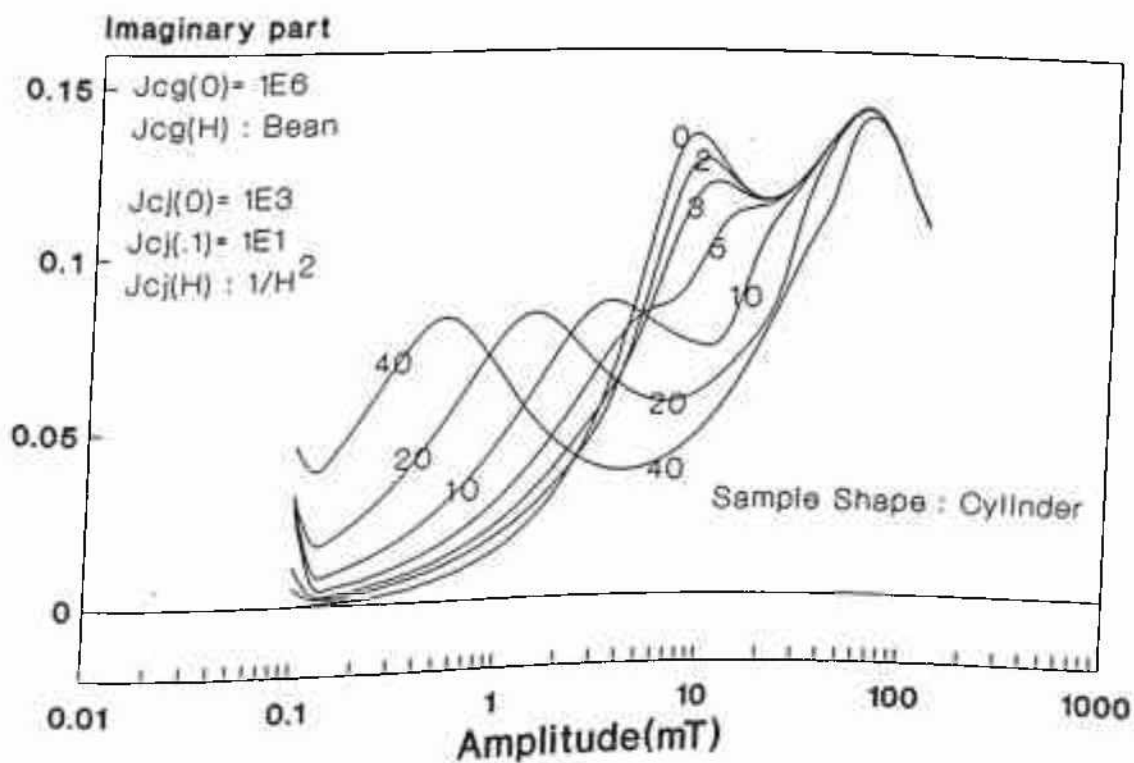


Figure 3.2.24b: Imaginary counter part of figure 3.2.24a.

amplitudes. But a third peak appears at an AC amplitudes lower than the GB peak position (figure 3.2.23b). This "third" peak becomes more prominent than the GB peak with increase of bias field to 5 mT or higher and shifts to lower values of AC amplitude as the DC bias field increases. But at the same time the GB peak starts diminishing and almost vanishes at around 40 mT. With the imposition of DC bias field this third peak occurs when the end points of the minor loops traced during AC cycling touch the major M-H loop corresponding to the GB. Further as the DC bias increases, J_{c1} decreases and the end points of minor loops touch the major M-H loop of the GB at lower and lower AC amplitudes causing this peak position to appear at a lower AC amplitude. The middle peaks which we have called as GB peaks, shifts to higher AC amplitude because with increase of DC bias a larger AC amplitude is required to reach the hump of the major M-H loop. The dependence of height of the peak on DC bias can also be explained by remembering that χ'' is proportional to the ratio of area of the minor loops to the square of AC amplitude. This clearly explains the reduction of middle peaks (GB peaks) with increase in DC bias field as - with increase in DC bias though the area of the minor loops may increase, the required amplitude to touch the major M-H loop also increases resulting in effect, decrease in the peak height. It is important to notice that the bias has hardly any effect on the grain contribution and at all DC bias the height and position of grain peaks remains unchanged. This is because the bias fields, as considered here, are lower than the grain penetration field, H_g^* .

The same qualitative description can be presented for the results in figures 3.2.24 and 3.2.25. In figures 3.2.24 and 3.2.25 β is 2. It can be seen that as the bulk penetration field for $\beta=2$ case (figure 3.2.24b) is higher than $\beta=1$ case (figure 3.2.23) while the grain penetration field in both cases ($\beta=1$ and 2) are same, the GB peaks become closer to grain peak and also the DC bias effect is less prominent.

3.2.2C) SIZE EFFECT - BULK AND GRAIN:

Here it will be important to see whether this amplitude dependance follows the right dependence of size of the bulk as well of the grains. In figure 3.2.26(a,b) bulk size dependance have been shown. It is clear that with decrease of size H_g^* decreases and thus the GB peaks appear at lower and lower amplitudes of AC field and gradually get reduced by height but the

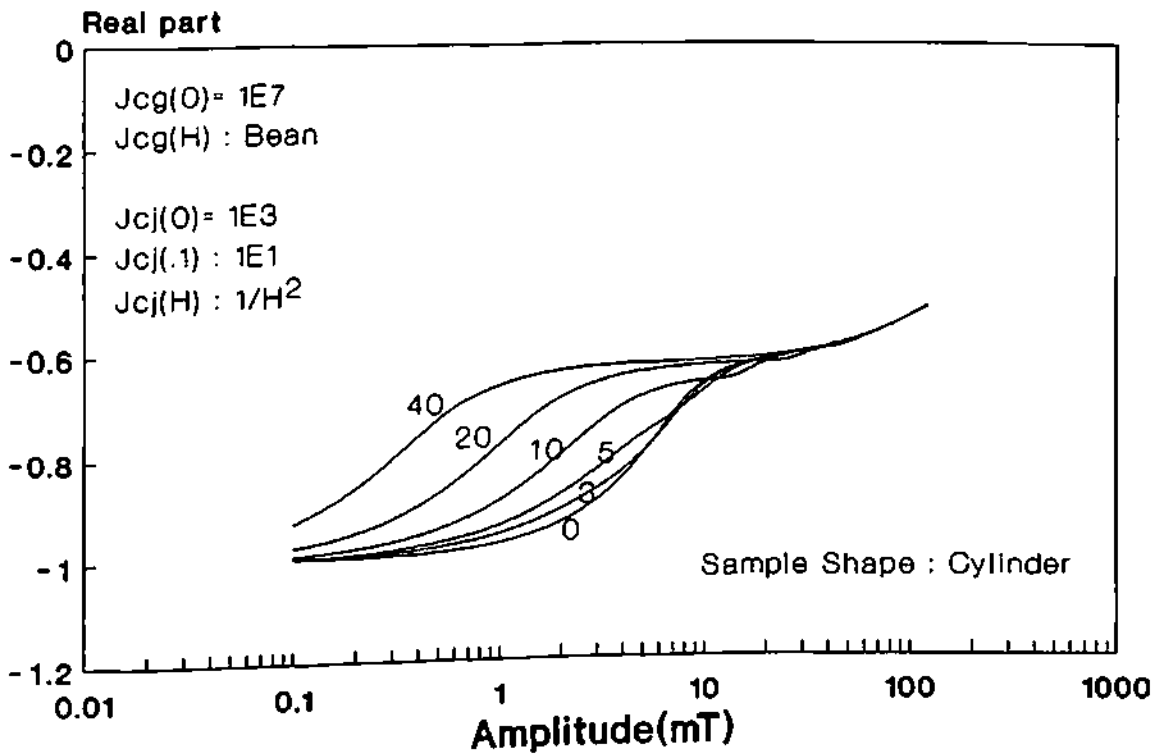


Figure 3.2.25a: χ' as a function of AC amplitude for DC bias field. [Numbers indicating DC bias in mT]

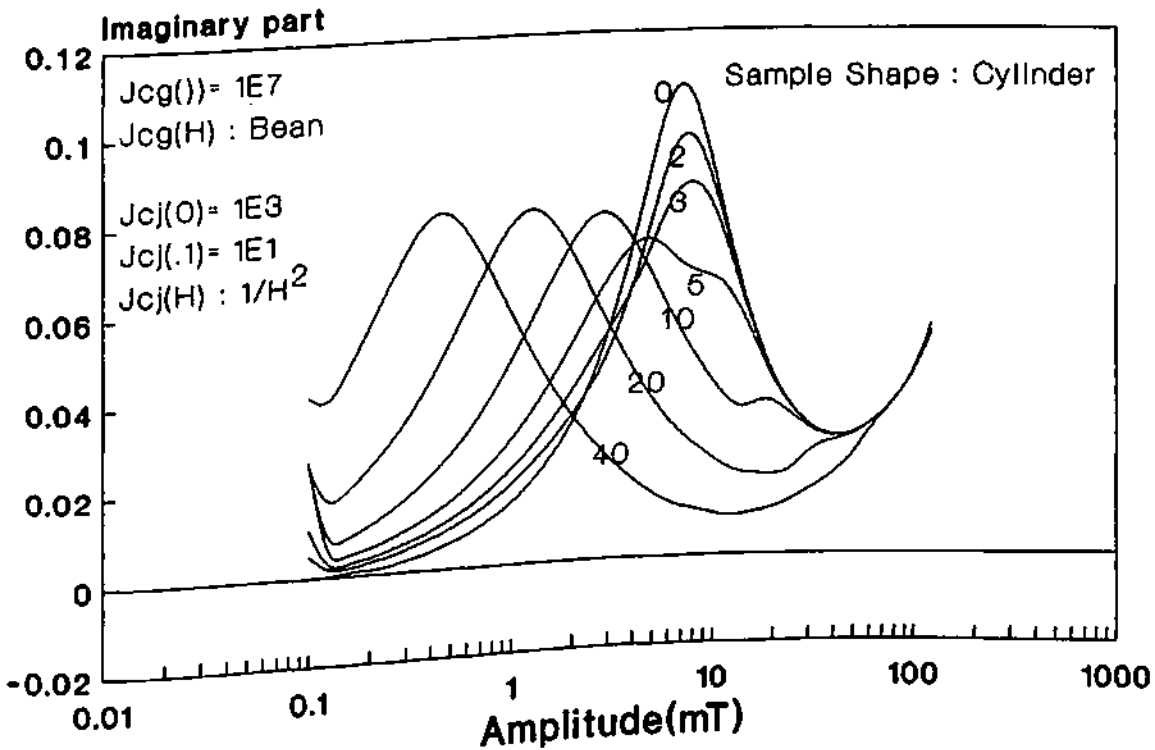


Figure 3.2.25b: Imaginary counter part of figure 3.2.25a.

grain peak remains almost unaltered.

In figure 3.2.27(a,b) the grain size effect has been demonstrated by plotting the same curves for different grain sizes while the bulk size is constant. Since only the grain size is being varied here, there is not much change in the GB contribution as compared to the grain contribution as long as the grain size is not too small. As the grain size decreases, the H_g^* also decreases and so the grain peaks shift to lower amplitudes. At the same time heights of the grain peaks are also decreased. At sufficiently small grain size when $H_g^* \simeq H_j^*$ the two peaks (GB and grain peaks) may convolute or even may merge together.

3.2.2D) EXPERIMENTAL EVIDENCE:

Amplitude dependence as discussed above has sufficient experimental support. In most of the experiments amplitude is not sufficiently high to see the grain peaks in χ'' as discussed above. However, the data of Chen et al.[32] clearly shows the two peaks in χ'' . They have also tried to fit their data to their model calculations. But their fit considers three different AC amplitude zones for which they have given different fitting processes resulting in discontinuity in the fitting. The calculations, as reported here, obviously give better fit and are continuous over the whole AC amplitude range. The appearance of the third peak due to imposition of DC bias field in the low amplitude region (figures 3.2.23b, 3.2.24b and 3.2.25b) also find evidence in the experimental data of Zeljko et al[33], where they obtained two peaks at a sufficiently high DC bias. Further, the relative heights of the two peaks, as reported in ref. [33], conform to the calculation as shown in figures 3.2.23b, 3.2.24b and 3.2.25b. The dependence on bulk size as described here are in excellent agreement with the data of ref. [36] where shift and decrease of GB peaks are in same order as reported here.

3.2.2E) SUM UP:

The following points are important derivation of the above discussion:

- * This model correctly shows two peaks in the imaginary part of AC susceptibility as a function of AC amplitude for zero DC bias in a continuous manner in the whole amplitude range.
- * In zero bias case, it is simple to identify the first peak, i.e., peak at the low AC

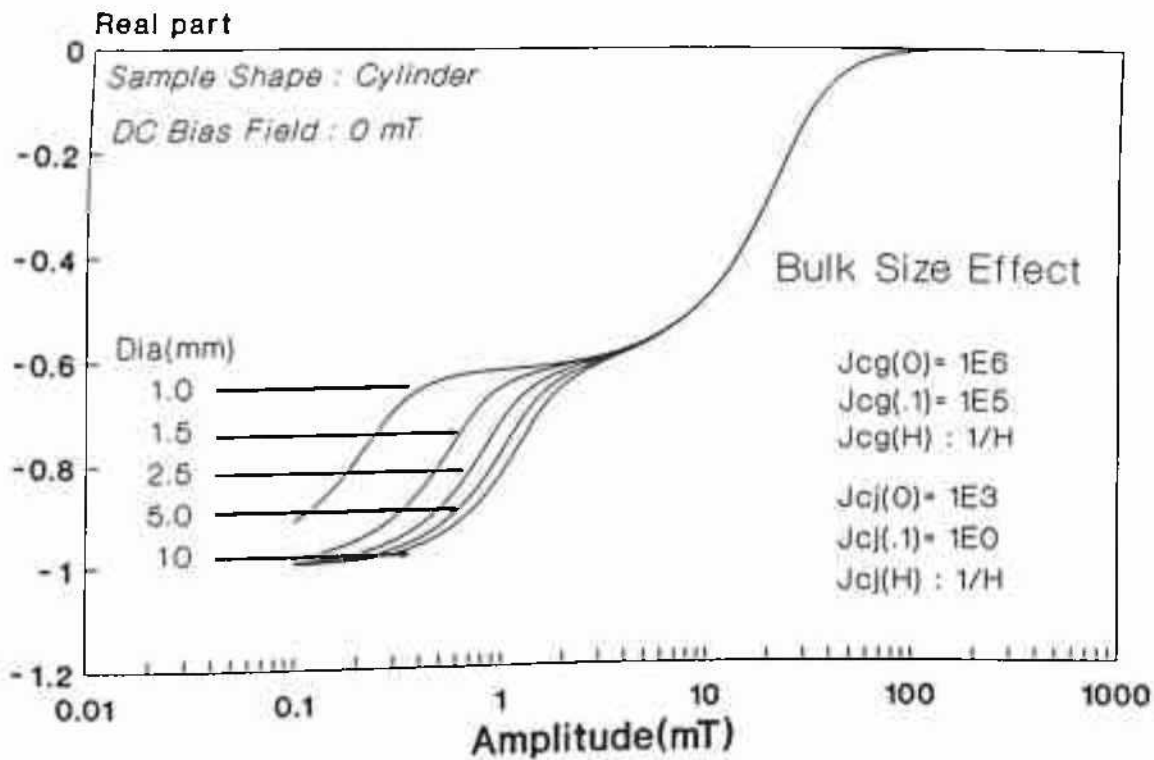


Figure 3.2.26a: χ' as a function of AC amplitude for different sample diameters.

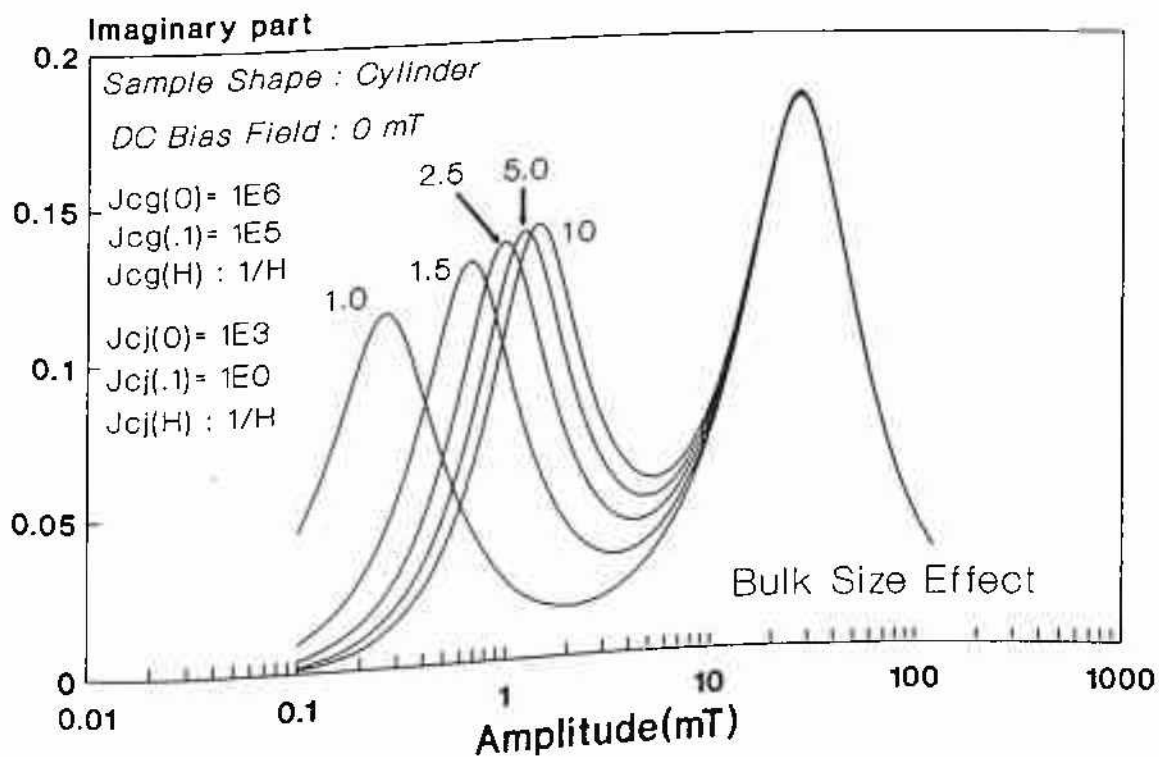


Figure 3.2.26b: Imaginary counter part of figure 3.2.26a.

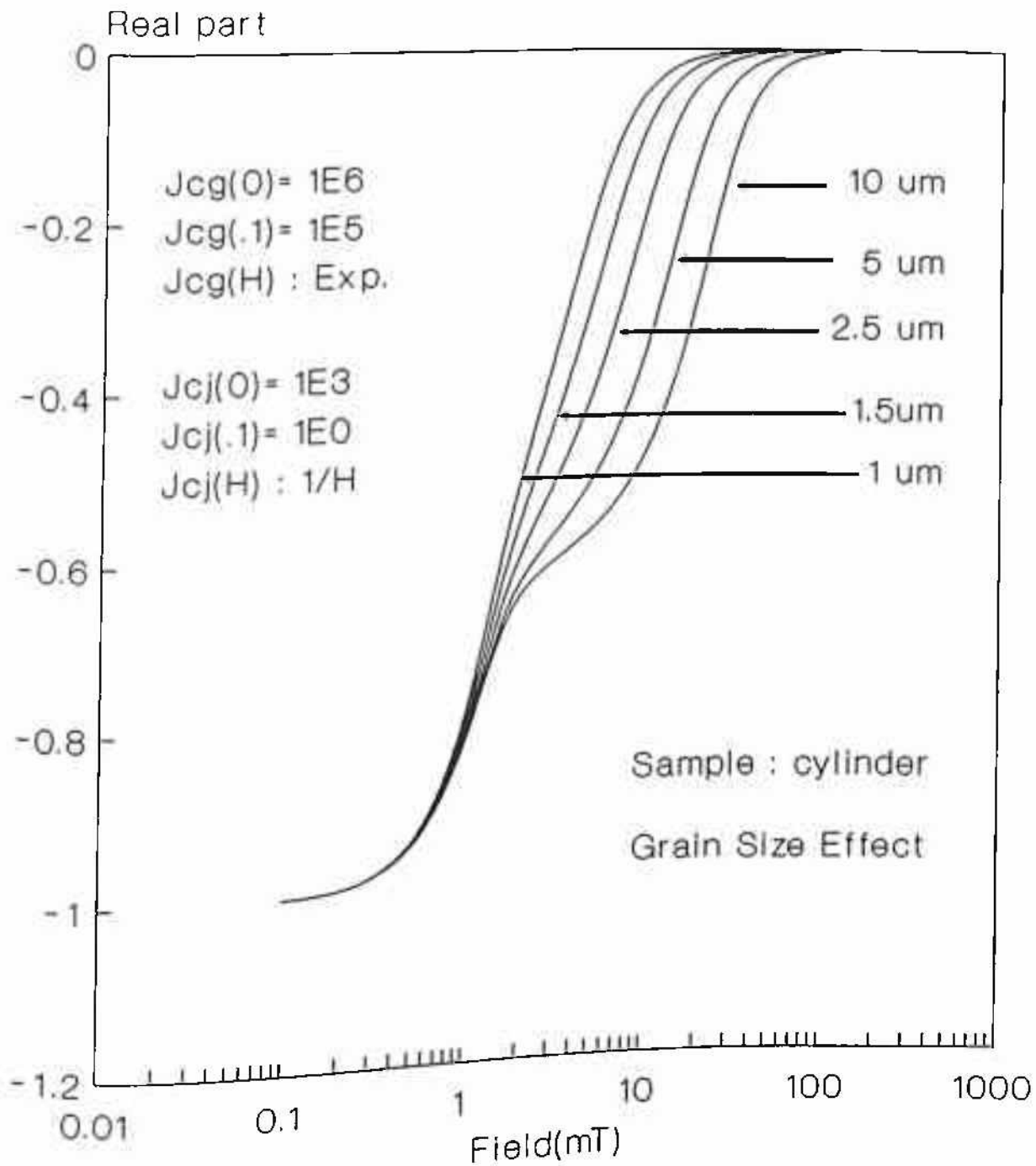


Figure 3.2.27a: χ' as a function of AC amplitude for different grain diameters (micron).

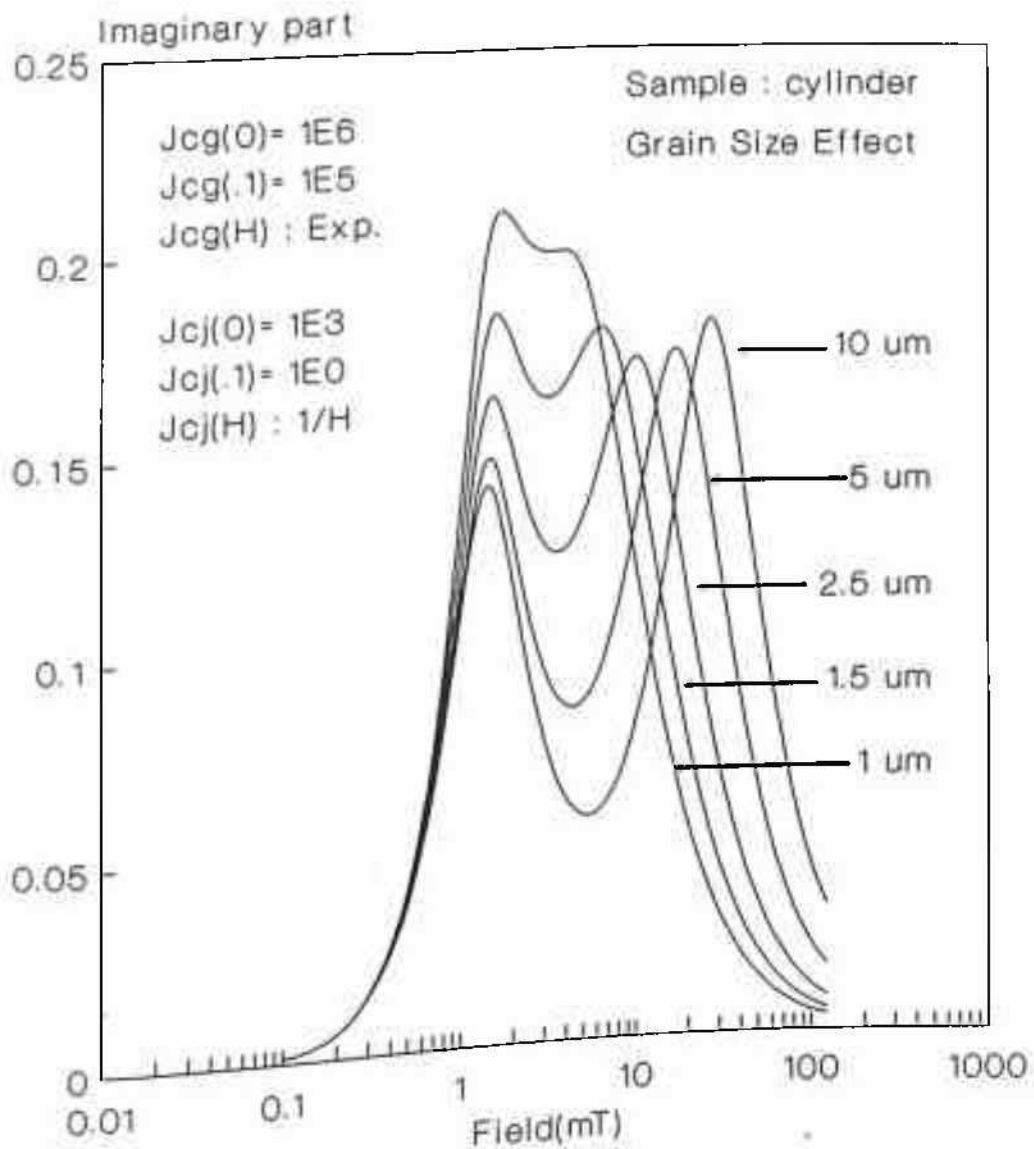


Figure 3.2.27b: Imaginary counter part of figure 3.2.27a.

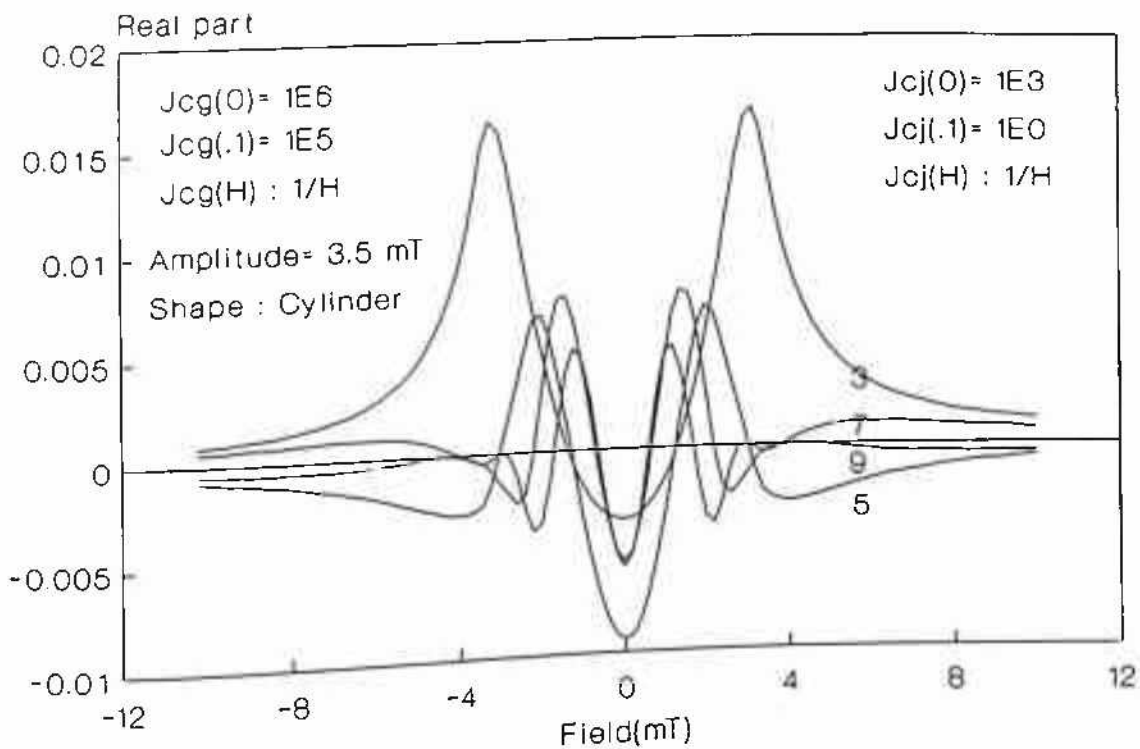


Figure 3.2.28a: Real part of odd harmonics as a function of DC bias field. (Numbers indicating order of harmonics)

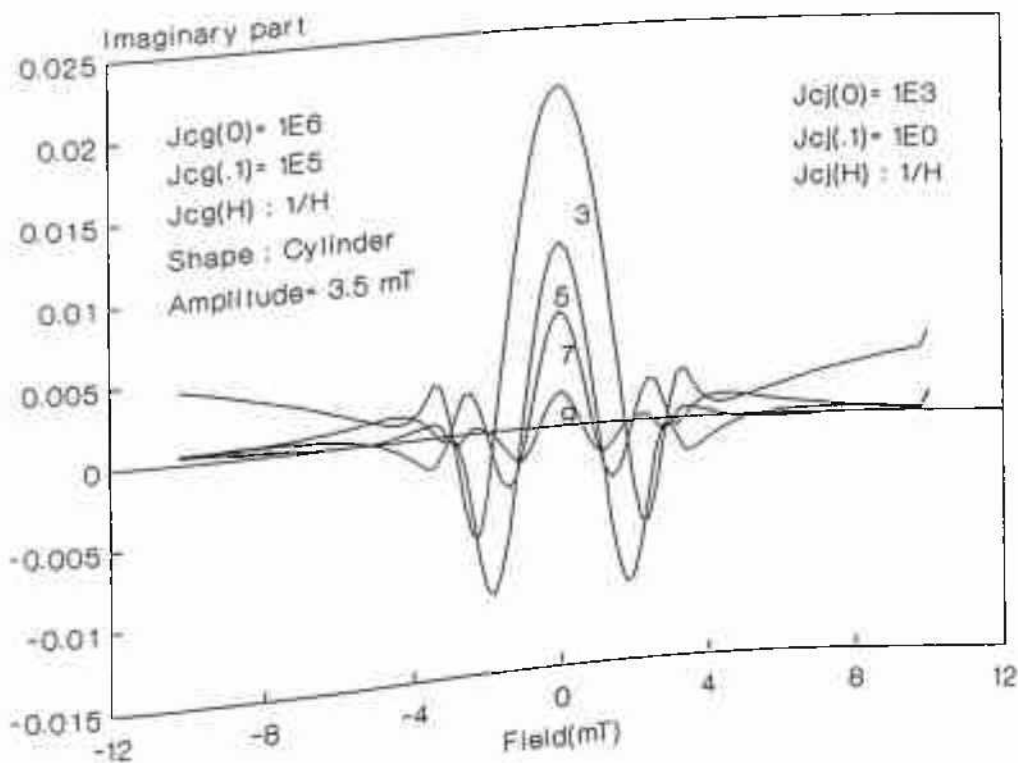


Figure 3.2.28b: Imaginary counter part of figure 3.2.28a.

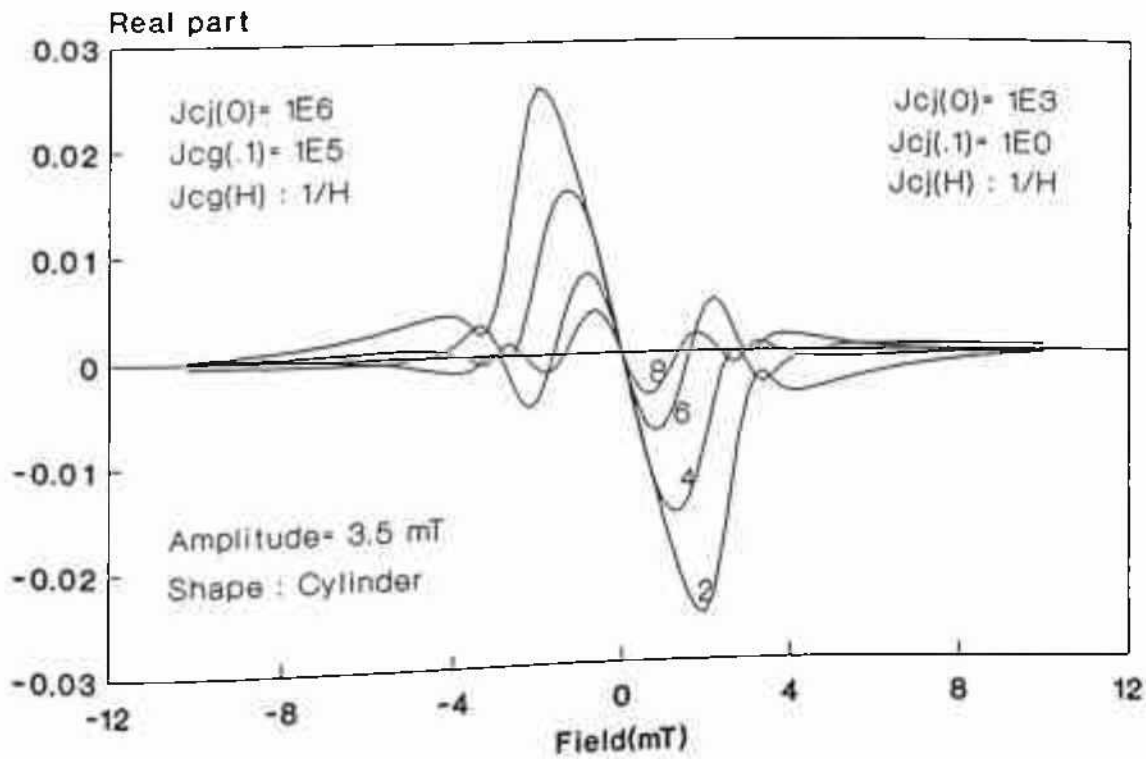


Figure 3.2.29a: Real part of even harmonics as a function of DC bias field. (Numbers indicating order of harmonics)

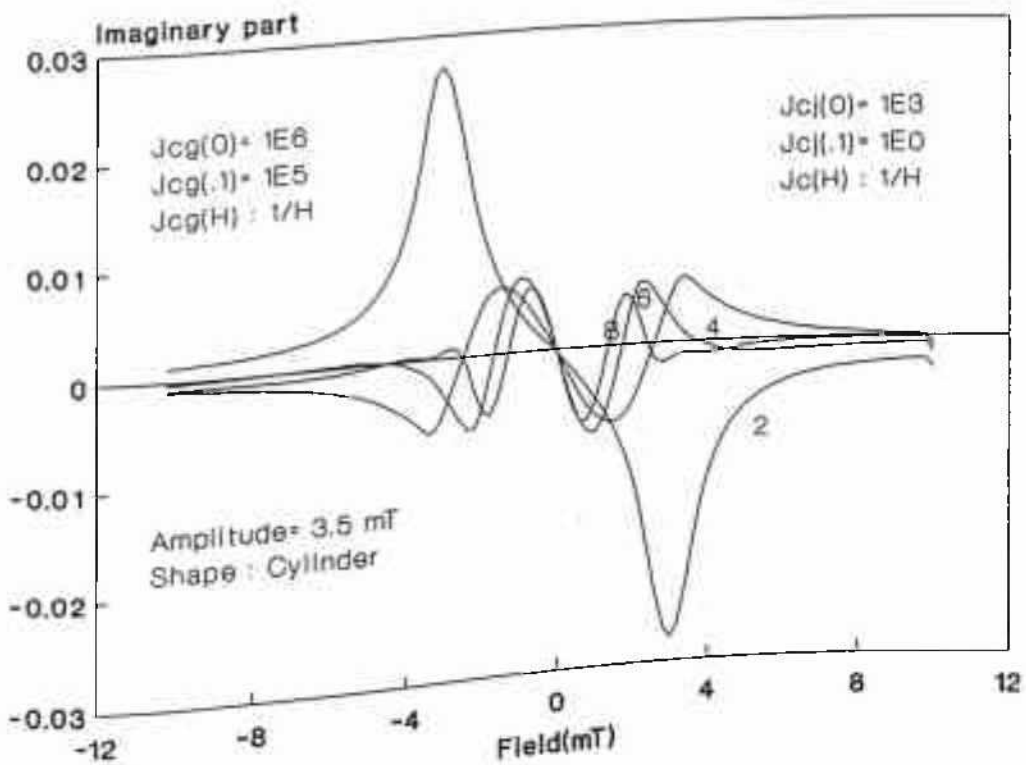


Figure 3.2.29b: Imaginary counter part of figure 3.2.29a.

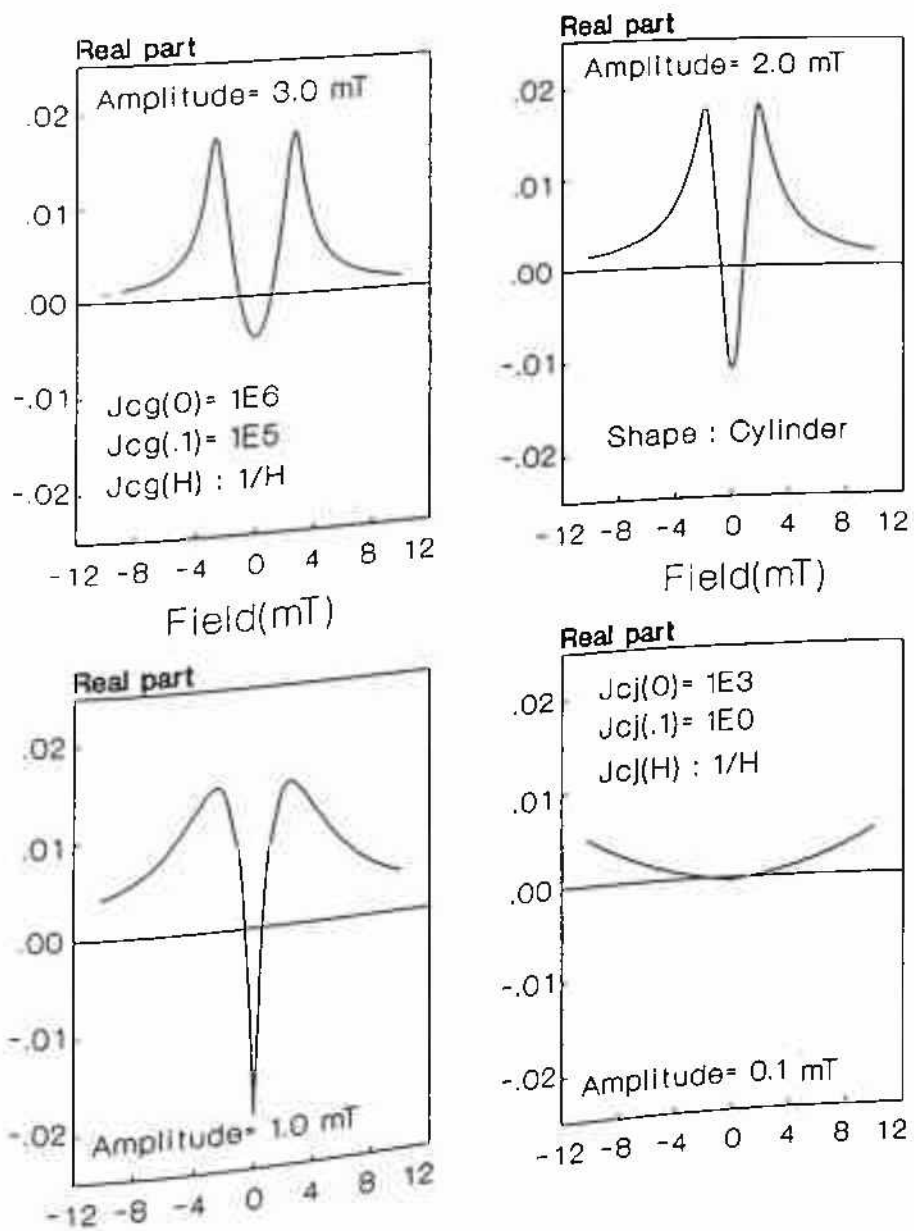


Figure 3.2.30a: Real part of 3rd harmonics as a function of DC bias field for 4 amplitudes. [demagnetization correction absent]

amplitude value to be due to the GB contribution while the other to be due to the grain contribution.

- At a sufficiently high DC bias, a third peak appears at an AC amplitude lower than that of the GB peak.
- In this model all these three peaks find good explanation.
- It is seen that variation of grain parameters affects not only the grain contribution but also the GB contributions. Thus it shows that the simplified method as proposed by different workers[*] for separating grain and GB contribution is not accurate and in principle should be avoided.
- The dependence of the curves on bulk size is quite physically reasonable and in excellent agreement to the experimental data.
- The dependence of the curves on grain size is also physically correct. However, there is no experimental data available to substantiate calculations here.

3.2.3. HIGHER HARMONICS - FIELD DEPENDENCE AND HYSTERESIS:

Study of higher harmonics of AC magnetic susceptibility has taken serious role in HTSC because of presence of non-zero even harmonics in contradiction to Bean's model prediction where all even harmonics are zero. Here a brief discussion will be presented.

3.2.3A) WITHOUT DEMAGNETIZATION CORRECTION:

In figure 3.2.28(a,b) real and imaginary parts of odd harmonics have been plotted as a function of DC bias field for a high AC amplitude of 3.5 mT while other parameters are given within the diagram. In figure 3.2.29(a,b) same curves as in figure 3.2.28(a,b) but for the even harmonics have been plotted. It is obvious that our calculations are well in agreement with already published data and calculated results[23,24]. By a proper selection of different parameters this agreement can be improved. The important feature in this figures is that all the even harmonics are present (upto 8th harmonics have been shown here). It is important to notice that at zero DC bias all the even harmonics (both real and imaginary parts) have zero values.

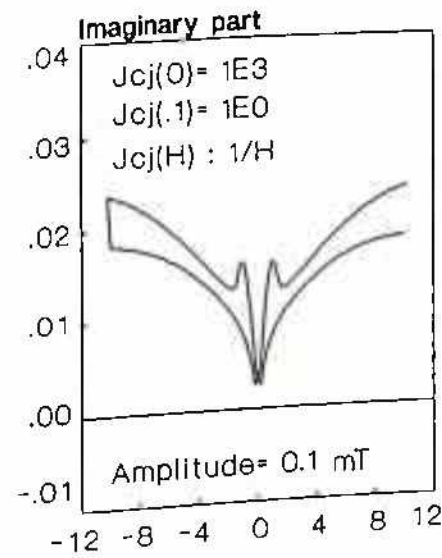
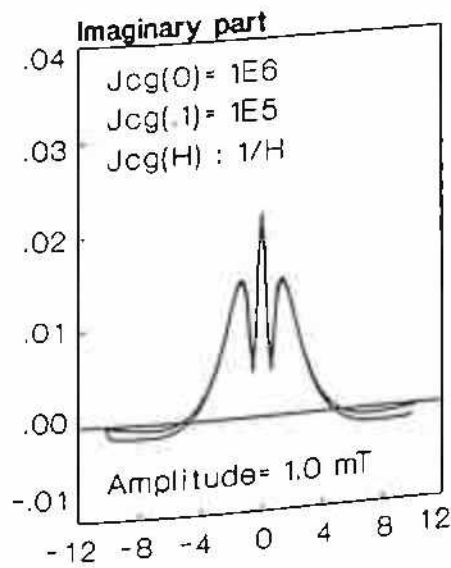
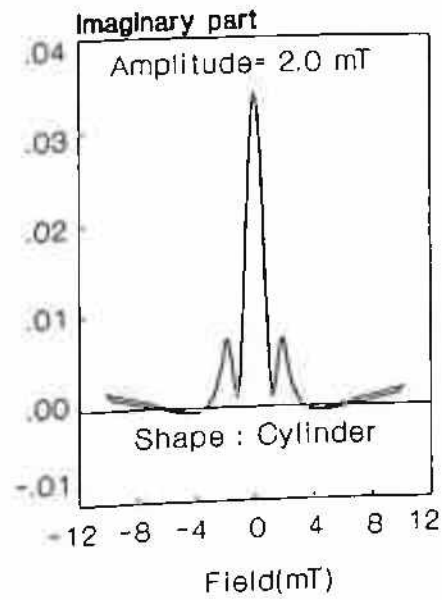
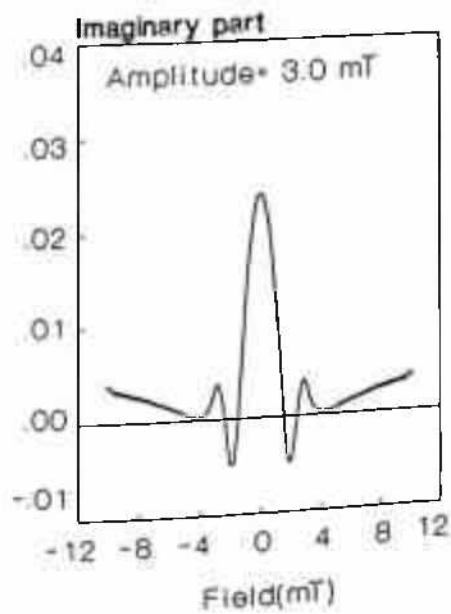


Figure 3.2.30b: Imaginary counter part of figure 3.2.30a.

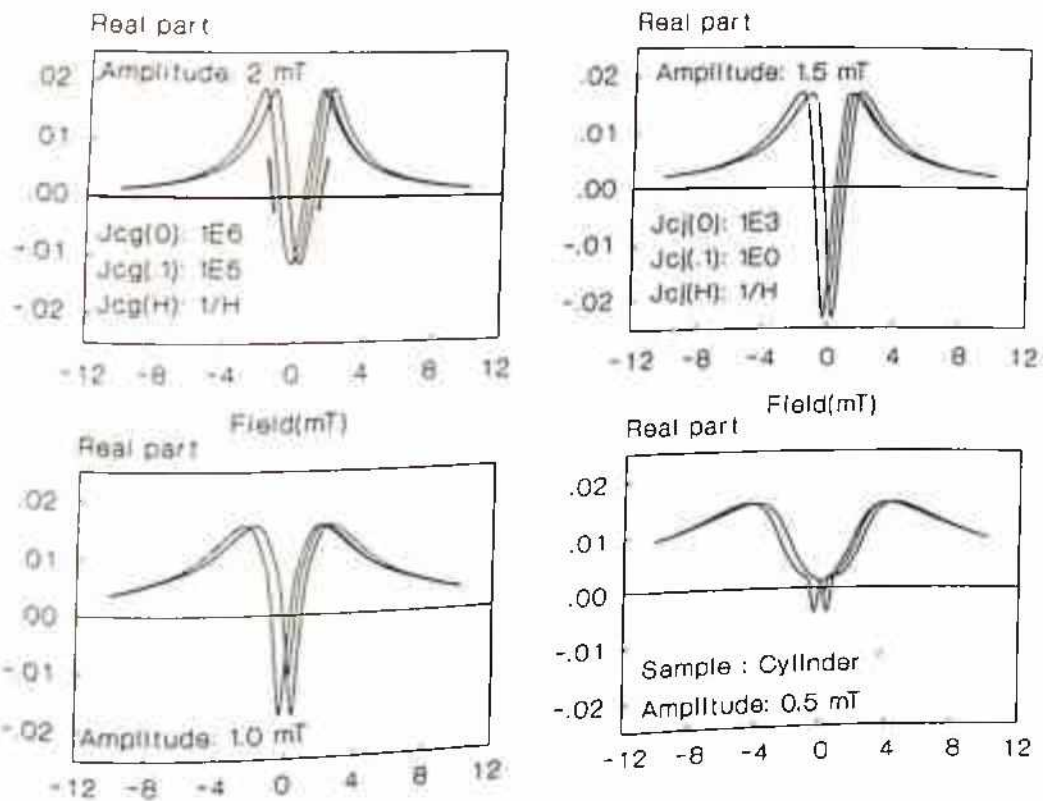


Figure 3.2.31a: Real part of even harmonics as a function of DC bias field. (Demagnetization correction included)

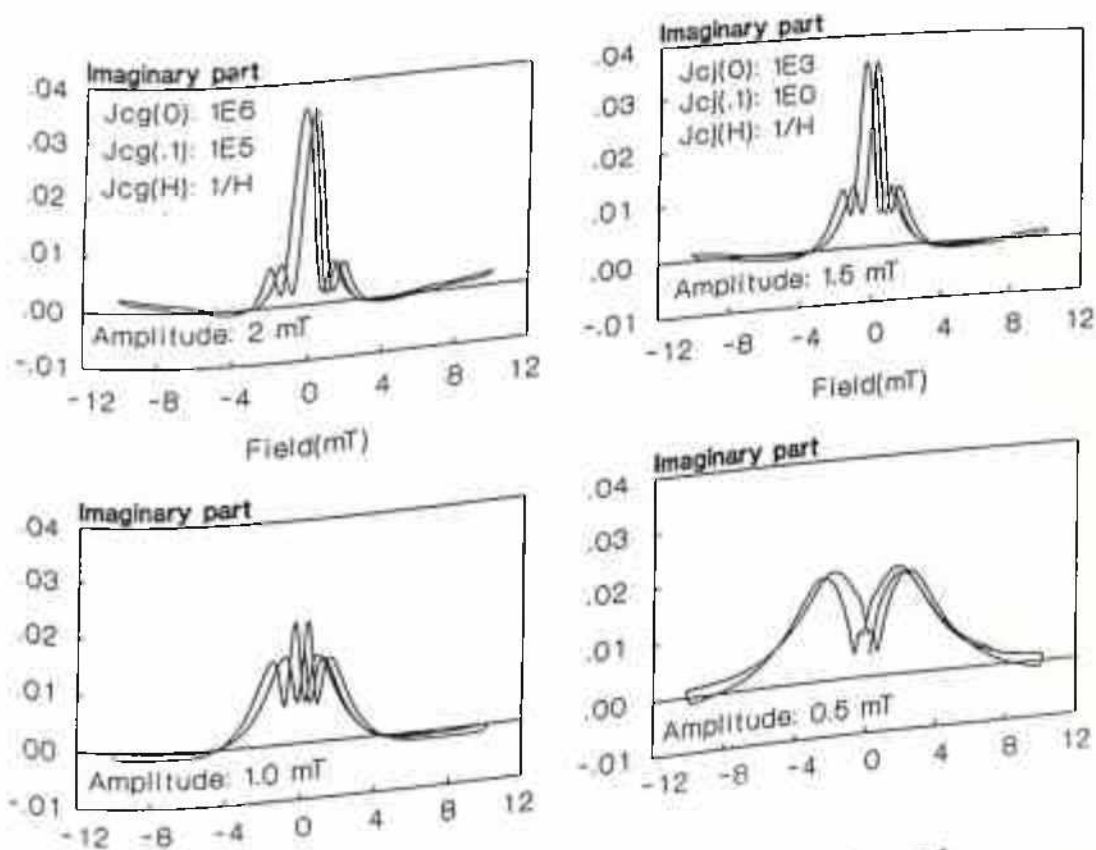


Figure 3.2.31b: Imaginary counter part of figure 3.2.31a.

This is in agreement with the theoretical expectation and results of others signifying the fact that even harmonics are not only due to field dependence but also a non-zero DC bias is required to produce them.

As it is already seen that the imaginary part of fundamental susceptibility shows hysteresis, one can expect the same hysteresis to be present even in other harmonics. Here the third harmonics will be considered. In figure 3.2.30(a,b) the third harmonics have plotted as a function of DC bias field for four different amplitudes. It is clear from the this figure that at lower amplitudes imaginary parts show hysteresis while the real parts do not exhibit any magnetic history at any amplitudes.

3.2.3B) DEMAGNETIZATION CORRECTION AND HYSTERESIS:

As in the case of fundamental case, here also demagnetization correction introduces hysteresis in both real and imaginary parts of the harmonics. In figure 3.2.31(a,b) real (χ'_3) and imaginary (χ''_3) parts of the third harmonic signals have been plotted as function of DC bias field for four different amplitudes. Other parameters in this figure are same as in figure 3.2.28. Experimental data of D. Sen et al.[2] have also shown the hysteresis in higher harmonics and have qualitative agreement with calculations here which can be checked by converting χ' and χ'' in this calculation into μ as shown in ref.[2]. It is to be noticed that other harmonics also exhibit hysteresis as in this case and need not to described any further. Calculation of hysteresis in higher harmonics of $\chi'(H)$ and $\chi''(H)$, to the author's knowledge, is reported for the first time.

3.2.4 MODIFICATION TOWARD NON-CRITICAL PHE-NOMENON.

3.2.4A. MODIFICATION IN THE MODEL - ACCOUNTING FOR FLUX CREEP:

So far in the model, it is assumed that an ideal critical state is present. However, in the light of different vortex related incidents (viz., flux melting or any other phase transitions, magnetic relaxations, thermally activated flux jumps or the giant flux creep) it is apparent that

the real situation is far from a true critical state. There is no elegant way in which one can take account of this vortex instability in a model like the one here. All that can be visualized is to include the effect through indirect impact of this on pinning potential or the critical current density.

The effect of flux creep is usually considered in a simple way following Campbell and Evetts[37] formulation of the Anderson and Kim theory of creep. In this model critical current density at given temperature and field can be written as[38];

$$J_c(H,T) = J_{c0} \left[1 - \frac{kT}{U_0(H,T)} \ln\left(\frac{f_0}{f}\right) \right] \quad (3.2.10)$$

where U_0 is the depth of the pinning potential well, f is frequency of measurements and f_0 is the characteristic attempt frequency having value in the range 10^9 - 10^{12} Hz. However, here more rigorous derivation will be followed as proposed by Müller[39] for a granular system. Müller has showed that the effect of creep of the Josephson vortices on the critical current density for cylinder of radius R is to modify the critical current density as follows;

$$J_c(H,T) = \frac{J_{c0}}{(H+\alpha)^\beta} + J_{creep} \quad (3.2.11)$$

where the second term is the actual creep component given by,

$$J_{creep} = \frac{kT}{2R_s^2 \phi_0} \ln\left(\frac{\nu_h}{\nu_0}\right) \quad (3.2.12)$$

Here ν_h is "minimal observable hopping rate" and is connected to the driving frequency as[40];

$$\nu_h = \frac{8\phi_0 H_{c2} R_s^2 f}{RkT} \quad (3.2.13)$$

In principle it is possible to accommodate eqn. 3.2.11 in the critical state model as described above. However, for an immediate visualization of the effect of creep a qualitative reasoning will be presented. As obvious from eqn. 3.2.11, the effect of creep is to add (or subtract) the J_{creep} component to the $J_{c0}(H,T)$ (because only the creep of the Josephson vortices

is being considered) depending on the frequency. For any practical situation this J_{creep} is negative (i.e., subtraction to be made) and with increase of frequency J_{creep} will decrease.

Obviously the same thing can be extended for creep due to intragrain vortices (Abrikosov vortices) when the creep contribution will modify J_{cg} in the same way.

3.2.4B. AC FIELD MEDIATED DEPINNING LEADING TO ENHANCE FLUX FLOW - FURTHER MODIFICATION IN THE MODEL:

In 1967 Fiory and Serin[42] first demonstrated that a flux flow state may be induced by superimposing an AC field of amplitude quite less than the upper critical field (H_{c2}). Cape and Silvera[43] also produced similar results and showed that for given frequency there was a threshold amplitude below which depinning was negligible. For their material (In+1.5% Bi) they observed that below 10 KHz amplitude required was close to H_{c2} . It is obvious that with decrease in frequency higher amplitude was required to produce the flux flow state. Cape and Silvera also showed that the threshold amplitude of the AC field to activate depinning is $H_T^{osc} \propto f^{1/2}$, f is the frequency of the AC field. This was then theoretically treated by Yamafuji et al. [44] for triangular pinning potential well and supported the experimental facts. In fact the extension of this principle is seen in microwave absorption measurements where the flux flow state is achieved by the microwave excitation and the measurements indicates properties of an "ideal" pinless type-II superconductors.

However, this effect has usually been overlooked in explaining the dependence of different magnetic properties of high temperature superconductor at low frequency but high enough amplitude of the AC excitation field. In the context of Josephson vortices, however, it appears that this effect may not be negligible. It will be shown here that the inclusion of this factor may result in better analysis of some of the experimental data.

Here a simple calculation will be followed as given by Gittleman and Rosenblum[45,46] to understand the actual process and to extend it for our case of HTSC. Assuming a pinning potential as;

$$U = A[1 - \cos(2\pi x/d)] , \tag{3.2.14}$$

where x is the displacement of a flux bundle [45,46] under AC field and d is the lattice parameter of the FLL. Thus the force exerted on each flux tube is

$$F = \frac{\partial U}{\partial x} = -\frac{2\pi A}{d} \sin \frac{2\pi x}{d} \quad (3.2.15)$$

The maximum of this force must be equal to the maximum of the Lorentz force per flux line that the pinning can withstand. Thus,

$$\frac{2\pi A}{d} = \frac{F_p \phi_0}{cH} \quad (3.2.16)$$

and we can write the equation of motion of a typical flux line as,

$$m\ddot{x} + \eta\dot{x} + \frac{F_p \phi_0}{cH} \sin \frac{2\pi x}{d} = \frac{J\phi_0}{c} \quad (3.2.17)$$

where η is flux flow viscosity defined in Chapter 1 and m is effective mass of the flux lines and also that J and H are mutually perpendicular.

The solution to this equation as such is difficult. However, for the usual microwave range eqn. 3.2.17 can be solved under assumption that x is small and so the sin function can be approximated by its argument and the third term in left hand of eqn. 3.2.17 will be given by

$$\frac{2\pi F_p \phi_0^{\frac{1}{2}}}{cH^{\frac{1}{2}}} x - kx \quad (3.2.18)$$

which reduces eqn. 3.2.17 to a simple equation of forced vibration. Further considering the effective mass to be negligible, the so called pinning frequency ($\omega_0 = 2\pi f$) can be derived as,

$$\omega_0 = \frac{k}{\eta} = \frac{2\pi c \rho_n F_p}{\phi_0^{\frac{1}{2}} H_{c2} H^{\frac{1}{2}}} \quad (3.2.19)$$

where ρ_n is the normal state resistivity.

Marcon et al.[47] have estimated ω_0 for HTSC (YBCO) to be around 10^{11} rad/sec from somewhat different expression of ω_0 as given by Gilchrist[47]. However, this is in fact too high a value to be accepted. Further for Josephson vortices, from a physical reasoning from $\omega_0 = k/\eta$, one can guess ω_0 to be low. Because in this case k which is in essence a restoring force of the pinning well is likely to be low and η should be high.

But here the interest is for low frequency range, $\omega \ll \omega_0$ and amplitude not too low. In fact in this range there is no work from which we can formulate our logic. However, without going into the complexity of mathematics in solving eqn. 3.2.17, it is instructive to consider, once again, the experimental results of Cape and Silvera[43] where they have reported similar behavior in a material (In +1.5% Bi) having $H_{c2} = 16.8$ Oe. They observed even at 2 Oe and 35 KHz noticeable shift of I-V towards linearity (i.e., Ohmic) and at 3.9 Oe they got full linearity in the I-V. Thus for the case of Josephson vortices it is plausible to get sufficient depinning even at a few KHz depending on the amplitude.

The weakening of flux pinning due to AC field has also seen in the experiment of Chen[49] for ceramic bulk of YBCO at 77 K even at frequency of 2000 Hz.

Thus the effect of depinning of flux lines due to AC field in the two component model is to modify the J_{cg} and J_{cj} according to

$$J_{cgj}(\omega) = J_{cgj}(\omega=0) - \Delta J_{depinning} \quad (3.2.20)$$

3.2.5. INCORPORATING THE NON-CRITICAL PHENOMENON IN THE MODEL:

In the case of granular system, it likely that the Josephson vortices are weakly pinned and the large flux flow, particularly at higher temperature (≈ 77 K), will be more important in the context of non-critical contributions, e.g., flux creep and flux flow. Therefore, here the effect of AC amplitude mediated depinning as well as flux creep contribution will be considered for the Josephson vortices only.

As it is clear from eqn. 3.2.11 and eqn. 3.2.20 that effective contribution of this non-

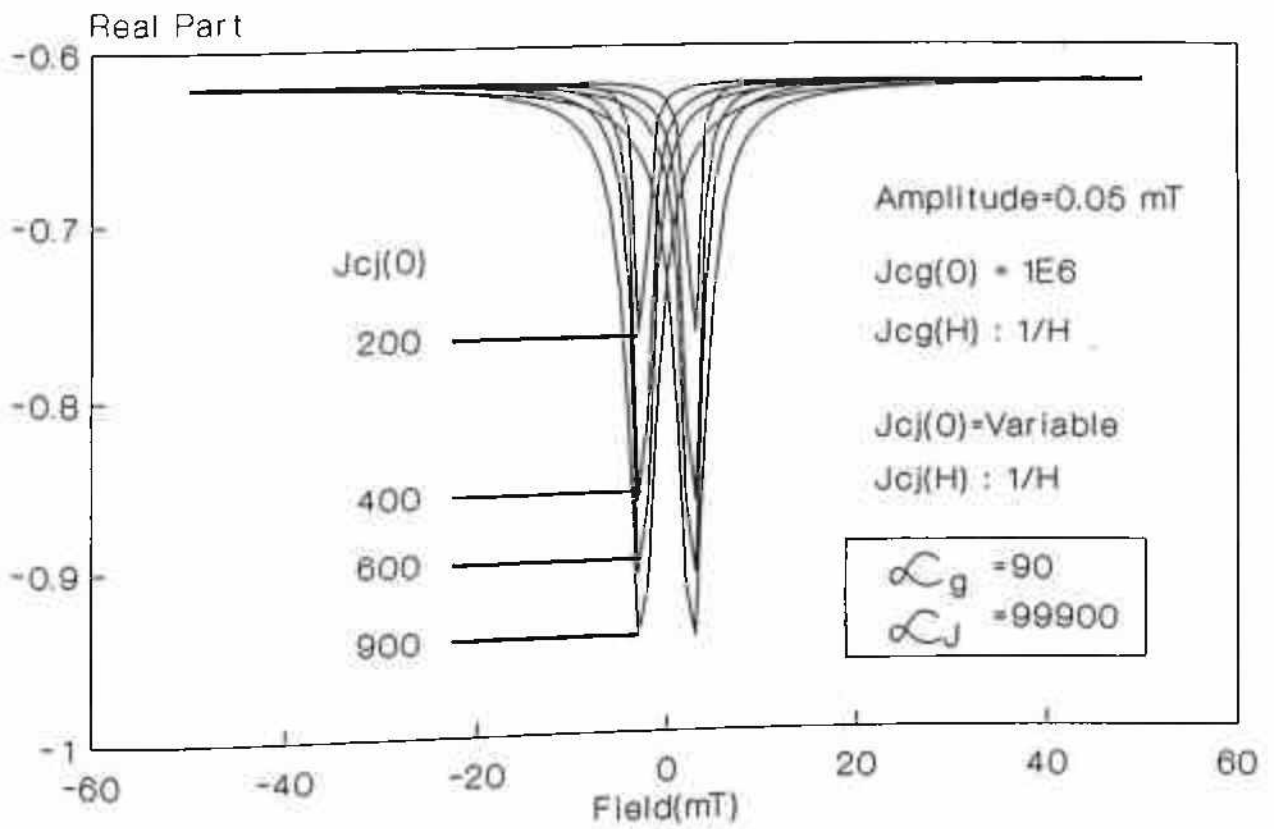


Figure 3.2.32a: χ' as a function of DC bias field for four different $J_{cj}(0)$ s. (see text)

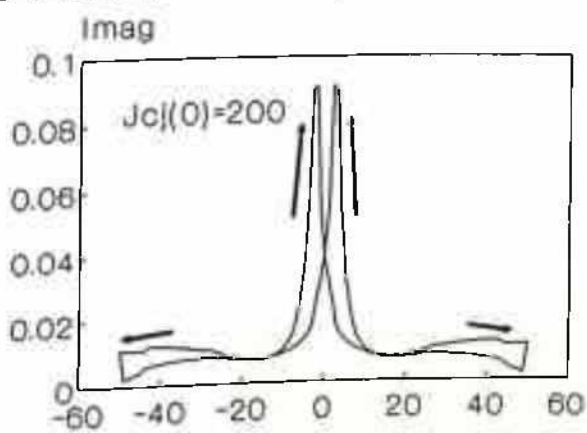
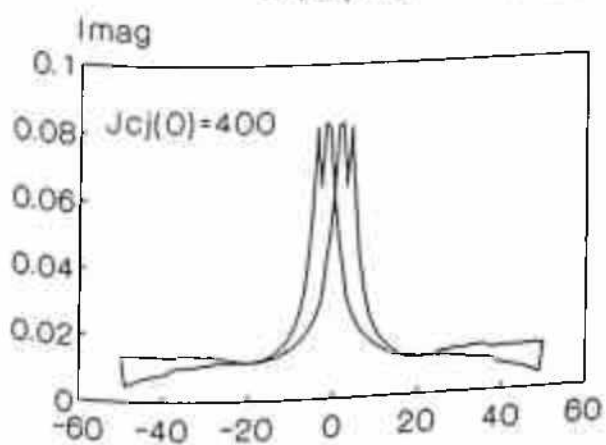
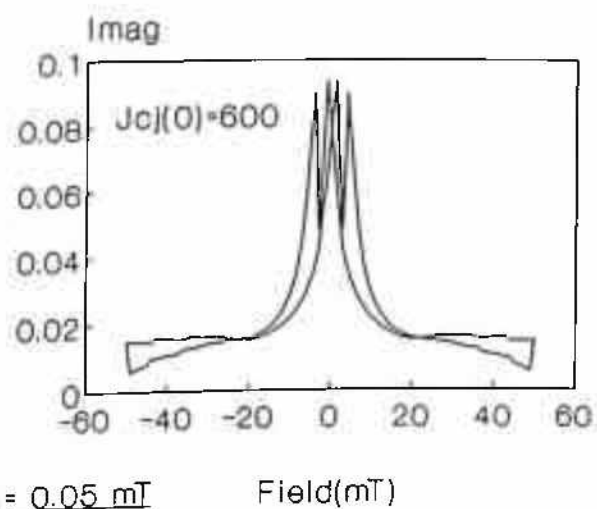
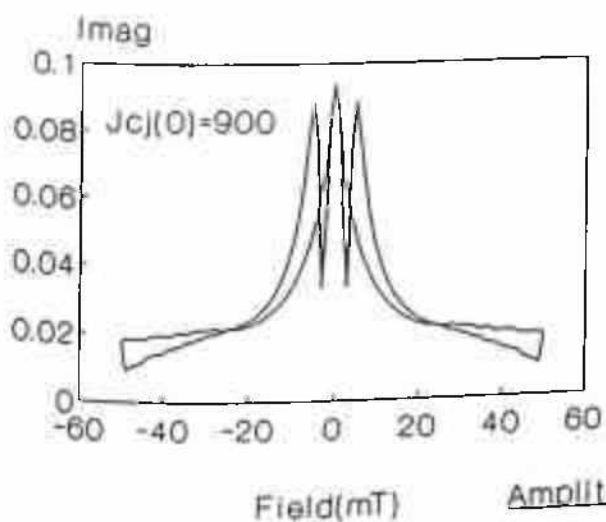


Figure 3.2.32b: Imaginary counterpart of figure 3.2.32a.

critical factor is to modify the actual critical state J_{c_j} (critical state J_{c_j} means J_{c_j} in absence of any creep or flow component) by an amount ΔJ . Here further simplification will be sought by assuming that this non-critical component is independent of magnetic field.

With this view in mind, in figure 3.2.32(a,b) the plot of the real and the imaginary part of AC susceptibility have been plotted for parameters as shown in the figure. In order to show clearly this effect of flow (or creep) through eqn. 3.2.20 (or eqn. 3.2.11), the model has been modified slightly. Instead of using the constants eg. $J_{cg/j}(0.1)$ or $J_{cg/j}(0.01)$, here directly the $J_{cg/j}(0)$ and $\alpha_{g/j}$ have been considered as input parameter and the value of the parameters have been shown within the diagram. Here the parameters are such that the results are useful to explain the experimental data in next chapter. The important features of this figure 3.2.32(a,b) are; i). the real parts show less screening with higher flow component, i.e., less effective $J_{c_j}(0)$. The field dependence of $\chi'(H)$ as a whole is also less with lesser effective $J_{c_j}(0)$, ii). in case of $\chi''(H)$, the sharp feature as described in figure 3.2.15b is quite clearly seen and this feature diminishes with decrease of effective $J_{c_j}(0)$. Below a certain low value of $J_{c_j}(0)$ this feature is no more seen. As will be seen in next chapter that this result will be helpful in explaining the experimental data.

3.2.6. EXPERIMENTAL EVIDENCE IN SUPPORT OF THE LAST TWO MODIFICATIONS:

This finding can be utilized to explain the frequency dependence of the M-H loops as reported by Gough et al.[41]. In this ref. M-H loops at three different frequencies have been studied at different temperatures by AC M-H loop tracer for ring shaped single crystal of YBCO and BSCCO (2212). The essential of the data in ref. [41] is that at high temperature M-H loops become larger in size with increase in frequency while at low temperature the reverse is seen.

Incorporating the modification due to creep in a one component M-H loop model it is possible to account for the observed frequency dependence in M-H loops of ref. [41]. At high temperature due to sufficient thermal energy (kT) more creep is liable to present. Thus as explained above at higher frequency this creep will contribute less to J_{cg} and hence effective J_{cg} at higher frequency will be higher than that at lower frequency and as a consequence M-H loops

will be wider at higher frequency. On the other hand at low temperature creep will be negligible and AC oscillation mediated depinning may overrun the flux creep contribution and as the flux flow is enhanced with higher frequency of AC field (because the amplitude is quite high) there will be decrease in M-H loops because of decrease of J_c .

REFERENCES:

- [1] Y. Kim, Q. H. Lamb and C. D. Jeffries 1991 Phys. Rev. **B43**, 11404
- [2] D. Sen, A. Mitra and S. K. Ghatak 1992 Supercond. Sci. Technol. **5**, 467
- [3] Y. Yang, C. Beduz, Z. Yi and R. G. Scurlock 1992 Physica C, **201**, 325
- [4] Subir Saha and B. K. Das 1993 Supercond. Sci. Technol. **6**, 685
- [5] Fedor Gomory 1992 Magnetic Susceptibility of Superconductors and Other Spin Systems, ed. R.A. Hein et al., Plenum Press, New York p:289
- [6] H. K pfer, I. Apfelstedt, R. Flukiger, C. Keller, R. Meier-Hirmer, B. Runtsch, A. Turowski, U. Wiech and T. Wolf 1988 Cryogenics **28**, 650
- [7] A. Kompany, Y. J. Qian, M-F. Xu, H-P. Baum, W. Millman and M. Levy 1990 Solid State Comm., **75**, 579
- [8] C.Y. Lee, L.W. Song and Y.H. Kao 1992 Physica C, **191**, 429
- [9] L. G. Mamsurova, K. S. Pigalskiy, V. P. Sakun and L. G. Scherbakova 1992 Physica C, **200**, 175
- [10] J. E. Evetts and B. A. Glowacki 1988 Cryogenics **28**, 641
- [11] R. B. Goldfarb and A. F. Clark (1985) march MAG21, 332
- [12] C.P. Bean 1962 Phys. Rev. Lett. **8**, 250
- [13] C.P. Bean 1964 Rev. Mod. Phys. **36**, 31
- [14] Y. B. Kim, C. F. Hempstead and A. R. Strand 1962 Phys. Rev. Lett. **9**, 306
- [15] Y. B. Kim, C. F. Hempstead and A. R. Strand 1963 Phys. Rev. **129**, 528
- [16] P. W. Anderson, 1962 Phys. Rev. Lett. **9**, 309
- [17] F. Irie and K. Yamafuji 1967 J. Phys. Soc. Jpn. **23**, 255
- [18] I. M. Green and P. Hlawiczka, 1967 Proc. IEE **114**, 1329
- [19] V. R. Karasik, N. G. Vasil'ev and V. G. Ershov 1964 Sov. Phys. Rev. **136**, A335
- [20] G. Ravi Kumar and P. Chaddah 1989 Phys. Rev. **B39**, 4704
- [21] D.-X. Chen, A. Sanchez, J. Nogu s, and J.S. Munoz 1990 Phys. Rev. **B41**, 9510
- [22] K. V. Bhagwat and P. Chaddah 1990 Physica C, **190**, 444
- [23] L. Ji, R.H. Sohn, G.C. Spalding, C.G. Lobb and M. Tinkham 1989 Phys. Rev. **B40**, 10936

- [24] T. Ishida and R. B. Goldfarb 1990 Phys. Rev. **B41**, 8937
- [25] K. H. Müller 1989 Physica C, **159**, 717
- [26] J. Clem 1988 Physica C, **153-155**, 50
- [27] J. R. Clem 1979 J. Appl. Phys. **50**, 3518.
- [28] D. -X. Chen, J. A. Brug and R. B. Goldfarb, IEEE Trans. Mag. **27**, 3601
- [29] S. Senoussi, S. Hajoudj, R. Maury and A. Fert 1990 Physica C **165**, 364
- [30] U. Yaron, Y. Korniyushin and I. Felner 1992 Phys. Rev. **B46**, 14823
- [31] U. Yaron, Y. Korniyushin and I. Felner, O. David and L. Patlagan 1993 Physica C **208**, 18
- [32] Du-Xing Chen and Alvaro Sanchez 1992 Phys. Rev. **B45**, 10793
- [33] Zeljko Marohnic and Emil Babic 1992 Magnetic Susceptibility of Superconductors and Other Spin Systems, ed. R.A. Hein et al., Plenum Press, New York p:267
- [34] M. Tinkham and C.J. Lobb 1989 Solid State Physics **42**, 91
- [35] K.-H. Müller and D.N. Matthews 1993 Physica C **206**, 275
- [36] D.-X. Chen, A. Sanchez, T. Puig, L.M. Martinez and J. S. Munoz 1990 Physica C **168**, 652
- [37] A.M. Campbell and J.E. Evettes 1972 Adv. Phys. **21**, 199
- [38] A.P. Malozemoff, T.K. Worthington, Y. Yeshurun and F. Holtzberg 1988 Phys. Rev. **B38**, 7230
- [39] K. H. Müller 1990 Physica C **168**, 585
- [40] K.H. Müller, N. Nikolo and R. Driver 1991 Phys. Rev. **B43**, 7976
- [41] C.E. Gough, A. Gencer, G. Yang, M.Z. Shoustari, A.I.M. Rae and J.S. Abell 1993 Cryogenics **33**, 339
- [42] A.T. Fiory and B. Serin 1967 Phys. Lett. **25A**, 557
- [43] J.A. Cape and I.F. Silvera 1968 Phys. Rev. Lett. **20**, 326
- [44] K. Yamafuji, N. Sakamoto and T. Kawashima 1971 Phys. Lett. **36A**, 341
- [45] J.I. Gittleman and B. Rosenblum 1966 Phys. Rev. Lett. **16**, 734
- [46] J.I. Gittleman and B. Rosenblum 1968 Journal Appl. Phys. **39**, 2617
- [47] R. Marcon. R. Fastampa, M. Giura and E. Silva 1991 Phys. Rev. **B43**, 2940
- [48] J. le G. Gilchrist 1966 Proc. R. Soc. London **A295**, 399

- [49] Q.Y. Chen 1991 *Magnetic Susceptibility of Superconductors and Other Spin Systems* Ed. R.A. Hein et al. Plenum pp 81.

EXPERIMENTAL DATA

STUDIES ON THE RESPONSE OF THE HIGH TEMPERATURE SUPERCONDUCTORS IN ALTERNATING CURRENTS:

This part contains the results of electrical measurements. The study includes FFT of voltage signal, I-V at different frequencies and magnetic fields and irreversibility of magneto-resistance. Some data on apparent contact resistance (3-probe) have also been included.

4.1.1. INTRODUCTION	164
4.1.2. EXPERIMENTAL DATA	167
A. DC RESULTS	169
B. AC RESULTS	171
I. HARMONICS THROUGH FFT	177
II. CURRENT VOLTAGE CHARACTERISTICS	180
III. IRREVERSIBILITY OF MAGNETO-RESISTANCE	190
4.1.3. SUM UP	192
REFERENCE	

4.1. STUDIES ON THE RESPONSE OF THE HIGH TEMPERATURE GRANULAR SUPERCONDUCTORS IN ALTERNATING CURRENT:

4.1.1. INTRODUCTION:

On application of a DC current, Type-I superconductors remain loss-less upto a limiting current known as depairing critical current. Ideal Type-II superconductors are lossy at all current values. But in the case of practical Type-II hard superconductors with pinned flux lines, there is no loss upto a limiting critical current density (J_c) above which flux lines get depinned resulting in losses. But on application of an alternating current, the situation becomes completely different and a complex situation arises in which a multitude of different processes can be present depending upon the frequency and the amplitude of the AC field. As this work is concerned with high temperature superconductors, which are extreme cases of Type-II superconductors, the discussion will be in that context only.

The experimental difficulties in doing this kind of study involving AC currents along with complexity in interpreting the results are reasons for the rare efforts in doing this kind of experiment [1-3].

The usual experiments involving AC currents involve AC loss measurements for superconducting wires due to technological importance [4-10]. AC loss is usually measured by calorimetric method or by measuring the imaginary part of the AC magnetic susceptibility. Though in principle resistive component (i.e., in-phase with the drive current) in AC transport measurements will also measure AC loss, this method is relatively rare. Moreover, though an AC current in principle will give more information on the microscopy of the pinning mechanism [1-3] there has not been much effort in that line.

Above a certain frequency, known as the "pinning frequency" as shown by de Gennes and Matricon [11] viscous forces dominate and pinning becomes completely ineffective (at microwave or higher frequencies). Fiory and Serin [12] showed from experimental data that, in presence of oscillatory magnetic field parallel to the current, pinning becomes less effective even at 30 KHz. This was also verified by Cape and Silvera [13] in their experiment where they further showed that there is a threshold value of the AC amplitude to inactivate pinning and that

this threshold amplitude increases to H_{c2} as the frequency decreases. Calculation of Yamafuji et al.[15] also supported these experimental findings.

The interest of the present work is in the low frequency range (a few Hz to a few KHz), a few order of magnitude less than the depinning frequency. Thus in order to have theoretical basis to explain our data this line of formulation is inadequate. In the early period (1960-70) there were some experiments involving AC transport measurements[20] which were explained on the basis of oscillation of flux lines[18,6]. Lowell[19] assumed the oscillation in the two regime distinguished by a limiting current density value (J_{0m} given by:

$$J_{0m} = \left(\frac{\eta \zeta_0}{m \phi_0} \right) \tanh(md) \quad (4.1.1)$$

where ζ_0 is the maximum reversible displacement of the flux line oscillation, $m^2 = \mu_0 \eta / \phi_0 B$, J_0 is the amplitude of AC current and $2d$ is the sample thickness and η is the restoring force per unit length of fluxon for unit reversible displacement[19]. Then the two regimes are; i). when $J_0 < J_{0m}$, the oscillation is reversible in the sense that no energy is spent at the pinning center and the field is harmonic and in quadrature with the current given by,

$$E_0 = \frac{1}{2} \omega m \phi_0 J_0 B \eta^{-1} \coth(md) \quad \text{out-of-phase} \quad (4.1.2)$$

and ii). if $J_0 > J_{0m}$, then the oscillation is no more reversible and anharmonicity is expected.

Then the two components of the electric field are given by;

$$E_{in} = \frac{\mu_0 J_0^2 \omega}{8 \pi J_c} \quad \text{(in-phase)} \quad (4.1.3)$$

$$E_{out} = \frac{\mu_0 J_0^2 \omega}{4 \pi J_c} \quad \text{(out-of-phase)} \quad (4.1.4)$$

This calculation implies that at a sufficient low AC amplitude, because of reversible oscillation of flux lines I-V will be straight line and at higher AC amplitude I-V will be parabolic. However, at all amplitudes the frequency dependence will be linear.

Though this calculation, more or less substantiated the experimental measurements[20], it is obviously not a rigorous one and can not be expected to be true in all cases, particularly in presence of flux flow as in the case of HTSC. In fact, recently there has been an attempt to formulate the electrodynamics in the mixed states in presence of AC current which probably will be a more accurate way to interpret the AC transport measurement data in HTSC. Here the proposition of Sonin et al[22] will be introduced. Usually the aim of these calculations is to account for the microwave range observations (eg. surface resistance) and the solution of the equation of motion in this range is easy. However, the intention in this work is different from that and hence a qualitative description will be sought. For a Josephson medium, Sonin et al.[22] considering the London equation and the equation of motion of flux lines as;

$$m \frac{d^2 X}{dt^2} + \eta \frac{dX}{dt} + kX - \frac{Jx\phi_0}{c} \quad (4.1.5)$$

have shown that the resistivity can be expressed as[22];

$$\rho_B(\omega) = \frac{4\pi\lambda^2\mu i\omega}{c^2} \left(1 + \frac{fB\phi_0}{4\pi\lambda^2\mu} \frac{1}{k-i\omega\eta} \right) \quad (4.1.6)$$

where f , the fraction of flux line that is unpinned. This fraction of unpinned vortices has been introduced following Marcon et al.[23]. Although this equation has been arrived at for Josephson medium this is equally valid for grains also. In that case the other parameters for the Josephson medium and for the grains, e.g., λ (effective penetration depth), μ (effective permeability), k (restoring force constant of the pinning potential) and η (coefficient of viscosity) are expected to be different. In this derivation, the effective mass of the flux lines have been considered to be negligible [24]. Eqn. 4.1.6 will form the basis for the explanation of the data considered here. Physical consequence of eqn. 4.1.6 is that due to oscillation of flux lines even at low current a voltage will appear which is proportional to AC current and also to the frequency (i.e.,

the first part of eqn. 4.1.6) while due to viscous loss another term will come in to force given by the second term of eqn. 4.1.6. Obviously the second term is linear in B and frequency dependence will be different in different regimes (above and below $\omega_0 = k/\eta$, the depinning frequency). Particularly at frequencies above ω_0 , the viscous term dominates and one can drop k from eqn. 4.1.6. In that case, the second term becomes frequency independent. However, in the low frequency range, k can not be omitted and the second part in eqn. 4.1.6 also becomes dependent on frequency.

The obvious generalization which restricts eqn. 4.1.6 to be applicable in all range of amplitude is that, here only the harmonic regime has been considered and so only the low amplitude case can be considered. As will be seen in the experimental data, in actual case one has to consider the non-linearity to account for the presence of different harmonics.

4.1.2. EXPERIMENTAL DATA:

4.1.2A. DC RESULTS.

Before discussing the AC results which are of importance here, it is better to go through some DC measurements. In figure 4.1.1 the plot of V-I with DC current for 4-probe has been shown for two different fields for a 10% Ag-doped YBCO sample. The inset is showing the V-I in the log-log scale for the high field data. It is clear from this figure that the sample in question had a critical current higher than 5 amp at zero field. But at a field of 100 mT critical current was only about 300 mA (assuming critical current to be measured at $1 \mu\text{V/cm}$). The log-log plot in the inset clearly indicates a power law relation between the current and the voltage, i.e., $V \propto I^n$. By fitting through least square method of the experimental data points, 'n' was calculated to be ≈ 1.588 . The dotted line in the inset is drawn to emphasize this power law behavior. This power law behavior is now well known and have been reported by many other[27-33]. Ban et al. have studied the power law I-V in $\text{ErBa}_2\text{Cu}_3\text{O}_{7-x}$ and calculated n as a function of temperature and magnetic field. Their study shows that n decreases with increase of temperature as well as magnetic field and $n = 3$ indicates to some critical value at which there is a jump in n values indicating some sort of phase transition. Thus $n = 1.588$ as seen in figure 4.1.1 is possibly below this critical value of n, i.e., above the phase transition.

Following the arguments of Brandt[34,37], the V-I in these materials can be characterized in the three different regions. In the low current limit, it is thermally assisted flux flow (TAFF) which rules the linear I-V curves[35]. At currents such that $J \approx J_c$, creep will dominate and non-linearity in I-V is expected. For $J \gg J_c$, Lorentz force will determine the I-V and in the limiting case of higher currents one will observe the usual flux flow regime where $E = \rho_{FF}J$. Thus both the TAFF and flux creep are the limiting cases of Anderson's [38] general expressions for the electric field $E(B,T,J)$ generated by thermally activated flux jumps out of pinning centers which may be written as[36]

$$E(J) = 2\rho_c J_c \exp(-U/k_B T) \sinh(JU/J_c k_B T) \quad , \quad (4.1.7)$$

where $J_c(B)$ (critical current density at $T = 0$), $\rho_c(B,T)$ (resistivity at $J = J_c$) and $U(B,T)$ (activation energy for flux jumps) are phenomenological parameters.

The physical idea behind eqn. 4.1.7 is that the Lorentz force acting on the FLL increases the rate of thermally activated jumps of the flux lines or flux bundles along the force, $\nu_0 = \exp[-(U-W)/K_B T]$, and reduces the jump rate for backward jumps, $\nu_0 = \exp[-(U+W)/K_B T]$. Here $W = JB\ell$ is energy gain during a jump, V is the jumping volume, ℓ is jump width and ν_0 is the attempt frequency[34,39].

Thus in the three current regimes one can write[34-36];

$$\rho = (2\rho_c U/k_B T) \exp(-U/k_B T) = \rho_{TAFF} \quad \text{for } J < J_c \quad (TAFF) \quad , \quad (4.1.8)$$

$$\rho = \rho_c \exp[(J/J_c - 1)U/k_B T] \quad \text{for } J \approx J_c \quad (Flux \text{ creep}), \quad (4.1.9)$$

$$\rho = \rho_{FF} (1 - J_c^2/J^2)^2 \quad \text{for } J > J_c \quad (flux \text{ flow}), \quad (4.1.10)$$

where $J_1 = J_c k_B T / U$.

Thus the I-V as shown in figure 4.1.1 is probably partly due to TAFF and partly due to flux creep because, for certainty current was well below the critical current value at $T=0$.

However, there was one important artifact that might have obscured the experimental data - the heating at the contact region when the voltage and current contacts are closer. This is further important in the context of the contacts here, because the contact resistivity in these experiments was also a function of the magnetic field. Thus in figure 4.1.2 the plots of 3-probe as well as 4-probe I-V have been given. As one can expect, the contact I-V (3-probe) had smaller value of n than the corresponding 4-probe I-V at same magnetic field. Further one must note that the magnetic field dependence in 3-probe I-V was at least a few times higher than that of 4-probe. This are probably sufficient argument to say that there is, if at all, not much mutual contribution. One more point is that the n values for 4-probe I-V from figures 4.1.1 ($n = 1.588$) and 4.1.2 ($n = 2.064$) are in agreement with Ban et al.'s findings, i.e., n decreases with increase in magnetic field.

4.1.2B. AC RESULTS.

AC transport measurements are usually difficult because of the presence of inductive voltage pickup in the measurement probes. In the experiments, being reported here, all the current and voltage leads used were shielded co-axial cable and one end of the all shields were earthed. This was expected to reduce the inductive pick-up. However, it was not possible to eliminate this pick up fully, because at least the silver rods of the contacts were not shielded which might be a possible source of pick-up. The details have been explained in the chapter 2 of this thesis. As these measurements were not accurate, here a relative comparison of the data at different frequencies and fields will be attempted. Though this kind of measurements are usually exploited for AC loss estimation, here the orientation will be towards response of flux lines in oscillatory field.

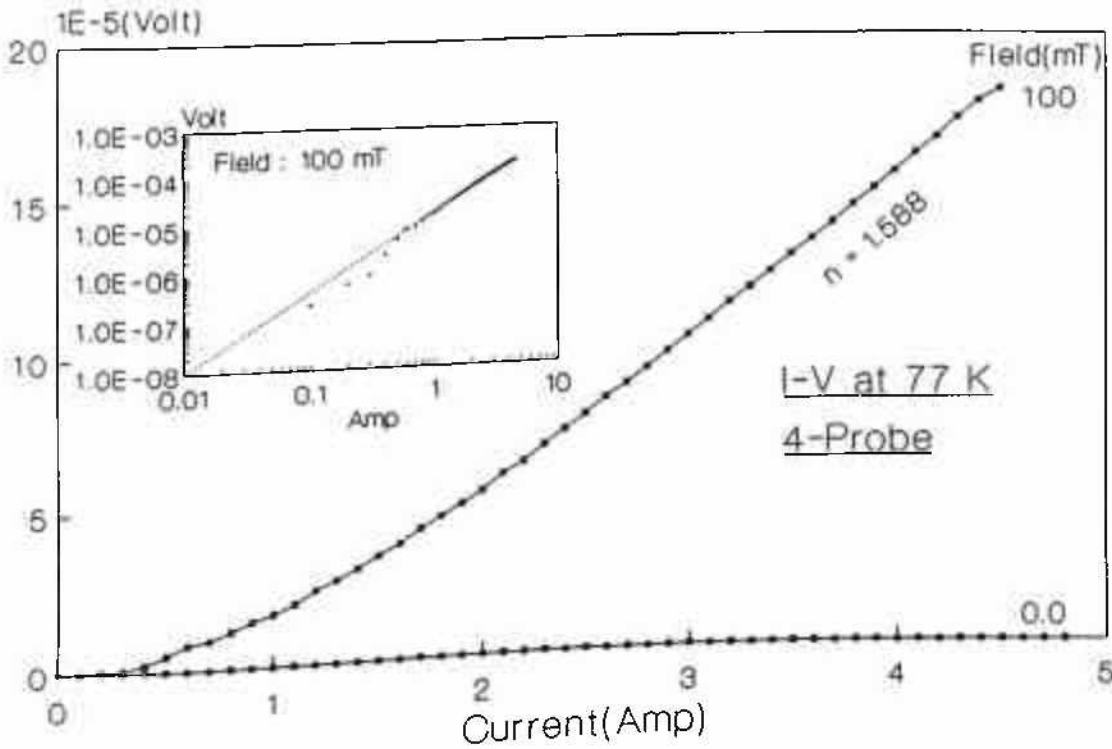


Figure 4.1.1: 4-probe DC I-V at 77 K for 10% Ag doped YBCO sample.

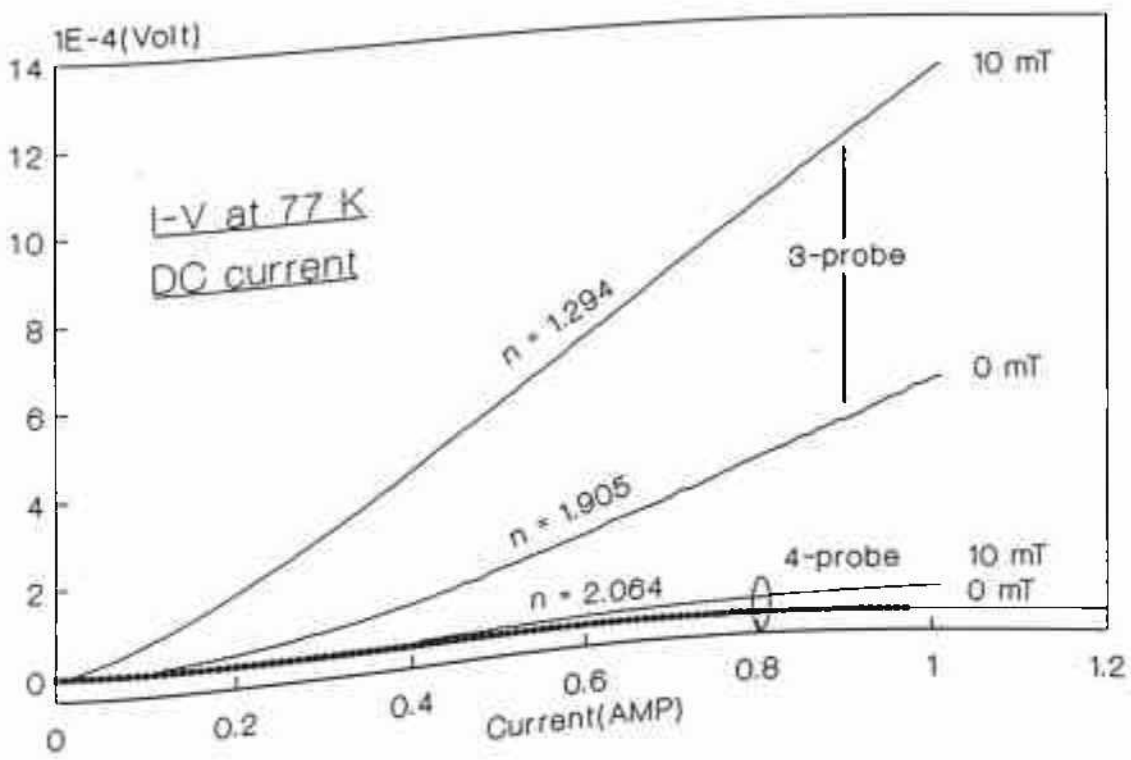


Figure 4.1.2: 4-probe and 3-probe DC I-V at 77 K for 10% Ag doped YBCO sample.

4.1.2A.D). HARMONICS THROUGH FFT:

To study the frequency response of a system Fourier transform is often used. Here the FFT of the voltage signal for a constant AC current has been done to illustrate the frequency response of the FLL. Exciting the sample by an AC current of a given constant rms value through the outer probes of the four probe configurations one can sample the voltage in the pair of middle probes. Obviously the sampling rate will determine the order of harmonics to be checked. Here a standard "Fast Fourier Transform (FFT)" was employed to analyze frequency components from the sampled wave form. Here the power spectrum was considered, i.e., the plot of $V(\text{FFT}) \cdot \text{conj}(V(\text{FFT}))$ (V is the complex function representing the FFT of the signal and "conj" stands for the conjugate of the corresponding complex function) as a function of frequency.

In figure 4.1.3 Fast Fourier Transform(FFT) of 4-probe signal of a pure YBCO sample at room temperature (300 K) have been presented. The important findings of this data was the absence of harmonics of the excitation signal (117 Hz), though the line frequency and it's harmonics were present. This also confirmed the current amplifier to be free from harmonics.

In figure 4.1.4 (3 Hz), 4.1.5 (7 Hz) and 4.1.6 (11 Hz) the FFT of 4-probe signal have been presented for liquid nitrogen temperature (77 K) at an AC current level (rms value) of 370 mA) for the sample as above. The excitation frequencies were different and are obvious in the diagrams. All the harmonics that were presents have been marked. As the sampling rate was 100 Hz one could identify the increase in signal level at the right end to be due to the line frequency noise(50 Hz). As can be seen in figure 4.1.4 for frequency close to 3 Hz upto (both even and odd) 11th harmonics were clearly seen. This strong anharmonicity, clearly indicated the hysteretic nature. In order to have some theoretical idea one must solve eqn. 4.1.5 with appropriate parameters to account for the non-linearity. The presence of power law relation $V \propto I^n \propto I_0^n \exp(in\omega t)$ directly indicates presence of different harmonic signal. However, it is difficult to calculate back the order of non-linearity by observing the order of harmonics.

Extending these studies for different excitation current levels, one can in principle make out the transition from reversible regime, where flux lines are oscillating across the pinning center without leaving it forever in phase with the driving force to the regime, where irreversibility prevents in-phase oscillation and anharmonicity appears. Here the same have been

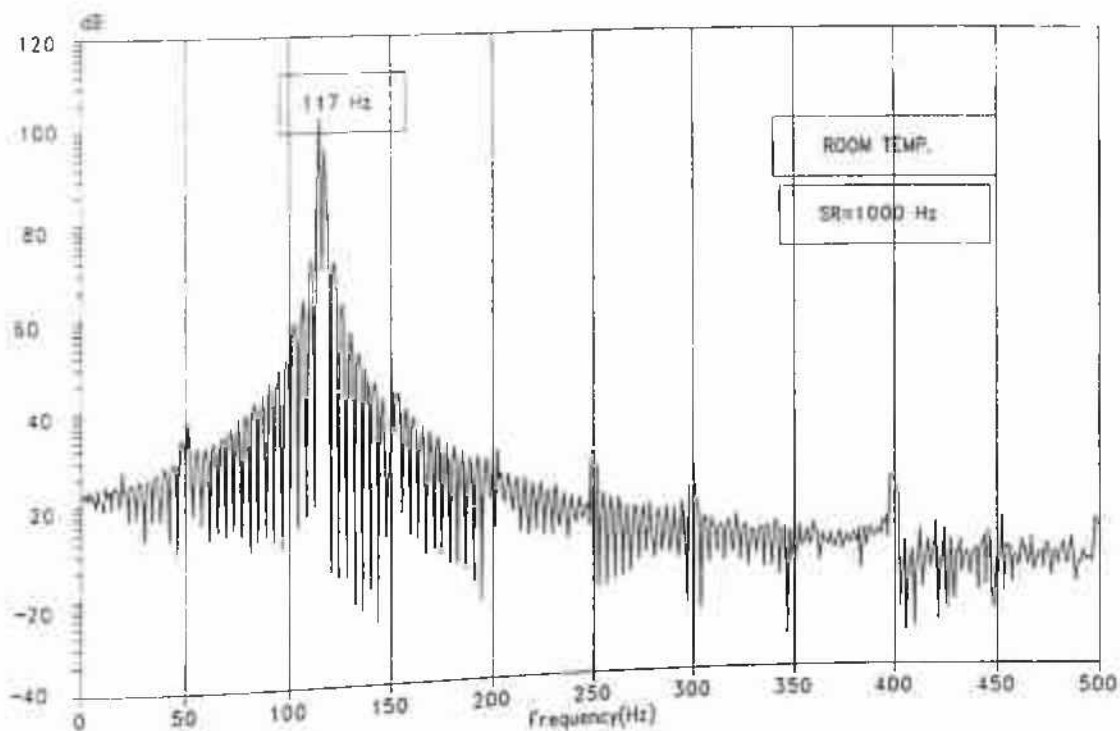


Figure 4.1.3: Power spectrum of 4-probe signal for frequency 117 Hz at room temperature for a YBCO sample.

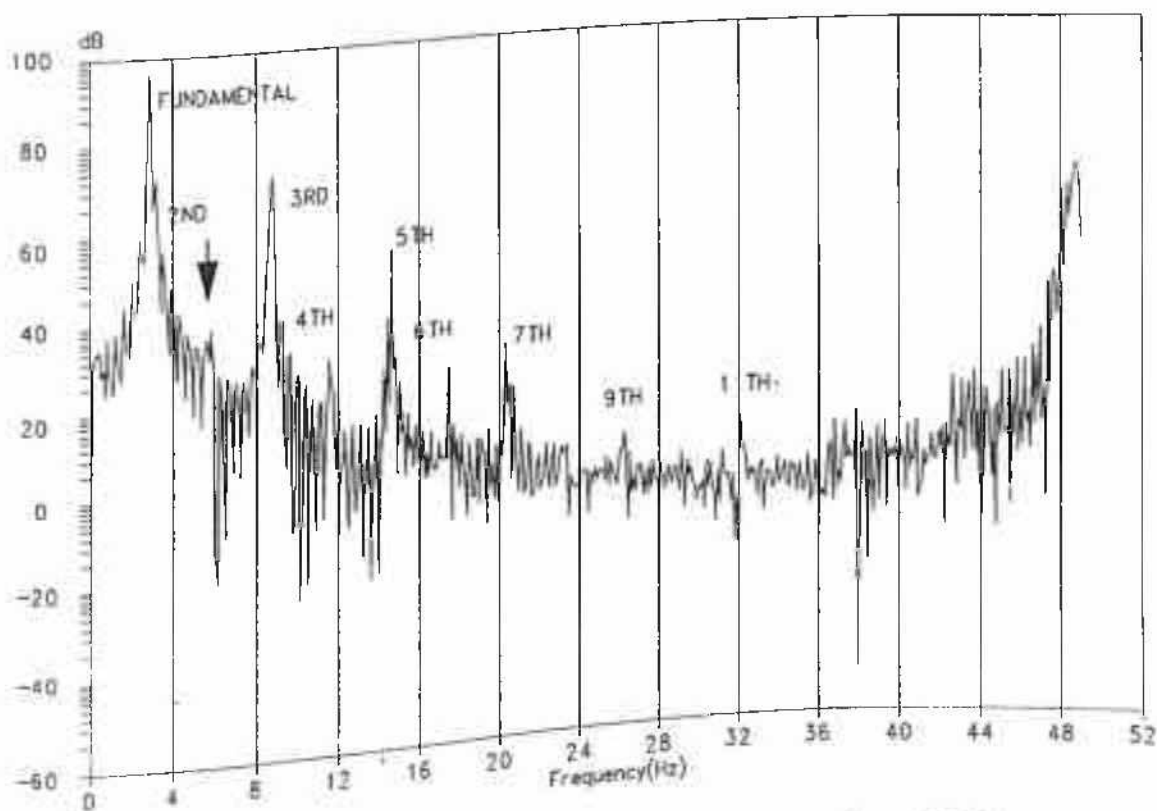


Figure 4.1.4: Power spectrum of 4-probe signal at 77 K for YBCO sample for frequency 3 Hz.

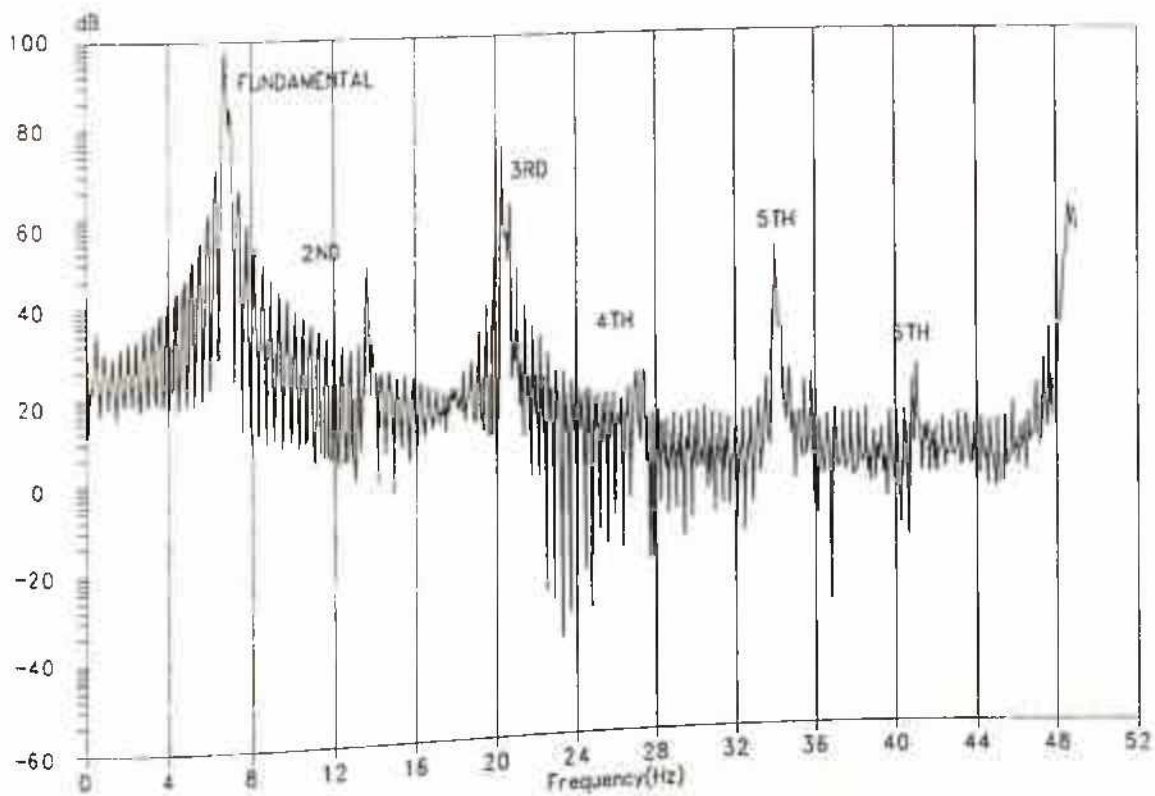


Figure 4.1.5: Power spectrum of 4-probe signal for frequency 7 Hz at 77 K for a YBCO sample.

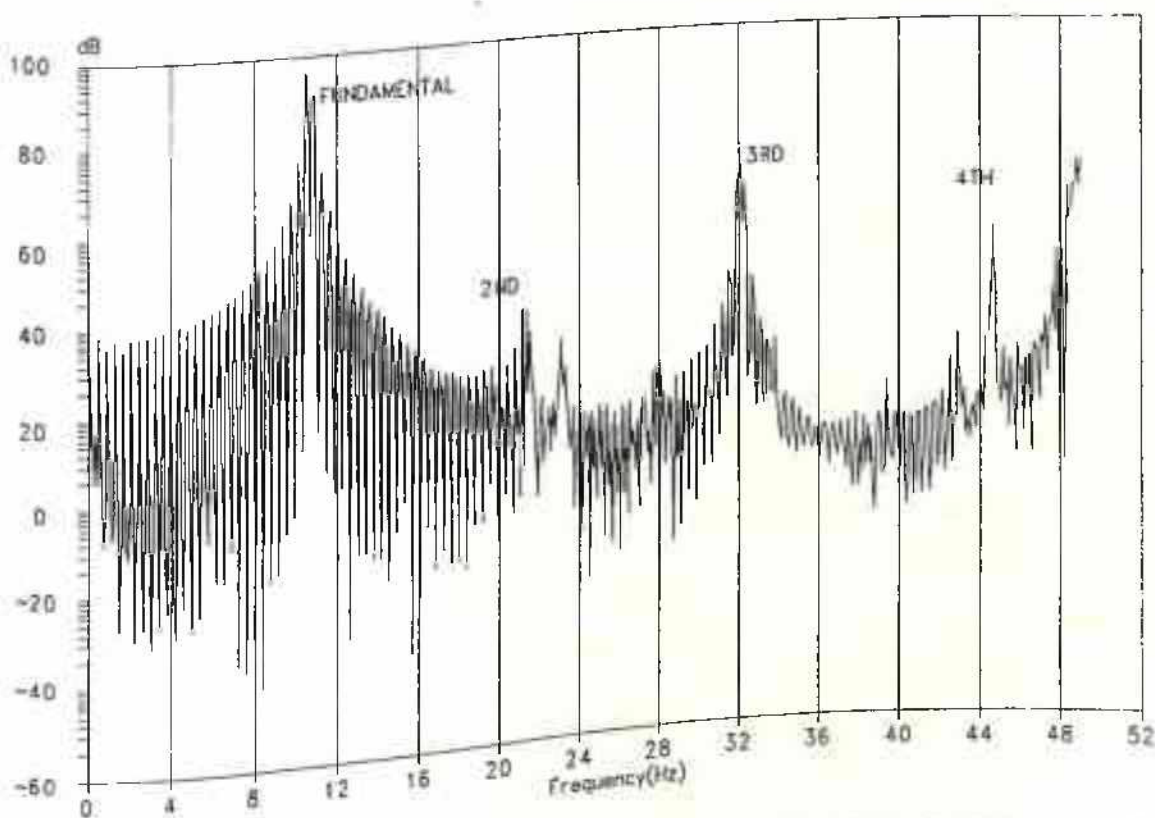


Figure 4.1.6: Power spectrum of 4-probe signal at 77 K for YBCO sample for frequency 11 Hz.

tried. However, the incapability to reduce the back ground noise particularly at low frequencies have posed serious problem. In figure 4.1.7 plots similar to figure 4.1.4 have been given for same frequency but 3 times lower current level. It is clear from this that the current level was still quite high and so anharmonicity was present. With further reduction of current the signal became too weak and different noises masked the actual signal.

In search of higher harmonics one must have a higher sampling rate. At the same time, with higher sampling rate at low frequency one will require larger number of points (this is to make it possible to cover at least few cycles of excitation to be sampled) and hence larger buffer memory. Because of this trade off, at lower frequencies higher sampling rate could not be achieved. However, here some data at higher frequencies with 1 KHz sampling rate have been included, which gave some new findings. In figures 4.1.8, 4.1.9, 4.1.10 FFT data at different frequencies have been shown for a current level somewhat higher (400 mA) than that of figure 4.1.4-4.1.6. As discussed above, at low frequencies (e.g. 11 Hz) number of cycles digitized being less, the harmonic resolution was very poor. However, it was not impossible to see some of the first harmonics along with 2nd harmonic (figure 4.1.8). But in case of 37 Hz of fundamental frequency (figure 4.1.9), it was quite interesting to see that there was no even harmonics though the other odd harmonics were quite prominent. Even at 73 Hz (figure 4.1.10) it was likely that the even harmonics were not present (the peak at around the position of 2nd harmonic (146 Hz) can not be accepted being close to the strong 3rd harmonic (150 Hz) of line frequency noise). It is further to be noticed that the case of 3 Hz (figure 4.1.4) at a sampling rate of 100 Hz was equivalent to the case of 37 Hz with sampling rate of 1 KHz (figure 4.1.9). But the striking thing is that though at 3 Hz even the 2nd, 4th and 6th of the even harmonics were present along with upto 11th of the odd harmonics, at 37 Hz there was no trace of any even harmonics although all the odd harmonics upto 11th harmonics were as prominent as in this case. There was, probably further indication that at higher frequencies the even harmonics might appear at lower current level (figures not given). However, the studies are not exhaustive and at lower amplitude there was line noise masking the actual signal. The reduction of even harmonics with increase of frequencies was probably beyond doubt and was a novel finding. This is important because the presence of strong even harmonics in this class of materials have been confirmed in magnetic measurements and have been attributed to the field dependence of

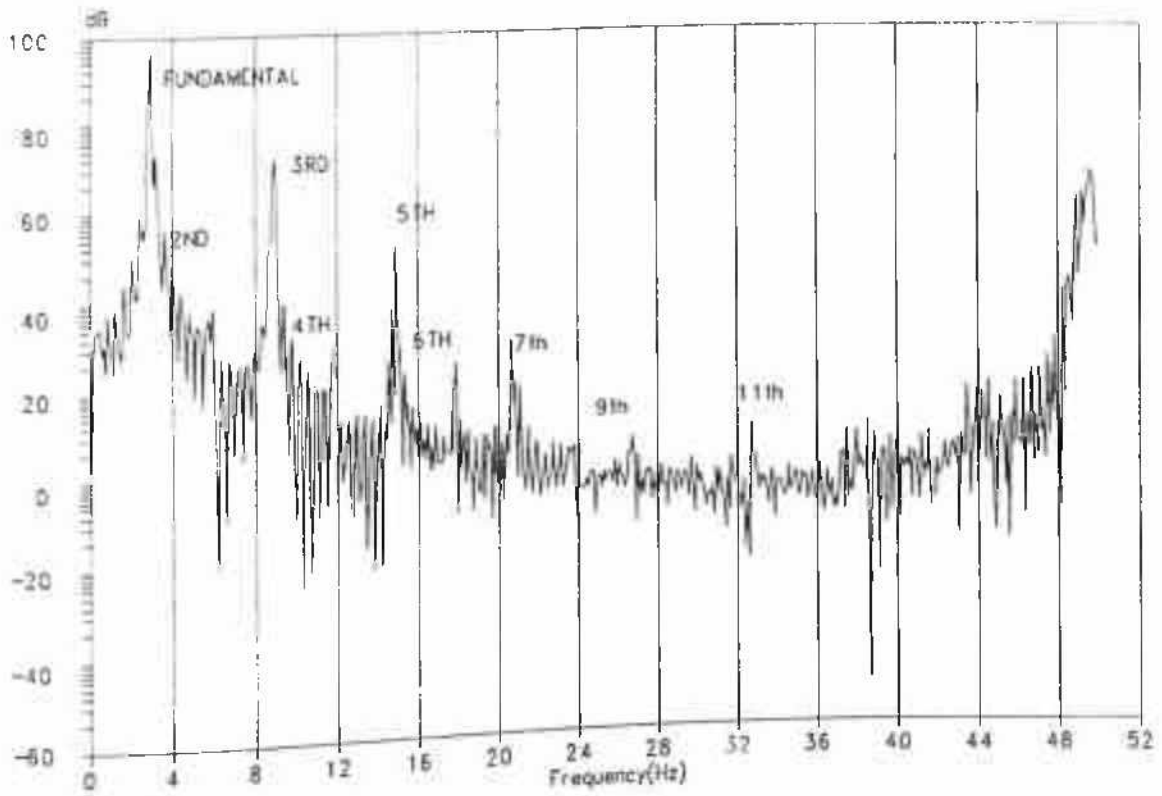


Figure 4.1.7: Power spectrum for frequency 3 Hz for a current level 3 times lower than that of figure 4.1.4.

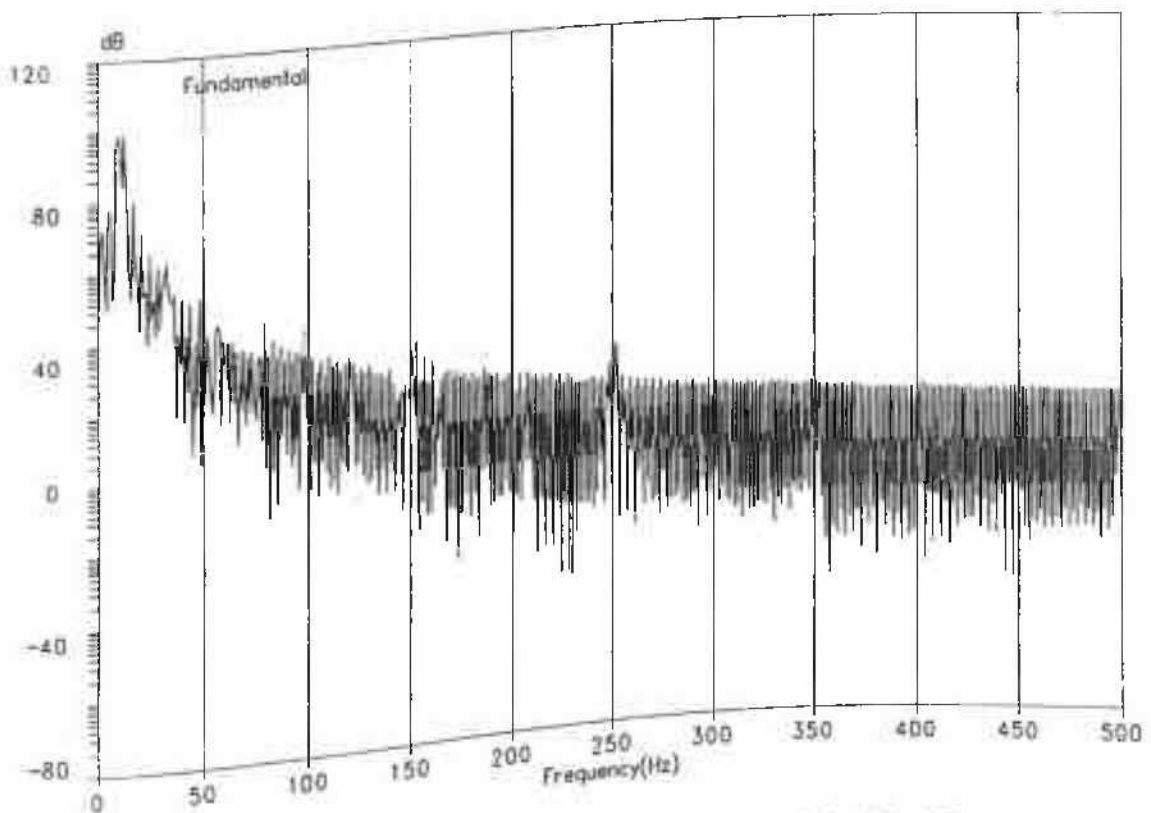


Figure 4.1.8: Power spectrum for frequency 11 Hz (Sampling rate 1000 Hz).

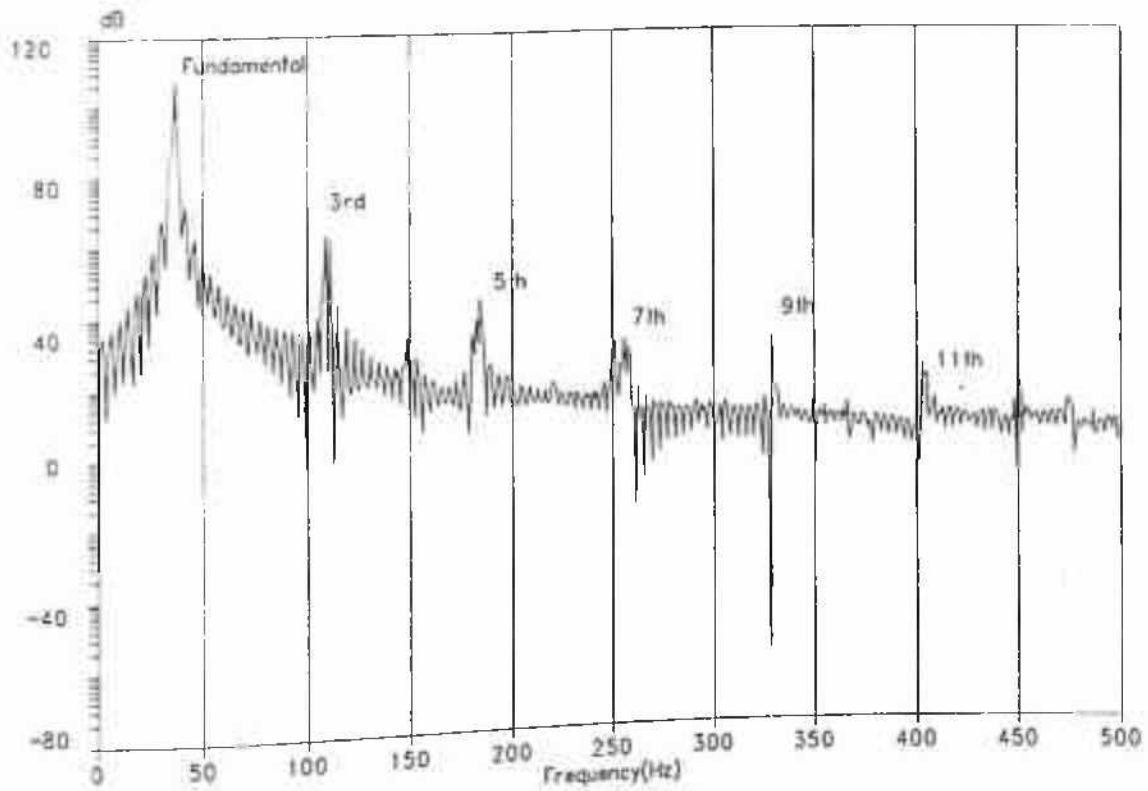


Figure 4.1.9: Power spectrum for frequency 37 Hz (sam ling rate 1000 Hz).

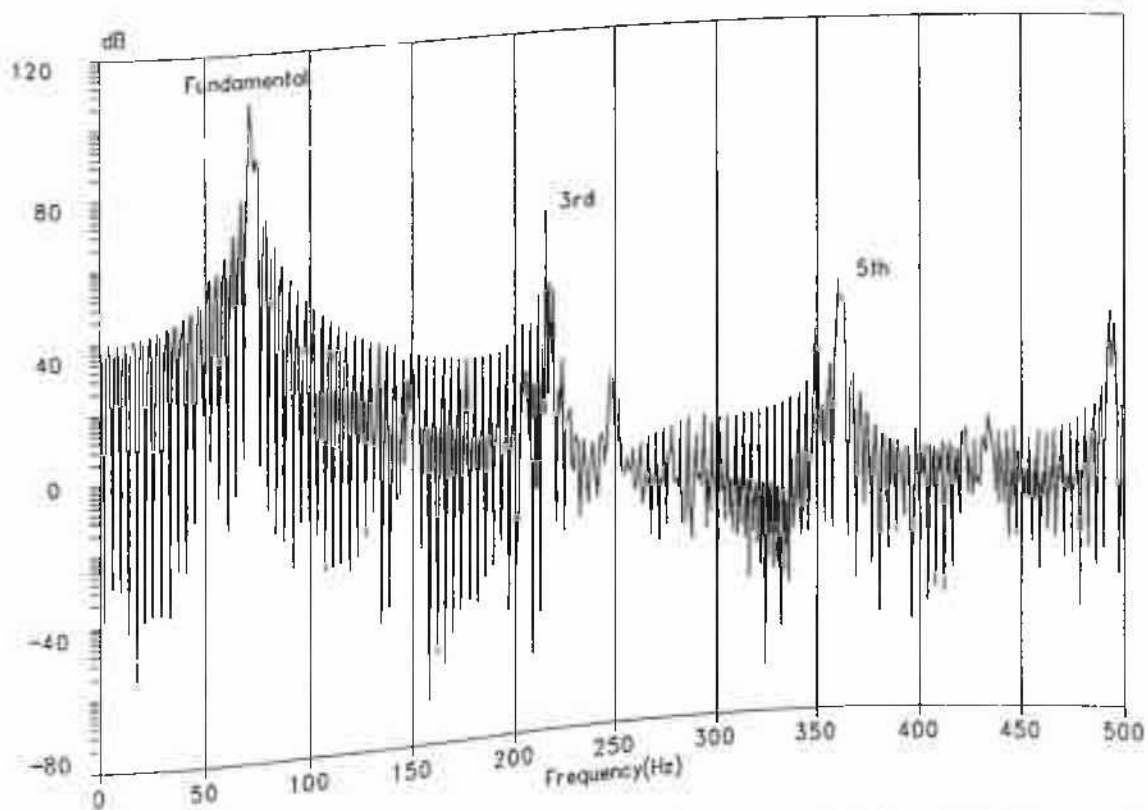


Figure 4.1.10: Power spectrum for frequency 73 Hz (Sampling rate 1000 Hz).

$J_c(H)$. In a Bean model there should be no even harmonics. The increase in the even harmonics at higher frequency with decrease of current level in these experiments, may be considered to justify this apparent contradiction as seen in magnetic measurements where even at a frequency of a few KHz non-zero 2nd (and other higher even harmonics) harmonics are seen with non-zero DC bias. Because in the magnetic experiments AC amplitudes are typically quite less (order of magnitude less) than what it was here. It may be remembered that if the current level is too high, probably the grain boundary contribution is not present and the grains being close to Bean type a reduction of 2nd harmonics can be expected. However, at lower frequencies but at same current level presence of 2nd harmonics may be indicative of the GB contribution which at higher frequencies may be absent because of "depinning of the weakly pinned Josephson vortices in the inter-granular regions by the higher frequency oscillation". However, it was a new finding and have to be further subjected to other possible tests before a possible explanation can be given.

4.1.2B.II). CURRENT-VOLTAGE CHARACTERISTICS:

It is now instructive to go through some further study in the line as above. In figure 4.1.11 the plots of I-V characteristics (in 4-probe) at room temperature for a sample with 10% Ag doped YBCO samples have been shown for different frequencies as indicated within the diagram. Here instead of plotting the real and imaginary parts separately, the magnitude of probe signal has been plotted as a function of the rms current. This result can be considered as a test of immunity of the measurement set-up to the inductive pick-up. In fact due to some technical limitations in this experiment, phase setting was not accurate (particularly at low frequencies) and so it was not possible to consider the in-phase and out-of-phase separately which could have given more information.

In figure 4.1.12 the same I-V characteristics as in the figure 4.1.11 for the same sample at 77 K have been shown for frequencies as indicated within the diagram. The linearity in the I-V as shown in figure 4.1.12 is quite obvious. As only the magnitude was being measured, it was not possible to define this as AC loss (because resistive component, i.e., the in-phase component represents the actual AC loss). However, the magnitude of the signal as considered here, was certainly composed of both the AC loss contribution and the out-of-phase component.

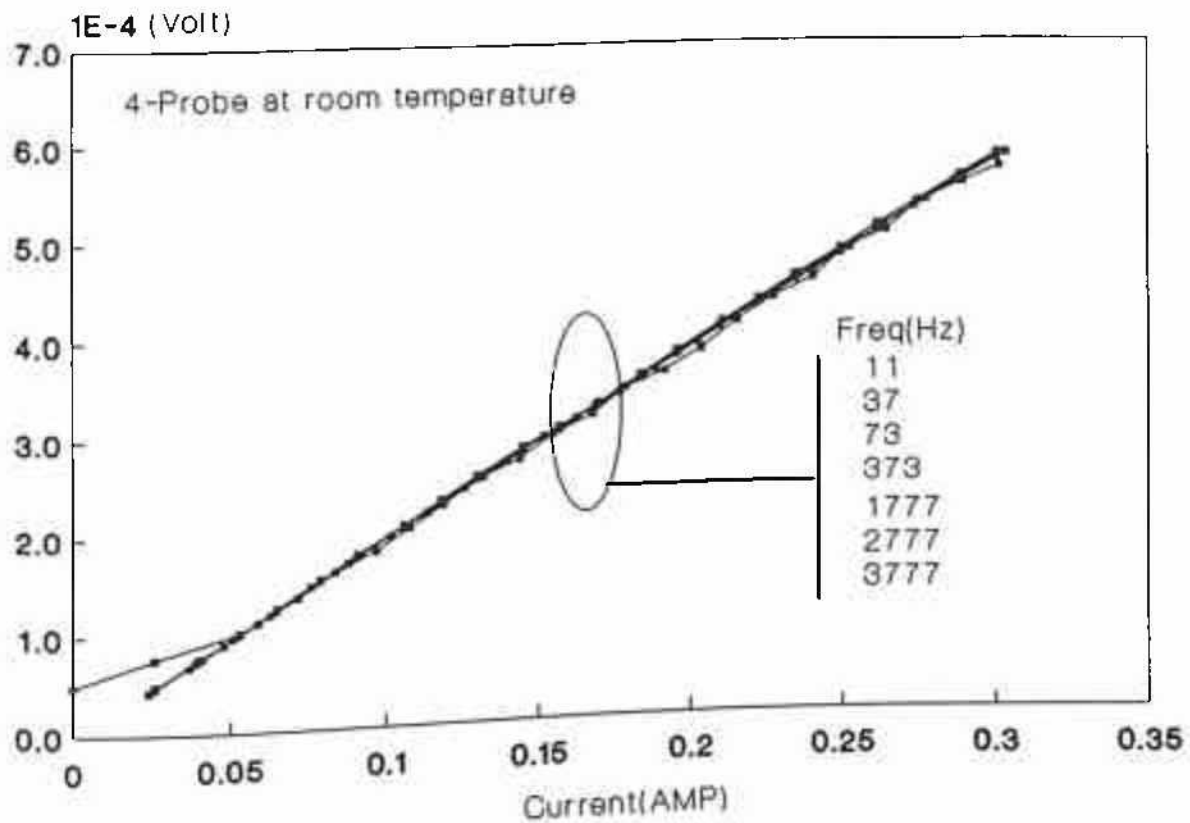


Figure 4.1.11: I-V's at different frequencies at room temperature for the sample (10% Ag doped YBCO) as in figure 4.1.1.

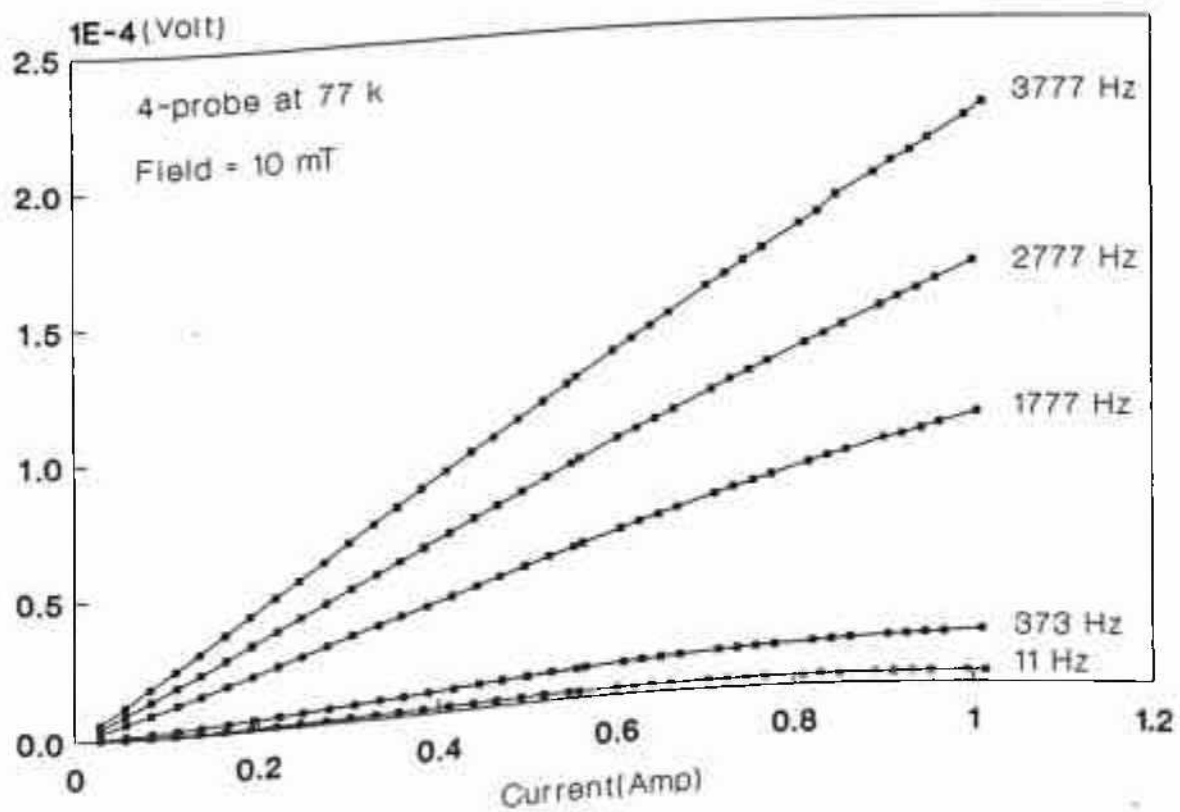


Figure 4.1.12: I-V's at 77 K for the sample as in figure 4.1.11.

Linearity in the I-V in case of AC current can be visualized in different situations: i). the reversible oscillations of flux lines in the low amplitude and so low current case ($J \ll J_c$)[19,20] as described by eqn. 4.1.2, ii) as a follow up from eqn. 4.1.6, iii). the TAFF in the low current case as a generalization from the DC case[35] and iv). the extreme flux flow case as in the case of DC I-V[35]. In figure 4.1.14 the plot of resistance at 10 mT as a function of frequency has been included. The striking feature was the linearity of resistance with frequency at all DC bias field upto 100 mT. Assuming the current density to be quite less than the critical value, the linear frequency dependence can be expected from both eqn. 4.1.2 and 4.1.6. As the phase resolution in this experimental arrangement was poor and so only magnitude was considered it was difficult to distinguish between the actual physical situation involved. Eqns. 4.1.3 and 4.1.4 are not appropriate, the I-V characteristics being non-linear. Further, in the eqn. 4.1.6 perfect linear dependence on frequency is expected when there is no flux flow ($f=0$). However, this is, most likely, not the actual case for HTSC material and one should expect at 77 K a finite flux flow to be present. Further though the frequency was quite low, still there is some obvious decrease in the effective pinning strength (eqn. 4.1.6) because of the increase in $\eta\omega$. It is probably true to say that there is **certainly** some flux flow. Because from eqn. 4.1.6, in case there is no flux flow one can normalize the I-V (i.e., plot V/ω vs. I) with respect to frequency and all the I-V's will superimpose. **But in the presence of flux flow contribution this normalization was not possible. In fact the normalization in the case of the data presented here did not superimposes all the curves. This clearly indicates that there was some contribution from flux flow.** This can further be substantiated by noting that in the Josephson medium (i.e., granular system) as Portis et al. have argued, the hypervortices or the Josephson vortices are subject to few order of higher flux flow[40] than the Abrikosov vortices within the grains. With this in view, the proposition of possibility of enhanced depinning of the Josephson vortices due to high amplitude oscillation may be a possible explanation. It is a plausible proposition remembering the fact that the Josephson vortices are weakly pinned and hence the transport J_c is quite low. But without further measurements and proper phase resolution of in- and out-of-phase components it is difficult to explain this confusing situation of AC I-V (i.e., $V(I)$ as well as $R(\omega)$ are linear). In fact, this situation is further complicated by already published data of Zannella et al.[42] on AC loss measurements where it is shown that the resistive component (AC

loss) is proportional to square of AC amplitude (in hysteretic situation AC loss is proportional to cube of amplitude of AC current[1,3]) and also linearly dependent on frequency. As argued by Zannella et al., the amplitude dependence is ambiguous where as the frequency dependence of AC loss, probably indicates the loss mechanism to be hysteretic.

In order to have a further look in to this complicated problem, in figure 4.1.13 the plot of I-V's at two different DC bias fields and different frequencies have been plotted. It is seen from this figure that at all frequencies I-V's at th higher field were above those at lower field for a given frequency. However, at higher frequencies field dependence was more. This increase of voltage with magnetic field at all frequencies can be justified on the basis of eqn. 4.1.2 and 4.1.6. In case of eqn. 4.1.6 field dependence will come if there is flux flow because if $f=0$ (in eqn. 4.1.6) there is no B dependent term. Thus these results were probably indicative of the fact that in HTSC there was finite flux flow at 77 K. This view will further be strengthened in the next few paragraphs where some data on the irreversibility of magneto-resistance will be discussed. This will probably show that there is a large contribution from flux flow regime which is present along with some irreversible contribution. It will be wise to consider that this flux flow contribution is actually due to flow of Josephson vortices while the irreversible contribution comes from the irreversibility of the intragranular Abrikosov vortices in the stronger intragranular pinning potential. As this results will be seriously dealt with, it is important to have a further description of the actual experimental situation in this measurements before going into actual data.

4.1.2B.III) IRREVERSIBILITY OF MAGNETO-RESISTANCE.

An AC current (for different frequencies) was passed through the sample and kept constant, while the DC magnetic field (perpendicular to the AC current direction) was ramped between $+H_{max}$ and the magnitude of the voltage across the voltage probes was dynamically monitored. So if this plot of the sample voltage as a function of DC bias field would give raise to some loops, it would indicate possible irreversibility present in the system. The loops, as described above, of magnitude of sample signal as a function of DC bias field for different frequencies have been plotted in figure 4.1.15 after making zero-offset (at point of lowest DC bias) and this zero-offset values as a function of frequency have been plotted in figure 4.1.16.

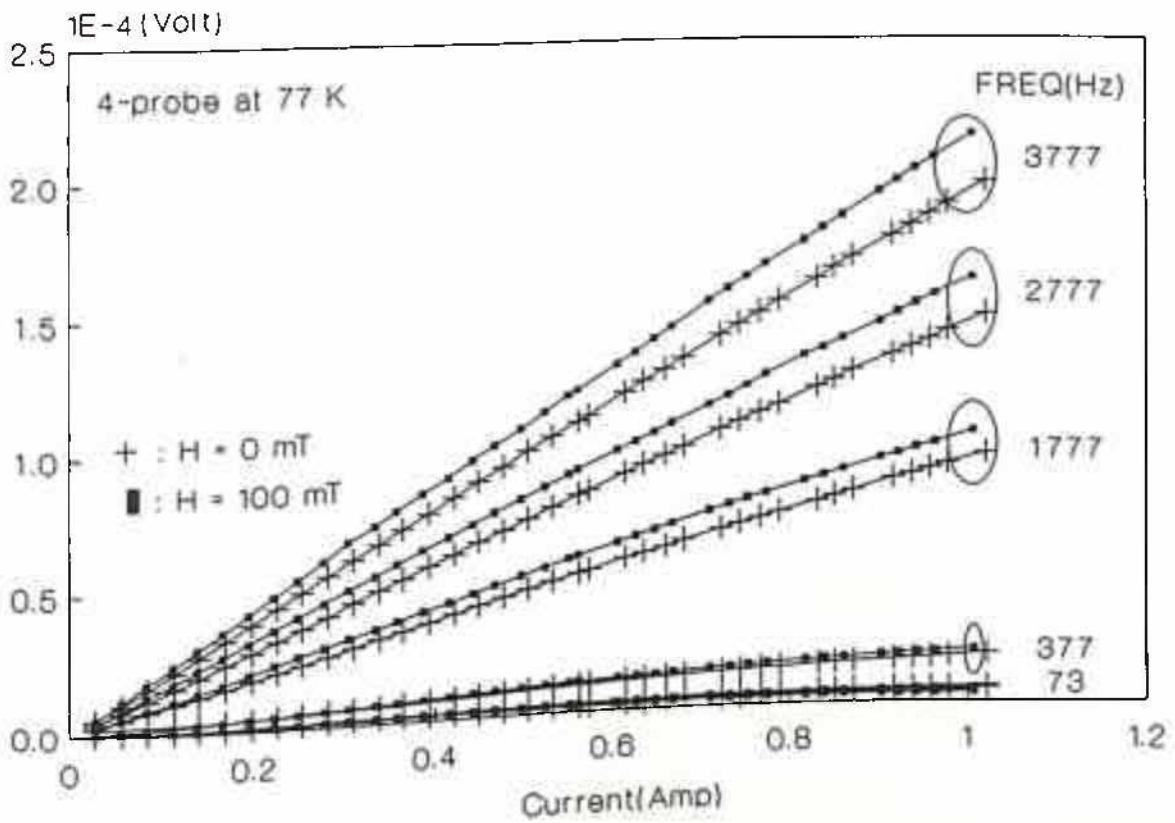


Figure 4.1.13: I-V's at different frequencies at 77 K for two different DC fields. (Sample same as in figure 4.1.11)

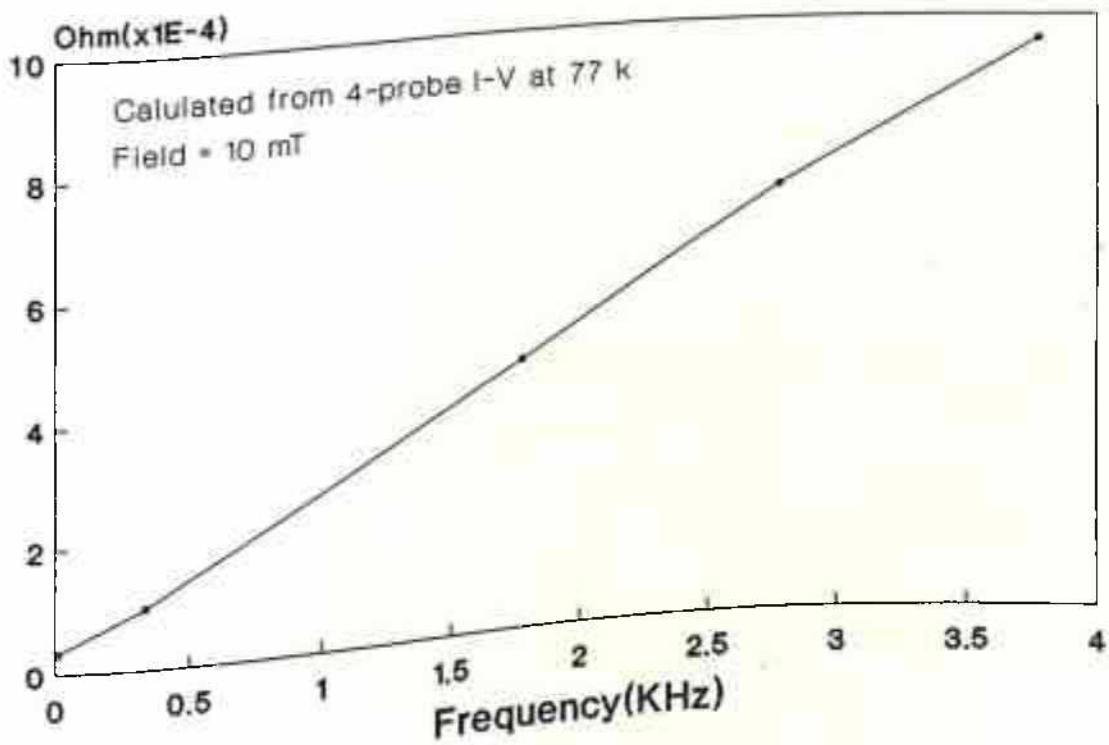


Figure 4.1.14: Resistance (V/I) as a function frequency (Calculated from figure 4.1.12).

The sample in question was the same one as described in the I-V studies above. It is clear from figure 4.1.16 that the offset values were linearly dependent on the frequency. Thus by comparing figure 4.1.16 with figure 4.1.14 it is possible to suggest that they relate to the same phenomenon. However, the result in figure 4.1.16 was for the same sample (as in figure 4.1.14) but after a few days (causing ageing of the sample and hence possible deterioration of J_c) an increase in the magneto-resistance was seen in this case. One more important point to be noted in figure 4.1.15 is that the total change in magnitude of magneto-resistance due to DC bias field excursion was a few orders of magnitude less than the offset values particularly at higher frequencies (the lowest curve in figure 4.1.15). This has created considerable difficulties in studying the irreversibility at higher frequencies.

The inference that one can have from these observations is that there are certainly two different contributions (for the sample considered here) to the magneto-resistance - i). the flux flow part (giving rise to the offset) which shows no irreversibility with respect to the DC bias field and but has a linear dependence on frequency and ii). the irreversible contribution which shows strong irreversibility as a function of DC bias field. This novel finding is being reported for the first time.

For the sample considered here, the irreversibility loops at low frequencies (e.g. 11 Hz and 37 Hz) were quite different from the expected one, on the basis of irreversibility of $J_c(H)$ as reported by different workers[50-53]. Though the loops at 11 Hz and 37 Hz were qualitatively same, in the later case loop area was considerably smaller than that at 11 Hz. As a general argument, one can extend this finding to infer that at 37 Hz irreversibility was considerably less than that at 11 Hz. Probably this can be considered to be true even for higher frequencies. However, at higher frequencies flux flow component, i.e., zero-offset became considerably higher than the total change in signal over the excursion of the bias field leading to lower sensitivity in resolving this irreversible contribution. In fact it was felt that a proper phase setting to differentiate the in- and out-of-phase components and the study of this irreversibility of the individual components would yield better results enlightening the complex situation.

The extreme care in preparing sample along with co-sintered silver contacts and other necessary precautions required in this experiment posed a serious problem in doing this studies on large number of samples. However, it was possible to study some other batches (having no

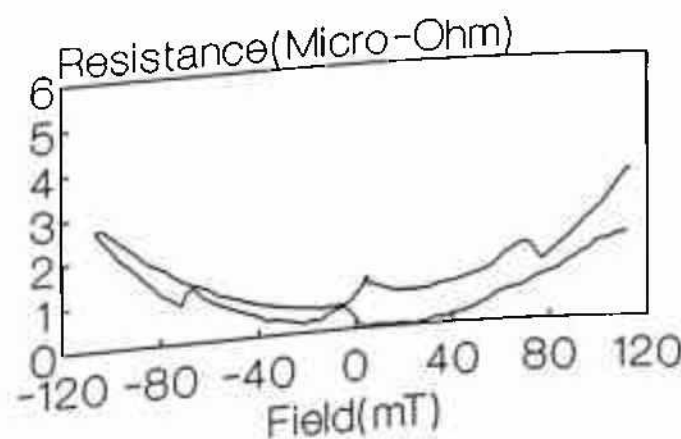
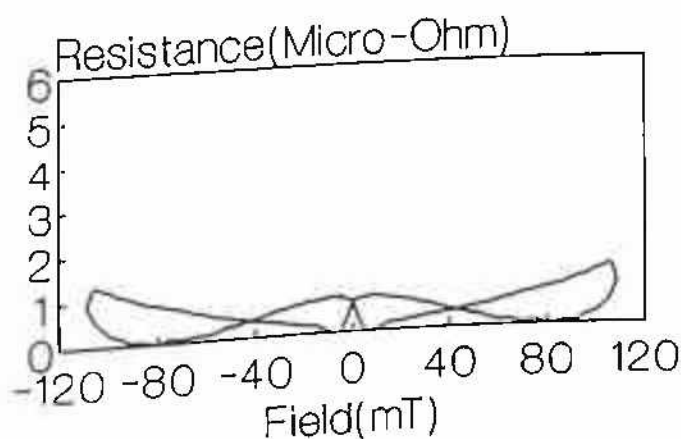
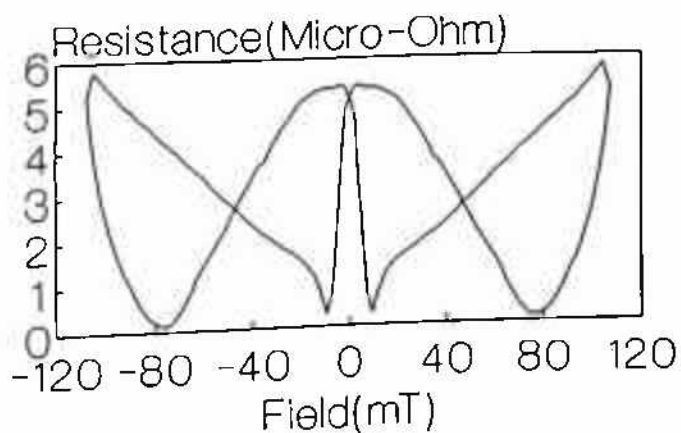


Figure 4.1.15: Irreversibility loops of the magneto-resistance.
 (Frequencies from top to bottom : 11, 37, 1117 Hz)

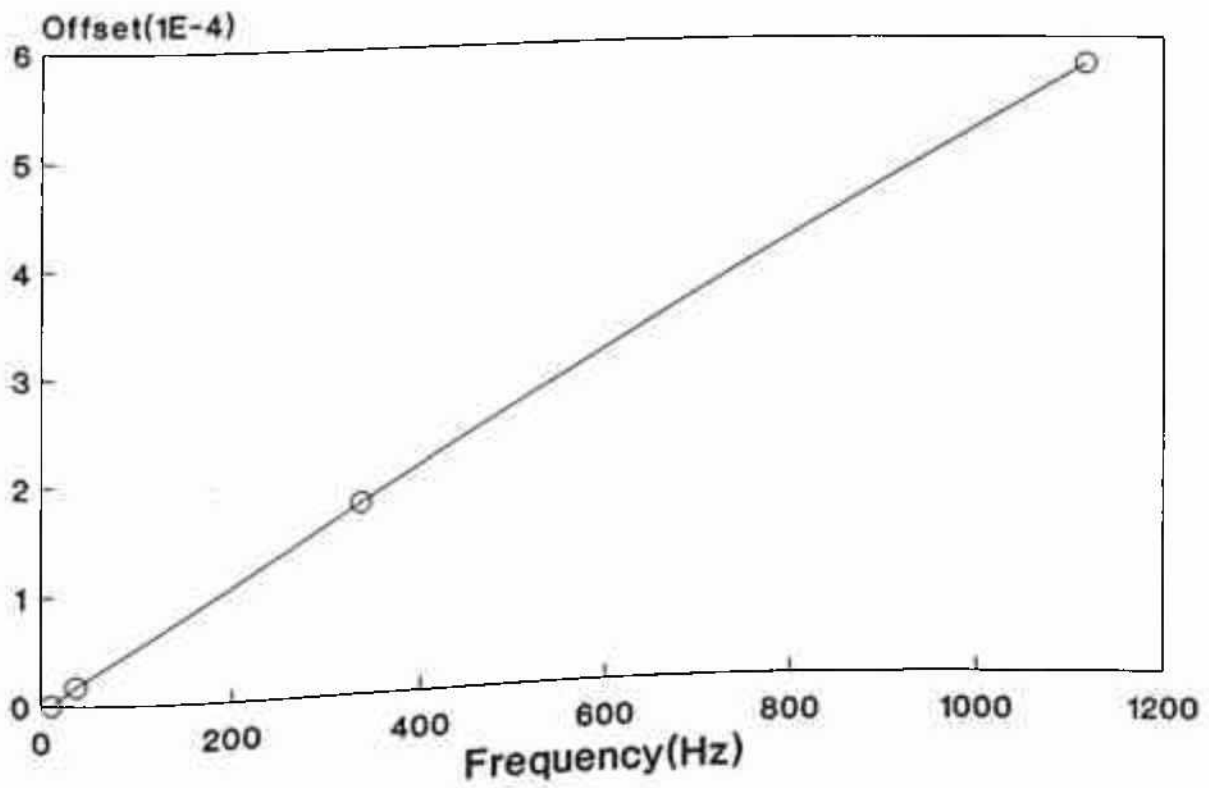


Figure 4.1.16: Offsets of figure 4.1.15 as a function of frequency.

silver additives - this sample is the same as the one considered in the FFT study) which offers a comparative study and a better realization of the process involved. In figure 4.1.17 irreversibility loops of the magnitude of sample signal with respect to the DC bias field have been given for different frequencies. These curves were also offsetted and the offsets as a function of frequency have been plotted in figure 4.1.18. These offsets, unlike the earlier sample showed negligible dependence on the frequency (figure 4.1.18). Further the loops were justified on basis of irreversibility of $J_c(H)$ (as reported by many workers) and were apparently independent of frequencies. This is a striking contradiction to the earlier case where strong dependence on the frequency have already been described. It is unfortunate that the I-V characteristic of this material has not been studied, making it difficult to have definite conclusions. However, from the apparent independence of the offsets on the frequency in this case clearly indicated that the flux flow loss contribution was dominating. This is further true because when $k = 0$ (i.e., pinning negligible) in eqn. 4.1.6 flux flow contribution become independent of the frequency. Because the sample was not a silver doped one, one can expect a poor J_c [44-48] and hence smaller k values. Further the magneto-resistance had a stronger field dependence as seen in figure 4.1.17 for the pure YBCO sample as compared to the silver doped one. Though it is difficult to convert the field dependence of magneto-resistance into $J_c(H)$, it is beyond question that the higher magneto-resistance must be indicative of lower J_c and vice versa. Also the offset values were order of magnitude higher in the pure sample (figure 4.1.18) than in the silver doped sample (figure 4.1.16) indicating larger flux flow in pure sample.

It is important to investigate the same irreversibility in case of 3-probe measurements which is supposed to be property of the contacts. In figure 4.1.19 and 4.1.20 the irreversibility loops of magneto-resistance for 3-probe have been included. In figure 4.1.19 the sample was the same as the one in figure 4.1.15 and in figure 4.1.20 sample was same as the one in figure 4.1.17. In the both cases the loops were offsetted. In the silver doped sample this offset had a small frequency dependence while in the other case (pure sample) offsets were almost frequency independent. The striking feature in these figures (figures 4.1.19 and 4.1.20) are that the shapes of the loops in both the cases were qualitatively the same (in 4-probe case, in figures 4.1.15 and 4.1.16 the two samples showed quite different nature). In figure 4.1.19 the DC loop have also been included - which also had same shape as the other to loops at different frequencies.

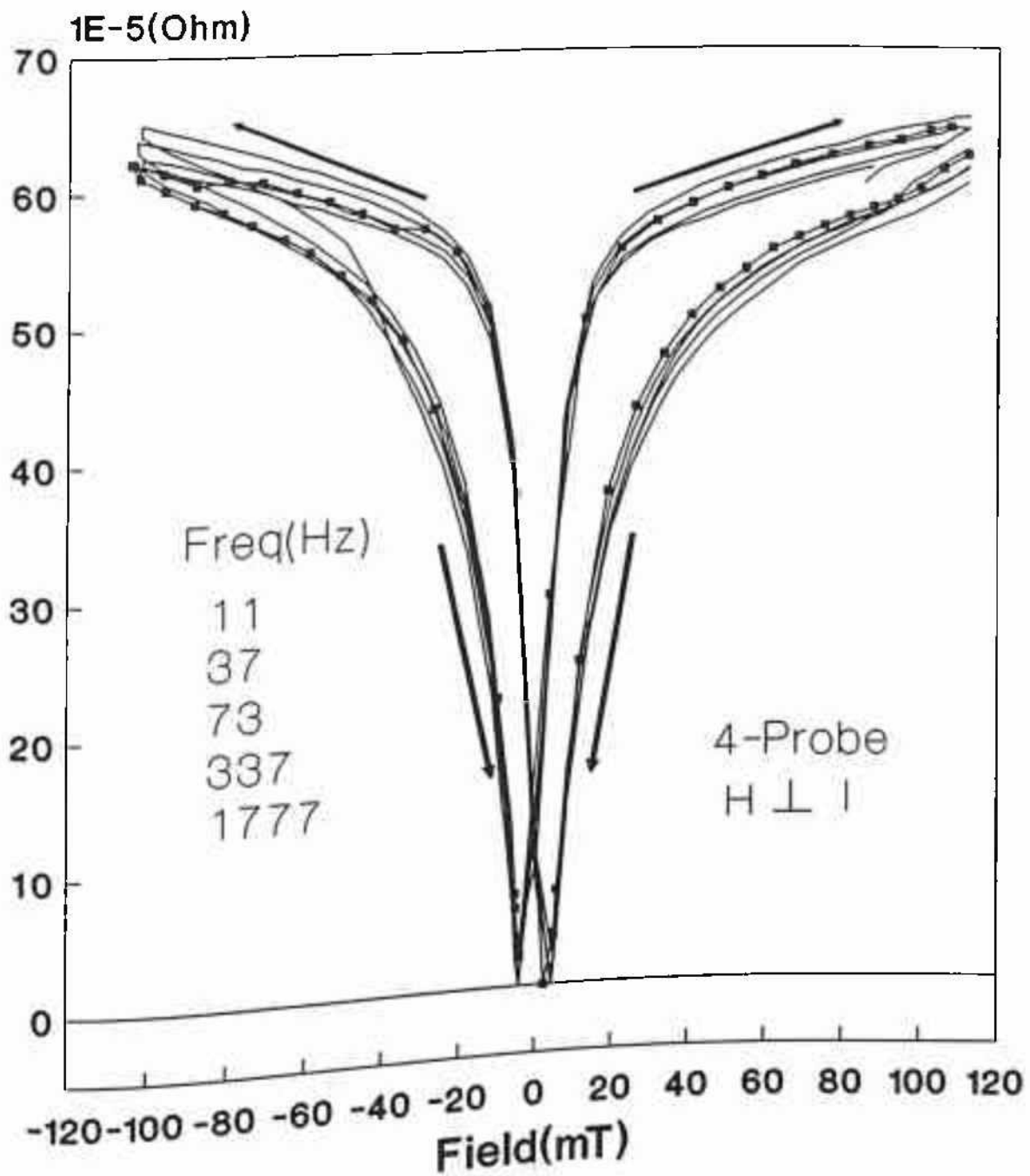


Figure 4.1.17: Irreversibility loops of the magneto-resistance. (Pure YBCO sample)

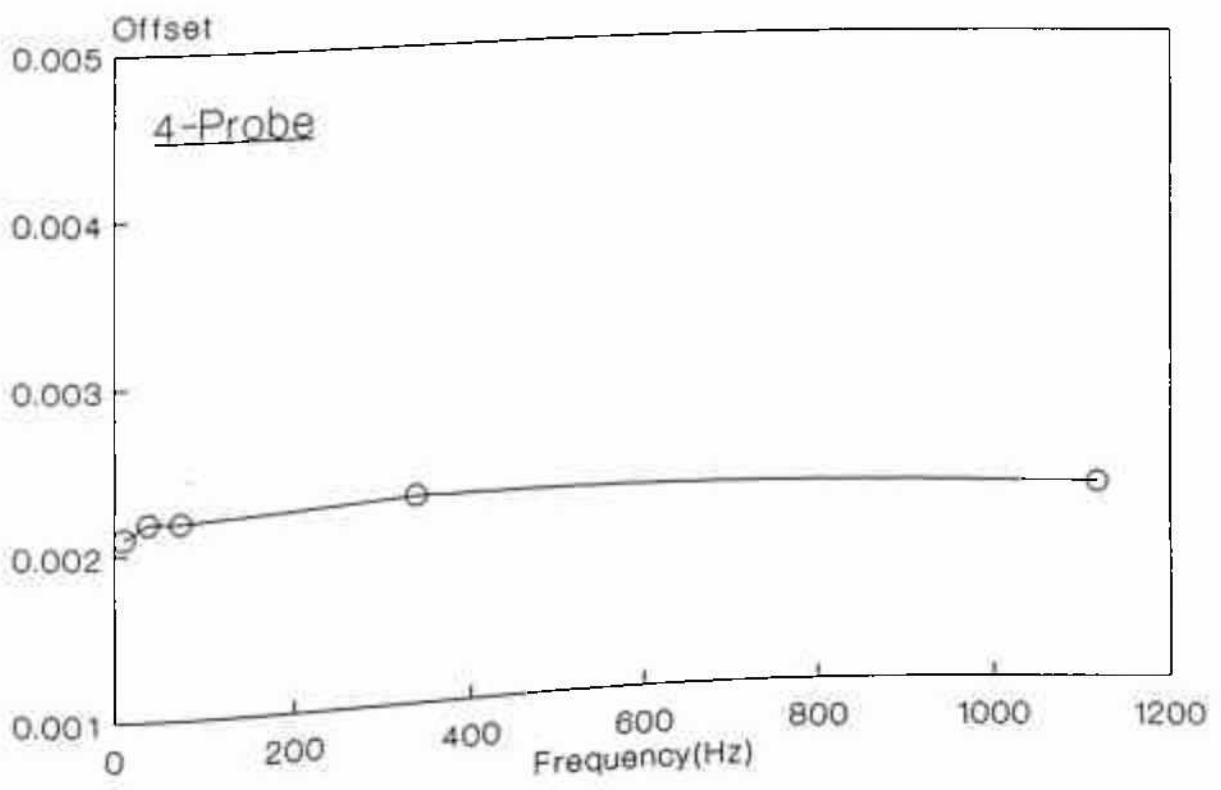


Figure 4.1.18: Offsets of figure 4.1.17 as a function of frequency.

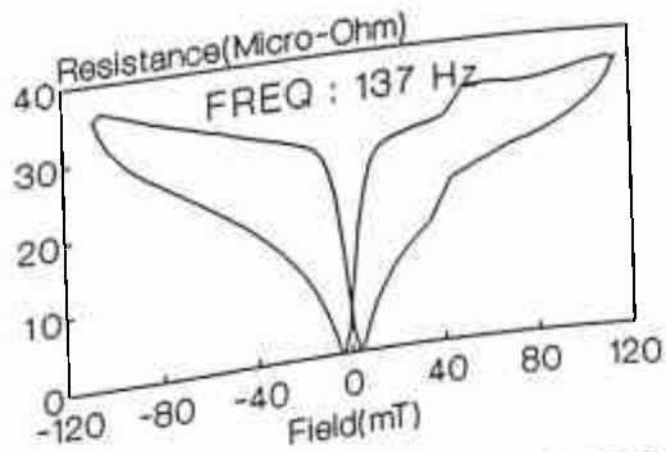
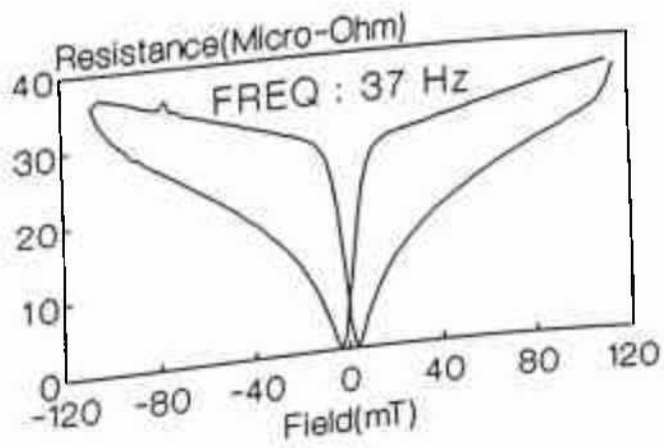
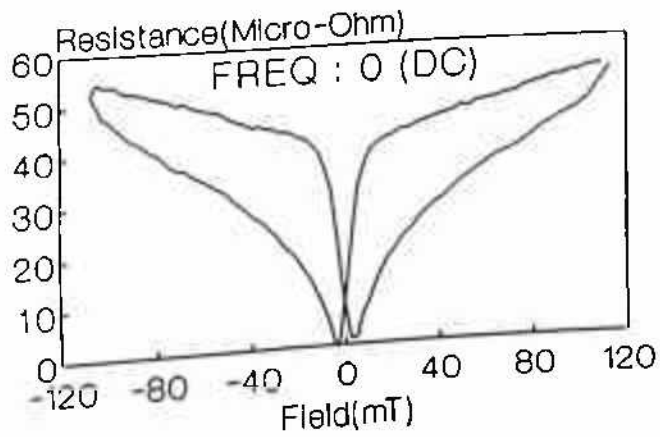


Figure 4.1.19: Irreversibility loops of the contact resistance (Silver doped sample).

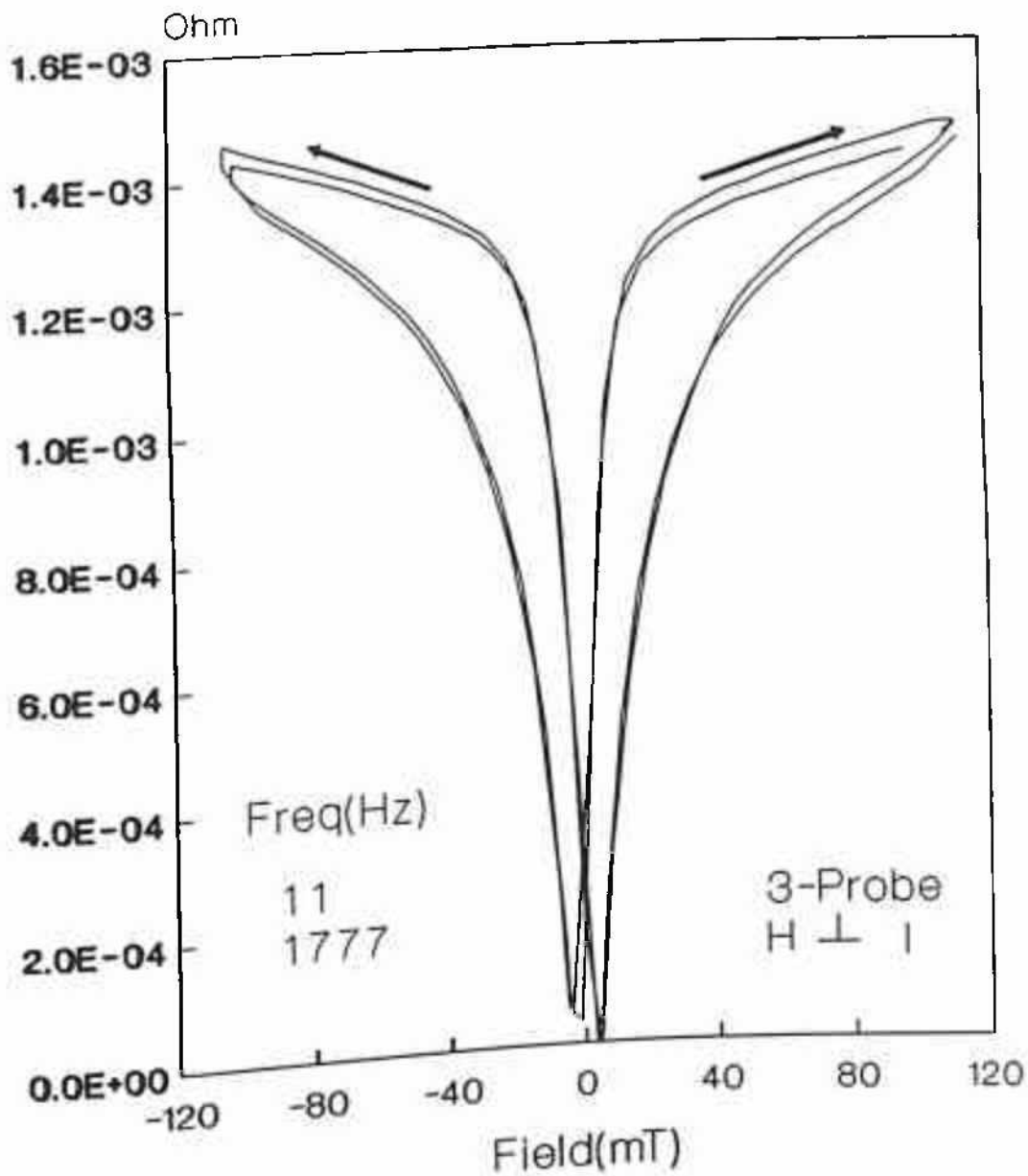


Figure 4.1.20: Irreversibility loops of the contact resistance (Pure YBCO sample).

One must note the higher (order of magnitude) magnitude in the 3-probe data as compared to corresponding 4-probe loops. Further in the silver doped sample (figure 4.1.15 and figure 4.1.19) the 3-probe loops were quite different from the corresponding 4-probe loops. This clearly indicates that the 3-probe loops were not dominated by the bulk contribution. For the pure sample, while the shapes of the loops were same in both the cases (i.e., 4-probe and 3-probe), the 3-probe loops indicated almost 2 orders of higher variation in than the corresponding 4-probe loops. This in all probability supports the fact that the 3-probe resistance was dominated by the corresponding "weak-link-like" behavior of the contact between the metal and the superconductor. The magnetic properties of the contact had been studied in detail and has already been published[49].

4.1.3 SUM UP:

Though the study is a preliminary one and there is not much data available still some conclusions can be arrived at;

1. FFT:

- * A study of frequency response and harmonics analysis showed presence of even and odd harmonics at low frequencies (≤ 11 Hz).
- * At higher frequencies for same current level as above, even harmonics were not seen.
- * With decrease of level of excitation, even harmonics were likely to reappear.

2. AC I-V:

- * Linear I-V characteristics were seen at all frequency at all DC bias field.
- * Resistance as calculated from I-V showed almost linear behavior with respect to frequency.

3. Irreversibility in magneto-resistance:

- * Peculiar irreversibility of magneto-resistance with respect to DC

bias field was observed in silver doped sample. This irreversibility of magneto-resistance can not be explained on the basis of standard $J_c(H)$ irreversibility as reported by Evettes et al.[50].

- * In case of pure YBCO sample irreversibility of magneto-resistance was as expected on the basis of the irreversibility of $J_c(H)$ as reported by Evettes et al.[50].
- * In silver doped sample the offsets of these irreversibility curves showed linear dependence on frequency.
- * In pure sample the same offsets show very less dependence on frequency.

Irreversibility in contact resistance:

- * Contact magneto-resistance measured by 3-probe also showed strong irreversibility and the shape of the loops was same for different samples.
- * The irreversibility in the three probe resistance as a function DC bias field, can not be attributed to the bulk contribution but to the presence "weak-link-like" behavior at the metal-superconductor interfaces.

REFERENCES:

- [1] A.M. Campbell and J.E. Evettes 1972 *Adv. Phys.* pp-294
- [2] P.H. Melville *Adv. Phys.* 647
- [3] J.E. Evettes 1992 *Coincise Encyclopedia of*
- [4] T. Matsushita, N. Harada, K. Yamafuji and M. Noda 1989 *J. JI. Appl. Phys.* **28**, 356
- [5] H. Tateishi and T. Onishi 1985 *Proc. Int. Symp. on Flux Pinning and Electromagnetic Properties in Superconductors.* p 259
- [6] F. Sumiyoshi, M. Matsuyama, M. Noda, T. Matsushita, K. Funaki, M. Iwakuma and K. Yamafuji 1986 *Jpn. J. Appl. Phys.* **25**, L148
- [7] R.B. Stephens 1992 *IEEE Trans. Appl. Supercond.* **2**, 122
- [8] S.A. Boggs, E.W. Collings and M. V. Parish 1992 *IEEE Trans. Appl. Supercond.* **2**, 122
- [9] S. Lofland, M.X. Huang and S.M. Bhagat 1992 *Physica C* **203**, 271
- [10] J. Rhyner 1993 *Physica C* **212**, 292
- [11] P. de Gennes and J. Matricon *Rev. Mod. Phys.* 1964 **36**, 45
- [12] A.T. Fiory and B. Serin 1967 *Phys. Lett.* **25A**, 557
- [13] J.A. Cape and I.F. Silvera 1968 *Phys. Rev. Lett.* **20**, 326
- [14] J.L. Zar 1964 *J. Appl. Phys.* **35**, 1610
- [15] K. Yamafuji, N. Sakamoto and T. Kawashima 1971 *Phys. Lett.* **36A**, 341
- [16] P.H. Melville 1971 *J. Phys. C: Solid St. Phys.* **4**, 2833
- [17] P.H. Melville 1972 *Phys. Lett.* **39A**, 373
- [18] A.M. Campbell 1971 *J. Phys. C* **4**, 3186
- [19] J. Lowell 1972 *J. Phys. F.: Metal Phys.* **2**, 547
- [20] J. Lowell 1972 *J. Phys. F.: Metal Phys.* **2**, 559
- [21] J. Lowell 1970 *J. Phys. C.: Solid State Phys.* **3**, 713
- [22] E.B. Sonin and A.K. Tagantev. 1989 *Sov. Phys. JETP* **68**, 572
- [23] R. Marcon, R. Fastampa, M. Giura and E. Silva 1991 *Phys. Rev. B* **43**, 2943

- [24] B. Rosenblum, M. Cardona and G. Fischer 1964] *RCA Rev.* **25**, 491
- [25] J.I. Gittleman and B. Rosenblum 1966 *Phys. Rev. Lett.* **16**, 734
- [26] J.I. Gittleman and B. Rosenblum 1968 *J. Appl. Phys.* **39**, 2617
- [27] M. Ban, T. Ichiguchi and Toshiyuki Onogi 1989 *Phys. Rev. B* **40**, 4419
- [28] P.C.E. Stamp, L. Forro and C. Ayache 1988 *Phys. Rev. B* **38**, 2847
- [29] M. Sugahara, M. Kojima, N. Yoshikawa, T. Akeyoshi and N. Haneji 1987 *Phys. Lett. A* **125**, 429
- [30] T. Onogi, T. Ichiguchi and T. Aida 1989 *Solid State Comm.* **69**, 991
- [31] S. Martin, A.T. Fiory, R.M. Fleming, G.P. Espinosa and A.C. Cooper 1988 *Phys. Rev. Lett.* **62**, 677
- [32] P.J. King, A. Kirk, J.S. Lees, K.A. Benedict, W.B. Roys, Y. Hioki and S. Iwama 1992 *Phase Transitions* **38**, 115
- [33] N.C. Yeh and C.C. Tsuei 1989 *Phys. Rev. B* **39**, 9708
- [34] E.H.Brandt 1992 *Physica C* **195**, 1
- [35] E.H. Brandt 1991 *Journal of Mod. Phys.* **B5**, 751
- [36] E.H. Brandt 1990 *Z. Phys. B (Cond. Matt)* **80**, 167
- [37] E.H. Brandt 1992 *Supercond. Sci. Technol.* **5**, S25
- [38] P.W. Anderson 1962 *Phys. Rev. Lett.* **9**, 309
- [39] Tinkham book
- [40] A.M. Portis and K. W. Blazey 1988 *Solid State Comm.* **68**, 1099
- [41] A.M. Portis, K.W. Blazey, K.A. Müller and J.G. Bednorze 1988 *EuroPhys Lett.* **5**, 467
- [42] S. Zannella, J. Tenbrink, K. Heine, V. Ottoboni, A. Ricca and G. Ripamonti 1990 *Appl. Phys. Lett.* **57**, 192
- [43] S. Zannella, L. Jansak, M. Majoros, V. Selvamanickam and K. Salama 1993 *Physica C* **205** 14
- [44] B. Souletie, M. Guillot, P. Lejay and J.L. Tholence 1991 *Solid State Comm.* **78**, 717
- [45] G. Kolowski, I. Maartense, R. Spyker R. Leese and C.E. Oberly 1991 *Physica C* **173**, 195
- [46] M. Itoh, H. Ishigaki, T. Ohyama, T. Minemoto H. Nojiri and M. Motokawa 1991 *J. Mater. Res.* **6**, 2272

- [47] T. Oka, Y. Itoh, Y. Yanagi, H. Tanaka, S. Takashima, Y. Yamada and U. Mizutani 1992 *Physica C* **200**, 55
- [48] J.A. Xia, H.T. Ren, Y. Zhao, C. Andrikidis, P.R. Munroe, H.K. Liu and S.X. Dou 1993 *Physica C* **215**, 152
- [49] S. Saha, R.B. Tripathy and B.K. Das 1992 *Supercond. Sci. Technol.* **5**, 703
- [50] J.E. Evettes and B.A. Glowacki 1988 *Cryogenics* **28**, 641
- [51] K.-H. Müller and D.N. Mathews *Physica C* 1993 **206**, 275
- [52] A.I. D'yachenko 1993 *Physica C* **213**, 176
- [53] W.F. Huang, K.J. Hung and J.G. Shen 1993 *Physica C* **208**, 7

EXPERIMENTAL DATA

HYSTERESIS IN COMPLEX AC SUSCEPTIBILITY WHEN THE AC AND THE DC FIELDS ARE CO-AXIAL

This part contains the data on the field dependence of the χ' and χ'' for different frequencies as well as amplitudes of AC excitation field when the two fields are coaxial. Study on the hysteresis in the χ' and χ'' with respect to DC field has been carried out in details. Effect of frequency and amplitude on the hysteresis loops has been studied.

4.2.1. REVIEW	196
4.2.2. EXPERIMENTAL RESULTS AND DISCUSSIONS	196
A. RANGE EFFECT OF DC BIAS FIELD	196
B. AMPLITUDE DEPENDENCE OF THE $\chi'(H)$ AND $\chi''(H)$ LOOPS	207
C. FREQUENCY DEPENDENCE OF THE $\chi'(H)$ AND $\chi''(H)$ LOOPS	220
4.1.3. SUM UP	241
REFERENCE	243

4.2. HYSTERESIS IN COMPLEX AC SUSCEPTIBILITY WHEN THE AC AND THE DC FIELDS ARE CO-AXIAL:

4.2.1. REVIEW:

Study of AC susceptibility as a function of DC bias field has been undertaken in order to have an insight into the magnetic behavior of granular HTSC. In the Chapter 3, a model calculation has been presented which has been successful, at least qualitatively, in explaining the already published data obtained by different workers. However most of the published data are in the low range of the DC bias field and are not exhaustive and the model predicts more curious results which are to be verified. With this in view, a detailed experimental study of AC susceptibility as a function DC field for YBCO samples was undertaken. In this section the co-axial configuration of the AC and the DC fields will be considered.

4.2.2. EXPERIMENTAL RESULTS AND DISCUSSIONS:

It has already been mentioned in the Chapter 2, that the DC field co-axial to the AC field was generated by a solenoid and that the maximum DC field that could be achieved was 20 mT only. The range of frequency in these experiments was 11 Hz to 97 KHz. However, because of noise, at lower amplitudes low frequencies had to be avoided in most of the cases.

4.2.2A. RANGE EFFECT OF DC BIAS FIELD:

In figure 4.2.1(a,b) the real(χ') and imaginary(χ'') parts of AC susceptibility as a function of DC bias field have been plotted for pure YBCO sample(A1). The amplitude of AC excitation was 0.3 mT, the highest amplitude employed in this work. In interpreting these results it has to be remembered that the measurements were in arbitrary units and that the individual curves were arbitrarily zero offsetted at the highest DC bias field of excursions. Because of the relative measurements, it was not always possible to compare the graphs for different parameters directly. However, in a given frame (diagram) all the curves were plotted in same scale and can be compared for the shape change for different parameters, e.g. range of DC bias field, amplitude and frequency of AC excitation etc.

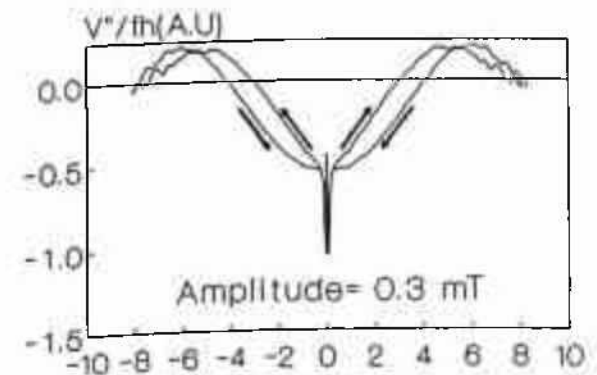
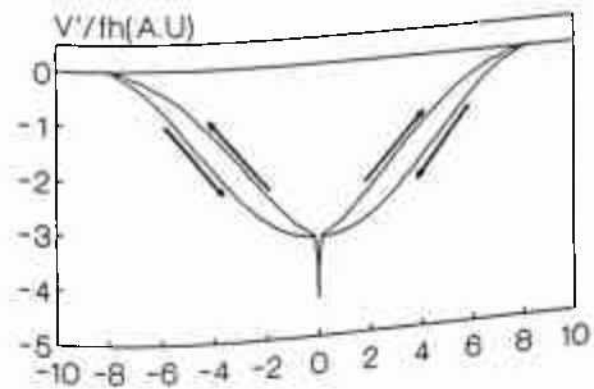
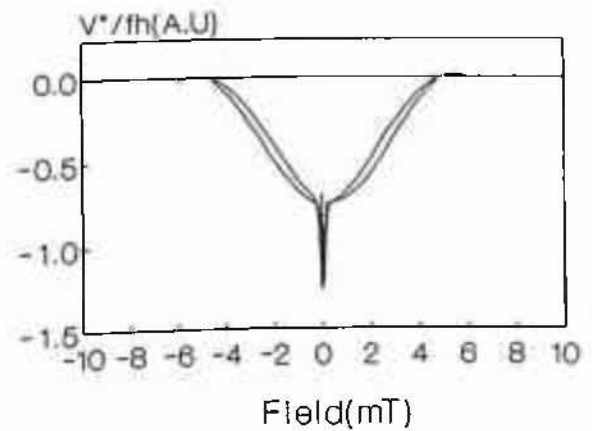
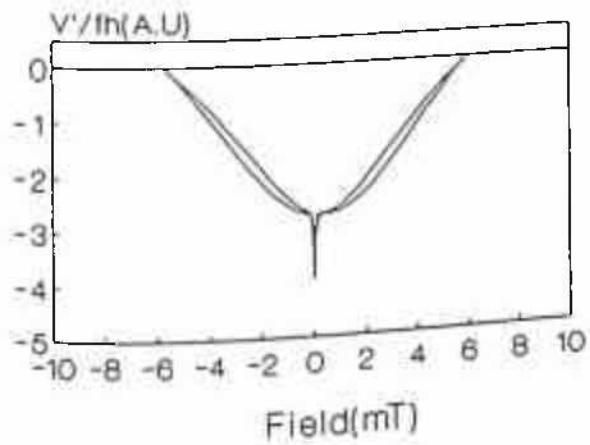
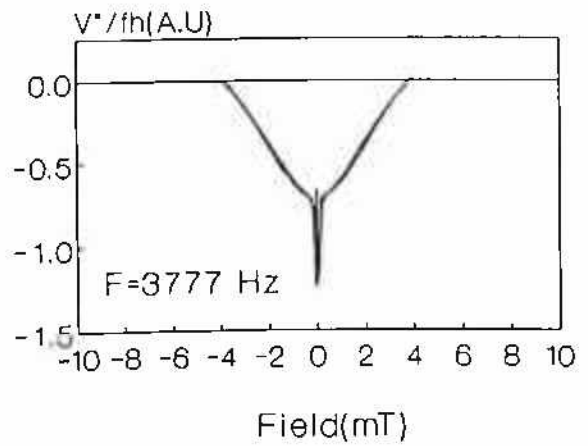
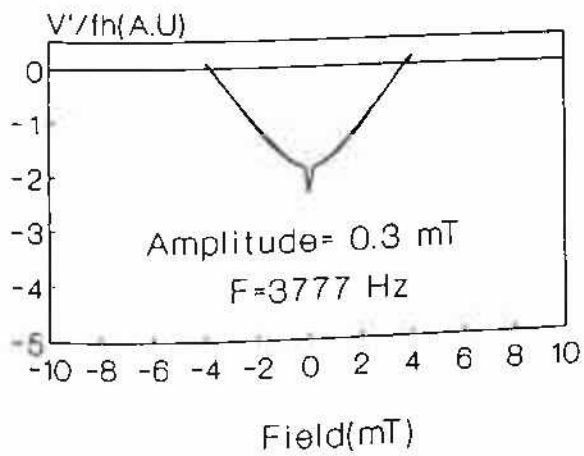


Figure 4.2.1a: $V'/fh(\approx \chi')$ as a function of DC bias field for three different ranges of DC field.

Figure 4.2.1b: $V''/fh(\approx \chi'')$ as a function of DC bias field for 3 different ranges of DC field.

The important findings in figure 4.2.1(a,b) are that i). below a maximum of the DC field excursion there was no hysteresis seen either in real or imaginary parts and ii). with the increase of the range of DC field excursion, the hysteresis in real parts increased monotonically whereas in imaginary parts, along with increase of hysteresis new features were seen to appear. The striking feature, that was seen in all the cases at the zero cross over points - the sharp change in χ' and χ'' near $H=0$, is being reported for the first time. It is difficult to explain the origin of this feature. However, it is likely to be due to the H_{c1} of the grain boundary. More over this feature is not seen in the model calculations in the previous Chapter which is indicative of the above argument that the feature may be due to H_{c1} , because the model assumes all the critical fields to be zero. The interesting feature about this zero-cross-over-feature(ZCOF) was that in case of real parts it increased with the increase in the range of DC field excursions whereas, in $\chi''(H)$ curves it was more or less independent of this range variation.

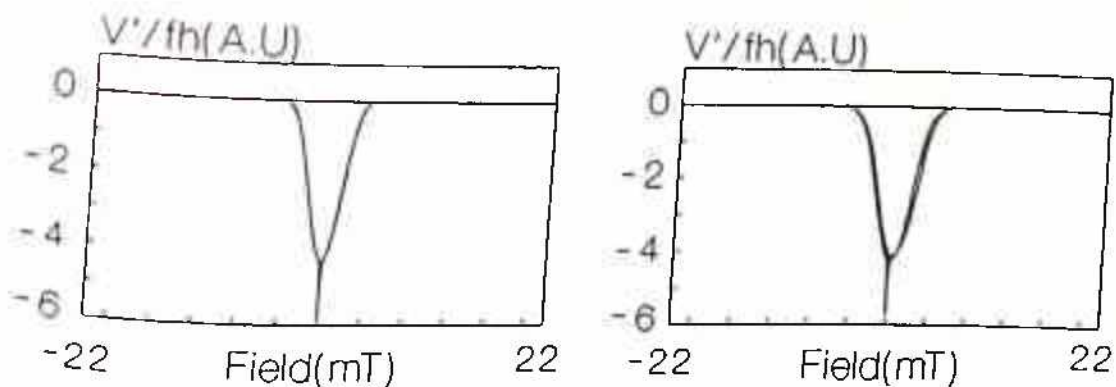
The presence of ZCOF as reported here and not seen in the already published data of others[1-5] can be understood due to the fact that in the experimental set up one usually employs a quasistatic variation of DC field using a constant current source (programmable), where as here a continuous voltage ramp was utilized to ramp the DC field. A constant current source, which drives the inductive load of the magnet in a feedback loop, can not provide a true zero current and hence in this kind of arrangement the ZCOF being sharp and close to zero bias field, will be missed. It was in fact verified in the experiments that the ZCOF was not present when the DC field variation was quasistatic. However, at lower frequencies (e.g., 373 Hz) even in the quasistatic case a small ZCOF was seen. In fact, it will be described in appropriate place that the sharpness of the ZCOF was dependent on the frequency and became narrower in width (i.e., sharper) with increasing frequency and so at lower frequencies, ZCOF being wider was noticeable even in the quasistatic case. It is better to keep this discussion aside for the time being and consider the other features of the $\chi'(H)$ and $\chi''(H)$ loops as a function of the range of the DC field excursion.

The other important feature of the real loops was that there was no change in shape of the curves, but the depths (i.e., the depth of the valley excluding the ZCOF) of these loops (figure 4.2.1a) increased with increase in the range of DC field. However, in case of $\chi''(H)$ loops, there was a substantial change in the shape of the curves with a peak seen to appear

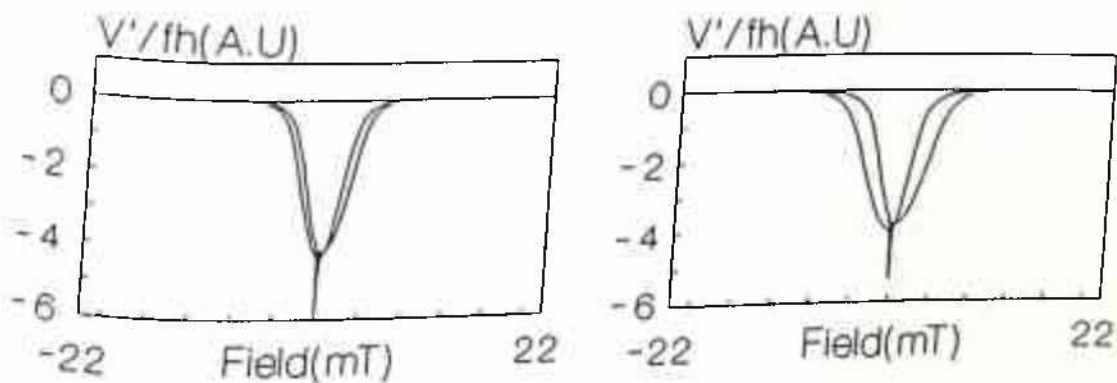
(bottommost loop in figure 4.2.1b) at high DC bias field values for the largest range of DC bias field. For $\chi''(H)$ loops as can be seen in figure 4.2.1b, the heights (the term "height" is introduced in view of the fact that if the loops were not offsetted they should be in +ve side of the y-axis) of these curves, excluding the ZCOF, i.e., the separation between the minimum (excluding the ZCOF) and the maximum of the curves were more or less independent of the variation of the range of DC field. However, the described behavior of χ' and χ'' loops was very much sample dependent and was not same in different samples. This peculiarity of range effect could also be seen in sample A2 (2% PbO doped YBCO). In figure 4.2.2a and 4.2.2b, same $\chi'(H)$ and $\chi''(H)$ loops have been plotted for six different ranges with amplitude of 0.3 mT for sample A2. It can be seen in figure 4.2.2a that the depth of $\chi'(H)$ loops remained almost unchanged upto a field range of 8 mT in this sample. Above this range, the hysteresis in $\chi'(H)$ loops increased significantly while the depth decreased. This effect of range of DC field on $\chi''(H)$ loops in this sample(A2) was also interesting and clearly showed the evolution of $\chi''(H)$ loops with range of DC field (figure 4.2.2b.). Unlike the first sample (figure 4.2.1b), here the height (excluding the ZCOF) of $\chi''(H)$ loops was apparently increasing with increase in the range, except for the lowest range where ZCOF was not quite narrow. However, this variation of height was not appreciable as compared to the variation of depths of the real loops.

It is interesting to consider another sample A4(10% PbO), where both increase and decrease of depths of real loops were seen. In figure 4.2.3a and 4.2.3b, the $\chi'(H)$ and $\chi''(H)$ loops have been plotted for sample A4 where the amplitude of AC excitation field was 0.012 mT, the lowest of the three amplitudes considered here. Here, three different ranges of the DC field have been considered and the clear variation of depths of $\chi'(H)$ loops was obvious - first strong increase in depth with increase in range from 2 mT to 5 mT and then once again decrease of depth with increase of range to 12 mT. But like the sample A2, here also the height (excluding the ZCOF) of $\chi''(H)$ showed a strong monotonic decrease with the increase of the DC field range.

The explanation of this peculiar dependence on the range of DC field can be given on the basis of the model calculations as given in Chapter 3. The closest similarity (excluding the ZCOF) of the shapes of the $\chi'(H)$ loops as seen here, was with that of in figures 3.2.8a and 3.2.9a of Chapter 3. However, the exact values were not same. The loops in figures 3.2.8a and



Amplitude: 0.3 mT



Frequency: 3777 Hz

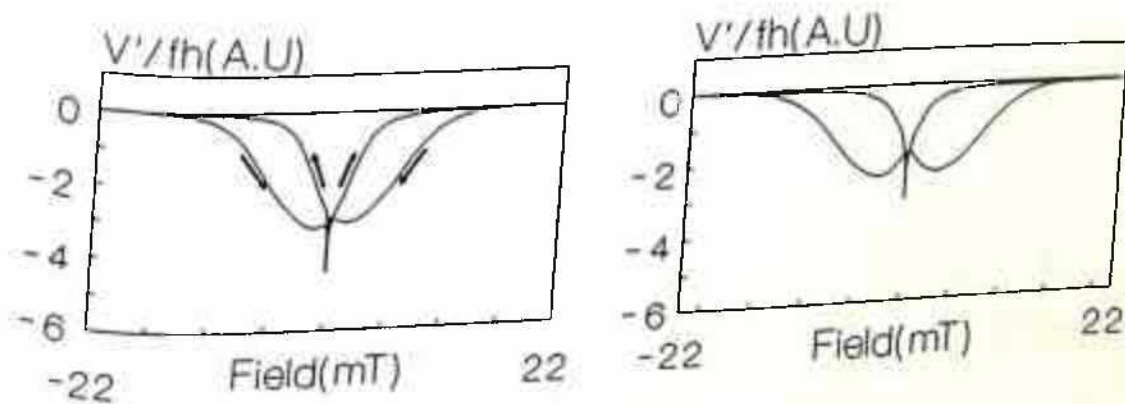
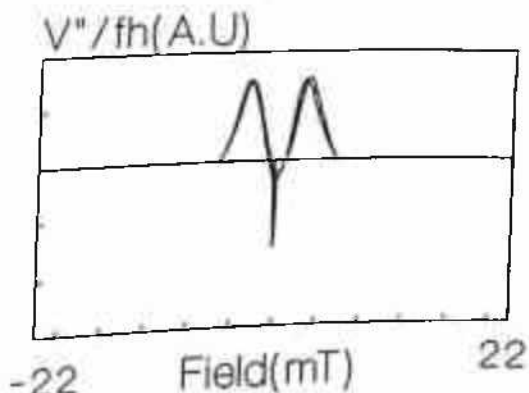
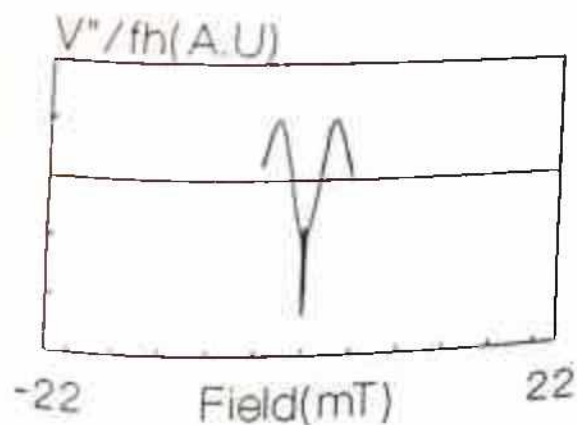
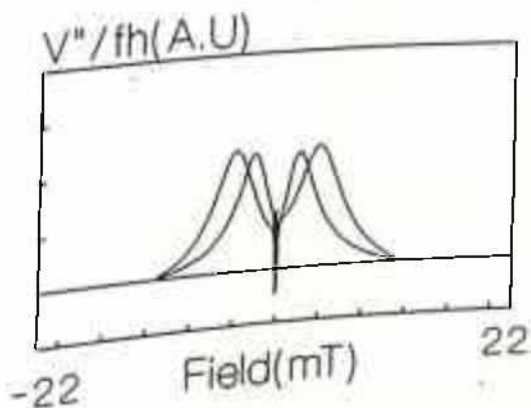
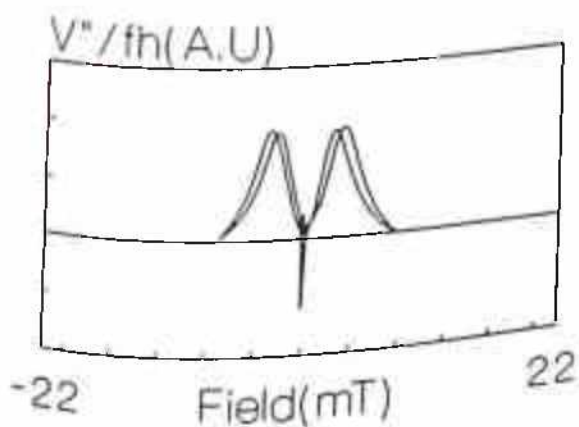


Figure 4.2.2a: V'/fh ($\approx \chi'$) as a function of DC bias for six different ranges. (Sample A2)



Amplitude: 0.3 mT



Frequency: 3777 Hz

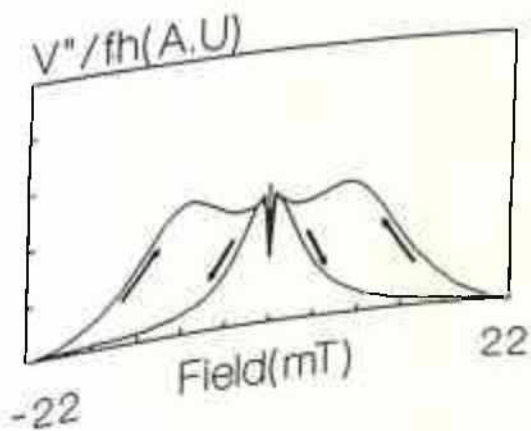
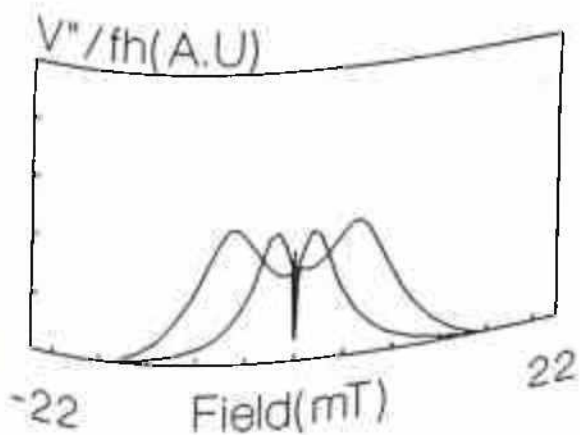


Figure 4.2.2b: $V''/fh(= \chi'')$ as a function of DC bias for six different ranges (Sample A2). For clarity in plotting, y-axis has 5 equal divisions but different ranges.

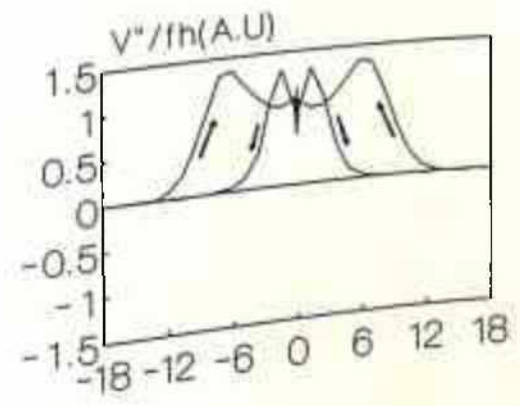
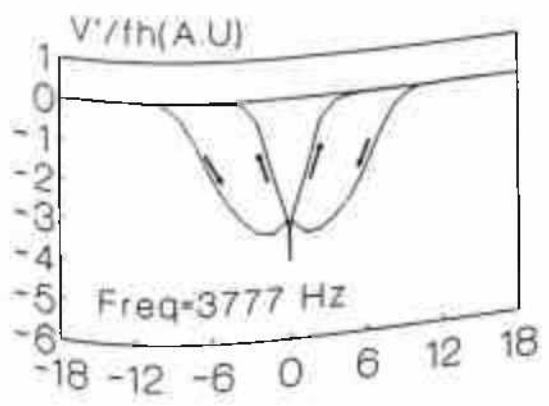
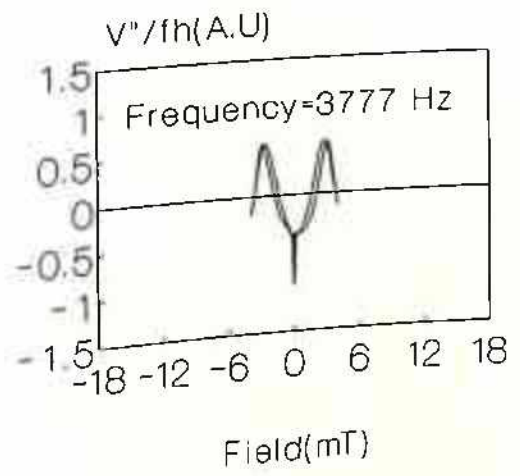
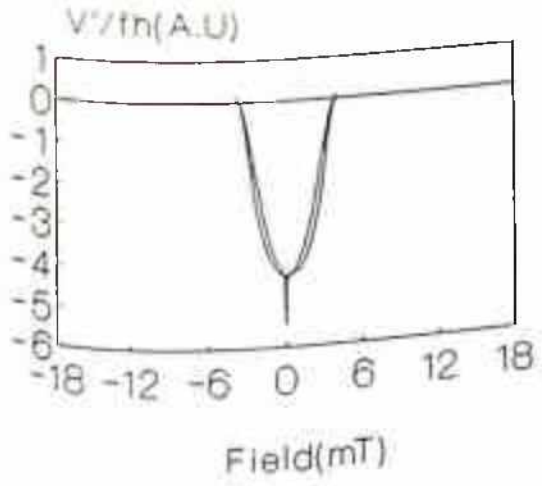
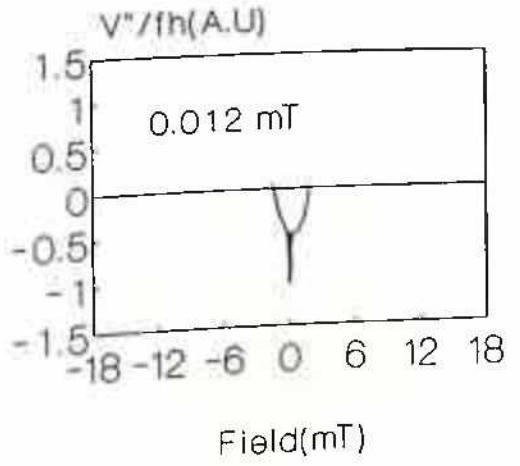
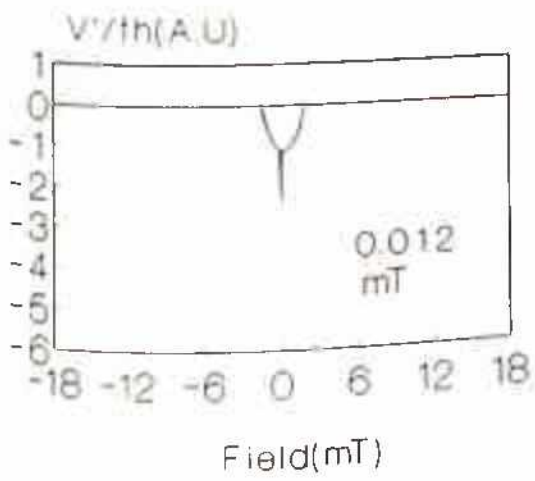
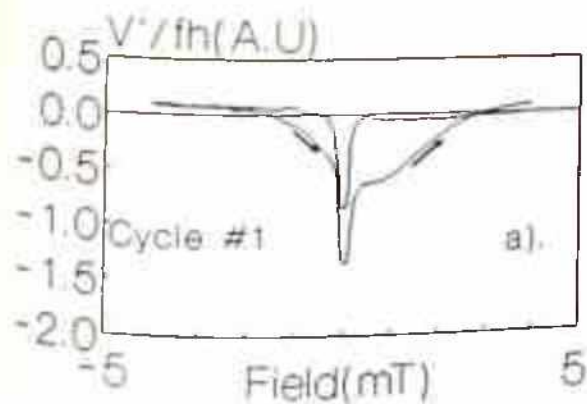


Figure 4.2.3a: $V'/fh(\approx \chi')$ as a function of DC bias field for three different ranges of DC field. (sample A4)

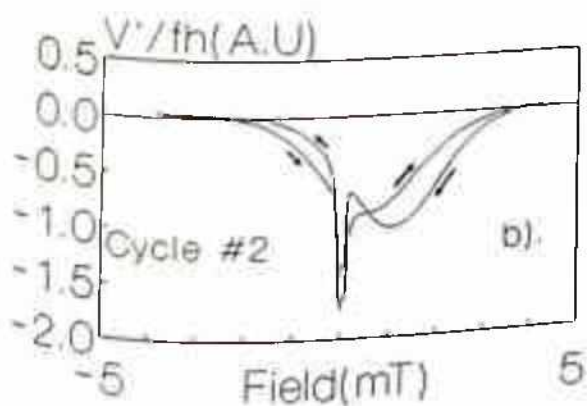
Figure 4.2.3b: $V''/fh(\approx \chi'')$ as a function of DC bias field for 3 different ranges of DC field. (Sample A4)

3.2.9a (of Chapter 3) clearly show that with increase of the range one will get similar behavior as have been seen in experimental loops, i.e., increase of depth of the $\chi'(H)$ with increase in the range of the DC field. If the amplitude is in the lower side, $\chi'(H)$ loops becomes flatter and so variation of the depth of $\chi'(H)$ must be less but a monotonic increase in the depth of the $\chi'(H)$ loops is expected. This may be the case in figure 4.2.1a. However, it is seemingly not possible to put forth an explanation for the decrease of the depth of the $\chi'(H)$ loops for higher range of the field. Any disagreement between the model calculations and the experimental data is obviously due to fact that the model still is an over simplified representation of the actual physical situation. This will be discussed at length in coming sections.

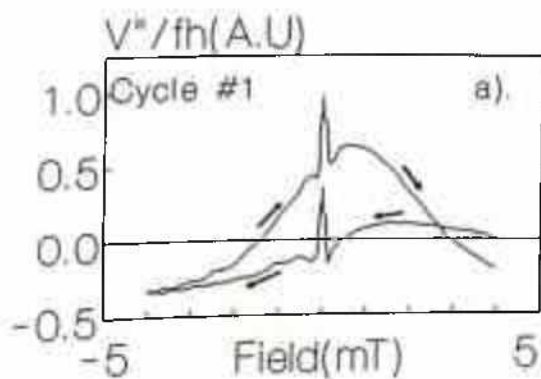
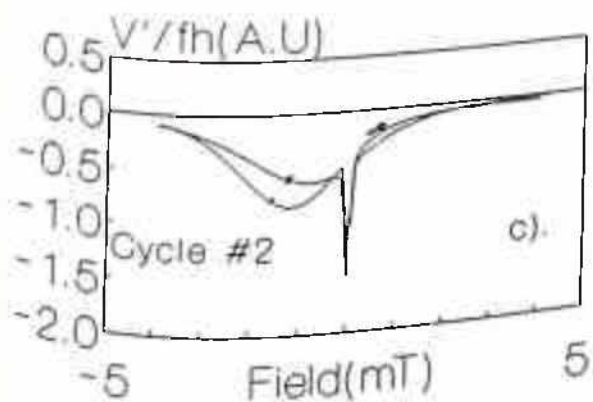
The presence of trapped flux can further be visualized in the following experiments. After taking the DC field to a maximum of +20 mT, the same $\chi'(H)$ and $\chi''(H)$ loops were drawn for lower field ranges (± 5 mT) as shown in figure 4.2.4(a and b) for amplitude of 0.012 mT for sample A4. As can be seen in these diagrams, the loops in the cycle #1 (+20 mT to -5 mT and then +5 mT) were quite different, because in this cycle there was large flux reorganization. However, in the cycle #2 (± 5 mT), only some excess flux remained trapped which distorted the symmetry of the loops (curve b's of figures 4.2.4a and 4.2.4b). That this asymmetry was certainly due to the trapped flux can be ascertained from a reverse field excursion (i.e., starting from -20 mT and then cycling ± 5 mT) as seen in curves c's of figures 4.2.4a,b where the asymmetry was reversed. It is further important to consider the effect of range on this trapped flux. In figures 4.2.5a and b (cycle #1), and figures 4.2.6a and b (cycle #2) the $\chi'(H)$ and $\chi''(H)$ loops have been plotted for three different field ranges (± 4 , ± 6 and ± 8 mT in the cycle #1 and #2) starting from a higher DC field of +20 mT. Here the amplitude was 0.3 mT and sample was A2(2% PbO). In comparison to figure 4.2.4, it can be seen here that with higher amplitude, the disturbance as well as hysteresis in cycle #1 were less at all ranges. This is plausible, because with higher amplitude, flux would be averaged over a larger volume during the AC cycling leaving less flux reorganization to occur over the DC field cycling. However, even at this higher amplitude, the disturbance in cycle #1 in figure 4.2.5 at all ranges was more than that at cycle #2 in figure 4.2.6. It was clear from these figures that though the asymmetry was present in all the cases, it was less with higher ranges which is also a physically obvious expectation. Moreover, this trapped flux acted like a bias field only and did not contribute to



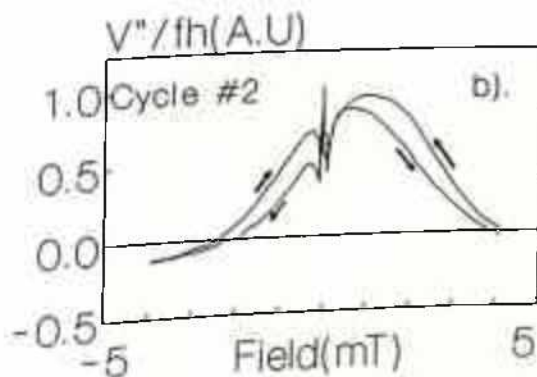
Amplitude = 0.012 mT



Frequency = 3777 Hz



Amplitude = 0.012 mT



Frequency = 3777 Hz

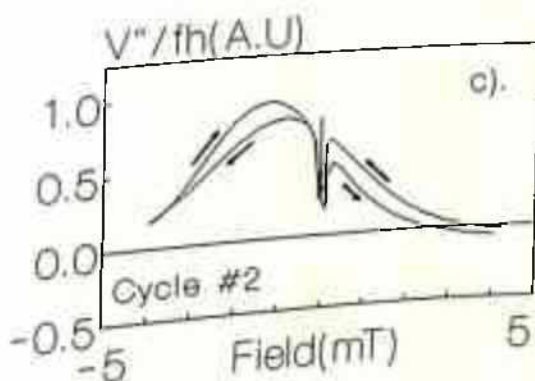


Figure 4.2.4b: $V''/fh (= \chi'')$ as a function of DC bias field for sample A4.

Figure 4.2.4a: $V'/fh (= \chi')$ as a function of DC bias field for sample A4.

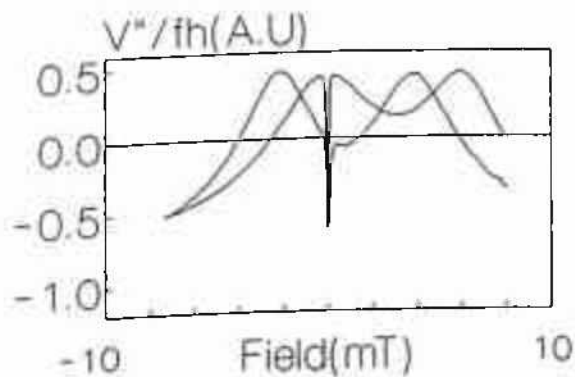
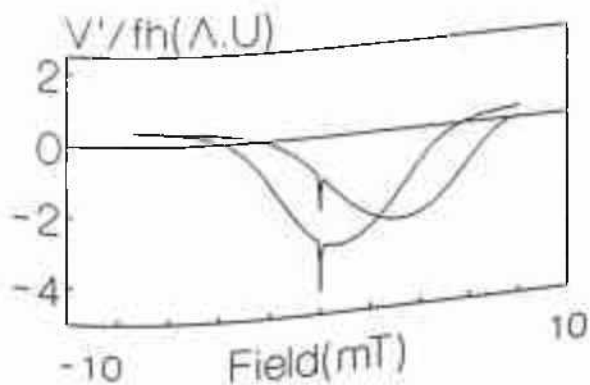
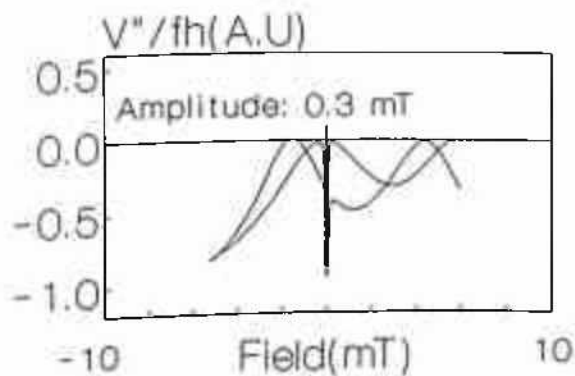
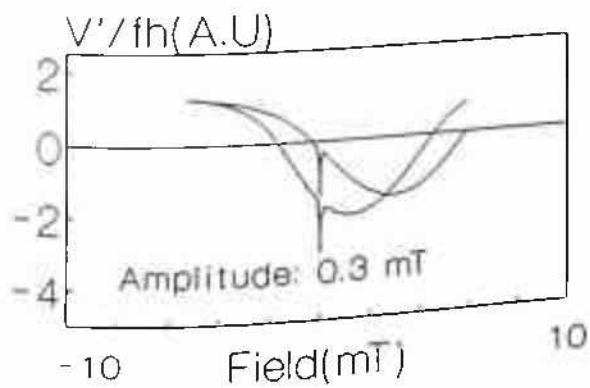
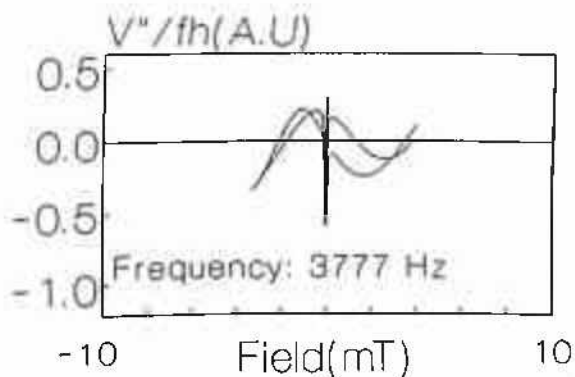
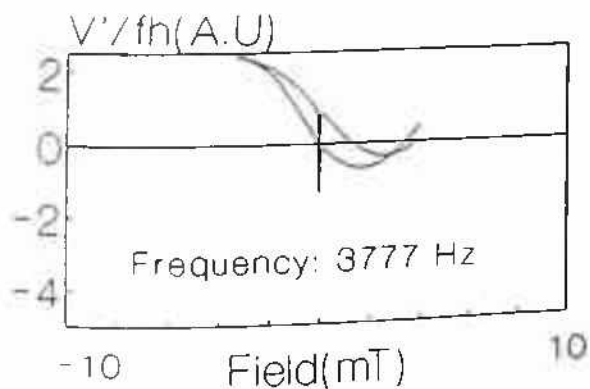


Figure 4.2.5a: $V'/fh (\approx \chi')$ as a function of DC bias field for sample A2 for different ranges of DC field. (Cycle #1)

Figure 4.2.5b: $V''/fh (\approx \chi'')$ as a function of DC bias field for sample A2 for different ranges of DC bias. (Cycle #1)

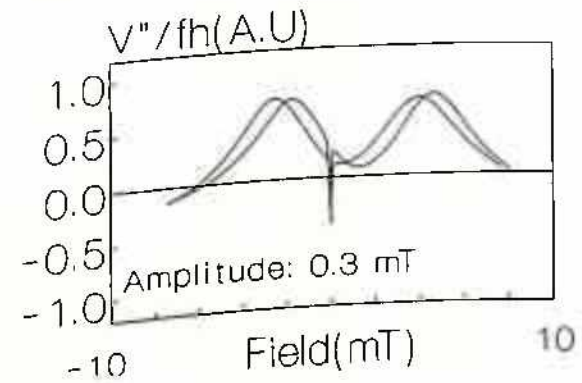
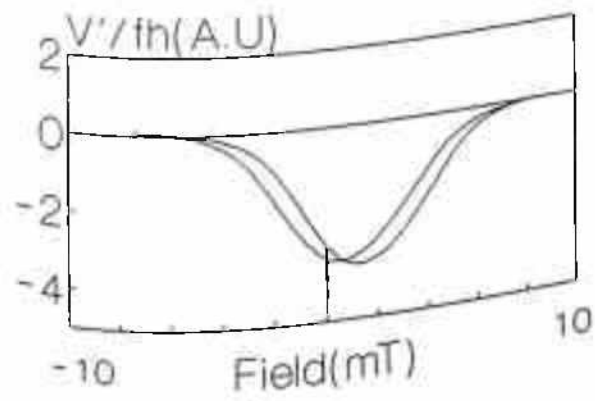
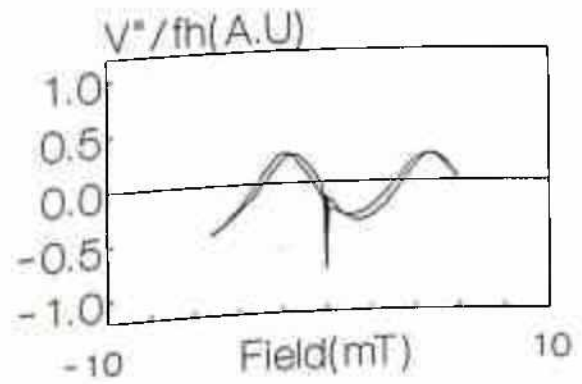
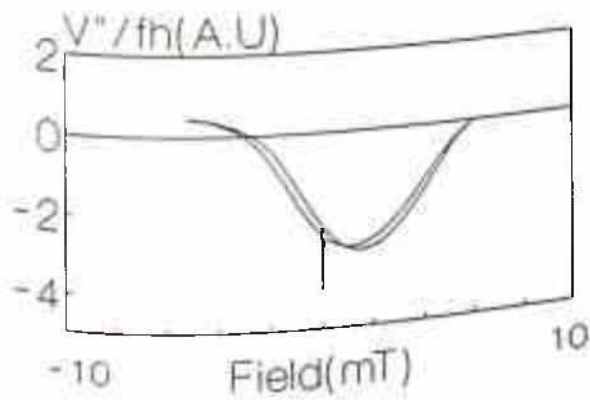
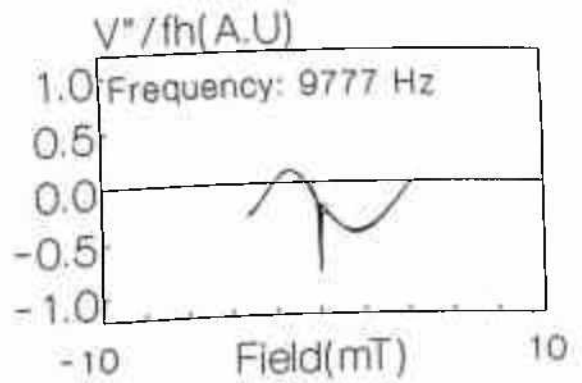
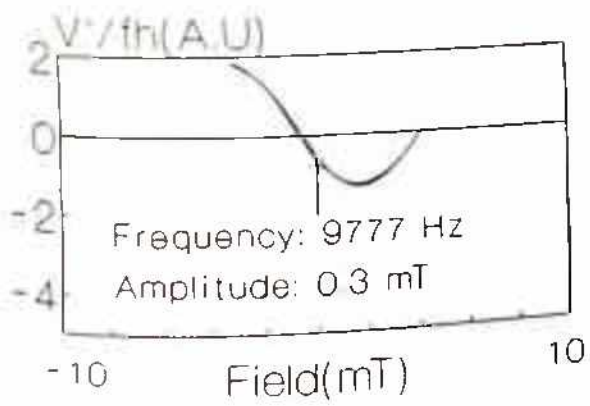


Figure 4.2.6a: $V''/fh (\approx \chi')$ as a function of DC bias field for sample A2 for different ranges of DC field. (Cycle #2)

Figure 4.2.6b: $V''/fh (\approx \chi'')$ as a function of DC bias field for sample A2 for different ranges of DC bias. (Cycle #2)

hysteresis as can be seen in the cycle #2 data where at the lowest field range no hysteresis was seen like the case of figure 4.2.2.

4.2.2B. AMPLITUDE DEPENDENCE OF THE $\chi'(H)$ AND $\chi''(H)$ LOOPS:

The dependence of the $\chi'(H)$ and $\chi''(H)$ loops on amplitude of the AC excitation field is quite large and provides rich information vide comparison with the model calculations. However, only three amplitudes had been considered here and they seemed to cover a wide range of behavior of the loops and showed a systematic variation. In figures 4.2.7(a,b) and 4.2.8(a,b) the $\chi'(H)$ and $\chi''(H)$ loops have been plotted for three different amplitudes for frequency of AC excitation field of 3777 Hz and for sample A1(pure) and sample A2(2% PbO) respectively. Except the ZCOF, the $\chi'(H)$ loops appeared to be justified in view of the model calculations (figure 3.2.8a, or 3.2.9a). As it is obvious (figures 4.2.7a and 4.2.8a), the DC field dependence of $\chi'(H)$ decreased with decrease of AC amplitudes and remembering the offsetting in this curves it was clearly in line with the field dependence of $\chi'(H)$ loops of the model calculation as seen in figure 3.2.8a in Chapter 3. But the comparison of $\chi''(H)$ loops in figure 4.2.7b and 4.2.8b with the calculated loops did not show much agreement. However, the basic tendency in the field dependence of $\chi''(H)$ was qualitatively same. Like in figure 3.2.8b, between 2.0 to 0.5 mT of amplitudes, the evolution of the field dependence of the $\chi''(H)$ loops was close to the case as shown in figure 4.2.8b.

The sample dependence is also clear from these figures. It was probably that the sample(A2 - 2% PbO) considered in figure 4.2.8 had worse critical current parameters for the GB than the sample(A1 - pure) concerned in figure 4.2.7 and hence the peak in the imaginary loops at higher amplitudes was seen to appear (to be compared with theoretical curve in figure 3.2.8b of Chapter 3)) in sample A2. Stronger variation of the field dependence in real parts in sample A2 (figure 4.2.8a) was also supportive of the fact. Because larger field dependence was seen in all calculation of real loops for lower J_{ci} parameters.

However, as already argued, the ZCOF can not be explained on the basis of the model. It is difficult to find out systematicity in the variation of ZCOF in these two figures. Once again it is better to avoid this peculiar behavior of ZCOF for the time being.

In figures 4.2.9(a,b) and 4.2.10(a,b), the $\chi'(H)$ and the $\chi''(H)$ loops have been plotted

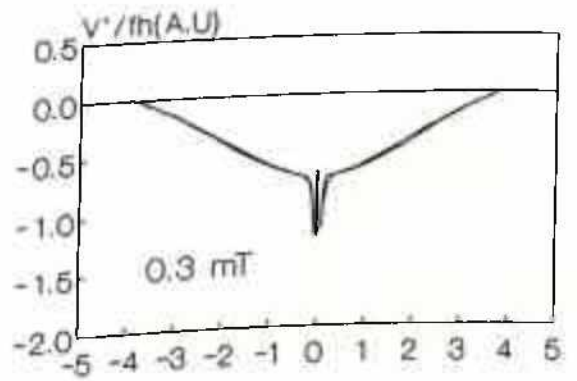
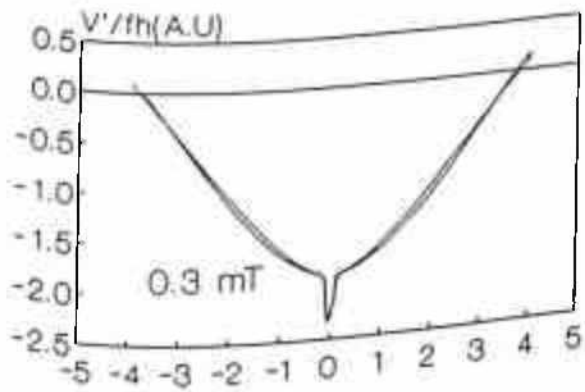
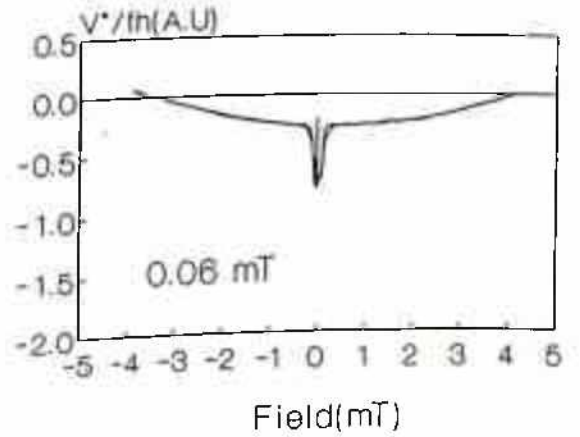
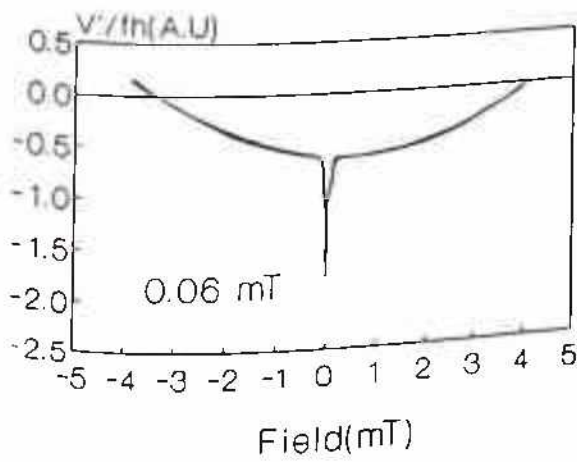
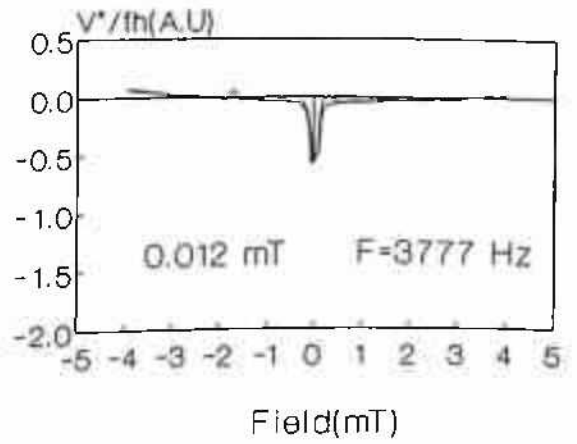
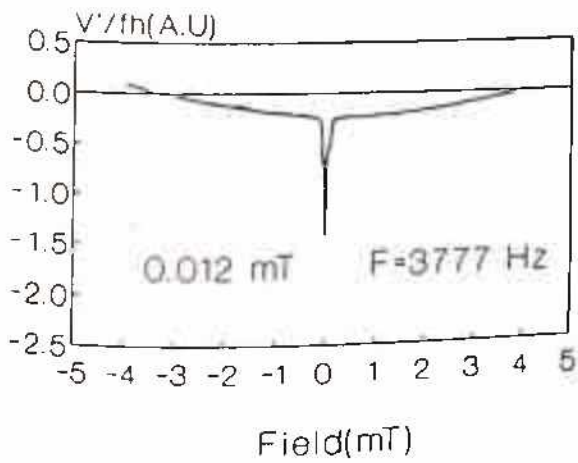


Figure 4.2.7a: $V'/fh (\approx \chi')$ as a function of DC bias field for sample A1 for different amplitudes.

Figure 4.2.7b: $V''/fh (\approx \chi'')$ as a function of DC bias field for sample A1 for different amplitudes.

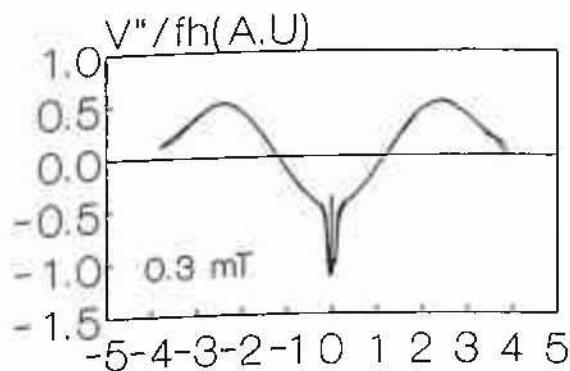
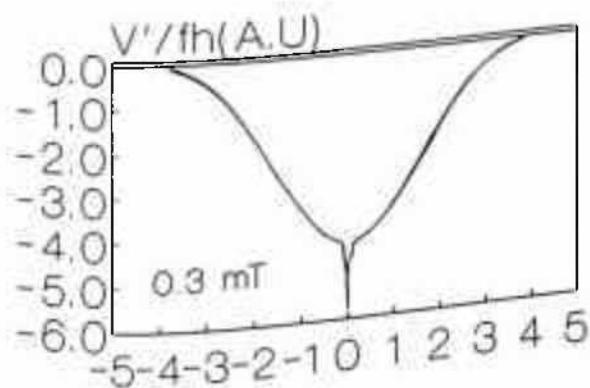
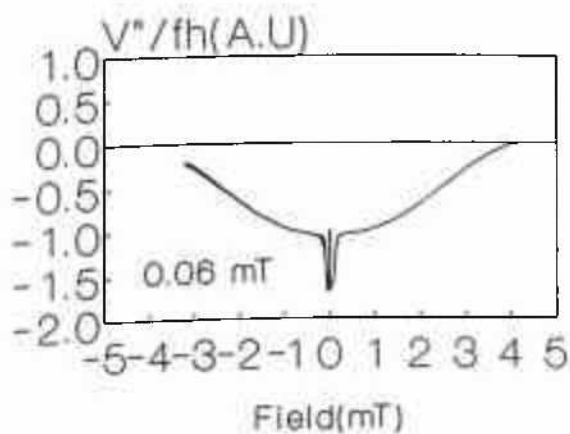
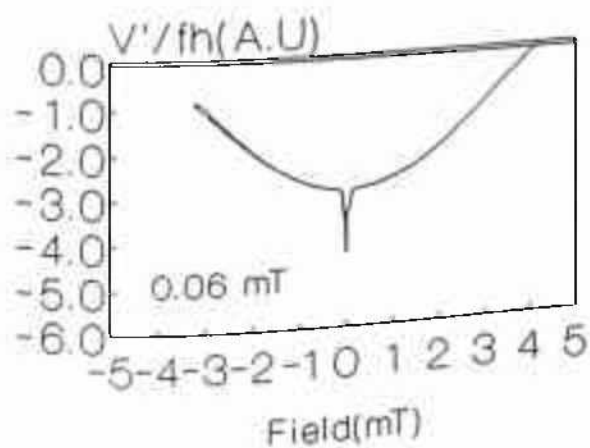
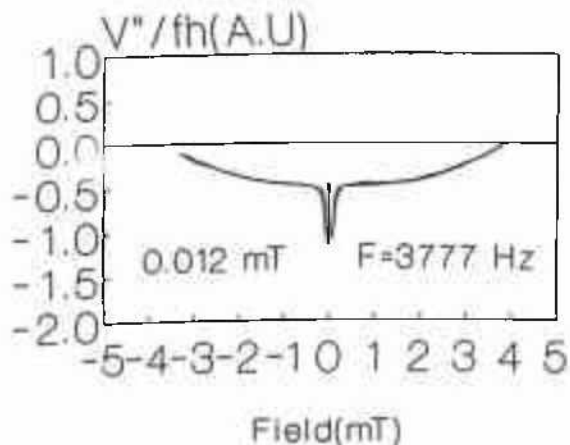
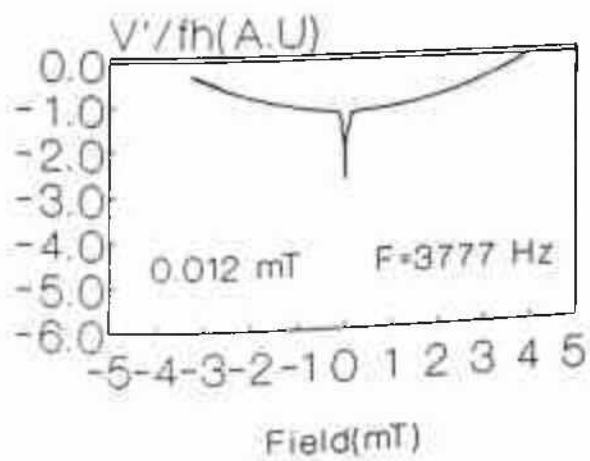


Figure 4.2.8a: V'/fh ($\approx \chi'$) as a function of DC bias field for sample A2 for different amplitudes.

Figure 4.2.8b: V''/fh ($\approx \chi''$) as a function of DC bias field for sample A2 for different amplitudes.

for two amplitudes for two different ranges for sample A4(10% PbO doped YBCO). In figure 4.2.9, the range being small, appreciable hysteresis was not seen and DC field dependence of χ' and χ'' showed the same tendency as in samples A1 and A2. In figure 4.2.10, substantial hysteresis was present and the DC field dependence of $\chi'(H)$ and $\chi''(H)$ loops was different from that of the low field cases. The important finding was that the sample A4 had critical current density worse than the other two as clear from appearance of peak on $\chi''(H)$ even at 1 mT of DC bias for amplitude 0.3 mT (in A1 this peak was not seen in this range and in A2 it was seen to appear at around 2.5 mT). One more important observation in figure 4.2.10a is the curvature of the $\chi'(H)$ loops. At higher amplitude the curvature of the $\chi'(H)$ loops was downward and that at lower amplitude it was upward. This behavior of the variation of curvature of the $\chi'(H)$ loops was in complete agreement with the low field calculation in the model and can be visualized through figures 3.2.5a, 3.2.8a and 3.2.9a in Chapter 3. When the field dependence of J_{cj} is $1/H^2$ type (i.e., $\beta=2$), this change over of curvature was seen in figure 3.2.8a (Chapter 3) and more clearly in 3.2.9a, whereas when $\beta=1$ as in figure 3.2.5a, the curvatures at all amplitudes were seen to be same (and were downward). This indicates that the materials here had a $J_{cj}(H)$ with $\beta=2$. The hysteresis in $\chi'(H)$ loops as was seen to be present in this sample A4 (figure 4.2.10a) and absent in samples A1 and A2 (figure 4.2.7a and 4.2.8a) is further indicative of the same fact that sample A4 had worse J_{cj} parameters. Because if one compares the calculated loops in figure 3.2.8a and figure 3.2.9a (both for $\beta=2$), the hysteresis was seen to be higher in the later case where $J_{cj}(0) = 100 \text{ amp/cm}^2$ compared to the other case where $J_{cj}(0) = 1000 \text{ amp/cm}^2$. On the contrary the imaginary loops as seen from these experimental data, once again did not show much resemblance with the calculated loops. However, the presence of peak in calculated $\chi''(H)$ loops (figure 3.2.8a and 3.2.9a) and shifting of this peak to higher DC bias with decrease of amplitude was supported by the data here and can be verified in figure 4.2.10b where the peak in $\chi''(H)$ loops for 0.3 mT of amplitude appeared at around 1.5 mT of DC bias while the same peak for 0.012 mT loops appeared at around 3 mT of the DC bias field. In fact the variety of shapes of $\chi''(H)$ loops, as will further be demonstrated in this work, has posed a serious problem in comparing them in terms of some parameters of the $\chi''(H)$ loops and hence the laborious way of plotting the full loops for different parameters have been resorted to.

In figures 4.2.11(a,b), 4.2.12(a,b), 4.2.13(a,b) the higher DC field range of $\pm 18 \text{ mT}$

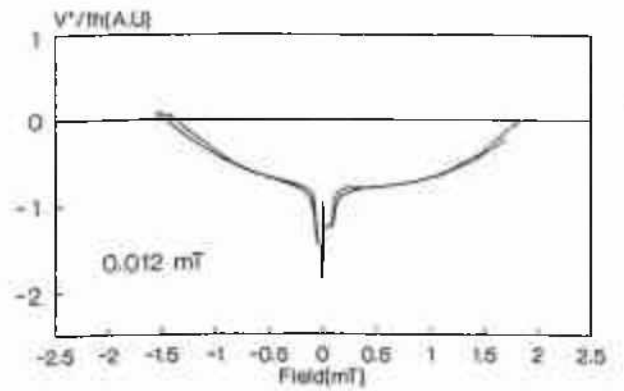
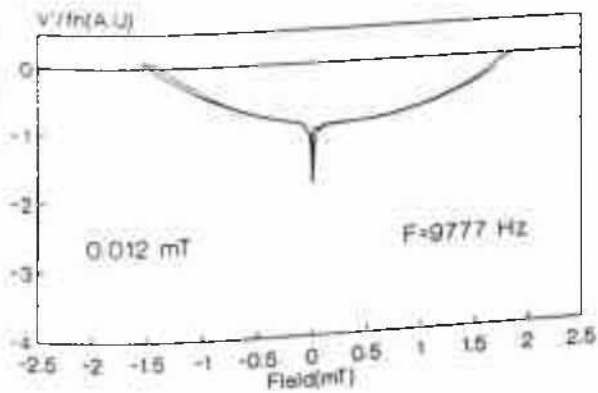
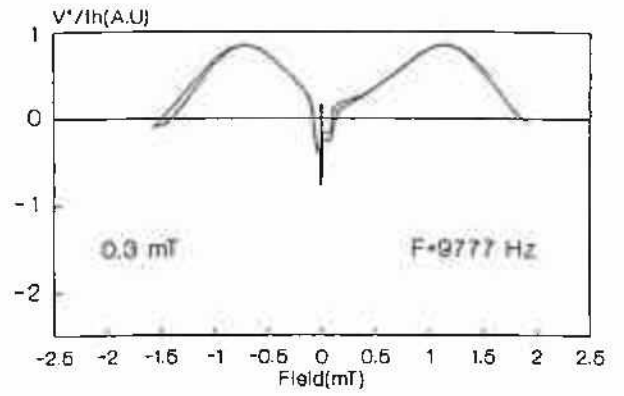
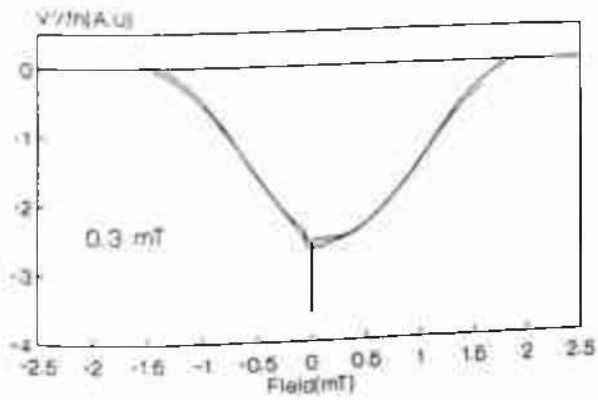


Figure 4.2.9a: $V'/fh (\approx \chi')$ as a function of DC bias field for sample A4 for different amplitudes.

Figure 4.2.9b: $V''/fh (\approx \chi'')$ as a function of DC bias field for sample A4 for different amplitudes.

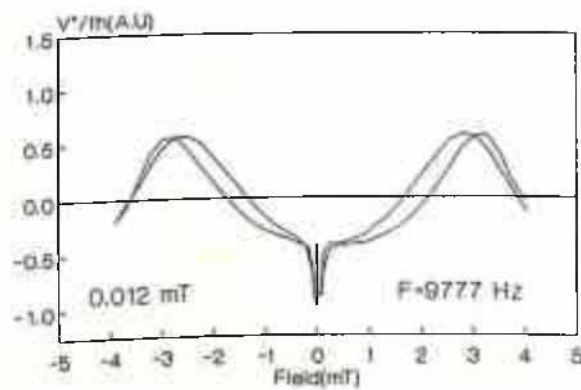
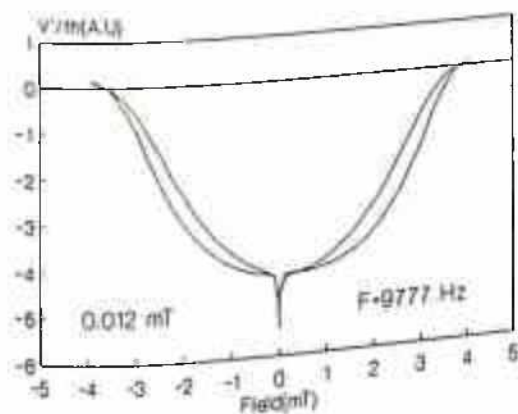
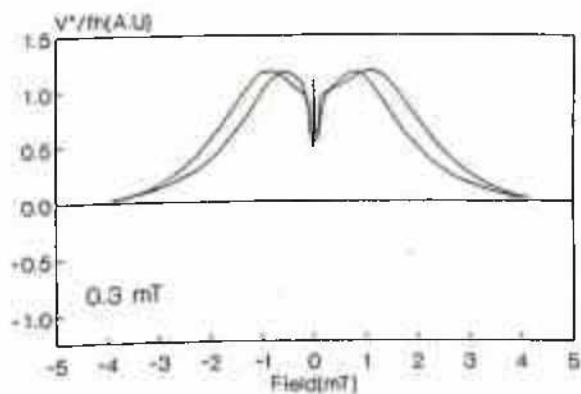
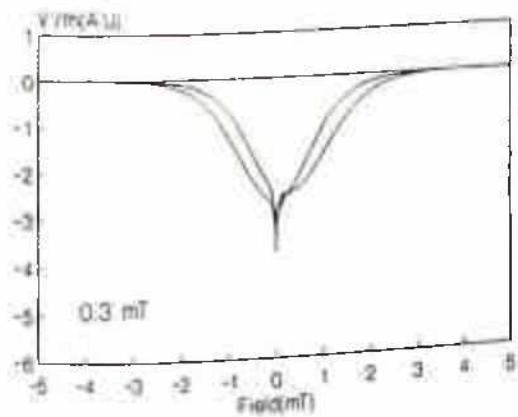


Figure 4.2.10a: $V''/fh(\approx\chi')$ as a function of DC bias field for sample A4 for different amplitudes.

Figure 4.2.10b: $V''/fh(\approx\chi'')$ as a function of DC bias field for sample A4 for different amplitudes.

have been considered for samples A2, A3 and A4 respectively. At this higher field range, amplitude dependence showed quite systematic evolution with amplitude. It is obvious from the real loops in these figures that the amplitude dependence of $\chi'(H)$ in all the cases was same as described above, i.e., decrease in field dependence with increase in AC amplitude. However, while in A2, the dependence was not sharp, in A3 and A4 the variation was quite large. It was likely that from A2 to A4 samples were gradually going towards poorer critical current parameters. This argument may further be ascertained from the observation of the amplitude dependence in the $\chi''(H)$ loops. The general feature of this $\chi''(H)$ loops was that there was a valley (V) at the zero-bias point and two peaks (P1 and P2) on each arm at a finite DC bias (indicated in figure 4.2.11b). It has already been explained that the peaks shifted to lower DC bias side with increase in amplitude and was also clearly seen here. Even, if the amplitude was too high, the peaks coincided and the valley could not be seen (viz., figure 4.2.13b - 0.3 and 0.06 mT). This movement of the peaks with amplitude variation caused an apparent shift of the valley upward and seen in figures 4.2.11b, 4.2.12b and 4.2.13b. Obviously these peaks were also seen in the calculations as obvious in figure 3.2.8b, where similar shift of this peak with amplitudes was demonstrated clearly (in between amplitude of 2 and 1 mT). In fact, if one can produce absolute measurements in these experiments, it is possible to compare the sample properties in a rigorous way.

Another aspect of the $\chi''(H)$ loops for different amplitudes as seen here (more clearly in figure 4.2.12b) was that with lower amplitude the split, of the increasing and decreasing arms of the loop, ΔH on each side (+ve or -ve H sides) was larger. It was also apparent that the hysteresis was higher with lower amplitudes in the $\chi''(H)$ loops. In the theoretical calculations, it was concluded that the hysteresis in $\chi''(H)$ loops should be higher with lower amplitudes (figures 3.2.1b, 3.2.5b, 3.2.8b and 3.2.9b in Chapter 3).

However, the obvious disagreement with the model calculations was that it indicated a decrease in hysteresis in $\chi''(H)$ loops with decreasing amplitude in contradiction to the finding here in the experimental data.

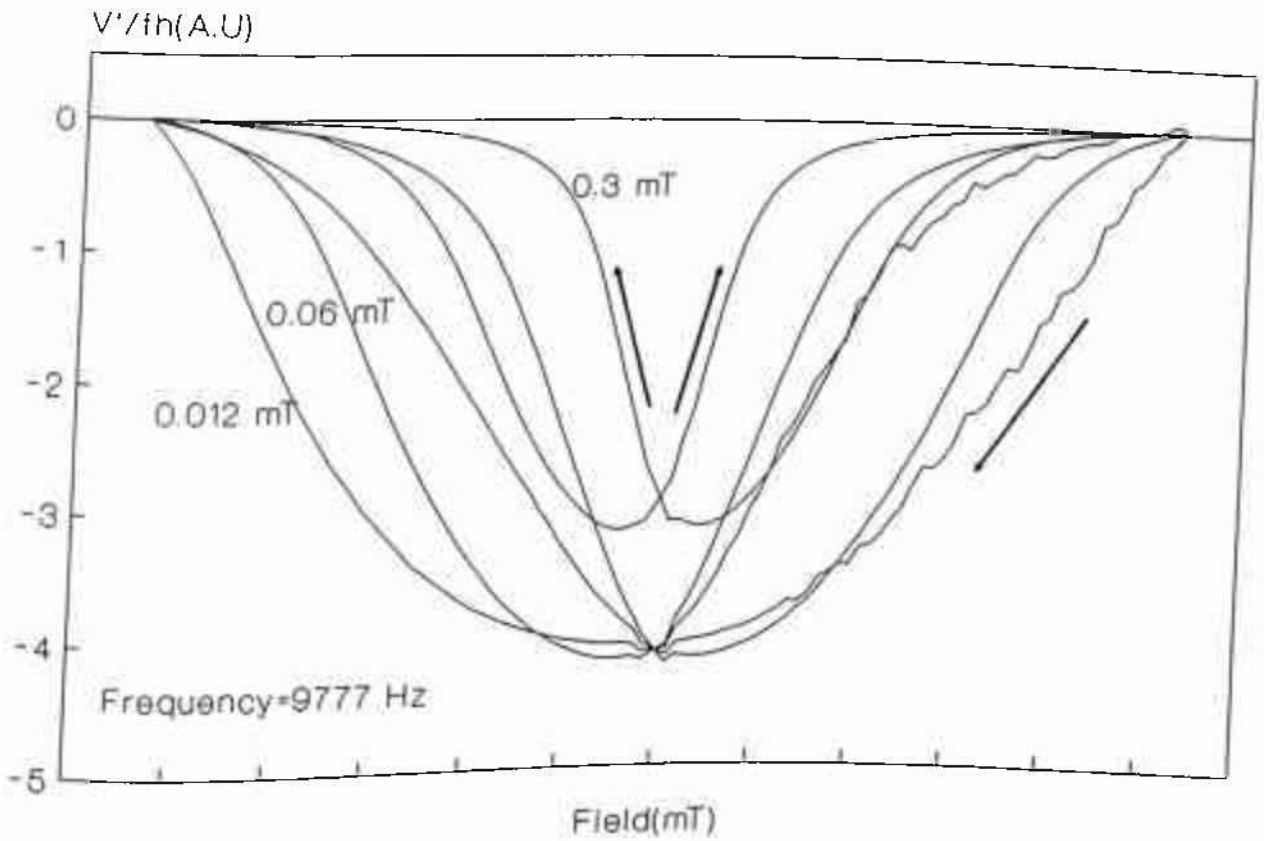
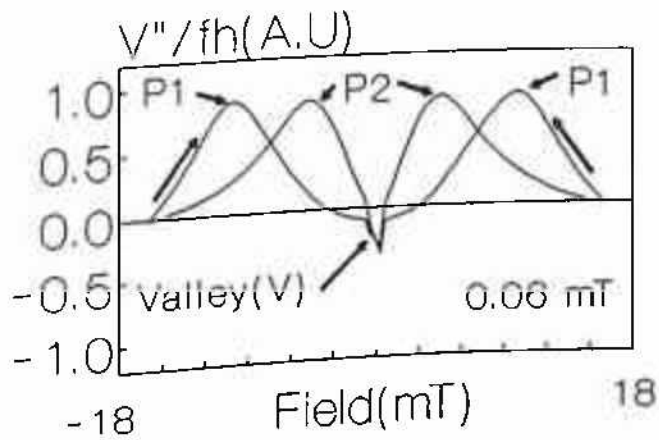
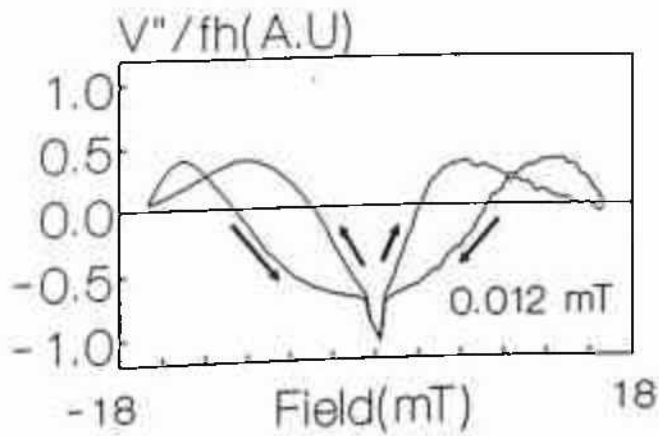


Figure 4.2.11a: $V'/fh (\approx \chi')$ as a function of DC bias field for sample A2 for different amplitudes. [DC bias field range: ± 18 mT]



Freq: 9777 Hz

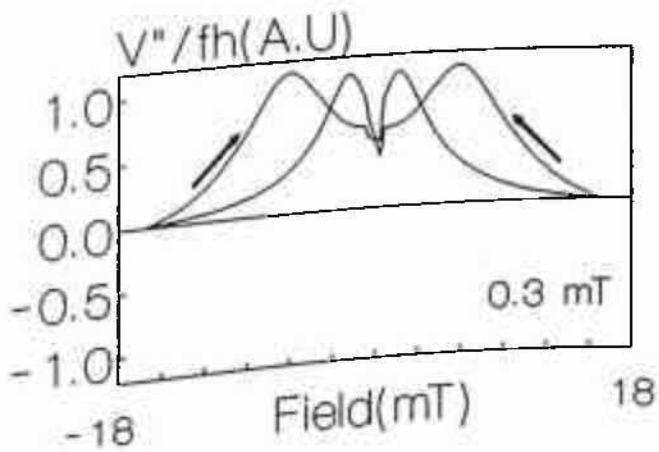


Figure 4.2.11b: $V''/fh(=x'')$ as a function DC bias field for sample A2 for different amplitudes.

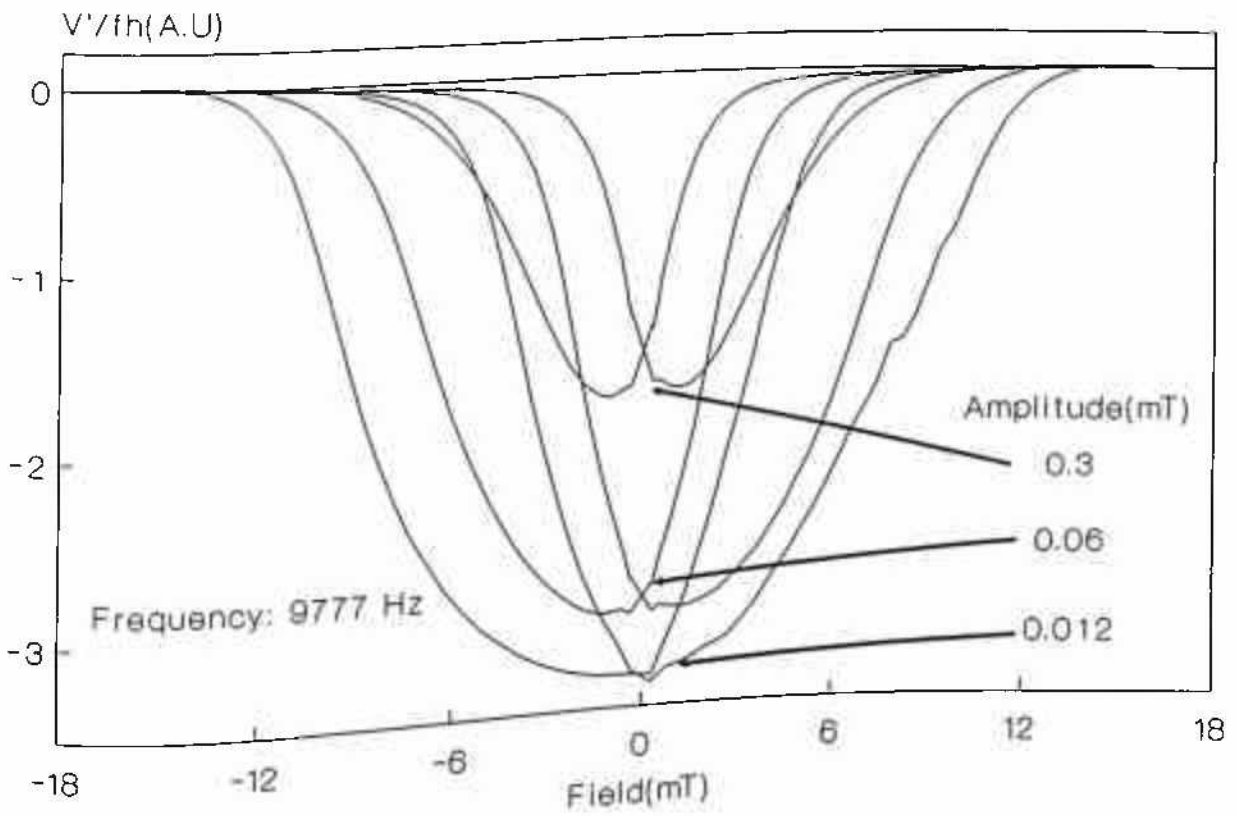


Figure 4.2.12a: $V'/fh(=x')$ as a function of DC bias field for sample A3 for different amplitudes.

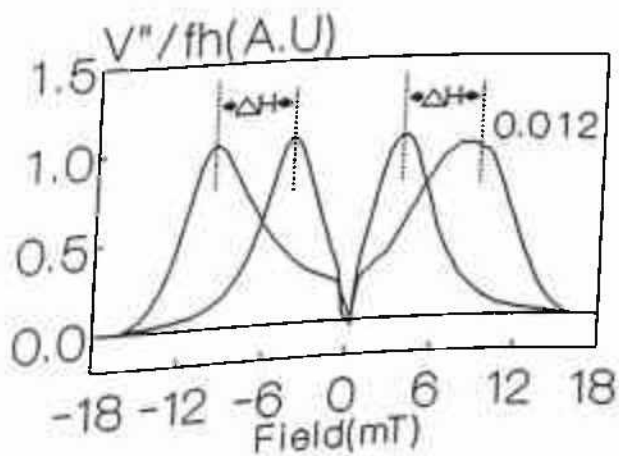
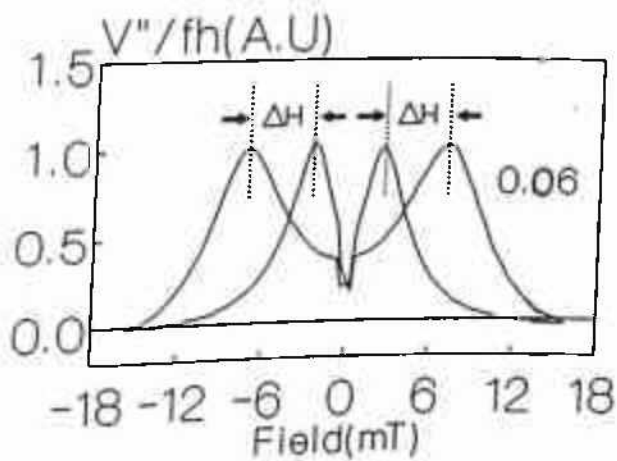
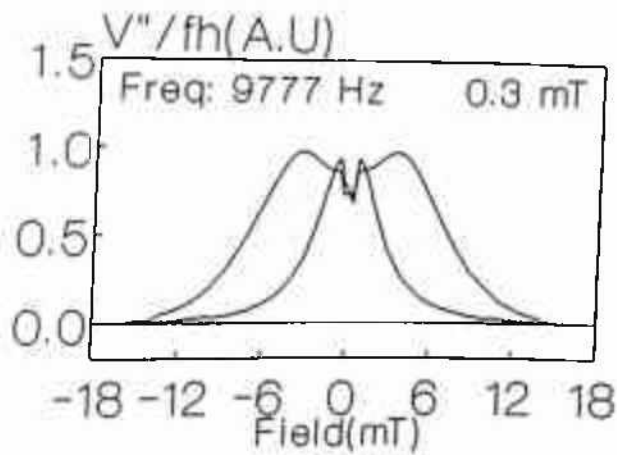


Figure 4.2.12b: $V''/fh (\approx \chi'')$ as a function DC bias field for sample A3 for different amplitudes.

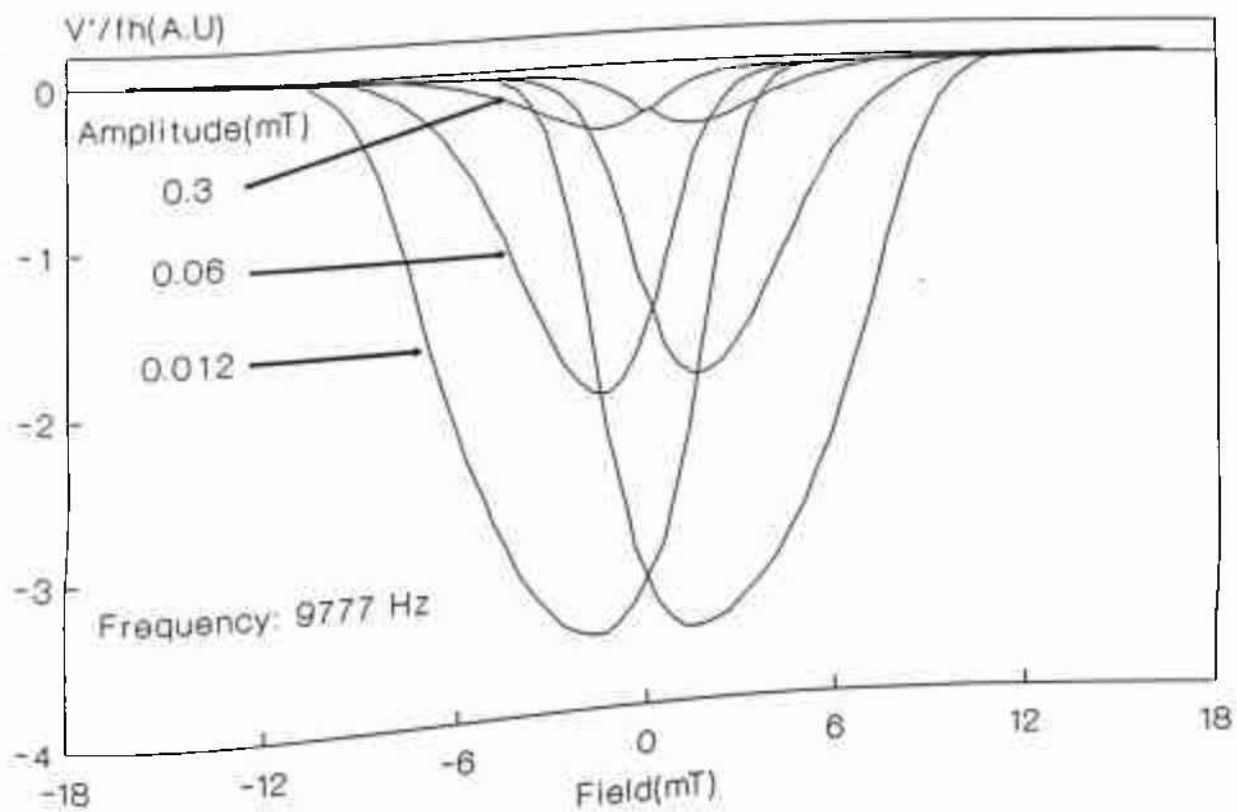


Figure 4.2.13a: V'/fh ($\approx \chi''$) as a function of DC bias field for sample A4 for different amplitudes.

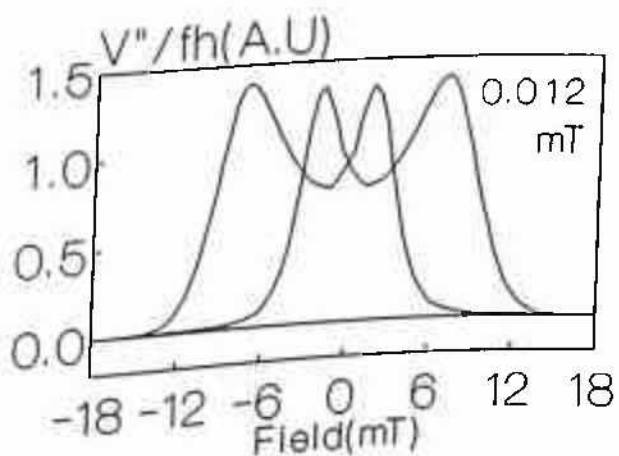
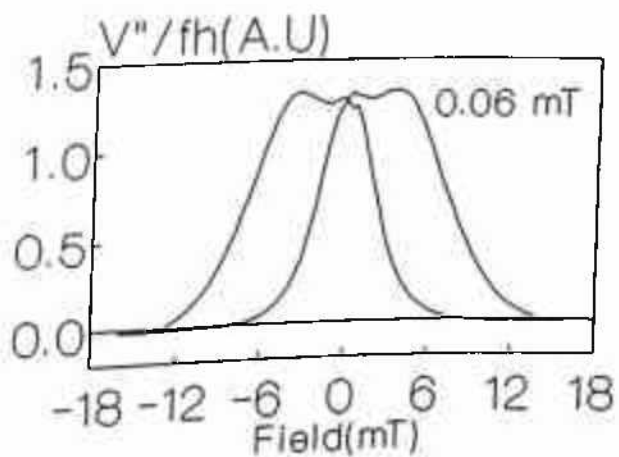
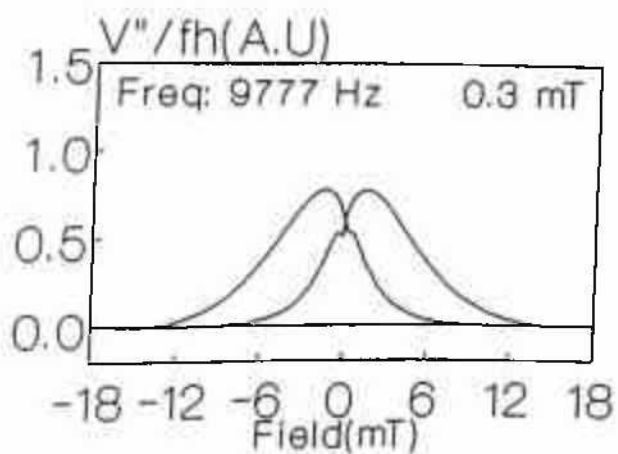


Figure 4.2.13b: $V''/fh(\approx \chi'')$ as a function DC bias field for sample A4 for different amplitudes.

4.2.2C. FREQUENCY DEPENDENCE OF $\chi'(H)$ AND $\chi''(H)$ LOOPS:

The frequency dependence of the $\chi'(H)$ and $\chi''(H)$ loops has also been studied in depth. Here a frequency range of few hundred Hz to 100 KHz has been considered. As discussed in Chapter 2, in describing the experimental arrangement that the coil set-up had a resonance frequency (due to self capacitance of the coil) close to 40 KHz and measurements at higher frequencies than this may not be acceptable. However, as here the effort was not to carry out absolute measurements but to study the relative changes in the shape of the $\chi'(H)$ and $\chi''(H)$ loops, it is probably not problematic to consider the higher frequencies too. It must be remembered that any non-linearity and capacitive drift at high frequencies were not expected to be a function of DC bias field. Thus the relative comparison as attempted here may not be erroneous so long as one confines to see the trend in the variation due to frequency only. As will be discussed in due course, that though here experimental data for frequencies higher than 40 KHz have been included, they are not must for making any conclusion. Further, it will also be seen that there was no discontinuity in the behavior of the loops over the change of frequency from few tens of Hz to few tens of KHz, rather a systematic variation of the shapes of the loops with frequency was seen in almost all samples. This merely indicated the same fact as above, i.e., that the offset and the non-linearity (as expected at higher frequencies) of coil set-up did not change with the DC bias field.

In figures 4.2.14(a,b) and 4.2.15(a,b) the $\chi'(H)$ and $\chi''(H)$ loops have been plotted for different frequencies for sample A1(pure) for an amplitude of 0.3 mT. It is quite clear from these figures (4.2.14a and 4.2.15a) that the shape of the $\chi'(H)$ loops, excluding the ZCOF, remained almost independent of frequency, while the depths of these loops initially decreased upto a frequency of 3777 Hz and then became almost constant in between 3777 Hz to 57770 Hz. Above 57770 Hz the depths started to increase significantly. The ZCOF also showed significant dependence on frequencies, particularly at low frequency range. The width of the ZCOF decreased and vanished as the frequency increased to 9777 Hz and ZCOF became almost a straight line. With further increase in frequency the length of the ZCOF line increased upto a frequency of 17777 Hz. In fact the length of the ZCOF showed a peculiar evolution with frequencies and it was difficult to explain its variation.

Though the basic shape of the $\chi''(H)$ loops, like the $\chi'(H)$ loops, did not change with

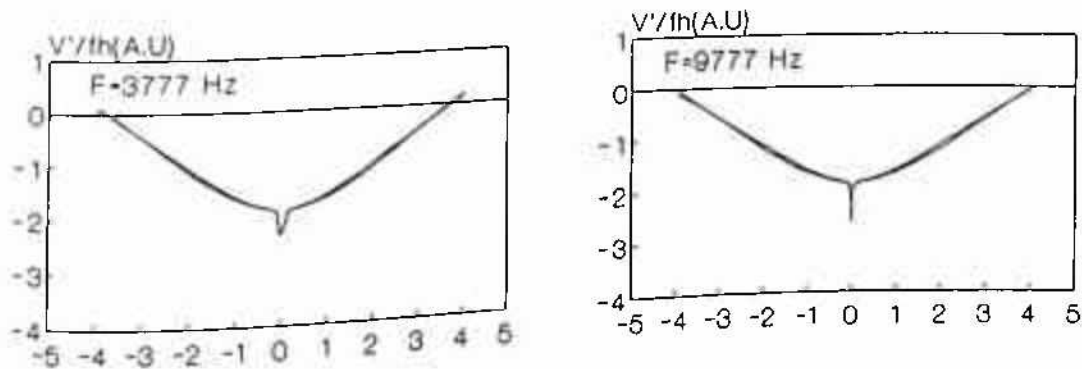
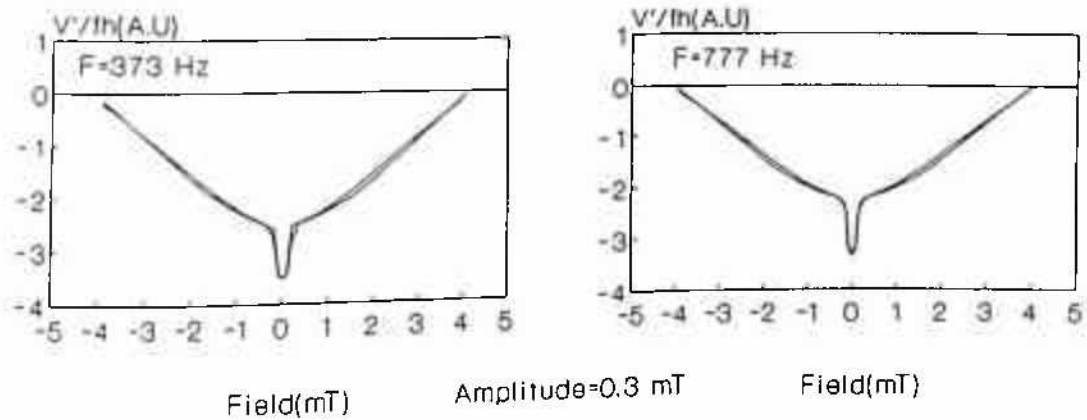


Figure 4.2.14a: V'/fh as a function of DC bias field for different frequencies.(sample A1)

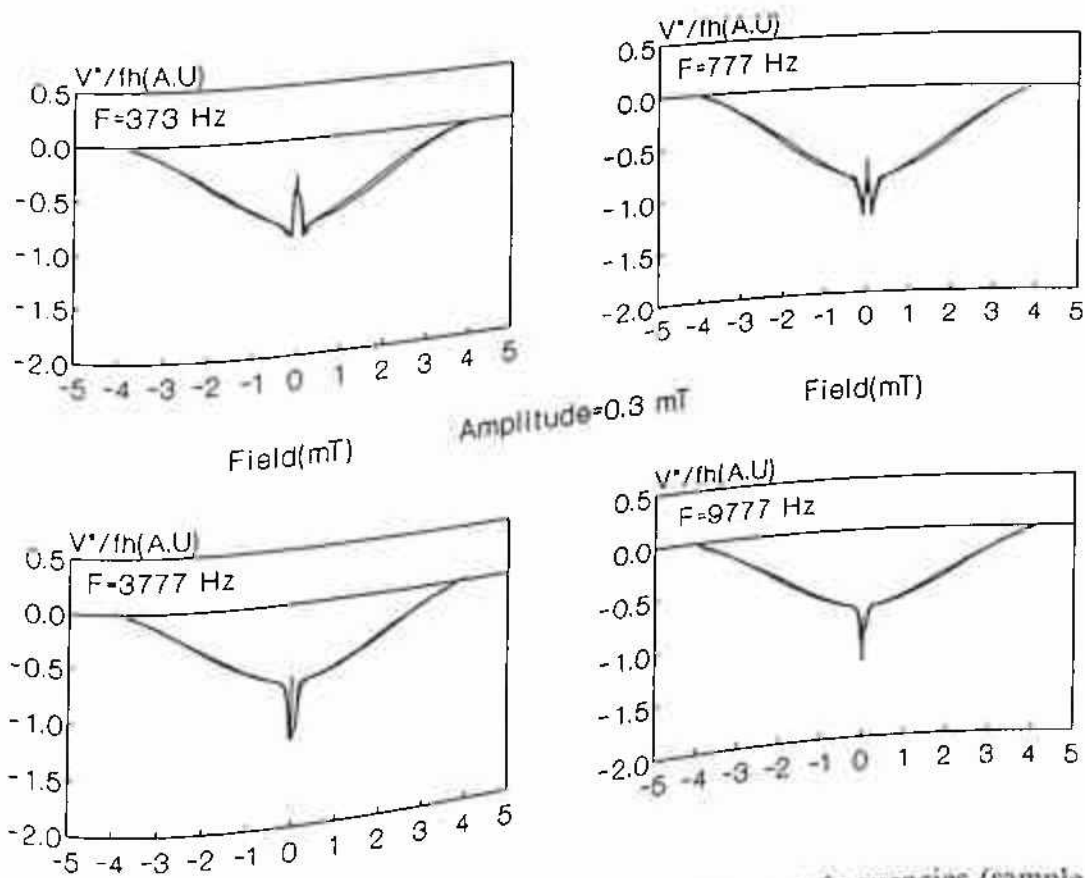
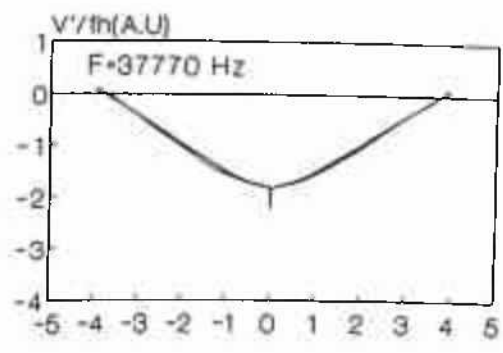
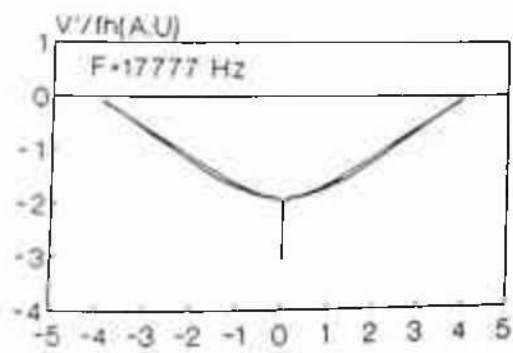


Figure 4.2.14b: V''/fh as a function of DC bias field for different frequencies.(sample A1)



Field(mT)

Amplitude=0.3 mT

Field(mT)

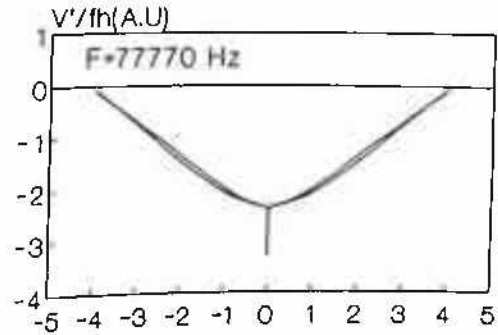
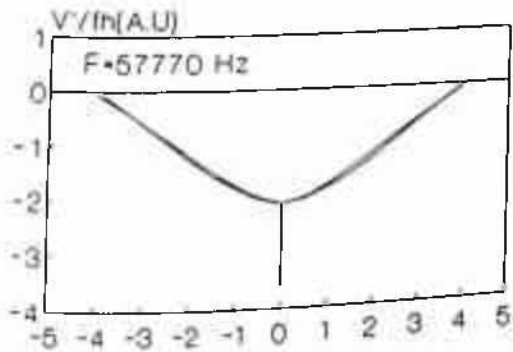
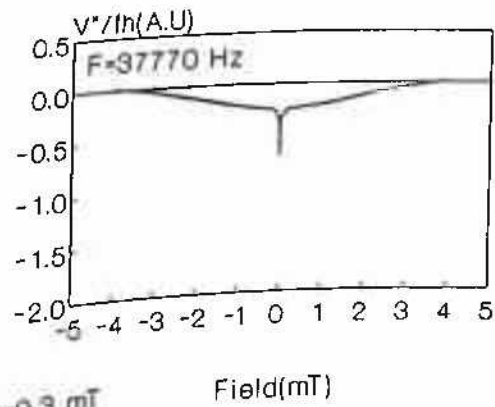
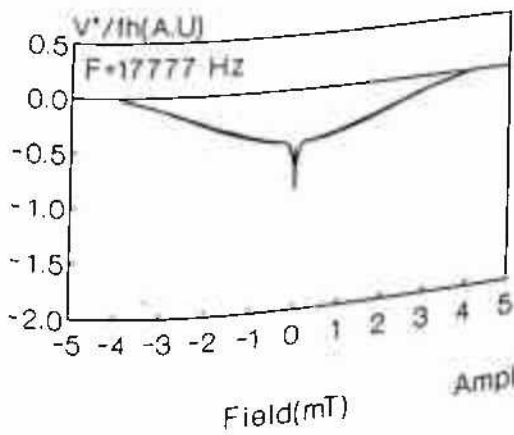


Figure 4.2.15a: V''/fh as a function of DC bias field for different frequencies. (sample A1)



Field(mT)

Amplitude=0.3 mT

Field(mT)

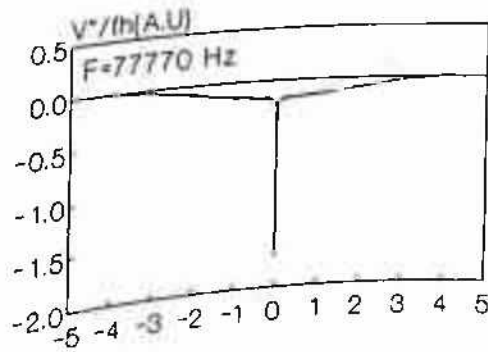
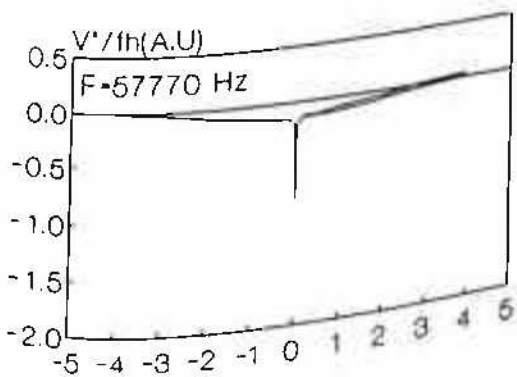


Figure 4.2.15b: V''/fh as a function of DC bias field for different frequencies. (sample A1)

frequency, once again the ZCOF showed strong variation with frequency. At the lower side of the frequencies, the ZCOF appeared as a peak in the upward direction. But as the frequency increased, the ZCOF came down and at around 37770 Hz ZCOF appeared as a sharp valley in the downward direction. However, at a sufficiently high frequency ZCOF increased drastically. But the height of the $\chi''(H)$ loops decreased almost monotonically with increasing frequency.

In figure 4.2.16(a,b) the $\chi'(H)$ and $\chi''(H)$ loops as in figure 4.2.14, have been plotted for the same sample(A1) but for a lower amplitude of 0.012 mT. It is clear from these figures that even at this amplitude the shapes of the real loops (excluding the ZCOF) were almost invariant (the hysteresis seen at 57770 Hz was due to the capacitive drift with time). The shapes of the $\chi''(H)$ loops as can be seen in the figure 4.2.16b were strongly dependent on frequency (the variation can be clearly seen if one plot the same curves removing the ZCOFs) and in the higher frequency range the $\chi''(H)$ loops took a downward curvature in contrast to the upward curvature as was seen in the lower frequency range for this amplitude. It is to be remembered that for the highest amplitude (0.3 mT) case, the curvature of the $\chi''(H)$ loops were upward at all frequencies considered here (figures 4.2.14b and 4.2.15b).

It will be now instructive to consider the same frequency dependence for the higher DC field ranges. In figure 4.2.17(a,b) the $\chi'(H)$ and $\chi''(H)$ loops as in figure 4.2.14 have been plotted for a field range of 8 mT for sample A1 with an AC amplitude of 0.3 mT. It is important to see that in this DC field range the frequency dependence of $\chi'(H)$ loops was not much different than what was seen in the low DC field range and within the range of frequency considered here, the $\chi'(H)$ loops including their shapes and hysteresis remained almost unchanged. But the $\chi''(H)$ loops showed strong dependence on frequency. Along with this decrease of the ZCOF) of the loops diminished with increase in frequency. As with this decrease of height, the hysteresis as apparent in figure 4.2.17b, decreased with increase in frequency.

The similar dependence on frequency was seen in sample A2 (2% PbO doped YBCO) as shown in figure 4.2.18(a,b) and 4.2.19 (only imaginary part) for the low range of DC field and for amplitude of 0.3 mT and 0.012 mT respectively. It can be seen in figure 4.2.18 that just like the sample A1 (pure), the depths of $\chi'(H)$ loops were almost independent of frequency whereas the $\chi''(H)$ loops showed more pronounced change with frequency as compared to sample A1(Pure). It was also seen in this case of sample A2, that in the lower amplitude case

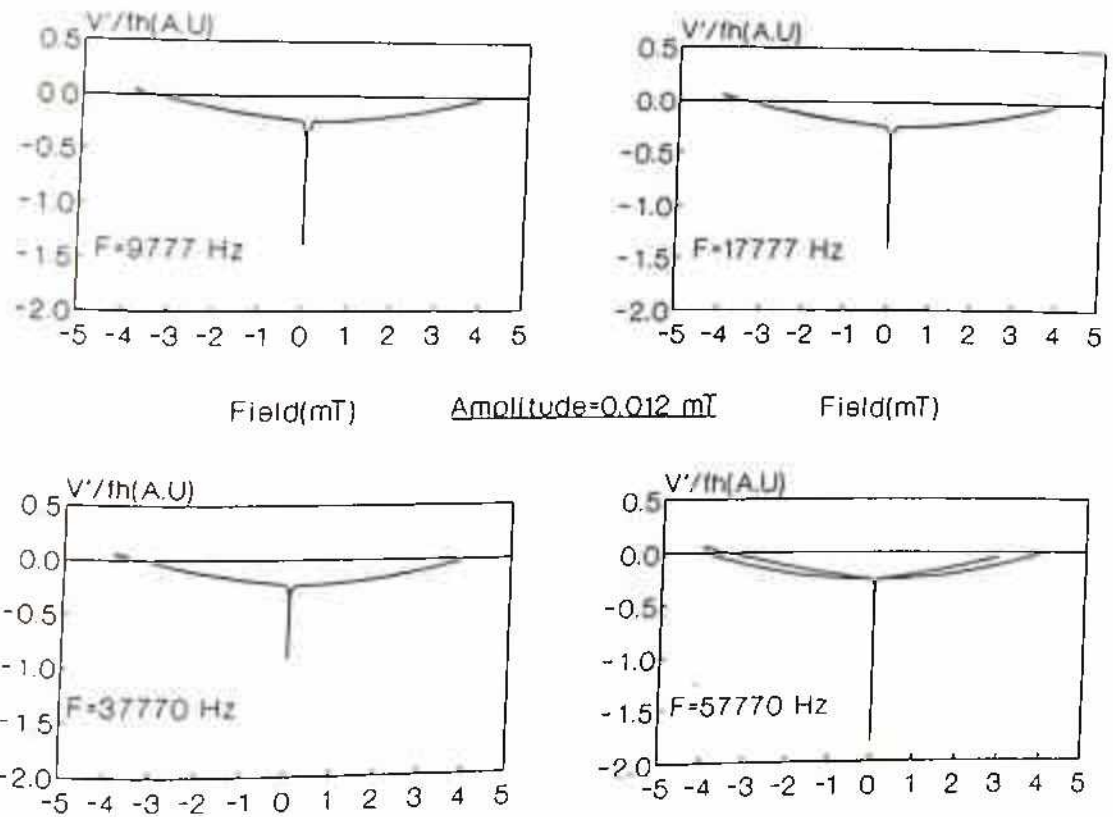


Figure 4.2.16a: V'/fh as a function of DC bias field for different frequencies.(sample A1)

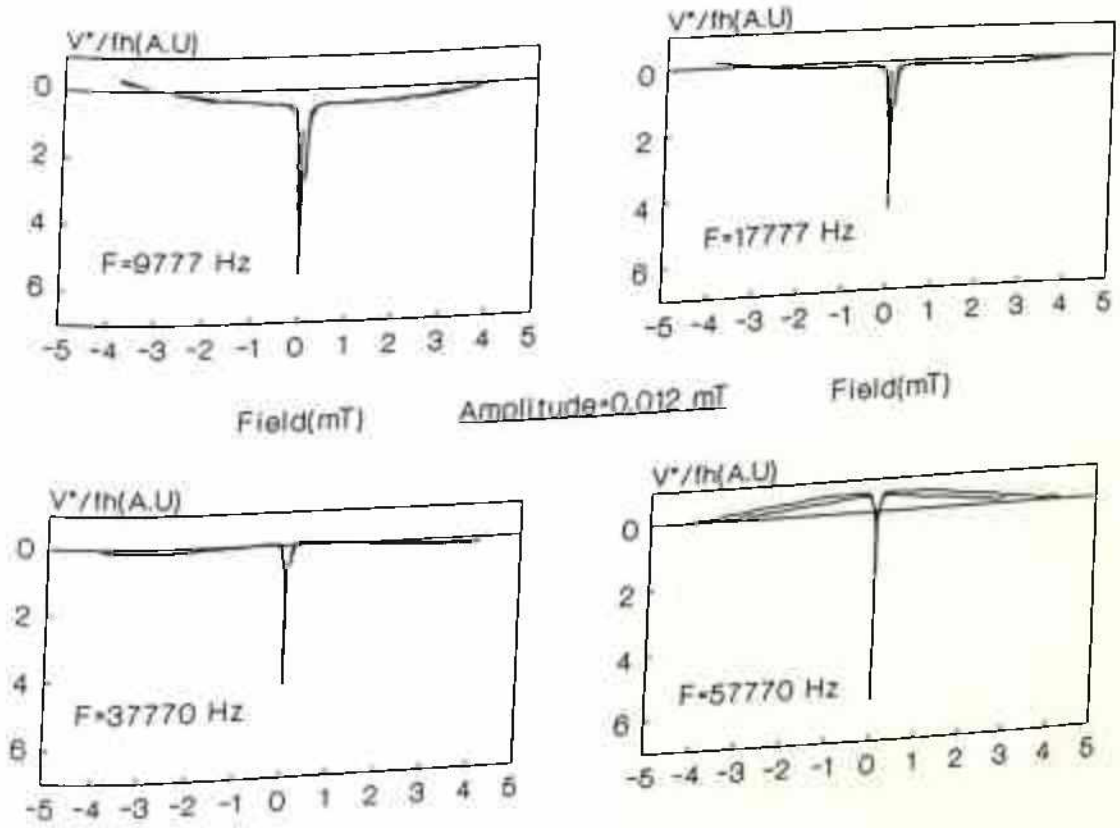
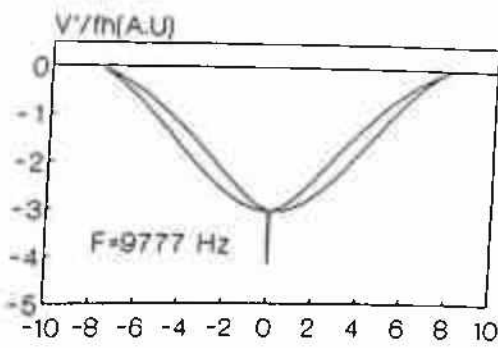
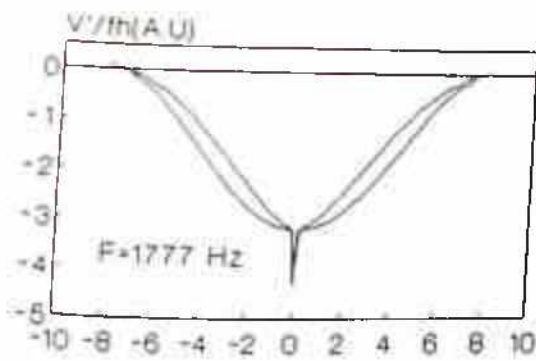


Figure 4.2.16b: V''/fh as a function of DC bias field for different frequencies.(sample A1)



Field(mT)

Amplitude=0.3 mT

Field(mT)

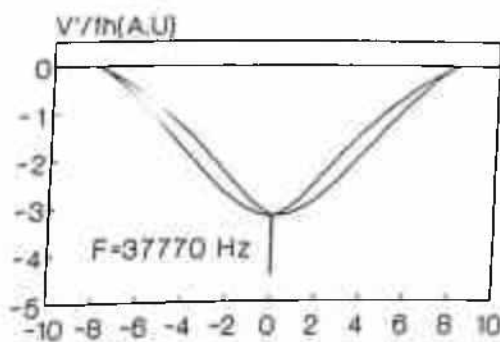
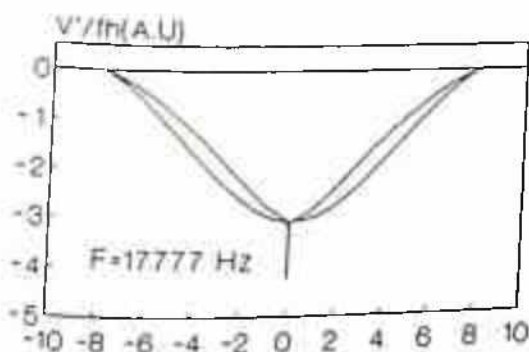
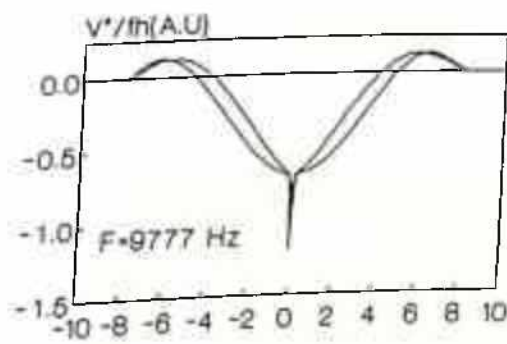
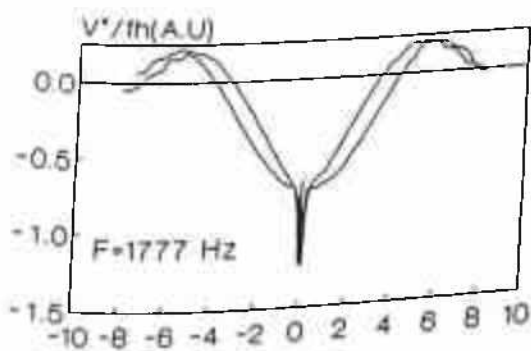


Figure 4.2.17a: V'/fh as a function of DC bias field for different frequencies.(sample A1)



Field(mT)

Amplitude=0.3 mT

Field(mT)

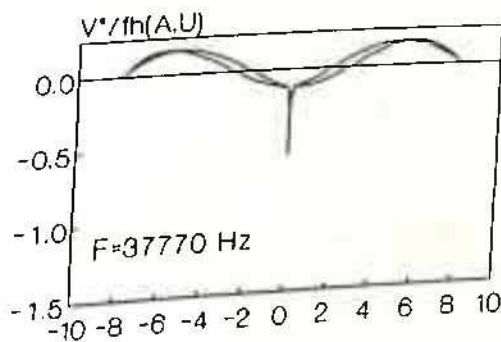
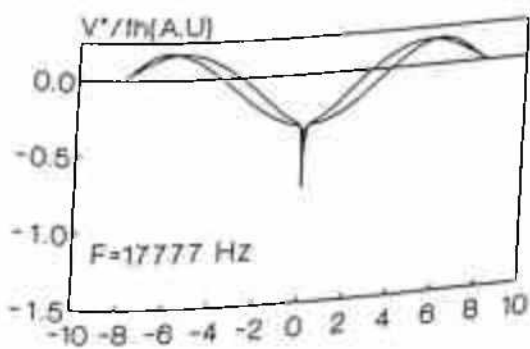


Figure 4.2.17b: V''/fh as a function of DC bias field for different frequencies.(sample A1)

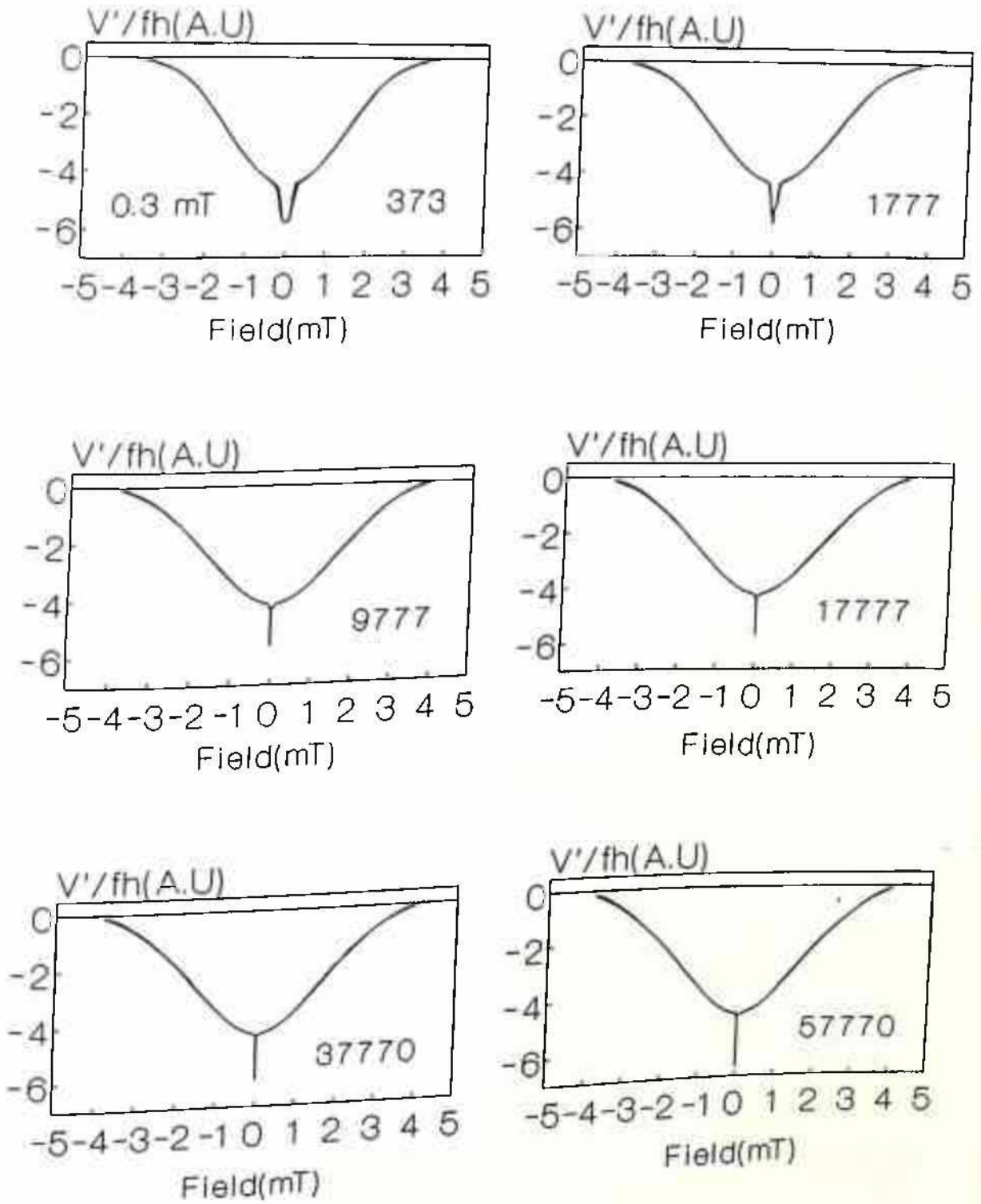


Figure 4.2.18a: V'/fh as a function of DC field for different frequencies(indicated by numbers).(Sample A2)

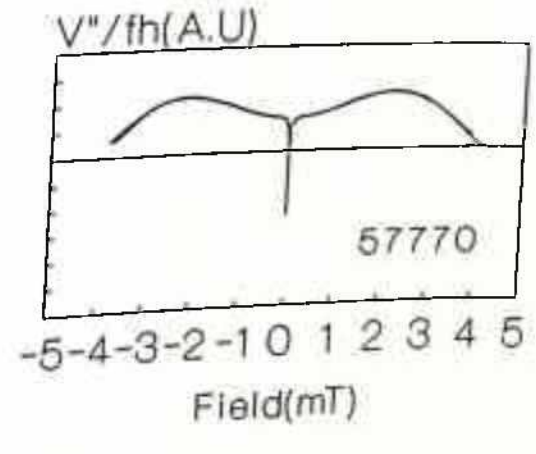
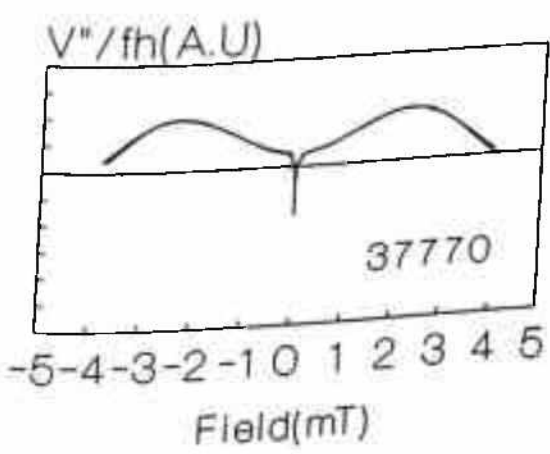
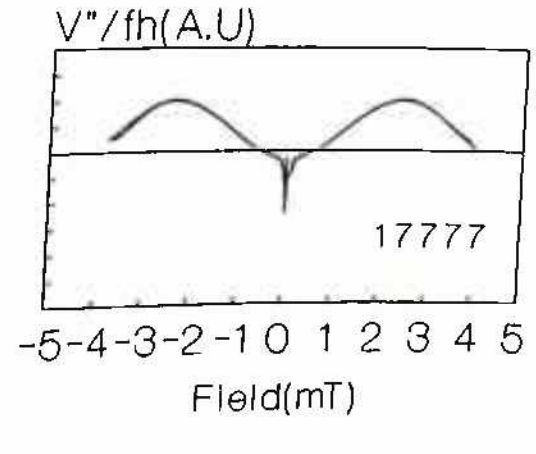
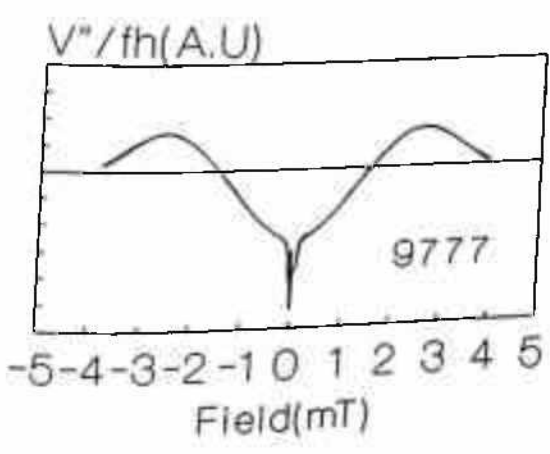
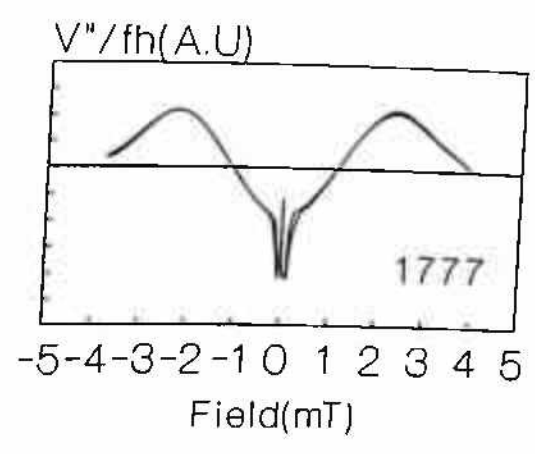
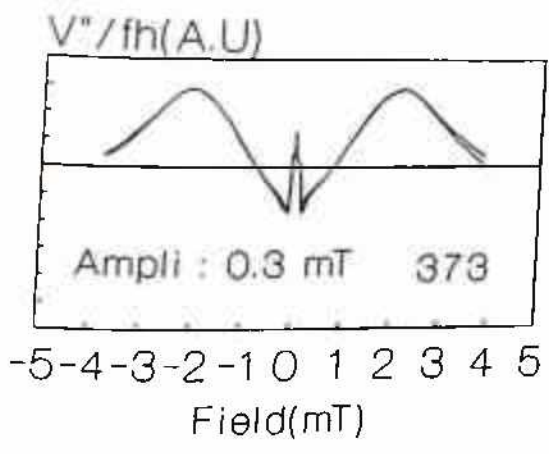


Figure 4.2.18b: V''/fh as a function of DC field for different frequencies(indicated by numbers).(Sample A2)

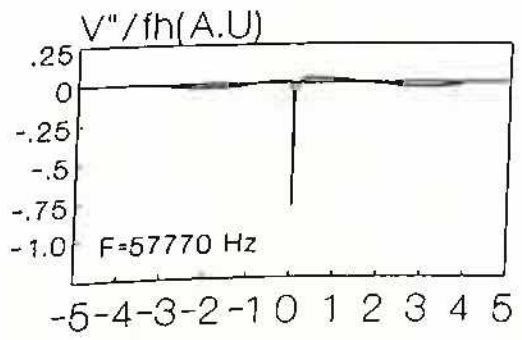
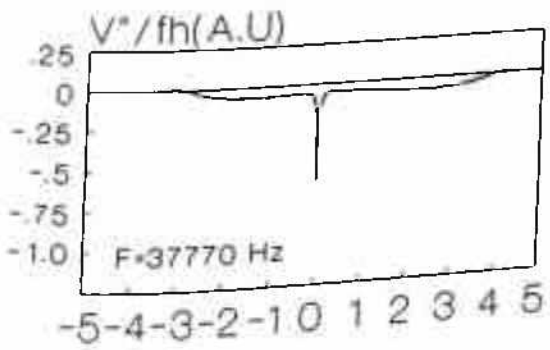
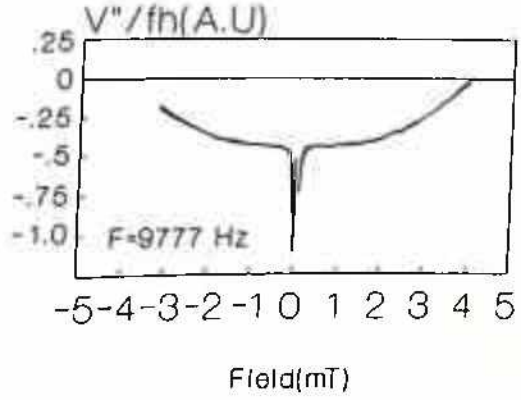
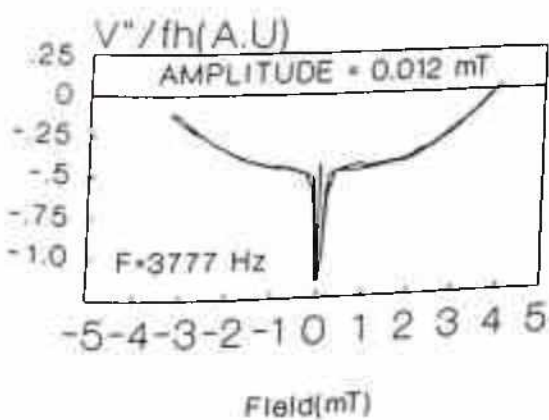
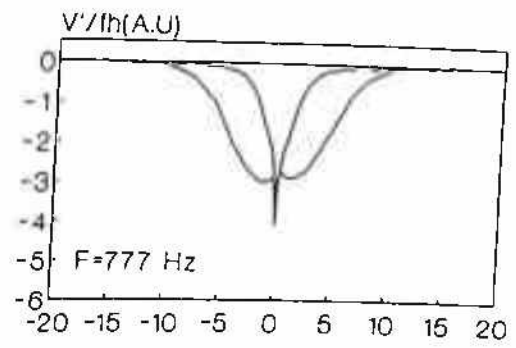
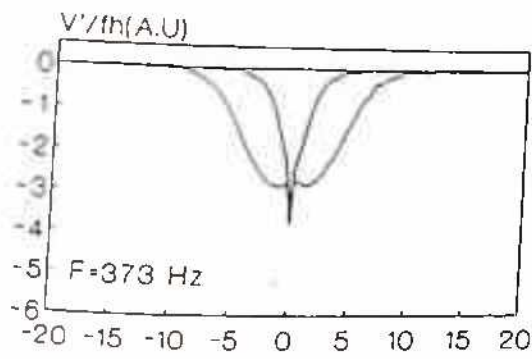


Figure 4.2.19: V''/fh as a function DC bias field for different frequencies.(Sample A2)

the upward curvature of the $\chi''(H)$ loops (figure 4.2.19) appeared at a higher frequency as compared to sample A1 (figure 4.2.16b).

In figure 4.2.20(a,b) and 4.2.21(a,b) the $\chi'(H)$ and $\chi''(H)$ loops for sample A2 (2% PbO doped YBCO) have been plotted for 18 mT of DC field range and for amplitude of 0.3 mT. In case of the high DC field range, the $\chi'(H)$ loops showed systematic dependence on frequencies. Like in figure 4.2.20a and 4.2.21a the depths of the loops (excluding ZCOF) were almost monotonically increasing as a function of frequency. It was further seen that the widths (measured at given value of χ') of the $\chi'(H)$ loops also increased with increase in the frequency. In case of $\chi''(H)$ loops (figure 4.2.20b) the heights of the loops for frequencies higher than 1777 Hz showed an increasing trend with frequencies. But below 1777 Hz (e.g. 373 to 777 Hz) there was a decrease in this height. The important observation in frequency dependence of $\chi''(H)$ loops was centered around the zero bias point. In the case of AC amplitude dependence of $\chi''(H)$ as described above in section 4.2.2b) where the peaks shifted closer to zero bias point with the increase in the AC amplitude and thus the valley at the origin (not the ZCOF) disappeared at higher amplitude. Here a similar disappearance (or diminishing) of the central valley was seen at higher frequency (figures 4.2.20b and 4.2.21b - from 373 Hz to 77770 Hz). However, here the positions of the peaks (both P1 and P2) with respect to the DC bias field were almost independent of frequency. It was seen that the substantial shift of the valley started around 17777 Hz. Apart from this variation of $\chi''(H)$ loops, ZCOF remained the same, i.e., from an upward peak at lower frequencies to a sharp downward valley at higher frequencies.

But the $\chi'(H)$ loops in the same DC field range but lower AC amplitudes (0.06 and 0.012 mT) for the same sample(A2) showed a different trend. This can be seen in figure 4.2.22(a,b) and 4.2.23(a,b) where same loops as in figure 4.2.20 have been plotted for amplitudes 0.06 and 0.012 mT respectively. For amplitude of 0.06 mT (figure 4.2.22a), the $\chi'(H)$ loops did not change much and the systematicity, if any, was difficult to find. But the imaginary part (figure 4.2.22b) was similar to the higher amplitude (0.3 mT) case (figure 4.2.20b, 4.2.21b) and showed large shift of the central valley in the upward direction. However, the heights of the $\chi''(H)$ loops (distance between the top and bottom of the curves excluding the ZCOF) was less dependent on frequency than the higher amplitude case (figure 4.2.20b and 4.2.21b). In the lowest amplitudes case of 0.012 mT (figure 4.2.23a), the $\chi'(H)$ loops apparently showed an opposite behavior to



Field(mT)

Amplitude=0.3 mT

Field(mT)

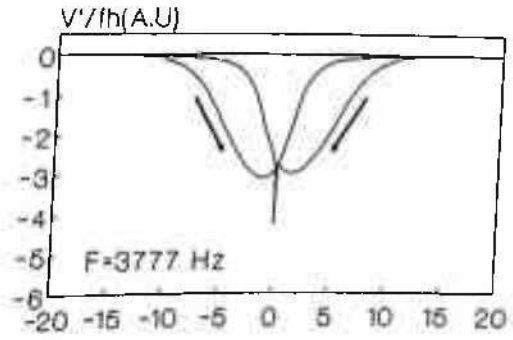
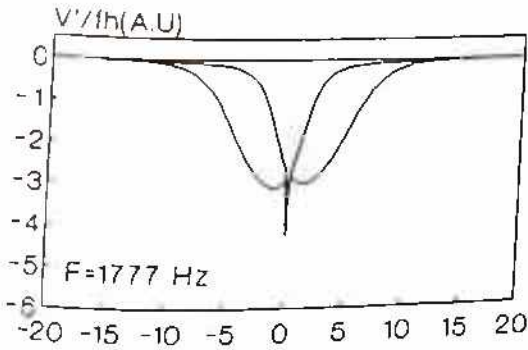
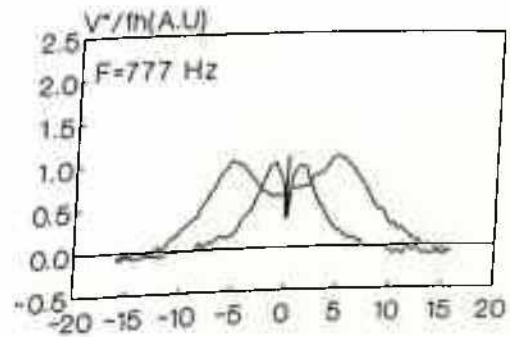
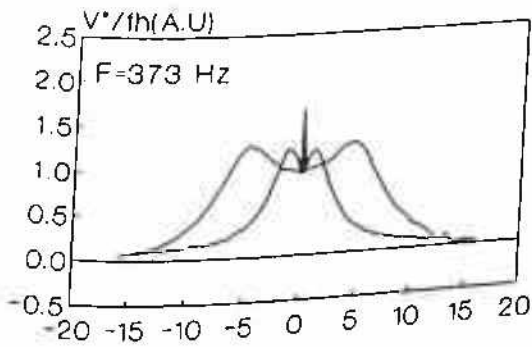


Figure 4.2.20a: V'/fh as a function of DC bias field for different frequencies.(sample A2)



Field(mT)

Amplitude=0.3 mT

Field(mT)

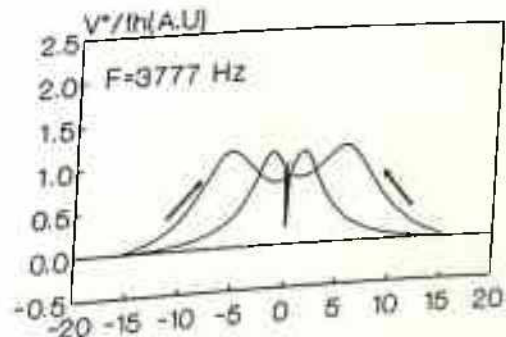
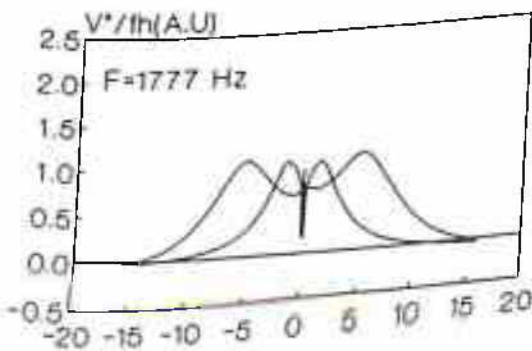
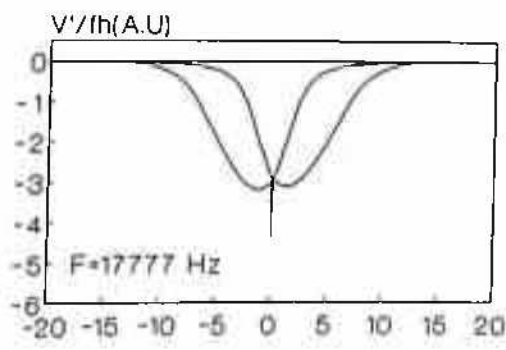
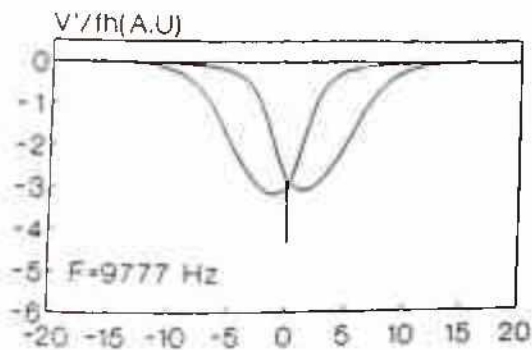


Figure 4.2.20b: V''/fh as a function of DC bias field for different frequencies.(sample A2)



Field(mT)

Amplitude=0.3 mT

Field(mT)

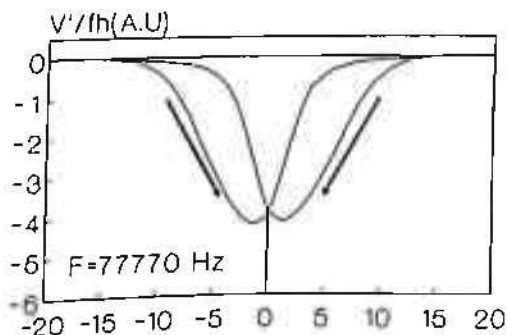
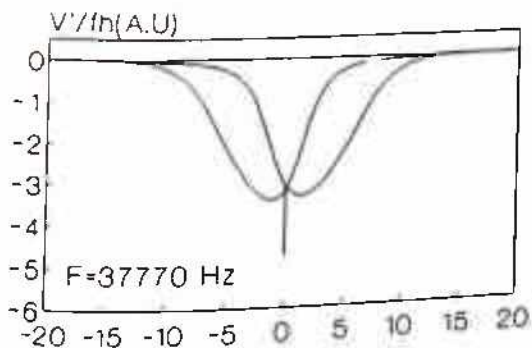
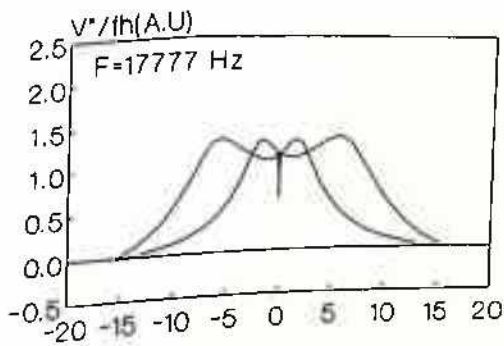
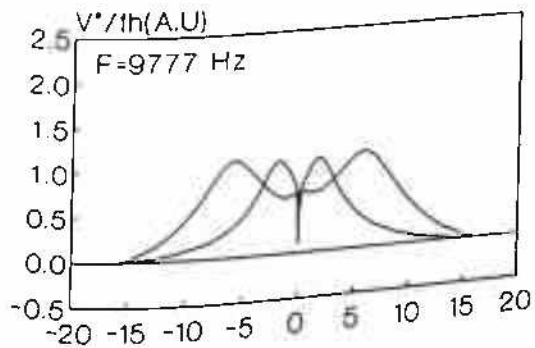


Figure 4.2.21a: V''/fh as a function of DC bias field for different frequencies.(sample A2)



Field(mT)

Amplitude=0.3 mT

Field(mT)

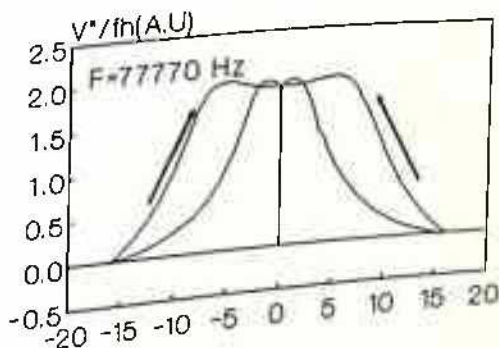
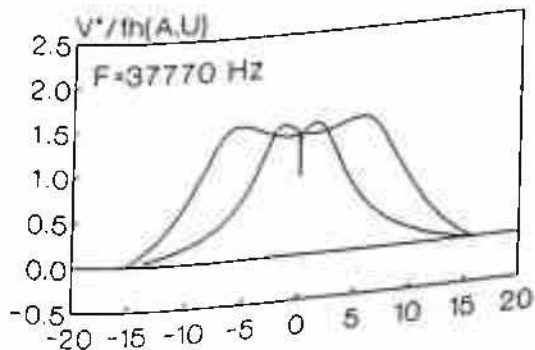


Figure 4.2.21b: V''/fh as a function of DC bias field for different frequencies.(sample A2)

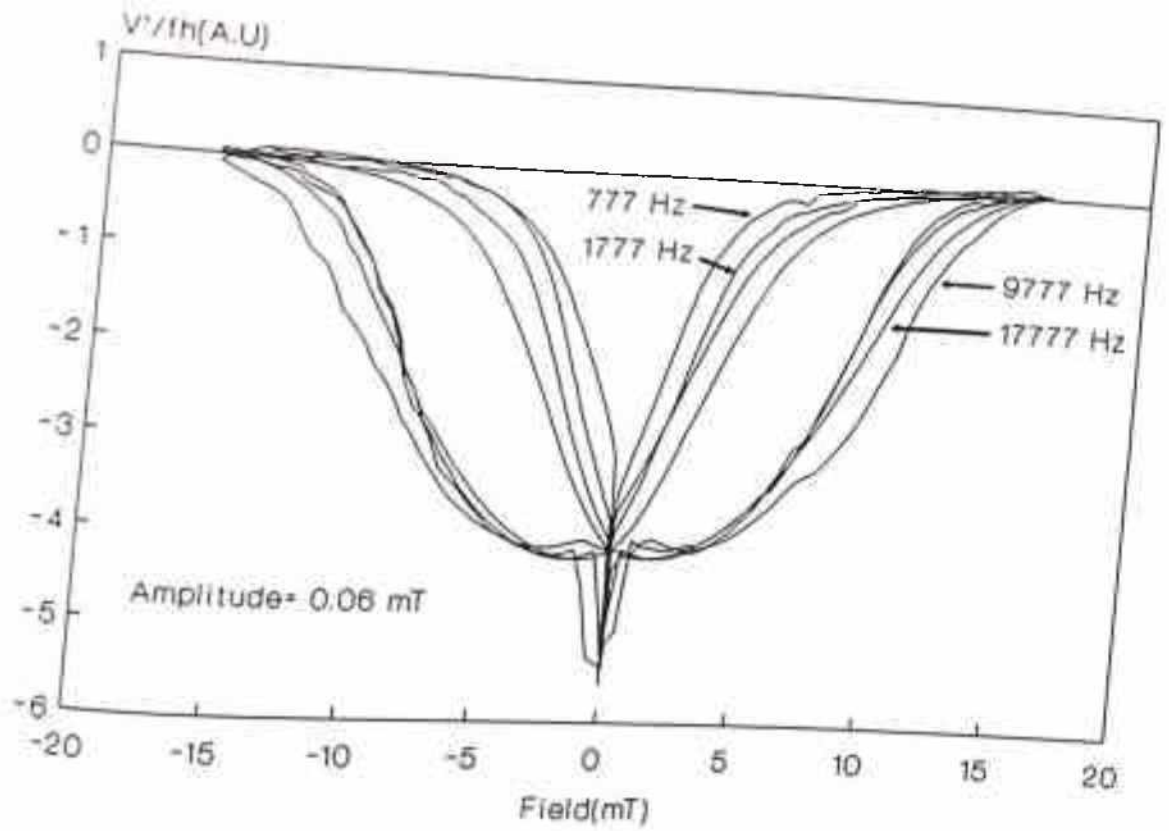


Figure 4.2.22a: V'/fh as a function of DC bias field for different frequencies. (sample A2)

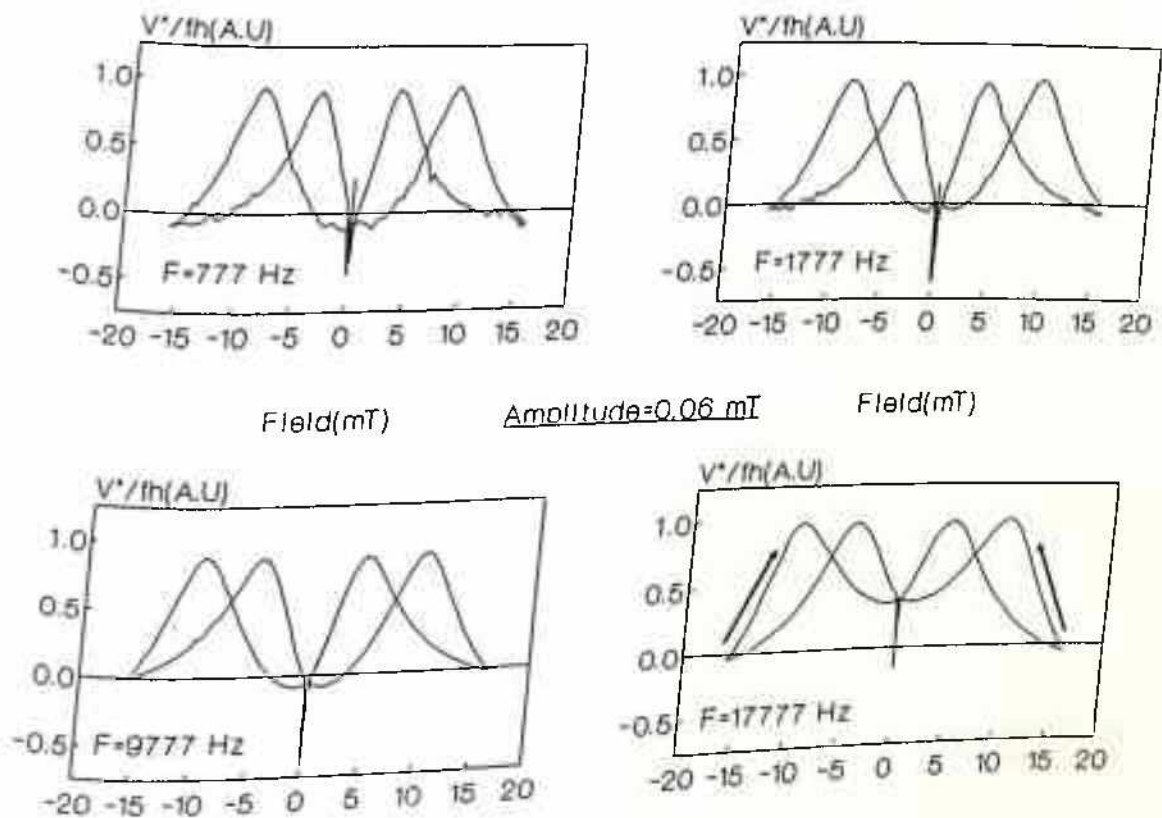


Figure 4.2.22b: V'/fh as a function of DC bias field for different frequencies. (sample A2)

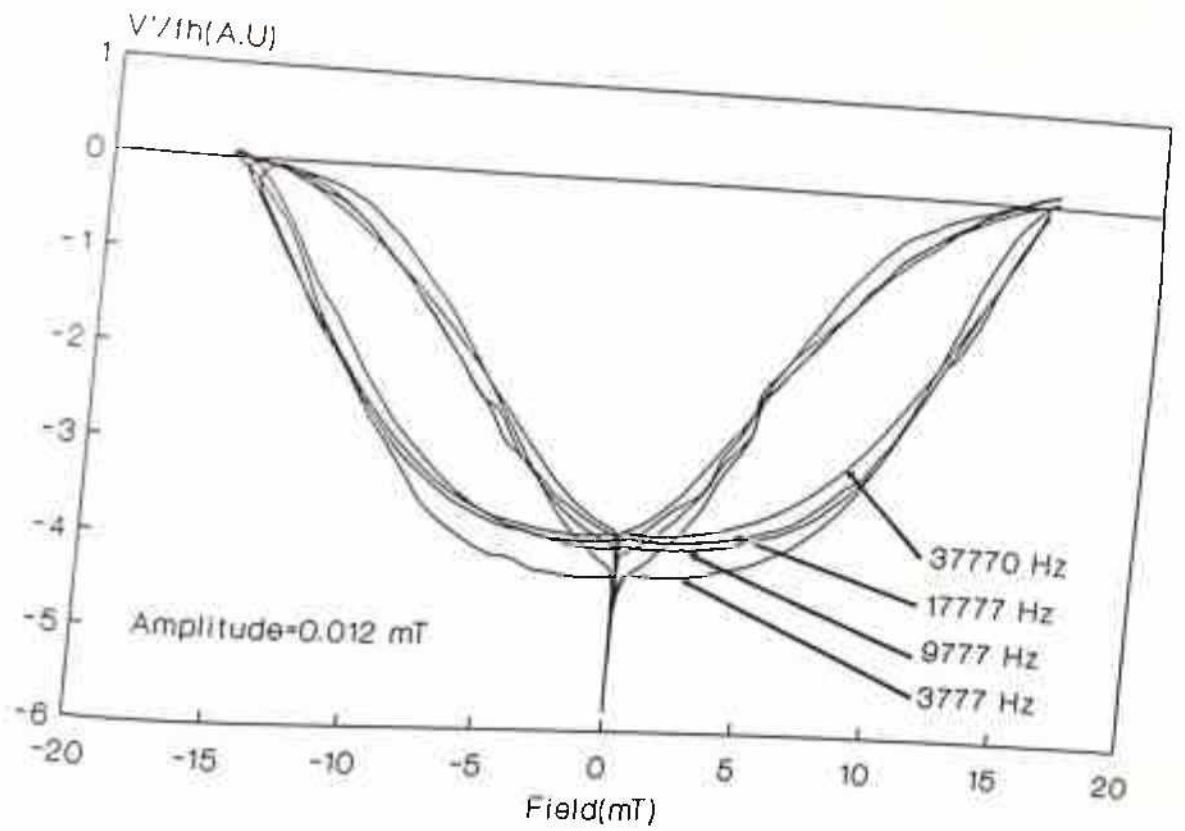


Figure 4.2.23a: V'/fh as a function of DC bias field for different frequencies. (sample A2)

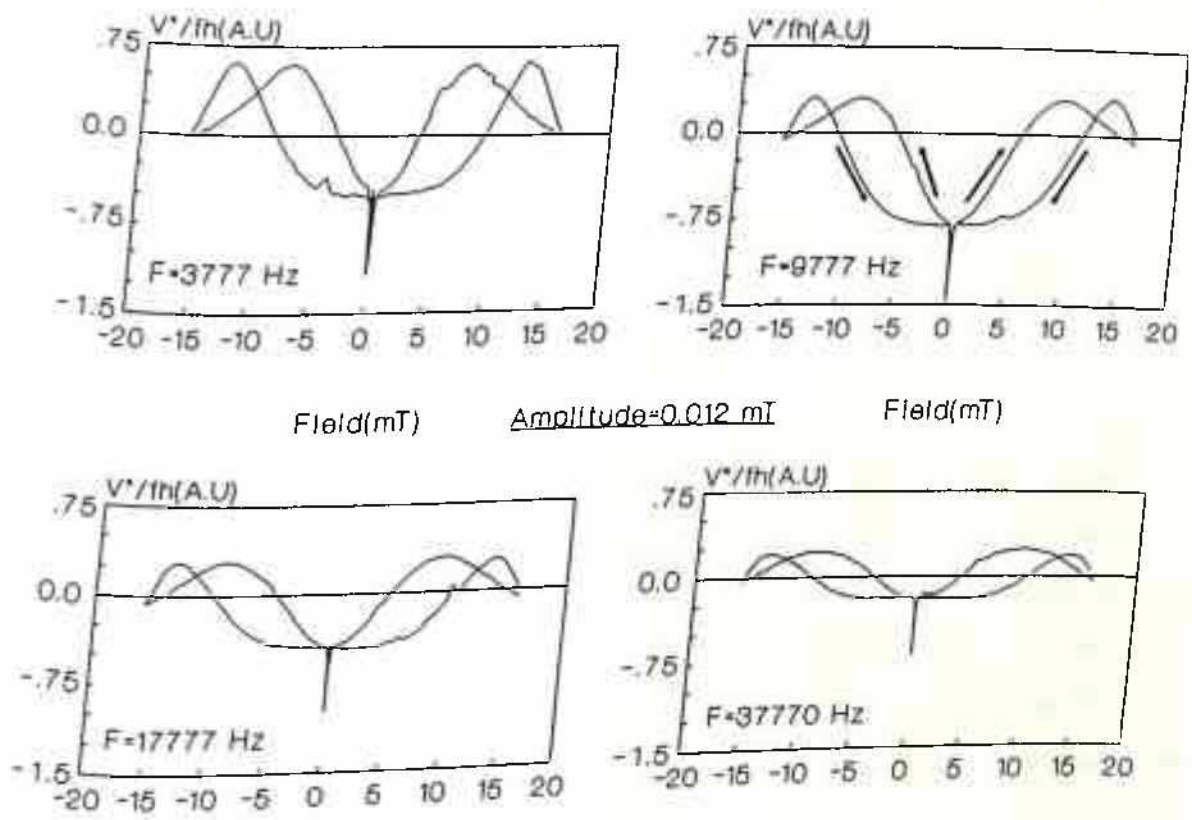


Figure 4.2.23b: V''/fh as a function of DC bias field for different frequencies. (sample A2)

that at the highest amplitude of 0.3 mT. Particularly, the depths, instead of increasing with increasing frequency as in the highest amplitude case, decreased with increase of frequency (figure 4.2.23a). The same behavior was seen in $\chi''(H)$ loops also (figure 4.2.23b). Here also, unlike the highest amplitude case, the height of the loops decreased rapidly at higher frequencies and the central valley was seen to be present even at 37770 Hz. This brought out one more important point of the frequency dependence by comparing the frequency dependence at the two extreme amplitudes, i.e., 0.3 mT (figure 4.2.20 and 4.2.21) and 0.012 mT (figure 4.2.23). It has already been explained that while at an amplitude of 0.3 mT, the depth of the $\chi'(H)$ loops and the height of the $\chi''(H)$ loops were monotonically increasing function of frequency, at an amplitude of 0.012 mT both of them were decreasing function of frequency. This finding is very important and indicates the presence of some kind of cross-over amplitude or critical amplitude below and above which the frequency dependence is exactly opposite.

The systematic frequency dependence of $\chi'(H)$ and $\chi''(H)$ loops as stressed above is an unique finding and is being reported for the first time.

At low amplitudes, the experimental setup was not as sensitive as at high amplitude and for this it was not possible to consider low frequencies with lower amplitudes. To elucidate this systematic dependence on frequency a careful study at an amplitude 0.3 mT has been made with quasistatic variation of DC field for the sample A2 (2% PbO doped YBCO). The results are shown in figure 4.2.24(a,b) where loops for all the frequencies have been drawn on a single frame. As this was the high AC amplitude case, the systematic increase in depths of $\chi'(H)$ loops (figure 4.2.24a) and in height of $\chi''(H)$ loops (figure 4.2.24b) have been clearly demonstrated. As already discussed, there was no discontinuity in the observed dependence on the frequency, can be justified from these figures 4.2.24a and 4.2.24b.

The effect of frequency became substantial only around 17777 Hz or higher. However, this frequency could be anywhere between 9777 Hz to 17777 Hz since no measurements were done in this frequency range. Though the resonance frequency of the coil setup was stated to be quite higher than this frequency range, however one would like to see the effect of frequency to be present even in frequency range below 17777 Hz. The different frequency dependence at different amplitudes, as seen in the data here indicated a complicated interaction of FLL in an oscillatory field. Without going into complexity involved in the process, it is probably not

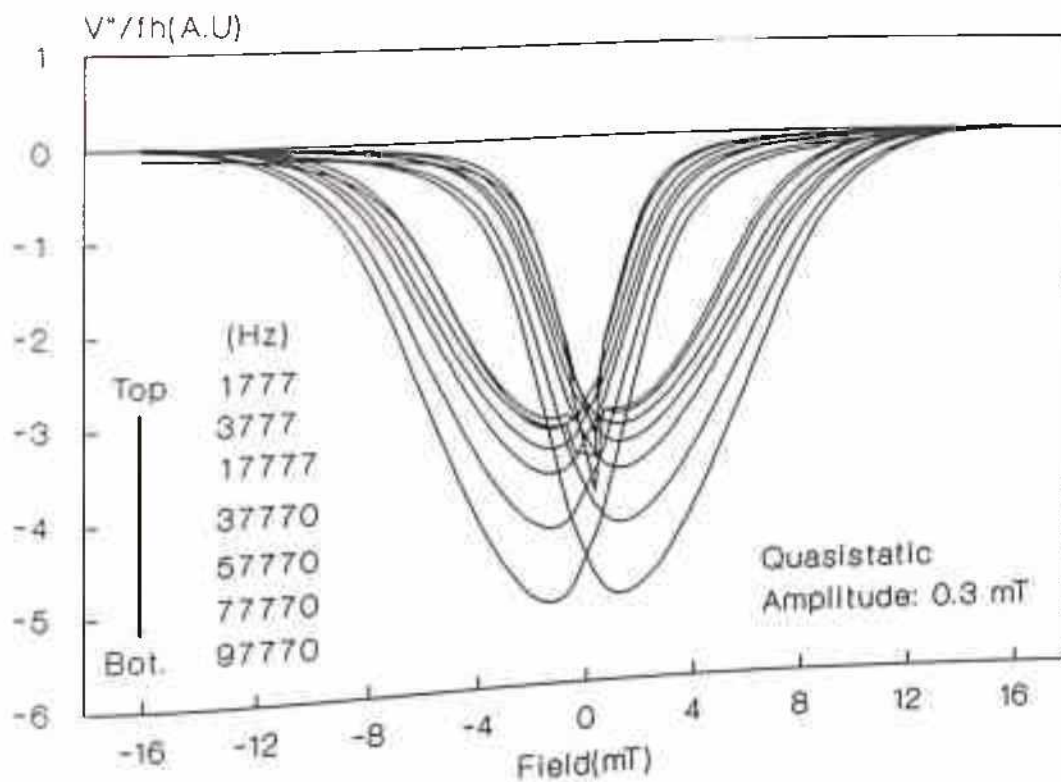


Figure 4.2.24a: V''/fh as a function of DC bias field for different frequencies. (sample A2)

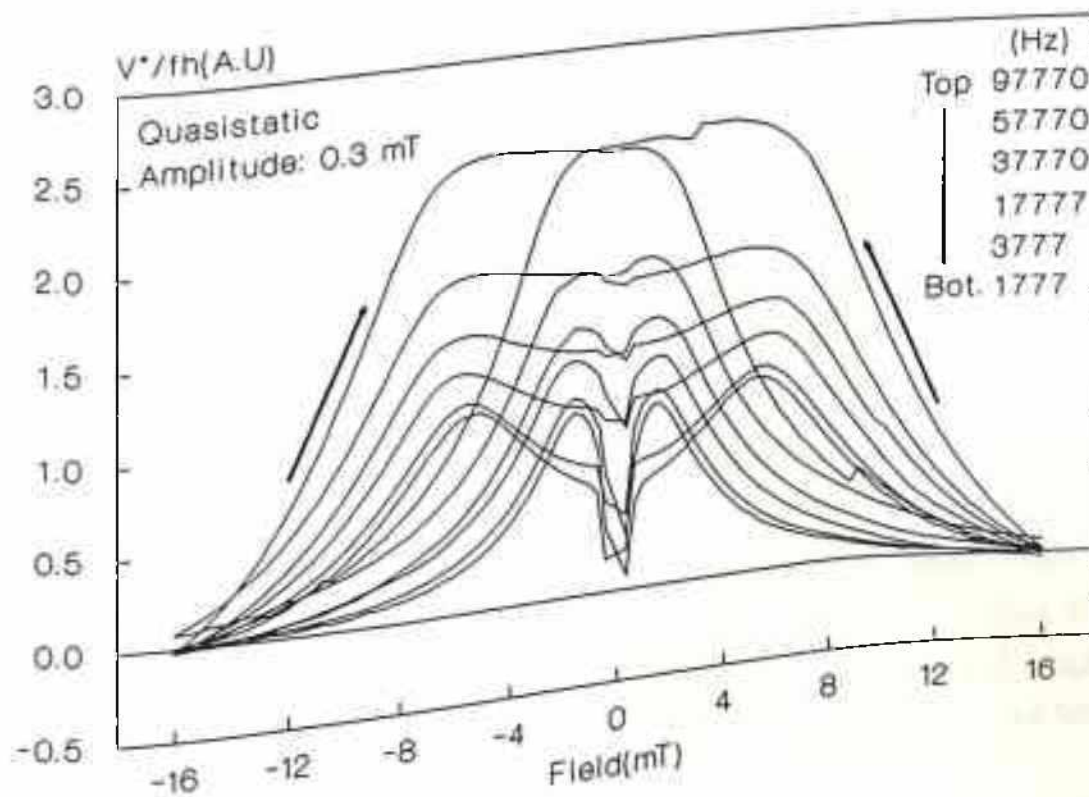


Figure 4.2.24b: V''/fh as a function of DC bias field for different frequencies. (sample A2)

improper to expect to see the effect of frequency at a lower frequency range in samples with lowest J_c values than the already considered sample.

With this view in mind, in figure 4.2.25(a,b) the $\chi'(H)$ and $\chi''(H)$ loops for the sample A4(10% PbO doped YBCO) have been plotted for an amplitude of 0.3 mT. It is obvious from this figure that 0.3 mT was too high an amplitude for this sample. This was also confirmed in the amplitude study as given earlier. It is quite important that the strong dependence on frequency was clear in $\chi''(H)$ loops where the heights of the loops were monotonically increasing with increase in frequency from 373 to 17777 Hz. In comparison to figure 4.2.24b for sample A2 (upto a frequency of 97770 Hz), the dependence on frequency of $\chi''(H)$ loops as seen here was more pronounced and seen at a quite lower frequency range. In case of $\chi'(H)$ loops, while at low frequencies ZCOFs were wider than other samples, they became narrower like other samples at higher frequencies. But the lengths of the ZCOFs, once again did not show much systematicity. However, it can be seen that the depths of the loops (excluding the ZCOFs) were increasing with increasing frequency and the variation was larger than that seen in sample A2 (figure 4.2.24a).

The effect of frequency at lower amplitudes for the same sample(A4) as above, can be seen in figure 4.2.26(a,b) and 4.2.27(a,b). As expected, with decrease of amplitude the dependence on frequency became less. This can be seen in figure 4.2.26a where the change in depth of $\chi'(H)$ loops (excluding the ZCOF) with frequency was less (around 40% from 777 to 9777 Hz) than that at amplitude of 0.3 mT (where the change was around 70% in the same frequency range) and with further decrease in amplitude to 0.012 mT as seen in figure 4.2.27a, the change in depth of $\chi'(H)$ loops with frequency became still smaller. Further important point in figure 4.2.26b was the narrowing of the central region even with increase of frequency from 777 to 9777 only, along with increase in heights of the loops with increasing frequency. At the lowest amplitude, the $\chi''(H)$ loops showed a valley(V) in the central region and it was seen that once again the depth of this valley decreased substantially 9777 Hz. This apparently indicated that with decrease of amplitude, the effect of frequency was less pronounced. It is further to be noticed that in this sample(A4), the cross-over amplitude might be lower than 0.012 mT and hence even at this amplitude increasing trend of depths of $\chi'(H)$ loops and heights of $\chi''(H)$ loops were seen. This finding is in line with the argument that the sample A4 had the lowest

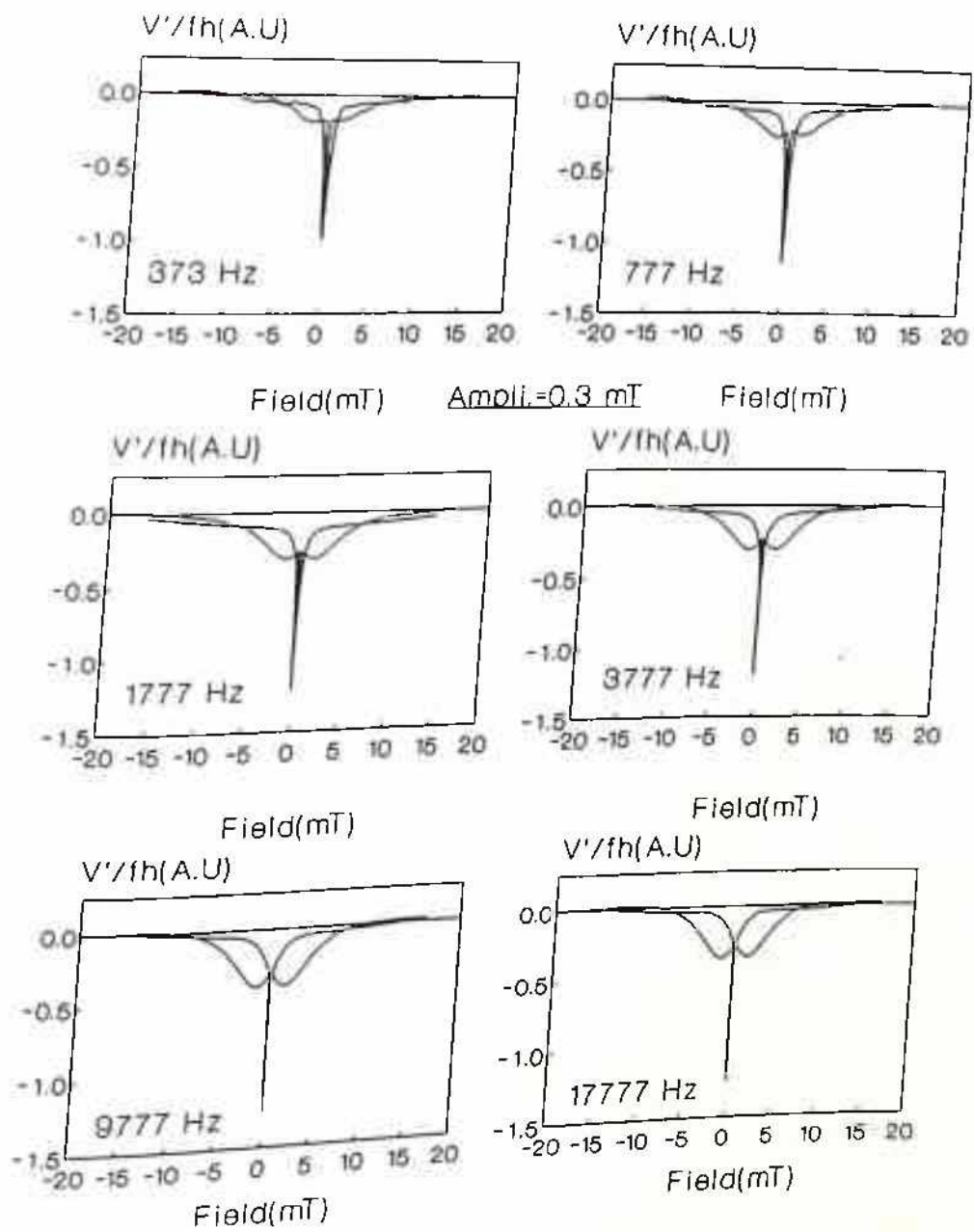


Figure 4.2.25a: V'/fh as function of DC bias field for different frequencies. (Sample A4)

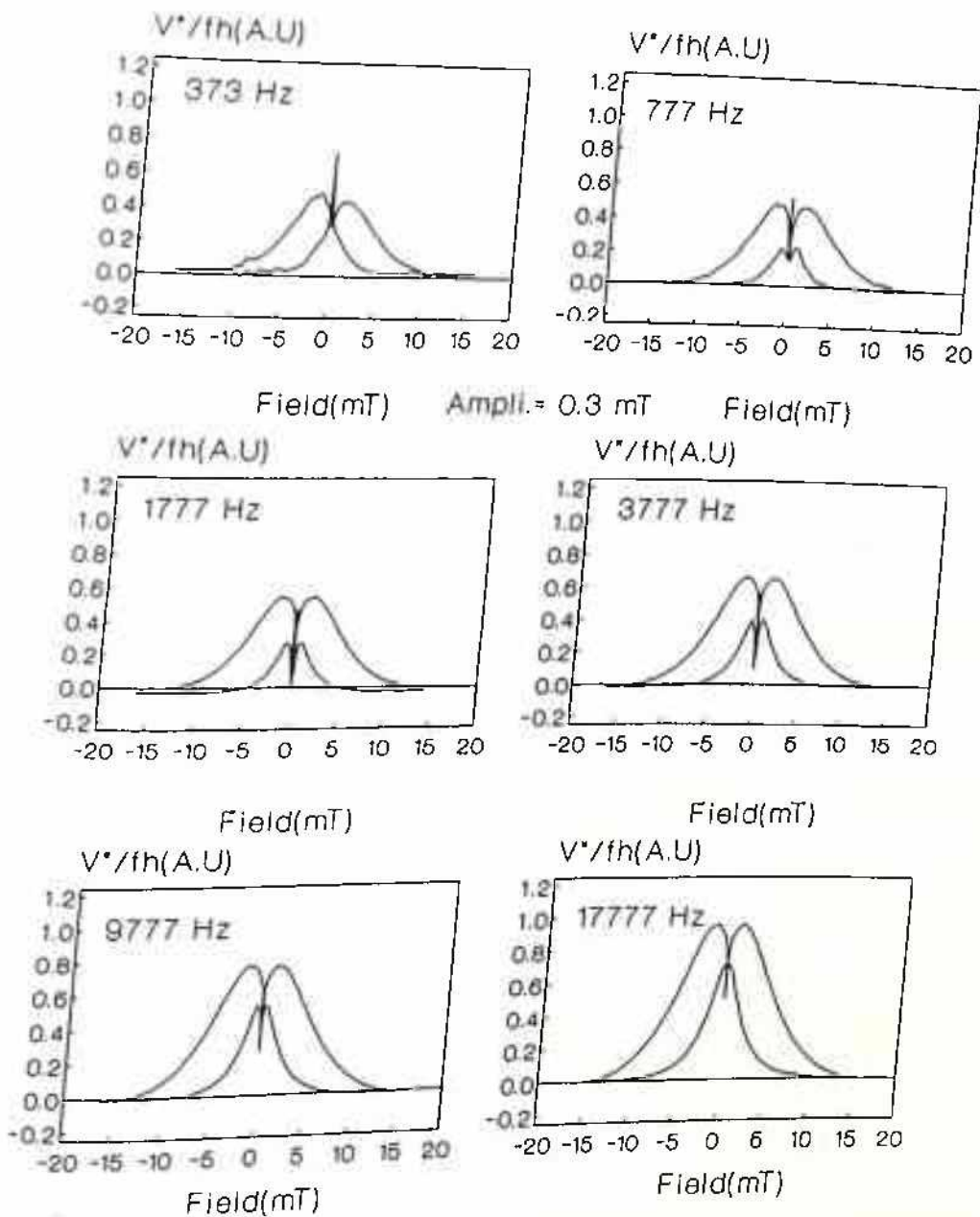


Figure 4.2.25b: V''/fh as function of DC bias field for different frequencies. (Sample A4)

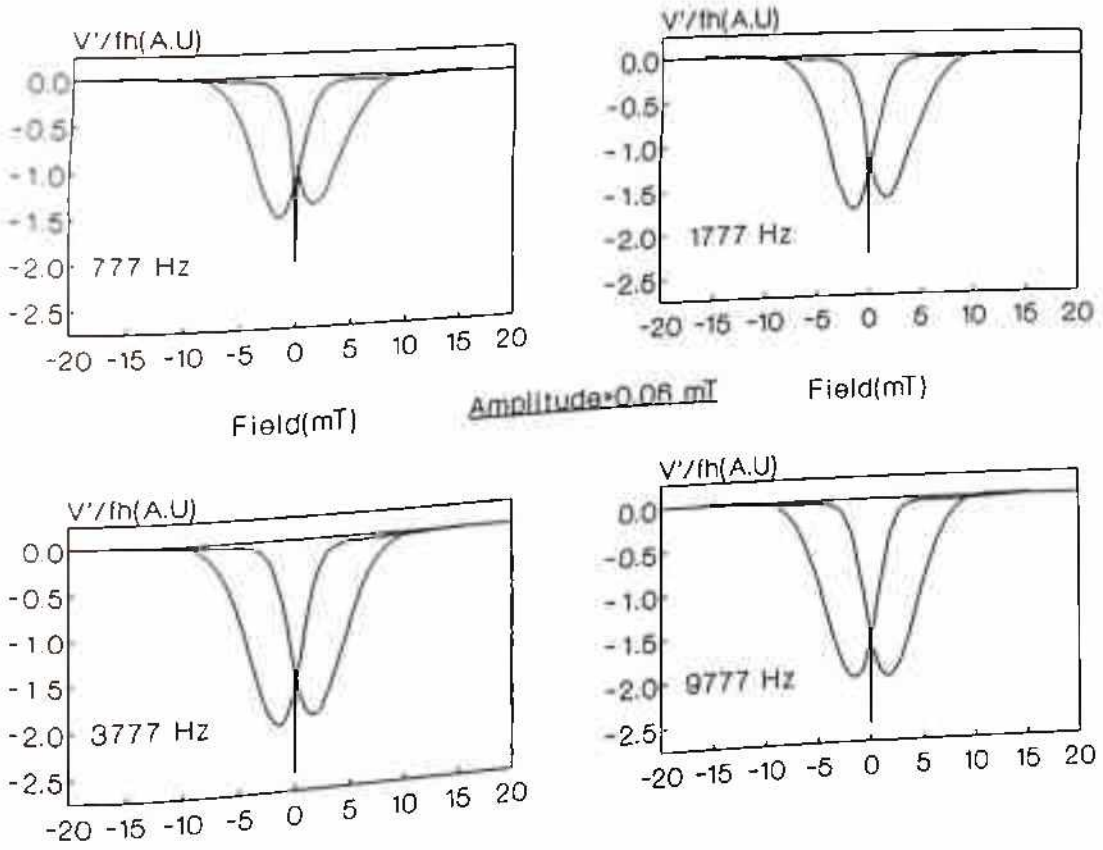


Figure 4.2.26a: V'/fh as a function of DC bias field for different frequencies. (sample A4)

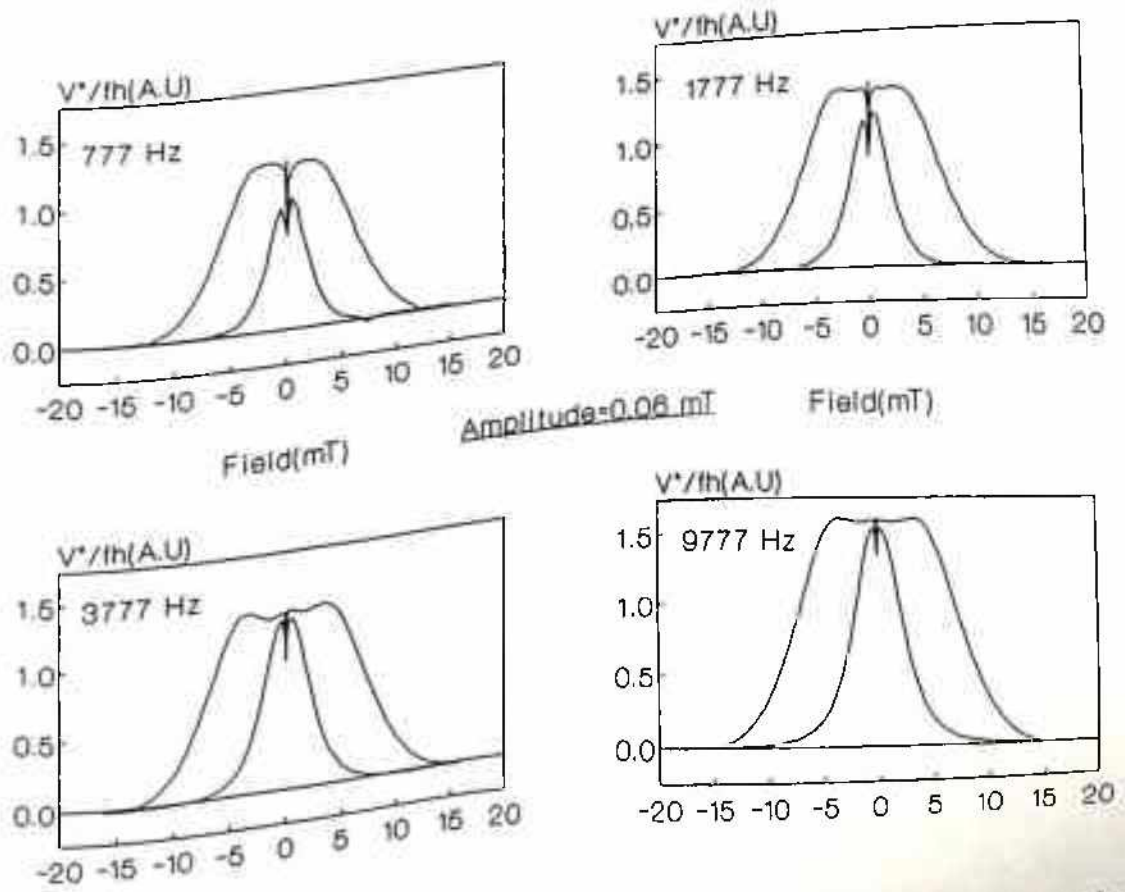


Figure 4.2.26b: V''/fh as a function of DC bias field for different frequencies. (sample A4)

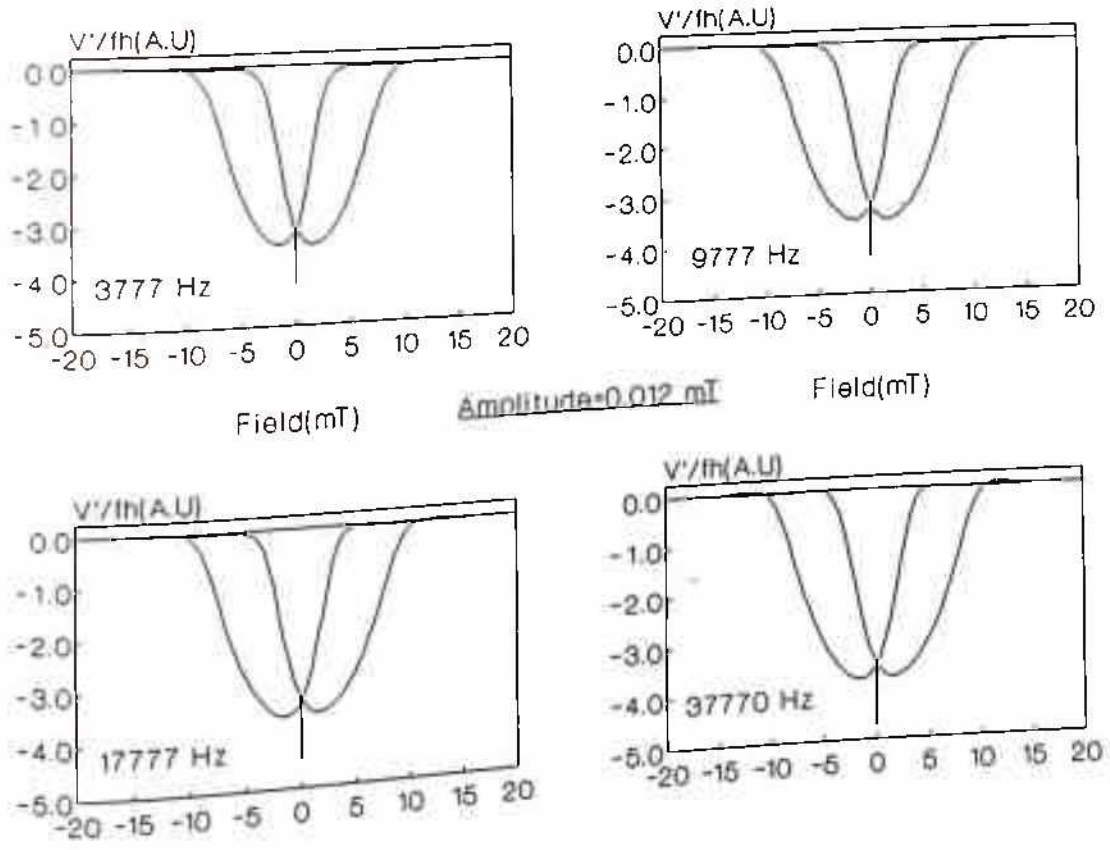


Figure 4.2.27a: V'/fh as a function of DC bias field for different frequencies. (sample A4)

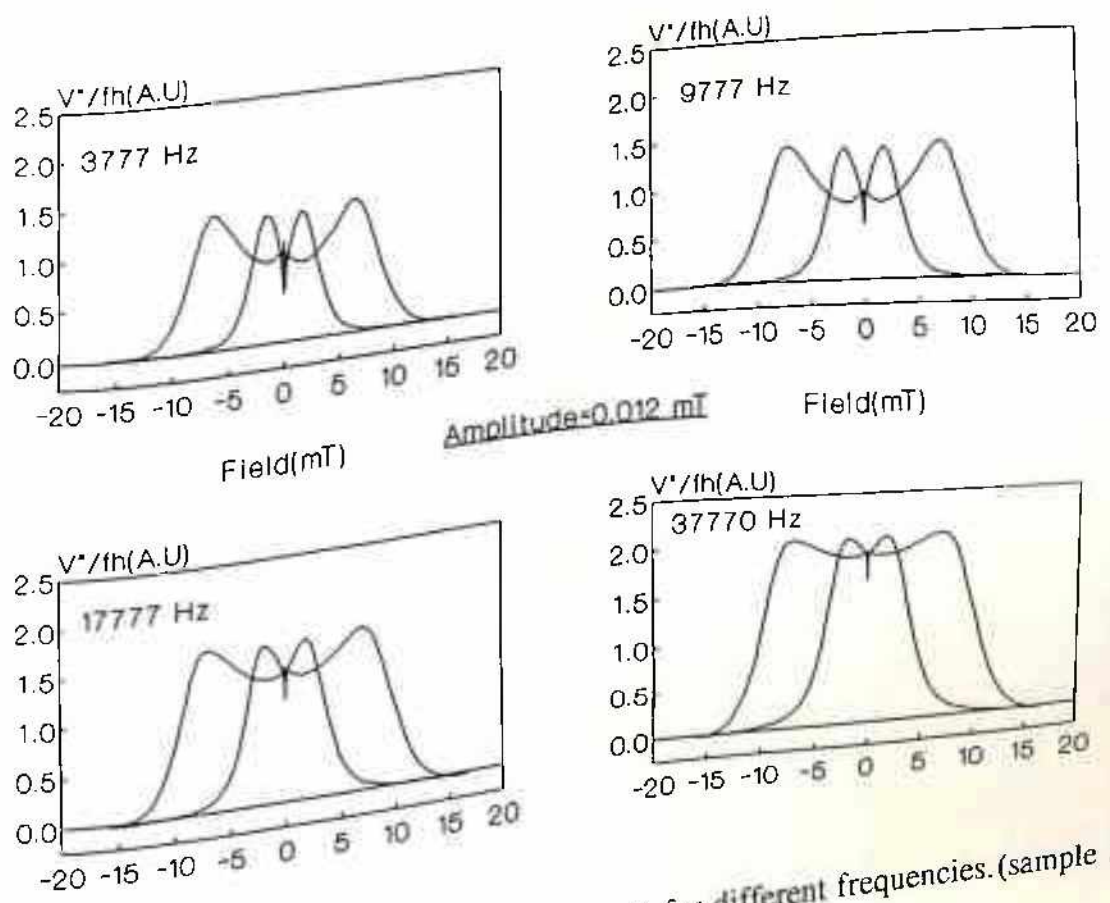


Figure 4.2.27b: V''/fh as a function of DC bias field for different frequencies. (sample A4)

$J_{c1}(0)$ and hence behavior similar to sample A2 would be expected at a correspondingly lower AC amplitude.

4.2.3. SUM UP:

As already mentioned, that the basic problem in interpreting the results is that there is not a single unique feature of all the curves which can be compared for different parameters to make the discussion easy to follow. Therefore always the full $\chi'(H)$ and $\chi''(H)$ loops have been plotted for different parameters which makes the study quite complicated. However, from the measurements the following essential features can be brought out;

1. STUDY OF RANGE EFFECT:

- * Excursions of DC bias field below certain limiting value did not yield hysteresis in the $\chi'(H)$ and $\chi''(H)$ loops.
- * The hysteresis in the $\chi'(H)$ and $\chi''(H)$ was seen to increase monotonically on increasing the range of DC bias field.
- * A peculiar feature (ZCOF) was seen at the zero-cross-over point of the DC bias field which is being reported for the first time. There is no apparent explanation for this ZCOF. This feature being very sharp is likely to be missed in quasistatic variation of DC bias field and hence not seen by any other worker.

2. STUDY ON AMPLITUDE DEPENDENCE:

- * The basic shape of the $\chi'(H)$ loops at all amplitudes and at all frequencies was same and similar to that of the calculated loops of Chapter 3.
- * The $\chi''(H)$ loops showed strong amplitude dependence and had a variety of shapes at different AC amplitudes and frequencies.
- * The peak seen on each side of $\chi''(H)$ loops shifted to lower DC bias with increasing amplitudes and vice versa in agreement with

the model calculation of Chapter 3.

For a given range of DC bias field, the peaks on the $\chi''(H)$ loop appeared at lower AC amplitude for a sample with worse GB parameters. This was also in agreement with the model prediction of Chapter 3.

3. STUDY ON FREQUENCY DEPENDENCE:

Other parameters remaining same, the $\chi'(H)$ and $\chi''(H)$ loops showed strong frequency dependence.

For poor samples with worse GB parameters, the frequency dependence was seen at a lower frequency.

Other parameters remaining same, the frequency dependence of the $\chi'(H)$ and $\chi''(H)$ loops for high range of DC field at different amplitudes were different. There was a clear cross-over amplitude above and below which the frequency dependence of the $\chi'(H)$ and $\chi''(H)$ was seemingly opposite. In the high amplitude case (above the cross-over amplitude), the depth of the $\chi'(H)$ loops and the height of the $\chi''(H)$ loops were a monotonically increasing function of frequency where as in low amplitude (below the cross over amplitude) case they were decreasing function of frequency.

* The cross-over amplitude was seen to be sample dependent and was lower for low J_c sample.

REFERENCES:

- [1] A. Kompany, Y. J. Qian, M-F. Xu, H-P. Baum, W. Millman and M. Levy 1990 Solid State Comm., **75**, 579
- [2] C.Y. Lee, L.W. Song and Y.H. Kao 1992 Physica C, **191**, 429
- [3] L. G. Mamsurova, K. S. Pigalskiy, V. P. Sakun and L. G. Scherbakova 1992 Physica C, **200**, 175
- [4] Y. Kim, Q. H. Lamb and C. D. Jeffries 1991 Phys. Rev. **B43**, 11404
- [5] D. Sen, A. Mitra and S. K. Ghatak 1992 Supercond. Sci. Technol. **5**, 467
- [6] Y. Yang, C. Beduz, Z. Yi and R. G. Scurlock 1992 Physica C, **201**, 325

EXPERIMENTAL DATA

HYSTERESIS IN COMPLEX AC SUSCEPTIBILITY WITH MUTUALLY PERPENDICULAR AC AND DC FIELDS:

This part contains the data on the field dependence of the χ' and χ'' for different frequencies as well as amplitudes of AC excitation field when the two fields are mutually perpendicular. Comparison of the $\chi'(H)$ and $\chi''(H)$ loops for different field configurations has been carried out. Bulk size dependence has been considered. Dependence on amplitude and frequency of the loops is also seen.

	244
4.3.1. INTRODUCTION	245
4.3.2. EXPERIMENTAL RESULTS AND DISCUSSIONS	245
A. CONTINUATION FROM CO-AXIAL FIELDS CASE	246
B. BULK SIZE DEPENDENCE OF THE $\chi'(H)$ AND $\chi''(H)$ LOOPS	253
C. AMPLITUDE DEPENDENCE OF THE $\chi'(H)$ AND $\chi''(H)$ LOOPS	262
D. FREQUENCY DEPENDENCE OF THE $\chi'(H)$ AND $\chi''(H)$ LOOPS	276
4.3.3. SUM UP	278
REFERENCE	

4.3. HYSTERESIS IN COMPLEX SUSCEPTIBILITY WITH MUTUALLY PERPENDICULAR AC AND DC FIELDS:

4.3.1. INTRODUCTION:

In last section (4.2), the hysteresis of the $\chi'(H)$ and $\chi''(H)$ has been considered for the case when DC and AC field were co-axial (parallel). In this section, the case of mutually perpendicular AC and DC fields will be considered. It is important to note that the model calculations, as have been attempted in chapter 3, are for the case of coaxial fields. It is, in fact, difficult to conceive a model with AC and DC fields perpendicular to each other. Nevertheless, from a theoretical point of view, the experimental results in perpendicular case is equally important to initiate possible theoretical background for a model, appropriate to the situation.

In the co-axial field case, because of some technical limitation, the DC field range higher than 20 mT could not be achieved. However, in the perpendicular case, as it was possible to use an electromagnet, a higher DC field range of 100 mT or higher could be used.

The case of co-axial fields, as one can visualize, is simple because both the fields being parallel, they can be considered as scalar quantities and the magnitude of the resultant field is the only parameter that comes in to the calculation. As discussed in chapter 3, the resultant process can be considered as tracing of minor loops for every AC cycle at different points of the major loop due to the DC bias field. When the DC field variation is continuous (ramped) one has to consider further variation of flux in a given AC cycle due to variation of the DC bias field within the cycle. However, considering the actual experimental case where the ramp rate was typically 2mT/min or less (this was typical ramp rate used in the co-axial case), the contribution of this ramp field in a given AC cycle of frequency 373 Hz is $\approx 2/60 \times 373 \approx 10^{-4}$ mT/cycle, which was two order lower than the lowest amplitude (obviously at higher frequencies this will be still smaller). In fact this is why, the effect of ramp rate was not addressed in the previous section. Thus if the ramp rate is not too high the situation within the frequency range as considered here, is equivalent to the case of quasistatic DC field variation. Now in a quasi-static case, the situation in a given AC cycle, in presence of constant DC bias, can be simplified as if tracing of M-H loops (minor) over the AC cycle with corresponding J_c parameters determined by the DC bias field, i.e., $J_c(B_{\text{bias}})$. In fact this proposition becomes more realistic when the AC

amplitude is quite lower than the DC bias field.

With this background, the case of AC and DC field mutually perpendicular can probably be dealt in the similar footing. On a physical reasoning, a small amplitude of AC field oscillation can be considered as a measuring probe for AC susceptibility, so the response is not likely to be different depending on whether the DC bias is parallel or perpendicular (obviously, here it is assumed that the sample does not have any anisotropy of $J(H)$). As will be seen in actual data, this argument is not far from truth. Indeed, it will be seen that in both configuration the loops are basically same except some quantitative difference which probably can be attributed to the different bulk demagnetization factors in the two cases.

Therefore, here the same model calculations of the co-axial fields will be extended for the perpendicular field case for a qualitative agreement.

Before going in to the actual data, here one further technical limitation and the consequence of it, must be addressed. This is about the ZCOF. It has been explained in chapter 2, that the DC field in this case was generated by driving an electromagnet powered by an analog integrator ramp current source (this was following a standard design from any text book) of which only the ramp rate could be programmed. Further, the driving current was monitored (not the field) as a measure of field which later on was corrected for the hysteresis of the pole pieces through software. Therefore, the slow variation of the drive current at the zero-cross-over of the ramp (an inherent problem of any ordinary analog integrator) appeared at finite DC bias field because of the hysteresis of the pole pieces. So it was not possible to detect the sharp ZCOF as seen in the case of parallel field configuration where zero current amounted to zero DC field. Thus in this case of perpendicular configuration of fields, the ZCOF will be totally absent.

4.3.2. EXPERIMENTAL RESULTS AND DISCUSSIONS:

4.3.2A. CONTINUATION FROM THE CO-AXIAL FIELD CASE.

Before going into the high field results in this case of perpendicular fields, which are main subject in this section, it is instructive to see that the proposition as conceived above that the basic behavior in both the field configurations would be same, is right.

In the low DC field range, in the perpendicular configuration because of the high remanence of the pole pieces it was difficult to study the hysteresis in the $\chi'(H)$ and $\chi''(H)$ loops. Thus here the study will be on the high DC field range(100 mT) loops. However, in order to show the continuity of the shapes of the loops in the two field configurations, here only one set of $\chi'(H)$ and $\chi''(H)$ loops at low field range (18 mT) have been plotted for the sample A4 with an amplitude of AC excitation of 0.012 mT (figure 4.3.1). Though care was taken to remove the remanence of the pole pieces, it is obvious from the figure 4.3.1 that the unbalanced remanence was still present in the pole pieces which shifted the axis of symmetry to some non-zero fields. Apart from this distortion due to unaccounted hysteresis of the pole pieces, the shapes of the loops were similar to that shown in figure 4.2.13(a,b) (in section 4.2 - with appropriate amplitude) for the co-axial fields configuration. It was not possible to compare the loops for different field configurations quantitatively.

The similar behavior of the loops in different field configurations was seen in all other samples and at all amplitudes and frequencies of the AC field. After seeing the continuity of the shapes of the loops in both configurations, it is now time to go into the detail study for the perpendicular configuration of fields.

4.3.2B. BULK SIZE DEPENDENCE OF THE $\chi'(H)$ AND $\chi''(H)$ LOOPS:

The study of the effect of bulk size is obviously one of the most important aspect to bring out the causality of the phenomena on the critical state. Because any critical state model must involve the macroscopic penetration field, H^* which certainly is a size dependent parameter. Though exact value of the penetration field is model dependent, it is always a monotonically increasing function of size of the sample concerned.

Though in principle study of size effect could have been simple, here it was difficult because of the two facts - i). preparation of sample with different diameters (because the apparatus as designed for maximum sensitivity could accommodate a maximum of 2 mm diameter of sample) and ii). with decrease of size the sample and hence mass, available signal became too weak. Thus only two diameters were studied(1.5 and 1.9 mm).

In figure 4.3.2(a,b) and 4.3.3(a,b) the $\chi'(H)$ and $\chi''(H)$ loops are plotted for sample A2(2% PbO in YBCO) for amplitudes 0.012 mT and 0.06 mT respectively. These data were

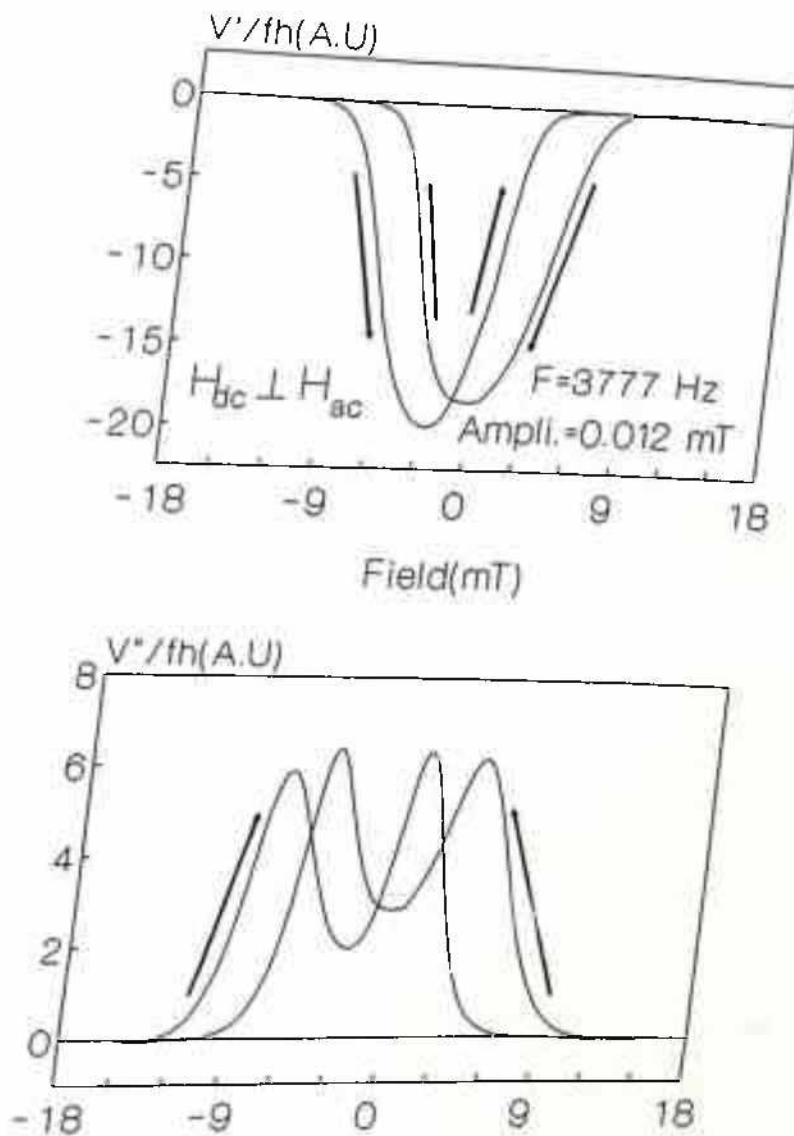


Figure 4.3.1: $\chi'(H)$ (upper) and $\chi''(H)$ loops for amplitude 0.012 mT when AC and DC fields are perpendicular. Shapes are noticeably similar to that in figure 4.2.13 (Co-axial fields). [Sample A4]

plotted after normalizing by respective weight of the samples. It is clear from figure 4.3.2a and 4.3.3a that in case of the $\chi'(H)$ loops, the field dependence became less with decreasing diameter. However, the split, ΔH between the valleys(V) of $\chi'(H)$ loops remained independent of the diameter of the samples. In case of the $\chi''(H)$ loops, similar behavior was seen. The position of the valleys(V) on the decreasing (magnitude wise) arms and that of the peaks on the increasing arms of the $\chi''(H)$ loops at lower DC bias fields (magnitude wise) remained unchanged with the variation of the size. But there was a noticeable change in the depth of the valleys(V) on the decreasing arms of the $\chi''(H)$ loops which was seen to increase with increasing diameter. There was another important variation of the shape of the $\chi''(H)$ loops with size. The broad maxima on the decreasing arms shifted considerably to lower DC bias field with decrease of diameter. However, the shift was larger in case of the smaller amplitude. Like in figure 4.3.2b for amplitude of 0.012 mT, the shift was from approximately 60 mT to 40 mT (a shift of 20 mT) for change of diameter from 1.9 mm to 1.5 mm and the corresponding shift in figure 4.3.3b for amplitude of 0.06 mT, was from 30 mT (approximately) to 20 mT (approximately) (a shift of 10 mT).

This findings of the experimental data can qualitatively be explained on the basis of the model calculations of chapter 3. However, before going in to that, one point must be noted which can make the comparison of the experimental data with the theoretical calculations of chapter 3 easy to follow. In any critical state model, as already discussed, the penetration field, H^* is a crucial parameter and is a function of diameter (for cylindrical sample) and as well as J_c parameters. Further it is seen, like the dependence of H^* on the size, it is a monotonically increasing function of $J_c(0)$ (obviously here the consideration is bulk size and hence $J_c(0)$) but exact nature, once again will be model dependent. Thus for a qualitative comparison, one can in effect treat the three quantities H^* , $J_c(0)$ and the diameter in the same footing, i.e., any increase in $J_c(0)$ or the diameter can equivalently considered as an increase in H^* and vice versa. It can further be stressed that the effect on the loops due to increase (or decrease) in amplitude can also be equivalently (obviously qualitatively) treated like a decrease (or increase) in H^* or $J_c(0)$ or diameter.

With the above proposition, it is now simple to compare the data in figures 4.3.2 and 4.3.3 with the calculated results. One can consider the figure 3.2.32(a,b) in chapter 3 which

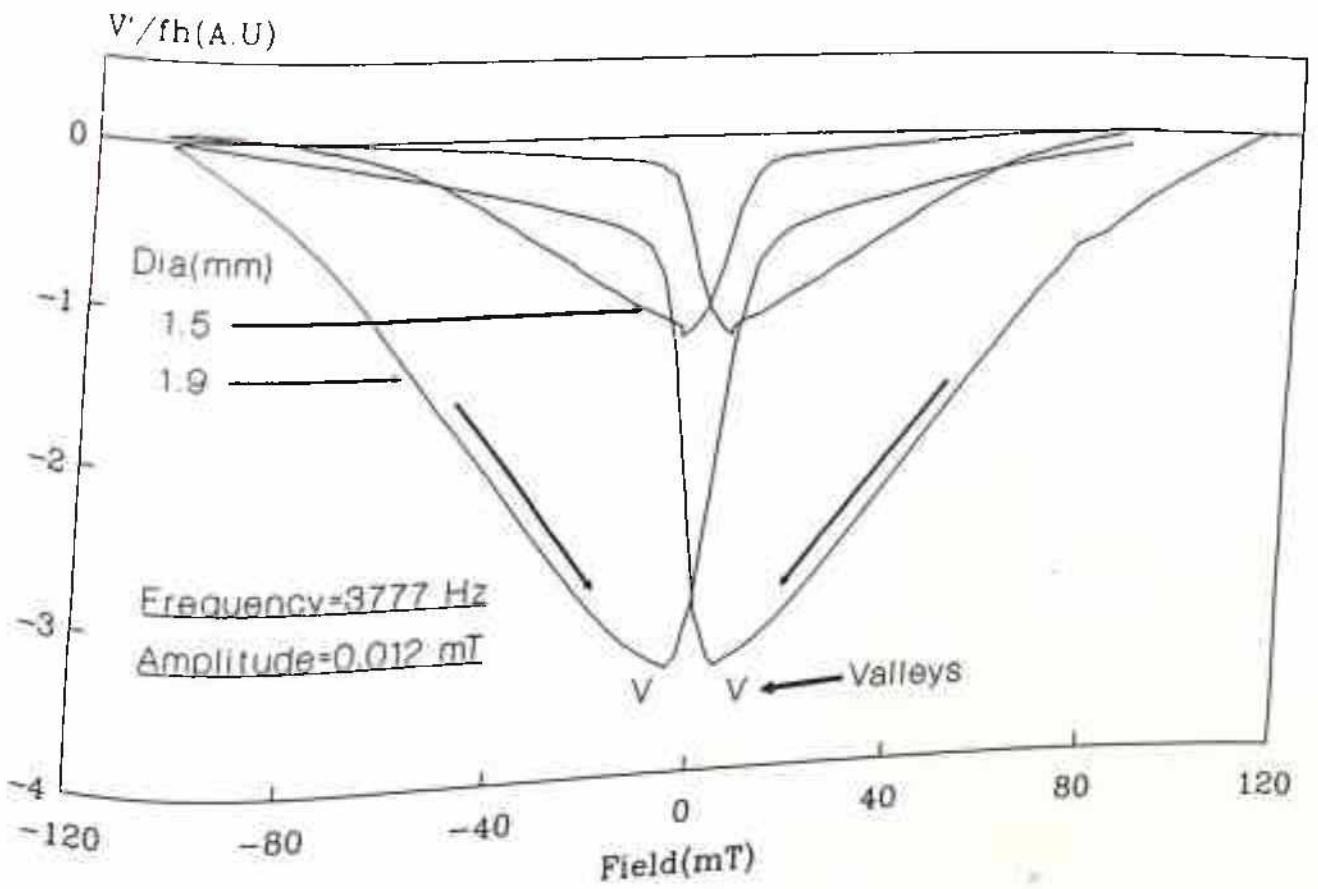


Figure 4.3.2a: $V'/fh (\approx \chi')$ for two different diameters for sample A2.

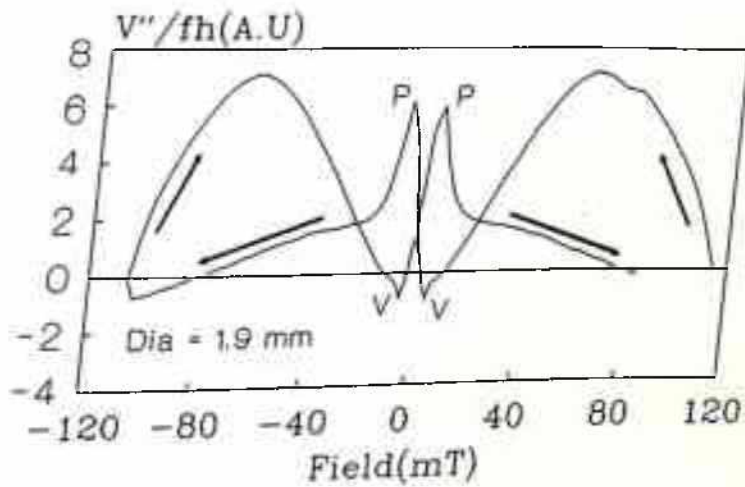
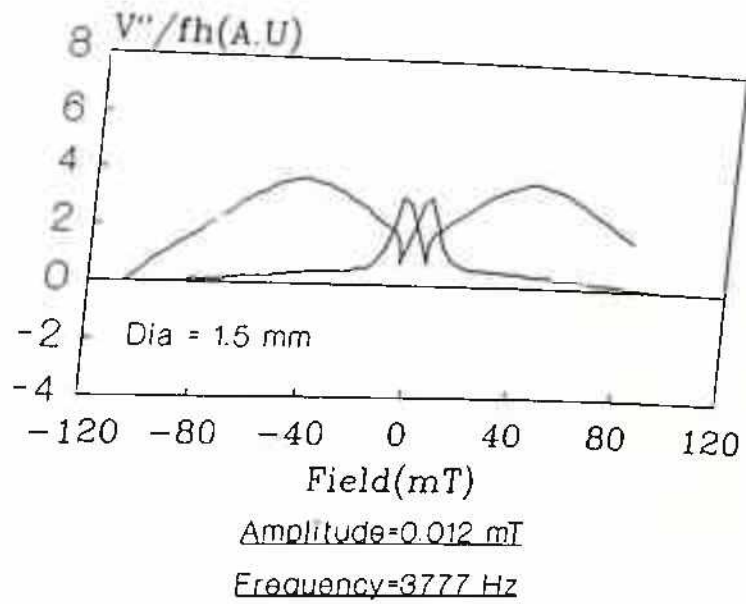


Figure 4.3.2b: $\chi''(H)$ loops for two different diameters for sample A2.

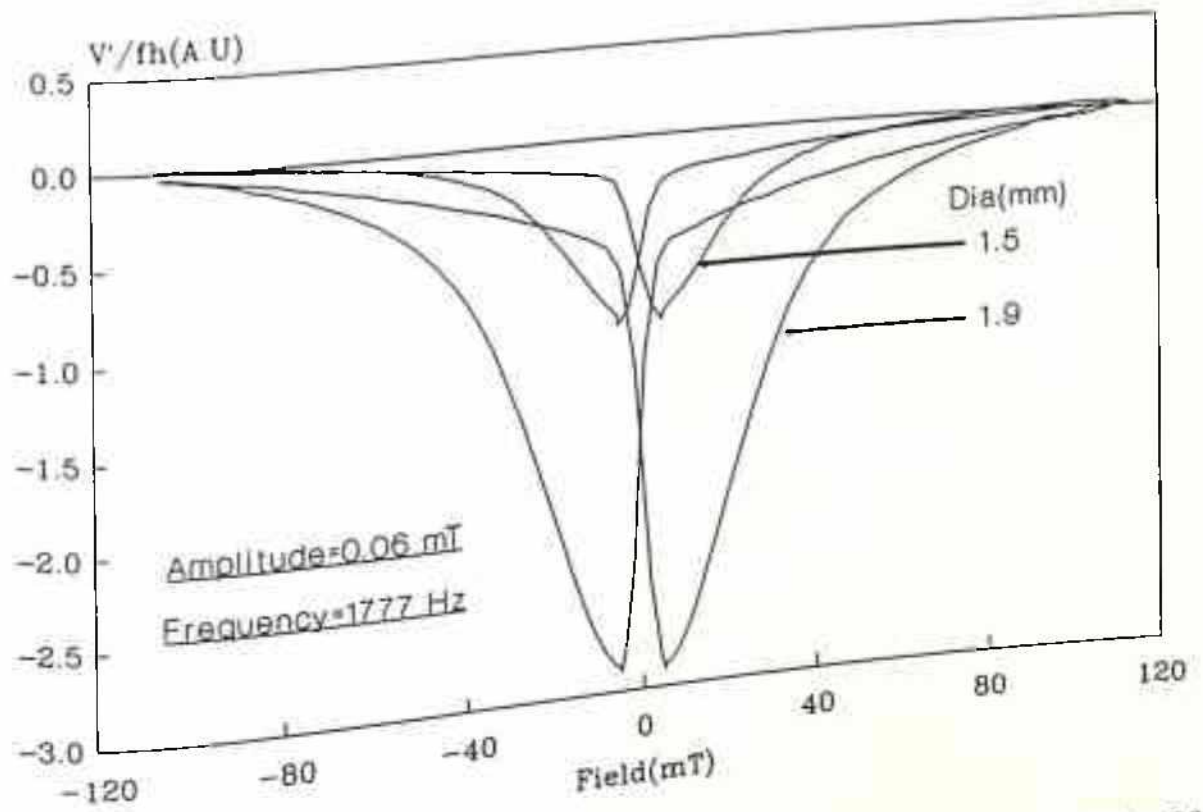
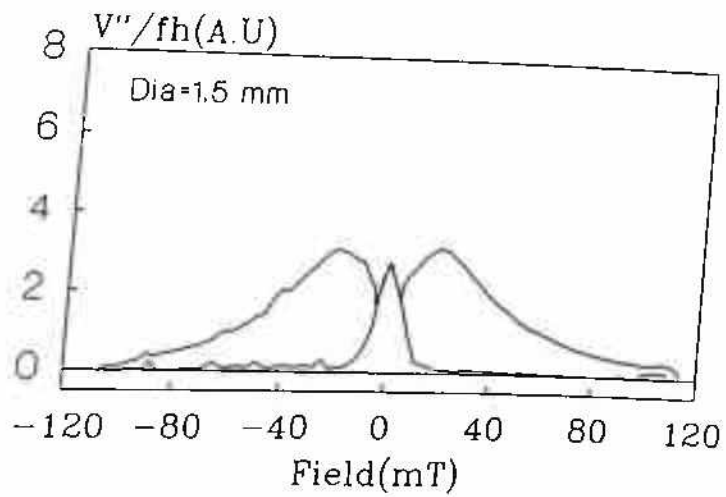


Figure 4.3.3a: $V'/fh (\approx \chi')$ for two different diameters for sample A2 for an amplitude of 0.06 mT.



Amplitude=0.06 mI

Frequency=1777 Hz

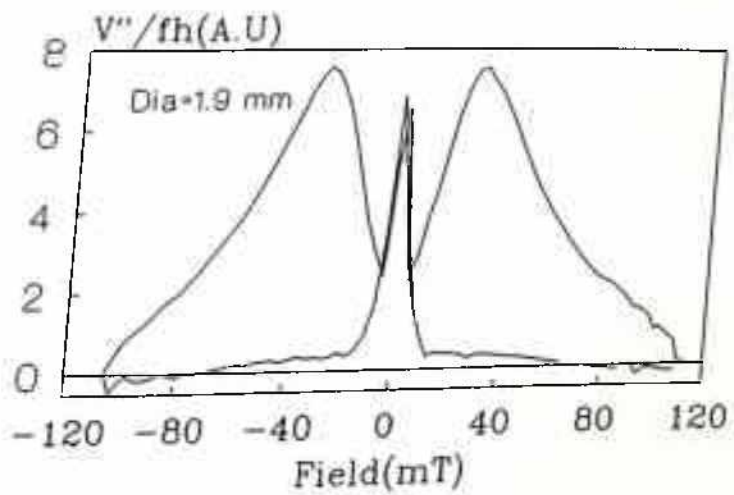


Figure 4.3.3b: Imaginary counterpart of figure 4.3.3a.

showed striking similarity with data here and reproduced most of the features of the experimental data correctly (however, the large hysteresis in the experimental data were not accountable in the present model). Like, in the calculation in figure 3.2.32b for $\chi''(H)$ loops, i). the peaks on the decreasing arms shifts to lower DC bias with decreasing $J_{c1}(0)$ (or equivalently decreasing H^* or diameter), ii). The depth of the valleys(V) on the decreasing arms decreased with decreasing $J_{c1}(0)$ (or equivalently decreasing H^* or diameter), iii). the peaks on the increasing arms shifted to lower DC bias fields with increasing $J_{c1}(0)$ (or equivalently increasing H^* or diameter) and merged together at a sufficiently high $J_{c1}(0)$ (the upper left-most curve) (or equivalently high H^* or diameter).

In case of the $\chi'(H)$ loops (figure 3.2.32a) also, the qualitative agreement was good and correctly showed the decrease of depth of the valleys(V) with decreasing $J_{c1}(0)$ ((or equivalently decreasing H^* or diameter) in agreement to the data in figures 4.3.2a and 4.3.3a.

However the model, as usual did not reproduce the large hysteresis as seen in the experimental $\chi'(H)$ and $\chi''(H)$ loops.

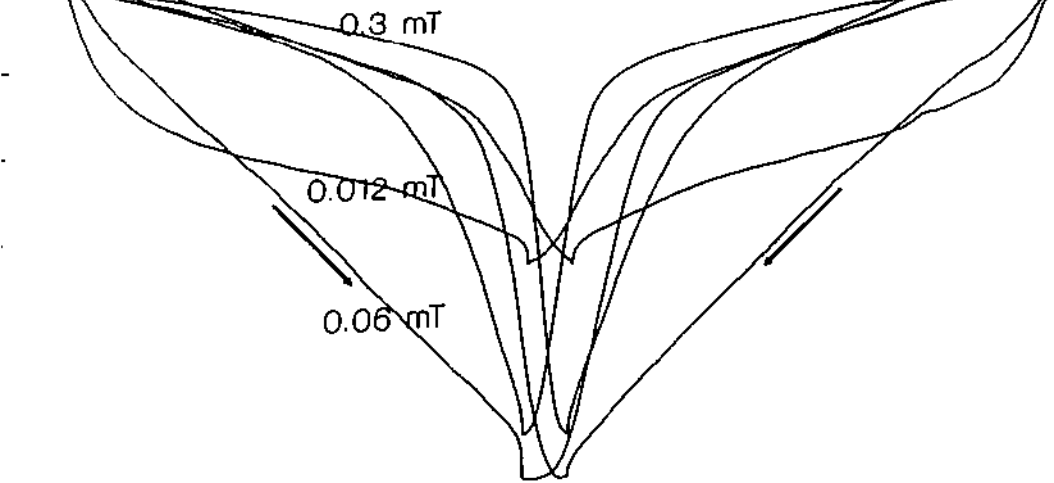
The excellent agreement of the calculations with the data here clearly certified the model to be in the right track in handling the field dependence of χ and in introducing the demagnetization factors to account for the hysteresis. However, it was clear that hysteresis must be due to more than the two factors accounted here, i.e., demagnetization and a small contribution from critical state at low amplitudes.

4.3.2C. AMPLITUDE DEPENDENCE OF THE $\chi'(H)$ AND $\chi''(H)$ LOOPS:

The inspiration in the last section (4.3.2b) naturally demanded the extension of the study for amplitude dependence of the $\chi'(H)$ and $\chi''(H)$ loops in this high field case.

In figures 4.3.4(a,b), 4.3.5(a,b), 4.3.6(a,b) and 4.3.7(a,b) the $\chi'(H)$ and $\chi''(H)$ loops have been plotted for a fixed frequency of 9777 Hz for sample A1(pure YBCO), A2(2% PbO doped YBCO), A3(6% PbO doped YBCO) and A4(10% PbO doped YBCO) respectively. In all of these curves ramp rate was 0.4mT/sec.

On the whole, it was seen that the $\chi'(H)$ loops for all the sample showed decreasing DC field dependence and decreasing hysteresis with increasing amplitude of AC field. This behavior was similar to that in the case of co-axial fields where the DC field range was low(18 mT max.).



Freq : 9777 Hz

Sample : Pure YBCO

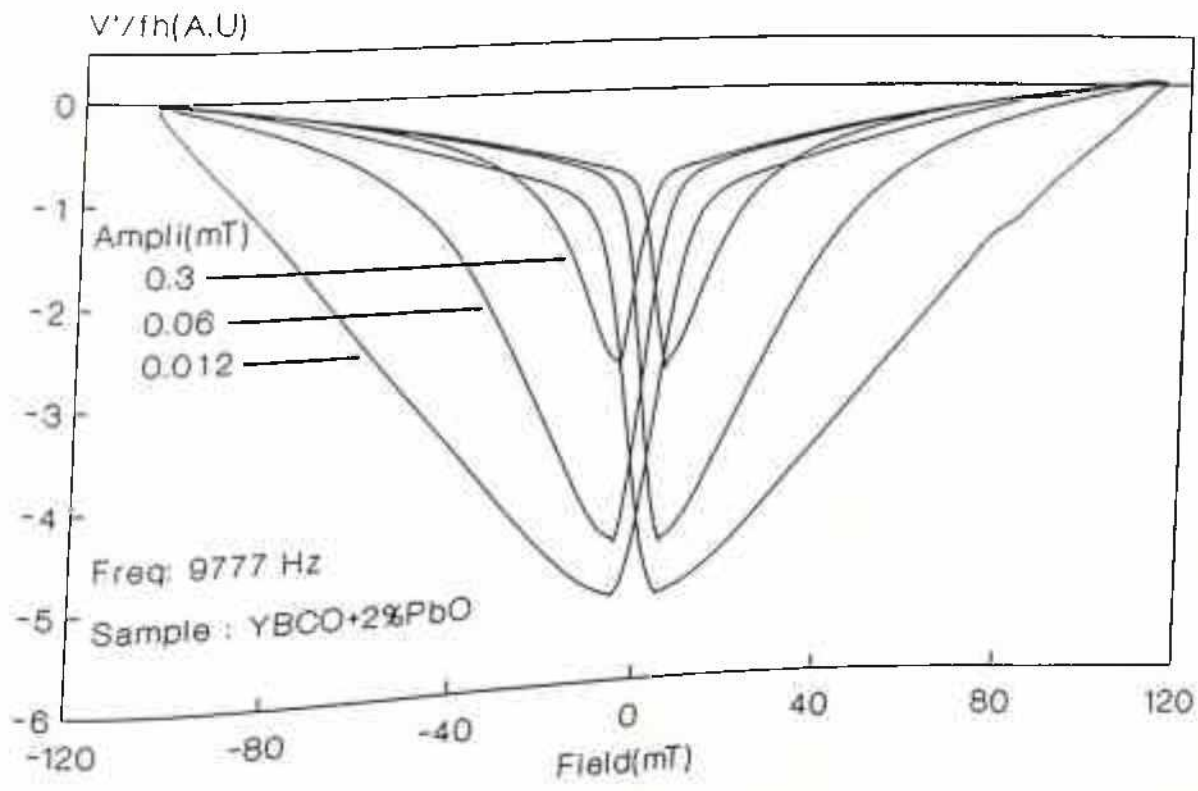


Figure 4.3.5a: $V'/fh (\approx \chi')$ for three different amplitudes for sample A2.

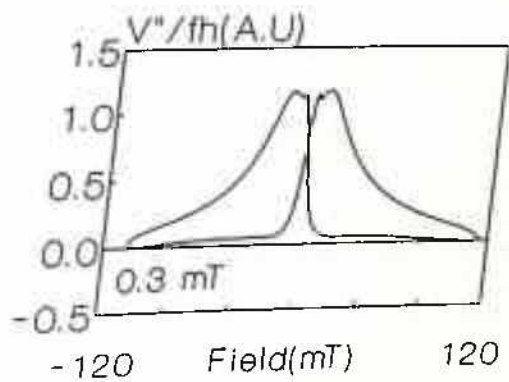
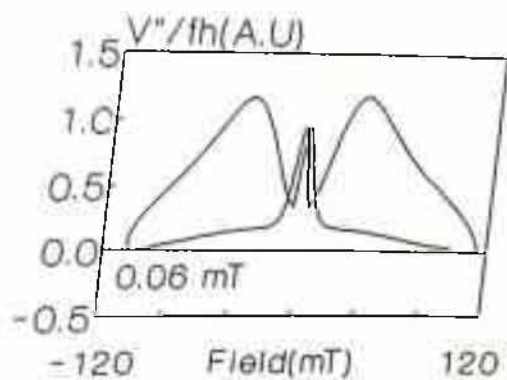
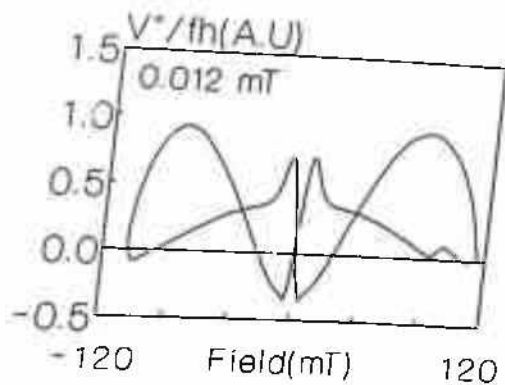


Figure 4.3.5b: $V''/fh(=\chi')$ for three different amplitudes for sample A2.

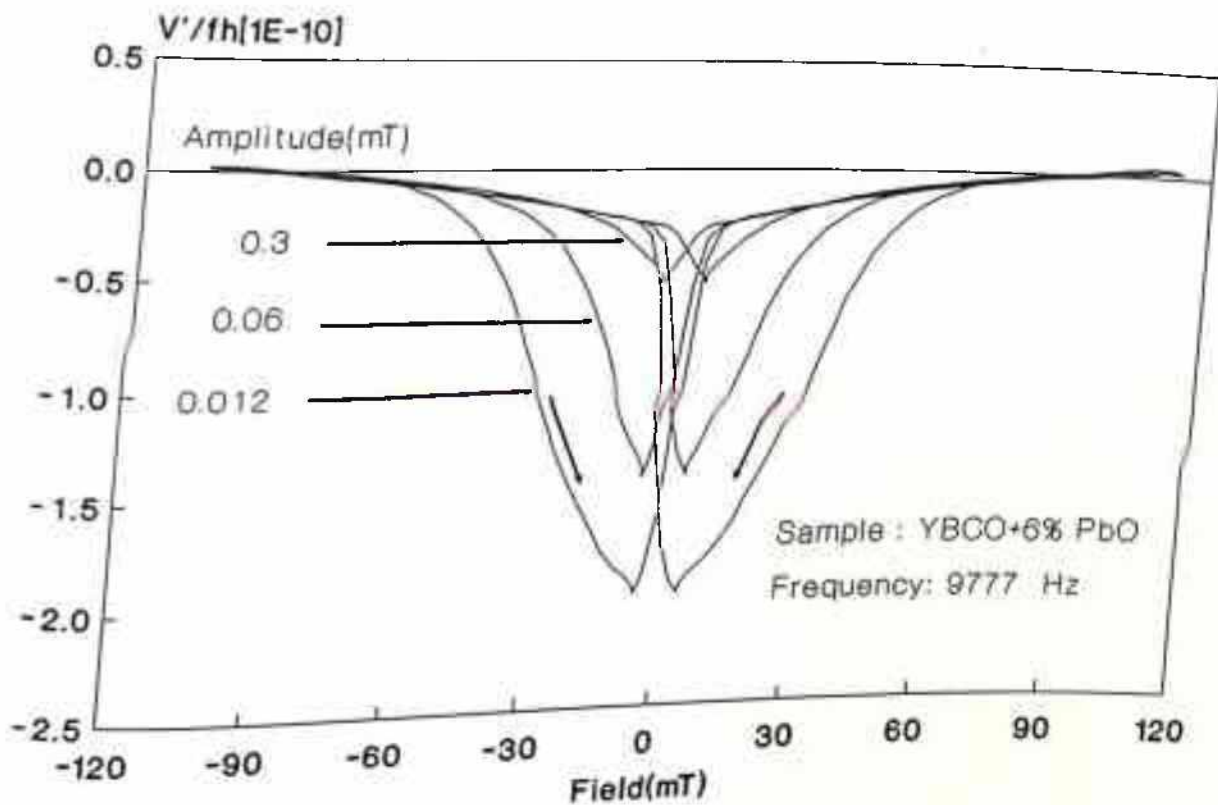


Figure 4.3.6a: $V'/fh (\approx \chi')$ for three different amplitudes for sample A3.

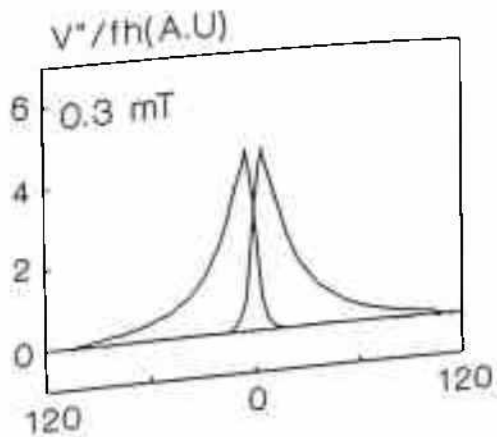
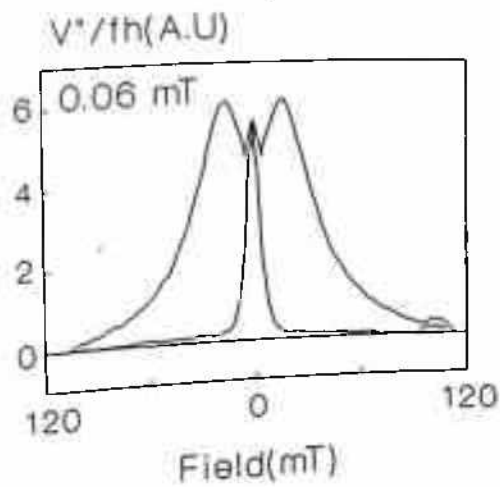
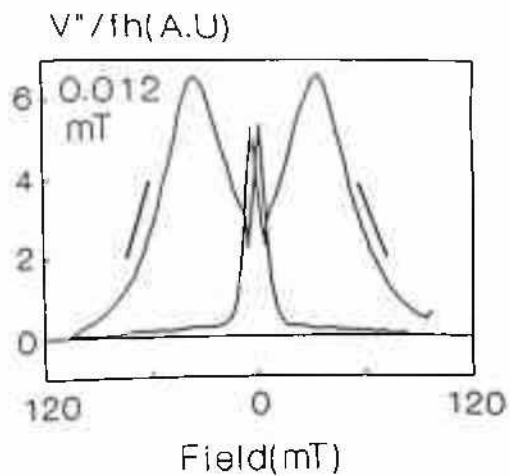


Figure 4.3.6b: $V''/fh(= \chi')$ for three different amplitudes for sample A3.

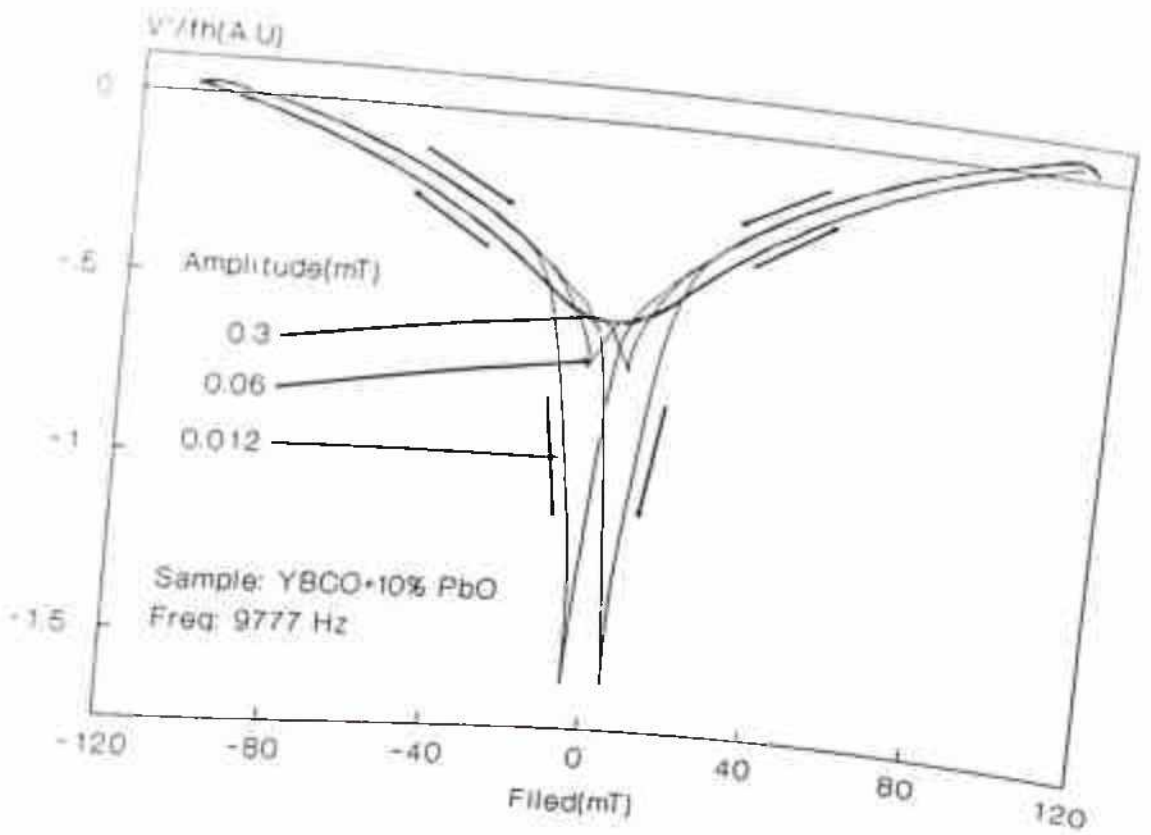


Figure 4.3.7a: V'/fh ($\approx \chi'$) for three different amplitudes for sample A4.

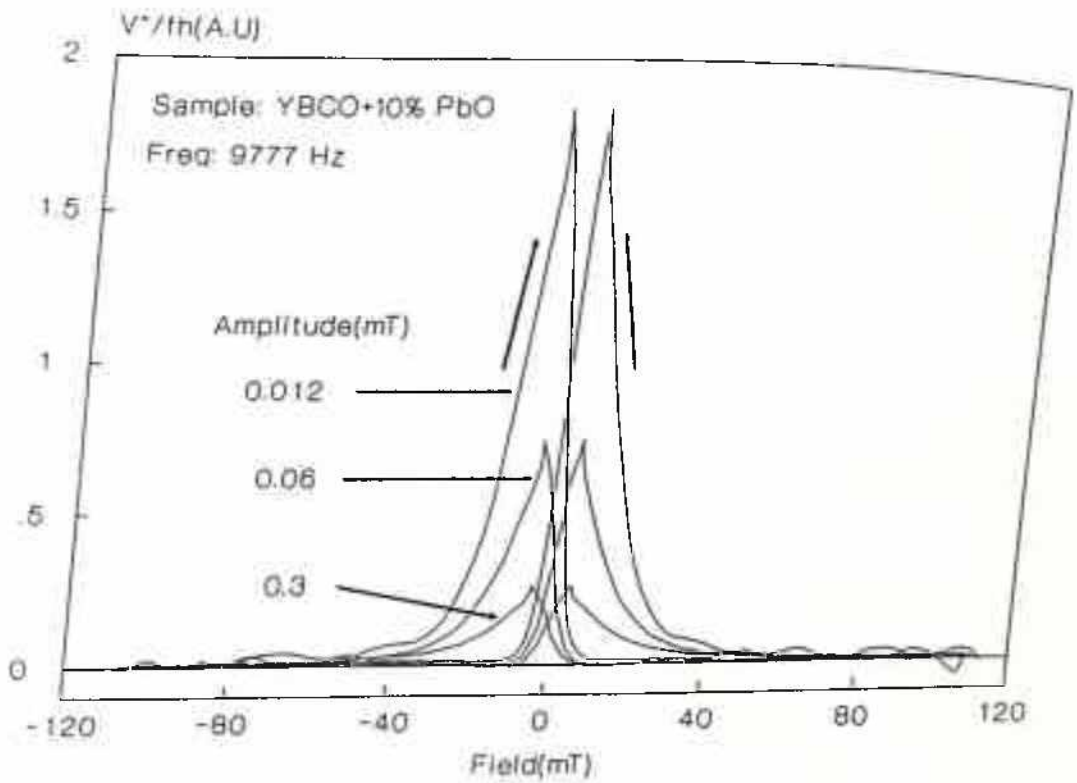


Figure 4.3.7b: V''/fh ($\approx \chi''$) for three different amplitudes for sample A4.

Assuming that the basic premise of the loops did not depend upon the field configurations, the model calculations could be extended to explain the loops as seen here for the higher DC field range. It can be seen that the experimental $\chi'(H)$ loops except for the extra-large hysteresis, were in qualitative agreement with the calculated loops as shown in figures 3.2.12a, 3.2.13a or 3.2.14a of chapter 3. In explaining these data, it will be assumed that PbO content does not change the grain parameters significantly but decreased the J_{ej} parameters substantially.

In explaining the data here, the above proposition (section 4.3.2b) of equivalence between different parameters of the critical state model will also be considered here.

The apparent anomaly in $\chi'(H)$ loops for sample A1 (in all other cases dependence on amplitude was monotonous) can probably be understood, considering the experimental limitations of offsetting at the highest field. As already seen in the last section, that sample A1 had the best J_{ej} parameters of the lot and the J_{ej} was such that even 0.3 mT was perhaps too low an amplitude for this sample. The equivalent behavior of figure 4.3.4a can be visualized in the calculated results in figure 3.2.12a (chapter 3) between amplitude 0.1 to 0.01 mT.

In figure 4.3.5a and figure 4.3.6a, the $\chi'(H)$ loops show best agreement to the model calculation. Further, sample A2 being worse than sample A1 (i.e., $J_{ej}(0)$ of sample A2 was less than $J_{ej}(0)$ of sample A1), the situation may be equivalent to that in figure 3.2.14a for the low amplitudes, viz., 0.1 to 0.01 mT and hence strongest field dependence as in figure 4.3.5a was obvious. But in sample A3 (figure 4.3.6a) $J_{ej}(0)$ ($J_{ej}(0)$ of sample A3 was less than that of sample A2) was such that the amplitudes of the experiment were in higher side for this sample. Therefore the field dependence was expected to be less as obvious in figure 3.2.12a, 3.2.13a or 3.2.14a in chapter 3, where total field dependence was seen to be less at too low or too high amplitudes as appropriate for given parameters. The $\chi'(H)$ loops in sample A4, as obvious in figure 4.3.7a took a new shape which was not seen within the parameters as considered in the model calculation in chapter 3. However, as it will be seen further from consideration of $\chi''(H)$ loops that sample A4 was likely to have $J_{ej}(0)$ less than that of all other samples. With this it is likely that the $\chi'(H)$ loops in figure 4.3.7a are expected to appear at quite higher amplitudes for a given J_{ej} parameters.

The main features of the experimental $\chi''(H)$ loops as seen in figure 4.3.4b for sample

At lower amplitudes:

- * there was a valley close to zero DC bias,
- * the depth of this valley decreased with increase in AC amplitudes,
- * apart from the presence of valley, the loss (proportionate to χ'') was a monotonically increasing function of DC bias,
- * $\chi''(H)$ showed large hysteresis on full excursion of the DC bias field.

At higher amplitudes:

- * with increase of amplitude the monotonic nature of $\chi''(H)$ was no more seen,
- * peaks and valleys(V) appeared on both sides of the decreasing (magnitude wise decrease of DC field) arms of the $\chi''(H)$ loops,
- * peaks(P) appeared on the increasing field arms at lower DC bias,
- * there was a flip of the decreasing arms (which were below the increasing arms at lower amplitudes) from below the increasing arms to above the increasing arms. This flip, in the long run resulted in the peaks.

In case of sample A2, the higher amplitude behavior as described above was seen. This was attributed to the fact that sample A2 had $J_{cj}(0)$ less (and hence H_j^*) than that of sample A1. Therefore, 0.012 mT appeared to be a higher amplitude in sample A2 than in sample A1. Thus the behavior of $\chi''(H)$ loops for 0.012 mT in figure 4.3.5b (sample A2) would be equivalent to the same in sample A1 for amplitude some where in between 0.06 to 0.3 mT in figure 4.3.4b. Similarly $\chi''(H)$ loops at 0.06 mT for sample A2 could be traced in sample A1 for an amplitude greater than 0.3 mT. This behavior as described here was quite systematic. For amplitude 0.3 mT in figure 4.3.5b for sample A2, the $\chi''(H)$ loop indicated the vanishing of the valleys(V) at higher amplitudes (as was seen in low DC field results in section 4.2). The similar evolution of the $\chi''(H)$ loops was repeated in sample A3 where it was obvious that $J_{cj}(0)$ was less than that of sample A2. In figure 4.3.7b, $J_{cj}(0)$ being further less (and hence effective amplitude quite

high) the valley(V) was no more seen and the height of the loops further decreased with increase in amplitude.

This systematic evolution of the $\chi'(H)$ and $\chi''(H)$ loops over the variation of amplitude of AC excitation field for different samples as described above did agree with similar evolution in the case of co-axial configuration of fields.

Now the effort will be to explain this systematic evolution on the basis of the model calculations. Here, once again the calculation of figure 3.2.32b will be considered, where the $\chi''(H)$ loops have been plotted for a given amplitude while $J_{ej}(0)$'s were different. Though the DC field range is different in this figure, it shows a similar evolution of the $\chi''(H)$ loops over different samples as described above. This same figure may be considered for the explanation of the evolution of $\chi''(H)$ loops over amplitude in a given sample. This is because the lowering of $J_{ej}(0)$ may equivalently considered as increasing of effective AC amplitude, however the scale of change in two cases is different. Considering the case of $\chi''(H)$ loops for samples A2, A3, and A4 for amplitude 0.06 mT, it was obvious by comparison with the calculated loops in figure 3.2.23b that the depth of the valley appearing on the decreasing arms would decrease with decrease in $J_{ej}(0)$ (or equivalently increase in amplitude in a given sample), i.e., from a good to poor samples. At quite low $J_{ej}(0)$ (or equivalently higher amplitude) the valley will vanish as seen in the experimental data. It is likely that to see the same behavior of sample A1 (figure 4.3.4b) for amplitude 0.012 mT, in the calculation an amplitude lower than 0.05 mT (figure 3.2.22b) or $J_{ej}(0)$ higher than 900 amp/cm² would be required. In fact, in figure 3.2.13b at the lowest amplitude of 0.01 mT a similar trend had been demonstrated. However in that case, as seen in figure 3.2.13b, there was a large asymmetry in the virgin $\chi''(H)$. In the experiment the virgin $\chi''(H)$ curves were not studied.

4.3.2D. FREQUENCY DEPENDENCE OF $\chi'(H)$ AND $\chi''(H)$ LOOPS:

As in the case when the AC and the DC fields were parallel, it was also seen in this case that the $\chi'(H)$ and $\chi''(H)$ loops showed systematic dependence on frequency. However, as will be seen while discussing the data, some differences in frequency dependence of the $\chi'(H)$ and $\chi''(H)$ were seen in comparison to the case of parallel field configuration. Here the aim was to substantiate the findings from the results in the case of parallel configuration of fields.

In figure 4.3.8(a,b) the $\chi'(H)$ and $\chi''(H)$ loops have been plotted for the sample A1 (pure YBCO) for an amplitude of 0.3 mT. Like in the case of parallel configuration of fields (figure 4.2.14 to 4.2.17 in section 4.2 - where a maximum of DC field range of 10 mT was tried) here also the real parts did not show much frequency dependence (figure 4.3.8a). However, in the case of $\chi''(H)$ loops, the valleys(V) on the decreasing arms showed strong frequency dependence. While from 373 Hz to 3777 Hz, there was an increase in the depth of the valleys(V), at higher frequencies there was a monotonic decrease of the depth of the valley(V) with increasing frequency. The over all heights of the loops (difference between maximum and minimum) decreased on increase of frequency from 373 Hz to 3777 Hz and then increased monotonically with increasing frequency. The data of low range of DC field in the parallel configuration of fields, as shown in figures 4.2.14b-17b, (section 4.2) showed a decrease of the over all height of the $\chi''(H)$ loops with increasing frequency. Combining these two findings from the data at high and low field range, it is clear that at low field range the GB contribution dominates and a monotonic decrease of height might be indicative of that only. But in case of data of high range of DC field, close to the zero bias, GB contribution is prominent and so is the frequency dependence (i.e., decrease of vertical width of the loops or decrease in the depth of the valleys(V)). But when DC bias is high, contribution of the grain will overtake that of the GB and hence the over all height of the loops may show different frequency dependence.

Here one further point is to be noted. In general the GB contribution is limited within a few mT of DC bias field (typically say 5 mT) above which "phase randomization" [1] will lead to vanishing of GB contribution. Thus one may expect to see the grain contribution even in all the 20 mT loops ($\chi''(H)$) in the coaxial configuration of fields (section 4.2) and hence the similar dependence on frequency as seen in the high field loops. Instead, one gets a regular dependence on frequency even in the 20 mT loops. This is probably due to the fact that the H_{c1} of the grains is usually few tens of mT (typically 30 mT) and hence even in 20 mT loops though grain contribution is present, it is from the Meissner state and hence reversible and that in the Meissner state one can not expect to have any frequency dependence. But in the case of 100 mT loops, irreversible contribution of the grain will come in to effect and hence a different frequency dependence at different range of DC field is expected.

In figure 4.3.9(a,b) the $\chi'(H)$ and $\chi''(H)$ loops have been plotted for the same sample A1

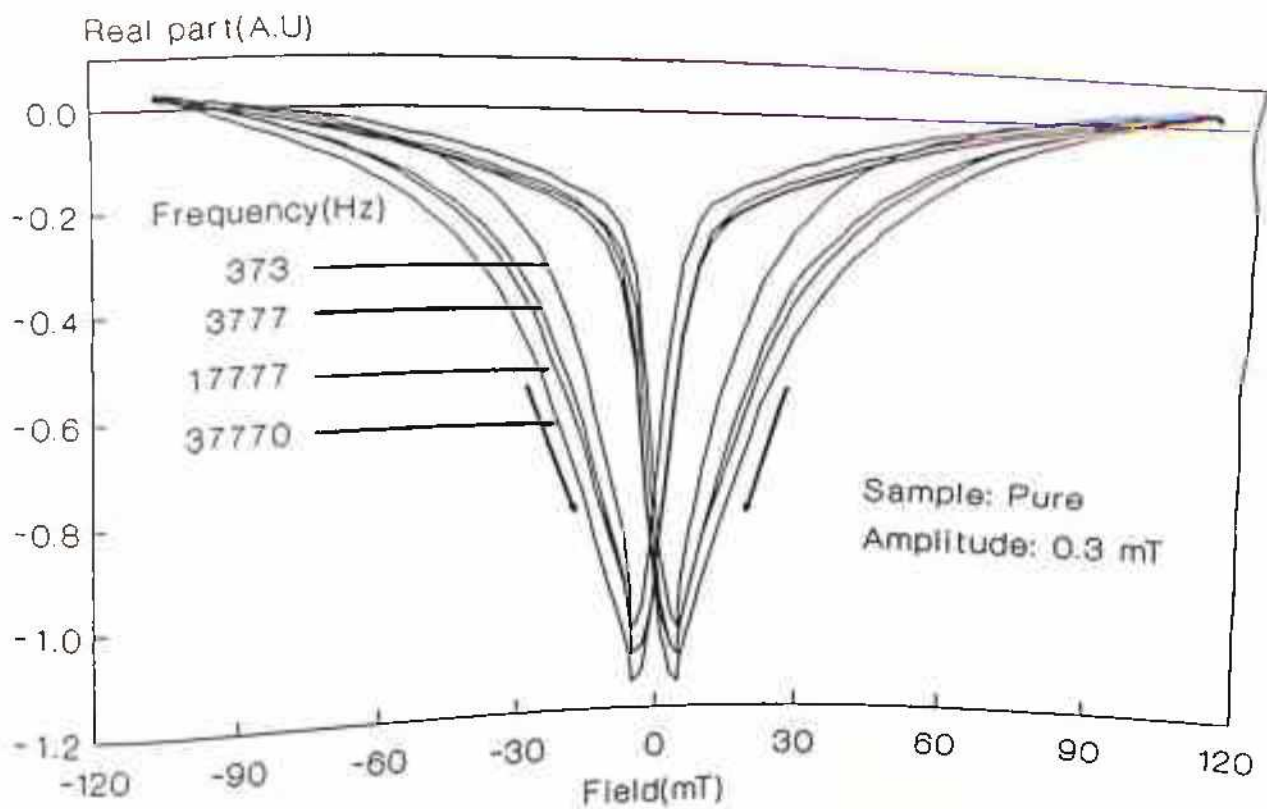


Figure 4.3.8a: $V'/fh(=\chi')$ for four different frequencies for sample A1.

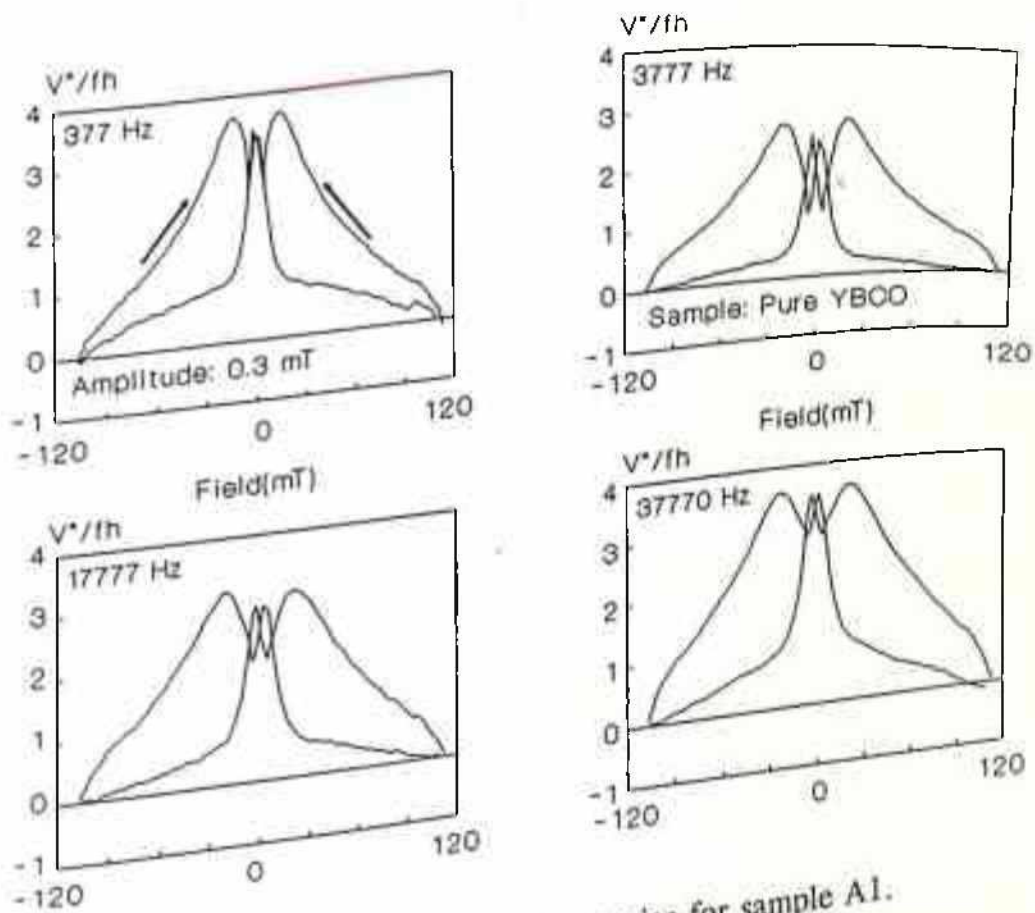


Figure 4.3.8b: $V''/fh(=\chi'')$ for four different frequencies for sample A1.

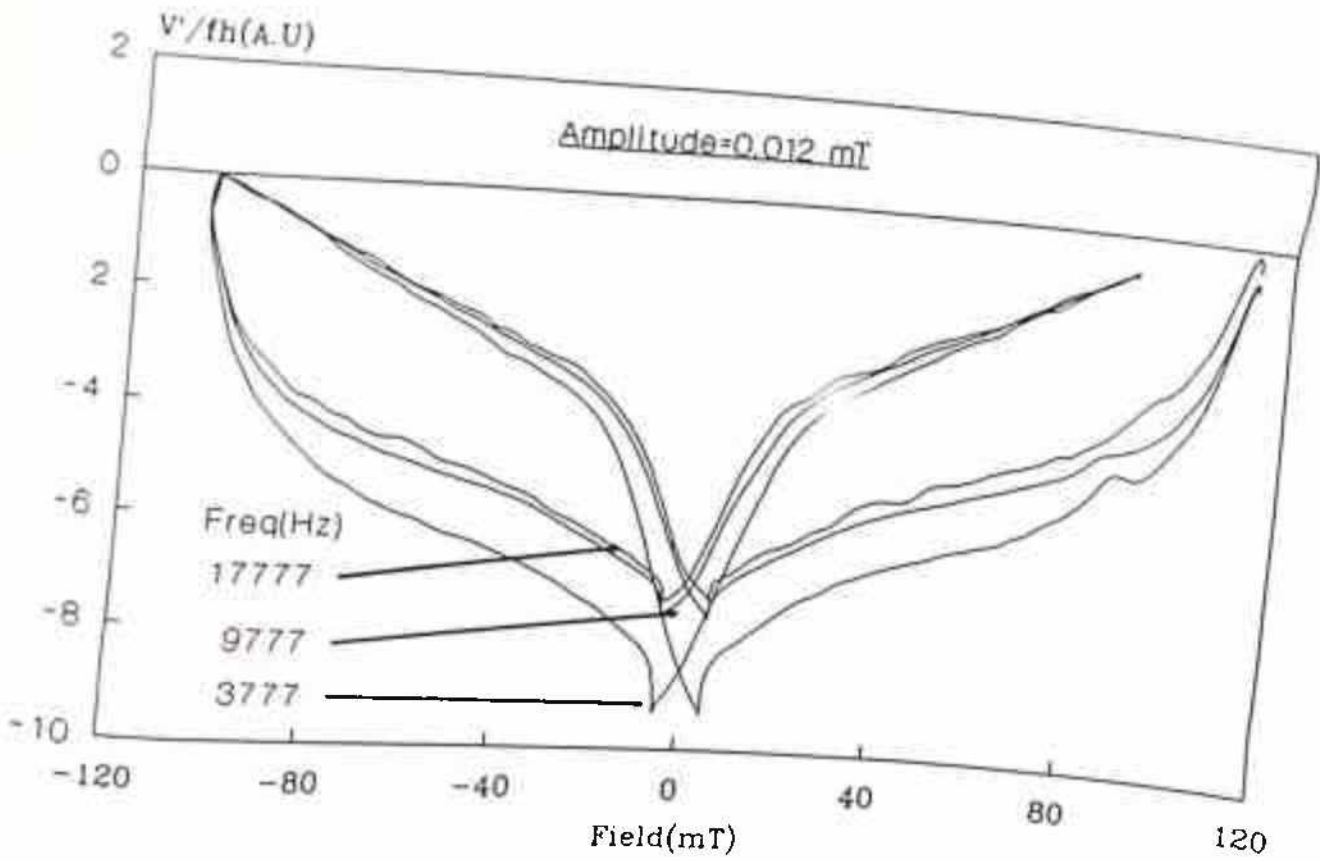


Figure 4.3.9a: $V'/fh (= \chi')$ for four different frequencies for sample A1.

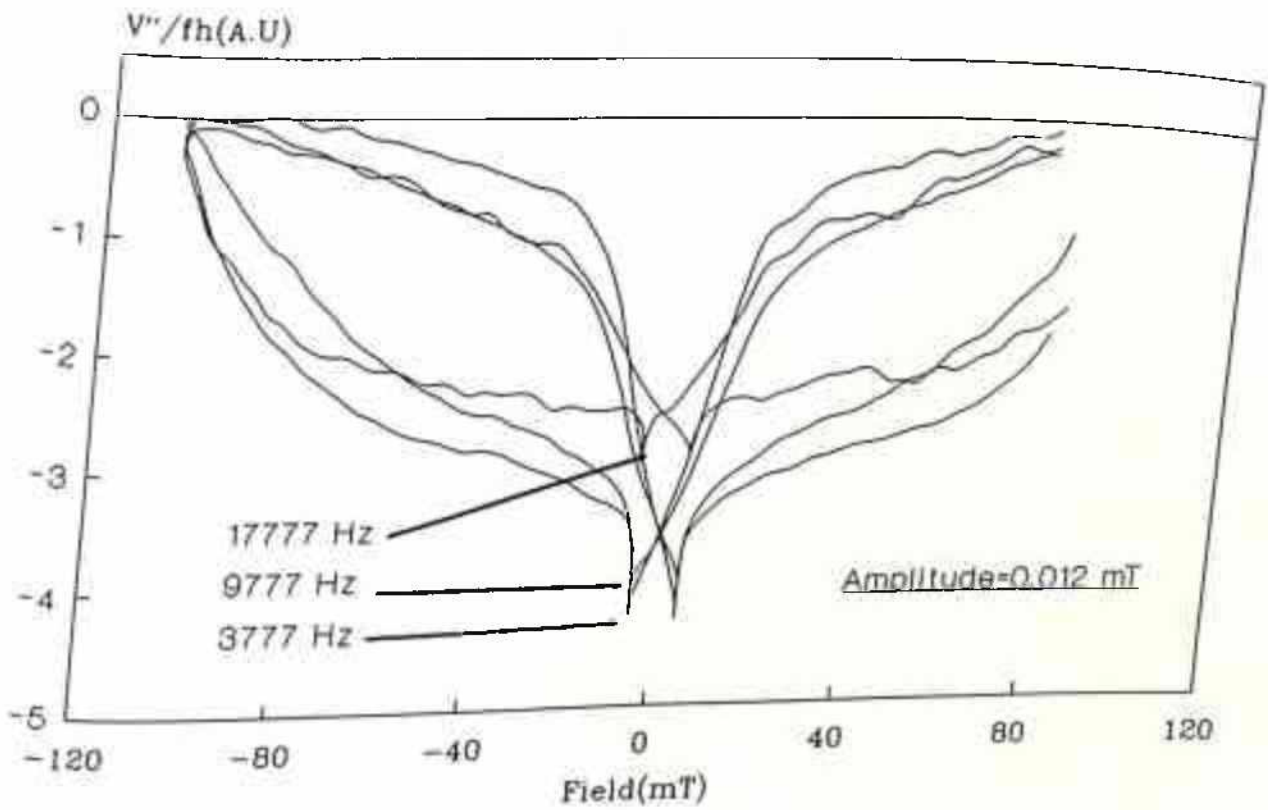
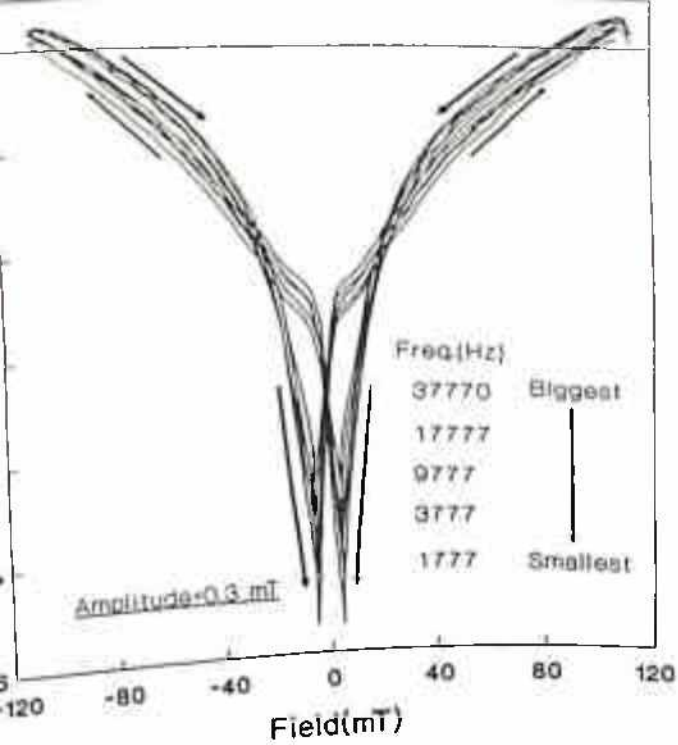


Figure 4.3.9b: $V''/fh (= \chi'')$ for four different frequencies for sample A1.

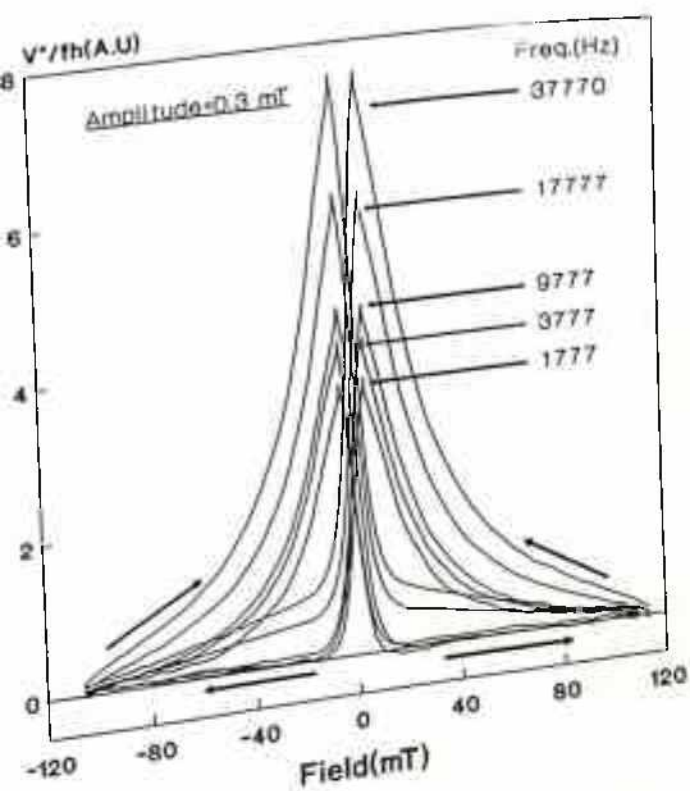
for an amplitude of 0.012 mT. As proposed earlier, *this amplitude may be below the "cross-over amplitude"* of the sample and hence the opposite trend in the frequency dependence was expected. Thus the decreasing trend in the depths of both $\chi'(H)$ and $\chi''(H)$ loops with increasing frequency in figure 4.3.9 was supportive of this fact.

In figures 4.3.10(a,b), 4.3.11(a,b) and 4.3.12(a,b) the $\chi'(H)$ and $\chi''(H)$ loops have been plotted for the sample A3(6% PbO) for amplitude of 0.3, 0.06 and 0.012 mT respectively for dependence. *The depth of the valleys increased with increasing frequency.* In figure 4.3.10a, for amplitude 0.3 mT, this frequency dependence was seen to be maximum and with decreasing amplitude the depths became less sensitive to frequency while the width increased with increasing frequency. There was a new feature in the real loops clearly seen in figure 4.3.10a for the highest amplitude of the experiment (in the study of amplitude dependence in section 4.3.3 this feature was missed because of lower resolution in plotting). This was the flipping of the increasing and decreasing arms at higher DC bias creating a further loops (say lobb) on both sides at higher DC bias fields (magnitude wise). In the parallel field configuration, this flip was not seen because the DC field range was small and in all cases of $\chi'(H)$ loops the decreasing arms were below the increasing arms at all DC field. Here it is further clear that the flip appeared at a higher DC bias (i.e., the lobbs reduced by size) with decrease in amplitude and disappeared at a lower amplitude depending on the sample. The interesting feature of the lobbs was that they were virtually independent of frequency. This probably ascertains the proposition that at higher DC bias grain contribution dominates and as will be addressed in later section, grain contribution is less dependent on frequency.

The $\chi''(H)$ loops as seen in figure 4.3.10b for amplitude 0.3 mT showed strong dependence on frequency and the heights of the loops increased steadily with increasing frequency along with obvious increase in hysteresis. With decrease in amplitude to 0.06 mT (figure 4.3.11b), the valley appeared near zero bias field and the depth of the valleys decreased with increasing frequency. Along with this, the heights of the $\chi''(H)$ loops were also seen to increase with increasing frequency like the 0.3 mT amplitude case. With further decrease of amplitude to 0.012 mT (figure 4.3.12b), the valleys were seen to be further prominent and the depth of the valleys also showed a strong decreasing trend with increasing frequency. However



3.10a: $V'/fh(= \chi')$ for different frequencies for sample



4.3.10b: $V''/fh(= \chi'')$ for different frequencies for sample

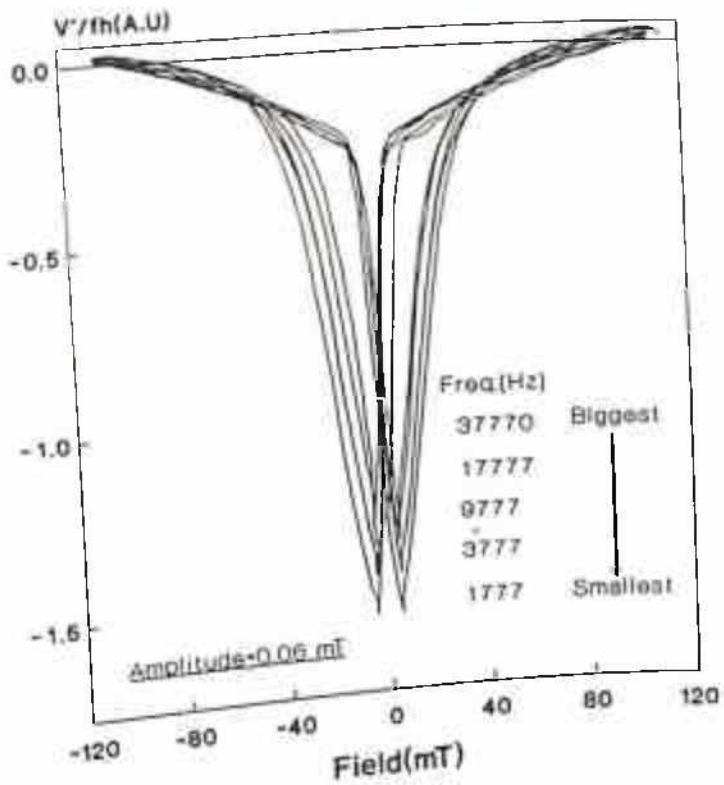


Figure 4.3.11a: $V'/fh (\approx \chi')$ for different frequencies for sample A3.

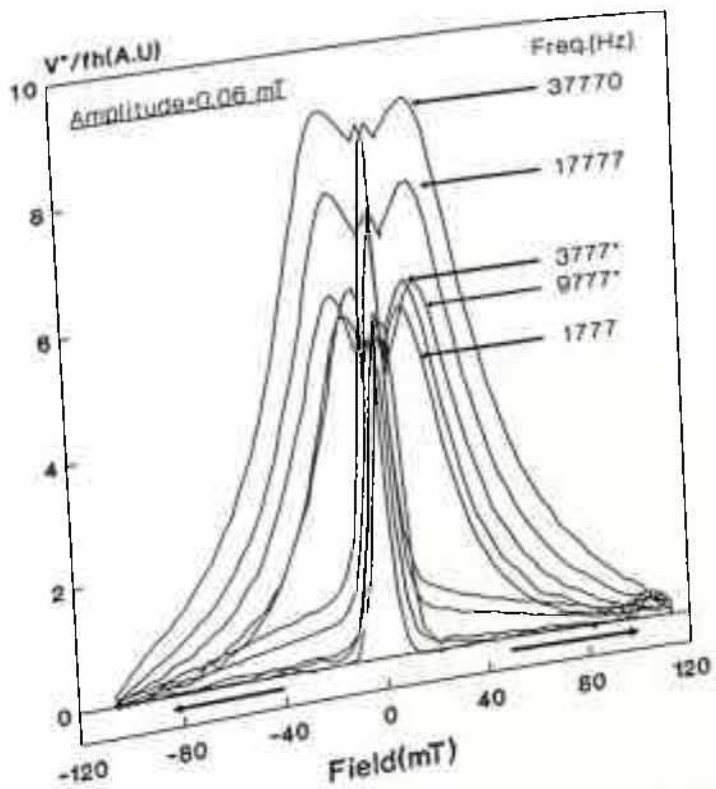


Figure 4.3.11b: $V''/fh (\approx \chi'')$ for different frequencies for sample A3.

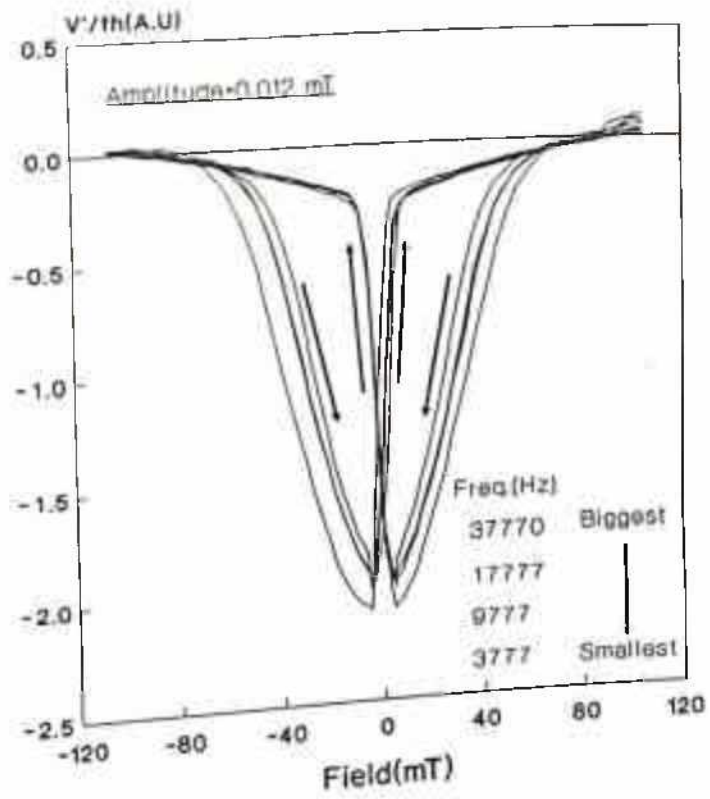


Figure 4.3.12a: $V'/fh (= \chi')$ for different frequencies for sample A3.

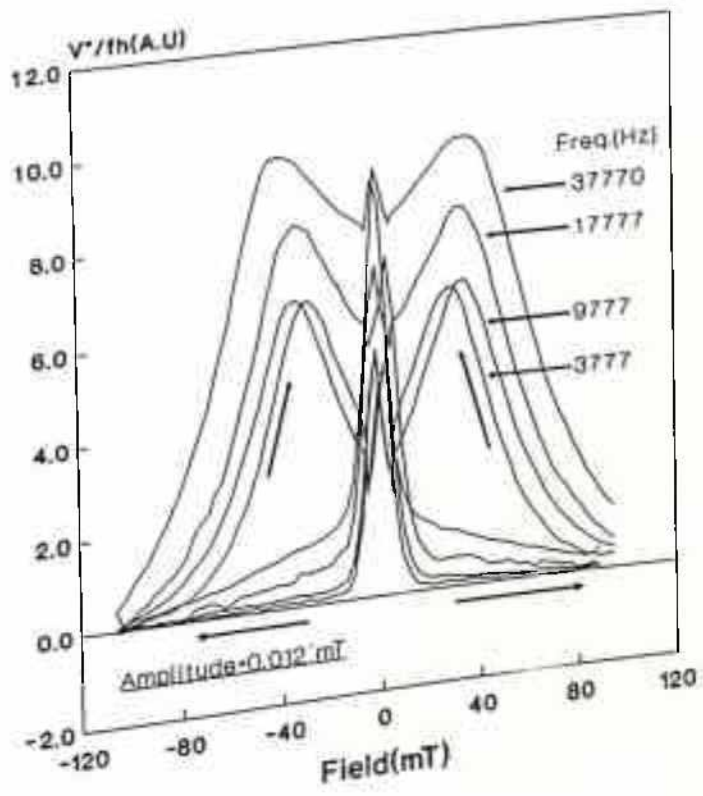


Figure 4.3.12b: $V''/fh (= \chi'')$ for different frequencies for sample A3.

the heights of the $\chi''(H)$ loops became less sensitive to frequency with decreasing amplitude (figures 4.3.10b to 4.3.12b). In continuation from section 4.2.2c (particularly sample A2), here even the lowest the amplitude of 0.012 mT was slightly higher than the cross-over amplitude. It was unfortunate that the experimental set up as used here, was not sensitive enough to work with amplitudes lower than 0.012 mT and hence the cross-over amplitude could not be decided for most of the samples except for samples A1 and A2 where it was within the range of amplitude covered. Further, as the dependence on frequency became less with lower amplitudes, it was seen that effective dependence on frequency below cross-over amplitude was obvious only around 17777 Hz or higher. However, the coil resonance frequency being 40 KHz, the result will attract criticism.

At amplitudes much higher than the cross-over amplitudes, dependence on frequency was large and seen to be monotonous over the full range of frequency - from 373 Hz (quite below the resonance frequency) to 97770 Hz (quite above the resonance frequency) and there was no discontinuity in the dependence on frequency in two regimes of frequencies. This was possibly due to the fact that with higher amplitudes total variation of signal over full excursion of DC field was quite large and hence was not masked by spurious effects. It must, further be noticed that with higher amplitudes basic inferences on the dependence on frequency of the $\chi(H)$ loops could be made even without considering data at higher frequencies (e.g > 17777 Hz). This argument can further be stressed in sample A4 which was seen to have the worst $J_{c1}(0)$.

The figures 4.3.13(a,b), 4.3.14(a,b) and 4.3.15(a,b) contain the $\chi'(H)$ and $\chi''(H)$ loops for sample A4 for amplitudes 0.3, 0.06 and 0.012 mT respectively for frequencies as shown within the diagrams (maximum frequency ≈ 17 KHz). Further in figures 4.3.16(a,b) and 4.3.17(a,b), the same $\chi'(H)$ and $\chi''(H)$ loops of figures 4.3.13 and 4.3.15 respectively have been plotted in a single frame with a frequency range of 3777 Hz to 57770 Hz.

At highest amplitude of 0.3 mT, the $\chi'(H)$ loops were almost independent of frequency. In fact these loops could be identified with the extended lobbs (as seen in sample A3 for higher amplitudes) which also showed negligible dependence on frequency. This feeble dependence of the $\chi'(H)$ loops on frequency must not be confused with the similar weak dependence on frequency in sample A1 (figure 4.3.8a). Because the amplitude 0.3 mT was effectively a low amplitude in sample A1 (but higher than cross-over amplitude) while in sample A4 it was effec-

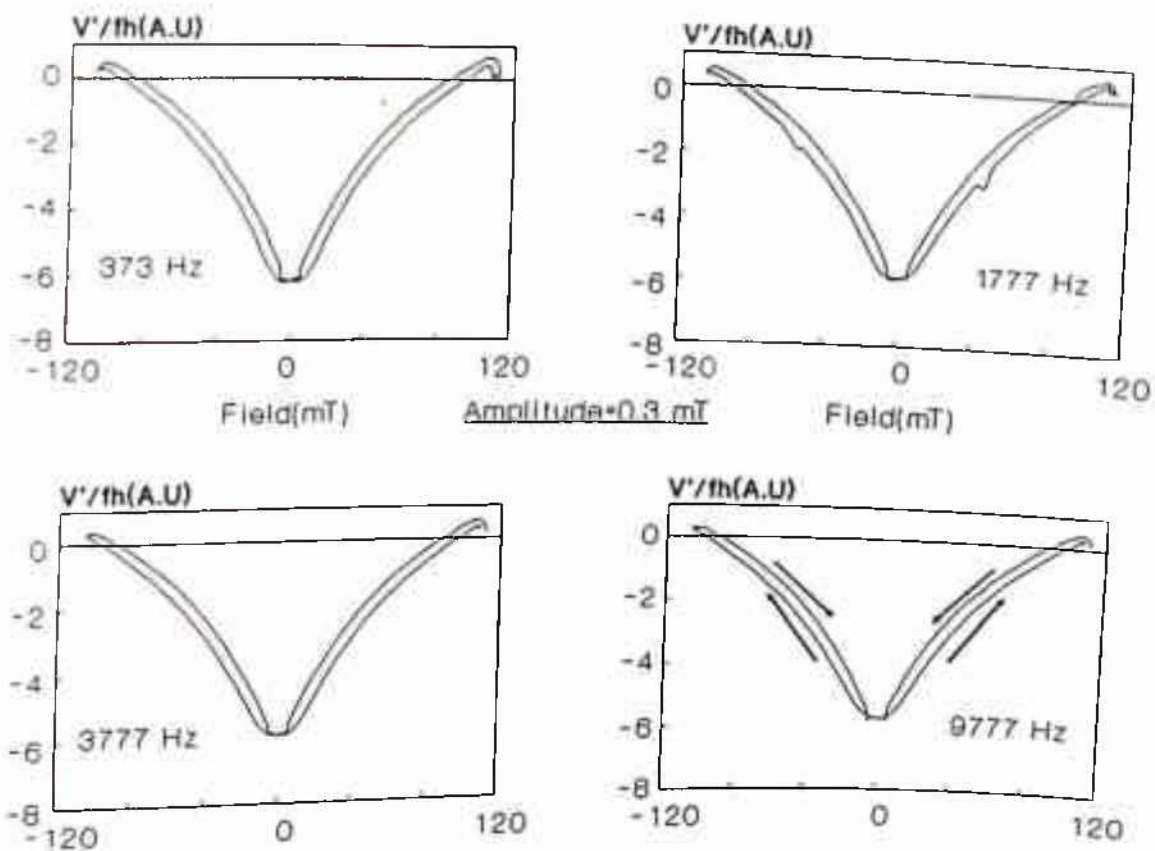


Figure 4.3.13a: $V'/fh (\approx \chi')$ for four different frequencies for sample A4.

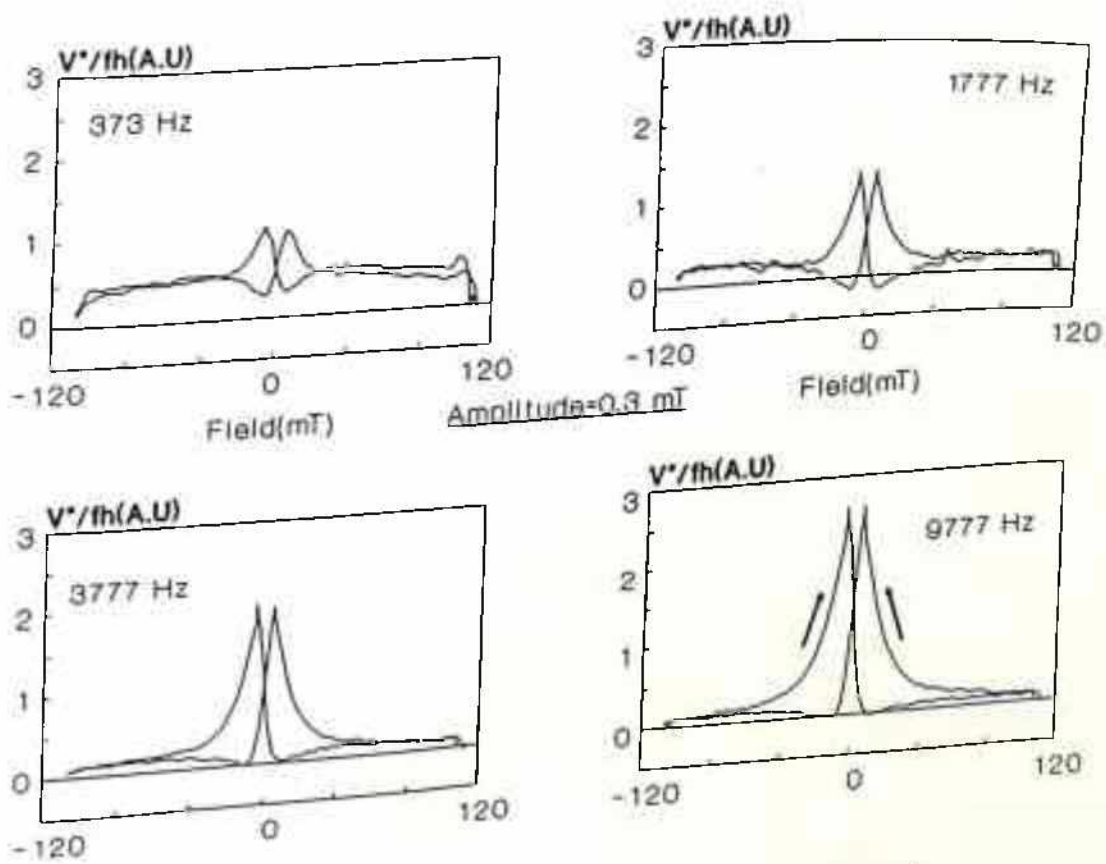


Figure 4.3.13b: $V''/fh (\approx \chi'')$ for four different frequencies for sample A4.

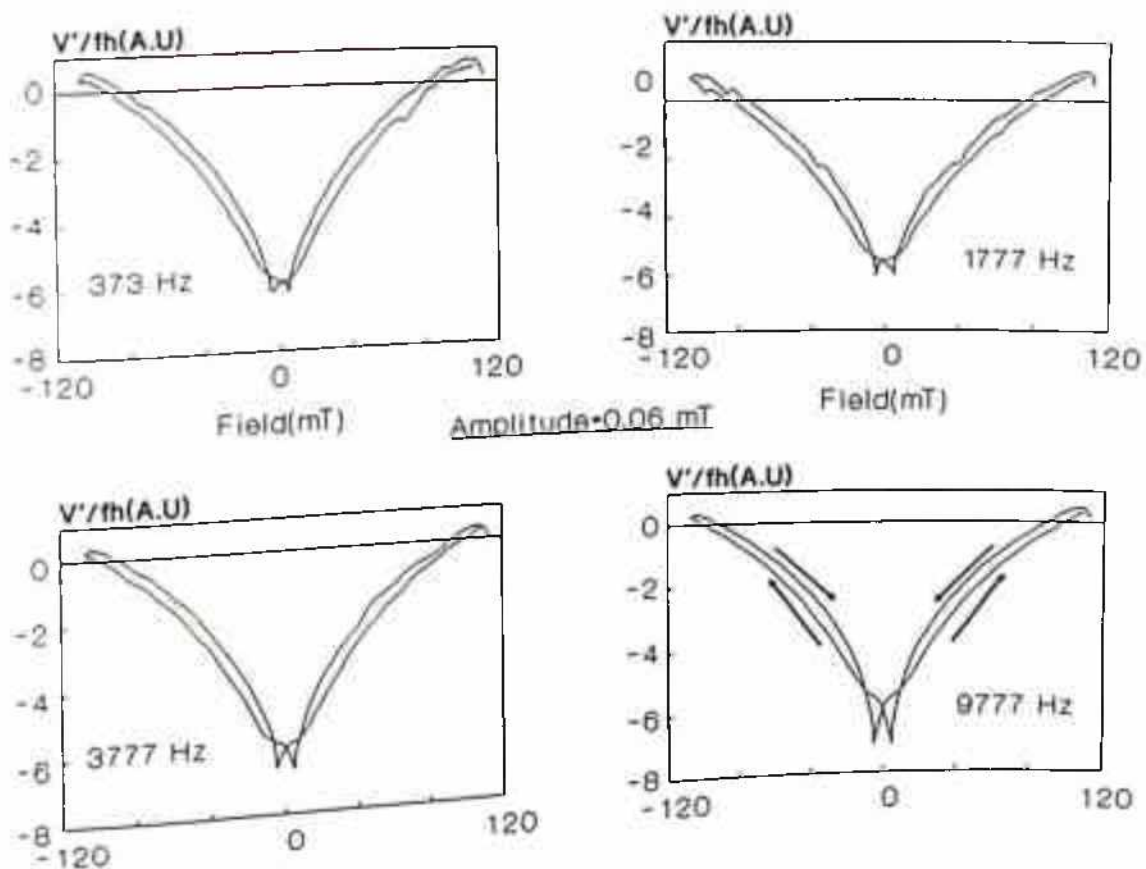


Figure 4.3.14a: $V'/fh (\approx \chi')$ for four different frequencies for sample A4.

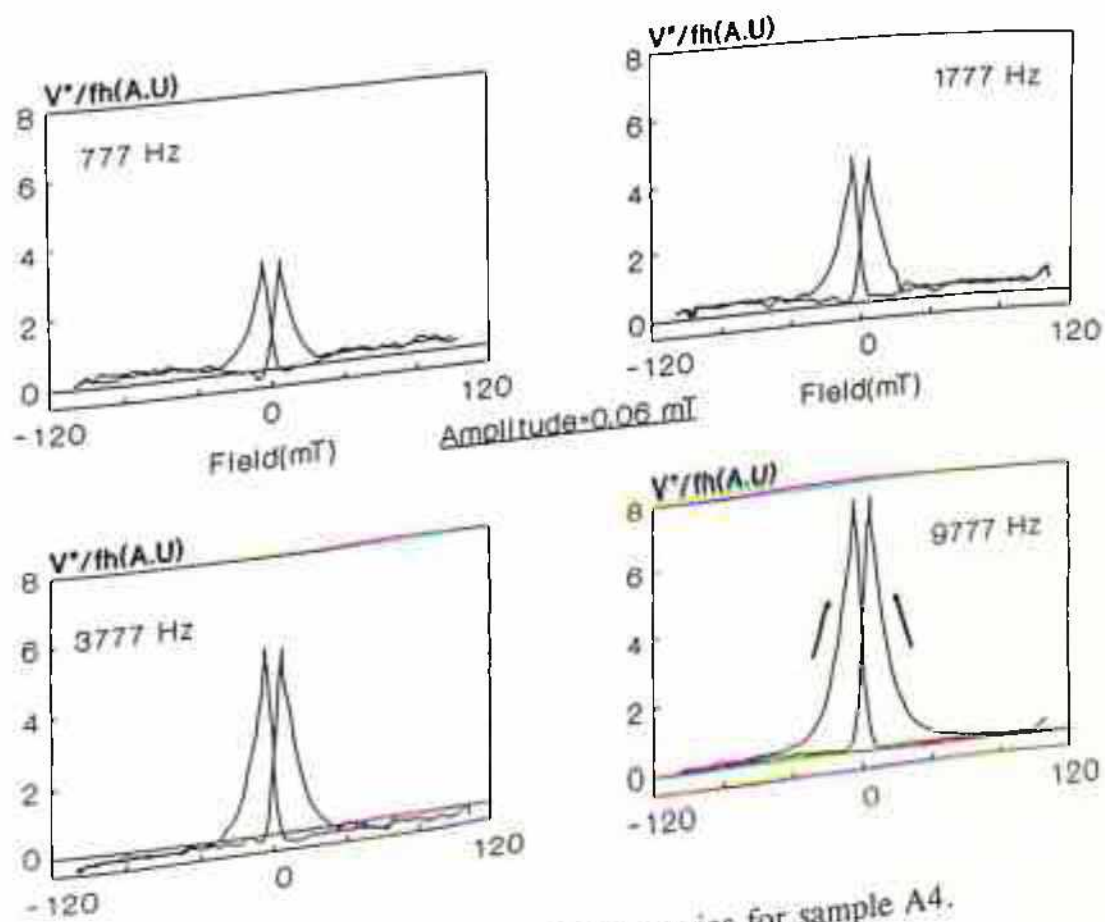
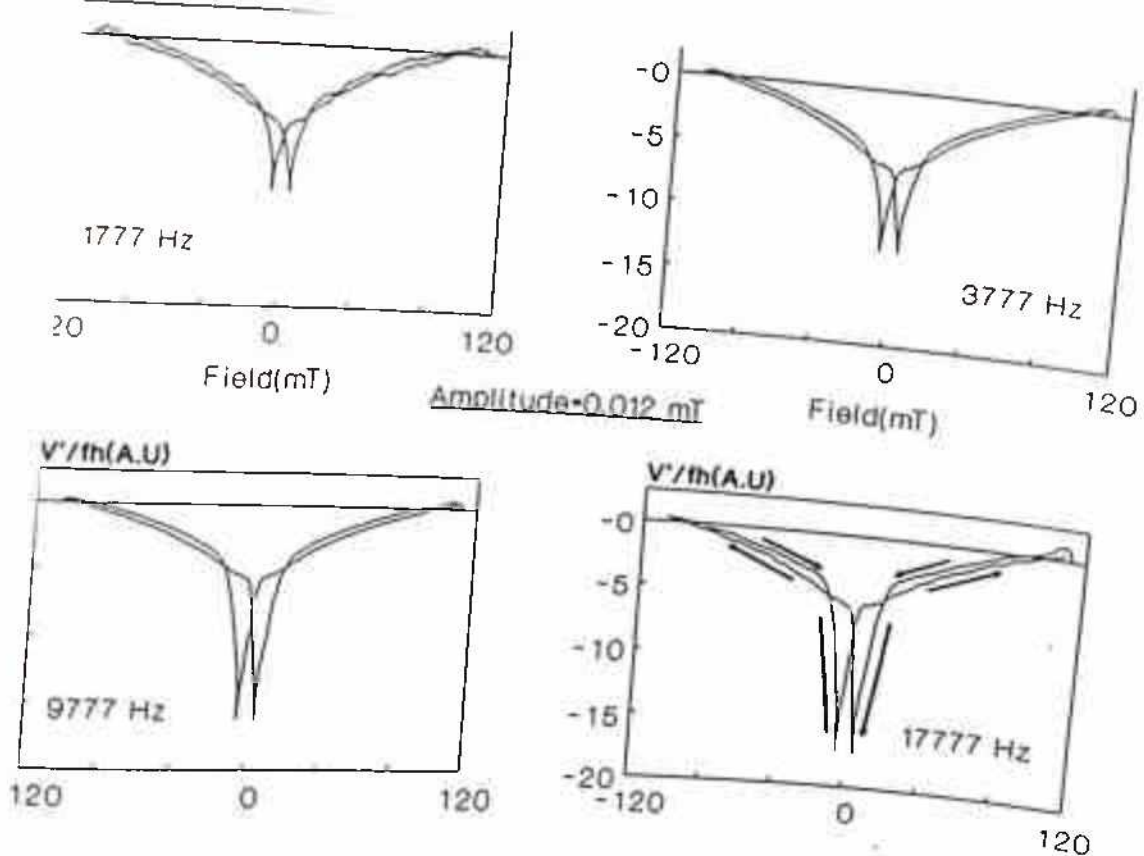
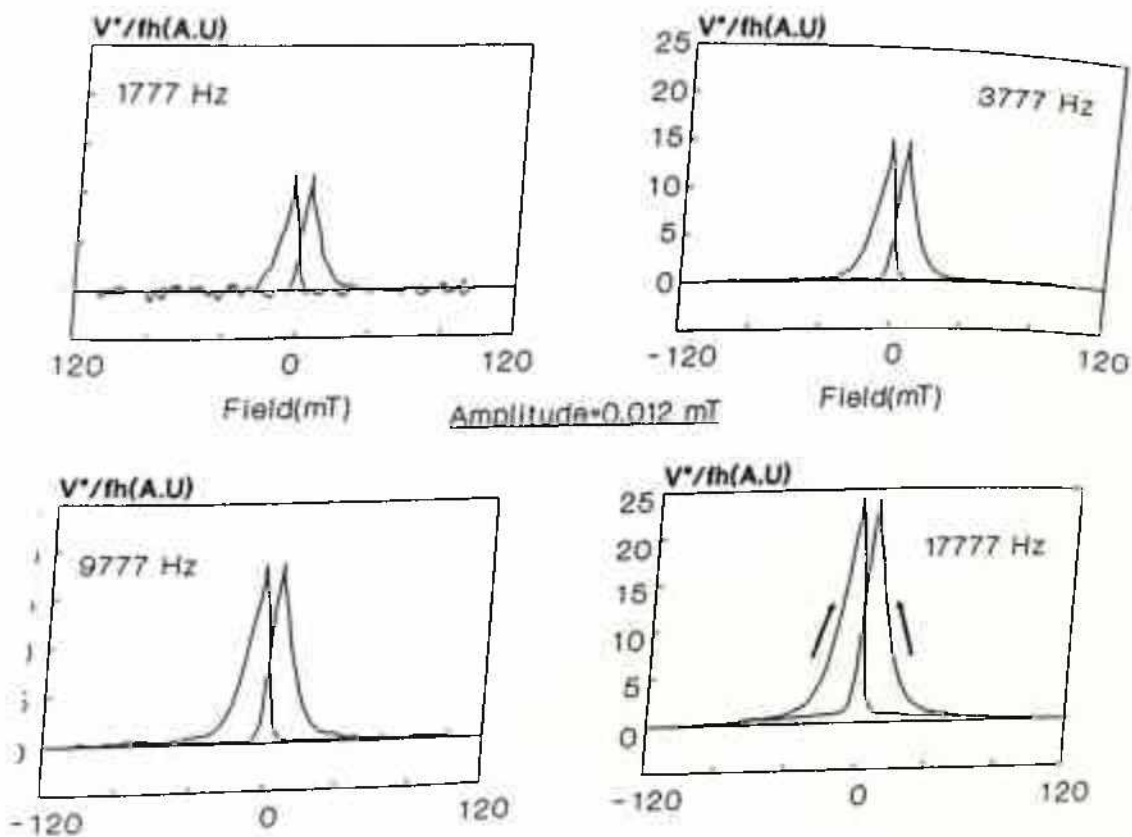


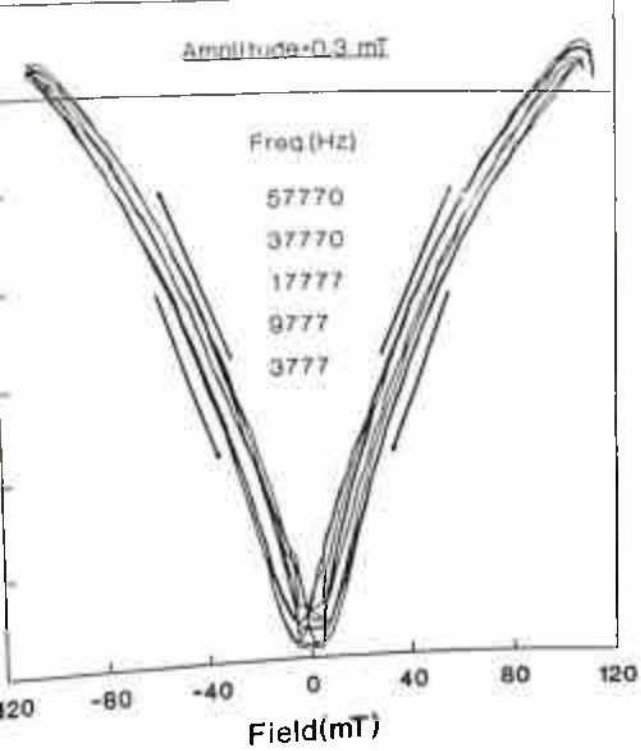
Figure 4.3.14b: $V''/fh (\approx \chi'')$ for four different frequencies for sample A4.



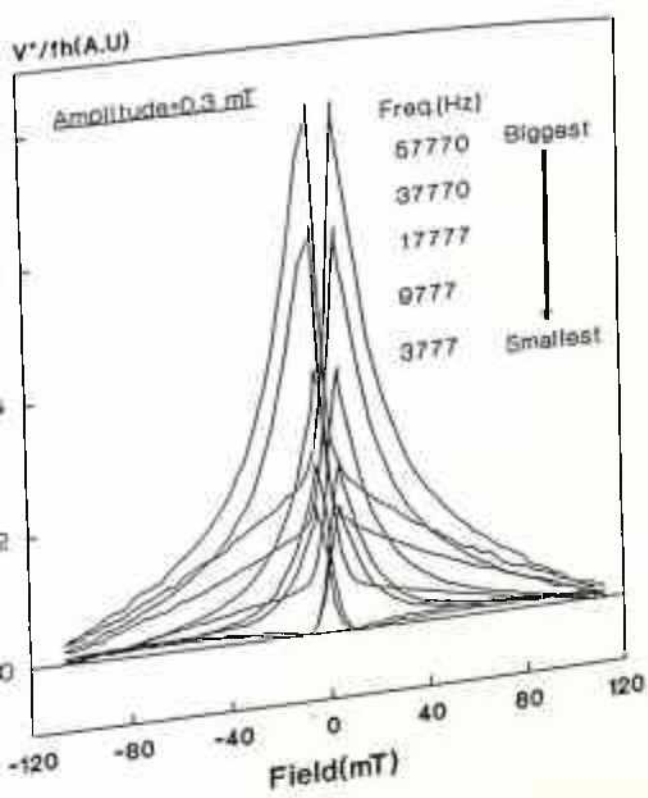
15a: $V'/fh(\approx \chi')$ for four different frequencies for sample A4.



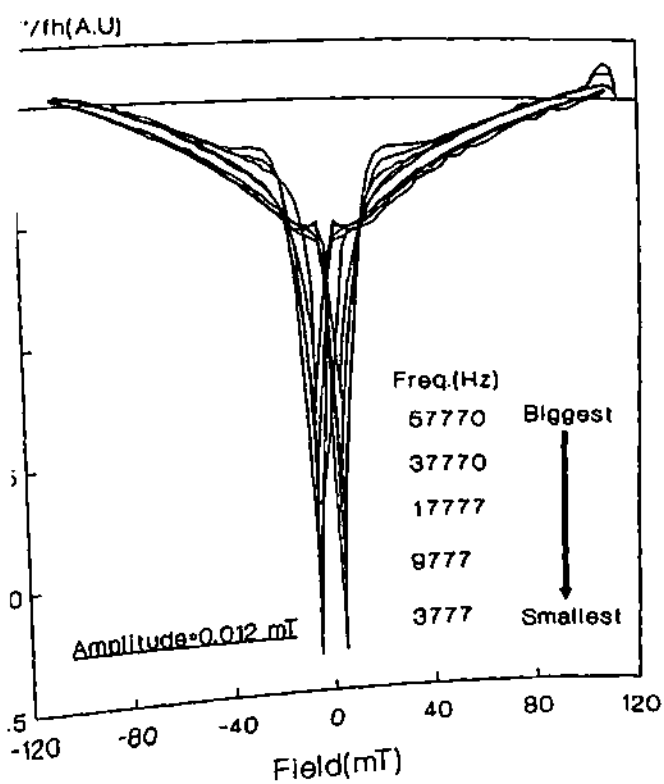
3.15b: $V''/fh(\approx \chi'')$ for four different frequencies for sample A4.



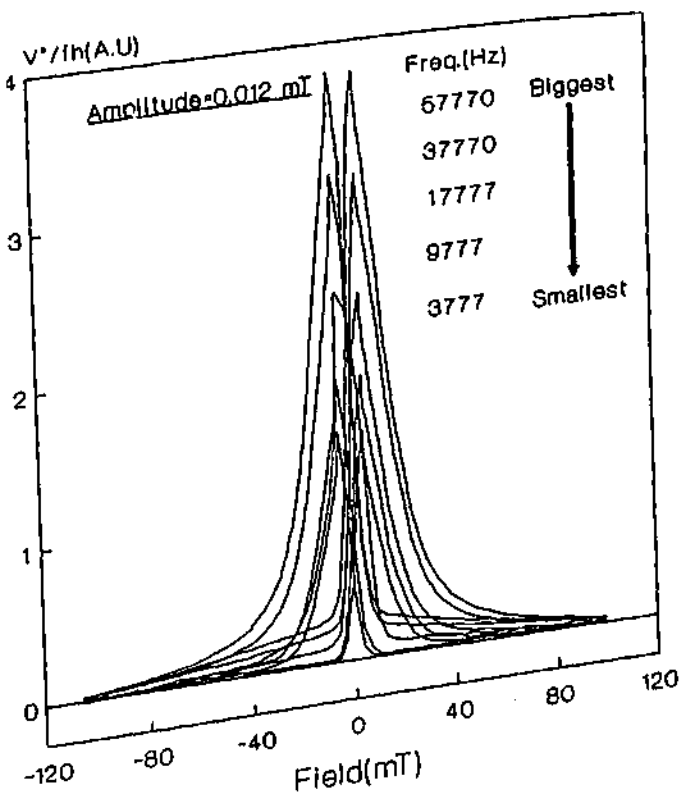
16a: $V'/fh (\approx \chi')$ for different frequencies for sample



3.16b: $V''/fh (\approx \chi'')$ for different frequencies for sample



3.17a: $V'/fh (= \chi')$ for different frequencies for sample



for sample

tively quite a high amplitude. This could also be ascertained from their $\chi''(H)$ loops also (in A4, amplitude being high, valleys(V) were not seen). As will be seen in next section, that this behavior in sample A4 might be due to vanishing of GB contribution at quite high amplitudes while in A1 GB contribution was present but J_{ω} being high frequency response was low. The

tively quite a high amplitude. This could also be ascertained from their $\chi''(H)$ loops also (in A4, amplitude being high, valleys(V) were not seen). As will be seen in next section, that this behavior in sample A4 might be due to vanishing of GB contribution at quite high amplitudes while in A1 GB contribution was present but J_c being high frequency response was low. The similar behavior of $\chi'(H)$ (figure 4.3.13a) was continued over the full range of frequency and have been clearly shown in figure 4.3.16a. With decrease of amplitude from 0.3 mT to 0.06 mT (figure 4.3.14a), valleys(V) appeared and the depths of these valleys(V) showed strong increasing trend with increasing frequency. With further decrease of amplitude to 0.012 mT (figure 4.3.15a) the valleys became more pronounced and showed a similar frequency dependence. This have been further emphasized in figure 4.3.17a for higher range of frequency.

The $\chi''(H)$ loops at an amplitude of 0.3 mT in figure 4.3.13b, showed strong dependence on frequency, i.e., the heights decreased strongly with increasing frequency from 373 Hz to 9777 Hz. The similar dependence on frequency were also seen for amplitude of 0.06 mT (figure 4.3.14b) and 0.012 mT (figures 4.3.15b and 4.3.17b) except that at lower amplitudes dependence on frequency became less pronounced.

It has already been mentioned that the aim of the discussion on data of sample A4 is to establish beyond doubt, that the effect of frequency can be seen to be present even at a range of frequency well below the resonance frequency of the coil. Obviously in that goal, the data was quite successful and showed strong dependence on frequency within a range of 373 to 9777 Hz.

The further importance of the data of sample A4 is that it once again emphasizes the fact that the signal involved being high, resonance of the coil does not limit the measurement below the resonance frequency. This is obvious from figures 4.3.13 and 4.3.16 (or 4.3.15 and 4.3.17) where the continuity in frequency dependence is clear.

4.3.3. SUM UP:

In this section basic aim was to emphasize the fact that the $\chi'(H)$ and $\chi''(H)$ is likely to be independent of the configuration of the fields (AC and DC). It is further stressed here that the observed frequency dependence is not an artifact of the experimental set-up and can be seen

in a frequency range below 10 KHz, far away from the resonance frequency of the coil set-up. The following findings are important;

- In a given range of DC field the $\chi'(H)$ and $\chi''(H)$ loops were almost independent of configuration of the AC and the DC fields except some quantitative change.
- A study on the bulk size dependence revealed strong variation of the $\chi'(H)$ and $\chi''(H)$ loops with change in diameter. The positions of the valleys and peaks close to zero bias remained almost unchanged with change in diameter. But the peaks on the decreasing (magnitude wise) arms shifted to a lower DC bias value with decreasing diameter.
- Amplitude dependence of the $\chi'(H)$ and $\chi''(H)$ showed systematic variation and was in line with the data of co-axial fields configuration.
- From amplitude dependence, it can be concluded qualitatively that the samples from A1 to A4 had gradually decreasing J_{c1} .
- Frequency dependence of the $\chi'(H)$ and $\chi''(H)$ was similar to the case of co-axial configuration of fields.
- In sample A4, frequency dependence was obvious even in frequency range below 10 KHz and thus confirmed the frequency dependence to be a material property.

References:

- [1] M. Tinkham and C.J. Lobb 1989 Solid State Physic 42, 91

EXPERIMENTAL DATA

A CLOSER LOOK INTO THE FREQUENCY DEPENDENCE:

This part contains a brief discussion on the experimentally observed frequency dependence of the $\chi'(H)$ and $\chi''(H)$. An attempt has been made to explain the frequency dependence by considering the the flux creep and "AC field mediated depinning". A comment on the IL has also been presented.

4.4.1. REVIEW	279
4.4.2. LOOKING BACK	280
4.4.3. COMMENT ON THE IL	282
REFERENCE	284

4.4. A CLOSER LOOK INTO THE FREQUENCY DEPENDENCE:

In Parts A, B and C of Chapter 4, the experimental data have been described in a straight forward manner along with possible explanation on the basis of the model calculations of Chapter 3. However, it is felt that the discussions, in a sense, were local and confined to the respective data. As the behavior of HTSC is more or less the response of FLs to the applied electric or magnetic fields, a global discussion on the data is essential to bring out the intricacy of the flux line dynamics. Here the discussion will be in that line - to enlighten the "non-critical" contributions from the Josephson vortices of the grain boundaries as well as the Abrikosov vortices of the grain.

4.4.1. REVIEW:

The effect of frequency in HTSC has received a great deal of attention. The effect of frequency was observed through the shift of the $\chi''(T)$ peak (the low temperature peak on $\chi''(T)$ as discussed in Chapter 2) with frequency. It was seen that the peak shifted to higher temperature with frequency[2,3]. Thus, the irreversibility line(IL) as predicted from this $\chi''(T)$ peak obviously showed frequency dependence and the IL was seen to shift towards a higher temperature and field[4] with increasing frequency. (An illuminating debate on the IL has been given in appendix of ref. [1] - here after to be referred as "debate")

There are different models explaining the origin of this $\chi''(T)$ peak and hence the IL, viz., vortex glass[5], flux creep[6], thermally activated flux flow[7] and flux lattice melting[8]. As Q. Y. Chen stressed in the "debate"[9], if the IL represents some sort of phase transition in the vortex state, it should be an intrinsic property and so independent of frequency, amplitude and sample size. Most of the data predict the opposite. However, below 1 KHz as discussed by Flippen[4], IL was almost independent of frequency. The frequency dependence of the IL can qualitatively be explained in the flux creep model[?], or in the thermally activated flux flow model(TAFF)[7]. However, the independence of the IL on frequency in the lower frequency range as such, is not expected in these models.

Q. Y. Chen[10] argued in his article as well as in the "debate" that with increasing frequency and field, weakening of flux pinning will lead to increasing flux-motion effect. This "depinning of flux lines" by oscillatory fields has been addressed in Chapter 3 and 4 to

some extend.

In this section, the aim is to bring out the essence of the frequency dependence from the data in Chapter 4 and then extend the finding to contribute in the explanation of the apparent confusion of the frequency dependence of the IL.

4.4.2. LOOKING BACK:

In a two component model one has two type of vortices, the Josephson vortices (here after to be referred as JV) prevalent in the grain boundaries and the Abrikosov vortices (here after to be referred as AV) within the grain. It is now well understood that the JVs are weakly pinned and are the cause of the most of the peculiarities in ceramic samples.

Let us first consider the high field $\chi'(H)$ and $\chi''(H)$ loops as described in Part C of Chapter 4. It was observed that the effect of frequency was more prominent in the low field (DC bias) region of the loops. It was seen that the valleys(V) (viz., figure 4.3.8b) on decreasing arms (magnitude wise) moved upward (i.e., the depths of the valleys decreased) with increasing frequency. However, there was some discontinuity in the frequency dependence at quite low frequency(e.g., below 3777 Hz) and it was seen that the depths as defined above increased with increasing frequency in this frequency range.

On the basis of the effect of the "non-critical" contribution as described in Chapter 3 on the model calculations, this frequency dependence can probably be explained qualitatively. With increasing frequency two exactly opposite processes may arise - i) if the frequency was lower than f_0 (eqn. 3.2.10) which was the case in almost every experimental situations as well as here, the creep component, J_{creep} is negative and decreases in magnitude with increasing frequency and so effective J_c will increase with increasing frequency, ii). $J_{depinning}$ (eqn. 3.2.20) will monotonously increase with increasing frequency causing decrease in effective J_c . Thus the overall effect will be decided by the dominance of the one or the other of the two factors.

Now let us consider the theoretical calculation as shown in figure 3.2.32(a,b) in Chapter 3, Part B, section 3.2.5. The depths of the valleys(V) as obvious in figure 3.2.32b, increased with increasing $J_{c1}(0)$. At lower frequency(< 3777 Hz), $J_{depinning}$ may be less effective than J_{creep} . Thus with increase of frequency from 377 Hz to 3777 Hz the effective $J_{c1}(0)$ may show an increasing trend hence increasing the depths of the valleys (clearly seen in figure 4.3.8b in Part C). With increasing frequency above this range, the balancing

process of the two components (J_{creep} and $J_{depinning}$) may change and it is likely that JVs being more susceptible to the "AC field mediated depinning", the effective $J_{c1}(0)$ will decrease with increasing frequency. This will decrease the depth of the valleys(V) as seen in the higher frequency range (> 3777 Hz). However, the apparent independence of the real part with frequency in the figure 4.3.8a is not justifiable from the prediction of the model (figure 3.2.32a).

At higher DC bias fields, grain contribution is dominant and the effect of frequency is likely to be less because the AVs of the grains are well pinned and hence depinning (and also the creep) is expected to be less effective. This argument can be substantiated from the experimental data at higher amplitudes for poor J_c samples. Because if $J_{c1}(0)$ is less, at a higher amplitude, the GB contribution is not likely to be present. Like, in sample A4, in figures 4.3.13a and 4.3.16a (Part C, Chapter 4) for an amplitude of 0.3 mT the loops did show negligible frequency dependence. But with decreasing amplitude (0.06 mT - figure 4.3.14a and 0.012 mT - figures 4.3.16a and 4.3.17a), sharp valleys appeared in the $\chi'(H)$ loops at low DC bias values and the depths of the valleys showed monotonic increase with increasing frequency. This monotonic increase in the depths of the $\chi'(H)$ loops in these figure can be compared with that of the model predictions of figure 3.2.32a where the increase in the depth of the valleys indicates increasing J_c . Thus, increasing depths of the valleys in the $\chi'(H)$ loops in experimental data in figures 4.3.14a and 4.3.16a was indicative of the fact that in this sample (A4) creep contribution overran the depinning contribution of the JVs. This was further true in the $\chi''(H)$ loops in figures 4.3.13b (and 4.3.16b), 4.3.14b and 4.3.15b (and 4.3.17b). The increase in the heights of these loops with increasing frequency in these figures can be justified on the basis of dominant flux creep. As obvious from figure 3.2.32b, this type of shape of $\chi''(H)$ loops was seen when $J_{c1}(0) (\approx 200 \text{ amp/cm}^2$ in this figure) was quite less. It was seen (not shown in figure 3.2.32b) that with further decrease in $J_{c1}(0)$ below 200 amp/cm^2 the height of the $\chi''(H)$ loop decreased. Thus, with increasing frequency due to decrease in J_{creep} , effective $J_{c1}(0)$ increased and so the height of the $\chi''(H)$ loop increased.

Thus one can expect the monotonous behavior with respect to frequency to appear either in the two extreme cases - the strong creep (e.g., sample A4) or the large depinning (e.g., sample A1 - though not at the extreme end).

As the effect of "AC field mediated depinning" must be amplitude dependent (whereas

creep is not likely to be amplitude dependent), the presence of a cross-over-amplitude can be visualized.

It is already discussed above, in the low frequency range (< 3777 Hz) in sample A1 there was an opposite behavior of the valley(V) of the $\chi''(H)$ loops than that at higher frequency range (< 3777 Hz). It is also obvious from above discussion that like a cross-over-amplitude one must expect to see some cross-over-frequency also. However, in the samples studied so far, this possible cross-over-frequency is in lower side of the frequency range and so there is not much data below this possible cross-over-frequency to see the exact cross-over from one regime to the other.

The search for a possible cross-over-frequency at a higher value, has no guideline. However, the sample B1 (pure YBCO of batch B) probably is probably indicating the same (it is unfortunate that this batch is not well characterized). In figure 4.4.1 the $\chi''(H)$ loops for different frequencies for sample B1 for an amplitude of 0.3 mT have been plotted (for mutually perpendicular fields).

It is obvious that with increasing frequency from 377 to 9777 Hz the valley(V) moved downward in a regular fashion. But above this frequency (17777 Hz and higher) there was a decrease in the depth of the valley(V). Thus the cross-over-frequency, in this sample was

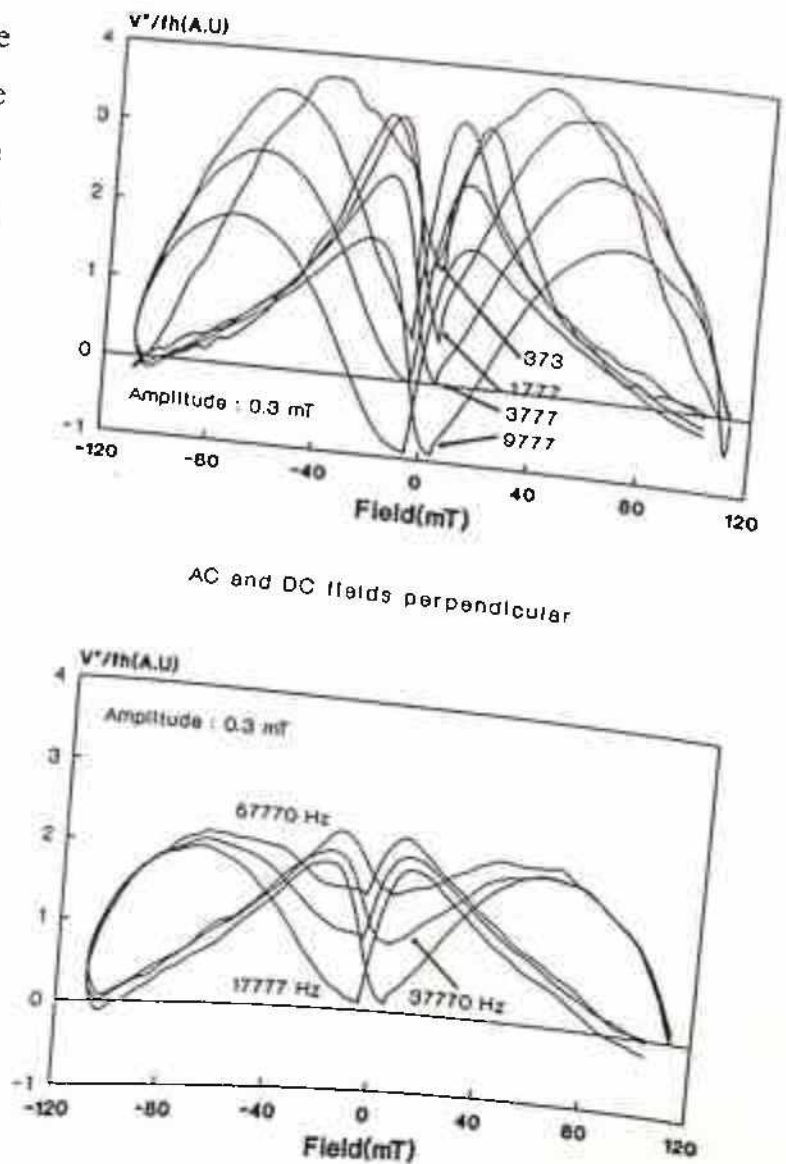


Figure 4.4: Possible cross-over-frequency in sample B1. In the upper frame, the valleys moving downward while in lower frame upward.

REFERENCES:

- [1] Magnetic Susceptibility of Superconductors and Others Spin Systems[S^d] 1991 ed. R.A. Hein, T. Francavilla and D.H. Liebenberg, Plenum Press
- [2] K.-H. Müller 1990 Physica C **168**, 585
- [3] A.P. Malozemoff, T.K. Worthington, Y. Yeshuran, F. Holtzberg and P.H. Kes 1988 Phys. Rev. B. **38**, 7230
- [4] R.B. Flippen 199 in S^d p353
- [5] K.A. Müller, M. Takashige and J.G. Bednorze 1987 Phys. Rev. Lett. **58**, 1143
- [6] M.R. Beasley, R. Labusch and W.W. Webb 1969 Phys. REv. **181**, 682
- [7] P.H. Kes, J. Arts, J. van den Berg, C.J. van den Beek and J. Mydosh 1989 Supercond. Sci. Technol. **1**, 242
- [8] P.L. Gammel 1990 J. Appl. Phys. **67**, 4676
- [9] Q.Y. Chen on "The Irreversibility Line" in the appendix of S^d
- [10] Q.Y. Chen in S^d p81

CONCLUSIONS:

1. A realistic two component critical state model was developed and solved numerically. This can successfully explain the low field anomalous M-H loops of the ceramic HTSC sample.
2. This model was extended for different field ranges and an exact evolution of the M-H loops over the variation of DC field range was observed.
3. Even the Z-shaped M-H loops could be explained by adding a shielding contribution.
4. Further the effect of the grain size studied in this model and the results were seen to be in agreement with already published data.
5. The same model was extended for AC susceptibility calculation as a function of DC bias field. The consideration of demagnetization factor led to hysteresis in the $\chi'(H)$ and $\chi''(H)$ loops.
6. Hysteresis of the $\chi'(H)$ and $\chi''(H)$ loops for different configurations of the fields was observed experimentally.
7. The low field $\chi'(H)$ and $\chi''(H)$ loops in the co-axial field configuration were in close qualitative agreement with the theoretical prediction. However the $\chi'(H)$ loops showed better agreement with calculation.
8. The features of the high field $\chi'(H)$ and $\chi''(H)$ loops in perpendicular configuration of fields showed good agreement to model predictions. But the extra large hysteresis of the experimental $\chi''(H)$ loops could not be explained by the model calculations.
9. The frequency dependence of the $\chi'(H)$ and $\chi''(H)$ loops was observed experimentally and an attempt was made to explain the data including flux creep and "AC field mediated depinning" in the model.
10. Frequency dependence of the $\chi'(H)$ and $\chi''(H)$ loops showed the presence of a cross-over-amplitude, above and below which frequency dependence is different.
11. On the basis of theoretical argument, a cross-over-frequency was predicted which was also substantiated experimentally.

LIST OF PUBLICATIONS

1. Title : **EFFECT OF LIQUID PHASE SINTERING OF YBCO**
Author(s) : **Subir Saha, R.B. Tripathy and B. K. Das.**
Journal : **Solid State Phenomenon, Vol. 25 & 26, pp. 387-392 (1992)**

2. Title : **PROPERTIES OF CO-SINTERED SILVER CONTACTS TO PURE AND SILVER DOPED BULK YBCO SUPERCONDUCTORS.**
Author(s) : **Subir Saha, R.B. Tripathy and B.K. Das**
Journal : **Superconductor Science and Technology, Vol. 5, pp703-706 (1992)**

3. Title : **A REALISTIC TWO COMPONENT CRITICAL STATE MODEL - SUCCESSFUL DERIVATION OF LOW FIELD M-H LOOPS OF GRANULAR SUPERCONDUCTORS.**
Author(s) : **Subir Saha and B. K. Das**
Journal : **Superconductor Science and Technology Vol. 6, pp 685-690 (1993)**

4. Title : **AC MAGNETIC SUSCEPTIBILITY OF HTSC AND ITS HYSTERESIS**
Author(s) : **Subir Saha and B. K. Das**
Journal : **Superconductor Science and Technology (To be published shortly)**